

BATTERY MANAGEMENT SYSTEMS

VOLUME I

Battery Modeling

Gregory L. Plett

Battery Management Systems

Volume I

Battery Modeling

For a listing of recent titles in the
Artech House Power Engineering and Power Electronics,
turn to the back of this book.

Battery Management Systems

Volume I

Battery Modeling

Gregory L. Plett



**ARTECH
HOUSE**

BOSTON | LONDON
artechhouse.com

Library of Congress Cataloging-in-Publication Data

A catalog record for this book is available from the U.S. Library of Congress.

British Library Cataloguing in Publication Data

A catalog record for this book is available from the British Library.

ISBN-13: 978-1-63081-023-8

Cover design by John Gomes

© 2015 Artech House

685 Canton Street

Norwood, MA 02062

All rights reserved. Printed and bound in the United States of America. No part of this book may be reproduced or utilized in any form or by any means, electronic or mechanical, including photocopying, recording, or by any information storage and retrieval system, without permission in writing from the publisher.

All terms mentioned in this book that are known to be trademarks or service marks have been appropriately capitalized. Artech House cannot attest to the accuracy of this information. Use of a term in this book should not be regarded as affecting the validity of any trademark or service mark.

10 9 8 7 6 5 4 3 2 1

Contents

Preface ix

1	<i>Battery Boot Camp</i>	1
1.1	<i>Preliminaries</i>	2
1.2	<i>How cells work</i>	4
1.3	<i>Materials choice</i>	8
1.4	<i>Insertion electrode cells</i>	11
1.5	<i>Lithium-ion cell preview</i>	12
1.6	<i>Manufacturing</i>	20
1.7	<i>Failure modes</i>	24
1.8	<i>Where to from here?</i>	28
2	<i>Equivalent-Circuit Models</i>	29
2.1	<i>Open-circuit voltage (OCV)</i>	30
2.2	<i>State-of-charge dependence</i>	30
2.3	<i>Equivalent series resistance</i>	33
2.4	<i>Diffusion voltages</i>	34
2.5	<i>Rough parameter values</i>	38
2.6	<i>Warburg impedance</i>	40
2.7	<i>Hysteresis voltages</i>	41
2.8	<i>Enhanced self-correcting cell model</i>	44
2.9	<i>Laboratory equipment for cell-data collection</i>	44
2.10	<i>Lab tests to determine OCV relationship</i>	45
2.11	<i>Lab tests to determine dynamic relationship</i>	53
2.12	<i>Example results</i>	57
2.13	<i>Where to from here?</i>	59
2.14	<i>Chapter appendix: MATLAB ESC model toolbox</i>	59
3	<i>Microscale Cell Models</i>	65
3.1	<i>Chapter goal: Derive microscale model equations</i>	67

3.2	<i>Charge conservation in the solid</i>	68
3.3	<i>Mass conservation in the solid</i>	75
3.4	<i>Thermodynamics</i>	80
3.5	<i>Physical chemistry</i>	86
3.6	<i>Basic characteristics of binary electrolytes</i>	91
3.7	<i>Concentrated solution theory: Electrolyte mass conservation</i>	94
3.8	<i>Concentrated solution theory: Electrolyte charge conservation</i>	106
3.9	<i>Butler–Volmer equation</i>	110
3.10	<i>Implementing the model</i>	119
3.11	<i>Cell-level quantities</i>	122
3.12	<i>Where to from here?</i>	130
3.13	<i>Chapter appendix: OCP sources</i>	130
3.14	<i>Partial glossary</i>	132
4	<i>Continuum-Scale Cell Models</i>	135
4.1	<i>Chapter goal: The continuum-scale cell model</i>	136
4.2	<i>Preliminaries</i>	137
4.3	<i>Volume-averaging theorem 1</i>	146
4.4	<i>Volume-averaging theorem 2</i>	148
4.5	<i>Volume-averaging theorem 3</i>	149
4.6	<i>Charge conservation in the solid</i>	152
4.7	<i>Mass conservation in the solid</i>	156
4.8	<i>Mass conservation in the electrolyte</i>	157
4.9	<i>Charge conservation in the electrolyte</i>	160
4.10	<i>Lithium movement between the solid and electrolyte phases</i>	161
4.11	<i>Boundary conditions for pseudo 2D model</i>	161
4.12	<i>Cell-level quantities</i>	163
4.13	<i>Model simulations</i>	164
4.14	<i>Running COMSOL</i>	169
4.15	<i>Where to from here?</i>	169
4.16	<i>Partial glossary</i>	170
5	<i>State-Space Models and the Discrete-Time Realization Algorithm</i>	173
5.1	<i>A quick introduction to state-space models</i>	174
5.2	<i>Equations describing the solid dynamics</i>	182
5.3	<i>State-space realization</i>	186
5.4	<i>Discrete-time realization algorithm (DRA)</i>	195
5.5	<i>Step-by-step examples of the DRA</i>	198
5.6	<i>Eigensystem realization algorithm (ERA)</i>	208
5.7	<i>Where to from here?</i>	212

5.8	<i>Partial glossary</i>	213
6	<i>Reduced-Order Models</i>	217
6.1	<i>A one-dimensional model of $j^{neg}(z, t)$</i>	217
6.2	<i>A one-dimensional model of $\tilde{c}_{s,e}^{neg}(z, t)$</i>	225
6.3	<i>A one-dimensional model of $\tilde{\phi}_s^{neg}(z, t)$</i>	226
6.4	<i>Positive-electrode variables $j^{pos}(z, t)$, $\tilde{c}_{s,e}^{pos}(z, t)$ and $\tilde{\phi}_s^{pos}(z, t)$</i>	227
6.5	<i>A one-dimensional model of $c_e(x, t)$</i>	229
6.6	<i>A one-dimensional model of $\tilde{\phi}_e(x, t)$</i>	241
6.7	<i>Summary of transfer functions</i>	244
6.8	<i>Computing cell voltage</i>	246
6.9	<i>Frequency response and cell impedance</i>	248
6.10	<i>Multiooutput DRA</i>	249
6.11	<i>Full cell model</i>	252
6.12	<i>Simulation example</i>	253
6.13	<i>Model blending</i>	256
6.14	<i>Where to from here?</i>	266
6.15	<i>Modal-solution code</i>	266
6.16	<i>Partial glossary</i>	269
7	<i>Thermal Modeling</i>	271
7.1	<i>Preliminary definitions</i>	272
7.2	<i>Microscale thermal model</i>	273
7.3	<i>Continuum thermal model</i>	277
7.4	<i>Parameter temperature variation</i>	280
7.5	<i>Reduced-order model</i>	281
7.6	<i>Gradient transfer functions</i>	281
7.7	<i>Heat-generation terms</i>	285
7.8	<i>Heat-flux terms</i>	292
7.9	<i>Uncoupled model results</i>	296
7.10	<i>Coupled model results</i>	297
7.11	<i>Where to from here?</i>	298
7.12	<i>Partial glossary</i>	300
A	<i>Supercapacitors</i>	303
A.1	<i>The same but different</i>	303
A.2	<i>Charge storage</i>	304
A.3	<i>Continuum model</i>	305
A.4	<i>A one-dimensional model of $\tilde{\phi}_{s-e}^{neg}(z, t)$</i>	307
A.5	<i>A one-dimensional model of $\tilde{\phi}_s^{neg}(z, t)$</i>	310

<i>A.6 A one-dimensional model of $\tilde{\phi}_e^{neg}(z, t)$</i>	311
<i>A.7 Positive-electrode variables $\tilde{\phi}_{s-e}^{pos}(z, t)$, $\tilde{\phi}_s^{pos}(z, t)$ and $\tilde{\phi}_e^{pos}(z, t)$</i>	312
<i>A.8 Supercapacitor voltage</i>	313
<i>A.9 Implementing the full-order model</i>	314
<i>A.10 Implementing the reduced-order model</i>	315
<i>A.11 Simulation results</i>	316
<i>A.12 Identifying parameters</i>	317
<i>A.13 Partial glossary</i>	322
<i>About the Author</i>	323
<i>Index</i>	325

Preface

This book constitutes the first volume in what is planned to be a three-volume series describing battery management systems. The intent of the series is not to be encyclopedic; rather, it is to put forward only the current best practices, with sufficient fundamental background to understand them thoroughly.¹

This first volume focuses on deriving mathematical sets of equations or *models* that describe how battery cells work, inside and out. The second volume applies equivalent-circuit style models to solve problems in battery management and control. The third volume shows how physics-based models can also be used to solve problems in battery management and control, leading to better results.

This particular volume is organized in the following way:

- Chapter 1 introduces the fundamental definitions pertaining to battery systems and gives an overview of how they work.
- Chapter 2 derives empirical models based on using linear circuits as an analog to input–output battery-cell behaviors.
- Chapter 3 presents the fundamental physics needed to understand physics-based internal battery-cell behaviors and derives microscale models.
- Chapter 4 introduces volume averaging as a means to convert microscale models to continuum-scale models, leading to the well-known pseudo-two-dimensional porous-electrode model.
- Chapter 5 reviews state-space models as the ultimate form of our development and develops the “discrete-time realization algorithm” (DRA) as a method for creating a state-space model.
- Chapter 6 derives cell-level discrete-time physics-based state-space models of similar computational complexity to the circuit models in Chapter 2, but able to predict internal cell behaviors in addition to input–output behaviors.
- Chapter 7 shows how a coupled electrochemical–thermal model can be derived—introducing concepts in heat generation and heat flux—leading to a physics-based reduced-order model of thermal effects.

¹ Certainly, what is meant by “best practices” is at least somewhat subjective, and I may well have overlooked approaches and methodologies that are better in some applications than those described herein. Perhaps I should say “best” from my own point of view, given what I happen to have tried, in application domains and problems I have attempted to address.

- Appendix A is a bonus chapter that applies the techniques from Chapters 3 through 7 to create a discrete-time physics-based state-space model of a supercapacitor.

The intended audience for this material is someone with an undergraduate degree in engineering—principally electrical or mechanical. Readers having a different background may find some of the material too basic (because they have studied it before, whereas engineering students have not) or not descriptive enough (because they are missing some background that would typically be encountered in an engineering degree program). Both problems have a remedy, although the solution to the second involves background research to become proficient in an unfamiliar discipline—not an easy undertaking.

The mathematical intensity—particularly for the topics presented in Chapters 3 through 7—can be intimidating even to someone having the intended background. However, I have found that the student who is willing to take the time to work the equations by hand, side by side with the derivations in the book, is able to validate every step and thus conquer the material. For the reader who is interested primarily in a higher-level understanding, the main derivation results to be proven are shared at the beginnings of the most mathematical chapters (i.e., Chapters 3, 4, and 7). The derivations themselves are necessary to understand the genesis of these results, but not to be able to implement the final equations in a simulation or some other application, and so may be skimmed on a preliminary reading.

The content in this book has been taught multiple times to students of diverse backgrounds in *ECE5710: Battery Modeling, Simulation, and Identification* at the University of Colorado Colorado Springs. Lecture videos are available at <http://mocha-java.uccs.edu/ECE5710/index.html>. As the lecture videos sometimes explain the concepts of this book in a somewhat different way, the additional perspective may be an advantage to the learner.

I am greatly indebted to a number of my students and colleagues who have assisted me over the years in understanding and developing the theory and methods presented in this work. Dr. Kan-Hao Xue prepared the first draft of the derivations in Chapter 3. Drs. Amit Gupta and Xiangchun Zhang explained to me the concepts of volume-averaging that are presented in Chapter 4. Dr. Mark Verbrugge introduced me to the pioneering work of Dr. Kandler Smith, which is the foundation of the work presented in Chapters 5 through 7 (and Dr. Smith himself was kind enough to answer questions I had on his work). Dr. Jim Lee developed the DRA presented in Chapter 5 and was the first to implement cell-scale optimum reduced-order models using the DRA, as presented in Chapter 6. Mr. Matt Aldrich developed the reduced-order thermal models in

Chapter 7. Finally, Dr. Al Mundy was the first to implement reduced-order supercapacitor models using the DRA techniques presented in Appendix A. My colleague and friend Dr. M. Scott Trimboli has also been a great encourager of this work and a true pleasure to work with.

Despite my best intentions, there are certain to be errors and confusing statements in this book. Please feel free to send me corrections and suggestions for improvements.

1

Battery Boot Camp

This book is all about developing a mathematical understanding of how electrochemical—and especially lithium-ion—battery cells work. This kind of knowledge is helpful when designing cells, when selecting cells to be used in an application, and for knowing how to use cells properly in an application. For some of these tasks, a high-level qualitative understanding is sufficient; however, for others, detailed quantitative insight into cell operation is critical. Here, we’re interested in both levels, with the ultimate goal of being able to predict both internal and external cell operational variables to a degree that enables optimized battery-pack controls.

This book has mission-critical single-cell or large battery-pack applications in mind, as these applications justify both the complexity of the models to be developed and an investment in advanced control methods that use the models, since such methods can prolong battery-pack life and improve total system performance. Example applications include battery systems for hybrid and electric vehicles or for utility-scale grid storage, backup, and frequency regulation. However, much of the material that is covered also applies to smaller battery packs, such as for personal electronics, and much of the material can also be applied to chemistries different from lithium-ion.

The three main foci of the book are:

1. *Modeling*: Deriving mathematical expressions that describe how battery cells work, both internally and externally. After several stages of development, the final models will comprise coupled sets of discrete-time ordinary difference equations (ODEs) that are functions of unknown but measurable or identifiable *parameter* values. The input to the models will be the cell current; the output will include cell voltage and possibly cell internal electrochemical states as well.
2. *Simulation*: Using computer tools to predict how a battery cell will respond to an input stimulus. The equations of the battery model are used to predict cell voltage and possibly internal

1.1	<i>Preliminaries</i>	2
1.2	<i>How cells work</i>	4
1.3	<i>Materials choice</i>	8
1.4	<i>Insertion electrode cells</i>	11
1.5	<i>Lithium-ion cell preview</i>	12
1.6	<i>Manufacturing</i>	20
1.7	<i>Failure modes</i>	24
1.8	<i>Where to from here?</i>	28

battery-cell states. We will see simulations involving different degrees of fidelity applied to different cell-length scales. We will describe simulations that use the finite-element software platform COMSOL Multiphysics[®], and we will give code to implement cell models in MATLAB[®].¹

3. *Identification*: Determining the values of model parameters, using data obtained via lab tests, to cause the model simulated predictions to match measured performance as closely as possible.

This chapter very quickly covers a lot of background material relating to battery terminology, function, and general application.² Later chapters will systematically develop models of battery-cell dynamics at different length scales for different kinds of application and show how to use these models to simulate performance and how to identify model parameters.

1.1 Preliminaries

Cells are the smallest individual electrochemical unit and deliver a voltage that depends on the combination of chemicals and compounds chosen to make the cell.³ Single-use cells are called *primary cells* and rechargeable cells are called *secondary cells*. *Batteries* or *battery packs* are made up from groups of cells.⁴ The schematic symbols for a cell and a battery are shown in Fig. 1.1.

Technically, a cell is different from a battery, but many people (including me, at times) use the term *battery* to describe any electrochemical energy source, even if it is a single cell, and this can lead to confusion. I will attempt to use the terms *cell* or *battery cell* consistently to refer to an individual electrochemical unit, and reserve the terms *battery* (used by itself) and *battery pack* to refer to an electrically connected group of cells. Note that it is not always obvious whether the correct term should be *cell* or *battery* since batteries are sometimes packaged in a single physical unit. For example, automotive “12 V” lead-acid batteries internally comprise six “2 V” cells wired in series;⁵ also, many high-capacity lithium-ion batteries consist of a number of cells wired in parallel in a single package.

CELL VOLTAGE depends a number of factors, as we will find out. The manufacturer-specified *nominal voltage* is “The value assigned to a cell or battery of a given voltage class for the purpose of convenient designation. The operating voltage of the cell or battery may vary above or below this value.”⁶ Cells with lead-acid (PbA) chemistry have a nominal voltage of 2.1 V; nickel-cadmium (NiCd) cells have a nominal voltage of 1.35 V; and nickel-metal-hydride (NiMH) chemistries

¹ COMSOL Multiphysics is a registered trademark of The COMSOL Group, and MATLAB is a registered trademark of The MathWorks. From now on, these products will be referred to simply as COMSOL and MATLAB, respectively.

² Much of the content of this chapter is adapted from the excellent Web site: <http://www.mpoweruk.com/>.

³ The National Electrical Code, document NFPA-70 defines a cell as “The basic electrochemical unit, characterized by an anode [i.e., negative electrode] and a cathode [i.e., positive electrode], used to receive, store, and deliver electrical energy.”

⁴ IEEE standard 446 defines a battery as “Two or more cells electrically connected for producing electric energy.”

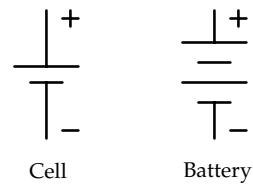


Figure 1.1: Schematic symbols for a cell and a battery.

⁵ Cells deliver a range of voltage depending on conditions such as temperature and how much charge they are holding. Table 1.1 lists the voltage of a single lead-acid cell as 2.1 V, which is more accurate under many conditions than the more commonly cited figure of 2 V, but either figure is roughly correct unless more specific operational factors are specified. One purpose of the models developed in this book is to be able to predict cell voltage under very general operating conditions.

⁶ From the National Electrical Code, document NFPA-70.

have a nominal voltage of 1.2 V (cf. Table 1.1). Most lithium-based cells have nominal voltages over 3 V.

CELLS STORE AND ARE ABLE TO DELIVER electrical charge to power a load circuit. The cell *nominal charge capacity* specifies the quantity of charge, in ampere-hours (Ah) or milliampere-hours (mAh), that a cell is rated to hold.⁷ The cell's nominal energy capacity (see below) is a different quantity. Both definitions of capacity have merit and can be computed from one another. However, as our focus in this book is on creating models that relate a cell's input current (i.e., rate of change of charge) to its internal electrochemical state and output voltage, charge capacity turns out to be the more relevant concept. Unless otherwise mentioned, the term *capacity* will refer to charge capacity and not to energy capacity in this book.

Related to the cell's charge capacity, the *C rate* is a relative measure of cell current. It is the constant-current charge or discharge rate that the cell can sustain for 1 hour—it is simply the nominal ampere hour rating of the cell multiplied by 1 h^{-1} . For example, a fully charged 20-Ah cell should be able to deliver 20 A (a “1C” rate) for 1 h or 2 A (a “C/10” rate) for about 10 h before the cell is completely discharged. If the cell is discharged at a 10C rate, it will be completely discharged in about 6 minutes. Note that the relationship between C rate and discharge time is not strictly linear, primarily because of the internal resistance of the battery cell and incomplete utilization of the active materials when the cell is exercised at high rates. In fact, a cell discharged at a 10C rate will reach a minimum operational voltage before 6 minutes has elapsed, but a cell discharged at a C/10 rate may be operated somewhat more than 10 h before reaching the minimum voltage.

A CELL STORES *energy* in electrochemical form, which it can later release to do work. The cell *nominal energy capacity* is the quantity of electrical energy in watt hours (Wh) or kilowatt hours (kWh) that the cell is rated to hold and is computed as the cell's nominal voltage multiplied by its nominal charge capacity.⁸ For example, a 2 V, 10-Ah lead-acid cell has an energy storage capacity of roughly 20 Wh. It is important to note that energy and power are different quantities for a particular rate of discharge. *Power* is the instantaneous rate at which energy is being released. Power is measured in watts (W) or kilowatts (kW). The maximum power that a cell can deliver is limited by the cell's internal resistance and is not an easy value to quantify. Power is usually regulated by enforcing minimum and maximum limits on cell terminal voltage.

⁷ Note that the SI unit for charge is the coulomb (C) and that $1\text{ Ah} = 3,600\text{ C}$, which is quite a lot of charge! The SI unit is not often used, probably because it is such a small amount of charge relative to the capacity of most cells.

⁸ The SI unit for energy is the joule (J), where $1\text{ J} = 1\text{ W}\cdot\text{s}$. A joule is a pretty tiny unit of energy compared to what a typical battery holds, which is probably why the SI unit is not usually used when working with batteries.

WHEN CELLS ARE CONNECTED IN *series*, the battery voltage is the sum of the individual cell voltages, by Kirchhoff's voltage law. However, by Kirchhoff's current law, the charge capacity of the series-connected battery is the same as the charge capacity of an individual cell since the same current passes through all of the cells. As an example, consider the battery in Fig. 1.2, which is constructed from three 2 V, 20-Ah cells connected in series. The battery voltage will be 6 V, the battery charge capacity will be 20 Ah, and the battery energy capacity will be 120 Wh.

When cells are connected in *parallel*, the battery voltage is equal to the cells' voltage, by Kirchhoff's voltage law. However, by Kirchhoff's current law, the charge capacity is the sum of the cells' charge capacities since the battery current is the sum of all the cell currents. For example, consider the battery in Fig. 1.3, which is constructed from five 2 V, 20-Ah cells connected in parallel. The battery will have a voltage of 2 V, a charge capacity of 100 Ah, and energy capacity of 200 Wh.

Specific energy AND *energy density* are measures of the maximum amount of stored energy per unit weight or volume, respectively. For a given weight, a higher specific energy cell design will store more energy, and for a given storage capacity, a higher specific energy cell will be lighter. For a given volume, a higher energy density cell chemistry will store more energy, and for a given storage capacity, a higher energy density cell will be smaller.

In general, higher energy densities and higher specific energies are obtained by using more reactive chemicals. The downside is that more reactive chemicals tend to be less stable and may require special safety precautions. Further, the quality of the active materials used in cell construction matters, with impurities limiting cell performance that can be achieved and with construction flaws reducing safety. Cells from different manufacturers with similar cell chemistries and similar construction may yield different performance. Cell construction also matters: overhead from packaging decreases the energy densities.

1.2 How cells work

Cells are built from a number of principal components. These include a negative electrode, a positive electrode, the electrolyte, and a separator. Certain types of cells also have current collectors that are distinct from the electrodes themselves. Fig. 1.4 shows a schematic of a lithium-ion cell, but the basic idea applies generally.

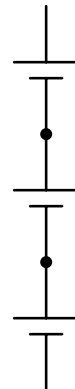


Figure 1.2: Three cells connected in series.

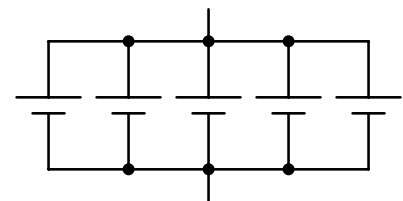


Figure 1.3: Five cells connected in parallel.

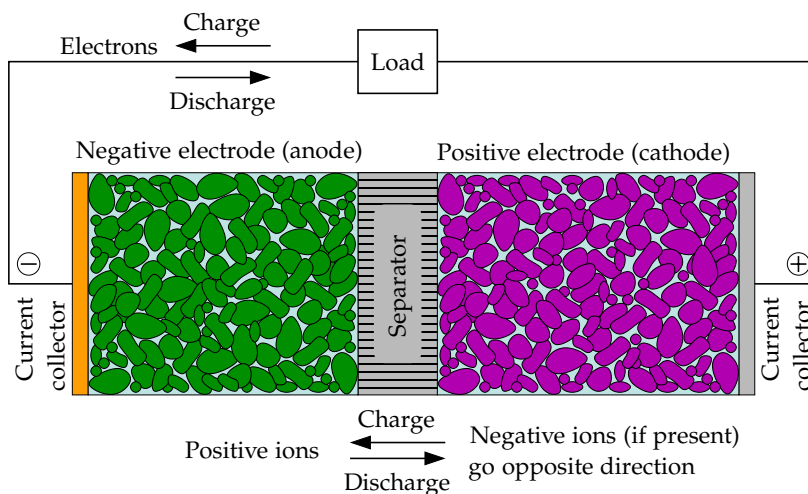


Figure 1.4: Schematic diagram of lithium-ion cell.

(Based on Fig. 1 of Stetzel, K., Aldrich, L., Trimboli, M.S., and Plett, G., "Electrochemical state and internal variables estimation using a reduced-order physics-based model of a lithium-ion cell and an extended Kalman filter," *Journal of Power Sources*, 278, 2015, pp. 490–505.)

THE *negative electrode* in an electrochemical cell is often a pure metal, or an alloy, or even hydrogen. For example, the negative electrode of a lead-acid cell is pure lead.⁹ Table 1.1 lists negative-electrode materials for common types of cells.

Electrochemistry	Negative electrode	Positive electrode	Electrolyte	Nominal voltage
Lead acid	Pb	PbO ₂	H ₂ SO ₄	2.1 V
Dry cell	Zn	MnO ₂	ZnCl ₂	1.6 V
Alkaline	Zn	MnO ₂	KOH	1.5 V
Nickel cadmium	Cd	NiOOH	KOH	1.35 V
Nickel hydrogen	H ₂	NiOOH	KOH	1.5 V
Nickel zinc	Zn	NiOOH	KOH	1.73 V
Silver zinc	Zn	Ag ₂ O	KOH	1.6 V
Zinc air	Zn	O ₂	KOH	1.65 V

During discharge, the negative electrode gives up electrons to the external circuit, a process by which the electrode is *oxidized*: oxidation of a species involves the loss of electrons or, equivalently, an increase in the oxidation state of the species (it becomes more positively charged). During charge, the negative electrode accepts electrons from the external circuit and is *reduced*: reduction of a species involves the gain of electrons or, equivalently, a decrease in its oxidation state (it becomes more negatively charged). Thus, the chemical processes that occur in an electrochemical cell are sometimes called reduction–oxidation or *redox* reactions.¹⁰

The negative electrode is often called the *anode*. Technically, the

⁹ This is realized in a practical lead-acid cell by spreading a lead paste on a lead-alloy grid.

Table 1.1: Components of some common electrochemical cells.

(Adapted from Table 1.2 in Linden, D., *Handbook of Batteries*, Linden, D. and Reddy, T.B. eds., 3d, McGraw-Hill, 2002.) The nominal voltages are representative only. For example, the open-circuit voltage of a lead-acid cell is related to the specific gravity of its electrolyte. Most vented lead-acid cells have a specific gravity of 1.215 and an open-circuit voltage of 2.05 V. Most valve-regulated lead-acid (VRLA) cells have a specific gravity of 1.3 and an open-circuit voltage of 2.15 V.

¹⁰ A mnemonic that may be helpful is "OIL RIG," which stands for "oxidation is loss (of electrons) and reduction is gain (of electrons)." Not a very "green" acronym for a "green" subject!

anode is the electrode where oxidation occurs. So, the negative electrode is really the anode only when the cell is discharging and is actually the cathode when the cell is charging! But this gets pretty confusing, so most people call it the anode regardless of whether the cell is being charged or discharged. To minimize this confusion, this book will avoid the term *anode* and will use the term *negative electrode* instead.

THE *positive electrode* in an electrochemical cell is often a metallic oxide, sulfide, or oxygen. For example, the positive electrode of a lead-acid cell is made from pure lead dioxide, often formed from a lead-oxide paste applied to a lead-alloy grid. Table 1.1 lists positive-electrode materials for common types of cells.

During discharge, the positive electrode accepts electrons from the external circuit, a process by which the electrode is reduced. During charge, the positive electrode gives up electrons to the external circuit and is oxidized.

The positive electrode is often called the *cathode*, but again, there are problems with this description. Technically, the cathode is the electrode where reduction occurs. So, the positive electrode is really the cathode only when the cell is discharging and is actually the anode when the cell is charging! Again, to minimize confusion, this book will avoid the term *cathode* and will use the term *positive electrode* instead.

THE *electrolyte* is an ionic conductor that provides the medium for internal ionic charge transfer between the electrodes.¹¹ The electrolyte most often comprises a liquid *solvent* containing dissolved chemicals (the *solute*) that provide this ionic conductivity (although solid polymer electrolytes are also possible). The chemistries listed in Table 1.1 use *aqueous* electrolytes, where the solvent is water, and the ionic charge transfer is accomplished via either an *acid* (H_2SO_4), a *base* (KOH), or a *salt* (ZnCl_2). Cells using aqueous electrolytes have terminal voltages limited to less than about 2 V because the oxygen and hydrogen in water dissociate in the presence of higher voltages. Lithium-ion cells must use nonaqueous electrolytes as their overall voltages are well above 2 V.

During discharge, positively charged ions or *cations* move through the electrolyte toward the positive electrode, and negatively charged ions or *anions* (if present) move through the electrolyte toward the negative electrode. During charge, the opposite occurs: cations move toward the negative electrode and anions move toward the positive electrode.

¹¹ The electrolyte must be an electronic insulator (it cannot conduct electrons). If it were an electronic conductor, a complete circuit would form internal to the cell, which would cause the cell to *self-discharge* or *short-circuit*.

THE *separator* physically isolates the positive and negative electrodes. It is an ionic conductor but an electronic insulator. Its function is to prevent internal short circuiting between the two electrodes, which would cause the cell to rapidly self-discharge and become useless.

Current collectors, if present, are electronic conductors onto which the electrode materials are adhered or with which the electrode materials are mixed. The current collectors take no part in the chemical reactions of the cell, but instead either allow simple electronic connection to materials that may otherwise be very difficult to connect to a cell terminal, or are included to reduce the electronic resistance of an electrode. In a lithium-ion cell, for example, the negative-electrode current collector is usually made from copper foil, and the positive-electrode current collector is usually made from aluminum foil. The current collector in the positive electrode of a dry cell is carbon.¹²

The observant reader will note the conspicuous absence of two very important chemistries in Table 1.1—nickel-metal hydride and lithium-ion cells. The principle of operation of these two advanced types of cell is somewhat different from the chemical processes that we are describing in this section, and so detailed discussion is reserved until Sections 1.4 and 1.5. For now, it is sufficient to note that these cells also have negative electrodes, positive electrodes, electrolyte, and a separator.

1.2.1 The discharge process

Electrochemical potential energy at the negative electrode favors a chemical process that would release electrons into the external circuit and positively charged ions into the electrolyte. Also, electrochemical potential energy at the positive electrode favors a chemical process that would accept electrons from the external circuit and positively charged ions from the electrolyte. The resulting electrical pressure or potential difference between the terminals of the cell is called the *cell voltage* or *electromotive force* (EMF).

This stored potential energy can be released and converted to useful work only when pathways are available for electrons and positively charged ions to travel from the negative electrode to the positive electrode. The electrolyte provides an always-available medium for positive-ion movement, but the separator prevents electron movement within the cell (hence preventing an internal short circuit). In order for electrons to move, an external electrical circuit must be completed, connecting the negative and positive electrodes electronically. When a circuit is completed, the cell *discharges* its energy through the

¹² Dry cells are sometimes called *zinc carbon* cells, and the positive electrode is sometimes identified as carbon. But, this is not actually true, as carbon takes no part in the chemical reaction—it serves only to collect current and reduce resistance of the manganese dioxide mix.

circuit, or *load*, and converts the stored chemical potential energy into electrical energy.

1.2.2 The charge process

In *primary cells*, this electrochemical reaction is not reversible. During discharge, the chemical compounds are permanently changed and electrical energy is released until the original compounds are completely exhausted. Primary cells can be used only once.

In *secondary* or *rechargeable cells*, the electrochemical reaction is reversible. The original chemical compounds can be reconstituted by the application of an electrical potential across the electrodes that is higher than the cell's own electrical potential. This injects energy into the cell, causing electrons and positive ions to move from the positive electrode back to the negative electrode, thus storing charge.

Secondary cells can be discharged and recharged many times. During charge, cations move from the positive to the negative electrode through the electrolyte, and electrons move from the positive to the negative electrode through the external circuit. The energy injected into the cell transforms the active chemicals to their original state.

1.3 Materials choice

The voltage generated across the terminals of a cell is directly related to the types of materials used in the positive and negative electrodes. When designing and analyzing a cell, it is often convenient to consider the electrodes separately. However, it doesn't make sense to talk about the voltage of an electrode by itself. Voltage is a *difference* in potential, and when dealing with a single electrode, what two potentials are being differenced?

There is a similar problem in the field of electrical circuit analysis. The solution in that case is to arbitrarily select a point in the circuit whose potential is defined to be "zero volts" or "ground," against which all other potentials in the circuit are measured. We apply the same basic solution when analyzing an electrochemical electrode. We consider a potential difference between the electrode under study and a hypothetical reference electrode, which may or may not be a part of the actual cell being designed or analyzed. Often, this reference is chosen to be in terms of the *standard hydrogen electrode*, and the potential at which $2\text{H}^+ + 2e^-$ spontaneously converts to $\text{H}_{2(\text{g})}$ is defined to be zero volts.¹³

The electrode potentials of some common electrode half reactions, known as an *electrochemical series*, are shown in Table 1.2. Compounds

¹³ Although, we will see that with lithium-ion cells, the reference is often chosen to be with respect to Li^+/Li , or the potential at which $\text{Li}^+ + e^-$ spontaneously converts to $\text{Li}_{(\text{s})}$.

Figure 1.5: Periodic table of the elements.

with more negative electrode potentials are used for negative electrodes and those with more positive electrode potentials for positive electrodes. The larger the difference between the electrode potentials of the negative and positive electrodes, the greater the cell voltage.

The values for the table entries are reduction potentials. Fluorine, $F_2(g)$, has the most positive number in the table, indicating that it reduces most easily, and therefore is the best oxidizing agent of those listed. Lithium, $Li_{(s)}$, has the most negative number in the table, indicating that it would rather undergo oxidation (and hence is the strongest reducing agent of those listed). If we were to create a cell combining the top and bottom reactions, the cell voltage would be $2.87\text{ V} - (-3.04\text{ V}) = 5.91\text{ V}$ (but so far we cannot, since there is no known electrolyte that will withstand that high a voltage without decomposing).

The electrochemical series is good for quantitative analysis, but an exhaustive table of all possible oxidation/reduction reactions is unwieldy and not necessarily intuitive. For qualitative analysis, we may consider the periodic table of the elements, such as in Fig. 1.5, where the relative reducing and oxidizing capabilities of the elements are indicated by the arrow below the table.

Each box in the periodic table corresponds to a particular element. The number in the top-left of each box is the element's *atomic number* (the number of protons in the nucleus of the atom). The number in the bottom-left of the box is the *atomic weight*, or the ratio of the average mass per atom of the element to 1/12 of the mass of an atom of ^{12}C . The series of numbers to the right of each box is arrangement of electrons in orbitals or shells in a *Bohr* or *classical model* of the atom.¹⁴ Some examples of the electron orbital occupancies are shown in Fig. 1.6.

¹⁴ It is still common to speak of shells despite the advances in understanding of the quantum-mechanical nature of electrons. For the purpose of this book, an understanding of the Bohr model is sufficient.

Cathode (reduction) half-reaction	Standard potential E^0 (volts)
$Li^+ + e^- \Rightarrow Li_{(s)}$	-3.01
$K^+ + e^- \Rightarrow K_{(s)}$	-2.92
$Ca^{2+} + 2e^- \Rightarrow Ca_{(s)}$	-2.84
$Na^+ + e^- \Rightarrow Na_{(s)}$	-2.71
$Zn^{2+} + 2e^- \Rightarrow Zn_{(s)}$	-0.76
$2H^+ + 2e^- \Rightarrow H_2(g)$	0.00
$Cu^{2+} + 2e^- \Rightarrow Cu_{(s)}$	0.34
$O_3(g) + 2H^+ + 2e^- \Rightarrow O_2(g) + H_2O_{(l)}$	2.07
$F_2(g) + 2e^- \Rightarrow 2F^-$	2.87

Table 1.2: Standard potentials of electrode reactions at 25 °C.
(Condensed from Table 2.2 in Broadhead, J. and Kuo, H.C., *Handbook of Batteries*, D. Linden and T.B. Reddy, eds., 3d, McGraw-Hill, 2002.)

The elements in the table are color-coded to highlight elements that behave in similar ways to each other. For example, we see that the strong reducing elements are grouped to the left, while the strong oxidizing elements are grouped to the right. Elements within each individual *group* (generally) have the same number of *valence electrons*, or number of electrons in their outer *valence shell* (but, transition metals are a little strange). Because the number of valence electrons determines how the atom reacts chemically with other atoms, elements within a particular group tend to have similar chemical properties. All the elements in any one *period* have the same number of electron shells or orbits, which corresponds to the number of possible energy levels of the electrons in the atom. The period number corresponds to the number of electron shells.

Atoms with one or two valence electrons more than a closed shell are highly reactive because the extra electrons are easily removed to form positive ions. Reducing agents have a surplus of valence-shell electrons, which they donate in a redox reaction, becoming oxidized. *Alkaline metals*, group 1, have only one valence electron, and *alkaline earth metals*, group 2, have only two valence electrons, so elements in these groups are highly reactive.

Atoms with one or two valence electrons fewer than a closed shell are also highly reactive because of a tendency either to gain the missing electrons and form negative ions, or to share electrons and form covalent bonds. Oxidizing agents have a deficit of valence-shell electrons and accept electrons in a redox reaction, becoming reduced. *Halogens*, group 17, are short only one valence electron, and so are highly reactive.

When the outer electron shell is full, as in the *noble gases* in group 18, there are no “free” electrons available to take part in chemical reactions. This is the lowest energy state for a species, and hence these atoms tend to be chemically nonreactive or *inert*.

1.4 Insertion electrode cells

Relatively recently, new cell chemistries have been developed using alternative chemical reactions to the traditional redox scheme. *Metal hydride* cells, such as nickel-metal hydride, depend on the ability of some metals to absorb large quantities of hydrogen without chemically changing the composition of the metal itself (much like a sponge absorbs water without undergoing a chemical change). These metallic alloys, termed *hydrides*, can provide a storage sink for hydrogen, which can reversibly react in battery-cell chemistry. Such metals or alloys are used for the negative electrodes. The positive electrode is nickel hydroxide (NiOOH) as in NiCd batteries. The electrolyte,

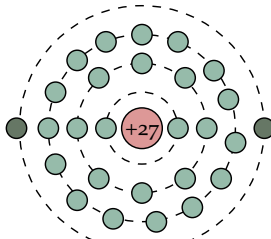
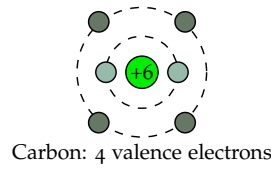
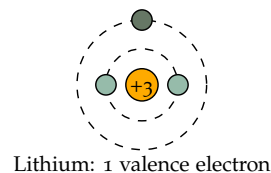


Figure 1.6: Schematic of some elements, showing electron configurations in different shells, and highlighting the number of valence electrons.

which is also a hydrogen-absorbent aqueous solution such as potassium hydroxide (KOH), takes no part in the reaction but serves to transport hydrogen H^+ ions (protons) between the electrodes. As we will see in the next section, lithium-ion cells work in a similar way.

1.5 *Lithium-ion cell preview*

This book focuses on lithium-ion cells (although much that we cover is quite general and could be applied to other chemistries). Lithium-ion cells have several advantages over other chemistries:

- They operate at higher voltages than other rechargeable cells, typically about 3.7 V for lithium-ion versus 1.2 V for NiMH or NiCd. Because of this, they tend to have higher energy density also.
- The higher voltage means that a single cell can often be used in a particular application rather than multiple NiMH or NiCd cells in series. While NiCd and NiMH do not require battery management circuitry for safe operation, all battery packs can potentially benefit from battery management: the battery management circuitry for lithium-ion can be simplified by this reduced cell count.
- Lithium-ion cells also have a lower self-discharge rate than other types of rechargeable cells. NiMH and NiCd cells can lose anywhere from 1–5 % of their charge per day, even if they are not installed in a device. Lithium-ion cells, on the other hand, will retain most of their charge even after months of storage.

Lithium-ion cells are at a disadvantage to other chemistries in other respects:

- Lithium-ion cells are more expensive than similar capacity NiMH or NiCd cells. This is in part because they are presently manufactured in much smaller numbers than NiMH or NiCd. As volumes increase, prices are expected to come down.
- Lithium-ion cells are very sensitive to overcharge and often include special circuitry that prevents damage by disconnecting the cell from the circuit if an attempt is made to operate the cell outside of its design voltage range. This adds to the cost and complexity of manufacture, and to the complexity of battery chargers. The cost of the protection circuitry may not scale as favorably with volume as the cost of the manufacturing process itself, and as it is possible for the circuitry itself to fail, the reliability of the overall battery system can be degraded.
- Lithium-ion cells are not available in standard cell sizes (AA, C, and D) like NiMH and NiCd cells.¹⁵ And, different lithium-ion

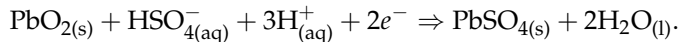
¹⁵ Note that the Energizer® “e² Lithium” is not a lithium-ion cell. It is a standard nonrechargeable 1.5 V galvanic cell with lithium/iron-disulfide (Li/FeS_2) chemistry.

cells in the reasonably common “18650” or “26650” form factors may internally comprise different types of lithium-ion electrochemistry that are not compatible with each other. So, because of their different shapes and sizes and internal chemistries, each type of lithium-ion cell tends to require a specific matching charger designed to accommodate it. This means that lithium-ion battery chargers are more expensive and more difficult to find than NiMH and NiCd battery chargers.¹⁶

Lithium-ion cells work differently from the electrochemical cells that we looked at earlier in this chapter. Traditional electrochemical cells depend on redox reactions that chemically change the reacting species at the electrode surfaces. Consider, for example, a lead-acid cell. On discharge, lead (Pb) from the negative electrode reacts with HSO_4^- in the electrolyte, producing hydrogen ions (protons), emitting two electrons to the external circuit, and forming solid lead sulfate (PbSO_4) crystals on the surface of the negative electrode. We can write,



In the positive electrode, lead oxide (PbO_2) and HSO_4^- from the electrolyte react with hydrogen ions, consuming electrons and forming solid lead sulfate crystals on the surface of the positive electrode. We can write,



Lithium-ion cells work differently. Like NiMH cells, they are insertion-electrode cells. Lithium does not react with the electrode materials, *per se*. Instead, lithium is either absorbed from the electrolyte and inserted into the structure of the electrode material (a process called *intercalation*), or is expelled from the electrode material into the electrolyte (*deintercalation*), depending on the direction of current flow.

For this to work, the electrodes must have two key properties. First, they must have open-crystal structures, pervaded with empty pathways or “corridors” that are large enough for lithium to move through freely. Thus, lithium can be inserted into the vacancies in the structure from the electrolyte, can be removed from the vacancies in the structure, and is free to move among the vacant spaces within the crystalline structure. Second, the electrodes must also be able to deliver or accept compensating electrons to/from the external circuit at the same time.

The crystal structure itself is not changed chemically by the insertion or removal of lithium. However, structural changes of the crystal lattice can occur. For example, small volume changes, generally on

¹⁶ In some applications, such as stationary battery systems for the telecom industry, standard chargers are specified, which largely mitigates this disadvantage.

the order of about 10% or less, are observed as lithium is added or removed. The presence of lithium can also cause nonuniform distortions to the shape of the crystalline structure, and these *phase transitions* can sometimes result in permanent damage to the material. To compensate, the cell is designed to be operated in regimes where these distortions are minimized.

WE BEGIN DESCRIBING lithium-ion cell operation using the simplified schematic of Fig. 1.7. (We will refine this understanding as the chapter proceeds.) In the figure, the negative and positive electrodes are drawn as crystal structures comprising layers of electrode material. Lithium, drawn as small spheres, can be added to or removed from the spaces between the layers.

Within the electrodes, lithium is stored as independent charge-neutral atoms. Each lithium atom's valence electron is very loosely shared with neighboring atoms in the crystal structure. As such, the lithium is not tightly bonded in one place and is actually quite free to move around. Lithium enters and exits the surface of the electrode, but diffuses within the layered open crystal structure to equalize the concentration of lithium within the vacant spaces of the electrode.

During discharge, lithium atoms at the surface of the negative electrode give up electrons—which travel through the external circuit—and become positive lithium ions, Li^+ —which exit the crystal structure of the electrode and dissolve into the electrolyte. We can write, $\text{Li} \Rightarrow \text{Li}^+ + e^-$. Conversely, lithium ions proximate to the surface of the positive electrode receive electrons from the external circuit, and the resulting charge-neutral lithium atoms enter the crystal structure of the electrode. We can write, $\text{Li}^+ + e^- \Rightarrow \text{Li}$.

The process is completely reversible. Thus the lithium ions pass back and forth between the electrodes during charging and discharging. This has given rise to the terms *rocking chair*, *swing*, or *shuttlecock* cells to describe lithium-ion cells. The intercalation mechanism is much gentler than an electrochemical reaction, so lithium-ion cells have much longer lives than other secondary cells.

UNTIL NOW, we have treated lithium-ion cell electrodes as homogeneous crystalline blocks. However, this is not actually the case. Instead, the electrodes are manufactured from millions of small electrode particles. This is done to increase the surface area of the electrodes, allowing easier lithium entrance/egress, decreasing overall cell resistance, and enhancing power delivery capability. For example, Fig. 1.8 shows a scanning electron microscope (SEM) image of a lithium-ion cell's negative electrode comprising graphite particles. The two images are of the same material at different magnifications.

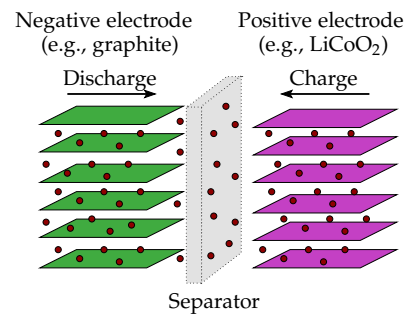


Figure 1.7: Simplified schematic of lithium-ion cell operation.

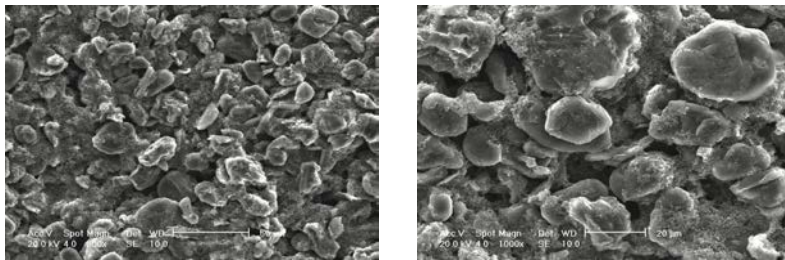


Figure 1.8: Scanning electron microscope (SEM) images of MTI-brand mesophase carbonaceous spheres (graphite).

(Images courtesy Sangwoo Han.)

Fig. 1.9 shows an SEM image of a positive electrode comprising lithium-manganese-oxide particles. The two images are of the same material at different magnifications. We see that the particles have distinctly different shape and size from the graphite particles.

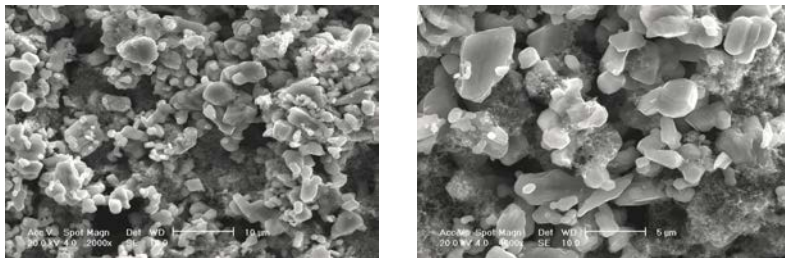


Figure 1.9: SEM images of Aldrich-brand lithium manganese oxide (LMO).

(Images courtesy Sangwoo Han.)

Fig. 1.10 shows cross-sections of an electrode. On the left, the electrode has been sliced by a razor blade; on the right, a focused ion beam (FIB) was used to mill a more precise cross-section, cutting through particles in the process. We see that the electrode structure is quite porous—electrolyte fills the pores between particles.

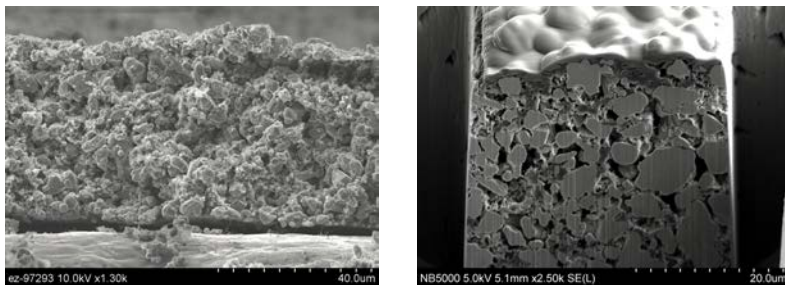


Figure 1.10: Focused ion beam (FIB) image of profile of LMO electrode (left) and FIB milled slice of LMO (right).

(Images courtesy Sangwoo Han.)

Mixed in with the primary electrode materials are binders, such as polyvinylidene fluoride (PVdF), to adhere the particles together, and conductive additives, such as carbon black, to enhance electron conduction, which is otherwise poor, especially in positive electrode materials. These additives are not “active” portions of the cell chemistry, and so are not always mentioned when discussing the composition of lithium-ion cells, but they are always present.¹⁷

¹⁷ The images shown above are of an electrode with a 90:5:5 ratio of active material to carbon black to PVdF.

1.5.1 Negative electrodes

We now begin to describe the materials that are commonly used as electrodes for lithium-ion cells. Presently, the vast majority of commercial lithium-ion cells use some form of graphite (C_6) for the negative-electrode material. Graphite comprises multiple graphene layers, in which hexagonal C_6 structures are tightly bonded together. The graphene layers are stacked loosely on top of each other, held together only by weak van der Waals forces; lithium intercalates between these layers. This is shown in Fig. 1.11, where carbon atoms are drawn as gray spheres joined by covalent bonds to neighboring carbon atoms in the graphene layers, and the lithium atoms are drawn as purple spheres. There is sufficient room between the graphene layers for the lithium atoms to be able to move freely.

Several different forms of graphite are used in lithium-ion cells. Two examples are illustrated in Fig. 1.12, where the lines depict graphene segments, and lithium is able to reside in the voids between graphene layers. The difference is in the degree of uniformity of the graphene layers within the microstructures of the particles. Natural and synthetic graphite tends to be the most uniform; natural “hard” or disordered carbons are less uniform, having many small pockets of graphene layers, arranged in random configurations. The different types of graphite have different voltage properties, capacities, and aging characteristics, but operate in essentially the same fashion.

The maximum amount of lithium that can be stored in graphite is one atom of lithium per six atoms of carbon; the minimum amount is zero. Therefore, when talking about the degree of lithiation of a graphite electrode, we use notation Li_xC_6 , where $0 \leq x \leq 1$. Clearly, when viewed at the atomistic level, there is either a single lithium atom or no lithium atom at all for any given C_6 site. But, when the entire electrode is considered, some fraction of the total number of C_6 sites is occupied, and that fraction is the value of x . When the cell is charged, the negative electrode is highly lithiated, and x is close to 1. When the cell is discharged, the negative electrode is largely depleted of lithium, and x is close to zero.

Alternative materials are being investigated for use as negative electrodes. Lithium titanate ($Li_4Ti_5O_{12}$, also known as *lithium titanate oxide* or *LTO*) allows much faster charging—without harmful side reactions—than graphite. The suppression of side reactions also yields cell lifetimes of many tens of thousands of charge/discharge cycles. However, the use of LTO also results in a cell voltages being reduced by about 1.4 V with respect to an equivalent cell having a graphite negative electrode and thus yields lower energy density. Silicon structures are also being researched, with the potential of

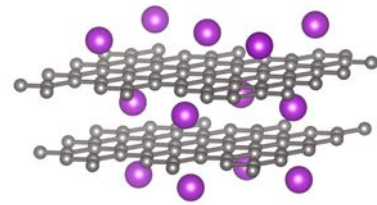


Figure 1.11: Atomic structure of lithiated graphite.

(Drawn with VESTA. See, Momma, K. and Izumi, F., “VESTA 3 for three-dimensional visualization of crystal, volumetric and morphology data,” *Journal of Applied Crystallography*, 44, 1272–1276 (2011).)

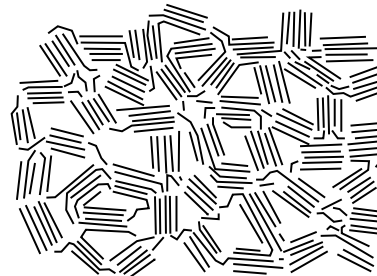
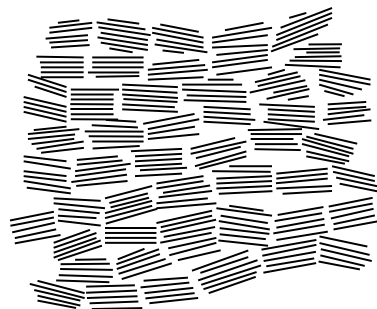


Figure 1.12: Microstructure of natural graphite (top) and hard carbon (bottom).

(Adapted from Fig. 4 in Wakihara, M. “Recent developments in lithium ion batteries,” *Materials Science and Engineering R33*, 2001, 109–134, with permission from Elsevier.)

much higher energy densities than graphite since up to four atoms of lithium can be stored per atom of silicon. However, this causes very large changes in the volume of the silicon structures when lithium intercalates, leading to rapid structural breakdown and poor cell lifetimes. At this point it remains to be seen what technology will replace graphite negative electrodes in the future.

1.5.2 Positive electrodes

There is much more variability in the choice of materials to be used in positive electrodes for lithium-ion cells. In 1980, John B. Goodenough discovered that lithium cobalt oxide (Li_xCoO_2 , also known as LCO) was a viable intercalation compound. Fig. 1.13 shows the crystal structure of LCO. The blue spheres represent cobalt atoms, the red spheres represent oxygen atoms, and the purple spheres represent lithium atoms. The amount of lithium in the structure is variable, but the cobalt-oxygen structures are fixed, and these are drawn as linked blue polyhedra (specifically, octahedra) to highlight the fact that the layers of cobalt oxide do not change—only the degree of lithiation of the structure can change. It is because of these layers, which behave somewhat like graphene in graphite, that this material is often called a *layered cathode*. A difference is that the lithium atoms in LCO act like pillars in the structure, keeping the cobalt-oxide layers apart. If too much lithium is removed, then the crystal structure collapses, and lithium can no longer enter between the layers. To avoid this collapse, only about half the theoretic capacity is usable (“ x ” in Li_xCoO_2 is permitted to use only about half of its theoretic range of 0 to 1).

LCO is commonly used in lithium-ion cells for portable electronics but suffers some problems when trying to scale up to larger cells for grid storage and vehicular applications. The principal problem is that cobalt is rare, toxic, and expensive. Nickel can be substituted for the cobalt sites, resulting in higher energy density (higher voltages at same capacity), but the resulting cell is not very stable thermally (it tends to catch fire). Aluminum, chromium, and manganese can be substituted as well, resulting in somewhat different properties. Often, a combination of transition metals is used. For example, a lithium nickel manganese cobalt oxide (NMC) electrode comprises a blend of nickel, manganese, and cobalt, which retains the layered structure, and has properties from all three constituent metals. A lithium nickel cobalt aluminum oxide (NCA) electrode blends nickel, cobalt, and aluminum.

In 1983, Goodenough and Thackery proposed lithium manganese oxide ($\text{Li}_x\text{Mn}_2\text{O}_4$, or LMO) as an alternate intercalation compound. This structure is drawn in Fig. 1.14. Manganese is drawn as blue

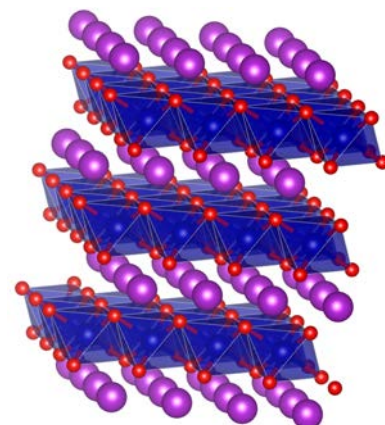


Figure 1.13: Crystal structure of lithium cobalt oxide (LCO).
(Drawn with VESTA. See, Momma, K. and Izumi, F., “VESTA 3 for three-dimensional visualization of crystal, volumetric and morphology data,” *Journal of Applied Crystallography*, 44, 1272–1276 (2011).)

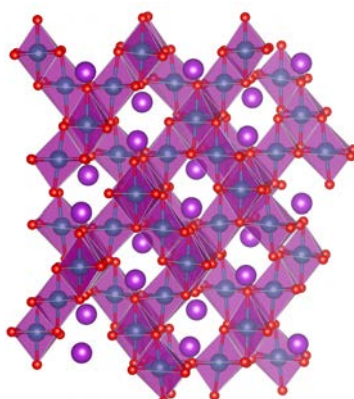


Figure 1.14: Crystal structure of lithium manganese oxide (LMO).
(Drawn with VESTA. See, Momma, K. and Izumi, F., “VESTA 3 for three-dimensional visualization of crystal, volumetric and morphology data,” *Journal of Applied Crystallography*, 44, 1272–1276 (2011).)

spheres, oxygen as red spheres, and lithium as purple spheres. The manganese oxide forms octahedral crystals in a pattern known as a *cubic spinel* structure, which is quite complicated and difficult to view in a two-dimensional projection. An interesting feature of this structure is that there are tunnels through it from each side, allowing lithium movement from front to back, from left to right, and from top to bottom.¹⁸ These degrees of freedom make it easy for lithium to move within the structure, decreasing the resistance of the cell.

The value of “ x ” in $\text{Li}_x\text{Mn}_2\text{O}_4$ typically varies between 0 and 1, but can go as high as 2. Values of x greater than one are usually avoided because the structure of LMO becomes unstable in acidic conditions when highly lithiated—the crystal structure disintegrates as manganese is attacked by the acid and dissolves into the electrolyte. Additives can be introduced to the electrolyte to neutralize acidity to help prevent this, but the “art” of additive design is presently in the realm of black magic and trade secrets. Despite this serious limitation, LMO is common because it is less expensive and safer than LCO and has similar energy-storage densities.

More recently, in 1997, Goodenough proposed *olivine* style phosphates as a third major category of positive-electrode material. Lithium iron phosphate (Li_xFePO_4 , or LFP) is the most common in this family. Its crystal structure is drawn in Fig. 1.15, where iron is represented by brown spheres, phosphorus by gray spheres, oxygen by red spheres, and lithium by purple spheres. Within this overall crystal structure, FeO_6 forms the brown octahedra, and PO_4 forms the gray tetrahedra.

Lithium is free to move only in one-dimensional linear tunnels, which makes this material quite resistive. In order to compensate for this high resistance, the electrode particle size is usually chosen to be very small, minimizing the diffusion length (and hence resistance). LFP is quite popular due to the material’s low-cost, low-toxicity, and very stable voltage profile. However, it also produces a lower cell voltage—by about 0.5 V—than other common positive-electrode materials and hence also a lower energy density. The amount of lithium by mass in LFP is also low, resulting in lower specific energies.

Alternative materials are being investigated for use as positive electrodes. Many of these are doped with vanadium, which tends to yield higher cell voltages. However, at present, the challenge is to develop an electrolyte that will function properly as a lithium ion conductor, but will not break down at the higher voltages.

¹⁸ For this reason, this material is said to have a “three-dimensional” or 3D structure. By referring back to Fig. 1.13, we see that LCO has a two-dimensional structure, and by looking forward to Fig. 1.15, we see that LFP has a one-dimensional structure.

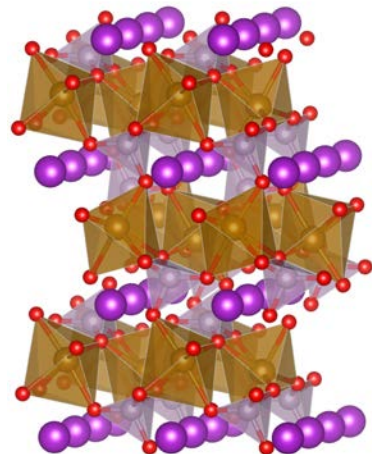


Figure 1.15: Crystal structure of lithium iron phosphate (LFP).
(Drawn with VESTA. See, Momma, K. and Izumi, F., “VESTA 3 for three-dimensional visualization of crystal, volumetric and morphology data,” *Journal of Applied Crystallography*, 44, 1272–1276 (2011).)

1.5.3 Electrolyte: Salt and solvent

The electrolyte is the media that conducts ions between electrodes. It comprises either a salt, an acid, or a base that is dissolved in a solvent. Since lithium reacts violently with water, the electrolyte in a lithium-ion cell is composed of nonaqueous organic solvents plus a lithium salt and acts purely as an ionic conducting medium, not taking part in the chemical reaction. The most commonly used salt is lithium hexafluorophosphate (LiPF_6), which dissociates in the solvent into Li^+ and PF_6^- , but other candidates include LiBF_4 and LiClO_4 .

Common solvents include ethylene carbonate (EC), propylene carbonate (PC), dimethyl carbonate (DMC), ethyl methyl carbonate (EMC), and diethyl carbonate (DEC). The chemical structure of each of these is drawn in Table 1.3. A distinguishing feature of each is the double-bonded oxygen at the top of the molecule, which has a slight negative charge. To compensate, the remainder of the molecule has a slight positive charge. This polarization is what supports ionizing the salt in the solution and conduction of an ionic current.

EC	PC	DMC	EMC	DEC

The solvent does not participate in the chemical processes of the cell, so we typically ignore it in our models (different solvents have different properties with regard to aging, low-temperature performance, and so forth, so the choice is important, but it doesn't factor in directly). So, we often talk about the salt as being the same thing as the electrolyte, even though the electrolyte also includes the solvent.

1.5.4 Separator

The separator in a lithium-ion cell is a permeable membrane with holes large enough to let lithium ions pass through unimpeded, but small enough that the negative- and positive-electrode particles do not make contact through the holes (which would short-circuit the cell). It is also an electronic insulator. An SEM image of a separator is shown in Fig. 1.16. To get a feel for the relative size of the pore

Table 1.3: Formulation of solvents commonly found in lithium-ion cells.

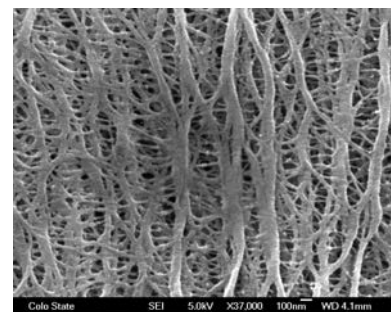


Figure 1.16: SEM image of raw separator material.
(Image courtesy Colorado State University.)

openings in the separator compared to an active-material particle, an atomic force microscopy (AFM) image of a lithium-manganese-oxide particle on top of a typical separator material is shown in Fig. 1.17. The fibrous nature of this particular type of separator is evident, where the pores are smaller than the most obvious depressions between the fibers. The vast scale differences between particle size and pore size of the separator material is also quite apparent. The separator is typically on the order of $20\ \mu\text{m}$ thick; pore size is on the order of $50\ \text{\AA}$; and this particular particle's size is on the order of $5\ \mu\text{m}$ in diameter.

1.6 Manufacturing

Some idea of how lithium-ion cells are manufactured can aid understanding how they work. The basic elements are the same for all kinds of lithium-ion cell, but there are some variations based on form factor:

- *Cylindrical* cells are ... cylindrical, and are encased in metal cans.
- *Prismatic* cells are ... prismatic, and are also encased in metal cans.
- *Pouch* cells are also flat and are encased in soft pouches.

Some examples of each form factor are shown in Fig. 1.18. In each case, the cells all contain one or more negative and positive electrodes (which are electrically connected inside the cell, forming a single logical negative and positive electrode), separator(s), and electrolyte (as previously discussed). Cylindrical cells are historically most common, but prismatic and pouch cells are finding heavy use for high-capacity battery applications to optimize the use of volume in high-capacity battery packs, since the more rectangular shapes pack together better.

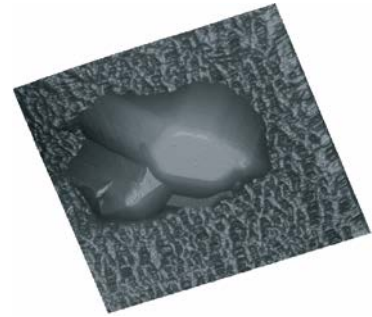


Figure 1.17: Lithium-manganese-oxide particle on top of separator material.
(Image courtesy Sangwoo Han.)

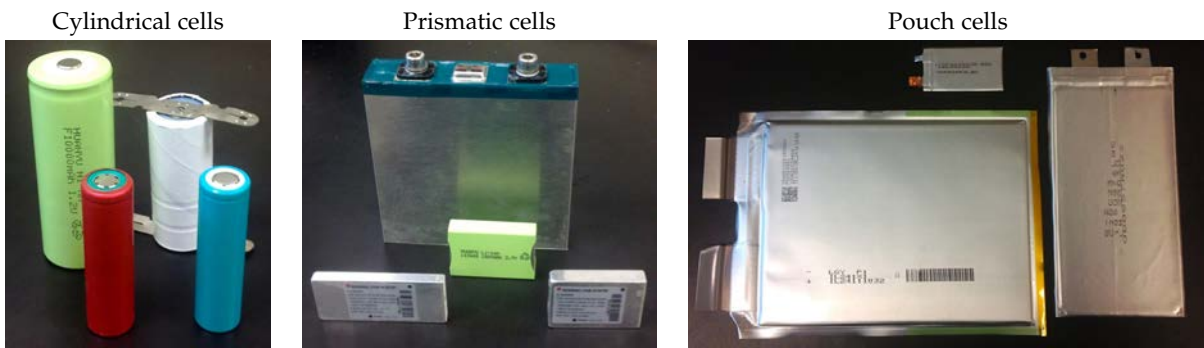


Figure 1.18: Different common form factors for lithium-ion cells.

1.6.1 Electrode coating

The negative and positive electrodes in lithium-ion cells are of similar form and are made by similar processes on similar or identical equipment. The active electrode materials are coated on both sides of thin metallic foils (the foils are on the order of $20\ \mu\text{m}$ thick) that act as the current collectors, conducting the current into and out of the cell. This is illustrated in Fig. 1.19.

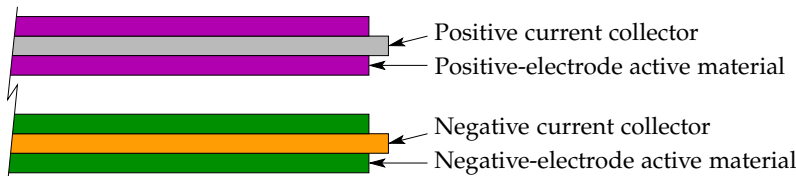


Figure 1.19: Electrode active material coats both sides of metal foil current collector.

Both negative- and positive-electrode active materials are delivered to the factory in the form of black powder.¹⁹ To the untrained eye they are nearly indistinguishable. Because contamination between negative- and positive-electrode materials would ruin a cell, great care must be taken to prevent these materials from coming into contact with each other. For this reason the different electrodes are usually processed in different rooms.

The metal electrode foils are delivered on large reels, typically about 0.5 m wide, with copper for the negative-electrode current collector and aluminum for the positive-electrode current collector. These reels are mounted directly on the coating machines where the foil is unreeled as it is fed into the machine through precision rollers.

The electrode active materials are mixed with a conductive binder and a solvent to form a slurry that is spread on the surface of the foil. A knife edge is located just above the foil, and the thickness of the electrode coating is controlled by adjusting the gap between the knife edge and the foil. (The thickness of the two electrodes will generally be different as the volumetric energy densities of the materials is generally different.) After being coated on both sides, the foil is fed directly into a long drying oven to evaporate the solvent from the slurry and to bake the electrode material onto the foil. As the coated foil exits the oven it is re-reeled. The process as described so far is accomplished by an electrode coating machine, which might look something like the illustration in Fig. 1.20.

The coated foils are subsequently fed into a *calendering* (i.e., pressing) and slitting machine. Calendering is done to compress the electrode active material, compacting the spaces between particles, pressing out porosity. Slitting cuts the foil into narrower strips of the desired width. Later they are cut to length. Any burrs on the edges

¹⁹ Green and purple coloring for the negative- and positive-electrode active materials, respectively, is used in this book purely for illustrative purposes. Orange and gray are used to represent copper and aluminum current collectors, respectively.

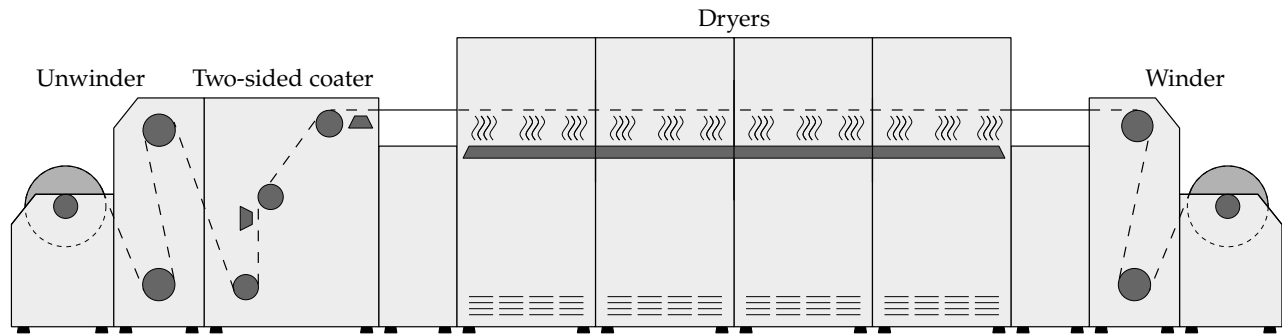


Figure 1.20: Electrode coating machine.

of the foil strips could give rise to internal short circuits in the cells so the slitting machine must be very precisely manufactured and maintained. The calendaring and slitting is accomplished by a machine that might look something like the illustration in Fig. 1.21.

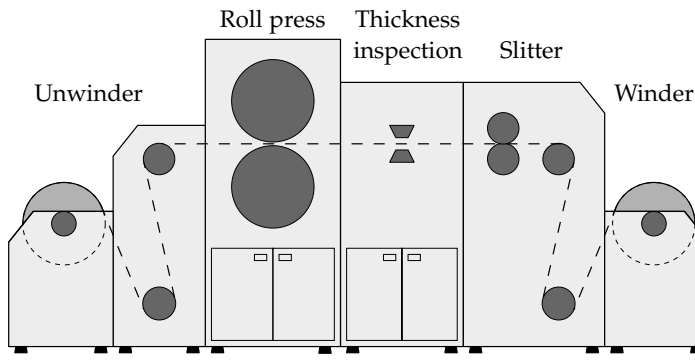


Figure 1.21: Calendaring and slitting machine.

1.6.2 Cell assembly

The electrodes are now ready to be assembled into cells. For cylindrical cells, the negative- and positive-electrode foils are cut into two long strips that are wound on a cylindrical mandrel, together with the separator that keeps them apart, to form a structure called a *jelly roll*. A cutaway diagram of a cylindrical cell is illustrated in Fig. 1.22. The mandrel is attached directly to the positive-electrode current collector and becomes the cell's positive terminal; the negative-electrode current collector is attached to the cell's negative terminal.

Prismatic cells are constructed similarly, but by winding the electrode-coated current-collector foils on a flat mandrel instead of a cylindrical mandrel. This is illustrated in Fig. 1.23. The flat mandrel causes the jelly-roll structure to be more prismatic than cylindrical in shape; once inserted into its can, the external appearance is prismatic.

The next stage is to connect the electrode structure to the terminals

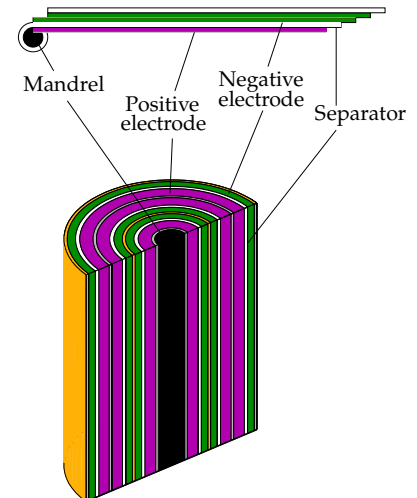


Figure 1.22: Construction of a cylindrical cell.

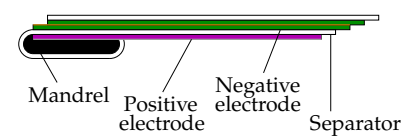


Figure 1.23: Construction of a prismatic cell.

and any internal electronic safety devices, and to insert this sub-assembly into a metal can. The can is then sealed via laser welding or ultrasonic heating, retaining a small opening. Electrolyte is injected into this opening, and the opening is closed. Addition of the electrolyte must be carried out in a *dry room* since the electrolyte reacts with water. Lithium hexafluorophosphate (LiPF_6), for instance, one of the most commonly used electrolyte salts, reacts with water to form toxic hydrofluoric acid (HF), which can attack the positive-electrode active materials and lead to premature cell failure. Afterward, the cell is given an identification code with a label or by printing a batch or serial number directly on the case. The final assembly is accomplished by a machine that might look something like the illustration in Fig. 1.24.

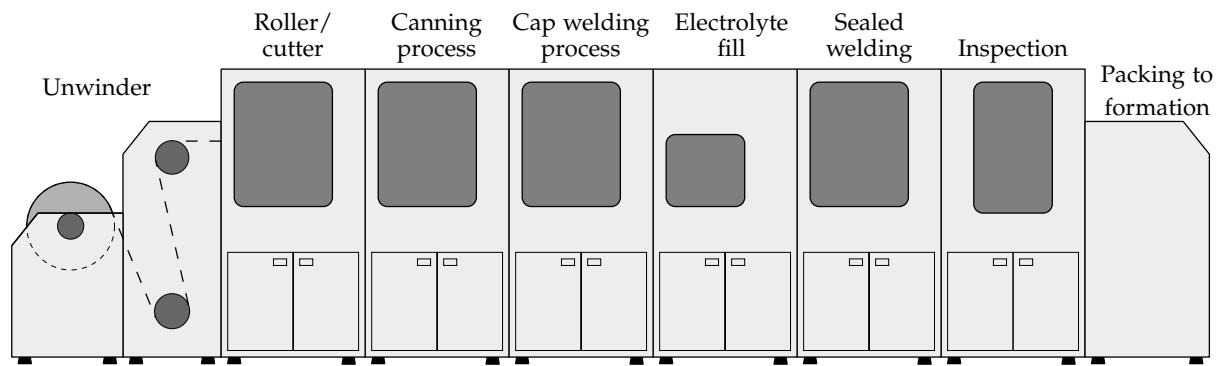


Figure 1.24: Cell construction machine.

Construction of pouch cells is somewhat different. Instead of winding long electrode strips around a mandrel, electrode plates are stamped out of the reels of electrode-coated foil. Negative- and positive-electrode plates are alternately stacked, with separator material between them, as shown in Fig. 1.25. All negative-electrode tabs are welded in parallel and to the cell's negative terminal; all positive-electrode tabs are welded in parallel and to the cell's positive terminal.

1.6.3 Formation

Lithium-ion cells are fabricated in a completely discharged state (all of the lithium is in the positive electrode). So, once the cell assembly is complete, the cell must be put through at least one precisely controlled charge cycle to activate the working materials, transforming them into their usable form. This first charge begins with a low voltage and builds up gradually until the cell is fully charged. This is called the *formation process*.

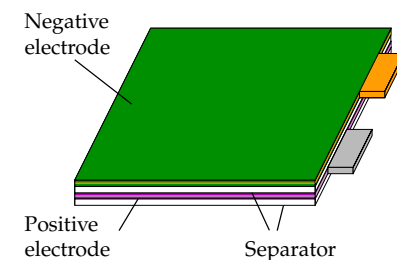


Figure 1.25: Stacked construction of a pouch cell.

THE ORGANIC SOLVENTS used in most lithium-ion cells naturally tend to react violently with graphitic negative electrodes. This would appear to be a “deal breaker,” but it turns out that the reaction is self-limiting. The process can be compared to what happens when aluminum is exposed to air. Aluminum reacts rapidly with oxygen to form a film of aluminum oxide on its surface. This aluminum oxide prevents oxygen from reaching the underlying aluminum metal and so inhibits further reaction. In lithium-ion cells, the reaction of the solvent with the graphite in the negative electrode creates a passivating film on the surface of the graphite, known as the *solid electrolyte interphase* (SEI) layer, which is electrically insulating yet provides sufficient ionic conductivity for lithium to intercalate into and deintercalate out of the electrode particles readily. This SEI layer inhibits solvents from reaching the underlying graphite and so protects the graphite from further reaction.

The SEI is both a blessing and a curse. It is necessary for the proper safe operation of the cell, but it also increases the resistance of the cell and consumes lithium when being formed, decreasing the cell’s capacity. Fortunately, once the SEI film is formed during the first charge cycle, it remains fairly stable and tends to grow only slowly as the cell is used. Even so, SEI growth is considered one of the principal aging mechanisms that lead to the cell wearing out.

DURING CELL FORMATION, data are also collected from the charger and recorded. The spread of the performance measurements across many cells gives an indication of whether the manufacturing process is under control. Although not the prime purpose of formation, the process allows a significant percentage of early-life cell failures due to manufacturing defects to occur in the manufacturer’s plant rather than in the customers’ products.

Tight tolerances and strict process controls are essential throughout the manufacturing process. Contamination, physical damage, and burrs on the electrodes are particularly dangerous because they can cause penetration of the separator and give rise to internal short circuits in the cell. There are no protection methods that can prevent or control this. Cleanliness is essential to prevent contamination, and cells are normally manufactured in clean-room conditions, with controlled access to the assembly facilities via air showers.

1.7 Failure modes

This book focuses on the operation of ideal cells, with the ultimate direction leading toward battery controls. To be able to effect optimal battery controls, however, an understanding of the potential cell

failure modes is essential. Failures occur because of cell design faults, poorly controlled manufacturing processes, aging, uncontrolled operations, and abuse. Battery controls can't do too much about the first two (it's too late!), but can do something about the others. Here, we briefly look at some qualitative aspects relating to postmanufacture cell failure.

1.7.1 “Normal” aging

Cell performance naturally deteriorates gradually with time due to unwanted chemical side reactions and physical changes to the active chemicals. Aging is generally irreversible and eventually results in cell failure. The following are some examples of causes (not all chemistries are susceptible to all of these mechanisms).

Corrosion refers to deterioration due to chemical interaction with the environment. It is a catch-all term for any number of undesirable side reactions that can occur within a cell. Some examples include reaction between the solvent and the current collectors and reaction between the solvent and the electrode active and inactive materials. In some cases, products of these reactions can themselves have a corrosive effect on other cell components.

Lithium-ion cells having graphitic negative electrodes are prone to a particular kind of corrosion known as *passivation*. The solvent in the electrolyte is not chemically stable at the high voltages found in most lithium-ion cells, and it reacts with the graphite particles. This forms a passivation layer of reaction products on the surface of the particles, which is known as the *solid-electrolyte interphase* or SEI film. This film protects the graphite against further reaction, greatly slowing down the process of passivation. However, SEI continues to grow at a slow rate throughout the cell's lifetime.

Some chemistries naturally produce gaseous products when charging, which ideally return to their prior aqueous state when discharging. However, if the gases leak due to a breach in the cell enclosure, capacity is lost. In many cases this can also be dangerous as in some cells the released gases are explosive (e.g., lead-acid cells give off oxygen and hydrogen when overcharged). In sealed cells, pressure buildup can lead to the rupture or explosion of the cell, unless the cell has a release vent to allow the escape of the gasses.

Chemical redox cells are also naturally susceptible to *crystal formation*. When material is removed from an electrode during discharge, it will not generally return to the same location when the cell is recharged. Instead, crystal structures will tend to form on the electrode surfaces. As the crystals grow, this reduces the effective surface

area of the electrodes, increasing resistance and hence decreasing their ability to deliver high power.

A particular example of crystal growth is when metallic *dendrites* form at the surface of an electrode. These treelike structures can grow through the separator, causing an increase in the cell's self-discharge rate or even a short circuit. For example, in lithium-ion cells, low-temperature operation or overcurrent during charging can cause deposition of lithium metal on the negative-electrode particles, leading to the growth of lithium dendrites.

Charging and discharging intercalation-based electrodes causes volume changes, which stress the electrodes and can lead to cracking of the active materials. In some lithium-ion positive-electrode materials, it can cause structural collapse, which prevents the electrode from intercalating or deintercalating lithium. Strains on the binder materials and conductive additives can lead to loss of contact between particles, increasing resistance.

Any of these causes lead to one or more of the following undesirable effects:

- *Increased internal impedance*: The resistance of the cell tends to increase as it ages. This limits the power that the cell is capable of delivering, leading to *power fade*.
- *Reduced capacity*: The capacity of a cell tends to decline as it ages. In some chemistries, some capacity can be recovered through reconditioning the cell by subjecting the cell to one or more deep discharges, but the general trend is in the downward direction. The decline of capacity over time is known as *capacity fade*.
- *Increased self-discharge*: Due to electrode swelling, which puts pressure on the separator; dendritic growth, which penetrates the separator; or local overheating, which melts and thins the separator, the self-discharge rate of a cell tends to increase as it ages as well.

Aging processes are generally accelerated by elevated temperatures. The best way to extend a cell's life is to maintain its temperature in an acceptable range.²⁰

1.7.2 Uncontrolled operating conditions and abuse

Good battery cells are not immune to failure, which can be provoked by the way they are used or abused. "Bad things" to do to a cell include using an unsuitable charging profile and/or overcharging, and exposing it to high ambient or storage temperatures.

Cells will also fail when subjected to physical abuse such as dropping, crushing, puncture, impact, immersion in fluids, freezing, or contact with fire, any of which could happen to an automotive

²⁰ A good rule of thumb for lithium-ion chemistries is that if you are comfortable at a certain temperature, the cell is also "comfortable" at that temperature. If it's too hot or too cold for your tastes, it's probably too hot or too cold for the cell as well.

battery during an accident, for instance. It is generally accepted that a cell is not required to survive all these trials; however, it should not itself cause an increased hazard or safety problem in these circumstances.

There are several possible failure modes associated with the complete breakdown of the cell, but it is rarely possible to predict which one will occur. It depends very much on the circumstances.

- *Open-circuit failure:* This is a fail-safe mode for the cell but possibly not for the application. Once the current path is cut and the cell is isolated, further damage to the cell is limited. This may not suit the user, however. If one cell of a multicell series-connected battery fails open-circuit, then the whole battery will be out of commission.
- *Short-circuit failure:* If one cell of a series-connected battery fails because of a short circuit, the rest of the cells may be slightly overloaded, but the battery will continue to provide power to its load. This may be important in emergency situations.

Short circuits may be external to the cell or internal within the cell. The *battery management system* (BMS) should be able to isolate cells from an external short, but there's not much the BMS can do to rescue a cell from an internal short circuit. However, the BMS and pack design must be able to prevent a single-cell failure from spreading to other cells; precautions include, for example, careful fusing, contactor control, and venting.

Within the cell there are different degrees of failure.

- *Hard short circuit:* Solid connection between electrodes causes extremely high current flow and complete discharge, resulting in permanent damage to the cell. The cell voltage collapses to 0 V, and the cell effectively acts as a resistor in the overall circuit.
- *Soft short circuit:* This is caused by small localized contact between electrodes. It may be self-correcting due to melting of the small regions in contact caused by the high current flow, acting as a local fuse, and interrupting the short-circuit current. A cell with a soft short is still operational, but has a high self-discharge rate.
- *Explosion and/or fire:* The rate of chemical reactions tends to double for every 10 °C increase in temperature. If the heat generated by these reactions cannot be removed as quickly as it is generated, this can lead to a further increase in temperature and set up a self-sustaining uncontrolled positive feedback known as *thermal runaway*, leading to a destructive result (fire/explosion). This is to be avoided at all costs, and the battery pack must incorporate protection circuits or devices to prevent it.

1.8 Where to from here?

In this chapter, we have covered a lot of fundamental background topics relating to how electrochemical cells—and especially lithium-ion cells—work at the level of the chemistry.²¹ We are now ready to begin looking at how a cell behaves electrically, making mathematical models that can predict the voltage response of a cell to an input-current stimulus.

The first model type that we look at is designed from a phenomenological point of view, using electric circuit elements as analogs to observed behaviors of cells. Later models will “look inside” the cell, using sophisticated analysis of the internal electrochemistry, to predict both internal and external behaviors.

Both types of model are useful, but the electrochemical models provide more physical insight than the circuit models and can be used by advanced battery control methods to derive an optimal trade-off between the performance delivered by a cell and the amount of incremental degradation experienced by the cell in doing so. However, the electrochemical models are computationally very complex. To overcome this limitation, we introduce reduced-order physics-based cell models that approximate the electrochemical model predictions very closely but have computational complexity similar to circuit models.

In the final chapter, we look at thermal aspects: how is heat generated or sunk in a cell? How does the temperature of the cell evolve over time? By the end of the book, we will have developed a solid understanding of how to model battery-cell operation with a high degree of accuracy.

²¹ It is not the intention of this book to cover every common chemistry. However, the phenomenological models discussed in Chap. 2 can be applied readily to any chemistry. The microscale models in Chap. 3 can also apply to any chemistry, with the understanding that the equations that describe intercalation compounds are not needed when modeling cells that do not have insertion electrodes. The continuum-scale models in Chap. 4 and the thermal models in Chap. 7 apply to any porous-electrode type cell, including NiMH. The methods presented in Chaps. 5 and 6 for reducing model-order complexity could be used on other similar sets of equations modeling different chemistries. In fact, this is illustrated in the appendix, which shows how to model the operation of a supercapacitor using the methods of this book.

2

Equivalent-Circuit Models

In this book, we will study two fundamentally different kinds of cell model. One is based on understanding the underlying physics that govern the cell's operation and building a model of the cell dynamics from the inside out. We will look at such physics-based models starting in Chap. 3.

In this chapter, we investigate the second, simpler approach to modeling cell operation, which uses electrical-circuit analogs to define a *behavioral* or *phenomenological* approximation to how a cell's voltage responds to different input-current stimuli. That is, we invoke knowledge of common electronic elements to define a circuit that has behavior that closely matches the observed behavior of the battery cell. The equations that describe the circuit therefore also closely describe the observed operation of the cell.

Such models are called *equivalent-circuit models*. We recognize that the circuit elements in the model are not meant to describe the construction of the cell. If we were to open up a cell, we should not expect to find voltage sources, resistors, capacitors, or the like! Rather, the circuit acts as a description of the cell's behavior, and the various circuit elements act as analogs to some of the internal processes. Because there is a great deal of knowledge relating to how circuit elements behave, circuit models leverage that knowledge to give a better "feel" for how cells will respond to different usage scenarios.

At present, the majority (if not all) of battery management systems for large battery packs use some flavor of equivalent-circuit cell model as a basis for maintaining the proper operating boundaries for the cells and for estimating critical internal cell states. The simplicity and robustness of equivalent-circuit models are the main reasons for this. Equivalent-circuit cell models don't have all of the features of physics-based models but are adequate for many applications.

2.1	<i>Open-circuit voltage</i>	30
2.2	<i>SOC dependence</i>	30
2.3	<i>Equivalent series resistance</i> . .	33
2.4	<i>Diffusion voltages</i>	34
2.5	<i>Rough parameter values</i>	38
2.6	<i>Warburg impedance</i>	40
2.7	<i>Hysteresis voltages</i>	41
2.8	<i>ESC cell model</i>	44
2.9	<i>Laboratory equipment</i>	44
2.10	<i>OCV-relationship lab tests</i> . .	45
2.11	<i>Dynamic-relationship tests</i> . .	53
2.12	<i>Example results</i>	57
2.13	<i>Where to from here?</i>	59
2.14	<i>MATLAB ESC toolbox</i>	59

2.1 Open-circuit voltage (OCV)

We take the approach of building up a circuit model element by element, starting with an explanation of the predominant observed behavior. Any difference between predictions by the circuit model and observed cell behavior is therefore deemed *modeling error*. This modeling error is analyzed, and circuit elements are proposed to refine the model to reduce this modeling error, until only a small level of error remains—small enough that we are satisfied to accept the model as “good enough.”

We start by explaining the most fundamental observed behavior of a battery cell: cells deliver a voltage at their terminals. If you place a voltmeter across the terminals of a cell, it will register some value. So, the first model we build represents the cell simply as an ideal voltage source. The schematic for this model is drawn in Fig. 2.1. In the model, cell terminal voltage $v(t)$ is not a function of load current $i(t)$, nor is it a function of past cell usage. In fact, voltage is constant. Period.

This is a pretty poor model of a battery cell because terminal voltage of a real cell *is* dependent on load current, recent usage, and other factors. However, this model provides a starting point for our development. Cells *do* supply a voltage to a load. And, when the cell is unloaded and in complete equilibrium (a condition that is termed *open circuit*), the voltage of the cell is fairly predictable. Hence, the voltage source in the model is labeled “OCV.” We’ll see that an ideal voltage source will remain a component of our final equivalent-circuit model.

2.2 State-of-charge dependence

The first improvement we make to the simple cell model is a result of recognizing that the voltage of a fully charged cell is generally higher than the voltage of a discharged cell. This is not, in fact, always the case, since the terminal voltage of the cell also depends on dynamic factors relating to how the cell has been used in the recent past. We can state, however, that the equilibrium unloaded rest voltage—or open-circuit voltage—of a fully charged cell is higher than that of a discharged cell.

So, we can improve our model by including a relationship between the open-circuit voltage and the charge status of the cell. To do so, we must first define what we mean by this “charge status.” We therefore define the *state of charge* (SOC) of a cell to be 100 % (or 1.0) when the cell is fully charged and 0 % (or 0.0) when the cell is fully discharged. If the cell is at an intermediate state between being fully charged and

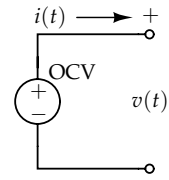


Figure 2.1: Trivial cell model having constant output voltage.

fully discharged, its state of charge is somewhere between 0 % and 100 %. State of charge is a unitless quantity and is denoted in this book by the symbol z .

To quantify state of charge, we need to know how much charge a cell holds when it is fully charged versus how much charge remains when it is fully discharged.¹ So, we define the *total charge capacity*—or more simply the *total capacity*—of a cell to be the total amount of charge removed when discharging a cell from $z = 100\%$ to $z = 0\%$. (This is different from the cell’s total *energy* capacity, as is discussed in Chap. 1.) Total capacity is usually measured in ampere-hours (Ah) or milliampere-hours (mAh), and is denoted by the symbol Q . The value of total capacity is a *parameter* of the cell model; that is, it is a constant that may differ from cell to cell. Total capacity is not a function of temperature or current, although the total capacity of a cell does tend to decrease very gradually as the cell ages due to undesired parasitic chemical side reactions and structural breakdown of the cell’s electrode materials.²

We can model changes to state of charge using an ordinary differential equation as

$$\dot{z}(t) = -\eta(t)i(t)/Q, \quad (2.1)$$

where we use the “dot” symbol in this book to indicate a time derivative (e.g., $\dot{z}(t) = dz(t)/dt$), and where the sign of $i(t)$ is positive on discharge. Hence, positive (discharge) current lowers the cell’s state of charge, and negative (charge) current increases the cell’s state of charge. Care must be taken with units: $i(t)$ is measured in amperes, and to be compatible, Q must be converted to ampere-seconds (i.e., coulombs). Both $z(t)$ and $\eta(t)$ are unitless.

The term $\eta(t)$ is the *coulombic efficiency* or *charge efficiency* of the cell.³ We model $\eta(t) = 1$ at time instants when the sign of current is positive (discharging), but $\eta(t) \leq 1$ at time instants when the sign of current is negative (charging). When charging, most of the charge that passes through the cell participates in the desired chemical reactions that raise the cell’s state of charge; however, a small fraction of the charge passing through the cell instead participates in unwanted side reactions, which do not increase the cell’s state of charge (and often cause irreversible degradation to the cell as well). Creating an accurate model of coulombic efficiency is a very challenging task, as its value depends on state of charge, charging rate, temperature, and the internal electrochemical state of the cell. However, due to the high coulombic efficiencies of lithium-ion cells, the first-order assumption that η is always equal to unity often gives reasonable overall model fidelity.

We can integrate the instantaneous relationship of Eq. (2.1) to

¹ Yes, a “fully discharged” cell still has charge in it! But, we don’t (intentionally) discharge a cell beyond a certain point because that can cause damage and possibly a safety concern.

² Note that *total capacity* is different from a cell’s *discharge capacity*. The latter is defined as the total amount of charge removed when discharging a cell at a constant rate from $z = 100\%$ until the cell terminal voltage reaches some minimum cutoff voltage. This will occur before $z = 0\%$ because real cells have internal resistance (and hence, a voltage drop across the internal resistance). So, a cell’s discharge capacities are always lower than its total capacity, unless discharge occurs at an infinitesimally slow rate.

³ Note that coulombic efficiency is different from *energy efficiency* of a cell. Coulombic efficiency in a typical lithium-ion cell is around 99 % or higher and is equal to (charge out)/(charge in). Energy efficiency is closer to 95 % and is equal to (energy out)/(energy in). Energy is lost in resistive heating on both charge and discharge.

obtain an aggregate equation for a change in state of charge over some time interval. Given known state of charge at initial time $t_0 < t$, and known current between times t_0 and t , we get

$$z(t) = z(t_0) - \frac{1}{Q} \int_{t_0}^t \eta(\tau) i(\tau) d\tau. \quad (2.2)$$

In this equation, we use τ as a placeholder for the time variable inside the integral so that we do not confuse the dummy variable of integration (which should disappear from the final result when the integral is performed) with the upper limit of integration (which should be retained in the final result).

Many times, we are more interested in a discrete-time model than a continuous-time model. Discrete-time models assume that the cell inputs and outputs are measured or *sampled* at a regular rate with period Δt seconds and frequency $1/\Delta t$ hertz. Such models are ready to be used inside inexpensive microcontrollers directly for battery management systems. To convert Eq. (2.2) to discrete time, let $t_0 = k\Delta t$ and $t = (k+1)\Delta t$. Then, if we assume that the cell's input current is constant over the sampling interval Δt , we have⁴

$$z((k+1)\Delta t) = z(k\Delta t) - \frac{\Delta t}{Q} \eta(k\Delta t) i(k\Delta t). \quad (2.3)$$

Noting that it is cumbersome to carry around the “ Δt ” factor in the time index of the model, we define a new notation. Square brackets “[.]” will be used to denote a discrete-time sample number, and parenthesis “(.)” will be used to denote an actual time. Then, for example, “[k]” is equivalent to “($k\Delta t$).” Rewriting Eq. (2.3) using this notation, we arrive at

$$z[k+1] = z[k] - \frac{\Delta t}{Q} \eta[k] i[k]. \quad (2.4)$$

Having a mathematical model for state of charge, we are now ready to revise our circuit model. We first recognize that a cell's open-circuit voltage is a function of its state of charge. Some examples are drawn in Fig. 2.2. There is some temperature dependence to this relationship—these curves are drawn for *room temperature* (25 °C). Also, while these curves are drawn as functions of the cell's state of charge, it is also common to see them expressed in terms of the cell's *depth of discharge* (DOD). Depth of discharge is the converse of state of charge and is expressed either as a fraction or in ampere-hours. $DOD = 1 - z(t)$ if it is being expressed as a fraction, and $DOD = Q(1 - z(t))$ if being expressed in ampere-hours.

The improved cell model, including open-circuit-voltage dependence on the cell's state of charge, is then depicted in Fig. 2.3. The ideal voltage source is replaced by a controlled voltage source having

⁴ This assumption is often reasonable if the sampling interval Δt is short. If means are available to measure average current $\bar{i}(k\Delta t)$ over the sampling interval, then this equation is exact if $i(k\Delta t)$ is replaced by $\bar{i}(k\Delta t)$.

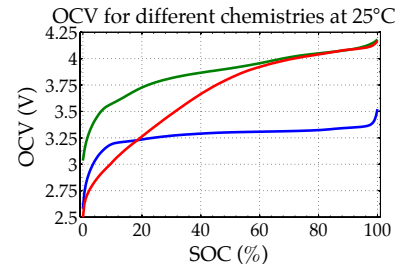


Figure 2.2: Open-circuit voltage as a function of state of charge for several common lithium-ion cell chemistries.

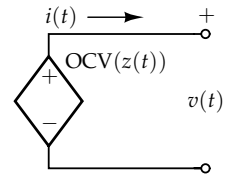


Figure 2.3: Improved cell model, with SOC-dependent voltage.

value equal to $OCV(z(t))$. If temperature dependence is required, we instead use $OCV(z(t), T(t))$, where $T(t)$ is the cell's internal temperature at time t .

The OCV values for a cell are determined empirically at numerous SOC points via laboratory procedures described in Sec. 2.10. These values can be stored in a lookup table, such that the OCV function is evaluated via interpolation between table entries. Alternatively, an analytic function such as a polynomial could be fit to the data using a regression technique. The OCV at some given SOC point would then be computed by evaluating this analytic function.

2.3 Equivalent series resistance

Up until this point, the cell model that we have developed is essentially static. It describes the rest behavior of the cell. Now, we begin to add dynamic features to the model to describe what happens when the cell is subjected to a time-varying input current.

The first observation that we would like the model to describe is that the cell's terminal voltage drops below the open-circuit voltage when the cell is subjected to a load, and the terminal voltage rises above the open-circuit voltage when the cell is being charged. This phenomenon can be explained in part by placing a resistance in series with the controlled voltage source. The revised model is drawn in Fig. 2.4. The added circuit component represents the so-called *equivalent series resistance* (ESR) of the cell.

In the revised model, the state-of-charge equation remains unchanged. However, we add a second equation to the model to describe how to compute the terminal voltage.⁵ In continuous time, we have

$$\begin{aligned}\dot{z}(t) &= -\eta(t)i(t)/Q \\ v(t) &= OCV(z(t)) - i(t)R_0.\end{aligned}$$

With this model, we see that $v(t) > OCV(z(t))$ when $i(t) < 0$ (i.e., when charging) and $v(t) < OCV(z(t))$ when $i(t) > 0$ (i.e., when discharging). This is in agreement with our observation of real cell performance. In discrete time, the equivalent model is

$$\begin{aligned}z[k+1] &= z[k] - \frac{\Delta t}{Q}\eta[k]i[k] \\ v[k] &= OCV(z[k]) - i[k]R_0.\end{aligned}$$

Note that the presence of this series resistance in the model also implies that power is dissipated by the cell internal resistance as heat, and therefore the energy efficiency of the cell is not perfect. The

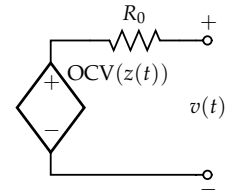


Figure 2.4: Improved cell model, with SOC-dependent voltage and equivalent series resistance R_0 .

⁵ It is important to understand that the model comprises both of these equations together. The model is not a single stand-alone equation.

power dissipated by the equivalent series resistance can be expressed as $i^2(t) \times R_0$.

Finally, we note that the cell's resistance is often a function of the cell's state of charge and is always a function of the cell's internal temperature. The fidelity of the model's predictions will be enhanced if these dependencies are taken into account in R_0 .

This model of a cell is sufficient for many simple electronic-circuit designs. However, it is not yet adequate for applications in large-scale battery packs, such as for electric-drive vehicles and grid-storage systems. There are several other dynamic features that must be addressed.

2.4 Diffusion voltages

Polarization refers to any departure of the cell's terminal voltage away from open-circuit voltage due to a passage of current through the cell. In the equivalent-circuit model that we have developed so far, we have modeled instantaneous polarization via the $i(t) \times R_0$ term. Real cells have more complex behavior, where the voltage polarization slowly develops over time as current is demanded from the cell and then slowly decays over time when the cell is allowed to rest.

Fig. 2.5 illustrates this slower behavior. The voltage plotted in the figure corresponds to the following scenario: (1) the cell is at rest for the first 5 min, and the voltage is constant; (2) the cell is then subjected to a discharge current pulse of constant magnitude from $t = 5$ min until $t = 20$ min; (3) the load is removed, and the cell is allowed to rest for the remainder of the test.

The model we have developed so far explains the cell behavior during the initial rest. It also explains the immediate voltage drop when current is applied and the immediate voltage recovery when the current is removed. It is difficult to predict, without further analysis, whether the cell model accurately predicts the voltage during the discharge interval, since we know that state of charge is decreasing, and so too the open-circuit voltage is decreasing. But we know for certain that the third section of the test is not being well modeled. In this section, we see that voltage is constantly changing, but we also know that the cell state of charge is not changing since the cell current is zero. There is something going on here that is not yet part of our model.

If you've ever played with a flashlight, you are certain to have seen this phenomenon in action. What happens when your battery is just about empty? The light produced by the flashlight grows dimmer and dimmer and becomes indiscernible. But turn the flashlight off and wait a minute or two. Then turn the flashlight back on—the bulb

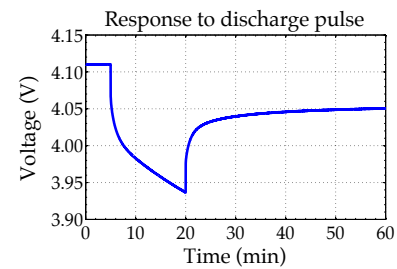


Figure 2.5: Polarization evident when a cell is subjected to a discharge pulse followed by a rest.

is brighter again! Did the battery magically recharge? No, but its voltage recovered somewhat from the slow decay in polarization that we observed in Fig. 2.5, and we are able to get (a little) more light from the flashlight with nearly empty batteries.

We will find out later that this phenomenon is caused by slow diffusion processes of lithium in a lithium-ion cell, so we will refer to this slowly changing voltage as a *diffusion voltage*. Its effect can be approximated closely in a circuit using one or more parallel resistor-capacitor subcircuits. In Fig. 2.6, the combination of R_1 and C_1 perform this function. In the model, the state-of-charge equation remains the same as before, but the voltage equation changes to

$$v(t) = \text{OCV}(z(t)) - v_{C_1}(t) - v_{R_0}(t)$$

for a continuous-time model and

$$v[k] = \text{OCV}(z[k]) - v_{C_1}[k] - v_{R_0}[k]$$

for a discrete-time model. When using data to identify model parameters, it turns out to be simpler if we write these expressions in terms of element currents instead:

$$v(t) = \text{OCV}(z(t)) - R_1 i_{R_1}(t) - R_0 i(t)$$

$$v[k] = \text{OCV}(z[k]) - R_1 i_{R_1}[k] - R_0 i[k].$$

We find an expression for the resistor current $i_{R_1}(t)$ as follows. First, we recognize that the current through R_1 plus the current through C_1 must equal $i(t)$. Further, $i_{C_1}(t) = C_1 \dot{v}_{C_1}(t)$, which gives

$$i_{R_1}(t) + C_1 \dot{v}_{C_1}(t) = i(t).$$

Then, since $v_{C_1}(t) = R_1 i_{R_1}(t)$,

$$\begin{aligned} i_{R_1}(t) + R_1 C_1 \frac{di_{R_1}(t)}{dt} &= i(t) \\ \frac{di_{R_1}(t)}{dt} &= -\frac{1}{R_1 C_1} i_{R_1}(t) + \frac{1}{R_1 C_1} i(t). \end{aligned} \quad (2.5)$$

This differential equation can be simulated as is to determine $i_{R_1}(t)$. Alternatively, we can convert it to a discrete-time form. It turns out that we'll have to make a similar conversion in the next section, so to encompass both cases we'll consider transforming a generic ordinary differential equation from continuous time to discrete time. Define

$$\dot{x}(t) = ax(t) + bu(t). \quad (2.6)$$

Then, we wish to evaluate $x(t)$ at discrete times $t = k\Delta t$, where $x[k] = x(k\Delta t)$. We assume that the input $u(t)$ is constant over the

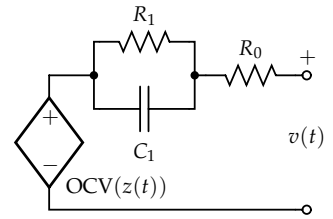


Figure 2.6: Circuit that now models diffusion voltages.

sampling interval. The general solution to Eq. (2.6) turns out to be

$$x(t) = e^{at}x(0) + \underbrace{\int_0^t e^{a(t-\tau)}bu(\tau) d\tau}_{\text{convolution}}. \quad (2.7)$$

This says that the time response of the ordinary differential equation comprises a portion depending on the initial condition $x(0)$, and another portion that depends on the input signal $u(t)$. If the ordinary differential equation is stable, then $a < 0$ and the contribution of the initial condition decays. The contribution due to the input signal dominates in steady state, and the integral that computes that contribution is known as a *convolution integral*.

But, where did Eq. (2.7) come from? First, we rearrange Eq. (2.6) as

$$\dot{x}(t) - ax(t) = bu(t).$$

Then, we multiply both sides of this equation by e^{-at} .⁶

$$e^{-at}(\dot{x}(t) - ax(t)) = e^{-at}bu(t).$$

⁶The reason for doing this is not immediately apparent. However, it does take us quickly to the final form we desire.

We notice that the left-hand side of this equation can also be written as

$$\frac{d}{dt}[e^{-at}x(t)],$$

so we can then write

$$\frac{d}{dt}[e^{-at}x(t)] = e^{-at}bu(t).$$

Now, we integrate both sides of this equation between times 0 and t , being careful to replace t inside the integral with a dummy variable of integration τ .

$$\begin{aligned} \int_0^t \frac{d}{d\tau}[e^{-a\tau}x(\tau)] d\tau &= \int_0^t e^{-a\tau}bu(\tau) d\tau \\ \int_0^t d[e^{-a\tau}x(\tau)] &= \int_0^t e^{-a\tau}bu(\tau) d\tau. \end{aligned}$$

Note that the left-hand side of this equation becomes

$$e^{-a\tau}x(\tau)|_0^t = e^{-at}x(t) - x(0),$$

so we have

$$e^{-at}x(t) - x(0) = \int_0^t e^{-a\tau}bu(\tau) d\tau.$$

Moving $x(0)$ to the right-hand side and multiplying both sides by e^{at} gives the desired result in Eq. (2.7).

Now, beginning with this result, we seek to find a discrete-time relationship. We substitute

$$\begin{aligned} x[k+1] &= x((k+1)\Delta t) \\ &= e^{a(k+1)\Delta t}x(0) + \int_0^{(k+1)\Delta t} e^{a((k+1)\Delta t-\tau)}bu(\tau) d\tau. \end{aligned}$$

With malice aforethought, break up the integral into two pieces

$$\begin{aligned} x[k+1] &= e^{a(k+1)\Delta t}x(0) + \int_0^{k\Delta t} e^{a((k+1)\Delta t-\tau)}bu(\tau) d\tau \\ &\quad + \int_{k\Delta t}^{(k+1)\Delta t} e^{a((k+1)\Delta t-\tau)}bu(\tau) d\tau. \end{aligned}$$

We factor $e^{a\Delta t}$ out of the first two terms

$$\begin{aligned} x[k+1] &= e^{a\Delta t}e^{ak\Delta t}x(0) + e^{a\Delta t} \int_0^{k\Delta t} e^{a(k\Delta t-\tau)}bu(\tau) d\tau \\ &\quad + \int_{k\Delta t}^{(k+1)\Delta t} e^{a((k+1)\Delta t-\tau)}bu(\tau) d\tau. \end{aligned}$$

We can then write this as

$$\begin{aligned} x[k+1] &= e^{a\Delta t} \left(e^{ak\Delta t}x(0) + \int_0^{k\Delta t} e^{a(k\Delta t-\tau)}bu(\tau) d\tau \right) \\ &\quad + \int_{k\Delta t}^{(k+1)\Delta t} e^{a((k+1)\Delta t-\tau)}bu(\tau) d\tau \\ &= e^{a\Delta t}x(k\Delta t) + \int_{k\Delta t}^{(k+1)\Delta t} e^{a((k+1)\Delta t-\tau)}bu(\tau) d\tau. \end{aligned}$$

Finally, we write the result using discrete-time notation

$$x[k+1] = e^{a\Delta t}x[k] + e^{a(k+1)\Delta t} \int_{k\Delta t}^{(k+1)\Delta t} e^{-a\tau}bu(\tau) d\tau.$$

In the integral that remains, we assume that $u(t)$ is constant from $k\Delta t$ to $(k+1)\Delta t$ and equal to $u(k\Delta t)$

$$\begin{aligned} x[k+1] &= e^{a\Delta t}x[k] + e^{a(k+1)\Delta t} \left(\int_{k\Delta t}^{(k+1)\Delta t} e^{-a\tau} d\tau \right) bu[k] \\ &= e^{a\Delta t}x[k] + e^{a(k+1)\Delta t} \left(-\frac{1}{a}e^{-a\tau} \Big|_{k\Delta t}^{(k+1)\Delta t} \right) bu[k] \\ &= e^{a\Delta t}x[k] + \frac{1}{a}e^{a(k+1)\Delta t} \left(e^{-ak\Delta t} - e^{-a(k+1)\Delta t} \right) bu[k] \\ &= e^{a\Delta t}x[k] + \frac{1}{a} \left(e^{a\Delta t} - 1 \right) bu[k]. \end{aligned}$$

This is the generic discrete-time *ordinary difference equation* (ODE) that is equivalent to the continuous-time ordinary differential equation of

Eq. (2.6).^{7,8} To use this result in our battery-cell model, we note the correspondences between constants in Eqs. (2.5) and (2.6)

$$a = -\frac{1}{R_1 C_1} \quad \text{and} \quad b = \frac{1}{R_1 C_1},$$

and the correspondences between signals

$$x[k] = i_{R_1}[k] \quad \text{and} \quad u[k] = i[k].$$

Substituting these values into the generic result, we get the following discrete-time equation for the resistor current

$$\begin{aligned} i_{R_1}[k+1] &= \exp\left(-\frac{\Delta t}{R_1 C_1}\right) i_{R_1}[k] \\ &\quad + (-R_1 C_1) \left(\exp\left(-\frac{\Delta t}{R_1 C_1}\right) - 1\right) \left(\frac{1}{R_1 C_1}\right) i[k] \\ &= \exp\left(-\frac{\Delta t}{R_1 C_1}\right) i_{R_1}[k] + \left(1 - \exp\left(-\frac{\Delta t}{R_1 C_1}\right)\right) i[k]. \end{aligned}$$

Summarizing to date, the continuous-time model that describes the circuit in Fig. 2.6 is

$$\begin{aligned} \dot{z}(t) &= -\eta(t)i(t)/Q \\ \frac{di_{R_1}(t)}{dt} &= -\frac{1}{R_1 C_1}i_{R_1}(t) + \frac{1}{R_1 C_1}i(t) \\ v(t) &= \text{OCV}(z(t)) - R_1 i_{R_1}(t) - R_0 i(t). \end{aligned}$$

The discrete-time model that describes the circuit comprises the following three coupled equations:

$$\begin{aligned} z[k+1] &= z[k] - \frac{\Delta t}{Q} \eta[k] i[k] \\ i_{R_1}[k+1] &= \exp\left(-\frac{\Delta t}{R_1 C_1}\right) i_{R_1}[k] + \left(1 - \exp\left(-\frac{\Delta t}{R_1 C_1}\right)\right) i[k] \\ v[k] &= \text{OCV}(z[k]) - R_1 i_{R_1}[k] - R_0 i[k]. \end{aligned} \tag{2.8}$$

Finally, we note that a cell's diffusion-voltage response is generally a function of the cell's state of charge and its internal temperature. If R_1 and C_1 are modeled as functions of $z(t)$ and $T(t)$, the model predictions can be improved.

2.5 Rough parameter values

We have not yet finished developing the final version of the equivalent-circuit model of a lithium-ion cell. However, before proceeding, we spend a short time discussing how one might be able to discern parameter values for the unknown constants in the model equations.

⁷ Continuous-time *ordinary differential equations* and the discrete-time *ordinary difference equations* both have the acronym ODE. We reserve the use of ODE in this book to describe the discrete-time equations only.

⁸ This same basic procedure also works with vector signals, but the exponential operator in the solution is then the matrix exponential function, which is different from the scalar exponential function.

We give a more general procedure later on, but at this point we can introduce a simple method that helps us understand how the parameters of the equations describe cell responses.

In this section, we assume a model type of the sort developed to this point, having a single parallel resistor–capacitor subcircuit, exactly as drawn in Fig. 2.6. To identify the model parameters, we subject the cell to a constant-current discharge pulse and then allow the cell to rest while recording the cell’s voltage response (such as is shown in Fig. 2.7).

At the instant when the discharge current pulse is removed, at time 20 min, and considering Eq. (2.8), the instantaneous change in voltage must be equal to the instantaneous change in current multiplied by the series resistance R_0 because the capacitor voltage cannot change instantly, and state of charge is not changing when current is zero. This gives us $\Delta v_0 = R_0 \Delta i$ (with signs computed such that R_0 is positive). We know the change in current Δi because we controlled its value during the test, and we measure the change in voltage; therefore, we can compute the value $R_0 = |\Delta v_0 / \Delta i|$.

Then, we look at the steady-state change in voltage, which we can approximate by the value around time 60 min. The overall steady-state voltage change can be found from Eq. (2.8) to be $\Delta v_\infty = (R_0 + R_1) \Delta i$, again with signs computed so that R_0 and R_1 are both positive, knowing that the capacitor voltage will converge to zero in steady state. Since we know Δi (it’s the same as when we were computing R_0), we measure this new value of Δv , and as we have already computed R_0 , we can compute $R_1 = |\Delta v_\infty / \Delta i| - R_0$.

For the cell test conducted to gather the data plotted in Fig. 2.7, $\Delta i = 5 \text{ A}$, the change in voltage at time 20 min was $|\Delta v| = 41 \text{ mV}$, and the change in voltage at time 60 min was $|\Delta v| = 120 \text{ mV}$. From these values, we compute $R_0 \approx 8.2 \text{ m}\Omega$ and $R_1 \approx 15.8 \text{ m}\Omega$.

Finally, the pulse response converges to a value close to steady state in about four time constants of the R–C circuit, where the time constant of the exponential decay is $\tau = R_1 C_1$. In the example, the time to convergence is about $60 \text{ min} - 20 \text{ min} = 40 \text{ min} = 2,400 \text{ s}$. So, for this example, we might estimate

$$4\tau \approx 2,400 \text{ s} \quad \text{and} \quad C_1 \approx \frac{2,400}{4R_1}.$$

Using our prior result for R_1 , we can compute $C_1 \approx 38 \text{ kF}$.

This method is designed to give rough estimates of the parameters. Fine-tuning can be done using the approach described in Sec. 2.11. Further, if the model uses multiple parallel resistor–capacitor subcircuits, themselves connected in series, this simple approach will not work, and the method of Sec. 2.11 must be used instead.

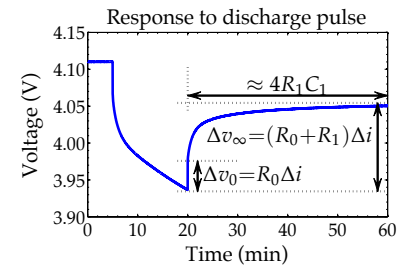


Figure 2.7: Measuring parameter values from a pulse response.

2.6 Warburg impedance

In the literature, it is not uncommon to see equivalent-circuit models containing a so-called *Warburg impedance* element. For example, the *Randles circuit* in Fig. 2.8 is a frequently seen equivalent-circuit model of a cell (less the open-circuit voltage) that is inspired by electrochemical principles, somewhat like we will see in later chapters.⁹

In the circuit, R_s models the electrolyte resistance, R_{ct} is the *charge-transfer resistance* that models the voltage drop over the electrode–electrolyte interface due to a load, C_{dl} is the *double-layer capacitance* that models the effect of charges building up in the electrolyte at the electrode surface, and Z_W is the Warburg impedance.

The Warburg impedance models diffusion of lithium ions in the electrodes. It is frequency dependent, modeled as $Z_W = A_W / \sqrt{j\omega}$, where the constant A_W is called the Warburg coefficient, $j = \sqrt{-1}$, and ω is the applied frequency in radians per second. The phase contributed to the circuit by this element is 45° , which is most easily observed in a *Nyquist plot* of a cell’s electrochemical impedance spectrum as a straight line at 45° at low frequency. Fig. 2.9 shows a simulated electrochemical impedance spectrum representing a realistic cell. The equivalent series resistance R_0 for this cell is on the order of $1.5 \text{ m}\Omega$, found by the intersection of the curve and the real axis; this point is the infinite-frequency impedance. The low-frequency impedance is represented by the straight line at 45° and models solid diffusion. At intermediate frequencies, the semicircular loop is dominated by charge-transfer dynamics, which are modeled in the equivalent circuit as a single resistor–capacitor pair.

There is no simple ordinary-differential equation for a Warburg impedance, which makes precise circuit simulation intractable. However, its effect can be approximated via multiple resistor–capacitor networks in series, as illustrated in Fig. 2.10.

⁹ Randles, J.E.B., “Kinetics of rapid electrode reactions,” *Discussions of the Faraday Society*, 1, 1947, pp. 11–19.

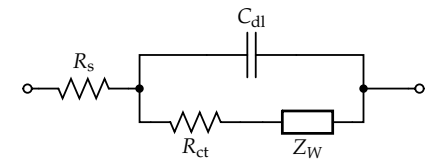


Figure 2.8: The Randles circuit.

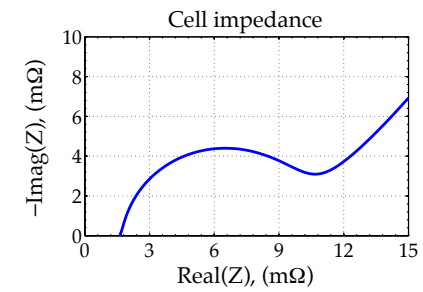
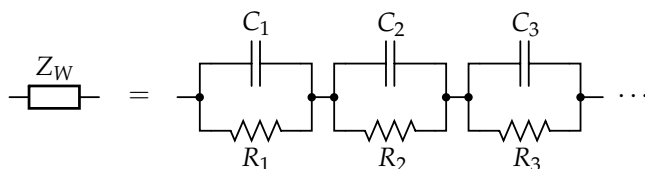


Figure 2.9: Nyquist plot of cell impedance.



For an exact equivalence, an infinite number of resistor–capacitor networks are needed; but, the circuit can often be modeled very well over some frequency range of interest using a small number of resistor–capacitor pairs. Also, since the double-layer capacitance has very little impact on the Randles circuit performance except at very high frequencies, it is often omitted. With the double-layer capacitor removed from the circuit, and with the Warburg impedance

Figure 2.10: Approximating a Warburg impedance with multiple resistor–capacitor subcircuits.

replaced by a small finite number of parallel resistor–capacitor circuits, themselves wired in series, the cell model collapses to the one in Fig. 2.6, with additional resistor–capacitor pairs.

When we discuss implementation of physics-based models, which have a Warburg-type impedance relationship built in intrinsically, we will see how to automatically create ordinary-difference equations that very accurately model the diffusion.

2.7 Hysteresis voltages

With the model we have developed so far, if the cell current is set to zero, the voltage drop across R_0 will immediately fall to zero, and the voltage drop across the capacitor C_1 will decay to zero over time as the capacitor discharges through R_1 . That is, the cell terminal voltage will converge to open-circuit voltage.

However, what we see in practice is different from this. The cell voltage decays to a value that is somewhat different from OCV, and the difference depends on the recent history of cell usage. For example, we find that if we discharge a cell to 50 % SOC and allow the cell to rest, the equilibrium voltage is lower than OCV. If we charge a cell to 50 % SOC and allow the cell to rest, the equilibrium voltage is higher than OCV. These observations indicate that there is hysteresis in the cell terminal voltage.

Fig. 2.11 shows data collected from a laboratory experiment designed to capture the nature of this hysteresis. The cell is first fully charged before the test begins. Then, the cell is very slowly discharged, at a C/30 rate, down to 0 % SOC. At this slow rate, the $i(t) \times R_0$ and diffusion voltages are very small, so the recorded voltage is very close to the equilibrium rest voltage of the cell. This voltage trace is the lowest line on the plot.

Then, the cell is very slowly charged, at a C/30 rate, to 95 % SOC; then the cell is discharged to 5 %, and so forth. Each point on the plot represents (at least approximately) an equilibrium point. Because of the space between the lower and upper curves, we discover that for every SOC there is a range of possible stable rest voltage values.

Vol. II in this book series addresses methods of estimating cell state of charge using equivalent-circuit cell models. To do this well, the cell model must be as accurate as possible. From the figure, we see that omitting hysteresis in our cell models can lead to large SOC estimation errors. For example, if we measure a fully rested terminal voltage of 3.3 V, that could correspond to any SOC between about 20 % and 90 %. We require a good model of hysteresis to know how different we expect the fully rested terminal voltage to be from open-circuit voltage.¹⁰

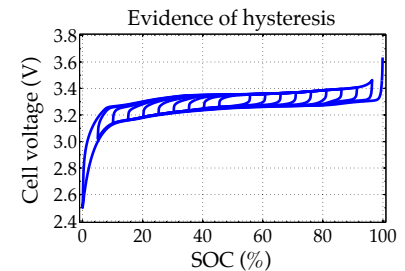


Figure 2.11: Cell test data giving evidence of hysteresis.

¹⁰ Note that this particular cell is a lithium-ion chemistry with an iron-phosphate positive electrode. The very flat OCV characteristics of this type of cell amplify the importance of a good hysteresis model. Other lithium-ion chemistries also exhibit hysteresis, but the higher slope to their OCV relationships dilutes the errors introduced by a poor hysteresis model.

NOTE THE DISTINCTION between hysteresis and diffusion voltages: diffusion voltages change with time but hysteresis voltages change only when SOC changes. They are not directly a function of time. If a cell is allowed to rest, diffusion voltages will decay to zero, but hysteresis voltages will not change at all. Any model of hysteresis must capture this behavior.

The challenge when modeling hysteresis is that it is not very well understood. A simple model jumps immediately from the lower to the upper branch of the plot in Fig. 2.11 when current changes from a discharge to a charge. A somewhat more advanced model changes hysteresis voltage linearly with a change in SOC. We introduce a combination of these two approaches here; however, the resulting model still struggles to explain hysteresis accurately.

2.7.1 SOC-varying hysteresis

Let $h(z, t)$ be the dynamic hysteresis voltage as a function of SOC and time, and let $\dot{z} = dz/dt$. Then, we model the change in hysteresis voltage as a function of change in SOC as

$$\frac{dh(z, t)}{dz} = \gamma \operatorname{sgn}(\dot{z}) (M(z, \dot{z}) - h(z, t)),$$

where $M(z, \dot{z})$ is a function that gives the maximum polarization due to hysteresis as a function of SOC and the rate-of-change of SOC. Specifically, we require that $M(z, \dot{z})$ be positive for charge ($\dot{z} > 0$) and negative for discharge ($\dot{z} < 0$). The $M(z, \dot{z}) - h(z, t)$ term in the differential equation states that the rate-of-change of hysteresis voltage is proportional to the distance of the present hysteresis value away from the major hysteresis loop, leading to a kind of exponential decay of voltage to the major loop. The term in front of this has a positive constant γ , which tunes the rate of decay, and $\operatorname{sgn}(\dot{z})$, which forces the equation to be stable both for charge and discharge.

To fit the differential equation for $h(z, t)$ into our model, we must manipulate it to be a differential equation with respect to time, not with respect to SOC. We accomplish this by multiplying both sides of the equation by dz/dt .

$$\frac{dh(z, t)}{dz} \frac{dz}{dt} = \gamma \operatorname{sgn}(\dot{z}) (M(z, \dot{z}) - h(z, t)) \frac{dz}{dt}.$$

We use the chain rule to write the left-hand side of the equation as $dh(z, t)/dt$, and we substitute $dz/dt = -\eta(t)i(t)/Q$ into the right-hand side, noting that $\dot{z} \operatorname{sgn}(\dot{z}) = |\dot{z}|$. Thus,

$$\dot{h}(t) = - \left| \frac{\eta(t)i(t)\gamma}{Q} \right| h(t) + \left| \frac{\eta(t)i(t)\gamma}{Q} \right| M(z, \dot{z}).$$

This may be converted into a difference equation for our discrete-time application using the technique from Sec. 2.4 (assuming that $i(t)$ and $M(z, \dot{z})$ are constant over the sample period):

$$\begin{aligned} h[k+1] &= \exp\left(-\left|\frac{\eta[k]i[k]\gamma\Delta t}{Q}\right|\right)h[k] \\ &\quad + \left(1 - \exp\left(-\left|\frac{\eta[k]i[k]\gamma\Delta t}{Q}\right|\right)\right)M(z, \dot{z}). \end{aligned}$$

Note that this is a nonlinear time-varying system as the factors multiplying the state and input change with $i[k]$.

The simplest representation is when $M(z, \dot{z}) = -M \operatorname{sgn}(i[k])$, when

$$\begin{aligned} h[k+1] &= \exp\left(-\left|\frac{\eta[k]i[k]\gamma\Delta t}{Q}\right|\right)h[k] \\ &\quad - \left(1 - \exp\left(-\left|\frac{\eta[k]i[k]\gamma\Delta t}{Q}\right|\right)\right)M \operatorname{sgn}(i[k]). \end{aligned}$$

With this representation $-M \leq h[k] \leq M$ at all times, and $h[k]$ has units of volts. When attempting to find the model parameters, we will find it valuable to rewrite this in an equivalent but slightly different representation, which has unitless hysteresis state $-1 \leq h[k] \leq 1$,

$$\begin{aligned} h[k+1] &= \exp\left(-\left|\frac{\eta[k]i[k]\gamma\Delta t}{Q}\right|\right)h[k] \\ &\quad - \left(1 - \exp\left(-\left|\frac{\eta[k]i[k]\gamma\Delta t}{Q}\right|\right)\right) \operatorname{sgn}(i[k]) \end{aligned}$$

Hysteresis voltage = $Mh[k]$.

This makes the output equation linear in M , which will make estimating M from lab-test data easier.

2.7.2 Instantaneous hysteresis

In addition to the type of dynamic hysteresis that changes as SOC changes, we also often see benefit in modeling an instantaneous change in hysteresis voltage when the sign of current changes. Define

$$s[k] = \begin{cases} \operatorname{sgn}(i[k]), & |i[k]| > 0; \\ s[k-1], & \text{otherwise.} \end{cases}$$

Then, the instantaneous hysteresis is modeled as

$$\text{Instantaneous hysteresis voltage} = M_0s[k],$$

and overall hysteresis is

$$\text{Hysteresis voltage} = M_0s[k] + Mh[k].$$

2.8 Enhanced self-correcting cell model

The *enhanced self-correcting* (ESC) cell model combines all the aforementioned elements. The model is called *enhanced* because it includes a description of hysteresis, unlike some earlier models. The model is called *self-correcting* because the model's predicted terminal voltage converges to OCV plus hysteresis when the cell rests, and converges to OCV plus hysteresis minus all the current times resistance terms on a constant-current event. The final circuit diagram for this model is shown in Fig. 2.12.

The figure shows an example with a single parallel resistor-capacitor pair, but the model easily accommodates multiple parallel resistor-capacitor pairs. To compact notation, define a resistor-capacitor subcircuit rate factor $F_j = \exp\left(\frac{-\Delta t}{R_j C_j}\right)$, and we have

$$i_R[k+1] = \underbrace{\begin{bmatrix} F_1 & 0 & \dots \\ 0 & F_2 & \\ \vdots & & \ddots \end{bmatrix}}_{A_{RC}} i_R[k] + \underbrace{\begin{bmatrix} (1-F_1) \\ (1-F_2) \\ \vdots \end{bmatrix}}_{B_{RC}} i[k].$$

Then, if we define $A_H[k] = \exp\left(-\left|\frac{\eta[k]i[k]\gamma\Delta t}{Q}\right|\right)$, we have the dynamic aspects of the model described by the matrix-vector relationship

$$\begin{bmatrix} z[k+1] \\ i_R[k+1] \\ h[k+1] \end{bmatrix} = \begin{bmatrix} 1 & 0 & 0 \\ 0 & A_{RC} & 0 \\ 0 & 0 & A_H[k] \end{bmatrix} \begin{bmatrix} z[k] \\ i_R[k] \\ h[k] \end{bmatrix} + \begin{bmatrix} -\frac{\eta[k]\Delta t}{Q} & 0 \\ B_{RC} & 0 \\ 0 & (A_H[k] - 1) \end{bmatrix} \begin{bmatrix} i[k] \\ \text{sgn}(i[k]) \end{bmatrix}.$$

This is the ESC model *state equation*. The model's *output equation* is

$$v[k] = \text{OCV}(z[k], T[k]) + M_0 s[k] + M h[k] - \sum_j R_j i_{R_j}[k] - R_0 i[k].$$

The ESC model comprises these two equations with associated parameter values filled in. Note that all model parameters must be nonnegative.

2.9 Laboratory equipment for cell-data collection

Parameter values for the ESC model are found by fitting the model equations to data collected from experiments performed on the cells of interest. These experiments are conducted with the aid of specially designed laboratory equipment known as *battery-cell cyclers*

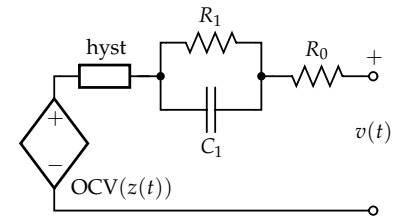


Figure 2.12: The enhanced self-correcting cell model equivalent circuit.



Figure 2.13: Sample cell-test equipment.

or *battery-cell test equipment*. An example cell cycler, manufactured by Arbin Instruments and resident in the University of Colorado Colorado Springs' High-Capacity Battery Research and Test Laboratory, is shown in Fig. 2.13. This particular cycler can perform independent experiments on up to 12 different cells simultaneously, controlling each cell's current according to a user-specified profile of demanded current versus time and recording actual cell current, voltage, and temperature. Each of the 10 thick white cables shown in the figure corresponds to a single *test channel*—the power electronics designed to conduct an independent test. Each cable contains four wires internally (two to carry current and two to measure voltage via a *Kelvin connection*) and can be connected to a single 0 V to 5 V cell, commanding current up to ± 20 A per test channel. The thinner white cables are connected to *thermistors* to measure cell temperature. The two pairs of thick black cables correspond to two high-current test channels, capable of commanding current up to ± 200 A each. Test channels may be connected in parallel if more current is needed than can be supplied or sunk from a single channel.

Battery-cell test equipment is generally custom designed to the user's specifications, so the cycler shown in Fig. 2.13 is discussed as a representative example only. Systems can be configured with more or fewer independent test channels, higher or lower maximum current, specialized measurement circuitry for three-terminal cells or for impedance-spectroscopy measurements, and more.

In addition, most tests must be conducted in controlled temperature settings. Fig. 2.14 shows an *environmental chamber* manufactured by Cincinnati Sub-Zero. This particular unit has 8 ft³ of interior space and is capable of maintaining constant temperatures between -45°C and 190°C and commanding profiles of temperature versus time. Systems can be configured with humidity control, wider temperature ranges, rapid cooling for thermal-shock testing, and more.

2.10 Lab tests to determine OCV relationship

A cell's open-circuit voltage is a static function of its state of charge and temperature. All other aspects of a cell's performance are dynamic in some sense. So, we perform separate experiments to collect data for the OCV versus SOC relationship and for the dynamic relationship. We first discuss experiments to determine the OCV relationship.

The general idea is straightforward. Before the cell test begins, the cell must be fully charged. Then, the cell is very slowly discharged to a minimum operating voltage while continuously measuring cell voltage and accumulated ampere-hours discharged. The cell is then very



Figure 2.14: Sample environmental chamber.

slowly charged to a maximum operating voltage while continuously measuring cell voltage and accumulated ampere-hours charged.

The purpose of the slow rate is to minimize the excitation of the dynamic parts of the cell model. We desire to keep the cell in a quasi-equilibrium state at all times. So, we generally use a C/30 rate, which is a compromise between the desire to have zero current to have a true equilibrium and the practical realization that the test will already require on the order of 60 h to complete with a C/30 discharge followed by a C/30 charge.

The collected data allow us to create a curve of “discharge OCV” versus discharge ampere-hours and a curve of “charge OCV” versus charge ampere-hours. With appropriate conversion between ampere-hours and state of charge, we then have discharge OCV and charge OCV versus SOC. These curves are different because (1) the test is not conducted at zero current, so there will still be some ohmic and diffusion polarization, and (2) hysteresis is present in the cell voltage response. We assume that the deviation from true OCV to the discharge OCV and charge OCV curves is equal in magnitude, so we approximate the cell’s true OCV as the average of these two values.

When multiple temperatures are considered, there are some important subtle issues that must be addressed, which somewhat modifies how we collect and process data. The first is that the initial step of fully charging a cell is generally defined by a process that is valid only at a specific temperature. Often, the manufacturer will state that the cell must be charged at 25 °C (i.e., “room temperature”) at a specific constant-current rate (e.g., 1C) until a particular voltage v_{\max} is reached. Then, the cell must be held at v_{\max} until the charging current drops below some threshold (e.g., C/30).

So, to charge a cell, we first soak the cell at 25 °C for at least 2 h to ensure a uniform temperature throughout the cell. We then charge the cell according to manufacturer specifications, using a cutoff current of C/30. The cell is now at 100 % state of charge at 25 °C. Then we run experiments at a number of temperatures spread over the operational range of the cell. These experiments are divided into four subexperiments, which we denote as *test scripts* (as different test programs or *scripts* must be implemented at different points in the overall experiment).

OCV test script #1 (at test temperature)

1. Soak the fully charged cell at the test temperature for at least 2 h to ensure a uniform temperature throughout the cell.
2. Discharge the cell at a constant-current rate of C/30 until cell terminal voltage equals manufacturer-specified v_{\min} .

OCV test script #2 (at 25 °C)

3. Soak the cell at 25 °C for at least 2 h to ensure a uniform temperature throughout the cell.
4. If the cell voltage is below v_{\min} , then charge the cell at a C/30 rate until the voltage is equal to v_{\min} . If the cell voltage is above v_{\min} , then discharge the cell at a C/30 rate until the voltage is equal to v_{\min} .

OCV test script #3 (at test temperature)

5. Soak the cell at the test temperature for at least 2 h to ensure a uniform temperature throughout the cell.
6. Charge the cell at a constant-current rate of C/30 until the cell terminal voltage equals v_{\max} .

OCV test script #4 (at 25 °C)

7. Soak the cell at 25 °C for at least 2 h to ensure a uniform temperature throughout the cell.
8. If the cell voltage is below v_{\max} , then charge the cell at a C/30 rate until the voltage is equal to v_{\max} . If the cell voltage is above v_{\max} , then discharge the cell at a C/30 rate until the voltage is equal to v_{\max} .

Voltage, accumulated ampere-hours discharged, and accumulated ampere-hours charged are recorded periodically (e.g., once per second) during every step. Because a very low current rate is used, there is negligible heat generation in the cell, and we can consider all data-points to be collected at the ambient test temperature for every script (though temperature data can be measured as well to verify this assumption).

Sample measured data from test scripts 1 and 3 for a lithium-ion cell having a lithium-manganese-oxide positive electrode are plotted in Fig. 2.15. These data were collected at -15°C , where the cell has a very high resistance. This resistance causes a significant ohmic voltage drop, so cutoff voltages are achieved at the end of test scripts 1 and 3 far before the cell is fully discharged or charged, respectively (which is why these tests lasted for less than 30 hours although a C/30 rate was used). The data processing methods must take this into account.

There are some subtle points if the test temperature is not 25 °C. Before step 2, the cell is still at 100 % state of charge, but its voltage will no longer be equal to v_{\max} because OCV is temperature dependent. At the end of step 2, the cell will be at 0 % state of charge *only*

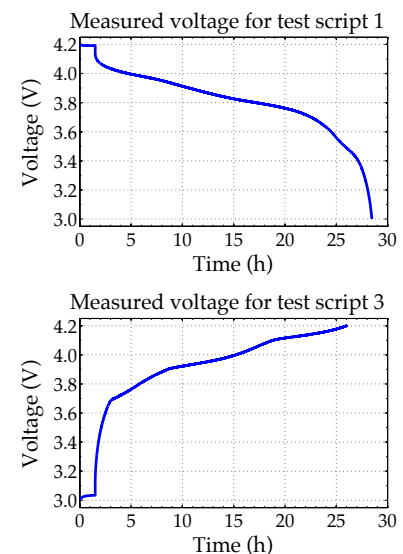


Figure 2.15: Unprocessed voltage data from slow-discharge and slow-charge test, used to determine OCV.

if the test temperature is 25 °C because, again, OCV is temperature dependent, and the v_{\min} specification defines 0 % SOC only for 25 °C. At other temperatures, the actual state of charge may be above or below 0 % at the end of step 2. Similarly, at the end of step 6, the cell will be at 100 % state of charge *only* if the test temperature is 25 °C. At other temperatures, the actual state of charge may be above or below 100 % at the end of step 6. This is why we must execute test scripts 2 and 4, to ensure that the cell is fully discharged and charged, respectively, before starting test scripts 3 and 1 (for the next temperature to be tested).

2.10.1 Determining coulombic efficiency

These factors impose a requirement that data must be very carefully processed. Let's consider processing data for test temperature equal to 25 °C first. This is the easiest case because all four scripts are then executed at 25 °C—no other temperatures are involved. And, because voltages v_{\max} and v_{\min} are calibrated to 25 °C, the net ampere-hours discharged over all steps is equal to the total capacity Q of the cell.

The net number of ampere-hours charged over all steps turns out to be slightly higher than Q since the coulombic efficiency of the cell is not perfect. We compute the coulombic efficiency at 25 °C as

$$\eta(25^\circ\text{C}) = \frac{\text{total ampere-hours discharged in all steps at } 25^\circ\text{C}}{\text{total ampere-hours charged in all steps at } 25^\circ\text{C}}.$$

At a test temperature T different from 25 °C, we must follow a somewhat different approach. We don't know *a priori* the cell state of charge at the end of steps 2 and 6. However, we do know that the cell is at 0 % SOC at the end of step 4 and is 100 % at the end of step 8. We use this information to compute first the coulombic efficiency at test temperature T :

$$\begin{aligned} \eta(T) = & \frac{\text{total ampere-hours discharged}}{\text{total ampere-hours charged at temperature } T} \\ & - \eta(25^\circ\text{C}) \frac{\text{total ampere-hours charged at } 25^\circ\text{C}}{\text{total ampere-hours charged at temperature } T}. \end{aligned}$$

Fig. 2.16 shows coulombic efficiency calculations for six different lithium-ion cells as a function of temperature. The efficiency *should* always be less than 1, but experimental accuracy of accumulated ampere-hours is inexact, and these calculations are reasonable, within experimental error. The figure shows that the quality of manufacture of different lithium-ion cells is by no means the same—some have efficiencies consistently above 99.5 %, while others have efficiencies as low as 98 %.

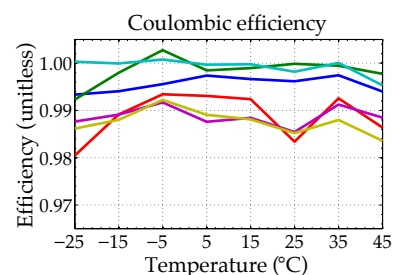


Figure 2.16: Sample coulombic efficiencies for six different lithium-ion cells.

2.10.2 Determining charge and discharge voltage versus SOC

Now, we can compute a state of charge corresponding to every data sample in every test. The depth of discharge (in ampere-hours) at every point in time is calculated as

$$\begin{aligned} \text{depth of discharge}(t) = & \\ & \text{total ampere-hours discharged until } t \\ & - \eta(25^\circ\text{C}) \times \text{total ampere-hours charged at } 25^\circ\text{C until } t \\ & - \eta(T) \times \text{total ampere-hours charged at temperature } T \text{ until } t. \end{aligned}$$

Using this metric, the cell capacity Q (measured at temperature T) is equal to the depth-of-discharge at the end of step 4. Likewise, the state of charge corresponding to every data sample is then

$$\text{state of charge}(t) = 1 - \frac{\text{depth of discharge}(t)}{Q}.$$

As a check, the state of charge at the end of step 4 must be 0 %, and the state of charge at the end of step 8 must be 100 %.

Fig. 2.17 plots discharge voltage from step 2 versus state of charge (lower solid curve) and charge voltage from step 6 versus state of charge (upper solid curve). These are the same data as shown in Fig. 2.15, but are now presented as functions of state of charge rather than test time. This example shows that there is a challenge in determining the open-circuit-voltage relationship at all states of charge; namely, we don't have discharge voltages at low states of charge because the test encountered a cutoff voltage of v_{\min} in step 2 before 0 % state of charge was reached, and we don't have charge voltages at high states of charge because the test encountered a cutoff voltage of v_{\max} in step 6 before 100 % state of charge was reached.

2.10.3 Determining approximate OCV at one temperature

There are perhaps many ways to use the available data to produce an approximate open-circuit-voltage relationship, but here we present one that has worked well for a number of different cells of different lithium-ion chemistries. First, we note that we are forced to base the open-circuit-voltage estimate on the discharge-voltage curve at high states of charge simply because there is no charge voltage information available. Similarly, we are forced to base it on the charge-voltage curve at low states of charge because there is no discharge-voltage information available. At intermediate states of charge, we could use both curves, but there should be no abrupt transitions because neither the discharge- nor charge-voltage curves have sharp transitions.

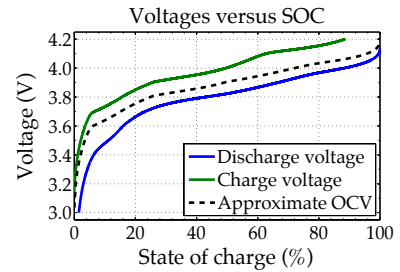


Figure 2.17: Unprocessed voltage data from slow-discharge and slow-charge test, used to determine OCV.

We can estimate the cell's ohmic resistance R_0 at high state of charge by looking at the instantaneous voltage change when the test moves from step 1 to step 2. We can similarly estimate the ohmic resistance at low state of charge by looking at the voltage change when the test moves from step 5 to step 6. Also, we can approximate the steady-state resistance at 50 % state of charge by considering the voltage change between the discharge voltage curve and the charge voltage curve at the 50 % state of charge point.

Then, suppose that we assume that the resistance changes linearly from its 0 % state of charge value to its 50 % state of charge value, and then linearly again from its 50 % state of charge value to its 100 % state of charge value. At states of charge lower than 50 %, the approximate open-circuit voltage is estimated as the charge voltage plus charge current times resistance at that state of charge, and at states of charge higher than 50 %, the approximate open-circuit voltage is estimated as the discharge voltage plus discharge current times resistance at that state of charge.

Fig. 2.17 shows this approximate open-circuit-voltage estimate as a dashed line. It is between the charge and discharge voltages, as it should be, and it also passes through a point exactly in the middle of these curves at 50 % state of charge, by design. Note that the curves in the figure are more widely separated than we would see at warmer temperatures, because cell resistance is much higher at cold temperatures, so the effects are more exaggerated than typical.

2.10.4 Determining final open-circuit-voltage relationship

Once we have an approximate open-circuit-voltage relationship at every test temperature, we further process these results to make a final model of the form

$$\text{OCV}(z(t), T(t)) = \text{OCV0}(z(t)) + T(t) \times \text{OCVrel}(z(t)),$$

where $\text{OCV}(z(t), T(t))$ is the open-circuit-voltage relationship as a function of present state of charge and temperature, $\text{OCV0}(z(t))$ is the open-circuit-voltage relationship at 0°C , and $\text{OCVrel}(z(t))$ ($\text{V}/^\circ\text{C}$) is the linear temperature-correction factor at each state of charge. Once $\text{OCV0}(z(t))$ and $\text{OCVrel}(z(t))$ are determined, $\text{OCV}(z(t), T(t))$ can be computed via two one-dimensional table lookups, which is very efficient computationally.

To make $OCV0(z(t))$ and $OCVrel(z(t))$, note that we can write

$$\underbrace{\begin{bmatrix} \text{Approx. OCV at SOC } z, \text{ temp. } T_1 \\ \text{Approx. OCV at SOC } z, \text{ temp. } T_2 \\ \vdots \\ \text{Approx. OCV at SOC } z, \text{ temp. } T_n \end{bmatrix}}_Y = \underbrace{\begin{bmatrix} 1 & T_1 \\ 1 & T_2 \\ \vdots & \vdots \\ 1 & T_n \end{bmatrix}}_A \underbrace{\begin{bmatrix} OCV0(z) \\ OCVrel(z) \end{bmatrix}}_X$$

at every state of charge z . We have already computed all values in Y and in A ; it remains only to determine the values in X . One way to do so is to use the least-squares solution, which is written mathematically as

$$X = A^\dagger Y,$$

where the dagger symbol (\dagger) represents a matrix pseudo-inverse and is computed in MATLAB as

```
X=A\Y;
```

We find that the approximate open-circuit-voltage relationships are more reliable for temperatures above about 0°C , so we tend to include only data from those temperatures in the calculation of $OCV0(z)$ and $OCVrel(z)$.

Fig. 2.18 plots the outcome of this overall process for six different lithium-ion cells. The top frame shows the $OCV0(z)$ relationship, and the bottom frame shows the $OCVrel(z)$ relationship. We can see that different choices in the active materials of the cells can produce significantly different OCV curves. The two lower-voltage cells have positive electrodes made from lithium-iron-phosphate (LFP); the higher-voltage cells have positive electrodes that are made from different combinations of lithium-manganese-oxide (LMO), lithium-cobalt-oxide (LCO), and lithium nickel-manganese-cobalt oxide (NMC). The negative electrodes of these cells are different mixtures of synthetic and natural graphites.

2.10.5 Modification to minimize impact of hysteresis

The procedure for collecting and analyzing data given so far can produce very accurate open-circuit-voltage curves. However, it does not take into account the fact that we know that voltage hysteresis exists. Therefore, unless hysteresis voltage is canceled somehow, the state of charge at the end of step 2 will not be exactly 0 %, and the state of charge at the end of step 6 will not be exactly 100 %.

While the mechanism of hysteresis is not well understood (and is probably different for different lithium-ion electrode chemistries), we find that a modification to the above testing methodology based on analogy to magnetic hysteresis seems to work to eliminate hysteresis

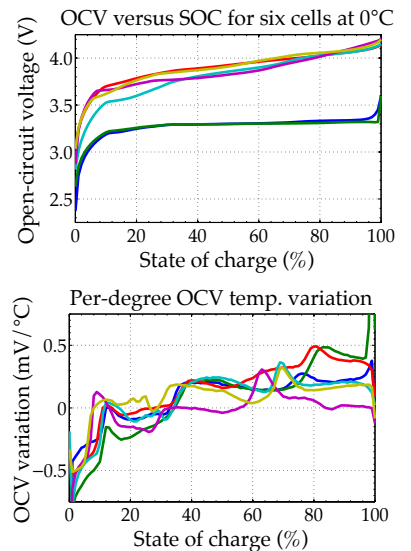


Figure 2.18: Final OCV relationships for six lithium-ion cells having different internal chemistries, stored as two table-lookup functions each.

voltage to a large degree. When a magnetic material is subjected to a frequency sweep, it tends to become demagnetized as its hysteresis profile follows a collapsing spiral to zero. Similarly, we propose, when the hysteretic phenomena in a lithium-ion cell is subjected to a frequency sweep, the hysteresis voltage is reduced or eliminated.

Fig. 2.19 shows a sample frequency sweep around $v_{\min} = 3$ V that could be executed at the end of step 4 to ensure that the cell was fully discharged before beginning step 5. A similar frequency sweep could be executed around v_{\max} at the end of step 8 before beginning the next test at step 1.

This frequency sweep is sometimes called a *chirp* signal in signal-processing literature and a *dither* signal in control-systems literature. It must have low-enough amplitude such that no damage is caused to the cell by slightly exceeding the cell's prescribed voltage limits. It may also be necessary to execute multiple iterations of this profile to achieve the desired state of charge. The rest voltage must stabilize very close to the desired voltage (e.g., to within about a millivolt) when the profile is complete. (All the prior examples included this dither approach in the test procedures.)

2.10.6 Illustrating difference between discharge and total capacity

Before leaving this section, we briefly discuss different measures of capacity. Fig. 2.20 shows three different measures of capacity for the six cells illustrated in this chapter. The blue solid lines show discharge capacity at the C/30 rate for the six cells, normalized by dividing by the cell's mean total capacity estimate Q . This is equal to the normalized number of ampere-hours discharged in step 2 and is not equal to the total capacity of the cell as additional ampere-hours are discharged in step 4. The green dashed lines show the normalized charge capacity at the C/30 rate for the six cells. This is equal to the normalized number of ampere-hours charged in step 6. This is not equal to the total capacity of the cell as additional ampere-hours are charged in step 8. Note that because cell resistance is a function of temperature, the discharge and charge capacities are also functions of temperature.

Total capacity is shown as the six red lines in the figure. Total capacity Q is calculated as the net ampere-hours discharged in steps 2 and 4. We see that (to within experimental error) total capacity is not a function of temperature. We point out this distinction since most cell data sheets will give discharge capacity at different discharge rates, but will not give total capacity; however, the ESC model requires total capacity Q .

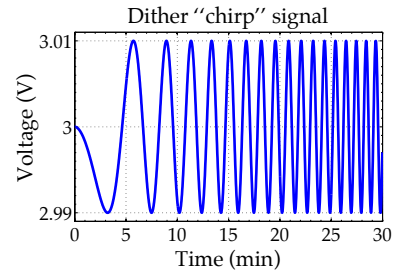


Figure 2.19: Sample frequency sweep around v_{\min} appended to step 4.

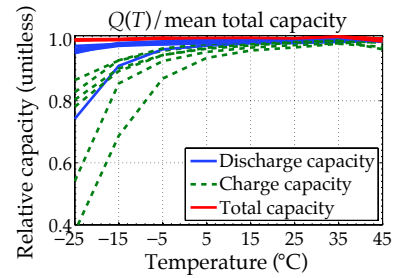


Figure 2.20: Illustrating different measures of capacity.

2.11 Lab tests to determine dynamic relationship

Now that we have determined the cell's OCV relationship, we turn our attention to finding the parameters of the dynamic parts of the ESC cell model. Different cell tests are performed to collect data to be used to determine these dynamic parameters. The cell must be exercised with profiles of current versus time that are representative of the final application for the resulting model to work best in that application. Fig. 2.21 shows a sample normalized profile for an automotive application: the urban dynamometer drive schedule (UDDS) profile. In practice, this profile is multiplied by the C-rate of the cell to convert to current in amperes.

Before any dynamic testing, the cell is first fully charged until it is at 100 % state of charge at 25 °C. Then we run experiments at a number of temperatures spread over the operational range of the cell. These experiments are divided into three subexperiments, which we denote as *test scripts* (as different test programs or *scripts* must be implemented at different points in the overall experiment).

Dynamic test script #1 (at test temperature)

1. Soak the fully charged cell at the test temperature for at least 2 h to ensure a uniform temperature throughout the cell.
2. Discharge the cell using a constant current at a C/1 rate long enough to deplete about 10 % of capacity (helping ensure we avoid over-voltage conditions during random charging portions of the dynamic profile).
3. Execute dynamic profiles over the SOC range of interest, nominally from 90 % SOC down to 10 % SOC.

Dynamic test script #2 (at 25 °C)

4. Soak the cell at 25 °C for at least 2 h to ensure a uniform temperature throughout the cell.
5. If the cell voltage is below v_{\min} , then charge the cell at a C/30 rate until the voltage is equal to v_{\min} . If the cell voltage is above v_{\min} , then discharge the cell at a C/30 rate until the voltage is equal to v_{\min} . Follow-on dither profile(s) can be used to eliminate hysteresis to the greatest degree possible.

Dynamic test script #3 (at 25 °C)

6. Charge the cell using a constant current at a C/1 rate until voltage is equal to v_{\max} . Then, maintain voltage constant at

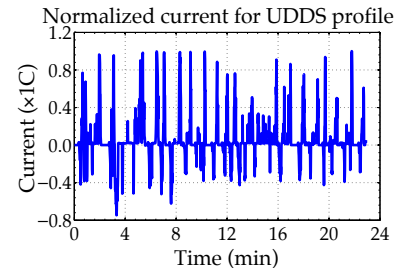


Figure 2.21: Profile of current versus time, representative of a UDDS cycle normalized for a passenger vehicle.

v_{\max} until current drops below $C/30$. Follow-on dither profile(s) at the end can be used to help eliminate hysteresis.

Voltage, current, temperature, ampere-hours charged, and ampere-hours discharged are recorded every second. These data are used to identify all ESC-model parameters, except for the OCV versus SOC relationship, which has already been described.

Sample output from this process is shown in Fig. 2.22. The top plot displays voltage versus time for 19 repetitions of the UDDS profile (with rests in between). The second plot shows a zoom on to one of those profiles. The third plot shows the output from test script 2 (with six repetitions of a dither profile), and the bottom plot shows the output from test script 3 (with six repetitions of a dither profile).

With these data, we wish to find parameter values for cell capacity Q , coulombic efficiency η , hysteresis rate constant γ , hysteresis parameters M_0 and M , equivalent-series resistance R_0 , and resistor-capacitor values for one or more parallel resistor-capacitor subcircuits. Most of these parameters cannot be computed directly from the measured data; instead, the parameter values must be found using some kind of optimization approach. This process, in general, is known as *system identification*.

The basic idea is to (1) choose a set of parameter values, somehow; (2) simulate the ESC model having those parameter values with the same input current as was measured during the cell test; (3) compare the ESC model voltage prediction to the measured voltage profile; and (4) intelligently modify the parameter values to improve the model prediction, going back to (2) until optimization is considered complete.

2.11.1 Simulink design optimization

One approach to this optimization is to use a commercial optimization toolbox, and one such example is the MathWorks' Simulink Design Optimization toolbox.¹¹ To use this automated approach, one must first create a block diagram to implement the model equations. Fig. 2.23 shows subsystems that compute the ESC-model state and output equations, assuming two parallel resistor-capacitor circuits, $\eta = 1$, $\gamma = 3600$, and $M_0 = 0$ (different block diagrams could be generated for different assumptions).

The toolbox automatically generates values for the cell capacity, resistor-capacitor time constants, the resistor values, and the maximum hysteresis value, then runs the model to see how well the voltage predictions agree with measured data, updates the parameter estimates, and iterates until it converges on a solution.

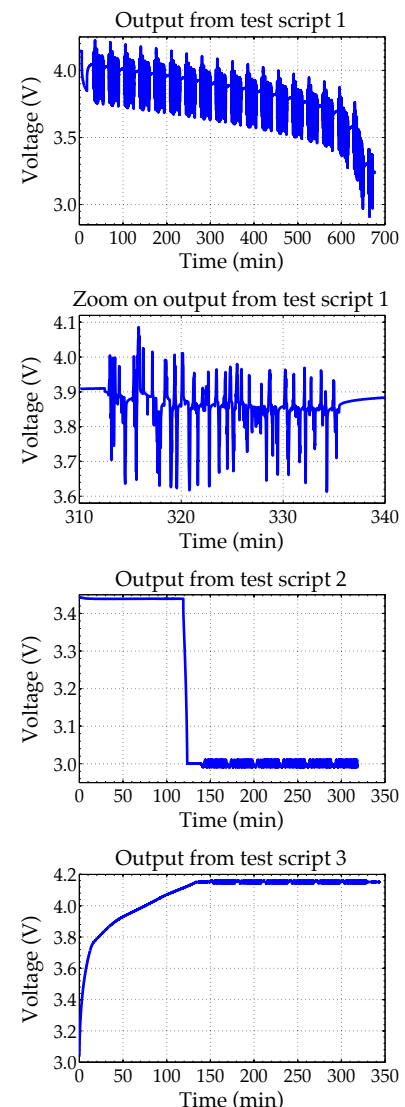


Figure 2.22: Dynamic test data.

¹¹ Jackey, R., Plett, G.L., and Klein, M., "Parameterization of a Battery Simulation Model Using Numerical Optimization Methods," in CD-ROM Proc. SAE World Congress 2009, Detroit, MI (April 2009).

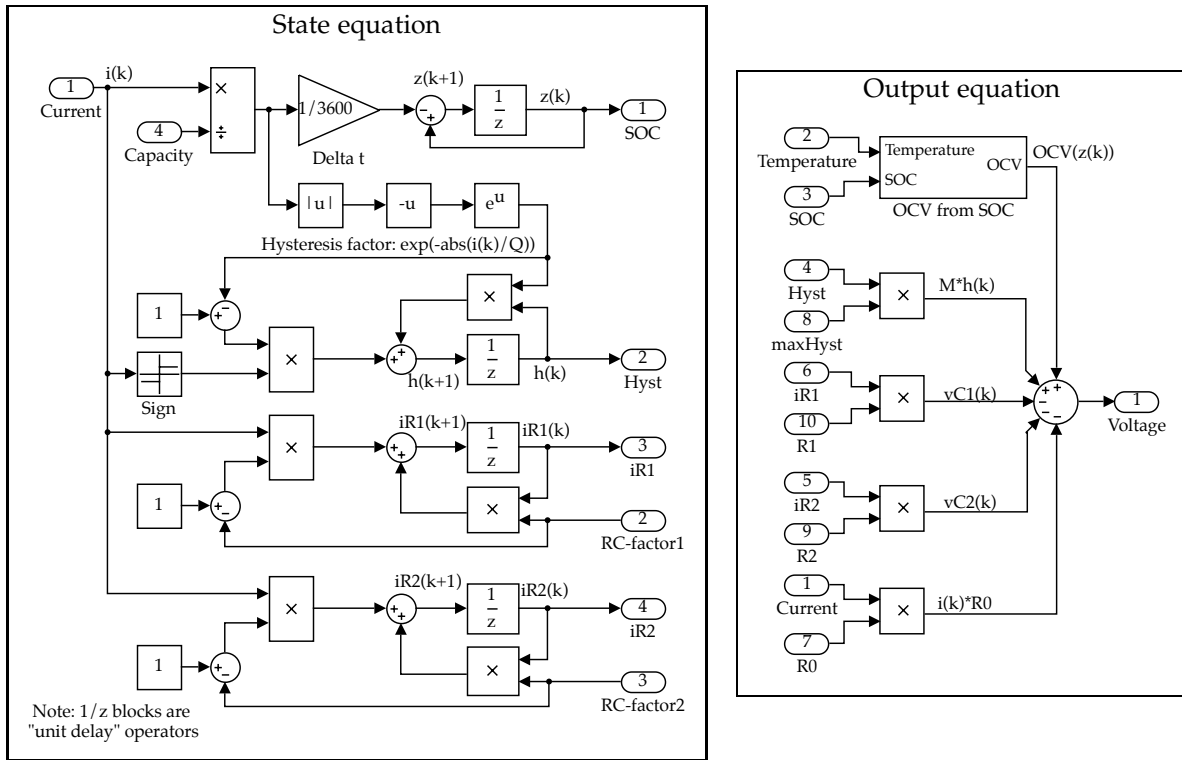


Figure 2.23: Simulink implementation of ESC model.

Nonlinear system identification—such as is implemented in the Simulink Design Optimization toolbox—is very powerful, but must be used with a great deal of care. There is no guarantee of arriving at the “globally optimal” solution; instead, the final parameter values may instead be only “locally optimal.” That is, small modifications to the parameter values will not result in a better match between measured and predicted voltage; however, large modifications may. Therefore, it is important to initialize the optimization with parameter values that are already quite good.

This is tricky—how do we find good initial guesses for the parameter values? The next sections give some guidance, which may in fact give the final answers that are wanted. Refinement is always possible using nonlinear optimization.

2.11.2 Direct measurement of capacity

One maxim of system identification is “Don’t estimate what you already know.” This is in part an efficiency concern: for every new parameter that must be estimated, computation increases. It is also an accuracy concern: system identification tries to match a model to an input–output dataset, but cannot guarantee that the internal states of the model make sense. If you know the actual value of a

parameter, you can remove the parameter from the list of those being estimated, speeding the process and ensuring that at least that one parameter value is accurate.

For the dynamic tests, cell coulombic efficiency and capacity can be computed using the same approach as in Sects. 2.10.1 and 2.10.2, recognizing that the dynamic tests also all start at 100 % SOC and end at 0 % SOC after the completion of test script 2. This eliminates two variables from the list of unknown parameters, simplifying the remaining computations.

2.11.3 Direct computation of resistor–capacitor time constants

Once the cell coulombic efficiencies and capacity are known, the cell state of charge can be computed for every point in time using Eq. (2.4). Then, the cell open-circuit voltage for every point can be computed, which leaves the following unexplained part of the measured cell voltage

$$\begin{aligned}\tilde{v}[k] &= v[k] - \text{OCV}(z[k], T[k]) \\ &= Mh[k] + M_0s[k] - \sum_j R_j i_{R_j}[k] - R_0 i[k].\end{aligned}\quad (2.9)$$

Note that we can compute $s[k]$ directly from the current profile. To compute $h[k]$ we also require γ ; for now, we assume that we know γ and will find a way to optimize its value later. Then, the unexplained part of the voltage is a linear-time-invariant system with input signals $h[k]$, $s[k]$, and $i[k]$, and methods exist to find the remaining parameters.

The trickiest part is in determining the time constants of the resistor–capacitor circuits. A method called *subspace system identification* is able to do so using only linear algebra techniques, which are very fast and have a unique solution.¹² It is beyond our scope to detail these methods here. However, we do note that there is code on the MathWorks web site that implements what we need.¹³

2.11.4 Direct computation of M , M_0 , R_0 , and R_j

Once we know these time constants, we can compute $i_{R_j}[k]$. Then, Eq. (2.9) becomes linear in the parameters. That is, we can assemble matrix

$$\underbrace{[\tilde{v}[k]]}_Y = \underbrace{\begin{bmatrix} h[k] & s[k] & -i[k] & -i_{R_j}[k] \end{bmatrix}}_A \underbrace{\begin{bmatrix} M \\ M_0 \\ R_0 \\ R_j \end{bmatrix}}_X.$$

¹² van Overschee, P., and De Moor, B., *Subspace Identification for Linear Systems—Theory, Implementation, Applications*, Springer (softcover reprint of the original 1st ed. 1996 edition), 2011.

¹³ Specifically, the function `subid.m` in “Subspace Identification for Linear Systems” toolbox on MATLAB CENTRAL file exchange, by P. Van Overschee, 1995.

Then, we can find the unknown parameter vector via least-squares solution $\mathbf{X} = \mathbf{A}^\dagger \mathbf{Y}$.

2.11.5 Optimization of γ

The only parameter we haven't actually computed from the data is the hysteresis rate constant γ . In Sec. 2.11.3, we assumed that this value was known, but in fact it is not. What we can do is to bound γ in some range, and then compute the goodness of fit for the models optimized to every γ in that range, keeping only the model that yields the best goodness of fit. Fig. 2.24 shows an example of the root-mean-squared modeling error resulting from different trial values of γ for one particular cell test. The data in this figure were determined by trying values of γ from 1 to 250, then optimizing all other model parameters based on that value of γ , and then computing the modeling error. In this case, a value of $\gamma \approx 90$ gives the best modeling results overall.

Because of the nonlinearities in the hysteresis model, and because subspace system identification does not necessarily provide a result that optimizes root-mean-squared error (but nonetheless provides a very good result), the output of optimizing γ , M_0 , M , R_0 , and R_j can then be used as a good initial guess for a nonlinear optimization, such as mentioned in Sec. 2.11.1.

2.12 Example results

To give a better feel for the capabilities of an equivalent-circuit type model, we present some modeling results in this section. Data were collected from a 25-Ah automotive battery cell using the procedures outlined in this chapter, and open-circuit voltage and dynamic modeling parameters were estimated from the data (using one resistor–capacitor subcircuit in the model). Here, we concentrate on simulating the optimized model open-loop, and comparing its predictions against the measured voltage data for a test conducted at 25 °C.

The top frame of Fig. 2.25 shows an overlay of true and model-predicted voltage over the entire 10-hour test. The root-mean-squared difference between the true and model results was 5.37 mV in this case. The lower frame of the figure zooms in to one UDDS cycle, more clearly showing that the circuit model captures the cell performance quite well.

Fig. 2.26 shows the optimized parameter values for this cell (as well as five others of different size and manufacture) as functions of test temperature (tests were conducted from –25 °C to 45 °C in

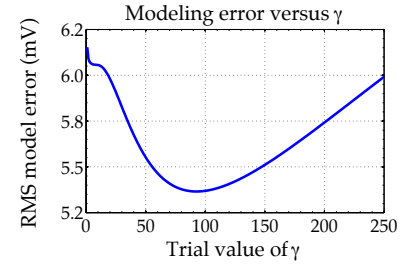


Figure 2.24: Finding optimum value of hysteresis parameter γ .

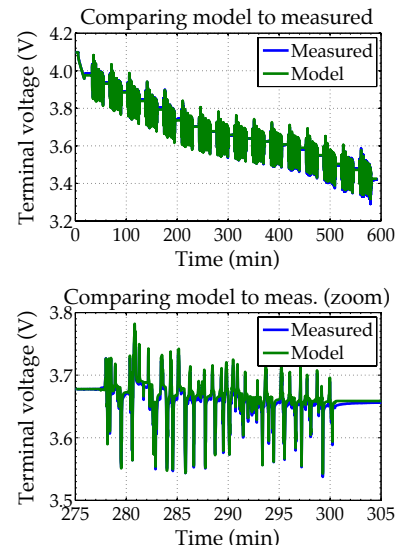


Figure 2.25: ESC-model comparison to measured voltage for a 25-Ah automotive battery cell at 25 °C.

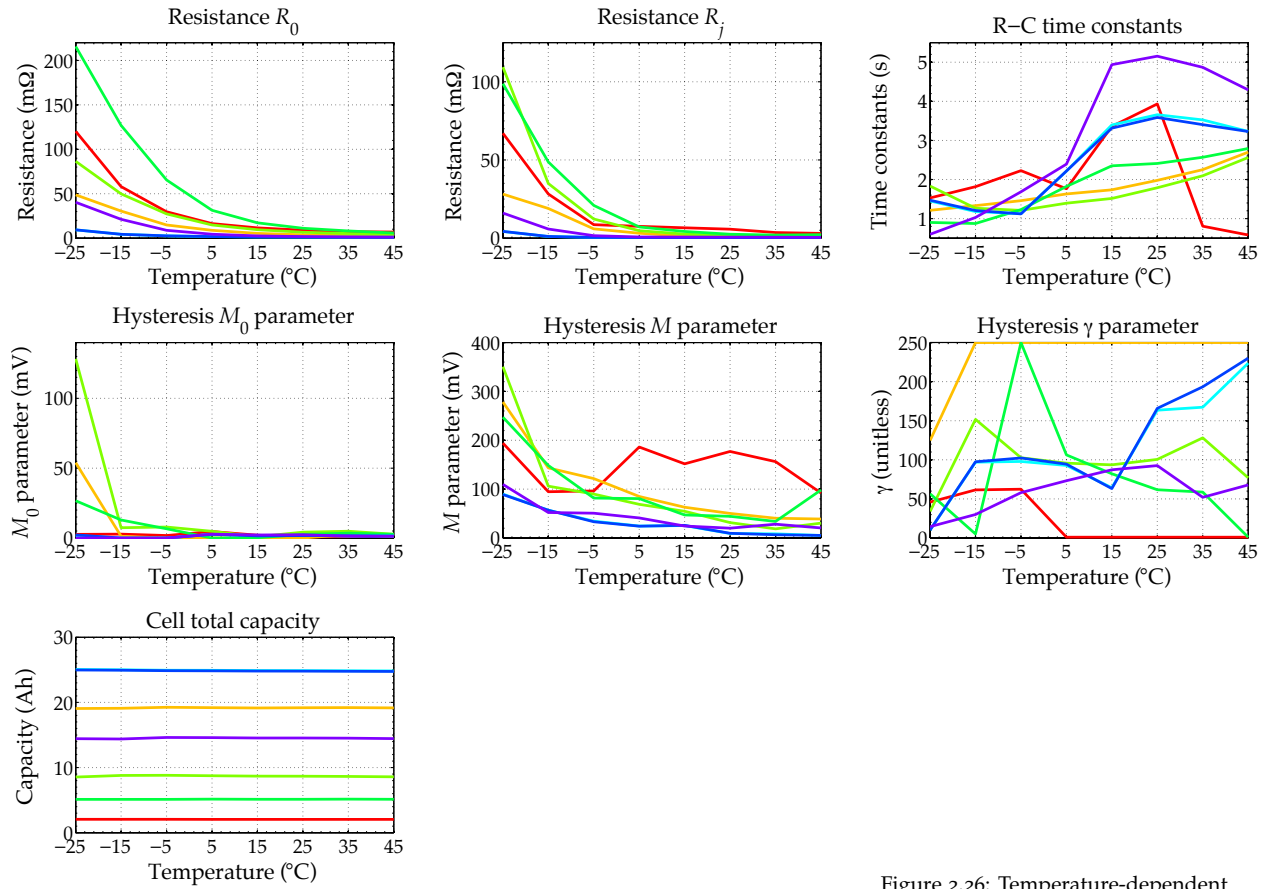


Figure 2.26: Temperature-dependent ESC-model parameter values identified for a sample cell.

increments of 10 C°). These particular results are characteristic, in a variety of ways.

- Equivalent-series resistance R_0 decreases exponentially as temperature increases. This is a near-universal result. Any model lacking this feature is suspect.
- Resistor-capacitor resistances R_j also decrease (roughly) exponentially as temperature increases. This is also expected.
- Resistor-capacitor time constants tend to increase with temperature. This might actually seem a surprising result, as we would expect the cell dynamics to speed up at warmer temperatures. However, results published by Lee et al. (based on physics models) show that at some states of charge the cell speeds up while at other states of charge the cell slows down overall. The result in Fig. 2.26 shows a single optimized time constant over all SOC, so it is not necessarily a surprising result. Moreover, Lee's results lead us to realize that this relationship should not be expected to be monotonic.¹⁴
- Hysteresis is generally “speeding up” (i.e., a smaller change in

¹⁴ Lee, J.L., Aldrich, L., Stetzel, K., and Plett, G.L., “Extended Operating Range for Reduced-Order Model of Lithium-Ion Cells,” *Journal of Power Sources*, 255, 2014, pp. 85–100.

SOC is required to effect a large change in the hysteresis state) and decreasing in magnitude as temperature increases. Hysteresis levels generally decrease as temperature increases.

- The measured capacity is very nearly constant across temperature (as it should be).

In practice, the model will need to be evaluated at temperatures not included in the testing protocol. To look up a parameter at an intermediate temperature, linear interpolation into the tables made via the system-identification process can be used to approximate the parameter values.

This assumes a smoothness in the functions as temperature varies. We don't always (i.e., rarely) see this from the initial system-identification output. In practice, some hand-smoothing of parameter relationships is usually necessary to make models that match measured data nearly as well as the automatically tuned versions, but which work better at intermediate temperatures.

2.13 Where to from here?

In this chapter, we have examined equivalent-circuit models of battery cells. We have seen that with optimized parameter values, there can be very good agreement between measured and predicted cell voltage to the same input stimulus. Therefore, they are sufficiently powerful for many circuit designs and for control algorithm development.

So, are we done? (No.) Circuit models lack predictive power over the long term. They do not answer the questions "How will a cell behave if it is subjected to stimuli quite different from that used during training of the model?" or "How will a cell behave as it ages?" or "Can we predict cell aging or impending failure?" or "How can we control a cell to maximize its utility while maximizing its life?"

So, we now start to look at physics-based models of cells, which enable us to increase the predictive power of our models. These physics-based models are mathematically very complex, but ultimately we will be able to reduce them to models of similar computational complexity to the equivalent-circuit models we have studied in this chapter.

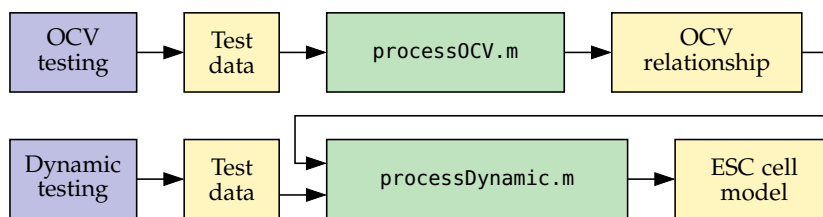
2.14 Chapter appendix: MATLAB ESC model toolbox

Sec. 2.10 discussed how to collect and process cell-test data in order to make an open-circuit-voltage relationship for a cell. Sec. 2.11 then discussed how to collect and process cell-test data to determine the

remaining parameters of a complete dynamic ESC model. A MATLAB toolbox and dataset comprising code implementing these steps and companion cell-test data collected from a number of cells are available on the book web site.¹⁵ In this appendix, we quickly introduce the main code components of the toolbox. A great deal of learning is possible if this discussion is coupled with a diligent examination of the code itself to see how the steps are implemented.

2.14.1 Creating the model

Fig. 2.27 depicts the overall process for creating an enhanced self-correcting (ESC) cell model. The blue boxes indicate laboratory processes; the yellow boxes indicate data files; and the green boxes indicate processing by MATLAB functions. The “OCV testing” box denotes cell tests of the sort described in Sec. 2.10, run at a number of temperatures. The “Dynamic testing” box denotes cell tests of the sort described in Sec. 2.11, also run at a number of temperatures. Later processing requires that 25 °C be one of those temperatures in both cases.



¹⁵ <http://mocha-java.uccs.edu/BMS1/CH02/ESCtoolbox.zip>

Figure 2.27: Process of creating an ESC cell model from cell-test data.

The “Test data” boxes abstractly denote the output of the laboratory testing. However, some format conversions are required for efficiency purposes. For example, cell-test equipment by Arbin Instruments produces a “.res” file as its output. Arbin also provides a Microsoft Excel macro that converts the “.res” format into an “.xlsx” format. The `makeMATfiles.m` code on the web site (one script each for the OCV and dynamic processing) then converts the “.xlsx” format into a MATLAB “.mat” file. The “.mat” files have variables properly set up for further processing.¹⁶

The `processOCV.m` function processes the raw cell-test data to produce an OCV relationship. In the toolbox, `processOCV.m` is called by the wrapper function `runProcessOCV.m`, which loads the raw cell-test data, organizes it into the prescribed format, calls `processOCV.m`, and saves the results to a file.

The `processDynamic.m` function likewise processes the raw cell-test data to produce the final ESC cell model. In the toolbox, `processDynamic.m` is called by the wrapper function `runProcessDynamic.m`, which loads

¹⁶ If a different brand of cell-test equipment is used, the user will need to implement new code to convert the testing output into a format compatible with the processing macros. The code and data on the web site should provide a template and an example for how this could be accomplished.

the OCV relationship and raw cell-test data, organizes it into the prescribed format, calls `processDynamic.m`, and saves the results to a file. Note that `processDynamic.m` requires MATLAB's optimization toolbox—if this is not available, the functionality of the line search performed by `fminbnd.m` will need to be rewritten by the user.

2.14.2 Using the model

Once the model is created, it is ready to be used. Fig. 2.28 depicts the process.

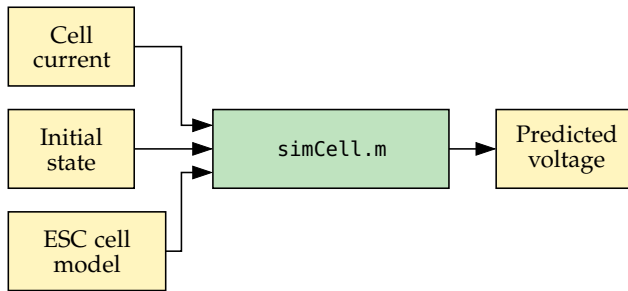


Figure 2.28: Process of using an ESC cell model to predict cell response.

The ESC cell model produced from cell-test data is loaded. An initial state comprising the initial cell state of charge, initial resistor currents, and initial normalized hysteresis value is assembled. Then the function `simCell.m` is called, along with the profile of cell current versus time to be simulated. The output of the function comprises predicted cell voltage, as well as the internal model states as functions of time.

The following code illustrates how to use the `simCell.m` function. The output of this code is presented in Fig. 2.29.

```

load DYN_Files/E2_DYN/E2_DYN_35_P25.mat % load data file
load DYN_Files/E2model.mat % load model file

time    = DYNDATA.script1.time; % make variables easier to access
voltage = DYNDATA.script1.voltage;
current = DYNDATA.script1.current;

ind = find(diff(time)<=0); % get rid of duplicate time steps
time(ind+1) = []; voltage(ind+1) = []; current(ind+1) = [];

t1=time(1); t2=time(end); % make sure evenly sampled in time
deltaT = 1; t = (t1:deltaT:t2) - t1; % one-second sampling
current = interp1(time,current,t1:deltaT:t2);
voltage = interp1(time,voltage,t1:deltaT:t2);

% change [0;0] to have same number of zeros as you have R-C states in
% model
vest = simCell(current,25,deltaT,model,1,[0;0],0); % simulate cell

figure(1); clf; plot(t/60,voltage,t/60,vest); % plot some results
legend('Truth','Model','location','southwest');
  
```

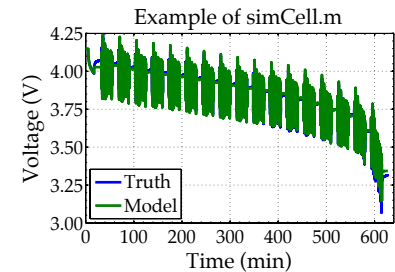


Figure 2.29: Output of `simCell.m` example.

```
xlabel('Time (min)'); ylabel('Voltage (V)');
title('Example of simCell.m');
```

2.14.3 Model internals

Sometimes, it may be important to query the parameters of the model. This may be done by accessing the fields in the MATLAB structure “model” directly. However, this is generally not considered good programming practice. Instead, the toolbox provides data accessor functions that do this task for you.

To determine the open-circuit voltage at one or more states of charge, the `OCVfromSOCtemp.m` function may be used. The inputs to this function are a vector of states of charge for which voltages are required, a temperature variable (either a scalar, which is applied to all outputs, or a vector of the same size as the state-of-charge input vector, where a different temperature is applied to each output), and the model data structure. For example:

```
load DYN_Files/E2model.mat % load model file
z = 0:0.01:1; % make SOC input vector
T = 25; % set temperature value
plot(z,OCVfromSOCtemp(z,T,model));
```

To determine the state of charge from one or more at-rest open-circuit-voltage values, the `SOCfromOCVtemp.m` function may be used. Its calling parameters are similar to those used for `OCVfromSOCtemp.m`. For example:

```
load DYN_Files/E2model.mat % load model file
v = 2.5:0.01:4.2; % make voltage input vector
T = 25; % set temperature value
plot(v,SOCfromOCVtemp(v,T,model));
```

Finally, to determine a model dynamic parameter value, the `getParamESC.m` function may be used. For example:

```
load DYN_Files/E2model.mat % load model file
T = 25; % set temperature value
gamma = getParamESC('GParam',T,model); % hysteresis rate factor
```

This requires that the user have some knowledge of the internal structure of the model data structure. (Again, it is not recommended that the user access the fields of this data structure directly. However, the field name is required as input to the `getParamESC.m` function.) These fields are listed in Table 2.1.

Identifier field

name An identifying string storing a name for the cell type

Table 2.1: Fields in the model data structure.

Fields pertaining to the OCV versus SOC relationship:

OCV0	Vector of OCV versus SOC at 0 °C [V]
OCVrel	Vector of change in OCV versus SOC per °C [V/°C]
SOC	SOC vector at which OCV0 and OCVrel are stored
SOC0	Vector of SOC versus OCV at 0 °C (unitless)
SOCrel	Vector of change in SOC versus OCV per °C [1/°C]
OCV	OCV vector at which SOC0 and SOCrel are stored

Fields pertaining to the dynamic relationship:

temps	Temperatures at which dynamic parameters are stored [°C]
QParam	Capacity Q at each temperature [Ah]
etaParam	Coulombic efficiency η at each temperature (unitless)
GParam	Hysteresis “gamma” parameter γ (unitless)
MParam	Hysteresis M parameter [V]
M0Param	Hysteresis M_0 parameter [V]
R0Param	Series resistance parameter R_0 [Ω]
RCParam	The R-C time constant parameter $R_j C_j$ [s]
RParam	Resistance R_j of the R-C parameter [Ω]

3

Microscale Cell Models

The focus of this book is on creating mathematical models of lithium-ion cells, finding values for the parameters in the models, and simulating the models to predict cell performance. We have already seen a phenomenological (equivalent-circuit) approach to modeling, and we now turn to exploring physics-based models. The two different approaches are compared and contrasted in Fig. 3.1.

Empirical models, such as the equivalent-circuit models we looked at in Chap. 2, are noted in the top of the figure. They comprise simple systems of cell-scale ordinary-difference equations (ODEs) that can be implemented readily on an inexpensive microprocessor. They are easily incorporated in battery-state estimation and control algorithms in battery management systems. The equations that make up these models can predict cell voltage accurately from measurements of cell input current, and the parameters of the model can be tuned to adapt to changing cell characteristics as the cell ages.

3.1	<i>Chapter goal: Microscale</i>	67
3.2	<i>Solid charge conservation</i>	68
3.3	<i>Solid mass conservation</i>	75
3.4	<i>Thermodynamics</i>	80
3.5	<i>Physical chemistry</i>	86
3.6	<i>Binary electrolytes</i>	91
3.7	<i>Electrolyte mass conserv.</i>	94
3.8	<i>Electrolyte charge conserv.</i>	106
3.9	<i>Butler–Volmer equation</i>	110
3.10	<i>Implementing the model</i>	119
3.11	<i>Cell-level quantities</i>	122
3.12	<i>Where to from here?</i>	130
3.13	<i>Appendix: OCP sources</i>	130
3.14	<i>Partial glossary</i>	132

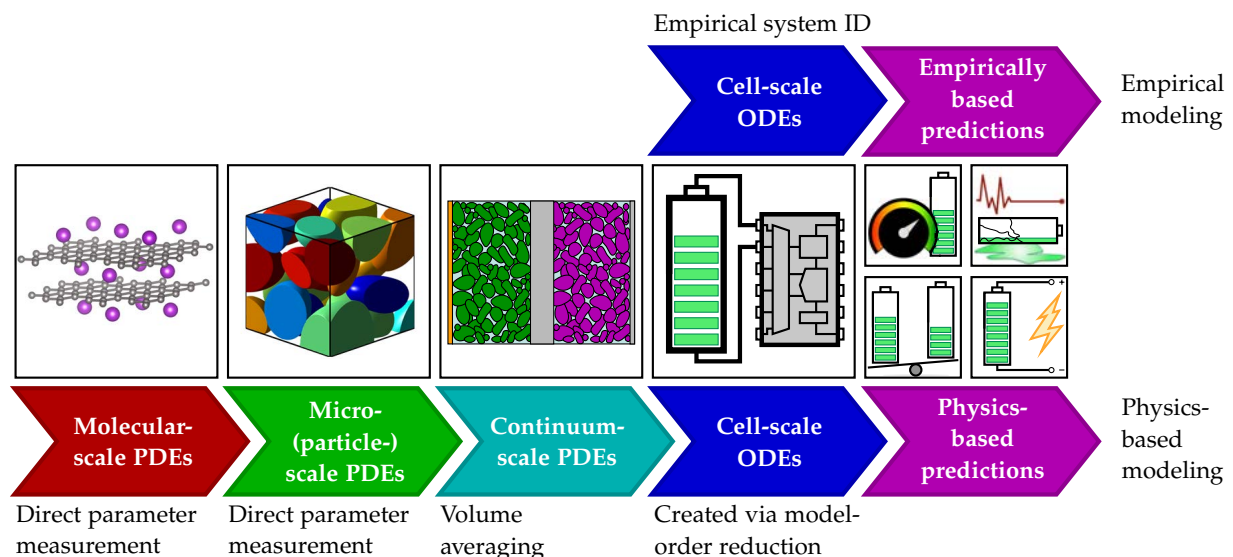


Figure 3.1: Different approaches to making models of lithium-ion cells.

However, these models are limited. Most important, they cannot predict cell internal dynamics, which is of critical importance to being able to predict how a cell will age and to being able to formulate battery-control algorithms to minimize cell aging due to out-of-bounds internal states. Further, the process of determining the parameter values for an empirical cell model uses empirical system identification, which is essentially a curve-fitting process, and so has its own limitations. In particular, the resulting model must not be used in scenarios that are very different from the ones from which data were collected to tune the model parameter values.¹

Physics-based models are more difficult to formulate but allow enhanced monitoring and prediction of individual mechanisms internal to the cell. Further, just as Newton's laws of motion allow accurate predictions of an object's acceleration over a very wide range of initial velocities given only measurements of its mass—so too physics-based models of cell dynamics allow accurate predictions of cell behaviors using only a small set of measured physical cell parameters. There is no concern of “extrapolation versus interpolation” as there is for empirical models.

The process for creating and using a physics-based model is illustrated in the bottom of Fig. 3.1. We see that there are multiple stages involved, starting at very short length scales and progressively moving up to the final cell-scale model.

Some physics-based models describe processes at the molecular scale.² Parameter values for these equations can be measured directly, replacing the need for empirical system identification. The resulting models are useful primarily for predicting diffusion rates of lithium within the crystalline structures of the solid particles that comprise the electrode active materials and for predicting open-circuit potential relationships for these materials. However, there are laboratory techniques for measuring diffusivity and open-circuit potentials directly without need of molecular-scale models, so we omit any further discussion of modeling cell dynamics at this scale.

The next higher scale is the particle-scale or microscale, where we look at homogeneous materials. These models predict what happens inside the solid electrode particles and what happens in the electrolyte, as considered separately. We can think of this scale as a volume average of the molecular scale, where impurities and imperfections are blended in, to create a homogeneous material. Model parameters are also measured directly via lab tests at this level.

The next higher scale is the continuum scale, where the solid and electrolyte are no longer considered separately. Continuum models are volume-averaged simplifications of the microscale, where each

¹ Curve fitting is good for interpolating data—predicting performance in an operating scenario similar to and within the operating regimes of the data-generating testing—but is bad for extrapolating data—predicting performance in scenarios outside the scope of the scenarios used to generate the model.

² These models are sometimes referred to as “microscale,” but as they operate at the atomic level, they might more appropriately be called “nanoscale.” We will refer to them as “molecular scale,” sidestepping the issue.

sample volume is assumed to contain a portion of the solid electrode material and a portion of the electrolyte. Activity in the solid and activity in the electrolyte are still thought of separately, but the equations take into account the interactions between the two regions.

The final scale converts the partial-differential equations from the continuum scale into a coupled set of ordinary difference equations at the cell scale, suitable for rapid simulation and controls purposes. The final complexity of these cell-scale ODEs is similar to those created via empirical modeling, but the predictive power is much greater.³ The physics-based path is much harder to develop and understand, but the final results are worth the effort.

Fig. 3.1 can be seen as a roadmap for the bulk of this book. Chap. 2 has already considered equivalent-circuit type empirical models. Chap. 3 focuses on developing microscale models. Chap. 4 will show how to invoke volume-averaging techniques to create continuum-scale models. Chaps. 5 and 6 will give the background and methods to convert continuum-scale models into low-complexity cell-scale models automatically. Finally, Chap. 7 will consider how thermal effects can be incorporated in physics-based models.

3.1 Chapter goal: Derive microscale model equations

The road ahead in this chapter involves concepts from vector calculus, thermodynamics, and physical chemistry that may not be familiar to all readers. Sufficient background in these fields will be developed to be able to derive the equations of the microscale model, but it will take time to do so. It's easy to get lost in the details and to miss the main results. So, before embarking on these topics, we present in summary the main results that we intend to develop.⁴ The reader can use these results as "mile markers" for the chapter, giving some sense of the progress that is being made.

In particular, our goal in this chapter is to develop the microscale model, which comprises a set of five coupled equations:

1. Charge conservation in the homogeneous solid:

$$\nabla \cdot \mathbf{i}_s = \nabla \cdot (-\sigma \nabla \phi_s) = 0. \quad (3.1)$$

2. Mass conservation in the homogeneous solid:

$$\frac{\partial c_s}{\partial t} = \nabla \cdot (D_s \nabla c_s). \quad (3.2)$$

3. Mass conservation in the homogeneous electrolyte:

$$\frac{\partial c_e}{\partial t} = \nabla \cdot (D_e \nabla c_e) - \frac{\mathbf{i}_e \cdot \nabla t_+^0}{F} - \nabla \cdot (c_e \mathbf{v}_0). \quad (3.3)$$

³ We can extrapolate beyond the data used to create the model, as the physics allows us to do so. Further, the equations can predict internal cell dynamics in addition to external cell voltage.

⁴ Special thanks to Dr. Kan-Hao Xue, who helped to derive many of the proofs of equations given in this chapter.

4. Charge conservation in the homogeneous electrolyte:

$$\nabla \cdot \mathbf{i}_e = \nabla \cdot \left(-\kappa \nabla \phi_e - \frac{2\kappa RT}{F} \left(1 + \frac{\partial \ln f_{\pm}}{\partial \ln c_e} \right) \left(t_+^0 - 1 \right) \nabla \ln c_e \right) = 0. \quad (3.4)$$

5. Lithium movement between the solid and electrolyte phases:

$$j = \frac{i_0}{F} \left\{ \exp \left(\frac{(1-\alpha)F}{RT} \eta \right) - \exp \left(-\frac{\alpha F}{RT} \eta \right) \right\}. \quad (3.5)$$

At this point, none of the variables in the equations will have meaning to the reader. However, note that a glossary of the most important variables used in this chapter can be found in Sect. 3.14. Vector-calculus gradient (∇) and divergence ($\nabla \cdot$) operators will also be reviewed when they first appear in the derivations.

3.2 Charge conservation in the solid

We begin by deriving the microscale equations for a lithium-ion cell that describe charge and mass conservation in the solid: Eqs. (3.1) and (3.2), respectively. These derivations are fairly straightforward, starting with basic physics laws, but do require some knowledge of vector calculus, which we will review. We'll then need to look at some concepts from thermodynamics and physical chemistry before proceeding to develop the remaining three model equations.

Fig. 3.2 illustrates activity in the solid particles of the electrode active material. Our final model will describe electron movement via conduction due to local differences in the electric potential and lithium-atom movement between vacancies in the crystalline structure of the active material via diffusion due to local differences in concentration. But first, we need to define terminology that allows us to quantify material and charge, and we need to discuss how we will define movement of material mathematically.

3.2.1 Moles and coulombs

For any appreciable current to flow in a battery cell, a *lot* of lithium must move. So, instead of counting individual lithium atoms, it is customary to count *moles* of lithium instead. A *mole* is a unit of measurement used in chemistry to express quantities of a chemical substance, equal to $N_A = 6.02214 \times 10^{23}$ molecules of that substance.⁵ The mole is one of the base units in the International System of Units and has the unit symbol mol. The number of molecules in a mole is defined so that the mass of one mole of a substance, expressed in grams, is exactly equal to the substance's mean molecular weight. For

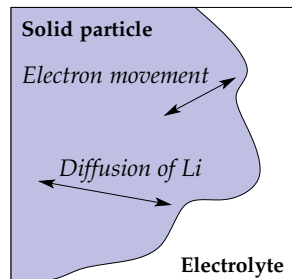


Figure 3.2: Dynamics in the solid.

⁵ N_A is known as Avogadro's number.

example, the mean molecular weight of natural water (H_2O) is about 18.015, so one mole of water is about 18.015 g.

The mole is widely used in chemistry—instead of units of mass or volume—as a convenient way to express the amounts of reactants and products of chemical reactions. For example, the reaction $2 \text{ H}_2 + \text{O}_2 \rightarrow 2 \text{ H}_2\text{O}$ implies that 2 mol of dihydrogen and 1 mol of dioxygen react to form 2 mol of water. The mole may also be used to express the number of atoms, ions, or other elementary entities in some sample.

Similarly, for any appreciable current to flow in a battery cell, a *lot* of electrons must move. So, instead of counting individual electrons, we also count moles of electrons. However, we're usually less interested in the quantity of electrons moving than we are in the quantity of charge moving. We express charge in coulombs or C, where there are $F = 96,485$ coulombs per mole of elementary charges.⁶ Electrical current is the flow of charge and is measured in amperes, where one ampere equals one coulomb per second ($1 \text{ A} = 1 \text{ C s}^{-1}$).

3.2.2 Flux density

We are about to discuss movement of electrons and lithium atoms and ions. More formally, we are going to consider their *flux*. Flux is the rate of something crossing a surface. Note that flux is a total quantity per unit time. If we are concerned with the movement of electrons, the flux will be measured in coulombs per second, or A. If we are considering the movement of lithium ions or atoms, the flux will be measured in moles per second, or mol s^{-1} . Later on, we'll be more interested in *flux density*, which is flux normalized per unit area or volume.⁷ When considering charge, we will measure flux density in A m^{-2} ; when considering lithium, we will measure flux density in $\text{mol m}^{-2} \text{ s}^{-1}$.

The surface across which the movement occurs can be a physical boundary, such as when considering the movement of lithium between the solid electrode particles and the electrolyte. However, the surface can also be a nonphysical boundary, such as some conceptual plane separating (x, y, z) and $(x + \delta x, y, z)$. In the latter case, we would be considering how much lithium is traveling in the x direction near the point (x, y, z) .

To measure the flux of electrons or lithium passing through a surface, we need to know

- The shape, size, and orientation of the surface,
- The strength and direction of the flow at any point in space

The latter is known as a *vector field*, which is a function of space that results in computing a vector value at every (x, y, z) location. Each

⁶ F is known as Faraday's constant.

⁷ In the literature, it is common to see flux density referred to as flux. The key is to look at the units to see what the author is really considering.

vector has a length, which says how quickly material is flowing at that point, and an orientation, which says in which direction the material is flowing. Fig. 3.3 shows how we might draw a vector field in two dimensions: every (x, y) point is associated with a vector indicating rate and direction of flow.

The local strength of the vector field has a direct impact on the flux. Doubling the strength will double the flux passing through a surface. Flux also depends on the orientation of the field and the surface. When the field passes directly through the surface (is at right angles to the surface), the flux is maximized. As the surface tilts away from the field, the flux decreases as less and less flux crosses the surface. Eventually, we get zero flux when the source and surface are parallel—the flux passes over the boundary but does not cross through it.

As an analogy, imagine wind (the source of flux) blowing past a window frame (the surface). If the wind is pointed straight at the window, the airflow through the window frame is maximized. If the wind is at an angle to the window, the airflow through the window frame is reduced. If the wind is blowing across the window, then no airflow will pass through the window frame.

This is illustrated in Fig. 3.4. The blue lines indicate the vector field $\mathbf{F}(x, y, z)$. The surface is illustrated in green, and a vector normal to the surface is denoted as $\hat{\mathbf{n}}$. The components of the vector field that make up the flux are illustrated by the orange lines—these are the parts of \mathbf{F} that are parallel to $\hat{\mathbf{n}}$ and perpendicular to the surface.

In this example, flux is positive because it is in the same direction as $\hat{\mathbf{n}}$. If it were in the opposite direction, it would have a negative sign. When the surface is physical, this has meaning. We define the normal vector $\hat{\mathbf{n}}$ pointing *outward* from the object. Then, positive flux means that the flow is out of the object, and the object is a source of the flux. Negative flux means that the flow is *into* the object, and the object is a sink to the flux.

Expressing this mathematically, if $\mathbf{F}(x, y, z)$ is the vector field and $\hat{\mathbf{n}}$ is the normal vector to a surface, then the dot product of these two vectors, $\mathbf{F}(x, y, z) \cdot \hat{\mathbf{n}}$, gives the component of the vector field that is perpendicular to the surface. The total flux is the integral of this dot product over the surface. We can write

$$\text{flux} = \iint_S \mathbf{F}(x, y, z) \cdot \hat{\mathbf{n}} \, dS,$$

where \iint_S means that we are integrating over the entire (generic) surface S . For a specific computation, the limits of integration would need to be supplied explicitly in order to be able to evaluate the integral and dS would need to be written in terms of the geometric variables describing the surface (e.g., perhaps dx and dy).

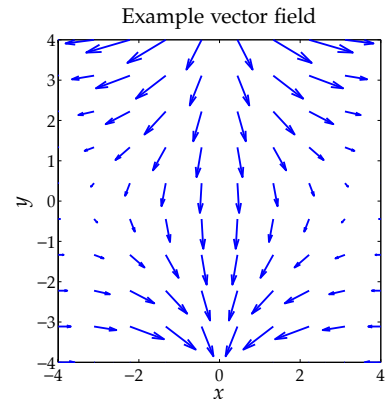


Figure 3.3: An example generic vector field in two dimensions.

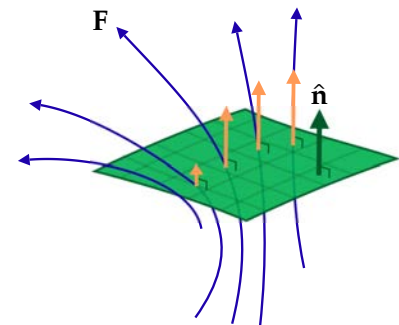


Figure 3.4: Orientation dependence of flux.

(Adapted from
[http://en.wikipedia.org/
 wiki/File:General_flux_diagram.svg](http://en.wikipedia.org/wiki/File:General_flux_diagram.svg))

Also note that sometimes we make the distinction between an *open surface* and a *closed surface*. An open surface does not completely enclose a volume and therefore has a distinct edge or boundary. A closed surface completely encloses some volume (e.g., the outer surface of a cube or a sphere). When talking about closed surfaces, we more correctly write flux as

$$\text{flux} = \iint_S \mathbf{F}(x, y, z) \cdot \hat{\mathbf{n}} \, dS,$$

where \iint_S means that we are integrating over the entire closed surface S . When the surface under consideration might either be open or closed, we write \iint_S .

3.2.3 Point form of Ohm's law

We are now ready to derive a relationship that models the movement of charge through the homogeneous solid crystalline structures of the electrodes. We will assume that the electron movement arises from drift motion of charges in a linear media, where Ohm's law applies.

In this scenario, current density is proportional to the applied electric field: $\mathbf{i} = \sigma \mathbf{E}$, where

- $\mathbf{i}(x, y, z, t)$ [A m^{-2}] is the (vector) current density flowing through a representative cross-sectional area centered at a given location. By convention, \mathbf{i} represents the flow of positive charges; negatively charged electrons flow in the direction opposite to \mathbf{i} .
- $\sigma(x, y, z, t)$ [S m^{-1}] is a material-dependent *conductivity* value. A high value of σ means that it is easy for current to flow, and a low value of σ means that it is difficult for current to flow. Conductivity is inversely proportional to resistivity.
- $\mathbf{E}(x, y, z, t)$ [V m^{-1}] is the (vector) electric field at that location.

If we assume that magnetic effects are negligible, the electric field can be written in terms of the local gradient of the electric potential⁸

$$\mathbf{E} = -\nabla\phi,$$

where $\phi(x, y, z, t)$ [V] is the scalar field (scalar function of space) representing the electric potential at each point. Substituting, we have

$$\mathbf{i} = -\sigma \nabla\phi. \quad (3.6)$$

Note that this relationship is a microscopic (point-form) version of Ohm's law, which states that $I = \Delta V/R$ for homogeneous linear media. Here we have had to introduce the negative sign to accommodate the different sign convention of the gradient operator $\nabla\phi$ versus the difference operator ΔV .

⁸Gradients tell us the rate of change of a function with respect to space. The gradient is a vector that points in the direction of greatest increase of a function, considered locally. Mathematically, the gradient symbol is an upside-down delta and is called "dell." We can write out the gradient of a function $F(x, y, z)$ as

$$\nabla F = \frac{\partial F}{\partial x} \hat{\mathbf{i}} + \frac{\partial F}{\partial y} \hat{\mathbf{j}} + \frac{\partial F}{\partial z} \hat{\mathbf{k}},$$

where $\hat{\mathbf{i}}$, $\hat{\mathbf{j}}$, and $\hat{\mathbf{k}}$ are the standard unit vectors in the x , y , and z directions, respectively.

As an example, consider the scenario depicted in Fig. 3.5. The left frame is an example scalar field, such as the local electric potential ϕ as a function of spatial coordinates x and y . The middle frame shows contours of equal function value as circles and local gradient values as vector symbols. We see that toward the center of the diagram, the gradient points upward toward the peak. Moving out from the center, after the valley is reached, the gradient vectors point toward the lower ridge-line of the function (i.e., the gradient does not point toward the globally maximum function value; it points upward in a local sense only). The right plot shows the flux density vectors. The flux density is of opposite sign to the gradient, implying that movement is “downhill.” That is, positive charges move from a high potential to a low potential under the effect of the electric field.

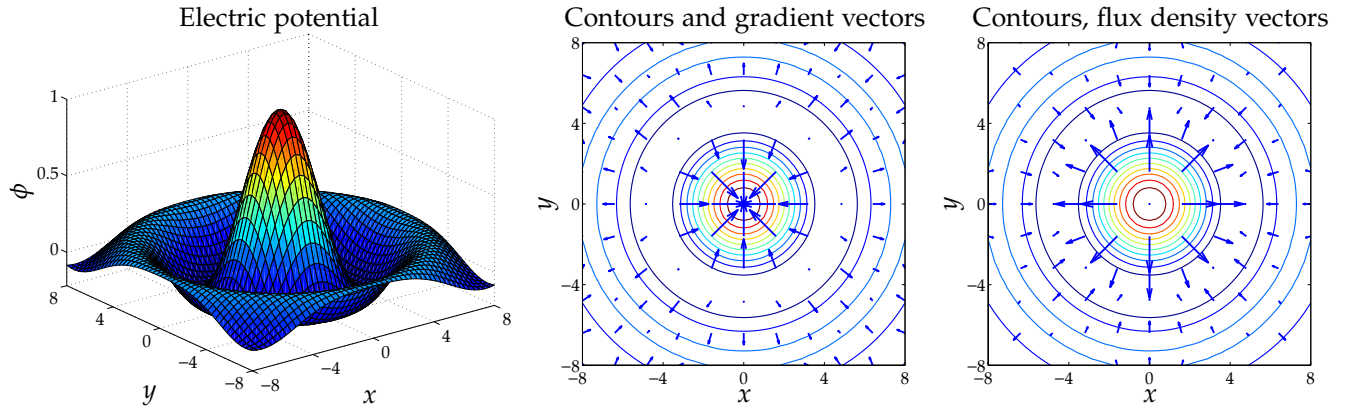


Figure 3.5: Example of gradient and flux density.

3.2.4 The continuity equation (Kirchhoff's current law)

Comparing Eq. (3.6) with Eq. (3.1), we see that we are beginning to develop the terms needed for the first microscale model equation, but that we do not yet have the desired final form. So far we have computed only a way to represent the flow of charge; we have not yet enforced conservation of charge. We do that now.

Consider representing a solid particle as a lot of tiny volumes. Now, consider one of those volumes V , where the material properties within that volume are homogeneous, the volume has closed boundary surface S , and current density \mathbf{i} is directed into the volume. Then, the net current i [A] *into* the region is

$$i = - \iint_S \mathbf{i} \cdot \hat{\mathbf{n}} dS,$$

the minus sign arising because of our usual convention that the normal $\hat{\mathbf{n}}$ points *out* of the volume.

A net charge dQ [C] is supplied to volume V by the current within a time dt , so we can write

$$i = \frac{dQ}{dt}.$$

Thus, the net charge in the volume changes in time dt by an amount $dQ = d \iiint_V \rho_V dV$ where ρ_V [C m⁻³] is the *charge density* (of positive charges) within volume V and hence

$$\oint_S \mathbf{i} \cdot \hat{\mathbf{n}} dS = -\frac{d}{dt} \iiint_V \rho_V dV. \quad (3.7)$$

Note that we've implicitly assumed that charge within V can be changed *only* by allowing it to enter or exit through the boundary. Charge already contained in V is neither created nor destroyed while this occurs. Thus, Eq. (3.7) is (the integral form of) the so-called *equation of continuity*. It is equivalent to a statement of conservation of charge.

3.2.5 Divergence

We're ultimately interested in converting the integral form of the charge-conservation relationship into a (differential) point form. To do so, we'll need to be able to take the limit of Eq. (3.7) as the volume V becomes vanishingly small.

To aid in this effort, we recognize that the *divergence* of a vector field \mathbf{F} is defined as

$$\nabla \cdot \mathbf{F} = \lim_{\Delta V \rightarrow 0} \frac{1}{\Delta V} \oint_S \mathbf{F} \cdot \hat{\mathbf{n}} dS. \quad (3.8)$$

We can come up with a way of understanding the notation $\nabla \cdot \mathbf{F}$ used to represent divergence if we write $\mathbf{F} = F_x \hat{\mathbf{i}} + F_y \hat{\mathbf{j}} + F_z \hat{\mathbf{k}}$, where F_x is the x component of \mathbf{F} , F_y is the y component of \mathbf{F} , and F_z is the z component of \mathbf{F} . Then, shrinking the volume of ΔV down to an infinitesimal cube, where the value of \mathbf{F} is constant on each face of the cube (but possibly different on different faces), Eq. (3.8) becomes the normalized summation of $\mathbf{F} \cdot \hat{\mathbf{n}}$ on the six different faces of the cube, multiplied by each face area

$$\begin{aligned} \nabla \cdot \mathbf{F} = \lim_{\Delta V \rightarrow 0} \frac{1}{\Delta V} & \left[(F_x(x + \delta x) - F_x(x)) A_{yz} \right. \\ & \left. + (F_y(y + \delta y) - F_y(y)) A_{xz} + (F_z(z + \delta z) - F_z(z)) A_{xy} \right], \end{aligned}$$

where A_{yz} is the area of the $y-z$ planar side of the cube, A_{xz} is the area of the $x-z$ side of the cube, and A_{xy} is the area of the $x-y$ side of

the cube. Then, realizing that $\Delta V = A_{yz}\delta x = A_{xz}\delta y = A_{xy}\delta z$,

$$\begin{aligned}\nabla \cdot \mathbf{F} &= \lim_{\delta x, \delta y, \delta z \rightarrow 0} \left[\frac{F_x(x + \delta x) - F_x(x)}{\delta x} \right. \\ &\quad \left. + \frac{F_y(y + \delta y) - F_y(y)}{\delta y} + \frac{F_z(z + \delta z) - F_z(z)}{\delta z} \right] \\ &= \frac{\partial F_x}{\partial x} + \frac{\partial F_y}{\partial y} + \frac{\partial F_z}{\partial z},\end{aligned}$$

which is how divergence is computed in practice in rectangular coordinates.

Notice that the notation for divergence combines the ideas of a gradient and a dot product:

$$\begin{aligned}\nabla \cdot \mathbf{F} &= \left(\frac{\partial}{\partial x} \hat{\mathbf{i}} + \frac{\partial}{\partial y} \hat{\mathbf{j}} + \frac{\partial}{\partial z} \hat{\mathbf{k}} \right) \cdot \left(F_x \hat{\mathbf{i}} + F_y \hat{\mathbf{j}} + F_z \hat{\mathbf{k}} \right) \\ &= \frac{\partial F_x}{\partial x} + \frac{\partial F_y}{\partial y} + \frac{\partial F_z}{\partial z}.\end{aligned}$$

By careful change of variables, divergence can also be expressed in other coordinate systems. For example, in cylindrical (ρ, ϕ, z) coordinates, divergence can be written as

$$\nabla \cdot \mathbf{F} = \frac{1}{\rho} \frac{\partial(\rho F_\rho)}{\partial \rho} + \frac{1}{\rho} \frac{\partial F_\phi}{\partial \phi} + \frac{\partial F_z}{\partial z}.$$

In spherical (r, θ, ϕ) coordinates, we have

$$\nabla \cdot \mathbf{F} = \frac{1}{r^2} \frac{\partial(r^2 F_r)}{\partial r} + \frac{1}{r \sin \theta} \frac{\partial(\sin \theta F_\theta)}{\partial \theta} + \frac{1}{r \sin \theta} \frac{\partial F_\phi}{\partial \phi}.$$

By examining Eq. (3.8), we can arrive at an intuitive sense of the meaning of divergence. The divergence of a vector field is a scalar quantity denoting the net flux density *out* of a volume through the enclosing surface. Positive divergence means that we have a point source; negative divergence means that we have a point sink. Considering that the term “to diverge” means “to move away from,” this mathematical definition is in agreement with standard understanding of how the word is used in other contexts as well. Positive divergence means that material is moving away from a point; negative divergence means that material is moving toward a point.

Fig. 3.6 illustrates this concept. A vector field is drawn, and three different regions (two-dimensional “volumes”) are highlighted. We see that more arrows point out of the top (red) volume than point into it. Hence this volume is acting as a net source, and divergence is positive. The same number of arrows point into and out of the middle (blue) volume, so this volume is neither a source nor a sink, so its divergence is zero. More arrows point into the bottom (green) volume than out of it, so this volume is acting as a net sink.

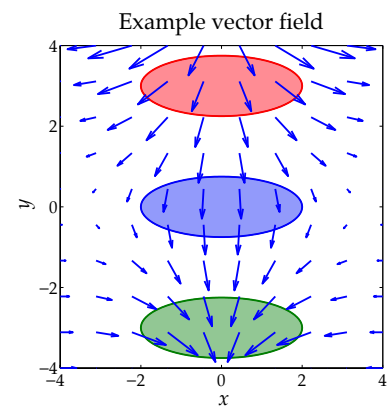


Figure 3.6: Illustrating positive (top, red region), zero (middle, blue region), and negative (bottom, green region) divergence.

3.2.6 Point form of charge conservation

We are now ready to convert the integral form of the equation of charge continuity to a point form. Starting with the integral form,

$$\iint_S \mathbf{i} \cdot \hat{\mathbf{n}} dS = -\frac{d}{dt} \iiint_V \rho_V dV,$$

we employ Liebnitz's rule for differentiating an integral⁹ and get

$$\iint_S \mathbf{i} \cdot \hat{\mathbf{n}} dS = - \iiint_V \left(\frac{\partial \rho_V}{\partial t} \right) dV,$$

assuming that charge density is continuous and that the volume V is not time varying.

We then divide both sides of the equation by the region's volume and take the limit as the volume shrinks to zero:

$$\begin{aligned} \lim_{V \rightarrow 0} \frac{1}{V} \iint_S \mathbf{i} \cdot \hat{\mathbf{n}} dS &= \lim_{V \rightarrow 0} -\frac{1}{V} \iiint_V \left(\frac{\partial \rho_V}{\partial t} \right) dV \\ \nabla \cdot \mathbf{i} &= -\frac{\partial \rho_V}{\partial t}. \end{aligned}$$

Applying Ohm's law to this identity, we get

$$\nabla \cdot \mathbf{i} = \nabla \cdot (-\sigma \nabla \phi) = -\frac{\partial \rho_V}{\partial t}.$$

At this point, we assume that the rate of electron movement in the solid lattice is much faster than the rate of other processes in the electrochemical cell. Therefore, ρ_V reaches an equilibrium state relatively quickly and so can be treated as being essentially constant over the time scales of the other processes. Then, $\partial \rho_V / \partial t \approx 0$. This gives us $\nabla \cdot (-\sigma \nabla \phi) = 0$.

To emphasize that this relationship applies to the solid particles in the cell and not to the electrolyte, we employ the subscript "s" on \mathbf{i} and ϕ :¹⁰

$$\nabla \cdot \mathbf{i}_s = \nabla \cdot (-\sigma \nabla \phi_s) = 0.$$

In words, this says that the divergence of the current density out of any sample volume within the homogeneous solid is zero. This means that the same amount of charge must exit the volume as enters it; that is, charge is neither created nor destroyed nor stored within any sample volume in the homogeneous solid.

We have now derived Eq. (3.1).

3.3 Mass conservation in the solid

We now set out to derive Eq. (3.2); that is, to develop an equation that defines mass conservation in the homogeneous solid electrode

⁹ Liebnitz' rule for differentiating an integral is

$$\begin{aligned} \frac{d}{d\theta} \int_{a(\theta)}^{b(\theta)} f(x, \theta) dx &= \int_{a(\theta)}^{b(\theta)} \frac{\partial f(x, \theta)}{\partial \theta} dx \\ &+ f(b(\theta), \theta) \frac{\partial b(\theta)}{\partial \theta} \\ &- f(a(\theta), \theta) \frac{\partial a(\theta)}{\partial \theta}, \end{aligned}$$

assuming that $f(x, \theta)$ is continuous and that the integral exists.

¹⁰ In this book, we use "s" to refer to the solid and "e" to refer to the electrolyte. It is also very common in the literature to use subscript "1" for the solid and "2" for the electrolyte. We feel that the alphabetic subscript is less confusing, but the reader should be prepared to encounter both conventions.

materials. In many ways, this derivation is parallel to the one we have just completed.

Again, we start with a relationship that models movement of the quantity of interest. This time, instead of being interested in the movement of charge, we are interested in the movement of lithium atoms within either the negative- or positive-electrode active material crystalline structures. We assume that movement occurs due to interstitial diffusion only, in a linear media.

That is, we assume that *molar flux density* is proportional to the concentration gradient via Fick's first law

$$\mathbf{N} = -D \nabla c, \quad (3.9)$$

where

- $\mathbf{N}(x, y, z, t)$ [$\text{mol m}^{-2} \text{s}^{-1}$] is the (vector) *molar flux density* of lithium flowing through a representative cross-sectional area of the solid that is centered at a given location.
- $D(x, y, z, t)$ [$\text{m}^2 \text{s}^{-1}$] is a material-dependent parameter called the *diffusivity*. A large value for D means that it is easy for lithium to move; a small value for D means that it is difficult for lithium to move.
- $c(x, y, z, t)$ [mol m^{-3}] is the concentration of lithium in the neighborhood of a given location.

This is illustrated in Fig. 3.7. The left frame shows an example plot of concentration versus space. The gradient vector field of the concentration, as shown in the middle frame, points locally in the direction of increasing concentration. The material flux density points in the opposite direction from the gradient as seen in the right frame, as lithium moves from a high-concentration to a low-concentration region.

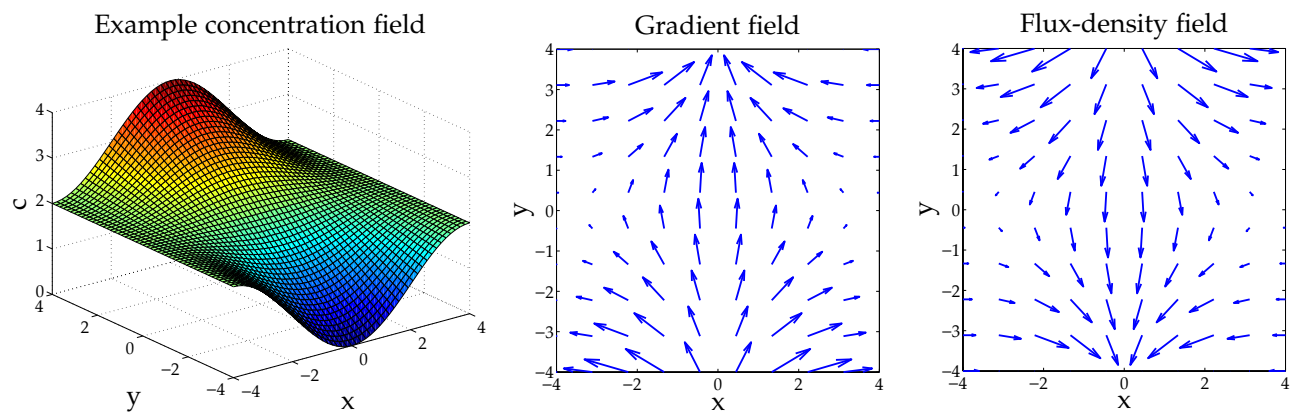


Figure 3.7: Movement of lithium atoms due to a concentration gradient.

3.3.1 The continuity equation

Eq. (3.9) describes the flow of lithium; we now proceed to derive from it a relationship that enforces conservation of mass.

As before, we consider representing a solid particle as many small volumes and examine a representative homogeneous volume V with boundary surface S and with lithium molar flux density \mathbf{N} directed into it. The net molar flux j [mol s⁻¹] into the region is

$$j = - \iint_S \mathbf{N} \cdot \hat{\mathbf{n}} dS,$$

where the minus sign arises because of the convention that the normal $\hat{\mathbf{n}}$ points *out* of the region. The flux can also be written as

$$j = \frac{dn}{dt},$$

where n is the number of moles of lithium in the volume V . Therefore, a net quantity of lithium dn is supplied to V by the molar flux j within a time dt . But, we can write $dn = \iiint_V c dV$, where c is the concentration of lithium within volume V , measured in moles per cubic meter. So, we conclude that

$$\iint_S \mathbf{N} \cdot \hat{\mathbf{n}} dS = - \frac{d}{dt} \iiint_V c dV.$$

This is the integral form of the so-called *equation of continuity* and is equivalent to a statement of conservation of mass. Note that we've implicitly made the same assumption as before; that is, that the mass within V can be changed *only* by allowing it to enter or exit through the boundary. Mass already contained in V is neither created nor destroyed while this occurs.

3.3.2 Point form of mass conservation

We are now ready to convert the integral form of the equation of continuity to a point form. Starting with the integral form

$$\iint_S \mathbf{N} \cdot \hat{\mathbf{n}} dS = - \frac{d}{dt} \iiint_V c dV,$$

we employ Liebnitz's rule for differentiating an integral and get

$$\iint_S \mathbf{N} \cdot \hat{\mathbf{n}} dS = - \iiint_V \left(\frac{\partial c}{\partial t} \right) dV,$$

assuming that concentration is continuous and that V is not time varying.

We then divide both sides of the equation by the region's volume and take the limit as the volume shrinks to zero:

$$\lim_{V \rightarrow 0} \frac{1}{V} \iint_S \mathbf{N} \cdot \hat{\mathbf{n}} dS = \lim_{V \rightarrow 0} -\frac{1}{V} \iiint_V \left(\frac{\partial c}{\partial t} \right) dV$$

$$\nabla \cdot \mathbf{N} = -\frac{\partial c}{\partial t}.$$

Applying Fick's first law to this identity, we get

$$\frac{\partial c}{\partial t} = \nabla \cdot (D \nabla c).$$

This is known as Fick's second law. Finally, adding subscript "s" to c and D to denote that these variables correspond to the solid phase, we get

$$\frac{\partial c_s}{\partial t} = \nabla \cdot (D_s \nabla c_s).$$

In words, this says that the total lithium flux density into any sample volume within the homogeneous solid is equal to the rate of change of concentration of lithium in that volume.¹¹ This means that any lithium entering a sample volume must either be compensated for by lithium exiting that volume or by an increasing concentration of lithium in that volume. That is, lithium is neither created nor destroyed within any sample volume in the homogeneous solid.

We have now derived Eq. (3.2).

3.3.3 1D example of linear diffusion

Eqs. (3.1) and (3.2) are diffusion equations. Furthermore, Eq. (3.3) has a dominant diffusion component. To understand the operation of lithium-ion cells, it is therefore very important to have an intuitive feel for how diffusion works.

To help visualize diffusion, we create a simulator for the special case of one-dimensional diffusion with constant D_s . In this case, the diffusion PDE reduces to

$$\frac{\partial c_s(x, t)}{\partial t} = D_s \frac{\partial^2 c_s(x, t)}{\partial x^2}.$$

We will partition time and space into small uniform divisions and use the *finite-difference* method to simulate the dynamics of the equation. That is, we first approximate the time derivative using Euler's forward rule

$$\frac{\partial c_s(x, t)}{\partial t} \approx \frac{c_s(x, t + \Delta t) - c_s(x, t)}{\Delta t}.$$

We can approximate the second spatial derivative using the forward or backward rule (repeated), or the central-difference (CD) rule

$$\frac{\partial c_s(x, t)}{\partial x} \approx \frac{c_s(x + \Delta x, t) - c_s(x, t)}{\Delta x} \quad (\text{Forward})$$

¹¹ To see this more clearly, we can write $\frac{\partial c_s}{\partial t} = -\nabla \cdot (-D_s \nabla c_s)$ and note that $-D_s \nabla c_s$ is flux density. Then, $-\nabla \cdot (\text{flux})$ is negative divergence and actually represents net flux density *into* a point rather than flux density *out of* a point.

$$\frac{\partial c_s(x, t)}{\partial x} \approx \frac{c_s(x, t) - c_s(x - \Delta x, t)}{\Delta x} \quad (\text{Backward})$$

$$\frac{\partial^2 c_s(x, t)}{\partial x^2} \approx \frac{c_s(x + \Delta x, t) - 2c_s(x, t) + c_s(x - \Delta x, t)}{(\Delta x)^2}. \quad (\text{CD})$$

Putting the equations together, using the central-difference rule, we get

$$c_s(x, t + \Delta t) = c_s(x, t) + D_s \Delta t \frac{c_s(x + \Delta x, t) - 2c_s(x, t) + c_s(x - \Delta x, t)}{(\Delta x)^2}. \quad (3.10)$$

To implement this method, we must take time steps of Δt seconds. Every time step, we compute c_s at every x location using this relationship. Selection of Δt and Δx cannot be done arbitrarily—this method is stable only for certain combinations of Δt and Δx . However, it is the simplest way to approximate a PDE in discrete time and space, so it is the method we choose to implement first. Other methods include the *finite-volume* method (introduced later in this chapter) and the *finite-element* method (introduced in Chap. 4). Either of these is generally preferred over finite difference for stability and accuracy, but is more complicated to explain.

The following MATLAB code implements the central-difference method, mirroring at edges.

```
D = 2; % diffusivity (m^2/s)
dt = 0.1; % time step (s)
dx = 1; % x step (m)
c = 1:32; % initial concentration profile (mol/(m^3))

figure(1); clf; colormap(jet(31));
for k = 0:1000,
    % implement finite-difference diffusion equation using
    % explicit method and central differences
    c = c + D*dt/(dx^2)*([c(2:end),c(end)] - 2*c + [c(1),c(1:end-1)]);

    if mod(k,100) == 0, % plot a snapshot
        subplot(11,1,k/100+1); image(c); grid on
        set(gca,'ytick',[],'xticklabel',[],'ticklength',[0 0]);
        set(gca,'xtick',1.5:1:100,'gridlinestyle','--','linewidth',4);
        h = ylabel(sprintf('t = %g (s)',k*dt));
        set(h,'rotation',0,'horizontal','right','vertical','middle')
    end
end
xlabel('x location');
text(16,-14.25,'Diffusion example','horizontal','center');
```

In the code, the first three lines set up the simulation constants, and the fourth line creates a vector c that represents c_s at different points in space at this particular moment in time. This vector is initialized as a concentration profile ranging from 1 to 32 mol m^{-3} across the x dimension. That is, the leftmost of the 32 spatial points being simulated has concentration 1 mol m^{-3} , the rightmost point has concentration 32 mol m^{-3} , and points in between vary linearly.

The majority of the remainder of the code is concerned with plotting the concentration vector at different moments in time, resulting in Fig. 3.8. Besides plotting, the code implements a “for” loop, which steps from the zeroth time step to the 1,000th time step, and the concentration update equation:

```
c = c + D*dt/(dx^2)*([c(2:end),c(end)] - 2*c + [c(1),c(1:end-1)]);
```

In this MATLAB vector equation, `[c(2:end),c(end)]` implements the $c_s(x + \Delta x, t)$ term, substituting the “mirrored” $c_s(31\Delta x, t)$ for the unknown $c_s(32\Delta x, t)$ and `[c(1),c(1:end-1)]` implements $c_s(x - \Delta x, t)$, substituting the “mirrored” $c_s(0, t)$ for the unknown $c_s(-\Delta x, t)$. Overall, this line implements Eq. (3.10) once per time iteration.

Fig. 3.8 illustrates the results of running this code, showing diffusion in action. At time $t = 0$, the figure shows a profile of concentration versus space ranging from 1 mol m^{-3} to 32 mol m^{-3} across the x dimension. The dark blue colors indicate low concentration, and the dark red colors indicate high concentration. Even as soon as time $t = 10$, the blues and reds are not as dark, indicating that there has been some material flux from a higher concentration region to a lower concentration region via diffusion, with the result being that the profile of concentration versus space is becoming more uniform. By time $t = 100$, the concentration is almost entirely uniform across the width of the simulated space, as illustrated by the nearly constant midrange green color.

We see that diffusion is actually pretty simple—explaining how material flows due to a concentration gradient—even though the PDE may look daunting at first. Soon, you’ll be able to glance at an equation that looks like

$$\frac{\partial c(x, t)}{\partial t} = \nabla \cdot (D \nabla c(x, t)) + r(x, t)$$

and say to yourself, “That’s just a diffusion equation” and

1. Know what you’re talking about;
2. Really think of it as pretty simple.

The good news is that battery-physics equations are predominantly diffusion equations. So we can look at the final forms and understand the internal cell processes as being dominated by diffusion effects similar to what we have seen illustrated in this example.

3.4 Thermodynamics

Now that we have addressed conservation of charge and mass in the solid particles of the electrode active material, we move on to establishing parallel conservation of charge and mass relationships for

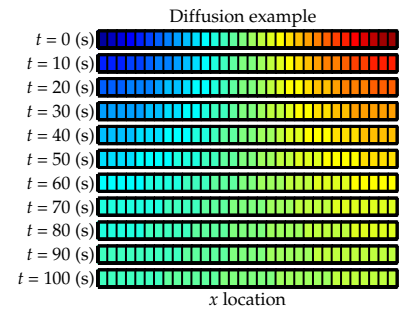


Figure 3.8: Diffusion example using the finite-difference method.

the electrolyte. Fig. 3.9 illustrates our new focus. Positively charged lithium ions move through the electrolyte due to diffusion, migration, and convection. In doing so, they set up an ionic current, which influences the electric potential in the electrolyte.

The derivation of electrolyte equations involves a topic of study known as *concentrated solution theory*. We follow the general outline of Newman's book, filling in some of the gaps that were left between equation steps.¹² However, before we can leap right into the derivation, we must first cover a number of critical foundational topics.

The first broad topic that we look at is a subject area known as *thermodynamics*, which looks at energy relationships in systems, including (but not limited to) heat/temperature aspects. Thermodynamics tells us whether or not a process or a reaction is able to occur by looking at energy states before and after the presumed reaction. It is applicable to systems in stable or metastable equilibrium.

We will eventually also look at *kinetics*, which concerns the rate of chemical reactions. How quickly or how slowly will the process occur? Kinetics is applicable to systems in transition from nonequilibrium to equilibrium or between two equilibrium states. Kinetics addresses how to overcome the energy barrier to finish the transformation from the starting (reactant) state to the final (product) state. We postpone any further discussion of kinetics until Sect. 3.9, where we consider the derivation of Eq. (3.5).

3.4.1 Energy

In thermodynamics, we define a *system* to be whatever part of the universe we select for study. Adjacent to the system is the *environment*. Thermodynamics is about energy relationships between and among systems and the environment.

It turns out that we can think about a system's energy in a number of different ways. Four quantities called *thermodynamic potentials* are useful. They are *internal energy U*, *enthalpy H*, *Helmholtz free energy A*, and *Gibbs free energy G*. All have units of joules (J), and the relationships between them are illustrated in Table 3.1.

The most basic of these is the internal energy *U*. Internal energy is defined as the energy associated with the random, disordered motion of molecules. It is separated in scale from the macroscopic ordered energy associated with moving objects; it refers to the invisible microscopic energy on the atomic and molecular scale. This includes translational, rotational, and vibrational kinetic energy of atoms and molecules, and potential energy associated with the static rest mass energy of the constituents of matter, static electric energy of atoms within molecules or crystals, and the static energy of chemical bonds.

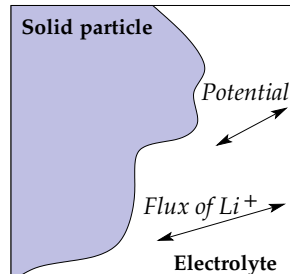


Figure 3.9: Dynamics in the electrolyte.

¹² Newman, J., and Thomas-Alyea, K.E., *Electrochemical Systems*, 3d, Chapter 12, Wiley-Interscience, 2004.

Table 3.1: Energy relationships.
(Adapted from Schroeder, D.V., *An Introduction to Thermal Physics*, Chapter 5, Addison Wesley, 2000.)

Subtract TS	
Internal energy U (energy needed to create a system)	Helmholtz free energy $A = U - TS$ (energy needed to create a system minus energy you can get from the environment)
Enthalpy $H=U+pV$ (energy needed to create a system plus the work needed to make room for it)	Gibbs free energy $G=U+pV-TS$ (energy needed to create a system and make room for it minus the energy you can get from the environment)

The internal energy then is the energy needed to create the system but excludes the energy required to displace the system's surroundings, any energy associated with a move as a whole, or energy due to external force fields.

To bring a system to internal energy U , we don't need to start from zero. For example, if the system is created in an environment of temperature T , then some of the energy can be obtained by spontaneous heat transfer from the environment to the system.¹³ The amount of this spontaneous energy transfer is TS where S is the final entropy of the system (defined in Sect. 3.4.3). The bottom line is that if you accept energy from the environment when creating the system, you don't have to put in as much energy as if you didn't. Note that if a more disordered (higher entropy) final state is created, less work is required to create the system. The Helmholtz free energy, computed as $A = U - TS$ (where A is from the German *arbeit*, or work), is then a measure of the amount of energy you have to put in to create a system once the spontaneous energy transfer to the system from the environment is accounted for. Note also that if the system is subjected to an external force field (e.g., an electric field), any energy received from that field is considered to be a part of A . The best way to think about Helmholtz free energy is that it is the maximum amount of work that a system can perform at constant temperature.

To understand enthalpy, first consider Fig. 3.10. In this example, constant air pressure p of the atmosphere is acting on surface area A of the system with force $F = pA$ and is compressing the volume V of the system of interest. The work that the atmosphere has done to the cylinder system is

$$\Delta w = F \Delta x = (pA) \Delta x = p(A \Delta x) = p(-\Delta V) = -p \Delta V,$$

noting that $\Delta V < 0$ and so $\Delta w > 0$.

Enthalpy is defined as $H = U + pV$. The internal energy U might be thought of as the energy required to create a system in the absence of changes in temperature or volume. But if the process changes the volume, as in a chemical reaction that produces a gaseous product, then work must be done to produce the change in volume. For a constant-pressure process, the work you must do to produce a volume change ΔV is $p\Delta V$. Then the term pV can be interpreted as the extra work you must do to "create room" for the system if you presume it started at zero volume. Since it turns out that heat and work change internal energy in equivalent ways (see Sect. 3.4.2), enthalpy can also be thought of as the total amount of energy stored by the system that could be released as heat. We will find the concept of enthalpy important when considering thermal effects in Chap. 7.

The *Gibbs free energy* is defined as $G = U + pV - TS$. This is the net

¹³ Here, and in the rest of this book, T is absolute temperature, measured in kelvin (K).

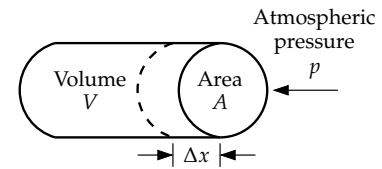


Figure 3.10: Atmospheric work.

energy required to create a system in an environment having temperature T , starting from a negligible initial volume. It can be thought of as the maximum amount of work obtainable from a reaction in a constant-temperature, constant-volume scenario.¹⁴ We will see that the change in Gibbs free energy, ΔG , in a reaction is a very useful parameter: it predicts the direction in which a chemical reaction will proceed spontaneously.

3.4.2 The first law of thermodynamics

The *first law of thermodynamics* deals with the internal energy of a system. An important property of the internal energy is that it is a *state function*. A state function is a precisely measurable physical property such as temperature that characterizes the state of a system, independently of how the system was brought to that state.¹⁵ For example, you might increase the temperature of an object and arrive at the same final temperature either by performing work (e.g., via friction), or by adding heat (e.g., by subjecting to a warm environment), or both. All that matters is the final temperature, which is a function of the system state.

We can define what we mean by a state function mathematically. Let the state of the system be defined by the vector \mathbf{x} of parameters, and let $f(\mathbf{x})$ be some state function. Then, if the change in parameters is from an initial state \mathbf{x}_i to a final state \mathbf{x}_f , then the change in f is

$$\Delta f = \int_{\mathbf{x}_i}^{\mathbf{x}_f} df = f(\mathbf{x}_f) - f(\mathbf{x}_i).$$

This relationship depends only on the initial and final points \mathbf{x}_i and \mathbf{x}_f . It does not depend on the path taken between these two endpoints. We say that df is an *exact differential*. In contrast, a quantity that is represented by an *inexact differential* is not a function of state.

A simple example of an exact differential is the function¹⁶ $f = xy$. Then, $df = d(xy) = y dx + x dy$. Integrating df from any initial (x_i, y_i) point to any final (x_f, y_f) point will give the same answer of $(x_f \times y_f) - (x_i \times y_i)$ regardless of the path taken.

On the other hand, a simple example of an inexact differential is the function ~~dg~~ $g = y dx$. (The strikeout through the d is used to show that this is an inexact differential.) Then, for example, integrating from $(0, 0)$ to $(1, 1)$ along a straight line $y = x$ gives

$$\Delta g_1 = \int_{(0,0)}^{(1,1)} y dx = \int_0^1 x dx = 1.$$

However, integrating from $(0, 0)$ to $(1, 0)$ along $y = 0$ and then to

¹⁴ Note also that if the system is subjected to an external force field (e.g., an electric field), any energy received from that field is considered to be a part of G .

¹⁵ Other common examples of state functions are pressure p , volume V , enthalpy H , Helmholtz free energy A , entropy S , and Gibbs free energy G .

¹⁶ From Blundell, S.J. and Blundell, K.M., *Concepts in Thermal Physics*, chapter 11, Oxford University Press, 2009.

(1,1) along $x = 1$ gives

$$\Delta g_2 = \int_{(0,0)}^{(1,0)} y \, dx + \int_{(1,0)}^{(1,1)} y \, dx = 0.$$

The calculations for Δg_1 and Δg_2 had the same initial and final points, but yielded different results.

Returning to the problem at hand, the first law of thermodynamics states that $dU = \text{dq} + \text{dw}$, where dq is the amount of heat added to a system and dw is the amount of work done on the system during an infinitesimal procedure. We use dq and dw rather than dq and dw because they turn out not to be exact differentials—they merely denote some infinitesimal amount.

Thus, heat added to a system and mechanical work done on the system are two equivalent ways to increase its internal energy, and the total energy is conserved. If the system is isolated from its environment, its internal energy does not change. Also, both heat and work are forms of energy. For example, considering infinitesimal changes rather than macroscopic changes now, the work that the atmosphere has done to the cylinder system in Fig. 3.10 is

$$\text{dw} = F \, dx = (pA) \, dx = p(A \, dx) = p(-dV) = -p \, dV.$$

3.4.3 The second law of thermodynamics

The second law of thermodynamics points out the spontaneous direction of chemical reactions, using a concept called *entropy*. The easiest way to understand entropy S is to define it as follows: S is a state function such that during an isothermal *reversible* (infinitesimally slow) process, we have

$$\text{dq} = T \, dS,$$

where temperature T is kept constant. Therefore $dS = \text{dq}/T$ during isothermal reversible processes.

The second law of thermodynamics simply states that for any system:

$$dS \geq \frac{\text{dq}}{T},$$

where equality is possible only in reversible processes.

Entropy can be intuitively understood as the amount of disorder in a system.¹⁷ If heat is applied to the system and temperature kept constant, entropy increases. If heat is removed from the system at constant temperature, entropy has an opportunity to decrease.

The second law of thermodynamics can also consider the system (denoted here by subscript 1) and the environment (denoted by subscript 2) together. Assume they are both at temperature T . The heat

¹⁷ This understanding is oversimplified but is sufficient for our purposes.

transfer process (from 1 to 2, or vice versa) must follow $\text{d}q_1 = -\text{d}q_2$. According to the second law of thermodynamics,

$$\text{d}S_1 \geq \frac{\text{d}q_1}{T} \quad \text{and} \quad \text{d}S_2 \geq \frac{\text{d}q_2}{T}.$$

Therefore, $\text{d}S_1 + \text{d}S_2 \geq \frac{\text{d}q_1 + \text{d}q_2}{T} = 0$ and $\text{d}S = \text{d}S_1 + \text{d}S_2 \geq 0$.

This equation is another form of the second law of thermodynamics, which states that a closed system's entropy never decreases.

3.4.4 Gibbs free energy

We return to discuss Gibbs free energy, as it turns out to be the most important measure of energy for our modeling purposes. The *Gibbs function* is defined to be: $G = U + pV - TS$. *Free energy* is how much energy a system contains that can be harnessed to do work—we cannot always bring energy down to zero.

Considering the different definitions of energies from Sect. 3.4.1, this is not too hard to understand. If we are able to shrink the volume of the system down to zero, we can release the pV component of G to do useful work. However, we cannot remove more than the Helmholtz energy from the system. If we were to try to bring the internal energy U down to zero, the environment would be fighting against us, wanting to add in its TS contribution. So, the minimum energy state of a system is $U = TS$ and G tells us the maximum amount of energy that can be removed from the system.

As an analogy, consider a rock on the top of a cliff.¹⁸ It has the potential to provide useful work (e.g., via a pulley). From elementary physics, we know that the gravitational potential energy is equal to mass times the acceleration of gravity times height. But, height can never become zero (i.e., at the center of Earth). The rock can be lowered only until it rests at the bottom of the cliff (not yet at zero energy because not yet at the center of Earth). The environment places a constraint on how much energy is free/available.

When pressure and temperature are held constant, the Gibbs function can be interpreted as Gibbs free energy. The sign of G determines in which direction a reaction will proceed spontaneously. Spontaneous reactions always cause a decrease in G (i.e., $\text{d}G < 0$). For a reaction to occur for which $\text{d}G > 0$, energy must be added to the system.

The tendency of spontaneous decrease of G derives from the tendency of increasing the total entropy of the system plus the environment. To show this, we need to write $G = U_1 + pV_1 - TS_1$ with the subscript “1” emphasizing that the entropy associated with G is only S_1 , the entropy of the system. We denote the entropy of the

¹⁸ This example deals with macroscopic energy, not internal energy, but the same kind of idea applies.

environment as S_2 . So, for system 1

$$\begin{aligned} dG &= dU_1 + pdV_1 - TdS_1 \\ &= dq_1 + dw_1 + pdV_1 - TdS_1 \\ &= dq_1 - pdV_1 + pdV_1 - TdS_1 \\ &= dq_1 - TdS_1. \end{aligned}$$

We assume that the environment has reversible process $dq_2 = T dS_2$ and recall $dq_1 = -dq_2$,

$$dG = -dq_2 - T dS_1 = -T dS_2 - T dS_1 = -T dS \leq 0.$$

This is the sense in which we will use Gibbs free energy. It will be a tool for us to understand the spontaneous direction of a chemical reaction, from one equilibrium state to another.

3.5 Physical chemistry

We now take the background topics we have reviewed from thermal physics and link them to topics in chemistry, yielding results generally considered to belong to the domain of the field of physical chemistry. This will prepare us to talk about electrolyte solutions generally, and concentrated solution theory specifically.

To begin, we reflect on an attribute that was the same between some of the physical parameters that we encountered while considering thermodynamics and was different between others. Specifically, some of the parameters were normalized or relative quantities; others were total or absolute quantities.

We say that a property is *intensive* if it is a normalized quantity. If everything in a system is doubled, the value of an intensive property remains unchanged. Examples of intensive properties are pressure, temperature, concentration, and density.

We say that a property is *extensive* if it is a total quantity. If everything in a system is doubled, the value of an extensive property also doubles. Examples of extensive properties are internal energy, Gibbs free energy, volume, and mass.

It is preferable to work with intensive properties, if possible. Then, the absolute size of the system is not a factor of the models, and the equations apply directly to any scale. To do so, we must normalize extensive properties, possibly by dividing by volume or possibly by dividing by mass.

3.5.1 Molarity and molality

The electrolyte is a solution—a mixture created by dissolving a solute in a solvent. There are two primary ways of creating an intensive property out of the amount of solute in the solution:

- The concentration of a solution is commonly expressed by its *molarity*, which is the number of moles of the dissolved solute per liter of solution (not per liter of the solvent). The molarity of a solution is defined as

$$c_i = \frac{n_{\text{solute } i}}{V_{\text{solution}}}. \quad (3.11)$$

We will use units of mol m^{-3} when describing concentrations, but it is also common to see units of mol L^{-1} . To convert from one unit system to the other, note that $1 \text{ mol L}^{-1} = 1,000 \text{ mol m}^{-3}$.

- This is not to be confused with the *molality*, which is the number of moles of the dissolved solute per kilogram of solvent (not per kilogram of solution). We compute molality as

$$m_i = \frac{n_{\text{solute } i}}{m_{\text{solvent}}} \quad (3.12)$$

in units of mol kg^{-1} .

We will find a need to understand both molarity and molality in the derivation of the electrolyte models. Molarity is the more readily understood conceptual framework, but molality provides an easier experimental approach (it's easier to measure a mass of solute and a mass of solvent before mixing than it is to measure a mass and a volume after mixing). At the appropriate time, we'll discuss how to convert between molarity and molality.

3.5.2 Electrochemical potential

To convert an extensive property of a substance to an intensive property, we recognize that the extensive property must be proportional to the total molar amount of the substance. But if there are multiple species in the solution, the relationship between the extensive property and the individual intensive properties is not immediately obvious.

For example, suppose that there are n_1 mol of species 1 and n_2 mol of species 2 in a solution. If we double only one of these quantities, will the Gibbs free energy of the system double? The answer is no. You must double the quantities of all species in the system for the Gibbs free energy of the system to double.

Consequently, in multispecies systems, one has to define partial molar quantities. Partial molar quantities describe how much an

extensive property changes if we add one mole of one species to the system or solution.

Electrochemical potential $\bar{\mu}$ is defined to be the partial molar Gibbs free energy in a multispecies system. For species i , we define:

$$\bar{\mu}_i = \left(\frac{\partial G}{\partial n_i} \right)_{T,p,n_j(j \neq i)},$$

where n_i is the molar amount of species i , and the subscript notation indicates that we are keeping temperature, pressure, and molar amounts of all other species constant. The electrochemical potential represents how easy or difficult it is to add more of species i at this particular location. If it is easy to add more of species i , then $\bar{\mu}_i$ will be small (or negative)—either it requires only a small amount of energy to do so, or energy is actually released by doing so. If it is difficult, then $\bar{\mu}_i$ will be large—it requires significant energy to do so. The units of $\bar{\mu}_i$ are J mol^{-1} .

The electrochemical potential $\bar{\mu}_i$ can be thought of as the summation of two parts:

$$\bar{\mu}_i = \bar{\mu}_{i,\text{internal}} + \bar{\mu}_{i,\text{external}},$$

where $\bar{\mu}_{i,\text{external}}$ refers to the sum of electric potential, magnetic potential, gravitational potential, and other forces from external fields, and $\bar{\mu}_{i,\text{internal}}$ includes everything else, such as density, temperature, and enthalpy. In electrochemistry, we define *chemical potential*, denoted as μ_i (without the overline), to be equal to the internal portion, and *electrochemical potential* $\bar{\mu}_i$ as the total amount, including effects from external fields.¹⁹

Assuming that gravitational and magnetic potentials are negligible, chemical and electrochemical potentials are related via

$$\bar{\mu}_i = \mu_i + z_i F \phi, \quad (3.13)$$

where z_i is the valency (charge number) of the species,²⁰ F is Faraday's constant, and ϕ is the local electrostatic potential.

So, we can express a species' electrochemical potential from the Gibbs free energy of the system. But, can we express the Gibbs free energy of a system in terms of the electrochemical potentials of all its species? The key question here is whether G is a first-order homogeneous function of n_i (i.e., whether $G(\alpha \mathbf{n}) = \alpha G(\mathbf{n})$ for vector \mathbf{n}). If temperature and pressure are kept constant, this is true because Gibbs free energy is an extensive quantity in thermodynamics. For example, if only two species are present, $G(2n_1, 2n_2) = 2G(n_1, n_2)$. Therefore at constant temperature and pressure, Gibbs free energy is a first-order homogeneous function of n_i .

¹⁹ Note that there is inconsistent usage of terminology between physics, electrochemistry, semiconductor physics, and solid-state physics. Some fields would name the quantity we have computed as $\bar{\mu}_i$ to be *chemical potential* or *total chemical potential*. We use the conventions of electrochemistry, denoting this term as *electrochemical potential* instead, and reserving the term *chemical potential* for the internal chemical potential.

²⁰ For example, $z = -1$ for an electron and $z = +2$ for Cu^{2+} .

According to Euler's theorem for homogeneous functions, we can then state

$$G(\mathbf{n}) = \mathbf{n} \cdot \nabla G(\mathbf{n}) = \sum_i n_i \frac{\partial G}{\partial n_i},$$

where $\mathbf{n} = (n_1, n_2, \dots)$ is treated as a vector for convenience. Applying the definition of electrochemical potential, we have

$$G = \sum_i n_i \bar{\mu}_i. \quad (3.14)$$

3.5.3 Gibbs–Duhem equation

The intensive quantities of a solution are not all independent: one can be derived from the others. This result will be helpful, as it allows us to remove one equation from the simultaneous set of equations we must later solve.

We start with the prior definition of the Gibbs function,

$$\begin{aligned} G &= U + pV - TS \\ dG &= dU + d(pV) - d(TS) \\ &= dq + dw + pdV + Vdp - TdS - SdT. \end{aligned}$$

We know that $dw = -pdV$, and if we choose a reversible process, then $dq = TdS$, giving

$$\begin{aligned} dG &= Vdp - SdT \\ \sum_{i=1}^r n_i d\bar{\mu}_i &= Vdp - SdT. \end{aligned}$$

This can be rearranged to be the Gibbs–Duhem equation:

$$SdT - Vdp + \sum_{i=1}^r n_i d\bar{\mu}_i = 0. \quad (3.15)$$

To understand the Gibbs–Duhem equation, it is easiest to consider the simplest case. Assume that temperature and pressure are constant and that there are only two species. Then

$$n_1 d\bar{\mu}_1 + n_2 d\bar{\mu}_2 = 0.$$

The Gibbs–Duhem equation states that in an isothermal and constant pressure two-species solution, if the electrochemical potential of one species increases, then it must decrease for the other species.

We will use the Gibbs–Duhem equation for a multispecies solution at constant temperature and pressure. This result can be written as

$$\sum_{i=1}^r n_i d\bar{\mu}_i = 0.$$

If we divide both sides of this equation by volume, we get the equivalent relationship

$$\sum_{i=1}^r c_i d\bar{\mu}_i = 0. \quad (3.16)$$

The key point to remember is this: if we know c_i for $i = 1 \dots r$ and $d\bar{\mu}_i$ for $i = 1 \dots r - 1$, then we can compute $d\bar{\mu}_r$ from that information. This will eliminate one equation from the set of equations that we need to solve.

3.5.4 Activity

In a solution, cations and anions are not located completely randomly. The positive charge of a cation tends to attract anions around it and to repel other cations. Similarly, the negative charge of an anion tends to attract cations around it and to repel other anions. This is illustrated in Fig. 3.11.

As a consequence, it is not as easy for an ion to move through solution as it would be for an uncharged particle. The ion appears to be larger than it truly is, since it attempts to drag other ions with it and to push apart other groups of charged particles that are in its way.

So, if we look at the ionic conductivity of a solution, it is lower than expected. Ions do not move as quickly from a region of high concentration to a region of low concentration as would be predicted by a naïve model. It is as if the concentration gradient of the solute has been diminished.

To reflect this phenomenon, you can introduce an “effective concentration” or *activity* $a_i < c_i$ for each species i . We can think about the activity of a species in a certain location as its “restlessness” there.²¹ The greater the activity, the more eager the species is to leave.

You can define a *molar activity coefficient* f_i such that for species i , the activity

$$a_i = c_i f_i,$$

where $0 \leq f_i \leq 1$ characterizes how activity differs from concentration. We call it the “molar” activity coefficient because the concentration used here is the molar concentration c_i .

3.5.5 Absolute activity based on molarity

Activity of species i is also related to the chemical potential μ_i for that species. Guggenheim defined an *absolute activity* λ_i for species i as

$$\lambda_i = \exp\left(\frac{\mu_i}{RT}\right).$$

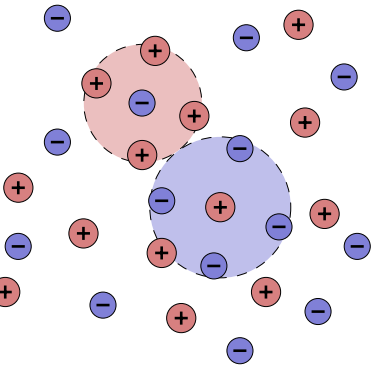


Figure 3.11: Nonrandom grouping of anions and cations in solution.

²¹ Oldham, K., Myland, J., and Bond, A., *Electrochemical Science and Technology: Fundamentals and Applications*, Wiley, 2011.

Conversely, we have

$$\mu_i = RT \ln \lambda_i. \quad (3.17)$$

This is related to the prior definition of activity via

$$\lambda_i = a_i a_i^\ominus,$$

where a_i^\ominus is a constant of proportionality, independent of the concentration or the electric potential, but dependent on the material types of solute and solvent, and on temperature as well as pressure (if there are gases). So it is defined at *standard temperature and pressure* (STP) $T = 0^\circ\text{C}$ and $p = 100\text{ kPa}$. This also allows us a different way to write relative activity if we define

$$a_i^\ominus = \exp\left(\frac{\mu_i^\ominus}{RT}\right),$$

which gives us

$$a_i = \exp\left(\frac{\mu_i - \mu_i^\ominus}{RT}\right).$$

Combining results, we see that λ_i can be broken down into three terms:

$$\lambda_i = c_i f_i a_i^\ominus, \quad (3.18)$$

and so

$$\mu_i = RT \ln (a_i a_i^\ominus) = RT \ln (c_i f_i a_i^\ominus).$$

3.5.6 Absolute activity based on molality

To define absolute activity, we have used concentration c_i (also known as molarity) of the species as a basis. It is also possible to define absolute activity in terms of molality m_i .

To do so, we must use the dimensionless “molal” activity coefficient, which is denoted by γ_i . The new relation is

$$\lambda_i = m_i \gamma_i \lambda_i^\ominus. \quad (3.19)$$

Again, λ_i^\ominus is a proportionality constant with units kg mol^{-1} .

No matter whether one uses molarity or molality, the computation will give exactly the same value of λ_i (dimensionless).

3.6 Basic characteristics of binary electrolytes

Our final major topic before beginning to derive the electrolyte conservation of mass and charge equations is that of understanding the electrolyte. We are particularly concerned with a *binary electrolyte*, that is, one having exactly two charged constituents. The electrolyte then comprises the solvent, the positively charged ions (cations), and the negatively charged ions (anions).

3.6.1 Stoichiometric coefficient ν

The electrolyte is formulated by dissolving either a charge-neutral acid, base, or salt into a charge-neutral solvent. Regardless of the choice of solute, the resulting solution has a fixed ratio of anions and cations corresponding to the ratio in the originating solute. The *stoichiometric coefficients* of the ions specify this ratio.

For a salt such as Na_2SO_4 , we define unsigned (positive) integer stoichiometric coefficients ν for both species (Na^+ and SO_4^{2-}). Since $\text{Na}_2\text{SO}_4 \rightarrow 2\text{Na}^+ + \text{SO}_4^{2-}$, we have $\nu_{\text{Na}^+} = 2$ and $\nu_{\text{SO}_4^{2-}} = 1$. Similarly, for $\text{LiPF}_6 \rightarrow \text{Li}^+ + \text{PF}_6^-$, we have $\nu_{\text{Li}^+} = 1$ and $\nu_{\text{PF}_6^-} = 1$. We also sometimes use $\nu = \sum_i \nu_i$.

Note that the symbol “ ν ” is not the letter “v”. It is the Greek letter “nu.” A memory mnemonic is to think “n” is for “number” (of each species), where ν is the Greek equivalent of “n.”

3.6.2 Charge number z

The *charge number* carried by an ion is represented by the signed integer z . In Na_2SO_4 , we have $z_{\text{Na}^+} = 1$ and $z_{\text{SO}_4^{2-}} = -2$ because the sodium ion has a charge of +1, and the sulphate ion has a charge of -2. Similarly, in LiPF_6 , $z_{\text{Li}^+} = 1$ and $z_{\text{PF}_6^-} = -1$. Notice that a cation has $z > 0$ while an anion has $z < 0$.

3.6.3 Electroneutrality in binary electrolytes

Since the electrolyte is formulated by combining a charge-neutral solute with a charge-neutral solvent, a macroscopic solution must satisfy the electroneutrality condition that $q = 0$, where q is the total charge. In an electrolyte, one must then have

$$\sum_i z_i \nu_i = 0. \quad (3.20)$$

If the electrolyte is a binary electrolyte, then we use subscripts “+” for the cation, “-” for the anion, and “0” for the solvent. This gives

$$z_+ \nu_+ + z_- \nu_- + z_0 \nu_0 = 0.$$

However, the solvent is uncharged. Therefore, this expression reduces to

$$z_+ \nu_+ + z_- \nu_- = 0. \quad (3.21)$$

There is another way of stating the same concept. In a binary electrolyte, the concentration of an ion is proportional to its stoichiometric coefficient. That is, $c_i \propto \nu_i$. Further, if we use “+” for the cation and “-” for the anion, then

$$\frac{c_+}{\nu_+} = \frac{c_-}{\nu_-}.$$

The ratio is the concentration of the solute. We particularly use symbol c (no subscript) for this ratio and obtain the following:

$$c = \frac{c_+}{v_+} = \frac{c_-}{v_-}, \quad (3.22)$$

where c is the concentration of the solute in the electrolyte.

By extension, we can rewrite Eq. (3.20) as

$$\sum_i z_i c_i = 0.$$

In particular, for a binary electrolyte,

$$z_+ c_+ + z_- c_- = 0. \quad (3.23)$$

The charge-neutrality and solute-concentration equations (3.21), (3.22), and (3.23) in this section are the characteristic equations for a binary electrolyte and will be used frequently in the forthcoming derivations.

3.6.4 An expression for current

Flux density \mathbf{N} , at a particular point, through an infinitesimal cross-sectional area, can be expressed as velocity \mathbf{v} multiplied by concentration c

$$\mathbf{N} = c \mathbf{v} \text{ mol m}^{-2} \text{ s}^{-1}.$$

We are particularly interested in the flux density of charged particles, which support the movement of electrical current.

An electrolyte contains both positively charged cations and negatively charged anions. The total current includes the contribution from both

$$\mathbf{i} = \mathbf{i}_+ + \mathbf{i}_-,$$

where \mathbf{i}_+ and \mathbf{i}_- represent contributions from the cations and anions, respectively.

We can immediately write the expression for the currents:

$$\begin{aligned} \mathbf{i}_+ &= z_+ F \mathbf{N}_+ = z_+ F c_+ \mathbf{v}_+ \\ \mathbf{i}_- &= z_- F \mathbf{N}_- = z_- F c_- \mathbf{v}_-, \end{aligned}$$

and

$$\begin{aligned} \mathbf{i} &= z_+ F c_+ \mathbf{v}_+ + z_- F c_- \mathbf{v}_- \\ &= F \sum_i z_i \mathbf{N}_i. \end{aligned} \quad (3.24)$$

3.6.5 Continuity equations for mass and charge

The mass continuity equation states that at any point in the solution,

$$\frac{\partial c_i}{\partial t} = -\nabla \cdot \mathbf{N}_i + R_i, \quad (3.25)$$

where R_i is the generation rate of species i at that particular point.

Note that $\nabla \cdot \mathbf{N}_i$ is the net flux density out of the point; thus, it is with a minus sign that it represents the contribution to the net increase of the concentration at that particular point.

This equation is written for only one species. One can first multiply both sides by $z_i F$:

$$F \frac{\partial z_i c_i}{\partial t} = -\nabla \cdot (z_i F \mathbf{N}_i) + z_i F R_i,$$

and then sum over all the species to obtain

$$\frac{\partial}{\partial t} F \sum_i z_i c_i = -\nabla \cdot \left(F \sum_i z_i \mathbf{N}_i \right) + F \sum_i z_i R_i.$$

We here allow “generation” because chemical reactions may generate new species. However, the species generated are charge balanced. That is, if a cation is generated, there would be certain number of anion(s) generated to balance the positive charge. Therefore, even if we have $R_i \neq 0$, we always have $\sum_i z_i R_i = 0$. Hence, this equation simplifies to

$$\frac{\partial}{\partial t} F \sum_i z_i c_i = -\nabla \cdot \left(F \sum_i z_i \mathbf{N}_i \right).$$

In fact, both sides of this equation are zero. The left-hand side is zero because $\sum_i z_i c_i = 0$ (as we have already shown, per Eq. (3.23)). We recognize the right-hand side to be $-\nabla \cdot \mathbf{i}$. Hence

$$\nabla \cdot \mathbf{i} = 0. \quad (3.26)$$

This equation implies that charge can neither be stored nor created nor destroyed in an electrolyte solution. It can be regarded as a charge continuity equation.

3.7 Concentrated solution theory: Electrolyte mass conservation

The goal of the next major section is to derive the mass-balance equation for the electrolyte

$$\frac{\partial c}{\partial t} = \nabla \cdot \left[D \left(1 - \frac{d \ln c_0}{d \ln c} \right) \nabla c \right] - \frac{\mathbf{i} \cdot \nabla t_+^0}{z_+ \nu_+ F} - \nabla \cdot (c \mathbf{v}_0).$$

This equation states that concentration changes occur due to three causes:

- *Diffusion*: The first term on the right-hand side of the equation is a diffusion term, and models ions moving because of a concentration gradient.
- *Migration*: The second term models movement of ions due to effects of an electric field. This effect is known as “migration.”
- *Convection*: The third term is a convection term, modeling movement due to a pressure gradient—solute ions are pulled along by the movement of the solvent.

The derivation is quite long, even with the background that we have developed in thermodynamics, physical chemistry, and binary electrolyte relationships. But, with patience we will arrive at our destination. In the process, we will discuss some important topics in solution theory, and specifically *concentrated solution theory*, which describes the electrolyte of a lithium-ion cell better than the simpler *dilute solution theory* approach.

As “mile-markers” to note progress in the definition, it may be helpful to know in advance that we will proceed by taking the following steps:

1. First, we look at the net force of collisions between species in the electrolyte. The result of this section is the Maxwell–Stefan relationship.
2. Then, we make a connection between the net force of collisions and the electrochemical potential of the species. The result is a multicomponent diffusion equation.
3. Third, we show how ion flux can be expressed in terms of the gradient of the chemical potential of the electrolyte.
4. Next, we find an expression for the gradient of the chemical potential in terms of the measurable quantities of interest.
5. Last, we derive the final relationship of mass balance via divergence of flux density.

3.7.1 Step 1. The Maxwell–Stefan relationship

We begin by looking at Maxwell–Stefan theory, which tells us about changes in momentum (and thus velocity) of multispecies systems due to collisions of the particles that make up those systems. The same basic result can be derived (differently) for ideal gases, dense gases, liquids, and polymers.²² Because the proof is clearer and more straightforward for ideal gases, we’ll proceed in that way, even though we recognize that the electrolyte of a lithium-ion cell is most frequently some kind of liquid or gel, and is sometimes even a solid polymer.

²² For dense gases, liquids, and polymers, the (concentration-dependent) diffusivities are not the same binary diffusivities as for an ideal-gas definition, however. See:

- Curtiss, C.F. and Bird, R.B., “Multicomponent diffusion,” *Industrial Engineering Chemical Research*, 38, 1999, pp. 2,515–2,522; (Correction in 40, 2001, p. 1,791).
- Curtiss, C.F., and Bird, R.B., “Diffusion-stress relations in polymer mixtures,” *Journal of Chemical Physics*, 111, 1999, pp. 10,362–10,370.

We start by considering collisions of particles in a two-species system and subsequently extend the result to a multispecies system. In particular, consider a unit volume containing two species of gas. Further, consider a single species-1 molecule with mass m_1 and original velocity \mathbf{v}_{m_1} , colliding with a single species-2 molecule with mass m_2 and original velocity \mathbf{v}_{m_2} . What happens?²³ What can we say about the velocity vectors of the particles after the collision?

We assume that the particle masses are not affected by the collision, and we denote the postcollision velocity of the species-1 molecule as \mathbf{v}'_{m_1} and the postcollision velocity of the species-2 molecule as \mathbf{v}'_{m_2} . We know that the total momentum must be conserved. So, we can write

$$m_1 \mathbf{v}_{m_1} + m_2 \mathbf{v}_{m_2} = m_1 \mathbf{v}'_{m_1} + m_2 \mathbf{v}'_{m_2}.$$

Considering only the species-1 molecule, we can write its momentum loss as

$$\Delta(m_1 \mathbf{v}_{m_1}) = m_1 (\mathbf{v}_{m_1} - \mathbf{v}'_{m_1}).$$

But, because of randomness, we cannot predict exactly what \mathbf{v}'_{m_1} will be. For example, if the particles collide “head on,” then the postcollision velocity vectors will be quite different from the case where one particle strikes the other with a glancing blow. Proceeding down the path of considering individual particle collisions appears to be a dead end.

However, we can make progress if we concern ourselves with the *average* velocities of the subsystems comprising species-1 and species-2 particles, instead of considering the individual particle velocities within those subsystems. Accordingly, we will change our notation slightly: \mathbf{v}_1 denotes the precollision velocity of the mass center of all particles of species-1, and \mathbf{v}'_1 denotes the postcollision velocity of the mass center of all particles of species-1. We will use \mathbf{v}_2 and \mathbf{v}'_2 in a similar way for the species-2 particles.

Next, we assume that the collisions are *elastic*; that is, that kinetic energy is conserved before and after the collision, implying that there is neither breakage, nor deformation, nor loss of energy due to heat, for example. This turns out to be a reasonable assumption for collisions between gas molecules in most cases.

Then, it is possible to derive the relationship²⁴

$$\mathbf{v}'_1 = \frac{m_1 \mathbf{v}_1 + m_2 \mathbf{v}_2}{m_1 + m_2}.$$

The average momentum loss of the species-1 molecule is then:

$$\begin{aligned} \Delta(m_1 \mathbf{v}_1) &= m_1 (\mathbf{v}_1 - \mathbf{v}'_1) \\ &= m_1 \left(\mathbf{v}_1 - \frac{m_1 \mathbf{v}_1 + m_2 \mathbf{v}_2}{m_1 + m_2} \right) \end{aligned}$$

²³ Fun factoid: Maxwell wrote and was known to sing,

“Gin a body meet a body,
flyin’ through the air;
Gin a body hit a body,
will it fly, and where? ...”

(From <http://www.haverford.edu/astronomy/songs/rigid.htm>)

²⁴ Present, R.D., *Kinetic Theory of Gases*, Section 8.2, McGraw-Hill, 1958.

$$\begin{aligned}
 &= m_1 \frac{m_2 \mathbf{v}_1 - m_2 \mathbf{v}_2}{m_1 + m_2} \\
 &= \frac{m_1 m_2}{m_1 + m_2} (\mathbf{v}_1 - \mathbf{v}_2).
 \end{aligned}$$

This result tells us that the average momentum transfer during a collision is proportional to the original average velocity difference between the two subsystems of molecules. If we consider the subsystem of species-1 molecules only or the subsystem of species-2 molecules only, we find that collisions within either subsystem do not cause a change to the total momentum of that subsystem—because of momentum conservation.

Therefore, considering subsystem-1, the only possibility to change its total momentum is when one (or more) of its molecules undergoes a collision with one (or more) of the species-2 molecules. That is, only the inter-subsystem collisions transfer momentum from species-1 to species-2, or vice versa.

Momentum change rate

The rate of change of momentum in a unit volume depends on

- The momentum change per collision, as just found;
- The frequency of collisions, which we now consider.

This frequency must be proportional to the concentration of species-1, as well as the concentration of species-2. Hence, we can write the momentum change rate of species-1 as

$$\left(\frac{dp}{dt} \right)_V^{\text{species-1}} \propto c_1 c_2 (\mathbf{v}_1 - \mathbf{v}_2), \quad (3.27)$$

where c_1 and c_2 are the concentrations of species-1 and species-2, respectively; \mathbf{p} denotes momentum,²⁵ and the subscript V on the left-hand side denotes “per unit volume.” Their values are defined by $c_1 = n_1/V$ and $c_2 = n_2/V$, where n_1 and n_2 are the number of moles of species-1 and species-2, respectively, and V is the volume of the system.

Next, we define the *mole fraction* of species i as $x_i = n_i/n$. So, $x_1 = n_1/n$ and $x_2 = n_2/n$. For a two-species system, we have that $x_1 + x_2 = 1$; for a multispecies system, we have $\sum_i x_i = 1$.

We also define a new quantity called *total concentration* as

$$c_T = \sum_i c_i, \quad (3.28)$$

where for a two-species system $c_T = c_1 + c_2$. Total concentration is the sum of the number of moles of all species, divided by the volume, n/V .

²⁵ Notation can be confusing, and care is needed: \mathbf{p} denotes the vector-quantity momentum; p is, however, the scalar-quantity pressure.

Then, we can write

$$x_i = \frac{n_i}{n} = \frac{n_i/V}{n/V} = \frac{c_i}{c_T}.$$

So, for example, $x_1 = c_1/c_T$ and $x_2 = c_2/c_T$.

Combining, we modify Eq. (3.27) to be

$$\left(\frac{dp}{dt} \right)_V^{\text{species-1}} \propto x_1 x_2 (\mathbf{v}_1 - \mathbf{v}_2).$$

According to Newton's second law, $\mathbf{F} = dp/dt$, and thus

$$\mathbf{F}_{1,V} \propto x_1 x_2 (\mathbf{v}_1 - \mathbf{v}_2),$$

where the subscript V , again, denotes "per unit volume," and $\mathbf{F}_{1,V}$ has units of newtons per cubic meter.

A problem remains: what is the coefficient of proportionality? From our latest result, one can argue that $\mathbf{F}_{1,V}$ is a kind of friction force since it is proportional to the difference between two velocities. So, we define the *Maxwell–Stefan friction coefficient* K_{12} so that $\mathbf{F}_{1,V} = K_{12} (\mathbf{v}_1 - \mathbf{v}_2)$.

We will find that working with equations written in terms of K_{ij} is straightforward. However, final models written in terms of K_{ij} are not desired, because this new proportionality "constant" is not constant. It depends on specific values of x_1 and x_2 . That is, $K_{12} = \text{constant} \times x_1 x_2$. The problem with this is that the equations are not written in terms of intrinsic material properties (which can be measured), but in terms of material properties weighted by the quantity of materials.

So, we will ultimately eliminate x_1 and x_2 by defining the *Maxwell–Stefan diffusion coefficient* or *Maxwell–Stefan diffusivity*,

$$\mathcal{D}_{ij} = \frac{x_i x_j}{K_{ij}} p,$$

where \mathcal{D}_{ij} is inversely proportional to the friction coefficient K_{ij} . Since K_{ij} characterizes how difficult it is for the species to diffuse (because of drag forces), \mathcal{D}_{ij} must characterize how easy it is for the species to diffuse.

Solving for K_{12} in terms of \mathcal{D}_{12} , we then have

$$K_{12} = \frac{x_1 x_2}{\mathcal{D}_{12}} p = \frac{n}{V} \frac{RT x_1 x_2}{\mathcal{D}_{12}},$$

where we have used the ideal gas law, $pV = nRT$. Since $c_T = n/V$, $x_1 = c_1/c_T$, and $x_2 = c_2/c_T$, we can write

$$K_{12} = c_T \frac{RT \frac{c_1 c_2}{c_T c_T}}{\mathcal{D}_{12}} = \frac{RT c_1 c_2}{c_T \mathcal{D}_{12}}.$$

If there are more than two species, we need to use subscripts i and j to denote species. In that case we can rewrite this as

$$K_{ij} = \frac{RTc_i c_j}{c_T \mathcal{D}_{ij}}. \quad (3.29)$$

Note that this relationship uses the *ideal gas law*, but the same result can be developed for liquids using electrochemical potentials instead.

According to Newton's third law, the friction forces must be mutual: $K_{ij} = K_{ji}$. Therefore, we must also have $\mathcal{D}_{ij} = \mathcal{D}_{ji}$. Finally, we substitute Eq. (3.29) for K_{12} into the force equation to write the force per unit volume as

$$\mathbf{F}_{1,V} = \frac{RTc_1 c_2}{c_T \mathcal{D}_{12}} (\mathbf{v}_1 - \mathbf{v}_2), \quad (3.30)$$

which is also the momentum change rate of species-1.

We have actually stopped short of deriving the full Maxwell–Stefan relationship, which states

$$\nabla x_i = - \sum_j \frac{x_i x_j}{\mathcal{D}_{ij}} (\mathbf{v}_i - \mathbf{v}_j).$$

We won't need this equation in our further development, but it is still interesting. The velocity of species- i is positively related to the velocity of the other species (they push species- i in the direction that they are going) and negatively related to the concentration gradient of species- i (the species' own concentration tends to equalize due to self-diffusion).

3.7.2 Step 2. Multicomponent diffusion equation

In deriving the Maxwell–Stefan relation, we assumed that the rate of change of momentum of species-1 (that is, the net force experienced by species-1) was due to collisions with other species. This is true at a microscopic level. Now, we relate that force to the gradient of electrochemical potential for charged species, which is how we would describe it at a macroscopic level.

Force is equal to the negative gradient of Gibbs free energy²⁶

$$\mathbf{F}_1 = -\nabla G_1 = -\frac{\partial G_1}{\partial \bar{\mu}_1} \nabla \bar{\mu}_1 = -n_1 \nabla \bar{\mu}_1,$$

where we have implied that $n_i = \partial G / \partial \bar{\mu}_i$ from Eq. (3.14). The force per unit volume is then

$$\mathbf{F}_{1,V} = \frac{\mathbf{F}_1}{V} = -\frac{n_1}{V} \nabla \bar{\mu}_1 = -c_1 \nabla \bar{\mu}_1.$$

Combining with Eq. (3.30), we now have

$$c_1 \nabla \bar{\mu}_1 = RT \frac{c_1 c_2}{c_T \mathcal{D}_{12}} (\mathbf{v}_2 - \mathbf{v}_1).$$

²⁶ We use the product rule from calculus:

$$\begin{aligned} \frac{\partial G_1}{\partial x} &= \frac{\partial G_1}{\partial \bar{\mu}_1} \frac{\partial \bar{\mu}_1}{\partial x} \\ \frac{\partial G_1}{\partial y} &= \frac{\partial G_1}{\partial \bar{\mu}_1} \frac{\partial \bar{\mu}_1}{\partial y} \\ \frac{\partial G_1}{\partial z} &= \frac{\partial G_1}{\partial \bar{\mu}_1} \frac{\partial \bar{\mu}_1}{\partial z}, \end{aligned}$$

and so can conclude that

$$\nabla G_1 = \frac{\partial G_1}{\partial \bar{\mu}_1} \nabla \bar{\mu}_1.$$

We can generalize to the multicomponent case, giving

$$c_i \nabla \bar{\mu}_i = RT \sum_j \frac{c_i c_j}{c_T \mathcal{D}_{ij}} (\mathbf{v}_j - \mathbf{v}_i) = \sum_j K_{ij} (\mathbf{v}_j - \mathbf{v}_i). \quad (3.31)$$

A sum over all the species gives

$$\sum_i c_i \nabla \bar{\mu}_i = \sum_i \sum_j K_{ij} (\mathbf{v}_j - \mathbf{v}_i).$$

3.7.3 Step 3. Concentrated binary electrolyte theory: Ion fluxes

Our next goal is to prove the following relationship regarding flux density of cations (and the corresponding relationship for anions), where c_0 is the concentration of the solvent

$$\mathbf{N}_+ = c_+ \mathbf{v}_+ = -\frac{\nu_+ \mathcal{D}}{\nu R T} \frac{c_T}{c_0} c \nabla \mu_e + \frac{\mathbf{i} t_+^0}{z_+ F} + c_+ \mathbf{v}_0. \quad (3.32)$$

Note that there are three new symbols in this equation:

- The electrolyte chemical potential μ_e ;
- The electrolyte average diffusivity \mathcal{D} ;
- The transference number t_+^0 .

The next subsections define these quantities, after which we prove Eq. (3.32), which is the flux-density equation that we will ultimately associate with Li^+ in the electrolyte.

Chemical potential of electrolyte

The chemical potential of a binary electrolyte represents how much its Gibbs free energy changes when 1 mol of salt is added. We define the chemical potential of the electrolyte as

$$\mu_e = \nu_+ \bar{\mu}_+ + \nu_- \bar{\mu}_-, \quad (3.33)$$

where the subscript “+” indicates the positively charged species and the subscript “-” indicates the negatively charged species.

Note that we refer to the *chemical potential* of the electrolyte and not the *electrochemical potential* because they turn out to be the same, as the salt as a whole is neutral.

$$\begin{aligned} \mu_e &= \nu_+ \bar{\mu}_+ + \nu_- \bar{\mu}_- \\ &= \nu_+ (\mu_+ + z_+ F \phi) + \nu_- (\mu_- + z_- F \phi) \\ &= \nu_+ \mu_+ + \nu_- \mu_- + (\nu_+ z_+ + \nu_- z_-) F \phi \\ &= \nu_+ \mu_+ + \nu_- \mu_- \end{aligned} \quad (3.34)$$

by Eqs. (3.13) and (3.21).

An example will illustrate the meaning of μ_e . Suppose we have an electrolyte comprising a solvent plus the salt Na_2SO_4 , which has $\nu_+ = 2$ and $\nu_- = 1$. According to the definition of electrochemical potential, if one mole of Na^+ is added, the Gibbs free energy of the system increases by $\bar{\mu}_+$. If one mole of SO_4^{2-} is added, the Gibbs free energy of the system increases by $\bar{\mu}_-$. So, if one mole of the whole salt Na_2SO_4 is added, then the Gibbs free energy of the system increases by $2\bar{\mu}_+ + \bar{\mu}_-$, or by, $\nu_+\bar{\mu}_+ + \nu_-\bar{\mu}_-$.

Eq. (3.32) requires the gradient of μ_e , which can be computed from Eq. (3.33) to be

$$\nabla\mu_e = \nu_+\nabla\bar{\mu}_+ + \nu_-\nabla\bar{\mu}_-.$$

We can compute the $c\nabla\mu_e$ term in Eq. (3.32) if we can first compute $c\nu_+\nabla\bar{\mu}_+ = c_+\nabla\bar{\mu}_+$ and $c\nu_-\nabla\bar{\mu}_- = c_-\nabla\bar{\mu}_-$ terms.

We get these by evaluating terms from Eq. (3.31):

$$\begin{aligned} c_+\nabla\bar{\mu}_+ &= K_{+0}(\mathbf{v}_0 - \mathbf{v}_+) + K_{+-}(\mathbf{v}_- - \mathbf{v}_+) \\ c_-\nabla\bar{\mu}_- &= K_{-0}(\mathbf{v}_0 - \mathbf{v}_-) + K_{-+}(\mathbf{v}_+ - \mathbf{v}_-). \end{aligned}$$

Adding these two equations together and using Eq. (3.22) gives

$$\begin{aligned} c\nabla\mu_e &= [K_{0+}(\mathbf{v}_0 - \mathbf{v}_+) + K_{+-}(\mathbf{v}_- - \mathbf{v}_+)] \\ &\quad + [K_{0-}(\mathbf{v}_0 - \mathbf{v}_-) + K_{-+}(\mathbf{v}_+ - \mathbf{v}_-)] \\ &= K_{0+}(\mathbf{v}_0 - \mathbf{v}_+) + K_{0-}(\mathbf{v}_0 - \mathbf{v}_-). \end{aligned} \quad (3.35)$$

This result will be used in the future.

Electrolyte average diffusivity

The electrolyte average diffusivity \mathcal{D} is a weighted average of the diffusivities of the anion and cation with respect to the solvent. It will be convenient to express this average diffusivity in terms of the Maxwell–Stefan friction coefficients.

When defining a weighted average diffusivity, it is important to recognize that diffusivities add like conductivities; that is, they add in reciprocal form. Accordingly, we define the weighted average diffusion coefficient \mathcal{D} in terms of the stoichiometric coefficients via the relationship

$$\frac{\nu}{\mathcal{D}} = \frac{\nu_+}{\mathcal{D}_{0+}} + \frac{\nu_-}{\mathcal{D}_{0-}},$$

where we recall that $\nu = \nu_+ + \nu_-$. Multiplying both sides of this expression by c and recalling Eq. (3.22) gives \mathcal{D} in terms of concentrations, which allows us to write it also in terms of the Maxwell–Stefan friction coefficients using Eq. (3.29)

$$\mathcal{D} = \frac{\nu c}{\frac{c_+}{\mathcal{D}_{0+}} + \frac{c_-}{\mathcal{D}_{0-}}}$$

$$\begin{aligned}
&= \frac{RTc_0}{c_T} \left(\frac{\nu c}{\frac{RTc_0c_+}{c_T\mathcal{D}_{0+}} + \frac{RTc_0c_-}{c_T\mathcal{D}_{0-}}} \right) \\
&= \frac{RTc_0}{c_T} \left(\frac{\nu c}{K_{0+} + K_{0-}} \right) \\
&= \frac{\nu RTc_0 c}{c_T (K_{0+} + K_{0-})}.
\end{aligned} \tag{3.36}$$

Transference numbers

A transference number states the fraction of ionic current \mathbf{i} that is carried by a certain species *when there is no gradient in chemical potential*.

We use the symbol t_+^0 to denote the transference number of the cation with respect to the solvent, and t_-^0 to denote the transference number of the anion with respect to the solvent. Since we are looking at a binary electrolyte, the transference number of the cation is proportional to the drag experienced by the anion, and vice versa. That is,

$$t_+^0 \propto K_{0-} \quad \text{and} \quad t_-^0 \propto K_{0+}.$$

To find the constants of proportionality, we recognize that the transference numbers must sum to one. So, we have

$$t_+^0 = \frac{K_{0-}}{K_{0-} + K_{0+}} \quad \text{and} \quad t_-^0 = \frac{K_{0+}}{K_{0-} + K_{0+}}. \tag{3.37}$$

Proving the ion-flux equation

We are now ready to prove Eq. (3.32). We repeat it here and highlight different parts of the equation for separate consideration:

$$\mathbf{N}_+ = c_+ \mathbf{v}_+ = - \underbrace{\frac{\nu_+ \mathcal{D}}{\nu RT} \frac{c_T}{c_0}}_A \underbrace{c \nabla \mu_e}_B + \underbrace{\frac{i t_+^0}{z_+ F}}_C + \underbrace{c_+ \mathbf{v}_0}_D.$$

We first look at the term identified as "A" and use Eq. (3.36)

$$\begin{aligned}
-\frac{\nu_+ \mathcal{D} c_T}{\nu RT c_0} &= -\frac{\nu_+ c_T}{\nu RT c_0} \frac{\nu RT c_0 c}{c_T (K_{0+} + K_{0-})} \\
&= -\frac{c \nu_+}{K_{0+} + K_{0-}} \\
&= -\frac{c_+}{K_{0+} + K_{0-}}.
\end{aligned}$$

We now recall the value of the term identified as "B" from Eq. (3.35)

$$c \nabla \mu_e = K_{0+} (\mathbf{v}_0 - \mathbf{v}_+) + K_{0-} (\mathbf{v}_0 - \mathbf{v}_-).$$

Multiplying terms "A" and "B" together gives

$$-\frac{\nu_+ \mathcal{D} c_T}{\nu RT c_0} c \nabla \mu_e = -\frac{c_+}{K_{0+} + K_{0-}} (K_{0+} (\mathbf{v}_0 - \mathbf{v}_+) + K_{0-} (\mathbf{v}_0 - \mathbf{v}_-))$$

$$= -c_+ \mathbf{v}_0 + \frac{c_+}{K_{0+} + K_{0-}} (K_{0+} \mathbf{v}_+ + K_{0-} \mathbf{v}_-).$$

Adding term "D" gives

$$-\frac{\nu_+ \mathcal{D} c_T}{\nu R T c_0} c \nabla \mu_e + c_+ \mathbf{v}_0 = \frac{c_+}{K_{0+} + K_{0-}} (K_{0+} \mathbf{v}_+ + K_{0-} \mathbf{v}_-).$$

Using Eq. (3.37), we write term "C" as

$$\begin{aligned} \frac{\mathbf{i}t_+^0}{z_+ F} &= \frac{z_+ F c_+ \mathbf{v}_+ + z_- F c_- \mathbf{v}_-}{z_+ F} \frac{K_{0-}}{K_{0-} + K_{0+}} \\ &= \frac{z_+ c_+ \mathbf{v}_+ - z_- c_+ \mathbf{v}_-}{z_+} \frac{K_{0-}}{K_{0-} + K_{0+}} \\ &= \frac{c_+}{K_{0+} + K_{0-}} (K_{0-} \mathbf{v}_+ - K_{0-} \mathbf{v}_-). \end{aligned}$$

Adding this term to the prior result gives

$$\begin{aligned} -\frac{\nu_+ \mathcal{D} c_T}{\nu R T} \frac{c_0}{c_0} c \nabla \mu_e + \frac{\mathbf{i}t_+^0}{z_+ F} + c_+ \mathbf{v}_0 &= \frac{c_+}{K_{0+} + K_{0-}} (K_{0+} \mathbf{v}_+ + K_{0-} \mathbf{v}_-) \\ &\quad + \frac{c_+}{K_{0+} + K_{0-}} (K_{0-} \mathbf{v}_+ - K_{0-} \mathbf{v}_-) \\ &= c_+ \mathbf{v}_+. \end{aligned}$$

So, we have now shown

$$\mathbf{N}_+ = c_+ \mathbf{v}_+ = -\frac{\nu_+ \mathcal{D} c_T}{\nu R T} \frac{c_0}{c_0} c \nabla \mu_e + \frac{\mathbf{i}t_+^0}{z_+ F} + c_+ \mathbf{v}_0. \quad (3.38)$$

Using the same approach, we can obtain the flux density of the anion as well:

$$\mathbf{N}_- = c_- \mathbf{v}_- = -\frac{\nu_- \mathcal{D} c_T}{\nu R T} \frac{c_0}{c_0} c \nabla \mu_e + \frac{\mathbf{i}t_-^0}{z_- F} + c_- \mathbf{v}_0. \quad (3.39)$$

3.7.4 Step 4. An expression for the gradient of the chemical potential

We have nearly reached our desired result—the derivation of Eq. (3.3). Before we finish, though, we need to express $\nabla \mu_e$ in terms of concentrations.

Note that by the chain rule of calculus $\nabla \mu_e = \frac{\partial \mu_e}{\partial c} \nabla c$. To achieve the standard form of the result, we further break up the first term into

$$\frac{\partial \mu_e}{\partial c} = \frac{\partial \mu_e}{\partial \ln m} \frac{\partial \ln m}{\partial c},$$

where m is the molality of the solution. It is helpful to note that $m = \frac{m_+}{\nu_+} = \frac{m_-}{\nu_-}$ and that the molality is related to molarity via $m_i = \frac{c_i}{c_0 M_0}$, where M_0 is the molar mass of the solvent.

Recall from our discussion of absolute activity (Eqs. (3.17) and (3.19)) that we can write $\mu_i = RT \ln(\lambda_i)$, where $\lambda_i = m_i \gamma_i \lambda_i^\ominus$, and from

Eq. (3.34) that the chemical potential of the electrolyte can be written as $\mu_e = \nu_+ \mu_+ + \nu_- \mu_-$, so we can write

$$\begin{aligned}
\mu_e &= \nu_+ RT \ln(m_+ \gamma_+ \lambda_+^\ominus) + \nu_- RT \ln(m_- \gamma_- \lambda_-^\ominus) \\
&= \nu_+ RT \ln(m \gamma_+ \lambda_+^\ominus) + \nu_- RT \ln(m \gamma_- \lambda_-^\ominus) \\
&= \nu_+ RT (\ln m + \ln \gamma_+ + \ln(\nu_+ \lambda_+^\ominus)) \\
&\quad + \nu_- RT (\ln m + \ln \gamma_- + \ln(\nu_- \lambda_-^\ominus)) \\
&= (\nu_+ + \nu_-) RT \ln m + RT (\ln \gamma_+^{\nu_+} + \ln \gamma_-^{\nu_-}) \\
&\quad + \nu_+ RT \ln(\nu_+ \lambda_+^\ominus) + \nu_- RT \ln(\nu_- \lambda_-^\ominus) \\
&= \nu RT (\ln m + \ln \gamma_\pm) + \nu_+ RT \ln(\nu_+ \lambda_+^\ominus) + \nu_- RT \ln(\nu_- \lambda_-^\ominus),
\end{aligned}$$

where we define $\gamma_\pm^\nu = \gamma_+^{\nu_+} \gamma_-^{\nu_-}$, and γ_\pm is known as the *mean molal activity coefficient*.

Therefore, we compute the first term to be

$$\frac{\partial \mu_e}{\partial \ln m} = \nu RT \left(1 + \frac{\partial \ln \gamma_\pm}{\partial \ln m} \right),$$

since none of the other terms are functions of m .

We now focus on the second term. We start by writing

$$\begin{aligned}
m &= \frac{m_+}{\nu_+} = \frac{c_+}{\nu_+ c_0 M_0} = \frac{c}{c_0 M_0} \\
\ln m &= \ln c - \ln c_0 - \ln M_0 \\
\frac{\partial \ln m}{\partial \ln c} &= 1 - \frac{\partial \ln c_0}{\partial \ln c} \\
\frac{\partial \ln m}{\partial c} &= \frac{1}{c} \left(1 - \frac{\partial \ln c_0}{\partial \ln c} \right).
\end{aligned}$$

Putting the two results together, we get

$$\nabla \mu_e = \frac{\nu RT}{c} \left(1 + \frac{d \ln \gamma_\pm}{d \ln m} \right) \left(1 - \frac{d \ln c_0}{d \ln c} \right) \nabla c. \quad (3.40)$$

3.7.5 Step 5. Mass balance equation

We are now ready to prove Eq. (3.3). We begin with Eq. (3.32), which we repeat here:

$$\mathbf{N}_+ = -\frac{\nu_+ \mathcal{D}}{\nu RT} \frac{c_T}{c_0} c \nabla \mu_e + \frac{\mathbf{i} t_+^0}{z_+ F} + c_+ \mathbf{v}_0.$$

We now substitute in the value for $\nabla \mu_e$ from Eq. (3.40),

$$\begin{aligned}
\mathbf{N}_+ &= -\frac{\nu_+ \mathcal{D}}{\nu RT} \frac{c_T c}{c_0} \frac{\nu RT}{c} \left(1 + \frac{d \ln \gamma_\pm}{d \ln m} \right) \left(1 - \frac{d \ln c_0}{d \ln c} \right) \nabla c + \frac{\mathbf{i} t_+^0}{z_+ F} + c_+ \mathbf{v}_0 \\
&= -\nu_+ \frac{\mathcal{D} c_T}{c_0} \left(1 + \frac{d \ln \gamma_\pm}{d \ln m} \right) \left(1 - \frac{d \ln c_0}{d \ln c} \right) \nabla c + \frac{\mathbf{i} t_+^0}{z_+ F} + c_+ \mathbf{v}_0.
\end{aligned}$$

Newman comments that the Maxwell-Stephan diffusivity (which he refers to as the “thermodynamic diffusion coefficient”) is not usually what is measured in a laboratory test, but rather the value D in²⁷

$$D = \mathcal{D} \frac{c_T}{c_0} \left(1 + \frac{d \ln \gamma_{\pm}}{d \ln m} \right),$$

where the difference between D and \mathcal{D} is due to the choice of the driving force and to the choice of the reference velocity in their definitions. Therefore, we can write

$$\mathbf{N}_+ = -\nu_+ D \left(1 - \frac{d \ln c_0}{d \ln c} \right) \nabla c + \frac{\mathbf{i} t_+^0}{z_+ F} + c_+ \mathbf{v}_0.$$

This can be put into the continuity equation, Eq. (3.25)

$$\frac{\partial c_+}{\partial t} = -\nabla \cdot \mathbf{N}_+,$$

(assuming that no species are generated and that mass is conserved) to obtain

$$\frac{\partial c_+}{\partial t} = \nabla \cdot \left[\nu_+ D \left(1 - \frac{d \ln c_0}{d \ln c} \right) \nabla c \right] - \nabla \cdot \left(\frac{\mathbf{i} t_+^0}{z_+ F} \right) - \nabla \cdot (c_+ \mathbf{v}_0).$$

Apply the identity that $c_+ = c \nu_+$,

$$\nu_+ \frac{\partial c}{\partial t} = \nu_+ \nabla \cdot \left[D \left(1 - \frac{d \ln c_0}{d \ln c} \right) \nabla c \right] - \nu_+ \frac{\nabla \cdot (\mathbf{i} t_+^0)}{z_+ \nu_+ F} - \nu_+ \nabla \cdot (c \mathbf{v}_0),$$

which can be rearranged to be

$$\frac{\partial c}{\partial t} = \nabla \cdot \left[D \left(1 - \frac{d \ln c_0}{d \ln c} \right) \nabla c \right] - \frac{\nabla \cdot (\mathbf{i} t_+^0)}{z_+ \nu_+ F} - \nabla \cdot (c \mathbf{v}_0).$$

Note that

$$\nabla \cdot (\mathbf{i} t_+^0) = \mathbf{i} \cdot \nabla (t_+^0) + t_+^0 \nabla \cdot \mathbf{i},$$

and according to the charge continuity equation $\nabla \cdot \mathbf{i} = 0$, we can obtain

$$\nabla \cdot (\mathbf{i} t_+^0) = \mathbf{i} \cdot \nabla t_+^0.$$

Finally, we get:

$$\frac{\partial c}{\partial t} = \nabla \cdot \left[D \left(1 - \frac{d \ln c_0}{d \ln c} \right) \nabla c \right] - \frac{\mathbf{i} \cdot \nabla t_+^0}{z_+ \nu_+ F} - \nabla \cdot (c \mathbf{v}_0),$$

which is the material-balance equation.

In practice, it is usually assumed that the concentration of the solvent is insensitive to the concentration of the salt, so²⁸

$$\frac{d \ln c_0}{d \ln c} \approx 0.$$

²⁷ Newman, J., Bennion, D., and Tobias, C.W., “Mass Transfer in Concentrated Binary Electrolytes,” *Berichte der Bunsengesellschaft*, 69, 1965, pp. 608–612. Corrections, *ibid.*, 70, 1966, p. 493.

²⁸ See Doyle, M., Fuller, T.F., and Newman, J., “Modeling the Galvanostatic Charge and Discharge of the Lithium/Polymer/Insertion Cell,” *Journal of the Electrochemical Society*, 140, 1993, pp. 1526–1533. However, note that this assumption implies that the partial molar volume of the salt is zero, which is true only in dilute solutions, not in concentrated solutions. To see how to handle this term a different way for concentrated solutions, refer to Xue, K-H, and Plett, G.L., “A convective transport theory for high rate discharge in lithium ion batteries,” *Electrochimica Acta*, 87, 2013, pp. 575–590.

The simplified version is then

$$\frac{\partial c}{\partial t} = \nabla \cdot (D \nabla c) - \frac{\mathbf{i} \cdot \nabla t_+^0}{z_+ \nu_+ F} - \nabla \cdot (c \mathbf{v}_0).$$

Specializing to a lithium-ion cell: the salt in the electrolyte is typically LiPF_6 . This dissociates into Li^+ and PF_6^- . Therefore, $\nu_+ = z_+ = 1$ (which is often true even if the salt is not LiPF_6). Further, we use subscripts “ e ” to distinguish between solid and electrolyte phases, which gives mass conservation equation:

$$\frac{\partial c_e}{\partial t} = \nabla \cdot (D_e \nabla c_e) - \frac{\mathbf{i}_e \cdot \nabla t_+^0}{F} - \nabla \cdot (c_e \mathbf{v}_0).$$

We have now derived Eq. (3.3).

3.8 Concentrated solution theory: Electrolyte charge conservation

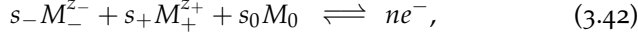
We next develop an expression for charge conservation in the electrolyte. Much of the background work has been done, so this derivation will go much more quickly.

First, we will find an expression for current \mathbf{i} in the electrolyte. Then, we apply Eq. (3.26), which states that $\nabla \cdot \mathbf{i} = 0$ to enforce charge conservation. Finally, we make some substitutions to put the equation in the final form of Eq. (3.4).

Our first step is to prove that

$$\mathbf{i} = -\kappa \nabla \phi - \frac{\kappa}{F} \left(\frac{s_+}{n \nu_+} + \frac{t_+^0}{z_+ \nu_+} - \frac{s_0 c}{n c_0} \right) \nabla \mu_e, \quad (3.41)$$

where the parameters s_i represent the *signed* stoichiometric coefficient of species i in the electrode reaction

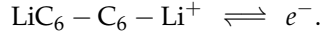


where $M_i^{z_i}$ is some “material” that takes place in the reaction, and for generality, we assume that the solvent may participate in the electrode reaction.

Note that s_i is different from ν_i . An example may help to illustrate this. Specializing to a lithium-ion cell, the negative-electrode reaction is

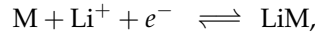


Putting this reaction into the form of Eq. (3.42) gives



From this, we conclude that $s_- = 0$ as no negatively charged species participate, $s_+ = -1$ because the coefficient of Li^+ is -1 , $s_0 = 0$ because the solvent does not participate in the reaction, and $n = 1$ because one electron is produced.

The positive-electrode reaction in a lithium-ion cell is



where the "M" in LiM stands for some metal oxide in the positive-electrode active material. Putting this reaction into the form of Eq. (3.42) gives



Again, $s_- = 0$, $s_+ = -1$, $s_0 = 0$, and $n = 1$.

The potential is introduced by recognizing that the Gibbs free energy of the n moles of electrons on the right-hand side of Eq. (3.42) is equal to $-nF\phi$, where ϕ is the local electrical potential. Since the energy of the product electrons must equal the energy of the reactants, we have the energy balance

$$\sum_i s_i \bar{\mu}_i = -nF\phi$$

(where the summation includes the solvent), and we therefore must also have

$$\sum_i s_i \nabla \bar{\mu}_i = -nF \nabla \phi.$$

We have seen expressions involving $\bar{\mu}_-$ and $\bar{\mu}_+$ before, but never any relating to $\bar{\mu}_0$. We create an expression for $\bar{\mu}_0$ by recalling the Gibbs–Duhem relationship of Eq. (3.16)

$$\begin{aligned} c_+ \nabla \bar{\mu}_+ + c_- \nabla \bar{\mu}_- + c_0 \nabla \bar{\mu}_0 &= 0 \\ \nabla \bar{\mu}_0 &= -\frac{1}{c_0} (c_+ \nabla \bar{\mu}_+ + c_- \nabla \bar{\mu}_-) \\ &= -\frac{c}{c_0} (\nu_+ \nabla \bar{\mu}_+ + \nu_- \nabla \bar{\mu}_-) \\ &= -\frac{c}{c_0} \nabla \mu_e. \end{aligned}$$

So, we now have

$$s_+ \nabla \bar{\mu}_+ + s_- \nabla \bar{\mu}_- - s_0 \frac{c}{c_0} \nabla \mu_e = -nF \nabla \phi. \quad (3.43)$$

For charge balance in the original reaction, we must have

$$\begin{aligned} s_+ z_+ + s_- z_- &= -n \\ s_- &= -\left(\frac{z_+}{z_-} s_+ + \frac{n}{z_-}\right), \end{aligned}$$

so the first terms in Eq. (3.43) can be found to be

$$\begin{aligned}
s_+ \nabla \bar{\mu}_+ + s_- \nabla \bar{\mu}_- &= s_+ \nabla \bar{\mu}_+ - \frac{z_+}{z_-} s_+ \nabla \bar{\mu}_- - \frac{n}{z_-} \nabla \bar{\mu}_- \\
&= \frac{s_+}{\nu_+} \left(\nu_+ \nabla \bar{\mu}_+ - \frac{z_+ \nu_+}{z_-} \nabla \bar{\mu}_- \right) - \frac{n}{z_-} \nabla \bar{\mu}_- \\
&= \frac{s_+}{\nu_+} (\nu_+ \nabla \bar{\mu}_+ + \nu_- \nabla \bar{\mu}_-) - \frac{n}{z_-} \nabla \bar{\mu}_- \\
&= \frac{s_+}{\nu_+} \nabla \mu_e - \frac{n}{z_-} \nabla \bar{\mu}_-.
\end{aligned}$$

Putting these results together, we now have

$$\begin{aligned}
\frac{s_+}{\nu_+} \nabla \mu_e - \frac{n}{z_-} \nabla \bar{\mu}_- - s_0 \frac{c}{c_0} \nabla \mu_e &= -nF \nabla \phi \\
\left(\frac{s_+}{n \nu_+} - \frac{s_0 c}{n c_0} \right) \nabla \mu_e - \frac{1}{z_-} \nabla \bar{\mu}_- &= -F \nabla \phi. \quad (3.44)
\end{aligned}$$

The next step is to find a relationship for $\nabla \bar{\mu}_-$, in terms of $\nabla \mu_e$ and \mathbf{i} . We start with a familiar result, via Eq. (3.31),

$$c_- \nabla \bar{\mu}_- = K_{0-} (\mathbf{v}_0 - \mathbf{v}_-) + K_{+-} (\mathbf{v}_+ - \mathbf{v}_-).$$

To find the terms $(\mathbf{v}_0 - \mathbf{v}_-)$ and $(\mathbf{v}_+ - \mathbf{v}_-)$, we look at the (slightly rearranged) flux-density equations, Eqs. (3.38) and (3.39),

$$\begin{aligned}
c_+ (\mathbf{v}_+ - \mathbf{v}_0) &= -\frac{\nu_+ \mathcal{D}}{\nu R T} \frac{c_T}{c_0} c \nabla \mu_e + \frac{\mathbf{i} t_+^0}{z_+ F} \\
c_- (\mathbf{v}_- - \mathbf{v}_0) &= -\frac{\nu_- \mathcal{D}}{\nu R T} \frac{c_T}{c_0} c \nabla \mu_e + \frac{\mathbf{i} t_-^0}{z_- F}.
\end{aligned}$$

We simplify these slightly before substitution by rewriting the \mathcal{D} term from Eq. (3.36) as

$$\mathcal{D} = \frac{\nu R T c_0 c}{c_T (K_{0+} + K_{0-})},$$

giving revised but equivalent equations

$$\begin{aligned}
\mathbf{v}_+ - \mathbf{v}_0 &= -\frac{c}{K_{0+} + K_{0-}} \nabla \mu_e + \frac{\mathbf{i} t_+^0}{c_+ z_+ F} \\
\mathbf{v}_- - \mathbf{v}_0 &= -\frac{c}{K_{0+} + K_{0-}} \nabla \mu_e + \frac{\mathbf{i} t_-^0}{c_- z_- F}.
\end{aligned}$$

Subtracting the second equation from the first gives

$$\begin{aligned}
\mathbf{v}_+ - \mathbf{v}_- &= \frac{\mathbf{i}}{F} \left(\frac{t_+^0}{c_+ z_+} - \frac{t_-^0}{c_- z_-} \right) \\
&= \frac{\mathbf{i}}{c_+ z_+ F} (t_+^0 + (1 - t_+^0)) = \frac{\mathbf{i}}{c_+ z_+ F}.
\end{aligned}$$

We can now find our expression for $\nabla\bar{\mu}_-/z_-$

$$\begin{aligned}
\frac{1}{z_-} \nabla \bar{\mu}_- &= \frac{1}{c_- z_-} [K_{0-} (\mathbf{v}_0 - \mathbf{v}_-) + K_{+-} (\mathbf{v}_+ - \mathbf{v}_-)] \\
&= \frac{1}{c_- z_-} \left[K_{0-} \left(\frac{c}{K_{0+} + K_{0-}} \nabla \mu_e + \frac{i t_-^0}{c_+ z_+ F} \right) + K_{+-} \left(\frac{\mathbf{i}}{c_+ z_+ F} \right) \right] \\
&= \frac{c}{c_- z_-} \frac{K_{0-}}{K_{0+} + K_{0-}} \nabla \mu_e + \mathbf{i} \left(\frac{K_{0-} t_-^0}{c_- z_- c_+ z_+ F} + \frac{K_{+-}}{c_- z_- c_+ z_+ F} \right) \\
&= -\frac{c_+}{\nu_+ c_+ z_+} t_+^0 \nabla \mu_e - F \mathbf{i} \left(\frac{-K_{0-} t_-^0 - K_{+-}}{c_- z_- c_+ z_+ F^2} \right) \\
&= -\frac{t_+^0}{\nu_+ z_+} \nabla \mu_e - \frac{F \mathbf{i}}{\kappa},
\end{aligned}$$

where we have recognized that the term multiplying \mathbf{i} has units reciprocal to molar conductivity, and we define

$$\frac{1}{\kappa} = \frac{-K_{0-} t_-^0 - K_{+-}}{c_- z_- c_+ z_+ F^2},$$

where κ is the *ionic conductivity* of the electrolyte and has units of S m^{-1} .

We are nearly done: we simply substitute this result for $\nabla\bar{\mu}_-/z_-$ into Eq. (3.44)

$$\begin{aligned}
-F \nabla \phi &= \left(\frac{s_+}{n \nu_+} - \frac{s_0 c}{n c_0} \right) \nabla \mu_e - \frac{1}{z_-} \nabla \bar{\mu}_- \\
-F \nabla \phi &= \left(\frac{s_+}{n \nu_+} - \frac{s_0 c}{n c_0} + \frac{t_+^0}{\nu_+ z_+} \right) \nabla \mu_e + \frac{F \mathbf{i}}{\kappa} \\
\mathbf{i} &= -\kappa \nabla \phi - \frac{\kappa}{F} \left(\frac{s_+}{n \nu_+} - \frac{s_0 c}{n c_0} + \frac{t_+^0}{\nu_+ z_+} \right) \nabla \mu_e.
\end{aligned}$$

We have now derived Eq. (3.41). However, in the literature, this equation is usually expressed in terms of $\nabla \ln c$ instead of $\nabla \mu_e$. We proceed by recognizing that

$$\nabla \mu_e = \frac{\partial \mu_e}{\partial \ln c} \nabla \ln c$$

and that $\mu_e = \nu_+ \bar{\mu}_+ + \nu_- \bar{\mu}_-$.

According to Eqs. (3.17) and (3.18), which connect the chemical potential to absolute activity,

$$\begin{aligned}
\mu_+ &= RT \ln (c_+ f_+ a_+^\ominus) = RT \ln (\nu_+ c f_+ a_+^\ominus) \\
&= RT \ln (\nu_+) + RT \ln (c) + RT \ln (f_+) + RT \ln (a_+^\ominus).
\end{aligned}$$

Also, $\bar{\mu}_+ = \mu_+ + z_+ F \phi$. So,

$$\frac{\partial \bar{\mu}_+}{\partial \ln c} = RT + RT \frac{\partial \ln f_+}{\partial \ln c} + z_+ F \frac{\partial \phi}{\partial \ln c},$$

as the remaining terms are not functions of c . Similarly,

$$\frac{\partial \bar{\mu}_-}{\partial \ln c} = RT + RT \frac{\partial \ln f_-}{\partial \ln c} + z_- F \frac{\partial \phi}{\partial \ln c}.$$

Therefore,

$$\begin{aligned} \frac{\partial \mu_e}{\partial \ln c} &= \nu_+ \frac{\partial \bar{\mu}_+}{\partial \ln c} + \nu_- \frac{\partial \bar{\mu}_-}{\partial \ln c} \\ &= (\nu_+ + \nu_-) RT + RT \frac{\partial \ln (f_+^{\nu_+} f_-^{\nu_-})}{\partial \ln c} + \underbrace{(\nu_+ z_+ + \nu_- z_-)}_0 F \frac{\partial \phi}{\partial \ln c}. \end{aligned}$$

If we define $f_+^{\nu_+} f_-^{\nu_-} = f_{\pm}^{\nu}$ (where f_{\pm} is known as the *mean molar activity coefficient*) and recall that $\nu = \nu_+ + \nu_-$, then,

$$\begin{aligned} \frac{\partial \mu_e}{\partial \ln c} &= \nu RT + RT \frac{\partial \ln f_{\pm}^{\nu}}{\partial \ln c} \\ &= \nu RT \left(1 + \frac{\partial \ln f_{\pm}}{\partial \ln c} \right). \end{aligned}$$

Therefore, our expression for ionic current Eq. (3.41) becomes

$$\mathbf{i} = -\kappa \nabla \phi - \frac{\nu \kappa RT}{F} \left(\frac{s_+}{n \nu_+} - \frac{s_0 c}{n c_0} + \frac{t_+^0}{\nu_+ z_+} \right) \left(1 + \frac{\partial \ln f_{\pm}}{\partial \ln c} \right) \nabla \ln c.$$

The conservation of charge equation says $\nabla \cdot \mathbf{i} = 0$, which gives us

$$\nabla \cdot \left(-\kappa \nabla \phi - \frac{\nu \kappa RT}{F} \left(\frac{s_+}{n \nu_+} - \frac{s_0 c}{n c_0} + \frac{t_+^0}{\nu_+ z_+} \right) \left(1 + \frac{\partial \ln f_{\pm}}{\partial \ln c} \right) \nabla \ln c \right) = 0.$$

Specializing to a lithium-ion cell, we have already found that $s_- = 0$, $s_+ = -1$, $s_0 = 0$, and $n = 1$. Also, $\nu_+ = \nu_- = z_+ = 1$ for most electrolyte salts, so the charge conservation equation for a lithium-ion cell is

$$\nabla \cdot \mathbf{i}_e = \nabla \cdot \left(-\kappa \nabla \phi_e - \frac{2 \kappa RT}{F} \left(1 + \frac{\partial \ln f_{\pm}}{\partial \ln c_e} \right) (t_+^0 - 1) \nabla \ln c_e \right) = 0,$$

where we have added the subscript “ e ” to denote the electrolyte.

We have now derived Eq. (3.4). Note that it is common to assume that $\partial \ln f_{\pm} / \partial \ln c_e = 0$ and to lump $\kappa_D = 2 \kappa RT (t_+^0 - 1) / F$, giving

$$\nabla \cdot (-\kappa \nabla \phi_e - \kappa_D \nabla \ln c_e) = 0.$$

3.9 Butler–Volmer equation

We have now developed the four microscale model partial-differential equations that describe the dynamics of a lithium-ion cell. We now develop the fifth equation, which couples the four PDEs together.

This final model equation computes the rate of lithium moving between solid and electrolyte. As it deals with reaction rate, it is often called the *kinetics* equation of the model.

Fig. 3.12 illustrates activity at the particle surface. In one direction, positively charged lithium ions from the electrolyte combine with an electron to become uncharged lithium, which intercalates into the crystalline structure of the solid active material. In the other direction, uncharged lithium deintercalates from the solid active material, giving up an electron to the outside circuit, and becoming positively charged lithium in the electrolyte.

3.9.1 Reaction rate

For a chemical reaction, reactants \rightleftharpoons products, the reaction rate can be defined using the rate of overall product concentration change,

$$r = \frac{d \prod_i c_{\text{product},i}}{dt},$$

where the \prod_i operation multiplies all of the reaction product concentrations together. For “first-order” processes—ones that happen in a single step—we can model this as

$$r = k \prod_i c_{\text{reactant},i}$$

where k is the reaction rate constant for this chemical reaction.

For now, we think about a single reactant species and a single product species, and later we generalize to the multispecies case, so

$$r = \frac{dc_{\text{product}}}{dt} = kc_{\text{reactant}}.$$

The reaction rate “constant” k generally depends on temperature, and this temperature dependence is usually modeled via an *Arrhenius relationship*,

$$k = k_f^0 \exp\left(-\frac{E_a}{RT}\right), \quad \text{or} \quad r = k_f^0 c_{\text{reactant}} \exp\left(-\frac{E_a}{RT}\right),$$

where E_a is the *activation energy* of the forward reaction. Both E_a and k_f^0 are constants that are determined by experiments.

3.9.2 Activated complex theory

Reaction kinetics deal with nonequilibrium dynamics. The forward direction of a reaction from reactants to products is favored if the Gibbs free energy of the products is lower than the Gibbs free energy of the reactants. However, there is generally an energy barrier to

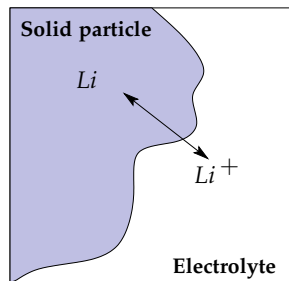
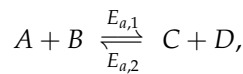


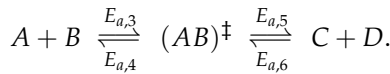
Figure 3.12: Dynamics at the particle surface.

overcome in order for the reaction to actually occur. This energy barrier is equal to the activation energy E_a of the chemical reaction. Fig. 3.13 illustrates the forward direction of a reaction in schematic form.

Activated complex theory states that there is a transition state (sometimes called the *activated complex*) in chemical reactions, where the activated complex is neither the same as the reactants, nor is it the same as the products. For example, in the reaction with reactants A and B , products C and D , and forward and reverse activation energies $E_{a,1}$ and $E_{a,2}$ respectively,



there is a transition state $(AB)^\ddagger$ where



The idea is that not every collision between reactants has enough energy to break the original chemical bonds and allow a reaction to occur. Most collisions result in elastic scattering events. Only when there is sufficient energy will the transition state form and the reaction continue.

This is illustrated in Fig. 3.14. In the upper part of the figure, blue and red reactants approach each other at a slow speed, with low kinetic energy. They collide, but with insufficient energy to break their chemical bonds, so the reactants simply “bounce” off each other without any change in chemical composition.

In the lower part of the figure, reactants approach each other at a high speed, with high kinetic energy. When they collide, the energy is sufficient to form the activated complex, and chemical bonds are broken and reformed as product species. When the molecules separate, they are now chemically altered.

3.9.3 Energy relationships in electrode reactions

Electrode reactions are different from standard chemical reactions because they produce or consume electrons. An electrode reaction has the form



where the forward reaction states that an oxidant o plus electron(s) forms a product r , and where the reverse reaction states that a reductant r forms a product o plus product electron(s).

The application of an external electric field can change the energy state of the electrons and hence can make the reaction more or

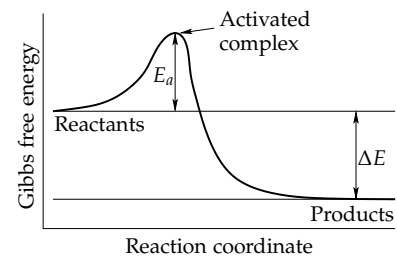


Figure 3.13: Progress of a chemical reaction in terms of energy.

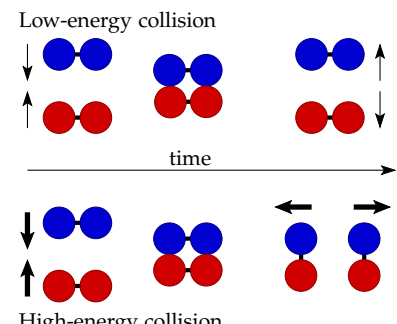


Figure 3.14: Results of low-energy and high-energy collisions.

less favorable. The progress of electrode reactions, where the electrons are subjected to an arbitrary original electric potential ϕ_0 and a second electric potential $\phi < \phi_0$, is shown in Fig. 3.15, where the original progress plot is drawn in green (the lower plot) and the second progress plot is drawn in blue (the upper plot).

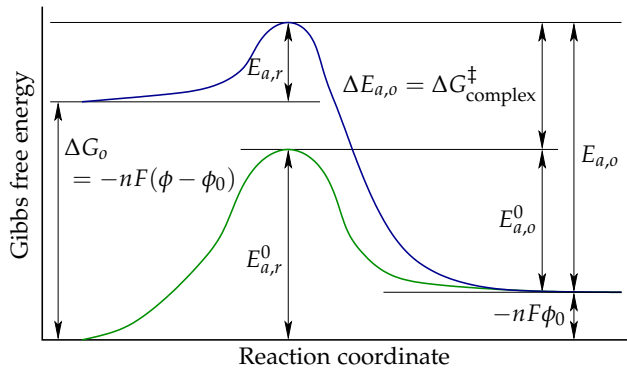


Figure 3.15: Energy relationships in an electrode reaction where potential ϕ is less than ϕ_0 .

In the figure, the activation energies for reduction and oxidation under the original potential ϕ_0 are denoted by $E_{a,r}^0$ and $E_{a,o}^0$, respectively. The modified activation energies under the lower potential ϕ are denoted by $E_{a,r}$ and $E_{a,o}$, respectively. As drawn, we see that the activation energies of the reaction are functions of the potential of the electrode.

When the potential of the electrode is changed from ϕ_0 to ϕ , the total Gibbs free energy of the left-hand side of Eq. (3.45) changes because there are electrons on the left-hand side; the total Gibbs free energy of the right-hand side remains unchanged, as there are no electrons. The change in the Gibbs free energy of the oxidants is

$$\Delta G_o = -nF(\phi - \phi_0),$$

where $-nF$ is the total charge of the electrons. The Gibbs free energy of the activated complex changes as well, but not as much as ΔG_0 :

$$0 < |\Delta G_{\text{complex}}^\ddagger| < |\Delta G_o|.$$

We see from the figure that $\Delta G_o + E_{a,r} = \Delta G_{\text{complex}}^\ddagger + E_{a,r}^0 = \Delta E_{a,o} + E_{a,r}^0$, or

$$\begin{aligned}\Delta E_{a,o} &= E_{a,r} - E_{a,r}^0 - nF(\phi - \phi_0) \\ &= \Delta E_{a,r} - nF(\phi - \phi_0),\end{aligned}$$

where we have defined $\Delta E_{a,r} = E_{a,r} - E_{a,r}^0$.

We deduce that decreasing electrode potential from ϕ_0 to $\phi < \phi_0$ results in a change in $\Delta E_{a,o}$ that is greater than the change in $\Delta E_{a,r}$.

We see this in the figure: $E_{a,o}$ increases, and $E_{a,r}$ actually decreases. This makes the forward reaction much more favorable than before.

We run into a problem when trying to solve for specific values of $\Delta E_{a,o}$ and $\Delta E_{a,r}$. By rearranging our result we further derive that

$$\Delta E_{a,o} - \Delta E_{a,r} = -nF(\phi - \phi_0) = \Delta G_o,$$

implying that neither quantity is found uniquely from only $(\phi - \phi_0)$. To be able to specify how much of the energy change is spent on decreasing $E_{a,r}$ while how much (the rest) is spent on increasing $E_{a,o}$, we define an *asymmetric charge-transfer coefficient* $0 < \alpha < 1$ such that

$$\alpha = \left| \frac{\Delta E_{a,r}}{\Delta G_o} \right|, \quad \text{and} \quad 1 - \alpha = \left| \frac{\Delta E_{a,o}}{\Delta G_o} \right|.$$

Then, we have $\Delta E_{a,r} = \alpha nF(\phi - \phi_0)$ and $\Delta E_{a,o} = -(1 - \alpha)nF(\phi - \phi_0)$. Putting all our results to date together,

1. Rate of reduction:

$$\begin{aligned} r_r &= k_o^0 c_o \exp \left(-\frac{E_{a,r}}{RT} \right) \\ &= k_o^0 c_o \exp \left(-\frac{E_{a,r}^0 + \alpha nF(\phi - \phi_0)}{RT} \right). \end{aligned}$$

2. Rate of oxidization:

$$\begin{aligned} r_o &= k_r^0 c_r \exp \left(-\frac{E_{a,o}}{RT} \right) \\ &= k_r^0 c_r \exp \left(-\frac{E_{a,o}^0 - (1 - \alpha)nF(\phi - \phi_0)}{RT} \right). \end{aligned}$$

In a charge-balanced reaction, the production rate of e^- is the same as the production rate of positive charge, and hence: $i_r = -nFr_r$ and $i_o = nFr_o$. This gives

$$\begin{aligned} i_r &= -nFk_o^0 c_o \exp \left(-\frac{E_{a,r}^0 + \alpha nF(\phi - \phi_0)}{RT} \right) \\ i_o &= nFk_r^0 c_r \exp \left(-\frac{E_{a,o}^0 - (1 - \alpha)nF(\phi - \phi_0)}{RT} \right). \end{aligned}$$

3.9.4 Specifying a neutral potential

Until now, we have assumed that the initial potential ϕ_0 was arbitrary. We now clean up our notation by setting $\phi_0 = 0$. Then, $E_{a,r}^0$ and $E_{a,o}^0$ correspond specifically to $\phi_0 = 0$, and

$$i_r = -nFk_o^0 c_o \exp \left(-\frac{E_{a,r}^0 + \alpha nF\phi}{RT} \right)$$

$$i_o = nFk_r^0 c_r \exp\left(-\frac{E_{a,o}^0 - (1-\alpha)nF\phi}{RT}\right).$$

Note that at equilibrium, $\phi = \phi_{\text{rest}}$. We define a new quantity, the *overpotential* $\eta = \phi - \phi_{\text{rest}}$, so that

$$i_r = -nFk_o^0 c_o \exp\left(-\frac{E_{a,r}^0 + \alpha nF(\phi_{\text{rest}} + \eta)}{RT}\right)$$

$$i_o = nFk_r^0 c_r \exp\left(-\frac{E_{a,o}^0 - (1-\alpha)nF(\phi_{\text{rest}} + \eta)}{RT}\right).$$

Now, at equilibrium, $\eta = 0$ and we have

$$i_r = -nFk_o^0 c_o \exp\left(-\frac{E_{a,r}^0}{RT}\right) \exp\left(-\frac{\alpha nF\phi_{\text{rest}}}{RT}\right)$$

$$i_o = nFk_r^0 c_r \exp\left(-\frac{E_{a,o}^0}{RT}\right) \exp\left(\frac{(1-\alpha)nF\phi_{\text{rest}}}{RT}\right).$$

Further, $i = i_o + i_r = 0$. We may define a quantity i_0 (note that the subscript is the numeral “0” and not the letter “o”) such that

$$i_0 = nFk_o^0 c_o \exp\left(-\frac{E_{a,r}^0}{RT}\right) \exp\left(-\frac{\alpha nF\phi_{\text{rest}}}{RT}\right)$$

$$= nFk_r^0 c_r \exp\left(-\frac{E_{a,o}^0}{RT}\right) \exp\left(\frac{(1-\alpha)nF\phi_{\text{rest}}}{RT}\right).$$

Then, even when not at rest,

$$i_r = -i_0 \exp\left(-\frac{\alpha nF\eta}{RT}\right)$$

$$i_o = i_0 \exp\left(\frac{(1-\alpha)nF\eta}{RT}\right).$$

The total electrode current density is then

$$i = i_o + i_r = i_0 \left\{ \exp\left(\frac{(1-\alpha)nF\eta}{RT}\right) - \exp\left(-\frac{\alpha nF\eta}{RT}\right) \right\},$$

which is the Butler–Volmer equation. Converting i from units of A m^{-2} to $\text{mol m}^{-2} \text{s}^{-1}$ by dividing both sides of this relationship by Faraday’s constant gives

$$j = \frac{i_0}{F} \left\{ \exp\left(\frac{(1-\alpha)nF\eta}{RT}\right) - \exp\left(-\frac{\alpha nF\eta}{RT}\right) \right\}.$$

We have now derived Eq. (3.5). But we’re not quite finished yet.

3.9.5 Exchange current density

The quantity i_0 is called the *exchange current density*. It is the value of oxidation and reduction currents when the electrode is at rest. That is, it is the rate at which electrons are continuously exchanged back and forth in a dynamic equilibrium.

Note that its value depends on the concentration of various species involved in the chemical reaction. Recall that we can write i_0 as

$$\begin{aligned} i_0 &= nFk_o^0 c_o \exp\left(-\frac{E_{a,r}^0}{RT}\right) \exp\left(-\frac{\alpha nF\phi_{\text{rest}}}{RT}\right) \\ &= nFk_r^0 c_r \exp\left(-\frac{E_{a,o}^0}{RT}\right) \exp\left(\frac{(1-\alpha)nF\phi_{\text{rest}}}{RT}\right). \end{aligned}$$

Setting $\mathcal{E}_{a,r}^0 = \exp\left(-\frac{E_{a,r}^0}{RT}\right)$ and $\mathcal{E}_{a,o}^0 = \exp\left(-\frac{E_{a,o}^0}{RT}\right)$ and equating these two equivalent versions of i_0 gives

$$\begin{aligned} k_r^0 c_r \mathcal{E}_{a,o}^0 \exp\left(\frac{(1-\alpha)nF\phi_{\text{rest}}}{RT}\right) &= k_o^0 c_o \mathcal{E}_{a,r}^0 \exp\left(-\frac{\alpha nF\phi_{\text{rest}}}{RT}\right) \\ \frac{\exp\left(\frac{(1-\alpha)nF\phi_{\text{rest}}}{RT}\right)}{\exp\left(-\frac{\alpha nF\phi_{\text{rest}}}{RT}\right)} &= \frac{k_o^0 c_o \mathcal{E}_{a,r}^0}{k_r^0 c_r \mathcal{E}_{a,o}^0} \\ \frac{(1-\alpha)nF\phi_{\text{rest}}}{RT} + \frac{\alpha nF\phi_{\text{rest}}}{RT} &= \ln\left(\frac{k_o^0 \mathcal{E}_{a,r}^0}{k_r^0 \mathcal{E}_{a,o}^0}\right) + \ln \frac{c_o}{c_r} \\ \phi_{\text{rest}} &= \underbrace{\frac{RT}{nF} \ln\left(\frac{k_o^0 \mathcal{E}_{a,r}^0}{k_r^0 \mathcal{E}_{a,o}^0}\right)}_{\phi^\ominus} + \frac{RT}{nF} \ln \frac{c_o}{c_r} \\ \phi_{\text{rest}} &= \phi^\ominus + \frac{RT}{nF} \ln \frac{c_o}{c_r}. \end{aligned}$$

This is the *Nernst equation* and describes the concentration dependence of the rest potential. Substituting ϕ_{rest} back into i_0 gives

$$\begin{aligned} i_0 &= nFk_o^0 c_o \mathcal{E}_{a,r}^0 \exp\left(-\frac{\alpha nF}{RT} \left(\phi^\ominus + \frac{RT}{nF} \ln \frac{c_o}{c_r}\right)\right) \\ &= nFk_o^0 c_o \mathcal{E}_{a,r}^0 \exp\left(-\frac{\alpha nF\phi^\ominus}{RT}\right) c_r^\alpha c_o^{-\alpha} \\ &= nFk_o^0 c_o^{1-\alpha} c_r^\alpha \mathcal{E}_{a,r}^0 \exp\left(-\frac{\alpha nF\phi^\ominus}{RT}\right), \end{aligned}$$

and

$$\begin{aligned} i_0 &= nFk_r^0 c_r \mathcal{E}_{a,o}^0 \exp\left(\frac{(1-\alpha)nF}{RT} \left(\phi^\ominus + \frac{RT}{nF} \ln \frac{c_o}{c_r}\right)\right) \\ &= nFk_r^0 c_r \mathcal{E}_{a,o}^0 \exp\left(\frac{(1-\alpha)nF\phi^\ominus}{RT}\right) c_o^{1-\alpha} c_r^{\alpha-1} \end{aligned}$$

$$= nFk_r^0 c_o^{1-\alpha} c_r^\alpha \mathcal{E}_{a,o}^0 \exp\left(\frac{(1-\alpha)nF\phi^\ominus}{RT}\right).$$

Since these two equations are equal, we can define an effective reaction rate constant

$$k_0 = k_o^0 \mathcal{E}_{a,r}^0 \exp\left(-\frac{\alpha nF\phi^\ominus}{RT}\right) = k_r^0 \mathcal{E}_{a,o}^0 \exp\left(\frac{(1-\alpha)nF\phi^\ominus}{RT}\right),$$

so we end up with the final result

$$i_0 = nFk_0 c_o^{1-\alpha} c_r^\alpha. \quad (3.46)$$

It is interesting to investigate the form of k_0 further, starting with either side of the equation. For example,

$$\begin{aligned} k_0 &= k_o^0 \mathcal{E}_{a,r}^0 \exp\left(-\frac{\alpha nF\phi^\ominus}{RT}\right) \\ &= k_o^0 \exp\left(\frac{-E_{a,r}^0}{RT} - \frac{\alpha nF\phi^\ominus}{RT}\right) \\ &= k_o^0 \exp\left(\frac{-E_{a,r}^0}{RT} - \frac{\alpha nF}{RT} \left(\frac{RT}{nF} \left(\ln\left(\frac{k_o^0}{k_r^0}\right) + \ln \mathcal{E}_{a,r}^0 - \ln \mathcal{E}_{a,o}^0\right)\right)\right) \\ &= k_o^0 \exp\left(\frac{-E_{a,r}^0}{RT} - \alpha \left(\ln\left(\frac{k_o^0}{k_r^0}\right) - \frac{E_{a,r}^0}{RT} + \frac{E_{a,o}^0}{RT}\right)\right) \\ &= k_o^0 \left(\frac{k_o^0}{k_r^0}\right)^{-\alpha} \exp\left(-\frac{1}{RT} \left((1-\alpha)E_{a,r}^0 + \alpha E_{a,o}^0\right)\right) \\ &= \left(k_o^0\right)^{1-\alpha} \left(k_r^0\right)^\alpha \exp\left(-\frac{1}{RT} \left((1-\alpha)E_{a,r}^0 + \alpha E_{a,o}^0\right)\right). \end{aligned}$$

So, we see that the reaction-rate “constant” is a function of the charge-transfer coefficient α and furthermore a function of temperature. It obeys an Arrhenius relationship, where the temperature-independent rate constant is $(k_o^0)^{1-\alpha}(k_r^0)^\alpha$ and the activation energy is $(1-\alpha)E_{a,r}^0 + \alpha E_{a,o}^0$.

Generalizing Eq. (3.46) to the case where there are multiple reactants and products, we have

$$i_0 = nFk_0 \left(\prod_i c_{o,i}\right)^{1-\alpha} \left(\prod_i c_{r,i}\right)^\alpha.$$

For a lithium-ion cell, $n = 1$. Lithium ions in the electrolyte are reduced to give lithium atoms in the solid. We then have

$$\prod_i c_{o,i} = c_e (c_{s,\max} - c_{s,e}),$$

where c_e is the concentration of lithium in the electrolyte, $c_{s,\max}$ is the maximum concentration of lithium in the solid, and $c_{s,e}$ is the

surface concentration of lithium in the solid. So $(c_{s,\max} - c_{s,e})$ is the concentration of available spaces for lithium atoms to enter.

For a lithium-ion cell, we also have $c_r = c_{s,e}$, and we typically denote ϕ_{rest} by U_{ocp} , where “ocp” stands for “open-circuit potential.”²⁹ The direction of lithium flux depends on whether the potential difference between solid and electrolyte is above or below U_{ocp} , so,

$$\eta = (\phi_s - \phi_e) - U_{\text{ocp}}.$$

The final Butler–Volmer relationship for a lithium-ion cell in A m^{-2} is then

$$i = Fk_0c_e^{1-\alpha}(c_{s,\max} - c_{s,e})^{1-\alpha}c_{s,e}^\alpha \left\{ \exp\left(\frac{(1-\alpha)F}{RT}\eta\right) - \exp\left(-\frac{\alpha F}{RT}\eta\right) \right\}.$$

We prefer using units of $\text{mol m}^{-2} \text{s}^{-1}$, which gives

$$j = k_0c_e^{1-\alpha}(c_{s,\max} - c_{s,e})^{1-\alpha}c_{s,e}^\alpha \left\{ \exp\left(\frac{(1-\alpha)F}{RT}\eta\right) - \exp\left(-\frac{\alpha F}{RT}\eta\right) \right\}.$$

Note that the sign of j is positive when lithium is moving from the solid to the electrolyte and is negative when lithium is moving from the electrolyte into the solid.

3.9.6 Normalizing units of k_0

Notice that the units of k_0 are rather awkward. The exponential terms of the Butler–Volmer equation are unitless, and j has units $\text{mol m}^{-2} \text{s}^{-1}$. Therefore, k_0 must have units of $\text{mol}^{\alpha-1} \text{m}^{4-3\alpha} \text{s}^{-1}$. Some computing platforms struggle with units having noninteger powers, so this poses a problem.

A solution is to define a normalized version of the exchange current density

$$\begin{aligned} i_0 &= Fk_0c_e^{1-\alpha}(c_{s,\max} - c_{s,e})^{1-\alpha}c_{s,e}^\alpha \\ &= \underbrace{Fk_0c_{e,0}^{1-\alpha}c_{s,\max}}_{k_0^{\text{norm}}} \left(\frac{c_e}{c_{e,0}} \right)^{1-\alpha} \left(\frac{c_{s,\max} - c_{s,e}}{c_{s,\max}} \right)^{1-\alpha} \left(\frac{c_{s,e}}{c_{s,\max}} \right)^\alpha, \end{aligned}$$

where $c_{e,0}$ is the at-rest equilibrium concentration of lithium in the electrolyte. We see that rearranging the exchange current density in this form makes the terms raised to noninteger powers themselves unitless, and gives k_0^{norm} units of $\text{mol m}^{-2} \text{s}^{-1}$, which is much easier to work with. We can rewrite the Butler–Volmer equation as

$$\begin{aligned} j &= k_0^{\text{norm}} \left(\left(\frac{c_e}{c_{e,0}} \right) \left(\frac{c_{s,\max} - c_{s,e}}{c_{s,\max}} \right) \right)^{1-\alpha} \left(\frac{c_{s,e}}{c_{s,\max}} \right)^\alpha \\ &\quad \times \left\{ \exp\left(\frac{(1-\alpha)F}{RT}\eta\right) - \exp\left(-\frac{\alpha F}{RT}\eta\right) \right\}. \end{aligned}$$

²⁹ For symmetry, one might expect to have $c_r = c_{s,e}(c_{e,\max} - c_e)$, but that form is rarely found in the literature. It could be used if the electrolyte salt concentration were approaching saturation.

Also note that most articles that discuss simulation of lithium-ion cells do not give values for k_0 . Instead, they give values of i_0 that apply at the beginning of the simulation, from which you must derive k_0 or k_0^{norm} .

3.10 Implementing the model

We have now developed the five equations that describe conservation of mass in the solid and electrolyte, conservation of charge in the solid and electrolyte, and the flux density of lithium between solid and electrolyte, corresponding to the microscale dynamics that occur within a lithium-ion cell.³⁰

At this point in history, computational power is not sufficient for it to be feasible to simulate an entire cell using these equations—the complexity is too high. Instead, some small volume, such as depicted in Fig. 3.16, comprising both particles and electrolyte is usually simulated instead. In the figure, the solid particles are drawn, and the electrolyte is assumed to fill the void between the particles.

To simulate this geometry, we need a PDE solver. We’re not going to discuss the simulation process in detail in this chapter, but we will look at it in the next chapter. We will see that, generally, the process is to

1. Define the three-dimensional geometries of every solid particle, the electrolyte, and the overall system. This is very challenging if anything but very simple shapes are used. For example, even the relatively simple truncated ellipsoids in Fig. 3.16 are quite difficult to describe. Usually, a computer-aided-design (CAD) tool is used to help draw the geometries, and these geometries are imported into the PDE solver.
2. Specify the PDEs and algebraic equations that operate in each geometry. Eqs. (3.1) and (3.2) apply to parts of the geometry describing the interior of solid particles, and Eqs. (3.3) and (3.4) apply to parts of the geometry describing voids between the particles that are filled with electrolyte.
3. Enter all parameters (such as conductivities, diffusivities, and so forth) and functions (such as open-circuit potential functions) for each geometry.
4. Define initial conditions, forcing functions, and boundary conditions.

We have not yet looked at boundary conditions, but these are critical to being able to simulate a system. Boundary conditions are equations that specify concentrations and potentials at the interface

³⁰ These equations can also apply to any chemistry, with the understanding that the equations that describe solid diffusion in intercalation compounds are not needed when modeling pure chemical cells that do not have insertion electrodes.

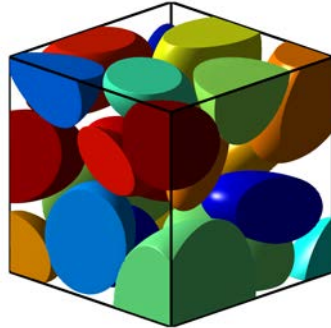


Figure 3.16: Example particle geometry in a small volume (colors are for illustrative purposes only).

between solid and electrolyte and at the edges of the simulation volume.

A boundary condition equation can be one of three generic types. *Dirichlet* boundary conditions specify a constant value or a function of time that is associated with a position on a boundary. *Neumann* boundary conditions give values to the normal derivative of the problem at positions on the boundary. *Cauchy* boundary conditions are a combination of Dirichlet and Neumann boundary conditions.

It turns out that the boundary conditions for the four PDEs that make up the microscale model are all of the Neumann type. We derive them here, and they will be important in the next chapter as well.

3.10.1 Boundary condition for charge conservation in the solid

We find a boundary condition on the solid charge-conservation equation by starting with the expression for current in the solid from Eq. (3.6):

$$\sigma \nabla \phi_s = -\mathbf{i}_s.$$

We notice that the left-hand side of this expression is a derivative, so we expect a Neumann-style boundary condition. So, we take the dot product of both sides of the equation with the normal vector, which points out from the solid into the electrolyte

$$\begin{aligned}\hat{\mathbf{n}}_s \cdot \nabla \phi_s &= -\frac{\mathbf{i}_s \cdot \hat{\mathbf{n}}_s}{\sigma} \\ \hat{\mathbf{n}}_s \cdot \nabla \phi_s &= -\frac{Fj}{\sigma}.\end{aligned}\quad (3.47)$$

This is the Neumann-style boundary condition that applies to the PDE that describes charge conservation in the solid.

3.10.2 Boundary condition for mass conservation in the solid

We find the boundary condition on the solid mass-conservation equation in a very similar way. We start with the expression for lithium flux density in the solid from Eq. (3.9):

$$D_s \nabla c_s = -\mathbf{N}.$$

We take the dot product of both sides of the equation with the normal vector, which points out from the solid into the electrolyte

$$\begin{aligned}\hat{\mathbf{n}}_s \cdot \nabla c_s &= -\frac{\mathbf{N} \cdot \hat{\mathbf{n}}_s}{D_s} \\ \hat{\mathbf{n}}_s \cdot \nabla c_s &= -\frac{j}{D_s}.\end{aligned}$$

This is the Neumann-style boundary condition that applies to the PDE that describes mass conservation in the solid.

3.10.3 Boundary condition for mass conservation in the electrolyte

Finding the boundary conditions for the electrolyte PDEs is a little more complex but still very manageable. Material flux entering and exiting the particle must be equal on both sides of the boundary. Flux densities of cations, anions, and solvent at the interface between the particle and the electrolyte are

$$\mathbf{N}_+ \cdot \hat{\mathbf{n}}_e = c\mathbf{v}_+ \cdot \hat{\mathbf{n}}_e = -j, \quad \mathbf{N}_0 \cdot \hat{\mathbf{n}}_e = c\mathbf{v}_0 \cdot \hat{\mathbf{n}}_e = 0, \\ \mathbf{N}_- \cdot \hat{\mathbf{n}}_e = c\mathbf{v}_- \cdot \hat{\mathbf{n}}_e = 0,$$

where $\mathbf{N}_+ \cdot \hat{\mathbf{n}}_e = -j$ as j is flux density from solid to electrolyte. The sign is negative because $\hat{\mathbf{n}}_e$ points outward from the electrolyte into the solid (that is, in the opposite direction from $\hat{\mathbf{n}}_s$).

Evaluating these equations using Eq. (3.32) for \mathbf{N}_+ (and corresponding result for \mathbf{N}_-)

$$-j = -\nu_+ D_e \left(1 - \frac{d \ln c_0}{d \ln c_e} \right) \nabla c_e \cdot \hat{\mathbf{n}}_e + \frac{\mathbf{i}_e \cdot \hat{\mathbf{n}}_e t_+^0}{z_+ F} + \nu_+ c_e \mathbf{v}_0 \cdot \hat{\mathbf{n}}_e \\ 0 = -\nu_- D_e \left(1 - \frac{d \ln c_0}{d \ln c_e} \right) \nabla c_e \cdot \hat{\mathbf{n}}_e + \frac{\mathbf{i}_e \cdot \hat{\mathbf{n}}_e t_-^0}{z_- F} + \nu_- c_e \mathbf{v}_0 \cdot \hat{\mathbf{n}}_e.$$

Specializing to the lithium-ion case, $\nu_+ = \nu_- = 1$, $z_+ = -z_- = 1$, and assuming that solvent velocity $\mathbf{v}_0 = 0$:

$$-j = -D_e \left(1 - \frac{d \ln c_0}{d \ln c_e} \right) \nabla c_e \cdot \hat{\mathbf{n}}_e + \frac{\mathbf{i}_e \cdot \hat{\mathbf{n}}_e t_+^0}{F} \\ 0 = -D_e \left(1 - \frac{d \ln c_0}{d \ln c_e} \right) \nabla c_e \cdot \hat{\mathbf{n}}_e - \frac{\mathbf{i}_e \cdot \hat{\mathbf{n}}_e t_-^0}{F}.$$

To eliminate \mathbf{i}_e , we add t_+^0 / t_-^0 times the second equation to the first

$$-j = -D_e \left(1 - \frac{d \ln c_0}{d \ln c_e} \right) \left(1 + \frac{t_+^0}{t_-^0} \right) \nabla c_e \cdot \hat{\mathbf{n}}_e \\ -t_-^0 j = -D_e \left(1 - \frac{d \ln c_0}{d \ln c_e} \right) \nabla c_e \cdot \hat{\mathbf{n}}_e.$$

This gives us the Neumann-style boundary condition for ∇c_e

$$\hat{\mathbf{n}}_e \cdot \nabla c_e = \frac{1 - t_+^0}{D_e \left(1 - \frac{d \ln c_0}{d \ln c_e} \right)} j. \quad (3.48)$$

3.10.4 Boundary condition for charge conservation in the electrolyte

To find the final boundary condition, we can substitute this value for $\hat{\mathbf{n}}_e \cdot \nabla c_e$ into the flux-density equation to solve for \mathbf{i}_e at the boundary

$$-j = -D_e \left(1 - \frac{d \ln c_0}{d \ln c_e} \right) \frac{(1 - t_+^0)j}{D_e \left(1 - \frac{d \ln c_0}{d \ln c_e} \right)} + \frac{\mathbf{i}_e \cdot \hat{\mathbf{n}}_e t_+^0}{F}$$

$$0 = -D_e \left(1 - \frac{d \ln c_0}{d \ln c_e} \right) \frac{t_-^0 j}{D_e \left(1 - \frac{d \ln c_0}{d \ln c_e} \right)} - \frac{\mathbf{i}_e \cdot \hat{\mathbf{n}}_e t_-^0}{F}.$$

Both expressions give identical results:

$$\mathbf{i}_e \cdot \hat{\mathbf{n}}_e = -jF. \quad (3.49)$$

Substituting this and the prior boundary condition into the \mathbf{i}_e equation gives

$$\begin{aligned} -\kappa \nabla \phi_e - \kappa_D \nabla \ln c_e &= \mathbf{i}_e \\ \hat{\mathbf{n}}_e \cdot \left(-\kappa \nabla \phi_e - \frac{\kappa_D}{c_e} \nabla c_e \right) &= \hat{\mathbf{n}}_e \cdot \mathbf{i}_e \\ \nabla \phi_e \cdot \hat{\mathbf{n}}_e &= \left(\frac{F}{\kappa} - \frac{\kappa_D}{\kappa c_e} \frac{t_-^0}{D_e \left(1 - \frac{d \ln c_0}{d \ln c_e} \right)} \right) j \end{aligned}$$

at the interface between the particle and the electrolyte.

In addition, ion flux density is zero at external boundaries of the cell.

3.11 Cell-level quantities

While simulating an entire cell using the equations developed in this chapter is unreasonable given present-day computing power, there are some cell-level variables that can be understood quite easily from these lower-level equations. We describe these in the following subsections.

3.11.1 Cell open-circuit voltage

As we saw in Chap. 2, the *open-circuit voltage* of a cell is the steady-state terminal voltage when the cell is allowed to rest. In terms of the model equations we have seen to date, this steady-state condition means that concentration of lithium is uniform in all solid particles in both electrodes, and the concentration of lithium is uniform in the electrolyte.

The cell open-circuit voltage can then be related to the *open-circuit potentials* of the two electrodes³¹

$$U_{\text{ocv}}^{\text{cell}} = U_{\text{ocp}}^{\text{pos}} - U_{\text{ocp}}^{\text{neg}}.$$

To develop high cell voltages (for high energy-density), the positive-electrode active material is chosen to have a high potential (versus a lithium metal reference), and the negative-electrode active material is chosen to have a low potential.

³¹ While the naming convention is a little arbitrary, we use the term *open-circuit voltage* for the cell-level quantity, as voltage refers to a difference between two potentials. We use the term *open-circuit potential* to refer to an electrode-level quantity: in actual fact, the potential of the electrode material is determined by constructing a cell whose negative electrode is lithium metal and whose positive electrode is the electrode material under consideration. Therefore, the open-circuit potential is the potential difference with respect to a lithium metal electrode, which may or may not be the electrode used in the final cell being considered.

Fig. 3.17 shows the open-circuit potential relationships of four materials commonly used for negative electrodes. Lithiated graphite of some kind is found in nearly all current lithium-ion cells. The chemical composition is Li_xC_6 , where x is a value between 0 and 1 indicating the stoichiometry of lithium in the electrode. (We compute $x = c_s^{\text{neg}} / c_{s,\text{max}}^{\text{neg}}$, where $c_{s,\text{max}}^{\text{neg}}$ is the total storage capability of the electrode solid material when the crystal lattice structure is completely full of lithium.)

The plot labeled “MCMB” is for “meso-carbon micro-beads,” or very nearly spherical particles of graphite. However, there are variations between the open-circuit potential relationships for different kinds of graphite (natural, synthetic) and hard or soft carbons with the same generic chemical composition, depending on the relative order or disorder of the layers. To illustrate this, we’ve also included plots of the open-circuit potential of petroleum coke and hard carbon (also having chemical composition Li_xC_6).

The other material shown in the figure is lithium-titanate oxide (LTO), with chemical composition $\text{Li}_{4+3x}\text{Ti}_5\text{O}_{12}$. While the high potential of LTO makes it less attractive as a negative-electrode active material, it is also relatively indestructible. Graphite electrodes tend to degrade relatively quickly due to the formation of a surface film known as the solid-electrolyte interphase (SEI); however, LTO electrodes do not appear to suffer from this same phenomenon and can be cycled tens of thousands of times.

Fig. 3.18 shows the open-circuit potential relationships of several materials commonly used for positive electrodes. Lithium-iron phosphate (LFP) has low voltage but long life, and has chemical composition Li_yFePO_4 , where y is a value between 0 and 1 indicating the stoichiometry of lithium in the electrode. (We compute $y = c_s^{\text{pos}} / c_{s,\text{max}}^{\text{pos}}$.)

Lithium-manganese oxide (LMO) has higher voltage than LFP, but suffers from rapid capacity degradation at high temperatures as the manganese tends to dissolve into the electrolyte. It has chemical composition $\text{Li}_y\text{Mn}_2\text{O}_4$.

Lithium-cobalt oxide (LCO) is more robust than LMO and has higher energy than LFP, but tends to be used mostly for small cells (such as used in portable electronics) as cobalt is expensive. The chemical formulation of LCO is Li_yCoO_2 .

There are other oxides that replace some of the cobalt in LCO with different transition metals in order to reduce cost but maintain the otherwise desirable qualities of LCO. For example, some of the cobalt may be substituted with nickel (which tends to make the cell have a higher voltage but be less thermally stable), aluminum, or manganese. So-called NCA cells replace some cobalt with nickel and some with aluminum: a common formulation is

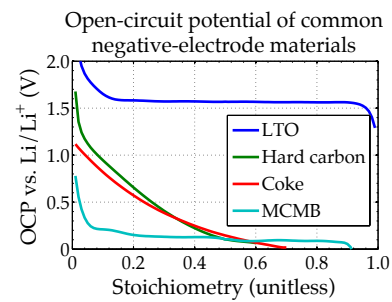


Figure 3.17: Open-circuit potential of two negative-electrode materials.

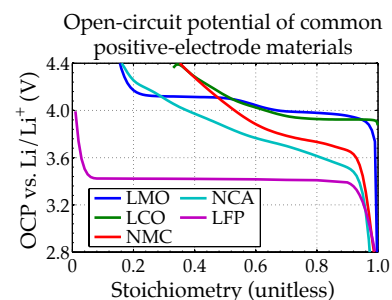


Figure 3.18: Open-circuit potential of common positive-electrode materials.

$\text{Li}_y\text{Ni}_{0.8}\text{Co}_{0.15}\text{Al}_{0.05}\text{O}_2$. Also, NMC cells replace some cobalt with nickel and some with manganese. Different relative amounts of nickel and manganese can be used, but a reasonably common formulation is $\text{Li}_y\text{Ni}_{1/3}\text{Mn}_{1/3}\text{Co}_{1/3}\text{O}_2$.

Open-circuit potentials of an electrode material are measured by constructing a test cell whose negative electrode is lithium metal and whose positive electrode material is the material under consideration. The test cell is very slowly charged and discharged, carefully taking into account the stoichiometry based on known amounts of material, and the voltages are recorded. This process is much the same as for measuring the open-circuit voltage of a full cell, as described in Chap. 2.

The data can be stored as table lookup, but most often the literature reports closed-form analytic curve fits based on approximating the data with different kinds of functions. Ad hoc fits with exponentials and hyperbolic tangents can be found; others based on polynomials or cubic splines are also popular. However, while these fits can describe the data well mathematically, they do not explain the underlying phenomena. Perhaps the first article that proposed a general fitting function with some theoretic interpretation was by Karthikeyan et al.³² In this work, a so-called Redlich–Kister expansion is used to create a fitting function. Here, we generalize their work by incorporating an empirical skew factor K into the expansion.³³ With this modification, the cell open-circuit potential is computed as

$$U(x) = U^0 + \frac{RT}{F} \ln \left(\frac{1-x}{x} \right) + \frac{1}{(K(2x-1)+1)^2} \times \\ \left[\sum_{k=0}^N \frac{A_k}{F} \left((2x-1)^{k+1} - \frac{2kx(1-x)}{(2x-1)^{1-k}} \right) \right. \\ \left. + K \sum_{k=0}^N \frac{A_k}{F} (2x-1)^k \left(2(k+1)x^2 - 2(k+1)x + 1 \right) \right].$$

In this equation, U^0 , K , and A_k for $k = 0 \dots N$ are the free fitting parameters. Curve fits for a number of commonly found electrodes are tabulated in Table 3.2. These coefficients were found by using a Levenberg–Marquardt method to minimize the summed least-squares error between the fitting function and data from numerous sources, cited in the chapter appendix.

3.11.2 Cell total capacity

Another cell-level quantity that can be quickly explained is the ampere-hour total capacity of the cell. We develop a relationship to compute this quantity in a sequence of steps, starting with expressions for capacity of each electrode.

³² Karthikeyan, D.K., Sikha, G., and White, R.E., "Thermodynamic model development for lithium intercalation electrodes," *Journal of Power Sources*, 185, 2008, pp. 1,398–1,407.

³³ Prausnitz, J.M., *Molecular Thermodynamics of Fluid Phase Equilibria*, Prentice Hall, NJ, 3d, 1999.

	MCMB	Petroleum coke	Hard carbon	LTO	LFP	LCO	LMO	NCA	NMC
K	1.000052×10^0	1.015189×10^{-5}	9.896854×10^{-1}	1.291628×10^{-1}	3.932999×10^{-2}	-2.369024×10^{-4}	-9.996536×10^{-1}	1.046644×10^{-4}	-6.359610×10^{-1}
U^0	-4.894122×10^{-1}	1.737471×10^1	5.839445×10^{-1}	1.596152×10^0	3.407141×10^0	-2.276828×10^1	4.004463×10^0	-4.419803×10^0	3.755472×10^0
A_1	1.115732×10^3	3.257341×10^6	6.433323×10^2	-2.730278×10^3	-2.244923×10^3	5.166082×10^6	2.888073×10^1	1.545979×10^6	-1.306411×10^3
A_2	-1.144052×10^5	3.324795×10^6	9.277734×10^4	5.232911×10^3	-2.090675×10^3	-5.191279×10^6	-1.928965×10^4	-1.598187×10^6	-5.799521×10^4
A_3	-9.895551×10^4	3.293786×10^6	1.208039×10^5	-8.075451×10^3	-6.045274×10^3	5.232986×10^6	2.751693×10^4	1.595170×10^6	1.285906×10^5
A_4	-8.472647×10^4	3.305070×10^6	3.909709×10^4	-4.993786×10^3	-6.046354×10^3	-5.257083×10^6	2.599759×10^4	-1.605545×10^6	-1.418605×10^5
A_5	-2.676683×10^5	3.341687×10^6	7.042733×10^4	3.643875×10^4	-1.395210×10^4	5.010583×10^6	4.795929×10^4	1.521194×10^6	1.281969×10^5
A_6	-4.761692×10^5	3.286297×10^6	4.527321×10^5	1.105087×10^5	4.928595×10^4	-4.520614×10^6	-2.773488×10^5	-1.645695×10^6	-3.281283×10^5
A_7	6.032508×10^5	2.786389×10^6	9.259981×10^5	-3.613702×10^5	5.768895×10^4	7.306952×10^6	-3.211625×10^5	1.809373×10^6	8.176398×10^2
A_8	1.867866×10^6	2.943793×10^6	1.111642×10^2	-5.025253×10^5	-2.706196×10^5	-1.463426×10^7	9.984391×10^5	-1.578053×10^6	1.373879×10^6
A_9	-1.698309×10^6	6.028857×10^6	-1.853447×10^6	1.401392×10^6	-2.623973×10^5	6.705611×10^6	1.227530×10^6	2.032672×10^6	6.511414×10^5
A_{10}	-5.707850×10^6	8.242393×10^6	-3.232663×10^5	1.148841×10^6	6.954912×10^5	3.389416×10^7	-2.722189×10^6	-2.281842×10^6	-7.315831×10^6
A_{11}	8.739993×10^5	1.365695×10^6	3.899277×10^6	-2.857197×10^6	4.805390×10^5	-6.352811×10^7	-1.973511×10^6	-1.678912×10^6	4.983891×10^6
A_{12}	7.780654×10^6	-1.036909×10^7	2.862280×10^6	-1.211581×10^6	-8.818037×10^5	3.048793×10^7	4.613775×10^6	2.858489×10^6	6.925178×10^6
A_{13}	1.486486×10^6	-1.328733×10^7	-2.837527×10^6	2.819998×10^6	-4.500675×10^5	2.144002×10^7	8.188394×10^5	5.443521×10^6	-6.123714×10^6
A_{14}	-4.703010×10^6	-6.890890×10^6	-4.19996×10^6	4.791029×10^5	4.255778×10^5	-2.773199×10^7	-4.157314×10^6	-9.459781×10^6	-3.595215×10^6
A_{15}	-2.275145×10^6	-1.366119×10^6	-1.406372×10^6	-1.091785×10^6	1.278146×10^5	8.206452×10^6	1.70975×10^6	3.600413×10^6	3.340694×10^6

Table 3.2: Modified Redlich–Kister expansion coefficients for OCP fits corresponding to commonly found electrode materials.

To compute the ampere-hour capacity of an electrode, we must first determine the capacity of the electrode in moles of lithium per unit volume. In an extreme case, this might be equal to $c_{s,\max}$. However, practical cells don't use this entire capacity (to stay away from boundaries which either lead to rapid cell degradation or power depletion)—we use only from $x_{0\%}$ to $x_{100\%}$ in the negative electrode and from $y_{0\%}$ to $y_{100\%}$ in the positive electrode, where x is the value between 0 and 1 in Li_xC_6 , for example, and y is the value between 0 and 1 in Li_yCoO_2 , for example. By combining the $c_{s,\max}$ and $x_{0\%}$, $x_{100\%}$, $y_{0\%}$, and $y_{100\%}$ values, we can find the total used capacities of the negative and positive electrodes, in moles per volume:

$$Q_V^{\text{neg}} = c_{s,\max}^{\text{neg}} |x_{100\%} - x_{0\%}| \text{ mol m}^{-3}$$

$$Q_V^{\text{pos}} = c_{s,\max}^{\text{pos}} |y_{100\%} - y_{0\%}| \text{ mol m}^{-3}.$$

Next, we need to determine the total volume of the solid material in each electrode. We start with the total volume of the electrode, which equals electrode plate area A multiplied by electrode thickness L . However, not all of this volume is filled with solid—some is filled with electrolyte, some with filler, some with binder or other non-active materials. The value ε_s is the fraction of the total electrode volume that is occupied by the solid electrode material. Knowing this, we can now compute the total used capacities of each electrode in moles:

$$Q^{\text{neg}} = AL^{\text{neg}} \varepsilon_s^{\text{neg}} c_{s,\max}^{\text{neg}} |x_{100\%} - x_{0\%}| \text{ mol}$$

$$Q^{\text{pos}} = AL^{\text{pos}} \varepsilon_s^{\text{pos}} c_{s,\max}^{\text{pos}} |y_{100\%} - y_{0\%}| \text{ mol.}$$

Finally, making use of Faraday's constant and knowing that there are 3,600 s in 1 h, we can find ampere-hour capacity.

$$Q^{\text{neg}} = AFL^{\text{neg}} \varepsilon_s^{\text{neg}} c_{s,\max}^{\text{neg}} |x_{100\%} - x_{0\%}| / 3600 \text{ Ah} \quad (3.50)$$

$$Q^{\text{pos}} = AFL^{\text{pos}} \varepsilon_s^{\text{pos}} c_{s,\max}^{\text{pos}} |y_{100\%} - y_{0\%}| / 3600 \text{ Ah.} \quad (3.51)$$

Often, one electrode has somewhat more capacity than the other, usually to minimize the occurrence of mechanisms that lead to cell degradation. The overall cell capacity is the minimum of the two electrode capacities:

$$Q = \min (Q^{\text{neg}}, Q^{\text{pos}}) \text{ Ah.} \quad (3.52)$$

3.11.3 Cell state of charge

Cell state of charge can be related either to the total amount of lithium in the negative electrode or to the total amount in the positive electrode. Similarly, by dividing the total amount of lithium in either

electrode by the total volume of the solid active material in which it resides, we can also relate state of charge to the *average* concentration of lithium in the negative electrode or to the *average* concentration of lithium in the positive electrode, where the average is computed over the entire electrode.

When the cell is fully charged, the amount of lithium in the negative electrode is at its maximum allowable level, and the amount of lithium in the positive electrode is at its minimum allowable level. In terms of stoichiometries, $c_{s,\text{avg}}^{\text{neg}}/c_{s,\text{max}}^{\text{neg}} = x_{100\%}$ and $c_{s,\text{avg}}^{\text{pos}}/c_{s,\text{max}}^{\text{pos}} = y_{100\%}$.

Similarly, when the cell is fully discharged, the amount of lithium in the negative electrode is at its minimum allowable level, and the amount of lithium in the positive electrode is at its maximum allowable level. In terms of stoichiometries, $c_{s,\text{avg}}^{\text{neg}}/c_{s,\text{max}}^{\text{neg}} = x_{0\%}$ (where $x_{0\%} < x_{100\%}$) and $c_{s,\text{avg}}^{\text{pos}}/c_{s,\text{max}}^{\text{pos}} = y_{0\%}$ (where $y_{0\%} > y_{100\%}$).

State of charge varies linearly as the stoichiometry of the negative electrode varies between $x_{0\%}$ and $x_{100\%}$ (or, equivalently, as the stoichiometry of the positive electrode varies between $y_{0\%}$ and $y_{100\%}$). Therefore, we can compute cell-level state of charge as:

$$z = \frac{c_{s,\text{avg}}^{\text{neg}}/c_{s,\text{max}}^{\text{neg}} - x_{0\%}}{x_{100\%} - x_{0\%}} \quad (3.53)$$

$$= \frac{c_{s,\text{avg}}^{\text{pos}}/c_{s,\text{max}}^{\text{pos}} - y_{0\%}}{y_{100\%} - y_{0\%}}. \quad (3.54)$$

3.11.4 Single-particle model

As we have learned to date, there are five coupled equations in a microscale cell model. These describe the movement of lithium in the solid and electrolyte, voltage (potential) of the solid and electrolyte, and the rate of reaction at the solid–electrolyte boundary at different points in the cell.

It turns out that the diffusion of lithium inside the solid particles is the slowest process, so its dynamic contribution dominates over the others. Hence, we can consider a single-particle model (SPM) of a cell, which simplifies each electrode by modeling it as a single spherical particle of active material representative of a typical particle within the electrode. The dynamics of electrolyte concentration and potential are ignored. While crude, the SPM is a good learning tool for understanding how lithium-ion cells should respond to different input stimuli, and they can be used within control designs to give good estimates of state of charge.

To simulate diffusion of lithium within a single solid particle, we might try several different approaches. Here, we introduce a finite-volume method for discretizing the diffusion equation. A single solid

particle is divided into spherical shells having equal thickness (like an idealized onion). At each time step the total flux of lithium from one shell to another is calculated, and the concentration of lithium within each shell is then updated. Lithium is forced into or out of the outermost shell via an imposed cell current.

Consider the following code for simulating a single particle, as the particle is discharged, rested, charged, and rested (the output of this code is plotted in Fig. 3.19).

```
% Replace constants below with relevant values for your problem
R = 10e-6; % particle radius [m]
Cmax = 12000; % [mol/m^3]
c0 = 9500; % initial concentration [mol/m^3]
j0 = 5000*R/3/1800; % lithium flux [mol/m^2/sec]
D = 1e-14; % solid diffusivity, [m^2/s]

jk = [j0*ones(1,1800), zeros(1,3600)]; % discharge and rest
jk = [jk -jk]; % discharge and rest, then charge and rest

% Simulation control
Nr = 20; % number of "shells" radially
dR = R/Nr; % width of each "shell"
Sa = 4*pi*(R*(1:Nr)).^2; % outer surface area of each shell
dV = (4/3)*pi*((R*(1:Nr)).^3 - (R*(0:Nr-1)).^3); % vol. of ea. shell
dt = 1; % time steps of 1 second

c = c0*ones(1,Nr); % concentration profile versus "r" dimension
cse = zeros(size(jk)); % concentration at surface
cse(1) = c0;

for timestep = 1:length(jk),
    N = -D*diff(c)/dR; % flux density at surfaces between "bins"
    M = N.*Sa(1:end-1); % total moles crossing surface between bins
    c = c + ([0 M] - [M 0]).*dt./dV; % conc. change via diffusion
    c(end) = c(end) - jk(timestep)*Sa(end)*dt/dV(end); % at boundary
    cse(timestep+1) = c(end);
end

figure(1); clf; plot((0:length(jk))/3600,cse/1000);
title('Surface concentration of particle')
xlabel('Time (h)'); ylabel('Concentration (kmol m^{-3})')
```

In the code, the spherical particle is assumed to have N_r equal-thickness onion-like “shells.” Thus, the thickness of any given shell is $dR = R_s/N_r$. We will also need to know the outer surface area of each shell and the volume of each shell:

- The innermost shell has volume $dV_1 = \frac{4}{3}\pi(dR)^3$ and outer surface area $Sa_1 = 4\pi(dR)^2$.
- The next shell has volume $dV_2 = \frac{4}{3}\pi(2dR)^3 - dV_1$ and outer surface area $Sa_2 = 4\pi(2dR)^2$.
- By extension, the n th shell has volume

$$dV_n = \frac{4}{3}\pi(ndR)^3 - \frac{4}{3}\pi((n-1)dR)^3$$

and surface area $Sa_n = 4\pi(ndR)^2$.

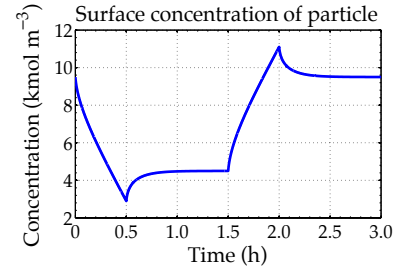


Figure 3.19: Output of code simulating a single particle.

The variables dV and Sa in the code are vectors containing the volumes and outer surface areas of all shells, respectively.

Now, consider converting molar flux density from a continuous function of distance r to a discrete function at the shell boundaries.

$$N = -D_s \nabla c_s = -D_s \frac{\partial c_s}{\partial r} \approx -D_s \frac{\Delta c_s}{\Delta r}.$$

The flux density at the n th boundary between shell n and shell $n + 1$ can then be written as

$$N_n \approx -D_s \frac{c_{n+1} - c_n}{\Delta R}.$$

When the sign of N_n is negative, then flux is entering the n th shell from the $(n + 1)$ st shell; when the sign is positive, flux is leaving the n th shell to the $(n + 1)$ st shell. The vector N in the code computes this flux density at all shell boundaries, except at the outer surface of the particle, which is computed separately. This flux has units $\text{mol m}^{-2} \text{s}^{-1}$.

In the code, we then multiply N by the surface area of the shell through which the flux is passing to get a rate of material transfer. This is the M variable in the code, in units mol s^{-1} .

Considering any shell, there are two boundaries through which this flux can come: the inner surface and the outer surface. The total increase in the number of moles in the n th shell is equal to $Sa_n N_n - Sa_{n-1} N_{n-1}$ in units mol s^{-1} . To get a change in concentration, we must multiply by Δt in seconds and divide by the volume of the n th shell. The concentration update equation uses this logic to implement the diffusion.

How about boundary conditions? We have an applied flux density j in $\text{mol m}^{-2} \text{s}^{-1}$. Multiplying j by $Sa_n \Delta t / V_n$ gives the change in concentration of the outer shell because of the applied flux every Δt seconds.

To find the average interphase lithium flux density in $\text{mol m}^{-2} \text{s}^{-1}$ for a given cell current in A, we must first convert the cell current from amperes to mol s^{-1} . Faraday's constant will help with this.

Next, we need to know how many square meters of interphase area can be found in each electrode. To arrive at this answer, we must first calculate the specific interfacial area in $\text{m}^2 \text{m}^{-3}$. If we assume that all electrode particles are spherical with radius R_s and that we have solid-phase volume fraction ε_s , then

$$a_s = \frac{\text{total surface area}}{\text{total volume}} = \underbrace{\frac{\text{volume of solid}}{\text{total volume}}}_{\varepsilon_s} \frac{\text{total surface area/particle}}{\text{volume of solid/particle}} \\ = \varepsilon_s \frac{4\pi R_s^2}{\frac{4}{3}\pi R_s^3} = \frac{3\varepsilon_s}{R_s}.$$

This result computes how many square meters of particle surface area there are per cubic meter of total electrode volume. So, $a_s AL$ gives the total square meters of particle surface area in an electrode, and

$$j = \frac{i_{app}}{a_s FAL} \text{ mol m}^{-2} \text{ s}^{-1}.$$

Finally, while state of charge is dependent on the average concentration of lithium in the electrode, voltage is dependent on the *surface* concentration of lithium (i.e., at the interface between the solid and electrolyte). The code defines a variable `cse`, which is what we denote $c_{s,e}$ elsewhere. When simulating an entire cell using the single-particle method, one particle models the negative electrode and a second particle (using a copy of the above code) models the positive electrode. Cell voltage is equal to positive-electrode potential minus negative-electrode potential. The positive-electrode potential is determined by evaluating the $U_{\text{ocp}}^{\text{pos}}(y)$ function at the value of y corresponding to the present surface concentration of lithium of the positive-electrode particle, where $y = c_{s,e}/c_{s,\text{max}}$. The negative-electrode potential is similarly determined by evaluating the $U_{\text{ocp}}^{\text{neg}}(x)$ function at the value of x corresponding to the present surface concentration of lithium of the negative-electrode particle, where $x = c_{s,e}/c_{s,\text{max}}$.

3.12 Where to from here?

We have now completed the most difficult derivations in the book! From now on, we depart from topics in thermodynamics, physical chemistry, and electrochemistry and work from the model we have now developed, successively bringing it up in scale until we arrive at ordinary-difference equations.

But, the microscale model is the most accurate set of model equations we will have in the book. From now on, our goal is to approximate these equations with versions that are simpler to implement. At the same time, we will attempt to minimize the error that we introduce into the models by the approximations.

3.13 Chapter appendix: OCP sources

This appendix offers citations to the original sources of the data from which Table 3.2 was constructed and from which Figs. 3.17 and 3.18 were plotted.

The MCMB data were digitized from Fig. A-1 in: S. Santhanagopalan,

Q. Guo, and R.E. White, "Parameter Estimation and Model Discrimination for a Lithium-Ion Cell," *Journal of the Electrochemical Society*, 154(3), 2007, pp. A198–A206.

The petroleum-coke data were digitized from Fig. B–2 in: M. Doyle, J. Newman, A.S. Gozdz, C.N. Schmutz, and J-M Tarascon, "Comparison of Modeling Predictions with Experimental Data from Plastic Lithium Ion Cells," *Journal of the Electrochemical Society*, 143(6), 1996, pp. 1,890–1,903.

The hard carbon data were digitized from Fig. 1 in: D.K. Karthikeyan, G. Sikha, R.E. White, "Thermodynamic Model Development for Lithium Intercalation Electrodes," *Journal of Power Sources*, 185, 2008, pp. 1,398–1,407.

The LTO data were digitized from Fig. 4 in: S. Stewart, P. Alber-

tus, V. Srinivasan, I. Plitz, N. Pereira, G. Amatucci, and J. Newman, "Optimizing the Performance of Lithium Titanate Spinel Paired with Activated Carbon or Iron Phosphate," *Journal of the Electrochemical Society*, 155(3), 2008, pp. A253–A261.

The LFP data were digitized from Fig. 3 in: M. Safari and C. Dela-

court, "Modeling of a Commercial Graphite LiFePO₄ Cell," *Journal of the Electrochemical Society*, 158(5), 2011, pp. A562–A571. From these (depth-of-discharge) data alone, it is not possible to determine the sto-

ichiometric coefficient y ; this was found by calibrating the discharge curve against Safari's own curve fit

$$U_{\text{ocp}}^{\text{LFP}} = 3.4323 - 0.8428 \exp \left(-80.2493(1-y)^{1.3198} \right) \\ - 3.2474 \times 10^{-6} \exp \left(20.2645(1-y)^{3.8003} \right) \\ + 3.2482 \times 10^{-6} \exp \left(20.2646(1-y)^{3.7995} \right)$$

to determine the correct stoichiometric range of y corresponding to the discharge curve.

The LCO data were digitized from Fig. A–2 in: S. Santhanagopalan, Q. Guo, and R.E. White, "Parameter Estimation and Model Discrimination for a Lithium-Ion Cell," *Journal of the Electrochemical Society*, 154(3), 2007, pp. A198–A206.

The LMO data were digitized from Fig. B–1 in: M. Doyle, J. New-

man, A.S. Gozdz, C.N. Schmutz, and J-M Tarascon, "Comparison of Modeling Predictions with Experimental Data from Plastic Lithium Ion Cells," *Journal of the Electrochemical Society*, 143(6), 1996, pp. 1,890–1,903.

The NCA data were digitized from Fig. 2 in: D.K. Karthikeyan, G. Sikha, R.E. White, "Thermodynamic Model Development for Lithium Intercalation Electrodes," *Journal of Power Sources*, 185, 2008, pp. 1,398–1,407.

The NMC data were digitized from Fig. 6 in: S.G. Stewart, V. Srinivasan, and J. Newman, "Modeling the Performance of Lithium-Ion Batteries and Capacitors during Hybrid-Electric-Vehicle Operation," *Journal of the Electrochemical Society*, 155(9), 2008, pp. A664–A671. From these (depth-of-discharge) data alone, it is not possible to determine the stoichiometric coefficient y ; this was found by calibrating the discharge curve against the paper's own curve fit

$$U_{\text{ocp}}^{\text{NMC}} = 6.0826 - 6.9922y + 7.1062y^2 - 0.54549 \times 10^{-4} \exp(124.23y - 114.2593) - 2.5947y^3$$

to determine the correct stoichiometric range of y corresponding to the discharge curve.

3.14 Partial glossary

This section gives a glossary of the most important variables defined in this chapter. Units are also given—the notation [u/l] is specified for a unitless quantity. Note that all variables are at least potentially functions of space and time.

- α [u/l] is the asymmetric charge-transfer coefficient $0 \leq \alpha \leq 1$ (cf. p. 114).
- a [mol m⁻³] is the activity of a species (cf. p. 90).
- a_s [m² m⁻³] is the specific interfacial surface area (cf. p. 129).
- A [J] is the Helmholtz free energy (cf. p. 82).
- A [m²] is the cell current-collector plate area (cf. p. 126).
- c [mol m⁻³] is the concentration of lithium in the neighborhood of a given location. c_s is used to denote concentration in the solid, and c_e is used to denote concentration in the electrolyte (cf. pp. 76 and 93). c_0 is the concentration of the solvent, and c_T is the total concentration (cf. pp. 100 and 97). $c_{s,e}$ is the surface concentration, and $c_{s,\text{max}}$ is the theoretic maximum lithium concentration (cf. pp. 130 and 126).
- c_+ and c_- [mol m⁻³] are the concentrations of the cation and anion in the electrolyte, respectively (cf. p. 92).
- D [m² s⁻¹] is a material-dependent *diffusivity*. D_s is used to denote diffusivity in the solid, and D_e is used to denote diffusivity in the electrolyte (cf. pp. 76 and 105).
- \mathcal{D} [m² s⁻¹] is the Maxwell–Stefan *diffusivity* of a concentrated solution (cf. pp. 98 and 101).
- ε_s [u/l] is the volume fraction of the solid in an electrode (cf. p. 126).
- \mathbf{E} [V m⁻¹] is the (vector) electric field at a point (cf. p. 71).

- $F = 96,485 \text{ [C mol}^{-1}]$ is Faraday's constant.
- $f_{\pm} \text{ [u/l]}$ is the mean molar activity coefficient (cf. p. 110).
- $G \text{ [J]}$ is the Gibbs free energy of a system or subsystem (cf. pp. 82 and 85).
- $\gamma_{\pm} \text{ [u/l]}$ is the mean molal activity coefficient (cf. p. 104).
- $H \text{ [J]}$ is the enthalpy of a system; dH is the heat added to or removed from a system by a chemical reaction (cf. p. 82).
- $\eta \text{ [V]}$ is the reaction overpotential (cf. p. 115).
- $\mathbf{i} \text{ [A m}^{-2}]$ is the (vector) current density flowing through a representative cross-sectional area centered at a given location. \mathbf{i}_s is used to denote current density in the solid, and \mathbf{i}_e is used to denote current density in the electrolyte (cf. pp. 71 and 93).
- $i_0 \text{ [A m}^{-2}]$ is the exchange current density (cf. p. 116).
- $j \text{ [mol m}^{-2} \text{ s}^{-1}]$ is the rate of positive charge flowing *out of* a particle across a boundary between the solid and the electrolyte (cf. p. 118).
- $k_0 \text{ [mol}^{\alpha-1} \text{ m}^{4-3\alpha} \text{ s}^{-1}]$ is the effective reaction-rate constant (cf. p. 117).
- $k_0^{\text{norm}} \text{ [mol m}^{-2} \text{ s}^{-1}]$ is a normalized version of the effective reaction rate constant with less awkward units (cf. p. 118).
- $K_{ab} \text{ [J s m}^{-4}]$ is the Maxwell–Stefan friction coefficient between species a and b (cf. p. 98).
- $\kappa \text{ [S m}^{-1}]$ is the ionic conductivity (cf. p. 109).
- $\kappa_D \text{ [V]}$ is an abbreviation of part of the electrolyte-potential equation: $\kappa_D = 2RT\kappa(t_+^0 - 1)/F$ (cf. p. 110).
- $\lambda \text{ [u/l]}$ is the absolute activity of a species and can be written in terms of molarity and molality (cf. pp. 90 and 91).
- $L \text{ [m]}$ is the electrode thickness (cf. p. 126).
- $\mu \text{ [J mol}^{-1}]$ is the chemical potential of a system (cf. p. 88).
- $\bar{\mu} \text{ [J mol}^{-1}]$ is the electrochemical potential of a system (cf. p. 88).
- $m \text{ [kg]}$ is mass of a species (cf. p. 87).
- $n \text{ [u/l]}$ is number of moles of a species (cf. p. 87).
- $\hat{\mathbf{n}} \text{ [u/l]}$ is a unit vector pointing in an outward direction from a surface, away from the phase of interest.
- $\mathbf{N}(x, y, z, t) \text{ [mol m}^{-2} \text{ s}^{-1}]$ is the (vector) *molar flux density* of lithium flowing through a representative cross-sectional area of the solid centered at a given location (cf. pp. 76 and 93).
- $N_A = 6.02214 \times 10^{23} \text{ [mol}^{-1}]$ is Avagadro's number.

- ν_+ and ν_- [u/l] are the unsigned stoichiometric coefficients of the cation and anion, respectively (cf. p. 92).
- $\mathbf{p}(t)$ [kg m s⁻¹] is the (vector) momentum of an object.
- p [Pa] is the pressure experienced by a system.
- ϕ [V] is the scalar field representing the electrostatic potential at a given point. ϕ_s is used to denote electric potential in the solid and ϕ_e is used to denote electric field in the electrolyte (cf. pp. 71 and 88).
- Q [C] is the charge in the vicinity of a given point (cf. p. 73).
- Q [Ah] is the total capacity of a battery cell (cf. p. 126).
- q [J] is the heat, usually considered as a delta Δq of added/removed heat to a system (cf. p. 84).
- $R = 8.314$ [J mol⁻¹ K⁻¹] is the universal gas constant.
- R_s [m] is electrode particle average radius (cf. p. 129).
- $\rho_V(x, y, z, t)$ [C/m³] is the *charge density* (of positive charges) in the vicinity of a given point (cf. p. 73).
- S [J K⁻¹] is the entropy of a system (cf. p. 84).
- s_+, s_-, s_0 [u/l] are the signed stoichiometric coefficients of cation, anion, and solvent, respectively (cf. p. 106).
- σ [S m⁻¹] is a material-dependent parameter called the *bulk conductivity* of homogeneous materials without inclusions in the vicinity of a given point (cf. p. 71).
- T [K] is the temperature at a point.
- t_+^0 and t_-^0 [u/l] are the transference numbers of the cation and anion with respect to the solvent, respectively (cf. p. 102).
- U [J] is the internal energy of a system (cf. p. 81).
- \mathbf{v} [m s⁻¹] is the (vector) velocity of a species.
- V [m³] is volume.
- w [J] is the work, usually considered as a delta Δw of work done on or by a system (cf. p. 84).
- x [u/l] is the mole fraction of a species (cf. p. 97).
- z_+ and z_- [u/l] are the signed charge numbers of the cation and anion, respectively (cf. p. 92).
- z [u/l] is cell state-of-charge (cf. p. 127).

4

Continuum-Scale Cell Models

Mathematical models of physical phenomena are expressed most readily at the microscopic scale. In Chap. 3, we saw that microscale models of lithium-ion cell dynamics describe, in three dimensions, the charge and mass balance within the solid particles and within the electrolyte, separately. They can be used to simulate small volumes inside electrodes, comprising small clusters of particles, in order to get ideas of how particle sizes and mixtures of geometries, and so forth, interact. However, it is infeasible with present technology to simulate an entire cell using microscale models. For cell-level models, we require reduced-complexity macroscale models that capture the dominant physics of the microscale.

We refer back to Fig. 3.1 to help gauge our progress in model development. We have completed deriving the microscale PDE model of lithium-ion dynamics. In this chapter, we consider deriving the next higher scale—the continuum-scale PDE model.

One approach to creating a macroscale model is by volume-averaging microscopic quantities over a finite but small unit of volume. The resultant model is called a *continuum model*. Modeling an object as a continuum assumes that the substance of the object completely fills the space it occupies. So, modeling the electrode's solid particles in this way ignores the details of the pores in between the particles, by which the solid electrode material is not continuous. Modeling the electrolyte this way ignores the details of the geometries of the particles that fill it. However, on length scales much greater than that of a particle's radius, such models can be highly accurate.

Any specific (x, y, z) coordinate inside an electrode corresponds either to a position inside a solid particle or to a position inside the electrolyte (or inside some inactive material such as a conductive additive or binder), but it cannot correspond to a point both in the solid and electrolyte. This is illustrated in Fig. 4.1, where particles are depicted by (truncated and artificially colored) ellipsoid shapes,

4.1	<i>Chap. goal: Continuum</i>	136
4.2	<i>Preliminaries</i>	137
4.3	<i>Averaging theorem 1</i>	146
4.4	<i>Averaging theorem 2</i>	148
4.5	<i>Averaging theorem 3</i>	149
4.6	<i>Solid charge conservation</i>	152
4.7	<i>Solid mass conservation</i>	156
4.8	<i>Electrolyte mass conserv.</i>	157
4.9	<i>Electrolyte charge conserv.</i>	160
4.10	<i>Butler–Volmer equation</i>	161
4.11	<i>Boundary conditions</i>	161
4.12	<i>Cell-level quantities</i>	163
4.13	<i>Model simulations</i>	164
4.14	<i>Running COMSOL</i>	169
4.15	<i>Where to from here?</i>	169
4.16	<i>Partial glossary</i>	170

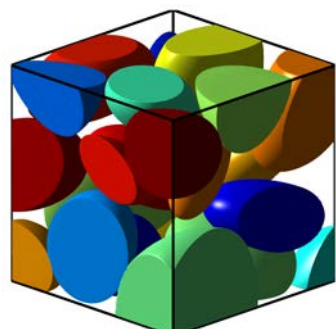


Figure 4.1: A small volume inside an electrode.

and electrolyte fills the voids between the particles. To simulate this portion of a lithium-ion cell's electrode most accurately, we use the microscale models from Chap. 3, which require complex geometric maps of the electrodes to be able to determine which points belong to the solid and which belong to the electrolyte. Equations of mass- and charge-conservation in the solid dynamics are applied to the solid regions; equations of mass- and charge-conservation in the electrolyte dynamics are applied to the electrolyte regions. The Butler–Volmer equation applies to the boundaries between regions.

Continuum models work differently. Because of the volume averaging performed to develop a continuum-scale model, the resulting equations assume that any (x, y, z) coordinate inside the electrode corresponds, in some sense, to a point both in the solid and electrolyte. That is, continuum models tell you what is the typical or average behavior inside the solid and electrolyte in the vicinity of a specific point. Solid and electrolyte *phases* are still considered separately, but their interactions within the volume must be factored in. Microscale geometries need not be known—an average geometry is assumed.

Referring again to Fig. 4.1, the solid potential equation defining $\phi_s(x, y, z, t)$ is no longer concerned about whether (x, y, z) corresponds to a point in the solid; the equation simply predicts the solid potential of particles in the neighborhood of (x, y, z) . Similarly, the equations defining solid lithium concentration, electrolyte potential, electrolyte lithium concentration, and solid–electrolyte flux density describe quantities that are representative of the true variables in a neighborhood of a specified point.

4.1 Chapter goal: The continuum-scale cell model

With all this in mind, the goal of this chapter is to derive the continuum-scale cell model from the microscale model that has already been developed. To be able to do so, we will need to first derive three theorems related to volume averaging:¹

1. Volume-averaging theorem 1 for scalar field ψ :

$$\varepsilon_\alpha \overline{\nabla \psi_\alpha} = \nabla (\varepsilon_\alpha \bar{\psi}_\alpha) + \frac{1}{V} \iint_{A_{\alpha\beta}(x,t)} \psi_\alpha \hat{\mathbf{n}}_\alpha \, dA. \quad (4.1)$$

2. Volume-averaging theorem 2 for vector field ψ :

$$\varepsilon_\alpha \overline{\nabla \cdot \psi_\alpha} = \nabla \cdot (\varepsilon_\alpha \bar{\psi}_\alpha) + \frac{1}{V} \iint_{A_{\alpha\beta}(x,t)} \psi_\alpha \cdot \hat{\mathbf{n}}_\alpha \, dA. \quad (4.2)$$

3. Volume-averaging theorem 3 for scalar field ψ :

$$\varepsilon_\alpha \overline{\left[\frac{\partial \psi_\alpha}{\partial t} \right]} = \frac{\partial (\varepsilon_\alpha \bar{\psi}_\alpha)}{\partial t} - \frac{1}{V} \iint_{A_{\alpha\beta}(x,t)} \psi_\alpha \mathbf{v}_{\alpha\beta} \cdot \hat{\mathbf{n}}_\alpha \, dA. \quad (4.3)$$

¹ The derivations rely heavily on: Gray, W.G., and Lee, P.C.Y., "On the Theorems for Local Volume Averaging of Multiphase Systems," *International Journal on Multiphase Flow*, 3, 1977, pp. 333–40.

The over-line notation “ \bar{x} ” will be explained at the appropriate time, as will the subscripts α and β .

Then, we will apply these volume-averaging theorems to the microscale model equations from Chap. 3 to derive

1. The volume-average approximation for charge conservation in the solid phase of the porous electrode, which is

$$\nabla \cdot (\sigma_{\text{eff}} \nabla \bar{\phi}_s) = a_s F \bar{j}. \quad (4.4)$$

2. The solid-phase mass conservation equation, which is

$$\frac{\partial c_s}{\partial t} = \frac{1}{r^2} \frac{\partial}{\partial r} \left(D_s r^2 \frac{\partial c_s}{\partial r} \right). \quad (4.5)$$

3. The volume-average approximation for charge conservation in the electrolyte phase of the porous electrode, which is

$$\nabla \cdot (\kappa_{\text{eff}} \nabla \bar{\phi}_e + \kappa_{D,\text{eff}} \nabla \ln \bar{c}_e) + a_s F \bar{j} = 0. \quad (4.6)$$

4. The volume-average approximation for mass conservation in the electrolyte phase of the porous electrode, which is

$$\frac{\partial (\varepsilon_e \bar{c}_e)}{\partial t} = \nabla \cdot (D_{e,\text{eff}} \nabla \bar{c}_e) + a_s (1 - t_+^0) \bar{j}. \quad (4.7)$$

5. The volume-average approximation to the microscopic Butler–Volmer kinetics relationship, which is

$$\bar{j} = j(\bar{c}_{s,e}, \bar{c}_e, \bar{\phi}_s, \bar{\phi}_e). \quad (4.8)$$

4.2 Preliminaries

Our first goal is to derive the volume-averaging theorems of Eqs. (4.1) through (4.3). To do so, we start by introducing some preliminary concepts.

4.2.1 The α and β phases

A helpful abstraction is to divide the sample volume into two phases: the phase-of-interest is denoted α ; all other phase(s) are lumped into β . When considering solid mass- and charge-conservation equations, the solid is denoted as phase α and everything else is phase β . When considering the electrolyte mass- and charge-conservation equations, the electrolyte is denoted as phase α and everything else is phase β .

4.2.2 The indicator function

Our interest then will be in finding the average value of some quantity in phase α . To help with notation, we define an indicator function for phase α as

$$\gamma_\alpha(x, y, z, t) = \begin{cases} 1, & \text{if point } (x, y, z) \text{ is in phase } \alpha \text{ at time } t; \\ 0, & \text{otherwise.} \end{cases}$$

We will need to take derivatives of this function, which we might imagine are zero everywhere except at the boundaries between phase α and phase β . But what is the value of the derivative right on the boundary?

4.2.3 The Dirac delta function

The derivative of the indicator function is known as a Dirac delta function $\delta(x, y, z, t)$. This function is unusual—it is defined in terms of its *properties* rather than by stating exactly its *value*. These properties are

$$\delta(x, y, z, t) = 0, \quad (x, y, z) \neq 0.$$

$$\iiint_V \delta(x, y, z, t) \, dV = 1.$$

We see that this function must have unit volume but zero extent. This is not an ordinary kind of function. It is a *generalized* function, which can have *many* different but equivalent equations that describe it.

In one dimension, an example Dirac delta function is drawn in Fig. 4.2 and is defined by

$$\delta(x) = \lim_{\epsilon \rightarrow 0} \begin{cases} \frac{1}{\epsilon}, & |x| \leq \epsilon/2; \\ 0, & \text{otherwise.} \end{cases} \quad (4.9)$$

This has an integral of 1 for all values of ϵ , and as ϵ approaches zero, it has zero width. We can make a more compact notation for this if we define the “pulse function”

$$\Pi(x) = \begin{cases} 1, & |x| < 1/2; \\ 0, & \text{otherwise.} \end{cases}$$

Then, we can write

$$\delta(x) = \lim_{\epsilon \rightarrow 0} \frac{1}{\epsilon} \Pi\left(\frac{x}{\epsilon}\right).$$

Sifting property of $\delta(x, y, z, t)$

The Dirac delta function has several properties that are important to know. The first we look at is the *sifting property*, which states that in

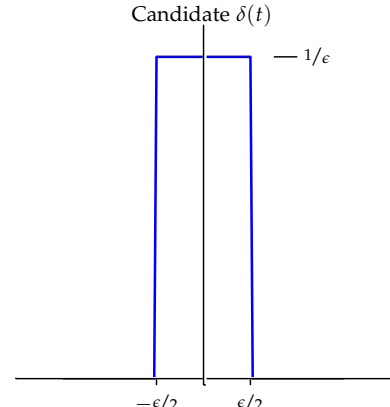


Figure 4.2: Sample one-dimensional Dirac delta candidate function.

one dimension

$$\int_{-\infty}^{\infty} f(x, t) \delta(x - x_0, t) dx = f(x_0, t).$$

The value of the function at the location of the Dirac delta is “sifted out,” and the integral of a function is replaced by the value of that function at a specific point. In three dimensions, using vector form, if $\mathbf{x} = (x, y, z)$, and $\mathbf{x}_0 = (x_0, y_0, z_0)$ we can write

$$\iiint_V f(\mathbf{x}, t) \delta(\mathbf{x} - \mathbf{x}_0, t) dV = \begin{cases} f(\mathbf{x}_0, t), & \text{if } \mathbf{x}_0 \text{ is inside } V; \\ 0, & \text{otherwise.} \end{cases}$$

We will sketch a proof of this relationship in one dimension for $x_0 = 0$. Consider using Eq. (4.9) as our candidate Dirac delta function, and consider also Fig. 4.3. We write

$$\int_{-\infty}^{\infty} f(x) \delta(x) dx = \lim_{\epsilon \rightarrow 0} \int_{-\infty}^{\infty} \frac{1}{\epsilon} \Pi\left(\frac{x}{\epsilon}\right) f(x) dx.$$

This operation is illustrated in Fig. 4.3.

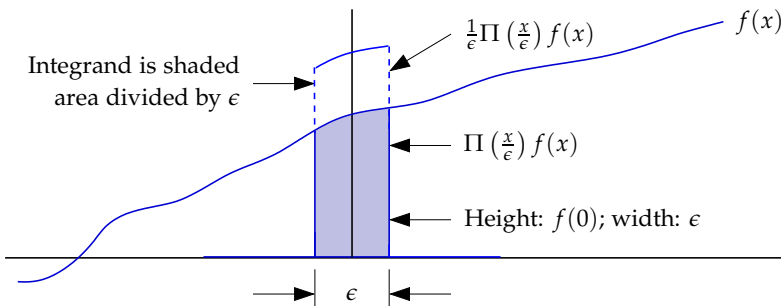


Figure 4.3: Illustrating the sifting property of the Dirac delta function.

From the figure, we see that $f(x)$ is being multiplied by zero at nearly every point inside the integral. In the ϵ neighborhood of $x = 0$, however, it is being multiplied by $1/\epsilon$. If $f(x)$ is continuous around $x_0 = 0$, then it will approach a constant value over the interval $-\epsilon/2$ to $\epsilon/2$, and that value will be $f(0)$. So, the integral becomes $f(0)$ times the ϵ width of the Dirac delta multiplied by the $1/\epsilon$ height of the Dirac delta. That is,

$$\int_{-\infty}^{\infty} f(x) \delta(x) dx = \frac{1}{\epsilon} \epsilon f(0) = f(0).$$

This proof sketch can be generalized to $x_0 \neq 0$ and higher dimensions quite readily.

Integrating a Dirac delta

Consider integrating a one-dimensional Dirac delta from $-\infty$ to x . That is, we wish to compute

$$\int_{-\infty}^x \delta(\chi) d\chi.$$

This is illustrated in Fig. 4.4. The left frame of the figure shows three candidate Dirac delta functions in different colors, starting with a short and wide function, and ending with a tall and narrow function. The taller and narrower the approximation, the closer it is to the true Dirac delta function that it is approximating.

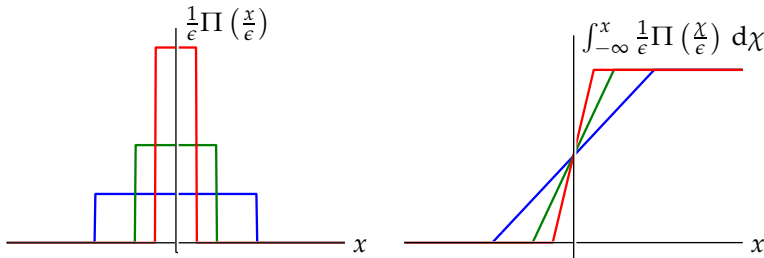


Figure 4.4: Integrating approximate Dirac delta functions of decreasing width.

In the integral, if the point x is to the left of the rectangle, the integral is summing up a lot of zero values, and the result is zero. If the point x is to the right of the rectangle, the integral contains the entire Dirac delta function inside of its limits, so the result must be one. If the point x falls in the middle of the rectangle, then the result is somewhere between zero and one.² This is illustrated in the right frame of the figure, where the colors of the integrated approximate Dirac delta functions correspond to the input functions in the left frame. We see that the more closely the approximate Dirac delta function approaches the true Dirac delta, the more closely the integral approaches a step function. In the limit, we have

$$\int_{-\infty}^x \delta(\chi) d\chi = \begin{cases} 0, & x < 0 \\ 1, & x > 0. \end{cases}$$

This tells us that the running integral of a Dirac delta function is a step function. Furthermore, the derivative of a step function is the Dirac delta function.

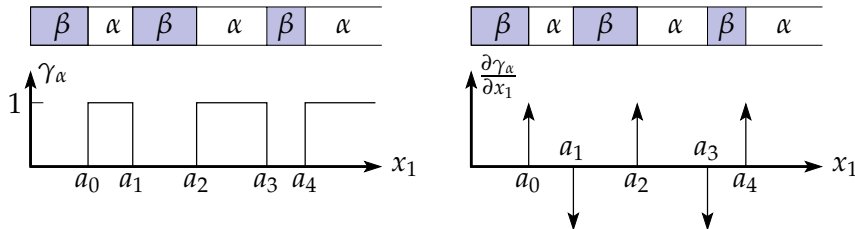
4.2.4 Gradient of the indicator function

Recalling that the indicator function is a steplike function, we expect that its gradient will involve the Dirac delta function.

Consider the simple one-dimensional example plotted in Fig. 4.5. The top of both frames shows segments of a sample volume, where

² However, for other candidate Dirac delta functions, this is not necessarily the case. So, the integral is actually undefined but finite at $x = 0$.

the shaded segments are phase β , and the clear segments are phase α . The indicator function γ_α is one for values of x_1 corresponding to phase α or else it is zero. This is plotted in the left frame of the figure.



The right frame of the figure considers the gradient of the indicator function. Specifically, the spatial derivative $\partial\gamma_\alpha/\partial x_1$ comprises Dirac delta functions, which are drawn as arrows in the figure.

$$\begin{aligned}\frac{\partial\gamma_\alpha(x_1, t)}{\partial x_1} = & \delta(x_1 - a_0(t)) - \delta(x_1 - a_1(t)) + \delta(x_1 - a_2(t)) \\ & - \delta(x_1 - a_3(t)) + \delta(x_1 - a_4(t)).\end{aligned}$$

We now define a unit-normal vector $\hat{\mathbf{n}}_\alpha$, which points *outward* from the α phase toward the β phase at all α - β interfaces. This allows us to write a more compact notation

$$\frac{\partial\gamma_\alpha(x_1, t)}{\partial x_1} = -\sum_{k=0}^4 \hat{\mathbf{n}}_\alpha \cdot \hat{\mathbf{i}} \delta(x_1 - a_k(t)),$$

where $\hat{\mathbf{i}}$ is a unit vector in the positive x_1 direction.

Now, consider a two-dimensional example, such as shown in Fig 4.6. In the left frame, the α phase is unshaded, and the β phase is shaded. In this instance, the spatial derivatives in the x_1 and x_2 directions are

$$\begin{aligned}\frac{\partial\gamma_\alpha(x_1, x_2, t)}{\partial x_1} &= -\hat{\mathbf{n}}_\alpha \cdot \hat{\mathbf{i}} \delta(\mathbf{x} - \mathbf{x}_{\alpha\beta}, t) \\ \frac{\partial\gamma_\alpha(x_1, x_2, t)}{\partial x_2} &= -\hat{\mathbf{n}}_\alpha \cdot \hat{\mathbf{j}} \delta(\mathbf{x} - \mathbf{x}_{\alpha\beta}, t),\end{aligned}$$

where \mathbf{x} is a position vector, $\hat{\mathbf{j}}$ is a unit vector in the positive x_2 direction, and $\mathbf{x}_{\alpha\beta}$ is the position vector of the α - β interface. The middle and right frames of the figure show the partial derivatives in the x_1 and x_2 directions, respectively.

Note that the varying heights of the impulse functions are due to the dot product between $\hat{\mathbf{n}}_\alpha$ and either $\hat{\mathbf{i}}$ or $\hat{\mathbf{j}}$. When these vectors are aligned, the dot product will be one; when they are at right angles, the dot product will be zero; otherwise, the dot product will be somewhere in between (by the law of cosines).

Figure 4.5: Representing a two-phase volume.

(Adapted from Fig. 1 in Gray, W.G., and Lee, P.C.Y., "On the Theorems for Local Volume Averaging of Multiphase Systems," *International Journal on Multiphase Flow*, 3, 1977, pp. 333-40, with permission from Elsevier.)

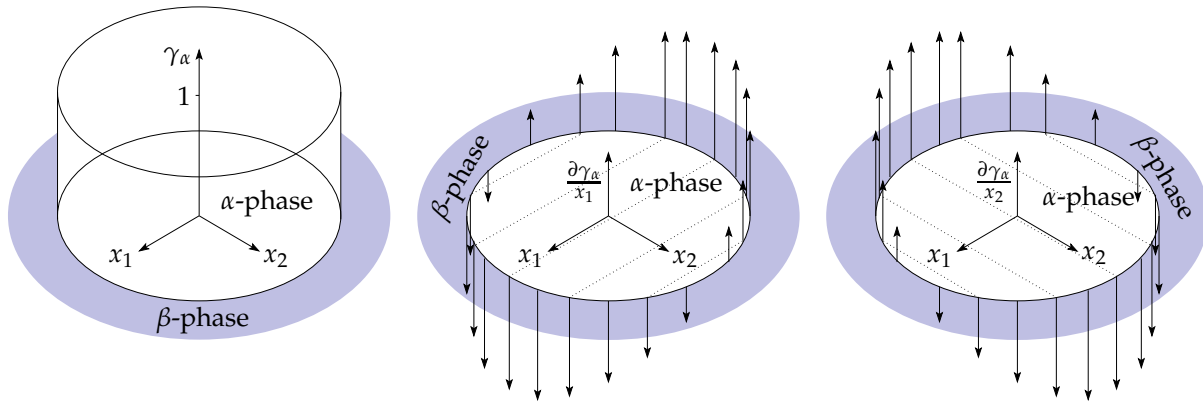


Figure 4.6: Two-dimensional example of a two-phase volume.

(Adapted from Fig. 2 in Gray, W.G., and Lee, P.C.Y., "On the Theorems for Local Volume Averaging of Multiphase Systems," *International Journal on Multiphase Flow*, 3, 1977, pp. 333–40, with permission from Elsevier.)

We generalize to three dimensions by defining the gradient operator over some scalar field $\psi(x, y, z, t)$ as

$$\nabla \psi(x, y, z, t) \triangleq \frac{\partial \psi}{\partial x} \hat{\mathbf{i}} + \frac{\partial \psi}{\partial y} \hat{\mathbf{j}} + \frac{\partial \psi}{\partial z} \hat{\mathbf{k}}.$$

Then, $\nabla \gamma_\alpha(\mathbf{x}, t) = -\hat{\mathbf{n}}_\alpha \delta(\mathbf{x} - \mathbf{x}_{\alpha\beta}, t)$.

4.2.5 Definitions for averaging

When applying averaging techniques to obtain continuum equations for porous media, it is necessary to select an averaging volume that will result in meaningful averages. This can be met when the characteristic length of the averaging volume is much greater than the dimension of the pore openings (between particles) in the medium, but much less than the characteristic length of the medium. In addition, the shape, size, and orientation of the averaging volume should be independent of space and time.

We define a local coordinate system ξ_1, ξ_2, ξ_3 , which has axes parallel with the x_1, x_2, x_3 system, but whose origin is located at position \mathbf{x} . The x_1, x_2, x_3 coordinate system is the fixed reference frame of the electrode under consideration. The vector \mathbf{x} determines the location of the averaging volume under consideration. The local coordinate system moves its origin with \mathbf{x} , and ξ_1, ξ_2 , and ξ_3 denote a position within that averaging volume. This is depicted in Fig. 4.7.

This double coordinate system representation allows us to define points inside the averaging volume with respect to the ξ coordinate system independently of \mathbf{x} . For example, we may set the centroid of the averaging volume to the origin of the ξ system.

With this in mind, we define two different kinds of volume averages. The *phase average* $\langle \theta_\alpha \rangle$ of a property θ over phase α is defined as

$$\langle \theta_\alpha(\mathbf{x}, t) \rangle = \frac{1}{V} \iiint_V \theta(\mathbf{x} + \xi, t) \gamma_\alpha(\mathbf{x} + \xi, t) dV_\xi,$$

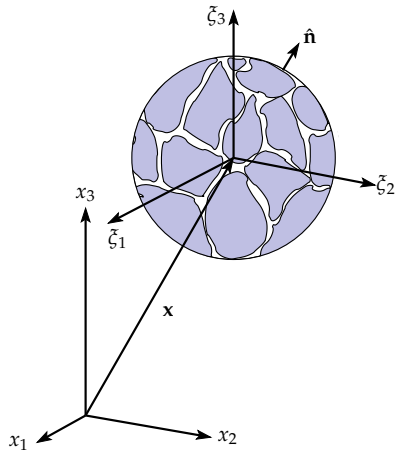


Figure 4.7: Coordinate system for volume-averaging theorems.

(Adapted from Fig. 3 in Gray, W.G., and Lee, P.C.Y., "On the Theorems for Local Volume Averaging of Multiphase Systems," *International Journal on Multiphase Flow*, 3, 1977, pp. 333–40, with permission from Elsevier.)

where volume $V = V_\alpha + V_\beta$ is independent of space and time. However, V_α and V_β themselves will depend on \mathbf{x} and will also depend on t if the medium is deformable (i.e., the phase boundary moves).

Physically, the phase average is a property of only the α phase averaged over the entire volume occupied by both the α and β phases in the averaging volume. Note that we could also write this integral as

$$\langle \theta_\alpha(\mathbf{x}, t) \rangle = \frac{1}{V} \iiint_{V_\alpha(\mathbf{x}, t)} \theta(\mathbf{x} + \boldsymbol{\xi}, t) dV_\xi,$$

but this is less useful because the limits of integration depend on spatial location and on time if the medium deforms.

The *intrinsic phase average* $\bar{\theta}_\alpha$ of some property θ with respect to phase α is given by

$$\bar{\theta}_\alpha(\mathbf{x}, t) = \frac{1}{V_\alpha(\mathbf{x}, t)} \iiint_{V_\alpha(\mathbf{x}, t)} \theta(\mathbf{x} + \boldsymbol{\xi}, t) dV_\xi.$$

This type of average describes a property of the α phase averaged over the volume occupied by that phase only. Comparing the two types of phase average, we see

$$\langle \theta_\alpha(\mathbf{x}, t) \rangle = \varepsilon_\alpha(\mathbf{x}, t) \bar{\theta}_\alpha(\mathbf{x}, t), \quad \text{or} \quad \bar{\theta}_\alpha(\mathbf{x}, t) = \frac{1}{\varepsilon_\alpha(\mathbf{x}, t)} \langle \theta_\alpha(\mathbf{x}, t) \rangle, \quad (4.10)$$

where the *volume fraction* of the α -phase in the medium is defined as

$$\varepsilon_\alpha(\mathbf{x}, t) = \frac{V_\alpha(\mathbf{x}, t)}{V} = \frac{1}{V} \iiint_V \gamma_\alpha(\mathbf{x} + \boldsymbol{\xi}, t) dV_\xi.$$

As an example to illustrate the difference between the phase average $\langle \theta_\alpha \rangle$ and the intrinsic phase average $\bar{\theta}_\alpha$, consider a beaker filled with rocks, where the porosity $\varepsilon_s = 0.5$. We have a second beaker filled with electrolyte solution where the salt concentration is $1,000 \text{ mol m}^{-3}$. We pour the solution into the first beaker until it is full, so that $\varepsilon_e = 0.5$.

Taking a phase average of salt concentration in the porous media,

$$\begin{aligned} \langle c_e \rangle &= \frac{1}{V} \iiint_{V_e} c_e(\mathbf{x} + \boldsymbol{\xi}, t) dV_\xi \\ &= c_e \frac{V_e}{V} = 0.5c_e = 500 \text{ mol m}^{-3}. \end{aligned}$$

Taking an intrinsic phase average of the salt concentration instead,

$$\begin{aligned} \bar{c}_e &= \frac{1}{V_e} \iiint_{V_e} c_e(\mathbf{x} + \boldsymbol{\xi}, t) dV_\xi \\ &= c_e \frac{V_e}{V_e} = c_e = 1,000 \text{ mol m}^{-3}. \end{aligned}$$

The phase average tells us, from the perspective of the entire volume, what is the concentration of salt in the volume (i.e., the total

number of moles of salt divided by the total volume). The intrinsic phase average tells us, from the perspective of the solution itself within the volume, what is the concentration of salt in the solution (i.e., the total number of moles of salt divided by the volume of the solution).

The intrinsic phase average is more readily related to the microscale models where physical measurements are made, so it is the one we will use. But, we will derive our equations in terms of the phase average first (because this is easier to do) and convert to intrinsic phase averages when finished.

4.2.6 Two equivalent forms of gradient operator

Because we have defined two coordinate systems, there will be an opportunity to take gradients of quantities with respect to either one or the other. Define ∇_x to refer to the gradient taken with respect to the x coordinates, holding ξ_1 , ξ_2 , and ξ_3 constant; define ∇_ξ to refer to the gradient taken with respect to the ξ coordinates, holding x_1 , x_2 , and x_3 constant; and define ∇ to refer either to ∇_x or ∇_ξ .

A result that we will need is this: if a function is symmetrically dependent on x and ξ (i.e., it depends on the sum $x + \xi$ rather than on x and ξ individually or in some other combination), the gradient in the x coordinate system is equal to the gradient in the ξ coordinate system:

$$\nabla_x \theta(x + \xi, t) = \nabla_\xi \theta(x + \xi, t) = \nabla \theta(x + \xi, t) \quad (4.11)$$

$$\nabla_x \gamma_\alpha(x + \xi, t) = \nabla_\xi \gamma_\alpha(x + \xi, t) = \nabla \gamma_\alpha(x + \xi, t). \quad (4.12)$$

To prove this result, first consider the gradient with respect to the x coordinate system

$$\begin{aligned} \nabla_x \theta(x + \xi, t) &= \nabla_x \theta(x_1 + \xi_1, x_2 + \xi_2, x_3 + \xi_3, t) \\ &= \frac{\partial \theta(x_1 + \xi_1, x_2 + \xi_2, x_3 + \xi_3, t)}{\partial x_1} \hat{\mathbf{i}} \\ &\quad + \frac{\partial \theta(x_1 + \xi_1, x_2 + \xi_2, x_3 + \xi_3, t)}{\partial x_2} \hat{\mathbf{j}} \\ &\quad + \frac{\partial \theta(x_1 + \xi_1, x_2 + \xi_2, x_3 + \xi_3, t)}{\partial x_3} \hat{\mathbf{k}}. \end{aligned}$$

We invoke the chain rule of calculus to introduce partials with respect to the symmetric dependencies $(x_1 + \xi_1)$, $(x_2 + \xi_2)$, and $(x_3 + \xi_3)$.

$$\nabla_x \theta(x + \xi, t) = \frac{\partial \theta(x_1 + \xi_1, x_2 + \xi_2, x_3 + \xi_3, t)}{\partial(x_1 + \xi_1)} \underbrace{\frac{\partial(x_1 + \xi_1)}{\partial x_1}}_1 \hat{\mathbf{i}}$$

$$\begin{aligned}
& + \frac{\partial\theta(x_1 + \xi_1, x_2 + \xi_2, x_3 + \xi_3, t)}{\partial(x_2 + \xi_2)} \underbrace{\frac{\partial(x_2 + \xi_2)}{\partial x_2}}_1 \hat{\mathbf{j}} \\
& + \frac{\partial\theta(x_1 + \xi_1, x_2 + \xi_2, x_3 + \xi_3, t)}{\partial(x_3 + \xi_3)} \underbrace{\frac{\partial(x_3 + \xi_3)}{\partial x_3}}_1 \hat{\mathbf{k}}.
\end{aligned}$$

This simplifies to

$$\begin{aligned}
\nabla_{\mathbf{x}}\theta(\mathbf{x} + \xi, t) &= \frac{\partial\theta(x_1 + \xi_1, x_2 + \xi_2, x_3 + \xi_3, t)}{\partial(x_1 + \xi_1)} \hat{\mathbf{i}} \\
& + \frac{\partial\theta(x_1 + \xi_1, x_2 + \xi_2, x_3 + \xi_3, t)}{\partial(x_2 + \xi_2)} \hat{\mathbf{j}} \\
& + \frac{\partial\theta(x_1 + \xi_1, x_2 + \xi_2, x_3 + \xi_3, t)}{\partial(x_3 + \xi_3)} \hat{\mathbf{k}}.
\end{aligned}$$

We then repeat the procedure, starting with the gradient with respect to the ξ coordinate system. Again, we first take the gradient with respect to ξ

$$\begin{aligned}
\nabla_{\xi}\theta(\mathbf{x} + \xi, t) &= \nabla_{\xi}\theta(x_1 + \xi_1, x_2 + \xi_2, x_3 + \xi_3, t) \\
&= \frac{\partial\theta(x_1 + \xi_1, x_2 + \xi_2, x_3 + \xi_3, t)}{\partial\xi_1} \hat{\mathbf{i}} \\
& + \frac{\partial\theta(x_1 + \xi_1, x_2 + \xi_2, x_3 + \xi_3, t)}{\partial\xi_2} \hat{\mathbf{j}} \\
& + \frac{\partial\theta(x_1 + \xi_1, x_2 + \xi_2, x_3 + \xi_3, t)}{\partial\xi_3} \hat{\mathbf{k}}.
\end{aligned}$$

We expand this as

$$\begin{aligned}
\nabla_{\xi}\theta(\mathbf{x} + \xi, t) &= \frac{\partial\theta(x_1 + \xi_1, x_2 + \xi_2, x_3 + \xi_3, t)}{\partial(x_1 + \xi_1)} \underbrace{\frac{\partial(x_1 + \xi_1)}{\partial\xi_1}}_1 \hat{\mathbf{i}} \\
& + \frac{\partial\theta(x_1 + \xi_1, x_2 + \xi_2, x_3 + \xi_3, t)}{\partial(x_2 + \xi_2)} \underbrace{\frac{\partial(x_2 + \xi_2)}{\partial\xi_2}}_1 \hat{\mathbf{j}} \\
& + \frac{\partial\theta(x_1 + \xi_1, x_2 + \xi_2, x_3 + \xi_3, t)}{\partial(x_3 + \xi_3)} \underbrace{\frac{\partial(x_3 + \xi_3)}{\partial\xi_3}}_1 \hat{\mathbf{k}}.
\end{aligned}$$

Finally, this simplifies to

$$\begin{aligned}
\nabla_{\xi}\theta(\mathbf{x} + \xi, t) &= \frac{\partial\theta(x_1 + \xi_1, x_2 + \xi_2, x_3 + \xi_3, t)}{\partial(x_1 + \xi_1)} \hat{\mathbf{i}} \\
& + \frac{\partial\theta(x_1 + \xi_1, x_2 + \xi_2, x_3 + \xi_3, t)}{\partial(x_2 + \xi_2)} \hat{\mathbf{j}} \\
& + \frac{\partial\theta(x_1 + \xi_1, x_2 + \xi_2, x_3 + \xi_3, t)}{\partial(x_3 + \xi_3)} \hat{\mathbf{k}}.
\end{aligned}$$

By comparing the final forms for $\nabla_x \theta(\mathbf{x} + \boldsymbol{\xi})$ and $\nabla_{\boldsymbol{\xi}} \theta(\mathbf{x} + \boldsymbol{\xi})$, we see that the two are equal. By the same argument, $\nabla_x \gamma_{\alpha}(\mathbf{x} + \boldsymbol{\xi}) = \nabla_{\boldsymbol{\xi}} \gamma_{\alpha}(\mathbf{x} + \boldsymbol{\xi})$ and $\nabla_x \cdot \boldsymbol{\psi}(\mathbf{x} + \boldsymbol{\xi}, t) = \nabla_{\boldsymbol{\xi}} \cdot \boldsymbol{\psi}(\mathbf{x} + \boldsymbol{\xi}, t) = \nabla \cdot \boldsymbol{\psi}(\mathbf{x} + \boldsymbol{\xi}, t)$.

4.3 Volume-averaging theorem 1

We are now ready to prove the three volume-averaging theorems. We begin by deriving Eq. (4.1), which states that for scalar field ψ , if ψ is continuous in the α phase,

$$\varepsilon_{\alpha} \overline{\nabla \psi_{\alpha}} = \nabla (\varepsilon_{\alpha} \bar{\psi}_{\alpha}) + \frac{1}{V} \iint_{A_{\alpha\beta}(\mathbf{x}, t)} \psi_{\alpha} \hat{\mathbf{n}}_{\alpha} dA.$$

We start with the definition of phase average of some general quantity θ

$$\langle \theta_{\alpha}(\mathbf{x}, t) \rangle = \frac{1}{V} \iiint_V \theta(\mathbf{x} + \boldsymbol{\xi}, t) \gamma_{\alpha}(\mathbf{x} + \boldsymbol{\xi}, t) dV_{\boldsymbol{\xi}}.$$

Then, the phase average of the gradient must be, by direct substitution of $\theta_{\alpha} = \nabla \psi_{\alpha}$,

$$\langle \nabla \psi_{\alpha}(\mathbf{x}, t) \rangle = \frac{1}{V} \iiint_V [\nabla \psi(\mathbf{x} + \boldsymbol{\xi}, t)] \gamma_{\alpha}(\mathbf{x} + \boldsymbol{\xi}, t) dV_{\boldsymbol{\xi}}.$$

Recall the product rule from calculus: $\nabla(AB) = (\nabla A)B + A(\nabla B)$, and let $A = \psi(\mathbf{x} + \boldsymbol{\xi}, t)$ and $B = \gamma_{\alpha}(\mathbf{x} + \boldsymbol{\xi}, t)$. Noticing that the integrand is of the form $(\nabla A)B$, we can then write

$$\begin{aligned} \langle \nabla \psi_{\alpha}(\mathbf{x}, t) \rangle &= \frac{1}{V} \iiint_V \nabla [\psi(\mathbf{x} + \boldsymbol{\xi}, t) \gamma_{\alpha}(\mathbf{x} + \boldsymbol{\xi}, t)] dV_{\boldsymbol{\xi}} \\ &\quad - \frac{1}{V} \iiint_V \psi(\mathbf{x} + \boldsymbol{\xi}, t) [\nabla \gamma_{\alpha}(\mathbf{x} + \boldsymbol{\xi}, t)] dV_{\boldsymbol{\xi}}. \end{aligned}$$

Substituting the known gradient of the indicator function $\nabla \gamma_{\alpha}(\mathbf{x}, t) = -\hat{\mathbf{n}}_{\alpha} \delta(\mathbf{x} - \mathbf{x}_{\alpha\beta}, t)$ gives

$$\begin{aligned} \langle \nabla \psi_{\alpha}(\mathbf{x}, t) \rangle &= \frac{1}{V} \iiint_V \nabla [\psi(\mathbf{x} + \boldsymbol{\xi}, t) \gamma_{\alpha}(\mathbf{x} + \boldsymbol{\xi}, t)] dV_{\boldsymbol{\xi}} \\ &\quad + \frac{1}{V} \iiint_V \psi(\mathbf{x} + \boldsymbol{\xi}, t) \hat{\mathbf{n}}_{\alpha} \delta(\mathbf{x} + \boldsymbol{\xi} - \mathbf{x}_{\alpha\beta}, t) dV_{\boldsymbol{\xi}}. \end{aligned}$$

The second integral involves the Dirac delta function, which is zero everywhere except at the α - β phase interface. By the sifting property of the Dirac delta function, this volume integral drops to a surface integral over the α - β phase interface

$$\frac{1}{V} \iiint_V \psi(\mathbf{x} + \boldsymbol{\xi}, t) \hat{\mathbf{n}}_{\alpha} \delta(\mathbf{x} + \boldsymbol{\xi} - \mathbf{x}_{\alpha\beta}, t) dV_{\boldsymbol{\xi}} = \frac{1}{V} \iint_{A_{\alpha\beta}(\mathbf{x}, t)} \psi_{\alpha}(\mathbf{x} + \boldsymbol{\xi}, t) \hat{\mathbf{n}}_{\alpha} dA,$$

and we get

$$\begin{aligned}\langle \nabla \psi_\alpha(\mathbf{x}, t) \rangle &= \frac{1}{V} \iiint_V \nabla[\psi(\mathbf{x} + \boldsymbol{\xi}, t) \gamma_\alpha(\mathbf{x} + \boldsymbol{\xi}, t)] dV_{\boldsymbol{\xi}} \\ &+ \frac{1}{V} \iint_{A_{\alpha\beta}(\mathbf{x}, t)} \psi_\alpha(\mathbf{x} + \boldsymbol{\xi}, t) \hat{\mathbf{n}}_\alpha dA.\end{aligned}$$

By Eqs. (4.11) and (4.12), we know that we are free to consider the gradient operator as either $\nabla = \nabla_x$ or $\nabla = \nabla_{\boldsymbol{\xi}}$. We choose to use $\nabla = \nabla_x$ in the first integral on the right-hand side of this equation, so that the gradient operator may be removed from the integral: we can do so because the volume of integration has been specified to be independent of \mathbf{x} . Thus, we obtain

$$\begin{aligned}\langle \nabla \psi_\alpha \rangle &= \nabla \left[\frac{1}{V} \iiint_V \psi(\mathbf{x} + \boldsymbol{\xi}, t) \gamma_\alpha(\mathbf{x} + \boldsymbol{\xi}, t) dV_{\boldsymbol{\xi}} \right] \\ &+ \frac{1}{V} \iint_{A_{\alpha\beta}(\mathbf{x}, t)} \psi_\alpha(\mathbf{x} + \boldsymbol{\xi}, t) \hat{\mathbf{n}}_\alpha dA \\ \langle \nabla \psi_\alpha \rangle &= \nabla \langle \psi_\alpha \rangle + \frac{1}{V} \iint_{A_{\alpha\beta}(\mathbf{x}, t)} \psi_\alpha \hat{\mathbf{n}}_\alpha dA.\end{aligned}$$

In words, it says that the phase average of the gradient is equal to the gradient of the phase average plus a correction term. The correction term sums up vectors pointing outward from the α phase into the β phase at every location on the α - β interface, scaling the vectors by the size of the field ψ_α at that point. Overall, this correction term points in the direction of largest surface field.

By extension, using Eq. (4.10), we can find the intrinsic phase average

$$\begin{aligned}\overline{\nabla \psi_\alpha} &= \frac{1}{\varepsilon_\alpha} \langle \nabla \psi_\alpha \rangle \\ &= \frac{1}{\varepsilon_\alpha} \left[\nabla \langle \psi_\alpha \rangle + \frac{1}{V} \iint_{A_{\alpha\beta}(\mathbf{x}, t)} \psi_\alpha \hat{\mathbf{n}}_\alpha dA \right] \\ &= \frac{1}{\varepsilon_\alpha} \left[\nabla (\varepsilon_\alpha \bar{\psi}_\alpha) + \frac{1}{V} \iint_{A_{\alpha\beta}(\mathbf{x}, t)} \psi_\alpha \hat{\mathbf{n}}_\alpha dA \right].\end{aligned}$$

Rearranging this expression gives

$$\varepsilon_\alpha \overline{\nabla \psi_\alpha} = \nabla (\varepsilon_\alpha \bar{\psi}_\alpha) + \frac{1}{V} \iint_{A_{\alpha\beta}(\mathbf{x}, t)} \psi_\alpha \hat{\mathbf{n}}_\alpha dA,$$

which proves volume-averaging theorem 1, Eq. (4.1). Be careful to note that ε_α is *inside* the gradient operator on the right-hand side, which is important if ε_α is a function of \mathbf{x} .

4.4 Volume-averaging theorem 2

The second volume-averaging theorem, Eq. (4.2), is very similar to the first, but the average operates on the divergence of a vector field rather than on the gradient of a scalar field. Here, we wish to show that, for vector field ψ , if ψ is continuous in the α phase,

$$\varepsilon_\alpha \overline{\nabla \cdot \psi_\alpha} = \nabla \cdot (\varepsilon_\alpha \bar{\psi}_\alpha) + \frac{1}{V} \iint_{A_{\alpha\beta}(\mathbf{x}, t)} \psi_\alpha \cdot \hat{\mathbf{n}}_\alpha \, dA.$$

The steps in the proof parallel the steps in the derivation of the first volume-averaging theorem directly.

We start with the generic definition of phase average:

$$\langle \theta_\alpha(\mathbf{x}, t) \rangle = \frac{1}{V} \iiint_V \theta(\mathbf{x} + \boldsymbol{\xi}, t) \gamma_\alpha(\mathbf{x} + \boldsymbol{\xi}, t) \, dV_\xi.$$

Then, the phase average of the divergence operation must be (by substituting $\theta_\alpha = \nabla \cdot \psi_\alpha$)

$$\langle \nabla \cdot \psi_\alpha(\mathbf{x}, t) \rangle = \frac{1}{V} \iiint_V [\nabla \cdot \psi(\mathbf{x} + \boldsymbol{\xi}, t)] \gamma_\alpha(\mathbf{x} + \boldsymbol{\xi}, t) \, dV_\xi.$$

The divergence operator also satisfies a product rule $\nabla \cdot (\gamma \mathbf{F}) = (\nabla \gamma) \cdot \mathbf{F} + \gamma (\nabla \cdot \mathbf{F})$. Let $\mathbf{F} = \psi(\mathbf{x} + \boldsymbol{\xi}, t)$ and $\gamma = \gamma_\alpha(\mathbf{x} + \boldsymbol{\xi}, t)$. Noticing that the integrand is of the form $\gamma (\nabla \cdot \mathbf{F})$, we can write

$$\begin{aligned} \langle \nabla \cdot \psi_\alpha(\mathbf{x}, t) \rangle &= \frac{1}{V} \iiint_V \nabla \cdot [\psi(\mathbf{x} + \boldsymbol{\xi}, t) \gamma_\alpha(\mathbf{x} + \boldsymbol{\xi}, t)] \, dV_\xi \\ &\quad - \frac{1}{V} \iiint_V \psi(\mathbf{x} + \boldsymbol{\xi}, t) \cdot [\nabla \gamma_\alpha(\mathbf{x} + \boldsymbol{\xi}, t)] \, dV_\xi. \end{aligned}$$

Substituting the known gradient of the indicator function $\nabla \gamma_\alpha(\mathbf{x}, t) = -\hat{\mathbf{n}}_\alpha \delta(\mathbf{x} - \mathbf{x}_{\alpha\beta}, t)$ gives

$$\begin{aligned} \langle \nabla \cdot \psi_\alpha(\mathbf{x}, t) \rangle &= \frac{1}{V} \iiint_V \nabla \cdot [\psi(\mathbf{x} + \boldsymbol{\xi}, t) \gamma_\alpha(\mathbf{x} + \boldsymbol{\xi}, t)] \, dV_\xi \\ &\quad + \frac{1}{V} \iiint_V \psi(\mathbf{x} + \boldsymbol{\xi}, t) \cdot \hat{\mathbf{n}}_\alpha \delta(\mathbf{x} + \boldsymbol{\xi} - \mathbf{x}_{\alpha\beta}, t) \, dV_\xi. \end{aligned}$$

As before, the second volume integral drops to a surface integral over the α - β phase interface

$$\frac{1}{V} \iiint_V \psi(\mathbf{x} + \boldsymbol{\xi}, t) \cdot \hat{\mathbf{n}}_\alpha \delta(\mathbf{x} + \boldsymbol{\xi} - \mathbf{x}_{\alpha\beta}, t) \, dV_\xi = \frac{1}{V} \iint_{A_{\alpha\beta}(\mathbf{x}, t)} \psi_\alpha(\mathbf{x} + \boldsymbol{\xi}, t) \cdot \hat{\mathbf{n}}_\alpha \, dA,$$

and we get

$$\begin{aligned} \langle \nabla \cdot \psi_\alpha(\mathbf{x}, t) \rangle &= \frac{1}{V} \iiint_V \nabla \cdot [\psi(\mathbf{x} + \boldsymbol{\xi}, t) \gamma_\alpha(\mathbf{x} + \boldsymbol{\xi}, t)] \, dV_\xi \\ &\quad + \frac{1}{V} \iint_{A_{\alpha\beta}(\mathbf{x}, t)} \psi_\alpha(\mathbf{x} + \boldsymbol{\xi}, t) \cdot \hat{\mathbf{n}}_\alpha \, dA. \end{aligned}$$

By extension to Eqs. (4.11) and (4.12), we are free to consider the divergence operator as either $\nabla \cdot = \nabla_x \cdot$ or $\nabla = \nabla_\xi \cdot$. We choose to use $\nabla \cdot = \nabla_x \cdot$ on the equation's right-hand side so that the divergence operator may be removed from the integral because the volume of integration has been specified to be independent of \mathbf{x} . Thus, we obtain

$$\begin{aligned}\langle \nabla \cdot \boldsymbol{\psi}_\alpha \rangle &= \nabla \cdot \left[\frac{1}{V} \iiint_V \boldsymbol{\psi}(\mathbf{x} + \boldsymbol{\xi}, t) \gamma_\alpha(\mathbf{x} + \boldsymbol{\xi}, t) dV_\xi \right] \\ &\quad + \frac{1}{V} \iint_{A_{\alpha\beta}(\mathbf{x}, t)} \boldsymbol{\psi}_\alpha(\mathbf{x} + \boldsymbol{\xi}, t) \cdot \hat{\mathbf{n}}_\alpha dA \\ \langle \nabla \cdot \boldsymbol{\psi}_\alpha \rangle &= \nabla \cdot \langle \boldsymbol{\psi}_\alpha \rangle + \frac{1}{V} \iint_{A_{\alpha\beta}(\mathbf{x}, t)} \boldsymbol{\psi}_\alpha \cdot \hat{\mathbf{n}}_\alpha dA.\end{aligned}$$

In words, this says that the phase average of the divergence is equal to the divergence of the phase average plus a correction term. The correction term is the volume-averaged total flux out of the surface of the α phase into the β phase within the volume V . That is, the divergence, which represents the rate at which something is leaving the α phase within a volume, must consider not only the flux through the surface of V , but must also consider the flux from α to β within V , which is happening at the α - β phase boundary inside of V .

By extension, using Eq. (4.10), the intrinsic phase average is

$$\varepsilon_\alpha \overline{\nabla \cdot \boldsymbol{\psi}_\alpha} = \nabla \cdot (\varepsilon_\alpha \bar{\boldsymbol{\psi}}_\alpha) + \frac{1}{V} \iint_{A_{\alpha\beta}(\mathbf{x}, t)} \boldsymbol{\psi}_\alpha \cdot \hat{\mathbf{n}}_\alpha dA,$$

which proves volume-averaging theorem 2.

4.5 Volume-averaging theorem 3

The derivation of the third volume-averaging theorem, Eq. (4.3), proceeds in a similar way to the first two, up to a point. However, we will see that the correction term is handled differently and requires some careful thought.

Here, we wish to show that, for scalar field ψ , if ψ is continuous in the α phase,

$$\varepsilon_\alpha \overline{\left[\frac{\partial \psi_\alpha}{\partial t} \right]} = \frac{\partial (\varepsilon_\alpha \bar{\psi}_\alpha)}{\partial t} - \frac{1}{V} \iint_{A_{\alpha\beta}(\mathbf{x}, t)} \psi_\alpha \mathbf{v}_{\alpha\beta} \cdot \hat{\mathbf{n}}_\alpha dA,$$

where $\mathbf{v}_{\alpha\beta}$ is the velocity of displacement of the α - β interface.

We start with the definition of phase average

$$\langle \theta_\alpha(\mathbf{x}, t) \rangle = \frac{1}{V} \iiint_V \theta(\mathbf{x} + \boldsymbol{\xi}, t) \gamma_\alpha(\mathbf{x} + \boldsymbol{\xi}, t) dV_\xi.$$

Then, we substitute the time derivative that we would like to average into the definition ($\theta_\alpha = \partial\psi_\alpha/\partial t$):

$$\left\langle \frac{\partial\psi_\alpha}{\partial t} \right\rangle = \frac{1}{V} \iiint_V [\partial\psi_\alpha(\mathbf{x} + \boldsymbol{\xi}, t)/\partial t] \gamma_\alpha(\mathbf{x} + \boldsymbol{\xi}, t) dV_\xi.$$

Recall the product rule from calculus: $\partial(AB)/\partial t = (\partial A/\partial t)B + A(\partial B/\partial t)$, and let $A = \psi_\alpha(\mathbf{x} + \boldsymbol{\xi}, t)$ and $B = \gamma_\alpha(\mathbf{x} + \boldsymbol{\xi}, t)$. Noticing that the integrand is of the form $(\partial A/\partial t)B$, we can write

$$\begin{aligned} \left\langle \frac{\partial\psi_\alpha}{\partial t} \right\rangle &= \frac{1}{V} \iiint_V \partial[\psi_\alpha(\mathbf{x} + \boldsymbol{\xi}, t) \gamma_\alpha(\mathbf{x} + \boldsymbol{\xi}, t)]/\partial t dV_\xi \\ &\quad - \frac{1}{V} \iiint_V \psi_\alpha(\mathbf{x} + \boldsymbol{\xi}, t) [\partial\gamma_\alpha(\mathbf{x} + \boldsymbol{\xi}, t)/\partial t] dV_\xi. \end{aligned}$$

Because V is independent of time, the order of differentiation or integration in the first term may be reversed, and we obtain

$$\left\langle \frac{\partial\psi_\alpha}{\partial t} \right\rangle = \frac{\partial \langle \psi_\alpha \rangle}{\partial t} - \frac{1}{V} \iiint_V \psi_\alpha(\mathbf{x} + \boldsymbol{\xi}, t) [\partial\gamma_\alpha(\mathbf{x} + \boldsymbol{\xi}, t)/\partial t] dV_\xi.$$

Now we consider the correction term—the remaining integral.

First note that if the α phase is *not* deforming, the partial derivative of the indicator function will be zero, and the integral term will be zero. This turns out to be the case we are most interested in.

However, for completeness, we also consider the more general case where the α phase *is* deforming. Then, γ_α will be a function of time, and the integral term will be nonzero in general.

We will use the chain rule of the total derivative of γ_α to write

$$\begin{aligned} \frac{d\gamma_\alpha}{dt} &= \frac{\partial\gamma_\alpha}{\partial t} + \frac{dx_1}{dt} \frac{\partial\gamma_\alpha}{\partial x_1} + \frac{dx_2}{dt} \frac{\partial\gamma_\alpha}{\partial x_2} + \frac{dx_3}{dt} \frac{\partial\gamma_\alpha}{\partial x_3} \\ &= \frac{\partial\gamma_\alpha}{\partial t} + \frac{d\mathbf{x}}{dt} \cdot \nabla\gamma_\alpha. \end{aligned} \tag{4.13}$$

In this equation, $\partial\gamma_\alpha/\partial t$ states how the indicator function is changing as a function of time only. The term $d\gamma_\alpha/dt$ instead states how an observer's measurement of the indicator function is changing as a function of all variables, including that observer's own velocity $d\mathbf{x}/dt$.

To understand this, first suppose that $\partial\gamma_\alpha/\partial t = 0$. This means that the γ_α function is not itself changing as a function of time. If we as an observer are located at some stationary (x_1, x_2, x_3) point within volume V , our velocity $d\mathbf{x}/dt$ is equal to zero, and we will look around and see that nothing is changing, so the (total) derivative will also be zero.

However, if we are moving around the function at some nonzero velocity $d\mathbf{x}/dt$, then we will experience a change in the value of γ_α that we measure, even when the function itself isn't changing, simply

because we are evaluating it at different points. Thus, $d\gamma_\alpha/dt \neq 0$ in general, even when $\partial\gamma_\alpha/\partial t = 0$. Further, we will get different values for $d\gamma_\alpha/dt$ when we move around the space at different velocities dx/dt .

Here, we choose to move our observation point at the same velocity as the α - β phase boundary movement: $dx/dt = \mathbf{v}_{\alpha\beta}$, so rearranging Eq. (4.13) to solve for the partial derivative gives

$$\frac{\partial\gamma_\alpha}{\partial t} = \frac{d\gamma_\alpha}{dt} - \mathbf{v}_{\alpha\beta} \cdot \nabla\gamma_\alpha.$$

For this choice of dx/dt , the total derivative becomes what is known as a *substantial derivative* that moves with the interface.

This velocity choice is a special case that simplifies the problem. As depicted in Fig. 4.8, an observer riding on (“surfing on”) the interfacial boundary and moving at the same velocity as the boundary movement will *notice* no change in γ_α versus time. It remains a step function that shifts with the moving boundary. The value of the function measured by the observer moving at velocity $\mathbf{v}_{\alpha\beta}$ doesn’t vary with time.

So, the total derivative is zero when $dx/dt = \mathbf{v}_{\alpha\beta}$, and we can write

$$\frac{\partial\gamma_\alpha}{\partial t} = -\mathbf{v}_{\alpha\beta} \cdot \nabla\gamma_\alpha.$$

This yields, when we substitute $d\gamma_\alpha/dt = -\mathbf{v}_{\alpha\beta} \cdot \nabla\gamma_\alpha$,

$$\begin{aligned} \left\langle \frac{\partial\psi_\alpha}{\partial t} \right\rangle &= \frac{\partial \langle \psi_\alpha \rangle}{\partial t} - \frac{1}{V} \iiint_V \psi_\alpha(\mathbf{x} + \boldsymbol{\xi}, t) [\partial\gamma_\alpha(\mathbf{x} + \boldsymbol{\xi}, t)/\partial t] dV_\xi \\ &= \frac{\partial \langle \psi_\alpha \rangle}{\partial t} + \frac{1}{V} \iiint_V \psi_\alpha(\mathbf{x} + \boldsymbol{\xi}, t) \mathbf{v}_{\alpha\beta}(\mathbf{x} + \boldsymbol{\xi}, t) \cdot \nabla\gamma_\alpha(\mathbf{x} + \boldsymbol{\xi}, t) dV_\xi \\ &= \frac{\partial \langle \psi_\alpha \rangle}{\partial t} + \frac{1}{V} \iiint_V \psi_\alpha(\mathbf{x} + \boldsymbol{\xi}, t) \mathbf{v}_{\alpha\beta}(\mathbf{x} + \boldsymbol{\xi}, t) \cdot (-\hat{\mathbf{n}}_\alpha \delta(\mathbf{x} + \boldsymbol{\xi} - \mathbf{x}_{\alpha\beta})) dV_\xi \\ \left\langle \frac{\partial\psi_\alpha}{\partial t} \right\rangle &= \frac{\partial \langle \psi_\alpha \rangle}{\partial t} - \frac{1}{V} \iint_{A_{\alpha\beta}(\mathbf{x}, t)} \psi_\alpha \mathbf{v}_{\alpha\beta} \cdot \hat{\mathbf{n}}_\alpha dA. \end{aligned}$$

In words, the phase average of a time derivative is equal to the time derivative of the phase average plus a correction term. The correction term accounts for a net dilution of the field ψ_α if the volume is expanding (phase interface is moving in the same direction as $\hat{\mathbf{n}}_\alpha$) or a concentration of the field ψ_α if the volume is contracting (phase interface is moving in the opposite direction as $\hat{\mathbf{n}}_\alpha$).

By extension, using Eq. (4.10),

$$\varepsilon_\alpha \overline{\left[\frac{\partial\psi_\alpha}{\partial t} \right]} = \frac{\partial (\varepsilon_\alpha \bar{\psi}_\alpha)}{\partial t} - \frac{1}{V} \iint_{A_{\alpha\beta}(\mathbf{x}, t)} \psi_\alpha \mathbf{v}_{\alpha\beta} \cdot \hat{\mathbf{n}}_\alpha dA,$$

which proves volume-averaging theorem 3. Here we note that if $\mathbf{v}_{\alpha\beta} \neq 0$, then ε_α is time varying, and we must be very careful to keep it inside the time derivative on the right-hand side of the equation.

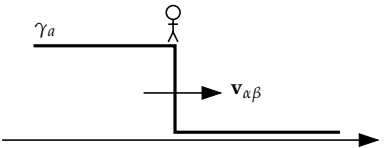


Figure 4.8: An observer “surfing on” the phase-boundary interface will *observe* no change in the indicator function as the observer is moving at the same rate that the indicator-function boundary is moving.

4.6 Charge conservation in the solid

With this rather long introduction, we are now ready to develop the volume-averaged continuum-scale lithium-ion cell model. This model can be used in three dimensions, but we will specialize to a one-dimensional description of cell dynamics, with an added “pseudo-dimension” that describes lithium concentration inside the solid. Accordingly, this model is often referred to as the *pseudo-two-dimensional model* in the literature.

Fig. 4.9 helps to illustrate this concept. The diagram shows, roughly to typical scale, the actual geometry of a lithium-ion cell cross section. Instead of using spatial x , y , and z coordinates, we will now specialize to an x coordinate only, where $x = 0$ at the negative-electrode current collector, and x takes on its maximum value at the positive-electrode current collector.

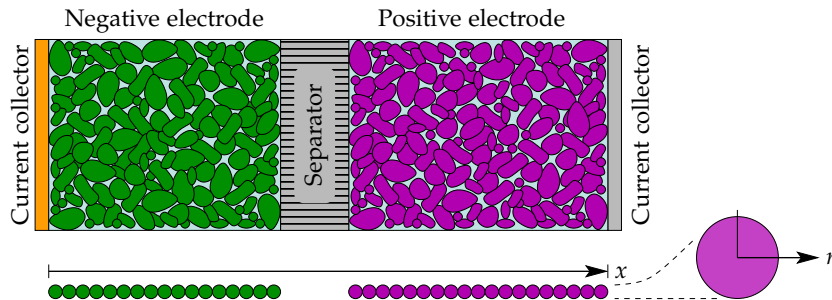


Figure 4.9: Schematic of a cell, from a continuum model perspective.
(Reproduced from Fig. 1 of Stetzel, K., Aldrich, L., Trimboli, M.S., and Plett, G., “Electrochemical State and Internal Variables Estimation using a Reduced-Order Physics-Based Model of a Lithium-Ion Cell and an Extended Kalman Filter,” *Journal of Power Sources*, 278, 2015, pp. 490–505.)

As we saw in the SEM and FIB images of electrodes in Figs. 1.8–1.10 of Chap. 1, true particle geometry is very complex. However, here we will simplify by assuming that all particles are perfect spheres, all having the same radius. This is an imperfect abstraction, but it helps us to make tractable models. In this abstraction, every x location corresponding to a point either in the negative- or positive-electrode is modeled as being the center of a spherical particle of radius R_s . The variable r such that $0 \leq r \leq R_s$ is the coordinate inside of this sphere and is referred to as the *pseudo-dimension* of the model.

Note that the figure shows a number of circular particles side by side in the negative-electrode region and another number of circular particles side-by-side in the positive-electrode region. This may mislead the reader into thinking that a discrete number of particles are being modeled. This is not the case; rather, there is assumed to be a particle for every real-valued x corresponding to a position in either the positive or negative electrode. The circular particles overlap infinitely in the model. This corresponds to the idea of continuum modeling, where every x location identifies a sample-volume

center, where the model predicts the average dynamics in the sample-volume-neighborhood of that x location, rather than the precise dynamics at that absolute location.

We now apply the volume-averaging theorems to develop continuum model equivalents of the five microscale model equations. We start with Eq. (3.1), the microscale model of charge conservation in the solid, which was

$$\nabla \cdot \mathbf{i}_s = \nabla \cdot (-\sigma \nabla \phi_s) = 0.$$

Using intrinsic averages and volume-averaging theorem 2 on the $\nabla \cdot (-\sigma \nabla \phi_s)$ term³

$$\varepsilon_s \overline{\nabla \cdot (-\sigma \nabla \phi_s)} = \nabla \cdot \left(\varepsilon_s \overline{(-\sigma \nabla \phi_s)} \right) + \frac{1}{V} \iint_{A_{se}} (-\sigma \nabla \phi_s) \cdot \hat{\mathbf{n}}_s \, dA.$$

But, $\nabla \cdot \mathbf{i}_s = 0$ so we must also have $\overline{\nabla \cdot \mathbf{i}_s} = 0$.

$$0 = \nabla \cdot \left(\varepsilon_s \overline{(-\sigma \nabla \phi_s)} \right) + \frac{1}{V} \iint_{A_{se}} (-\sigma \nabla \phi_s) \cdot \hat{\mathbf{n}}_s \, dA.$$

We look at the integral term first. Notice that the surface integral is over the boundary between the solid electrode particles and the electrolyte. The integrand, then, can be found from the boundary conditions on the ϕ_s equation that were developed in Chap. 3. Specifically, we found in Eq. (3.47) that

$$\hat{\mathbf{n}}_s \cdot \sigma \nabla \phi_s = -Fj.$$

We know that the Butler–Volmer flux density j is a function of c_s , c_e , ϕ_s , and ϕ_e at the particle surface. We will assume that our sample volume V is small enough that c_e , ϕ_s , and ϕ_e are relatively uniform and that c_s at the surface of particles in V is relatively uniform. This allows us to write

$$\frac{1}{V} \iint_{A_{se}} (-\sigma \nabla \phi_s) \cdot \hat{\mathbf{n}}_s \, dA \approx \frac{1}{V} \iint_{A_{se}} Fj(\bar{c}_{s,e}, \bar{c}_e, \bar{\phi}_s, \bar{\phi}_e) \, dA,$$

where $c_{s,e}$ is the *surface* concentration of lithium in the solid (i.e., at the solid–electrolyte interface; hence, the notation “ s, e ”). Because j is now using volume-averaged inputs, its value is constant over the sample volume, and we have

$$\begin{aligned} \frac{1}{V} \iint_{A_{se}} Fj(\bar{c}_{s,e}, \bar{c}_e, \bar{\phi}_s, \bar{\phi}_e) \, dA &= \frac{A_{se}}{V} Fj(\bar{c}_{s,e}, \bar{c}_e, \bar{\phi}_s, \bar{\phi}_e) \\ &= a_s Fj(\bar{c}_{s,e}, \bar{c}_e, \bar{\phi}_s, \bar{\phi}_e) \\ &= a_s F\bar{j}, \end{aligned}$$

where $\bar{j} = j(\bar{c}_{s,e}, \bar{c}_e, \bar{\phi}_s, \bar{\phi}_e)$, and we define a_s to be the *specific interfacial surface area* of the particles, equal to the total surface area of the solid

³Notice that we have chosen the α phase to correspond to the solid, denoted as “ s ,” and the β phase to correspond to everything else. “Everything else” includes electrolyte plus inert materials, but we denote β as “ e ” for “electrolyte” as it is the dominant contributor to phase β .

particles within the volume V divided by the volume of V . It has units of $\text{m}^2 \text{m}^{-3}$, which can be shortened to m^{-1} , but the reduced form loses the intuitive meaning of the variable.

For spherical particles with radius R_s and volume fraction ε_s , we can calculate a_s as

$$a_s = \frac{\text{total surface area}}{\text{total volume}} = \underbrace{\frac{\text{volume of solid}}{\text{total volume}}}_{\varepsilon_s} \frac{\text{total surface area/particle}}{\text{volume of solid/particle}}$$

$$= \varepsilon_s \frac{4\pi R_s^2}{\frac{4}{3}\pi R_s^3} = \frac{3\varepsilon_s}{R_s}.$$

So, we now have the result

$$0 = \nabla \cdot \left(\varepsilon_s \overline{(-\sigma \nabla \phi_s)} \right) + a_s F \vec{j}$$

$$\nabla \cdot \left(\varepsilon_s \overline{(-\sigma \nabla \phi_s)} \right) = -a_s F \vec{j}.$$

But, what to do with the $\overline{(-\sigma \nabla \phi_s)}$ term? We might consider using volume-averaging theorem 1, but note that we don't know what $\phi_s \hat{\mathbf{n}}$ is at the boundary, and so we are unable to evaluate the correction term in Eq. (4.1).

Instead, the common approach is to model $\varepsilon_s \overline{(-\sigma \nabla \phi_s)} \approx -\sigma_{\text{eff}} \nabla \bar{\phi}_s$. The *effective conductivity* σ_{eff} is modeled as $\sigma_{\text{eff}} = \frac{\varepsilon_s \sigma \delta}{\tau}$, where $\delta < 1$ is the *constrictivity* of the media and $\tau \geq 1$ is the *tortuosity* of the media. That is, σ is the bulk conductivity of homogeneous materials without inclusions and σ_{eff} is the *effective* conductivity of the solid matrix in the porous media.

Note that $\sigma_{\text{eff}} < \sigma$ since there are restrictions to flow of current. The constrictivity δ models the fact that the entire volume is not available for current to flow; instead, current must in some places flow through restricted paths due to the porosity of the media, with restriction being a factor of δ compared to the nonporous media. The tortuosity models the fact that the path from one side of the volume to the other is not direct, but must wind around a tortuous pathway with length greater than the dimension of the volume by a factor τ .

Values of δ and τ are rarely known precisely. Based on experimental results of a variety of porous media, it is frequently assumed that $\sigma_{\text{eff}} = \sigma \varepsilon_s^{\text{brug}}$, where "brug" is *Bruggeman's exponent*. This coefficient is normally assumed to take on the value of 1.5, although there is considerable evidence that this value can be quite inaccurate in real electrode materials. To get better values for "brug" we would either need to do microscale simulations with realistic particle geometries⁴ or create experiments to measure the value directly.

Collecting the above results, we now have the final continuum model of charge conservation in the solid,

$$\nabla \cdot (-\sigma_{\text{eff}} \nabla \bar{\phi}_s) = -a_s F \vec{j}.$$

⁴ See, for example, Gupta, A., Seo, J.H., Zhang, X., Du, W., Sastry, A.M., and Shyy, W., "Effective Transport Properties of LiMn_2O_4 Electrode via Particle-Scale Modeling," *Journal of the Electrochemical Society*, 158(5), 2011, pp. A487–A497.

Also note for future reference that

$$\begin{aligned}\varepsilon_s \bar{\mathbf{i}}_s &= \varepsilon_s (\overline{-\sigma \nabla \phi_s}) \\ &= -\sigma_{\text{eff}} \nabla \bar{\phi}_s.\end{aligned}\quad (4.14)$$

4.6.1 How well does the Bruggeman relationship work?

We now illustrate with an example how well an effective property in a volume-average equation can represent the effect of an intrinsic property in a microscale equation. We will use the PDE simulation software system COMSOL to help find results, and the example is adapted from the COMSOL documentation.

We're going to use a concentration model for this example, which corresponds closely to Eq. (4.7)—which we have yet to prove but will do so shortly—when there is no flux j between solid and electrolyte. The equation that models the microscale is Eq. (3.3), which when migration and convection terms are ignored becomes

$$\frac{\partial c}{\partial t} + \nabla \cdot (-D \nabla c) = 0.$$

The geometry that we consider is shown in Fig. 4.10. The rectangular objects are obstacles, which are similar in a sense to the solid particles in an electrode. The space between the rectangular objects is open, and material can flow through these voids. This space is similar in a sense to the pores in an electrode through which electrolyte can move.

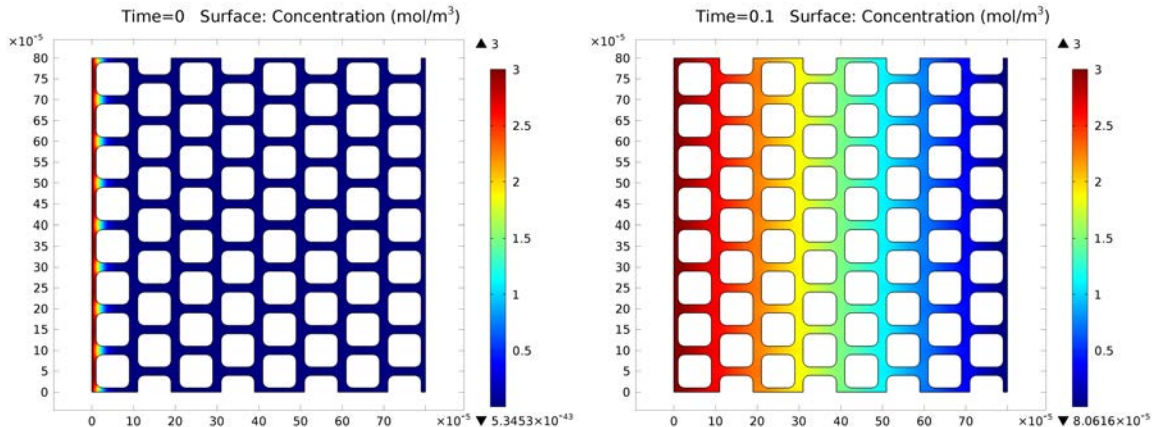


Figure 4.10: Microscale simulation of diffusion through a porous medium.

At the beginning of the simulation (left frame of figure), there is a high concentration of material at the left boundary of the porous lattice, but zero concentration of the material elsewhere. By time 0.1 s (right frame of figure), there is a uniform concentration gradient

established through the porous structure, as indicated by the colored shading.

We're interested in modeling the flux density of material out of the right edge of the structure. It is zero at time $t = 0$ and increases to some steady-state value over time. We can simulate the high-fidelity PDE model over the complex geometry, and we can also make a one-dimensional continuum model via

$$\varepsilon \frac{\partial \bar{c}}{\partial t} + \nabla \cdot (-D_{\text{eff}} \nabla \bar{c}) = 0,$$

where $D_{\text{eff}} = D_{\varepsilon^{\text{brug}}}$ (see Eq. (4.17) for the case where there is no reaction flux j).

Results are plotted in Fig. 4.11. The microscale solution is drawn as the solid blue line. Continuum-model solutions are drawn using dashed and dash-dot lines for $\text{brug} = 1.58$ and $\text{brug} = 1.60$, respectively. We see that with the correct choice of the Bruggeman constant, the continuum model gives predictions that are very close to the exact solution. The two models produce nearly indistinguishable results when $\text{brug} = 1.59$.

So, this example shows us that representing an effective property as a constant times the intrinsic property can produce very good results. However, the Bruggeman constant may need to be different from the commonly used value of 1.5 to achieve the best match.

4.7 Mass conservation in the solid

As mentioned earlier, the continuum-scale cell model has spatial dimension(s) *plus* a pseudo-dimension r . This pseudo-dimension is a coordinate used in the solid mass-conservation equation to specify a radial point inside a solid particle presumed to reside at some spatial location.

We could make a continuum model with three spatial dimensions plus an additional pseudo-dimension, resulting in a pseudo-four-dimensional model. The math we develop here is general enough to encompass this case, but in this book we ultimately specialize to a model with one spatial dimension plus the additional pseudo-dimension, resulting in a pseudo-two-dimensional model.

We assume that there is a particle centered at every spatial location in the electrode, that the particle is spherical, and that the concentration of lithium within the particle is spherically symmetric. So, to create the continuum equation for mass conservation within the solid, we don't need to use any volume-averaging theorems, because we are not volume averaging! Instead, we're specializing the microscale equation to these assumptions.

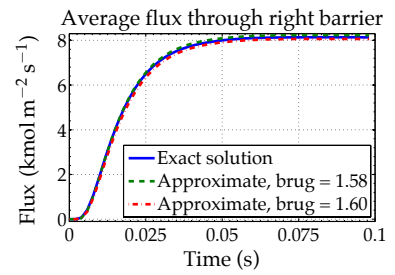


Figure 4.11: Flux-density comparison between microscale and continuum model.

Recall the microscale model, from Eq. (3.2)

$$\frac{\partial c_s}{\partial t} = \nabla \cdot (D_s \nabla c_s).$$

Also recall that the divergence of a vector field can be written in spherical coordinates as

$$\nabla \cdot \mathbf{F} = \frac{1}{r^2} \frac{\partial(r^2 F_r)}{\partial r} + \frac{1}{r \sin \theta} \frac{\partial(\sin \theta F_\theta)}{\partial \theta} + \frac{1}{r \sin \theta} \frac{\partial F_\phi}{\partial \phi}.$$

If we assume spherical particles, with symmetry in both the θ and ϕ axes, this reduces to

$$\nabla \cdot \mathbf{F} = \frac{1}{r^2} \frac{\partial(r^2 F_r)}{\partial r}.$$

Applying this to the right-hand side of the microscale model equation gives

$$\frac{\partial c_s}{\partial t} = \frac{1}{r^2} \frac{\partial}{\partial r} \left(D_s r^2 \frac{\partial c_s}{\partial r} \right).$$

We have now “proven” Eq. (4.5).

4.8 Mass conservation in the electrolyte

We next proceed to develop a continuum-scale equation for mass conservation in the electrolyte. We begin with the corresponding microscale Eq. (3.3)

$$\frac{\partial c_e}{\partial t} = \nabla \cdot (D_e \nabla c_e) - \frac{\mathbf{i}_e \cdot \nabla t_+^0}{F} - \nabla \cdot (c_e \mathbf{v}_0). \quad (4.15)$$

We will specialize immediately to consider the case where we assume that $\nabla t_+^0 = 0$ and $\mathbf{v}_0 = 0$, as is commonly done.⁵ We also assume that the phases do not deform, so $\mathbf{v}_{se} = 0$.

Taking the intrinsic volume average of the left-hand side of Eq. (4.15) using volume-averaging theorem 3 gives

$$\overline{\left[\frac{\partial c_e}{\partial t} \right]} = \frac{1}{\varepsilon_e} \left(\frac{\partial(\varepsilon_e \bar{c}_e)}{\partial t} \right).$$

Taking the intrinsic volume average of the right-hand side of Eq. (4.15) using volume-averaging theorem 2 gives

$$\overline{\nabla \cdot (D_e \nabla c_e)} = \frac{1}{\varepsilon_e} \left(\nabla \cdot (\varepsilon_e \overline{D_e \nabla c_e}) + \frac{1}{V} \iint_{A_{se}} D_e \nabla c_e \cdot \hat{\mathbf{n}}_e \, dA \right). \quad (4.16)$$

We first address the integral on the right-hand side of Eq. (4.16). Recall from the boundary conditions in Eq. (3.48) that $\hat{\mathbf{n}}_e \cdot (D_e \nabla c_e) =$

⁵ However, for high-rate operation, these terms should be considered. See Xue, K-H, and Plett, G.L., “A Convective Transport Theory for High Rate Discharge in Lithium Ion Batteries,” *Electrochimica Acta*, 87, 2013, pp. 575–590.

$(1 - t_+^0)j$. Using the same approach as with charge conservation in the solid, we assume uniform flux over the solid–electrolyte interface and write

$$\begin{aligned} \frac{1}{V} \iint_{A_{se}} D_e \nabla c_e \cdot \hat{\mathbf{n}}_e \, dA &= \frac{1}{V} \iint_{A_{se}} (1 - t_+^0)j(c_s, c_e, \phi_s, \phi_e) \, dA \\ &= \frac{A_{se}}{V} (1 - t_+^0) \bar{j} \\ &= a_s (1 - t_+^0) \bar{j}. \end{aligned}$$

Therefore, the intrinsic volume average of the right-hand side of Eq. (4.15) becomes

$$\overline{\nabla \cdot (D_e \nabla c_e)} = \frac{1}{\varepsilon_e} \left(\nabla \cdot (\varepsilon_e \overline{D_e \nabla c_e}) + a_s (1 - t_+^0) \bar{j} \right).$$

We now address the $\nabla \cdot (\varepsilon_e \overline{D_e \nabla c_e})$ term. Following the same kind of reasoning as before, we write this as

$$\nabla \cdot (\varepsilon_e \overline{D_e \nabla c_e}) \approx \nabla \cdot (D_{e,\text{eff}} \nabla \bar{c}_e),$$

where the effective diffusivity is defined as $D_{e,\text{eff}} = \varepsilon_e D_e \delta / \tau$, and we often assume $D_{e,\text{eff}} = D_e \varepsilon_e^{\text{brug}}$ where “brug” is frequently taken to be equal to 1.5.

So, combining all results,

$$\frac{1}{\varepsilon_e} \left(\frac{\partial(\varepsilon_e \bar{c}_e)}{\partial t} \right) = \frac{1}{\varepsilon_e} \left(\nabla \cdot (D_{e,\text{eff}} \nabla \bar{c}_e) + a_s (1 - t_+^0) \bar{j} \right).$$

Rewriting this gives our mass balance equation for the electrolyte,

$$\frac{\partial(\varepsilon_e \bar{c}_e)}{\partial t} = \nabla \cdot (D_{e,\text{eff}} \nabla \bar{c}_e) + a_s (1 - t_+^0) \bar{j}. \quad (4.17)$$

We have now proven Eq. (4.7). In words, this says that the local volume-average concentration of lithium in the electrolyte can increase due to a concentration gradient if material flows into the volume or if there is a local flux from the solid into the electrolyte in the volume.

4.8.1 Commenting on the $(1 - t_+^0)$ term

The $(1 - t_+^0)$ term in this result may seem a little odd. Why is only a fraction of the lithium flux from the solid to the electrolyte contributing to increasing the local lithium concentration in the electrolyte?

We briefly look at an intuitive explanation of what is happening. Consider a volume element having an interface between a solid particle and the electrolyte, such as is drawn in Fig. 4.12. Lithium flux density j is out of the particle, across the solid–electrolyte boundary, which denotes the particle’s surface.

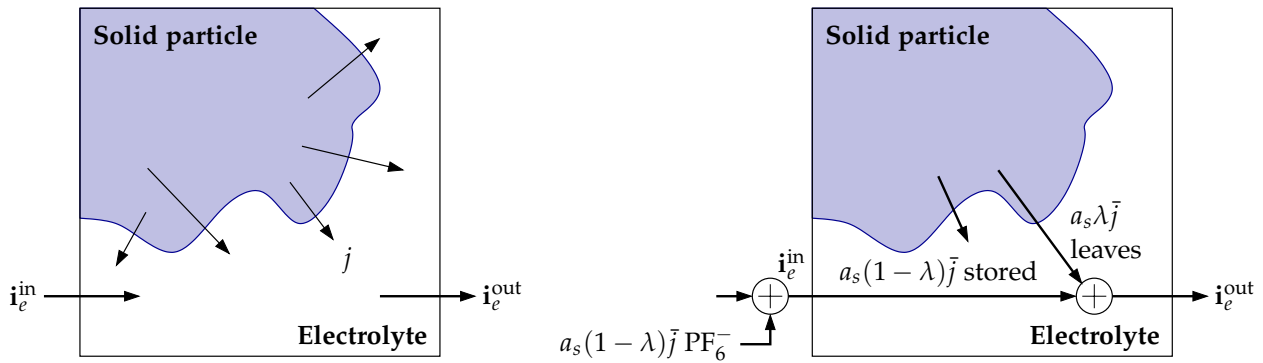


Figure 4.12: Explaining the $(1 - t_+^0)$ factor.

Per our earlier assumptions, the total volume-averaged lithium flux density from the solid to the electrolyte is

$$a_s \bar{j} = \frac{1}{V} \iint_{A_{se}} j(c_s, c_e, \phi_s, \phi_e) dA.$$

It turns out that not all of this total flux density remains in the volume element being considered (which would cause the concentration to increase by $a_s \bar{j}$). Some of the lithium escapes the local volume element into an adjacent volume element. But, neither does *all* of the flux escape the volume (which would keep c_e the same).

Let λ be the fraction of the flux density that escapes the local volume and $1 - \lambda$ be the fraction that remains. This is depicted in the right frame of the figure. To determine λ , we need to remember our assumption that the electrolyte must maintain macroscopic charge neutrality. This requires an anion flux density of $a_s(1 - \lambda)\bar{j}$ (e.g., of PF_6^- ions) into the local volume from a neighboring volume in order to balance the cation flux density of $a_s(1 - \lambda)\bar{j}$ positively charged lithium ions that is stored in the local volume.

The fraction of electrolyte current in the volume element that is added by the anion flux density required to maintain charge neutrality is $(1 - \lambda)$ times the added flux density; the fraction of the electrolyte current in the volume element that is added by the cation flux density that leaves the volume element is λ times the added flux density. Recognizing that the transference number t_+^0 is defined to be the fraction of current carried by the cation and that $t_-^0 = 1 - t_+^0$ is the fraction of the current carried by the anion, then we must have $\lambda = t_+^0$. Therefore, the amount of lithium that stays in the local volume and contributes to changing the local concentration is $a_s(1 - t_+^0)\bar{j}$.

4.9 Charge conservation in the electrolyte

The fourth continuum-scale model equation that we consider is the one describing charge conservation in the electrolyte. Recall the microscale Eq. (3.4)

$$\nabla \cdot \mathbf{i}_e = \nabla \cdot \left(-\kappa \nabla \phi_e - \frac{2\kappa RT}{F} \left(1 + \frac{\partial \ln f_{\pm}}{\partial \ln c_e} \right) \left(t_+^0 - 1 \right) \nabla \ln c_e \right) = 0.$$

For simplicity, we rewrite this as

$$\nabla \cdot \mathbf{i}_e = \nabla \cdot (-\kappa \nabla \phi_e - \kappa_D \nabla \ln c_e) = 0,$$

where we have defined

$$\kappa_D = \frac{2\kappa RT}{F} \left(1 + \frac{\partial \ln f_{\pm}}{\partial \ln c_e} \right) \left(t_+^0 - 1 \right).$$

Using volume-averaging theorem 2 on the left-hand side gives

$$\overline{\nabla \cdot \mathbf{i}_e} = \frac{1}{\varepsilon_e} \left(\nabla \cdot (\varepsilon_e \bar{\mathbf{i}}_e) + \frac{1}{V} \iint_{A_{se}} \mathbf{i}_e \cdot \hat{\mathbf{n}}_e \, dA \right).$$

We can compute the value of the integral by recalling from Eq. (3.49) that $\mathbf{i}_e \cdot \hat{\mathbf{n}}_e = -jF$ on the interface. Therefore, we approximate the integral by $-a_s F \bar{j}$.

$$\begin{aligned} \overline{\nabla \cdot \mathbf{i}_e} &= \frac{1}{\varepsilon_e} \left(\nabla \cdot (\varepsilon_e \bar{\mathbf{i}}_e) - a_s F \bar{j} \right) = 0 \\ 0 &= \nabla \cdot (\varepsilon_e \bar{\mathbf{i}}_e) - a_s F \bar{j}. \end{aligned}$$

Now, considering the right-hand side, note that

$$\varepsilon_e \bar{\mathbf{i}}_e = \varepsilon_e \left(\overline{-\kappa \nabla \phi_e} + \overline{-\kappa_D \nabla \ln c_e} \right).$$

As before, we approximate

$$\begin{aligned} -\varepsilon_e \overline{\kappa \nabla \phi_e} &\approx -\kappa_{\text{eff}} \nabla \bar{\phi}_e \\ -\varepsilon_e \overline{\kappa_D \nabla \ln c_e} &\approx -\kappa_{D,\text{eff}} \nabla \ln \bar{c}_e, \end{aligned}$$

where $\kappa_{\text{eff}} = \kappa \varepsilon_e^{\text{brug}}$ and $\kappa_{D,\text{eff}} = \kappa_D \varepsilon_e^{\text{brug}}$.

Combining, we get two results:

$$\varepsilon_e \bar{\mathbf{i}}_e = -\kappa_{\text{eff}} \nabla \bar{\phi}_e - \kappa_{D,\text{eff}} \nabla \ln \bar{c}_e, \quad (4.18)$$

and

$$\nabla \cdot (\kappa_{\text{eff}} \nabla \bar{\phi}_e + \kappa_{D,\text{eff}} \nabla \ln \bar{c}_e) + a_s \bar{j} F = 0.$$

We have now proven Eq. (4.7).

4.10 Lithium movement between the solid and electrolyte phases

Finally, we consider the continuum-scale equation of flux across the solid–electrolyte interface. We have already used this result, but for completeness we recall the Butler–Volmer equation

$$j = k_0 c_e^{1-\alpha} (c_{\max} - c_{s,e})^{1-\alpha} c_{s,e}^\alpha \left\{ \exp \left(\frac{(1-\alpha)F}{RT} \eta \right) - \exp \left(-\frac{\alpha F}{RT} \eta \right) \right\}. \quad (4.19)$$

This shows up in models as

$$\begin{aligned} \frac{1}{V} \iint_{A_{se}} j(c_s, c_e, \phi_s, \phi_e) dA &\approx \frac{A_{se}}{V} j(\bar{c}_{s,e}, \bar{c}_e, \bar{\phi}_s, \bar{\phi}_e) \\ &\approx a_s j(\bar{c}_{s,e}, \bar{c}_e, \bar{\phi}_s, \bar{\phi}_e) = a_s \bar{j}. \end{aligned}$$

If we choose to use normalized units for the exchange current density

$$\bar{i}_0 = \underbrace{F k_0 c_{e,0}^{1-\alpha} c_{s,\max}}_{k_{0,\text{norm}}} \left(\frac{\bar{c}_e}{c_{e,0}} \right)^{1-\alpha} \left(\frac{c_{s,\max} - \bar{c}_{s,e}}{c_{s,\max}} \right)^{1-\alpha} \left(\frac{\bar{c}_{s,e}}{c_{s,\max}} \right)^\alpha,$$

and

$$\bar{j} = \frac{\bar{i}_0}{F} \left\{ \exp \left(\frac{(1-\alpha)F}{RT} \bar{\eta} \right) - \exp \left(-\frac{\alpha F}{RT} \bar{\eta} \right) \right\},$$

where $\bar{\eta} = \bar{\phi}_s - \bar{\phi}_e - U_{\text{ocp}}(\bar{c}_{s,e})$. We note that in continuum models it is common to add a term to the overpotential to model the ionic resistance of a solid–electrolyte interphase film layer on the surface of the particle, and so we replace $\bar{\eta}$ with the calculation

$$\bar{\eta} = \bar{\phi}_s - \bar{\phi}_e - U_{\text{ocp}}(\bar{c}_{s,e}) - FR_{\text{film}} \bar{j}.$$

We have now derived Eq. (4.8).

4.11 Boundary conditions for pseudo 2D model

As with the partial-differential equations that we derived for the microscale, we must also specify boundary conditions for the continuum-scale PDEs. These boundary conditions are defined based on a physical understanding of movement of charge and mass at the boundaries of each region.

4.11.1 Charge conservation in the solid

At the current-collector–electrode boundary, charge is transferred between the current collector and the solid particles via electron movement; charge is not transferred between the current collector

and the electrolyte, since the electrolyte supports ionic currents only. Therefore, the electrical current through the solid at the current collector boundary must equal the total current entering/exiting the cell. That is,

$$\varepsilon_s \bar{\mathbf{i}}_s = -\sigma_{\text{eff}} \nabla \bar{\phi}_s = \frac{i_{\text{app}}}{A},$$

where i_{app} is the total cell applied current in amperes, and A is the current-collector plate area in m^2 .

By similar reasoning, at the electrode–separator boundary current is supported by movement of ions between the electrode region and the separator region. Electronic current is zero, and ionic current is equal to i_{app}/A .

Summarizing, for the positive electrode, we have

$$\frac{\partial \bar{\phi}_s}{\partial x} \Big|_{x=L^{\text{neg}}+L^{\text{sep}}} = 0, \quad \text{and} \quad \frac{\partial \bar{\phi}_s}{\partial x} \Big|_{x=L^{\text{tot}}} = \frac{-i_{\text{app}}}{A\sigma_{\text{eff}}},$$

and for the negative electrode we have

$$\frac{\partial \bar{\phi}_s}{\partial x} \Big|_{x=L^{\text{neg}}} = 0.$$

It is also true that in the negative electrode $\frac{\partial \bar{\phi}_s}{\partial x} \Big|_{x=0} = \frac{-i_{\text{app}}}{A\sigma_{\text{eff}}}$, but when all PDEs of the battery model are integrated together, this condition is redundant and is not implemented.

Since voltage is a potential difference, we must define a “ground reference” point against which to measure all internal cell voltages. We define

$$\bar{\phi}_s|_{x=0} = 0,$$

although other choices of reference voltage are possible.

4.11.2 Charge conservation in the electrolyte

At the electrode–separator boundaries, the ionic current must equal the total current entering/exiting the cell.

$$\varepsilon_e \bar{\mathbf{i}}_e = -\kappa_{\text{eff}} \nabla \bar{\phi}_e - \kappa_{D,\text{eff}} \nabla \ln \bar{c}_e = \frac{i_{\text{app}}}{A}.$$

And, the ionic current must be zero at the current collectors.

$$\kappa_{\text{eff}} \frac{\partial \bar{\phi}_e}{\partial x} + \kappa_{D,\text{eff}} \frac{\partial \ln \bar{c}_e}{\partial x} \Big|_{x=0} = \kappa_{\text{eff}} \frac{\partial \bar{\phi}_e}{\partial x} + \kappa_{D,\text{eff}} \frac{\partial \ln \bar{c}_e}{\partial x} \Big|_{x=L^{\text{tot}}} = 0.$$

As before, we have boundary conditions at the separator interfaces, but these are redundant and not implemented.

$$-\kappa_{\text{eff}} \frac{\partial \bar{\phi}_e}{\partial x} - \kappa_{D,\text{eff}} \frac{\partial \ln \bar{c}_e}{\partial x} \Big|_{x=L^{\text{neg}}} = -\kappa_{\text{eff}} \frac{\partial \bar{\phi}_e}{\partial x} - \kappa_{D,\text{eff}} \frac{\partial \ln \bar{c}_e}{\partial x} \Big|_{x=L^{\text{neg}}+L^{\text{sep}}} = \frac{i_{\text{app}}}{A}.$$

4.11.3 Mass conservation in the solid

At the particle surface, the flux of lithium out of the particle has been denoted by \bar{j} . Therefore, we must have

$$D_s \frac{\partial c_s}{\partial r} \Big|_{r=R_s} = -\bar{j}.$$

Because we have assumed radial symmetry in the lithium concentration in the particles, there can be no net flux through the particle center.⁶ This gives an internal “boundary” condition

$$\frac{\partial c_s}{\partial r} \Big|_{r=0} = 0.$$

⁶ Lithium flowing through the particle center would end up on the other side of the particle, but at the same radial location; hence, the net flux through the center would be zero.

4.11.4 Mass conservation in the electrolyte

There must be no flux of lithium through the electrolyte at the cell boundaries. This gives

$$\frac{\partial \bar{c}_e}{\partial x} \Big|_{x=0} = \frac{\partial \bar{c}_e}{\partial x} \Big|_{x=L^{\text{tot}}} = 0.$$

4.12 Cell-level quantities

As we did with the microscale model in Chap. 3, we would now like to extract several cell-level quantities from the continuum model developed in this chapter. These include: cell voltage, total capacity, and state of charge.

4.12.1 Cell voltage

The cell voltage is equal to the positive current-collector’s potential minus the negative current-collector’s potential. Since the solid phase is in direct electrical contact with the current collector, we then compute the cell voltage as

$$v(t) = \bar{\phi}_s(L^{\text{tot}}, t) - \bar{\phi}_s(0, t).$$

Because we have defined $\bar{\phi}_s(0, t) = 0$, we can further simplify to

$$v(t) = \bar{\phi}_s(L^{\text{tot}}, t).$$

4.12.2 Cell total capacity

Cell total capacity is determined in the same manner as in Chap. 3, using Eqs. (3.50), (3.51), and (3.52). For reference, we repeat the equations here:

$$Q^{\text{neg}} = AFL^{\text{neg}} \varepsilon_s^{\text{neg}} c_{s,\text{max}}^{\text{neg}} |x_{100\%} - x_{0\%}| / 3600 \text{ Ah},$$

$$Q^{\text{pos}} = AFL^{\text{pos}} \varepsilon_s^{\text{pos}} c_{s,\text{max}}^{\text{pos}} |y_{100\%} - y_{0\%}| / 3600 \text{ Ah},$$

and

$$Q = \min(Q^{\text{neg}}, Q^{\text{pos}}) \text{ Ah.}$$

4.12.3 Cell state of charge

Similarly, cell state of charge is determined in the same manner as in Chap. 3, using Eqs. (3.53), and (3.54). For convenient reference, we repeat the equations here:

$$\begin{aligned} z &= \frac{c_{s,\text{avg}}^{\text{neg}} / c_{s,\text{max}}^{\text{neg}} - x_{0\%}}{x_{100\%} - x_{0\%}} \\ &= \frac{c_{s,\text{avg}}^{\text{pos}} / c_{s,\text{max}}^{\text{pos}} - y_{0\%}}{y_{100\%} - y_{0\%}}. \end{aligned}$$

4.13 Model simulations

We are now at the point where we have derived the full set of continuum-scale model equations, which is great, but not especially useful unless we can do something with them. One very important application of the model is to use it in simulation to help understand how a cell works, and then use that to inform how a cell should be built and/or how a cell should be operated.

Digital simulation of continuous phenomena require discretizing the problem in time and space. There are three commonly used approaches to numeric solution:⁷

- *Finite difference*: Divide the spatial and temporal dimensions into small segments. Discretize the derivatives in the equations using Euler's rule or similar over these segments (some discretization methods work better than others: being more stable, resulting in less modeling error, etc.). Write the resulting system of equations, and solve using a linear algebra solver at each time step. The linear diffusion example in Sect. 3.3.3 introduced this method.
- *Finite volume*: Time is still divided up into small segments, but space is divided into volumes. Flux terms at volume boundaries are evaluated, and concentrations are updated to reflect the material fluxes. This method enforces mass balance: because the flux entering a given volume is identical to that leaving the adjacent volume, these methods are conservative. Another advantage of the finite volume method is that it is easily formulated to allow for unstructured meshes. The method is used in many computational fluid dynamics packages. The spherical diffusion example in Sect. 3.11.4 introduced this method.

⁷These methods are discussed in more detail, and applied to the battery-model simulation problem, in: Christopher D. Rahn and Chao-Yang Wang, *Battery Systems Engineering*, Wiley, 2013.

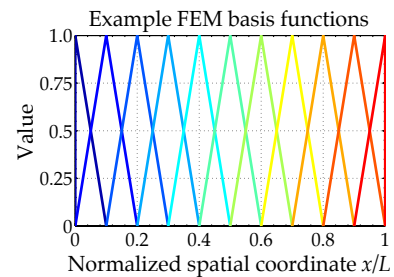


Figure 4.13: Example basis functions for the finite-element method.

- *Finite element*: Time is discretized as with the other two methods.

The spatial dimension, however, is formulated as a summation over N quadratic or linear basis or *finite-element* functions $\psi_m(x)$ for $1 \leq m \leq N$. One example is shown in Fig. 4.13, where each color represents a linear (triangular-shaped) basis function such that the summation of these $N = 11$ functions is equal to 1 at every x location. Then, the variable being studied is written as a weighted sum. For example, if we are interested in some variable $\theta(x, t)$, we write it as

$$\theta(x, t) = \sum_{m=1}^N \theta_m(t) \psi_m(x).$$

This simplifies the problem since the $\psi_m(x)$ are fixed—we convert a two-dimensional problem $\theta(x, t)$ into N one-dimensional problems $\theta_m(t)$, which are then evaluated by rewriting the PDEs in vector form for these one-dimensional variables, and solving. The shape and spacing of the elements can be varied to improve simulation accuracy in specific areas, as long as they always sum to 1.

Each method has advantages and disadvantages, and each has been used to simulate models of battery cells.⁸ Here, we introduce COMSOL, a commercial finite element multiphysics solver code, primarily because it is driven by a graphical user interface that makes it relatively straightforward to implement and modify model equations, allowing for very flexible exploration of battery dynamics (and many other applications as well).

We have implemented a “pseudo 2D” battery model in COMSOL and introduce it here. This model can be downloaded from the book web site, but will be useful only if you have a license to the COMSOL software.⁹ We describe this model in the following subsections.

4.13.1 Charge conservation in the solid

When entering a model into a PDE solver such as COMSOL for simulation, one must first specify the geometry of the object being simulated. The continuum model is primarily a one-dimensional construct where x represents the cross-sectional dimension of the cell. This dimension is itself divided into three regions: the negative-electrode, separator, and positive-electrode regions.

It would be most natural for us to specify geometries and to enter equations with physical lengths, so that the negative electrode spanned the range from $x = 0$ to $x = L^{\text{neg}}$, the separator spanned the range from $x = L^{\text{neg}}$ to $x = L^{\text{neg}} + L^{\text{sep}}$, and the positive electrode spanned the range from $x = L^{\text{neg}} + L^{\text{sep}}$ to $x = L^{\text{tot}}$. However, if we

⁸ V. Ramadesigan, P.W.C. Northrop, S. De, S. Santhanagopalan, R.D. Braatz, and V.R. Subramanian, “Modeling and Simulation of Lithium-Ion Batteries from a Systems Engineering Perspective,” *Journal of the Electrochemical Society*, 159(3), 2012, pp. R31–R45.

⁹ See <http://mocha-java.uccs.edu/BMS1/CH04/LiIon.mph>.

enter a model into COMSOL this way, we would have to “start from scratch” every time we wished to simulate a cell having different dimensions, as it is not possible to resize a geometry in COMSOL once it is defined.

So, instead of using natural lengths, we use normalized lengths. We will use symbol \bar{x} to represent position with respect to normalized length, and x to denote physical position. In the negative electrode we have $\bar{x} = x/L^{\text{neg}}$, in the separator we have $\bar{x} = (x - L^{\text{neg}})/L^{\text{sep}}$, and in the positive electrode we have $\bar{x} = (x - L^{\text{neg}} - L^{\text{sep}})/L^{\text{pos}}$. Generically, we see that $\bar{x}_{\text{region}} = x/L^{\text{region}} + \text{constant}$.

Using normalized variables, each region’s length is fixed at 1.0, regardless of the values of L^{neg} , L^{sep} , and L^{pos} . We can change the effective dimensions by changing the *variables* L^{neg} , L^{sep} , and L^{pos} without needing to change the COMSOL *geometries* of the different cell regions.

However, this requires that we modify the equations to use the normalized lengths rather than physical lengths. Starting with $\bar{x}_{\text{region}} = x/L^{\text{region}} + \text{constant}$, we have

$$\begin{aligned}\frac{\partial(\cdot)}{\partial\bar{x}} &= \frac{\partial(\cdot)}{\partial x} \frac{\partial x}{\partial\bar{x}} = L^{\text{region}} \frac{\partial(\cdot)}{\partial x} \\ \frac{\partial(\cdot)}{\partial x} &= \frac{\partial(\cdot)}{\partial\bar{x}} \frac{\partial\bar{x}}{\partial x} = \frac{1}{L^{\text{region}}} \frac{\partial(\cdot)}{\partial\bar{x}}.\end{aligned}$$

For the solid charge-conservation equation, we start with

$$\nabla_x \cdot (\sigma_{\text{eff}} \nabla_x \bar{\phi}_s) = a_s F \bar{j},$$

where the subscript x on the ∇ operators indicates the quantity with respect to which the derivative is being taken. Rewriting this equation in terms of \bar{x} instead of x gives

$$\frac{1}{L^{\text{region}}} \nabla_{\bar{x}} \cdot \left(\frac{\sigma_{\text{eff}}}{L^{\text{region}}} \nabla_{\bar{x}} \bar{\phi}_s \right) = a_s F \bar{j}.$$

Beyond the mechanical need to rescale equations to normalized geometries, there is an art to making PDE simulations work reliably. To solve the coupled nonlinear equations, a PDE solver uses nonlinear optimization at every time step to make the left-hand and right-hand sides of all equations match as closely as possible, within some tolerance. Coupling equations where some have very large values and others have very small values causes problems, as the PDE solver will tend to place more emphasis on making the large-valued equations match than on making the small-valued equations match (to reduce the total error).

Noting that a_s and F are rather large values, and L is a rather small value, we get better numeric performance if we instead implement

$$\nabla_{\bar{x}} \cdot \left(\frac{\sigma_{\text{eff}}}{L^{\text{region}}} \nabla_{\bar{x}} \bar{\phi}_s \right) = L^{\text{region}} a_s F \bar{j}.$$

In COMSOL, we input this equation into a predefined PDE form as

$$\nabla \cdot (\sigma_{\text{eff}}/L * \phi_{\text{sx}}) = L * a_s * F * j,$$

where the following variables are defined:

σ_{eff}	a_s	\bar{j}	L^{region}	$\bar{\phi}_s$	F
<code>sigma_eff</code>	<code>a_s</code>	<code>j</code>	<code>L</code>	<code>phi_s</code>	<code>F</code>

Note that in COMSOL syntax,

$$\phi_{\text{sx}} = \frac{d}{dx} \phi_s,$$

and recall that COMSOL's "x" is our normalized dimension " \bar{x} ".

4.13.2 Mass conservation in the solid

Mass conservation in the solid is described by the equation

$$\frac{\partial}{\partial t} c_s = \frac{1}{r^2} \frac{\partial}{\partial r} \left(D_s r^2 \frac{\partial c_s}{\partial r} \right),$$

which operates in the "pseudo" dimension, r , instead of the linear dimension, x . That is, at every " x " location, a copy of this radial equation operates, representing the radially symmetric concentration profile of lithium in a representative spherical particle located at that " x " location.

To implement this equation, we also normalize the radial dimension: let $\bar{r} = r/R_s$. Then, $r^2 = \bar{r}^2 R_s^2$ and $\frac{\partial(\cdot)}{\partial r} = \frac{1}{R_s} \frac{\partial(\cdot)}{\partial \bar{r}}$. This allows us to rewrite the PDE as

$$\frac{\partial}{\partial t} c_s = \left(\frac{1}{\bar{r}^2 R_s^2} \right) \frac{1}{R_s} \frac{\partial}{\partial \bar{r}} \left(D_s (\bar{r}^2 R_s^2) \frac{1}{R_s} \frac{\partial c_s}{\partial \bar{r}} \right).$$

We multiply both sides of the equation by $\bar{r}^2 R_s$ and rearrange to get the actual equation implemented in COMSOL:

$$\bar{r}^2 R_s \frac{\partial}{\partial t} c_s + \frac{\partial}{\partial \bar{r}} \left(-D_s \frac{\bar{r}^2}{R_s} \frac{\partial c_s}{\partial \bar{r}} \right) = 0,$$

except that COMSOL uses y instead of \bar{r} as the name of its radial coordinate.

When visualizing solid concentration, we are presented with an image like the one shown in Fig. 4.14. In this figure, the horizontal dimension is the cell " x " spatial dimension; the vertical dimension is the radial " r " pseudo-dimension (particle surface $r = R_s$ is at top; particle center $r = 0$ is at bottom); the left block represents the negative electrode and the right block represents the positive electrode. The color at any location indicates lithium concentration at

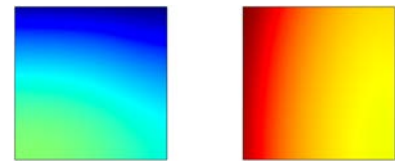


Figure 4.14: Visualizing solid concentration.

that spatial and radial coordinate: dark red is high concentration; dark blue is low concentration. In this example, we see a snapshot of the concentrations where the cell is at a low state-of-charge *immediately* following a long discharge (so the solid concentrations are not yet in equilibrium). Hence particle surface concentration in the negative electrode is low, while the particle interior concentrations in the negative electrode are still relatively high. And, for this simulation, the positive-electrode parameters were such that it was easier for the particles near the separator to “fill up” than it was for lithium to diffuse through the electrolyte to fill up other particles closer to the current collector.

Note that there is no diffusion of lithium in the solid in the horizontal x dimension. Lithium diffusion in the horizontal dimension happens only in the electrolyte. In the solid, lithium diffuses only in the “vertical” or radial dimension. This is represented in COMSOL by parameterizing a built-in PDE as

$$y^2 * R_s * \frac{\partial c_s}{\partial t} + \nabla \cdot \left(\begin{bmatrix} 0, & 0 \\ 0, & y^2 * D_s / R_s \end{bmatrix} * \nabla c_s \right) = 0,$$

where $\nabla = \left[\frac{\partial}{\partial x}, \frac{\partial}{\partial y} \right]$ and where the following variables are defined:

$$\begin{array}{c|c} R_s & D_s \\ \hline R_s & D_s \end{array}$$

4.13.3 Charge conservation in the electrolyte

To represent charge conservation in the electrolyte, we desire to implement

$$\nabla \cdot (\kappa_{\text{eff}} \nabla \bar{\phi}_e + \kappa_{D,\text{eff}} \nabla \ln \bar{c}_e) + a_s F \bar{j} = 0.$$

Once again, we use normalized lengths, which converts the equation to

$$\frac{1}{L^{\text{region}}} \nabla \cdot \left(\frac{\kappa_{\text{eff}}}{L^{\text{region}}} \nabla \bar{\phi}_e + \frac{\kappa_{D,\text{eff}}}{L^{\text{region}}} \nabla \ln \bar{c}_e \right) = -a_s F \bar{j}.$$

We implement $\nabla \ln \bar{c}_e$ as $\frac{1}{\bar{c}_e} \nabla \bar{c}_e$ and multiply both sides of the equation by L^{region} (for better convergence), so the equation that is actually implemented is

$$\begin{aligned} \nabla \cdot (\kappa_{\text{eff}} / L * (\phi_{\text{ex}} + \kappa_{D,\text{eff}} * 1 / c_e * c_{\text{ex}})) \\ = -L * a_s * F * j, \end{aligned}$$

where the following variables are defined:

$$\begin{array}{c|c|c|c|c|c|c|c} \kappa_{\text{eff}} & \kappa_{D,\text{eff}} / \kappa_{\text{eff}} & a_s & \bar{j} & L^{\text{region}} & \bar{\phi}_e & c_e & F \\ \hline \kappa_{\text{eff}} & \kappa_{D,\text{eff}} & a_s & j & L & \phi_{\text{ex}} & c_{\text{ex}} & F \end{array}$$

Note again that in COMSOL syntax,

$$\text{phi_ex} = \frac{d}{dx} \text{phi_e} \quad \text{and} \quad \text{c_ex} = \frac{d}{dx} \text{c_e},$$

and COMSOL's “ x ” is our normalized dimension “ \bar{x} ”.

4.13.4 Mass conservation in the electrolyte

The final PDE that we wish to implement describes mass conservation in the electrolyte

$$\frac{\partial(\epsilon_e \bar{c}_e)}{\partial t} = \nabla \cdot (D_{e,\text{eff}} \nabla \bar{c}_e) + a_s (1 - t_+^0) \bar{j}.$$

Once again, we normalize lengths, which converts the equation to

$$\frac{\partial(\epsilon_e \bar{c}_e)}{\partial t} = \frac{1}{L^{\text{region}}} \nabla \cdot (D_{e,\text{eff}} \frac{1}{L^{\text{region}}} \nabla \bar{c}_e) + a_s (1 - t_+^0) \bar{j}.$$

What is actually implemented is

$$\text{eps_e} * L * \frac{\partial c_e}{\partial t} + \nabla \cdot (-D_{e,\text{eff}} / L * \nabla c_e) = L * a_s * (1 - t_{\text{plus}}) * j,$$

where the following variables are defined

$D_{e,\text{eff}}$	t_+^0	a_s	\bar{j}	L^{region}	ϵ_e
$D_{e,\text{eff}}$	t_{plus}	a_s	j	L	eps_e

4.14 Running COMSOL

It is beyond the scope of this book to describe in detail how to use COMSOL or any other battery solver. However, we do show a screenshot taken when running COMSOL in Fig. 4.15. The left frame contains selectable elements that define constants, equations, meshes, and so forth. The details of the currently selected element are shown in the middle frame. The right frame shows simulation output: in this case, the voltage response of a cell that is subjected to a rest followed by a constant-current charge pulse, followed by a rest, followed by a constant-current discharge pulse, followed by a rest.

4.15 Where to from here?

We're making excellent progress. We're now at a point where we can fairly readily simulate cell performance and behavior. But, the equations are still far too complicated to implement in a real-time embedded system, which would be needed for battery controls. So, our

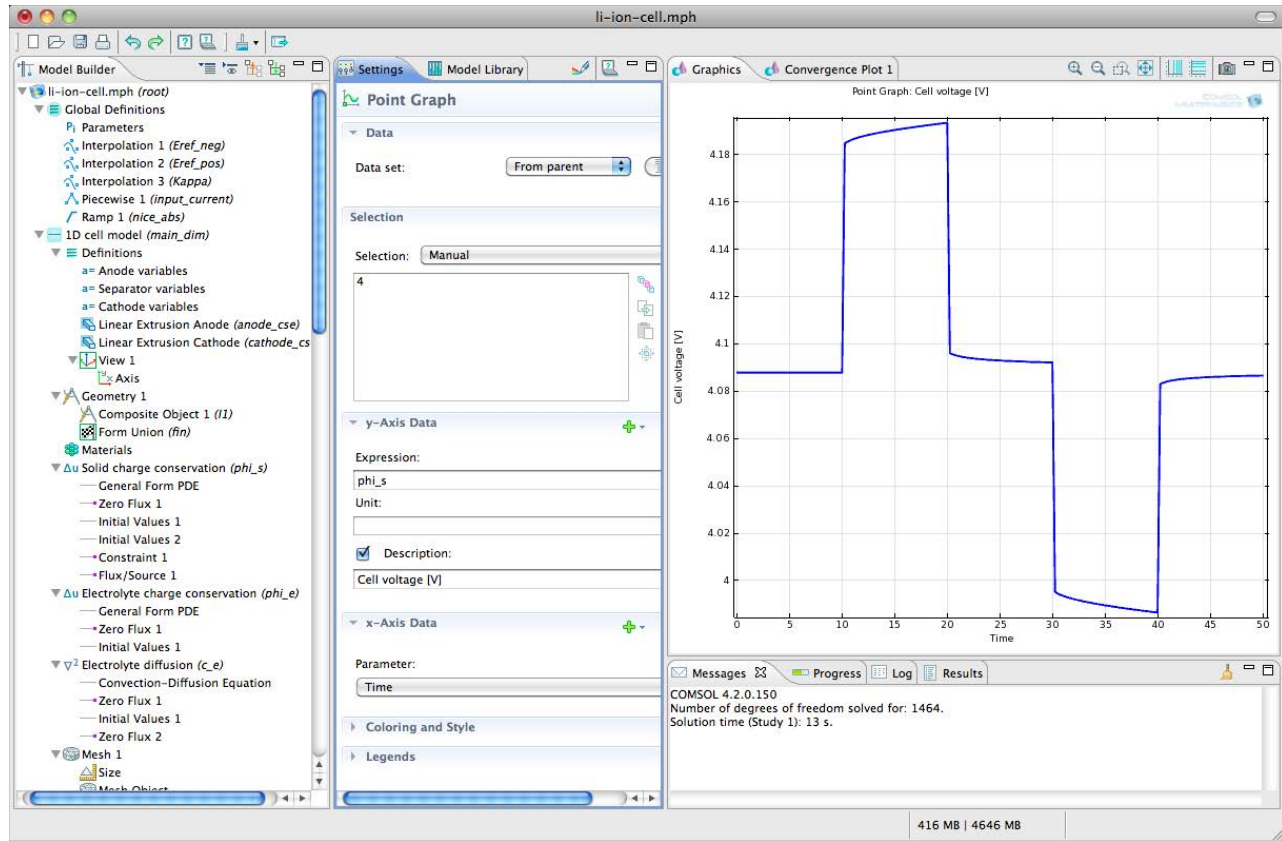


Figure 4.15: Screenshot of COMSOL user interface.

next step is to look at ways to reduce the complexity of the model equations, while still retaining the physics behind them. We devote the next two chapters of this book to doing so.

In Chap. 5, we introduce the discrete-time state-space model form, which is how our final equations will be expressed. We also introduce a method that can convert Laplace-domain transfer functions into the state-space model form. Then, in Chap. 6, we convert the PDEs from this chapter into transfer functions and create a reduced-order version of the continuum equations. The resulting model is of similar computational complexity to the equivalent-circuit models that we investigated in Chap. 2, but capable of predicting both the internal dynamics of the cell as well as the cell's voltage.

4.16 Partial glossary

This section gives a glossary of the most important variables defined in this chapter. Units are also given—the notation $[u/l]$ is specified for a unitless quantity. Note that all variables are at least potentially functions of space and time.

- $\langle \psi \rangle$ denotes the *phase average* of quantity ψ and has the same units as ψ (cf. p. 142).
- $\bar{\psi}$ denotes the *intrinsic phase average* of quantity ψ and has the same units as ψ (cf. p. 143).
- $a_s(x, y, z, t)$ [$\text{m}^2 \text{m}^{-3}$] is the *specific interfacial area*: the area of the boundary between solid and electrolyte per unit volume (cf. p. 154).
- brug [u/l] is *Bruggeman's exponent* for computing effective material properties. Often, we approximate $\text{brug} = 1.5$ (cf. p. 154).
- $\delta(x, y, z, t)$ [u/l] is the *constrictivity* of a porous media in the vicinity of a point. $\delta < 1$ (cf. p. 154).
- $\delta(x, y, z, t)$ [u/l] is also the symbol for the *Dirac delta function* (cf. p. 138).
- $\varepsilon_\alpha(x, y, z, t)$ [u/l] is the *volume fraction* of phase α in the vicinity of a point (cf. p. 143).
- $D_{e,\text{eff}}(x, y, z, t)$ [$\text{m}^2 \text{s}^{-1}$] is a short form for $D_{e,\text{eff}} \approx D_e \varepsilon_e^{\text{brug}} = D_e \varepsilon_e^{1.5}$ (cf. p. 158).
- $\gamma_\alpha(x, y, z, t)$ [u/l] denotes the *indicator function* for phase α (cf. p. 138).
- $\kappa_{\text{eff}}(x, y, z, t)$ [S m^{-1}] is the *effective conductivity* of the electrolyte, representing a volume-averaged conductivity of the electrolyte phase in a porous media in the vicinity of a given point. We often model $\kappa_{\text{eff}} \approx \kappa \varepsilon_e^{\text{brug}} = \kappa \varepsilon_e^{1.5}$ (cf. p. 160).
- $\kappa_{D,\text{eff}}(x, y, z, t)$ [V] is a short form for $\kappa_{D,\text{eff}} \approx \kappa_D \varepsilon_e^{\text{brug}} = \kappa_D \varepsilon_e^{1.5}$, where $\kappa_D = 2RT\kappa(t_+^0 - 1)/F$ (cf. p. 160).
- $\sigma_{\text{eff}}(x, y, z, t)$ [S m^{-1}] is an electrode-dependent parameter called the *effective conductivity*, representing a volume-averaged conductivity of the solid matrix in a porous media in the vicinity of a given point. We often model $\sigma_{\text{eff}} \approx \sigma \varepsilon_s^{\text{brug}} = \sigma \varepsilon_s^{1.5}$ (cf. p. 154).
- $\tau(x, y, z, t)$ [u/l] is the *tortuosity* of the porous media in the vicinity of a point. $\tau \geq 1$ (cf. p. 154).

5

State-Space Models and the Discrete-Time Realization Algorithm

The coupled PDE models derived in earlier chapters are useful for understanding how a cell works and (via a suitable design of experiments) can be used to explore design factors that might limit the cell's performance. Cell geometries, particle sizes, and material properties can be varied, in simulation, to optimize a cell's characteristics without the need to build numerous experimental cells.

For the purpose of real-time battery management, however, these models are too complex. For example, they are "infinite dimensional." For every point in time t , there are an infinite number of x - and r -dimension variables to solve for. That is, $c_s(x, r, t)$, $\bar{c}_e(x, t)$, $\bar{\phi}_s(x, t)$, and $\bar{\phi}_e(x, t)$ must be found for every x and r location.

We desire to create cell-scale ordinary difference equations (ODEs) that retain, as much as possible, the fidelity of the continuum-scale PDEs, but which reduce their order from infinite order to some (small) finite order. The result is a compact coupled set of ODEs, similar in computational complexity to the equivalent-circuit models developed in Chap. 2, which can be simulated very easily and quickly. This is the final step in the physics-based modeling approach of Fig. 3.1.

In this chapter, we introduce discrete-time state-space models, which are the final form of the physics-based reduced-order models that we will develop. We then preview the approach we will use to generate the state-space models from the PDEs of the variables of interest: we start by generating transfer functions for each PDE; we then use the *discrete-time realization algorithm* (DRA) to convert transfer functions to state-space form. In this chapter, we develop the DRA and give an important example to illustrate its behavior.

5.1	<i>Intro. to state-space models</i>	174
5.2	<i>Solid-dynamics equations</i>	182
5.3	<i>State-space realization</i>	186
5.4	<i>Discrete-time realization algo.</i>	195
5.5	<i>Examples of the DRA</i>	198
5.6	<i>Eigensystem realization algo.</i>	208
5.7	<i>Where to from here?</i>	212
5.8	<i>Partial glossary</i>	213

5.1 A quick introduction to state-space models

5.1.1 Continuous-time LTI system models

A linear-time-invariant (LTI) system's dynamics may be captured in (at least) three different ways. First, if we know the system's time response $h(t)$ to a Dirac delta impulse function $\delta(t)$ (i.e., its continuous-time *impulse response*), then we can compute the system's output corresponding to any input signal $u(t)$ via convolution as

$$y(t) = \int_{-\infty}^{\infty} u(\tau)h(t - \tau) d\tau. \quad (5.1)$$

Second, if we know the system's *transfer function* $H(s)$ or its *frequency response* $H(j\omega)$, then we can compute the output via Laplace or Fourier-transform techniques.

Third, we may write the system dynamics in a *state-space* form. While impulse responses, transfer functions, and frequency responses provide a system's input–output mapping only, state-space models provide access to what is going on *inside* the system in addition to the input–output mapping. These internal dynamics are summarized by the system's state.

We define the internal *state* of a system at time t_0 as a minimum amount of information at t_0 that, together with the input $u(t)$, $t \geq t_0$, uniquely determines the behavior of the system for all $t \geq t_0$.¹ Past inputs do not need to be stored as they do when computing system output using Eq. (5.1). Instead, the total net effect of all past inputs is captured by the present system state.

State-space models comprise two coupled equations. A linear-time-invariant continuous-time state-space model has the form

$$\dot{x}(t) = A_c x(t) + B_c u(t) \quad (5.2)$$

$$y(t) = C_c x(t) + D_c u(t), \quad (5.3)$$

where $u(t) \in \mathbb{R}^m$ is the input, $y(t) \in \mathbb{R}^p$ is the output, and $x(t) \in \mathbb{R}^n$ is the state vector.² Eq. (5.2) is called the *state equation* and describes how the input $u(t)$ influences the state $x(t)$. The matrix A_c is called the *state transition matrix*, and the matrix B_c is called the *input matrix*. Eq. (5.3) is called the *output equation* and describes how the state and input both directly influence the output. The matrix C_c is called the *output matrix*, and the matrix D_c is called the *feedthrough matrix*.³ Different linear systems have different A_c , B_c , C_c , and D_c matrices (all of which may be time-varying) and different state dimension n .

¹ We will see that the state itself is not necessarily unique; in general, different linear combinations of one state description form a second state description that encodes the same information.

² Boldfaced lowercase characters are used to denote quantities that may be vectors, and boldfaced uppercase characters are used to denote quantities that may be matrices.

³ The subscript “*c*” is used to refer to a continuous-time system and to underscore the fact that the A , B , C , and D matrices are different for continuous-time and discrete-time representations of the same system.

5.1.2 Discrete-time LTI system models

Linear-time-invariant (LTI) discrete-time state-space models have a very similar basic form:

$$\mathbf{x}[k+1] = \mathbf{A}\mathbf{x}[k] + \mathbf{B}\mathbf{u}[k] \quad (5.4)$$

$$\mathbf{y}[k] = \mathbf{C}\mathbf{x}[k] + \mathbf{D}\mathbf{u}[k], \quad (5.5)$$

where $\mathbf{u}[k] \in \mathbb{R}^m$ is the input, $\mathbf{y}[k] \in \mathbb{R}^p$ is the output, and $\mathbf{x}[k] \in \mathbb{R}^n$ is the state vector. Similar to before, Eq. (5.4) is the discrete-time model's state equation, and Eq. (5.5) is its output equation. It is important to note that the \mathbf{A} and \mathbf{B} matrices of the continuous-time and discrete-time models are not the same, even if describing the same system. As previewed in Chap. 2, we can convert from a continuous-time state-space model to a discrete-time model via

$$\mathbf{A} = e^{\mathbf{A}_c \Delta t}$$

$$\mathbf{B} = \mathbf{A}_c^{-1} (e^{\mathbf{A}_c \Delta t} - I) \mathbf{B}_c$$

$$\mathbf{C} = \mathbf{C}_c$$

$$\mathbf{D} = \mathbf{D}_c,$$

provided that \mathbf{A}_c^{-1} exists.⁴ Note that the exponential operation in the \mathbf{A} and \mathbf{B} equations is a matrix exponential, which can be evaluated as

$$e^{\mathbf{A}_c \Delta t} = \mathcal{L}^{-1} [(sI - \mathbf{A}_c)^{-1}]_{t=\Delta t}.$$

That is, one first computes the matrix function $(sI - \mathbf{A}_c)^{-1}$, then the inverse Laplace transform of this function, which is evaluated at the time instant $t = \Delta t$. There are other ways to evaluate a matrix exponential, including infinite series expansion, which are generally well described in introductory textbooks to multivariable control systems.⁵ In MATLAB, the `expm` command is used.

A block diagram can help visualize the signal flows. Consider Fig. 5.1. In the diagram, the z^{-1} block represents a unit delay; the input to this block is $\mathbf{x}[k+1] = \mathbf{A}\mathbf{x}[k] + \mathbf{B}\mathbf{u}[k]$, and the output is $\mathbf{x}[k]$, which is used to compute $\mathbf{y}[k] = \mathbf{C}\mathbf{x}[k] + \mathbf{D}\mathbf{u}[k]$. A MATLAB Simulink block diagram can be created that looks exactly like this figure in order to implement a discrete-time state-space system, providing that the \mathbf{A} , \mathbf{B} , \mathbf{C} , and \mathbf{D} blocks are matrix-multiply blocks.

5.1.3 Converting transfer function to state space

As an example of working with different discrete-time model forms, we consider how we might transform the following single-input single-output difference equation into a state-space form:

$$y[k] + a_1y[k-1] + a_2y[k-2] + a_3y[k-3] = b_1u[k-1] + b_2u[k-2] + b_3u[k-3].$$

⁴ If not, then $\mathbf{B} = \int_0^{\Delta t} e^{\mathbf{A}_c \tau} \mathbf{B}_c d\tau$, which must generally be evaluated manually to find a solution.

⁵ The definitive summary can be found in: Moler, C., and Van Loan, C., "Nineteen Dubious Ways to Compute the Exponential of a Matrix, Twenty-Five Years Later," *SIAM Review*, 45(1), 2003, pp. 3–49.

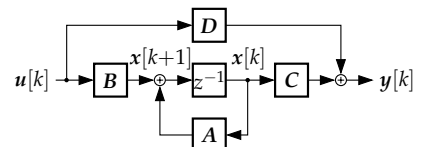


Figure 5.1: Block diagram implementing discrete-time state-space system.

First, we take the z -transform of both sides of the equation (assuming that initial conditions are zero) to get

$$\left[1 + a_1z^{-1} + a_2z^{-2} + a_3z^{-3}\right] Y(z) = \left[b_1z^{-1} + b_2z^{-2} + b_3z^{-3}\right] U(z).$$

Rearranging gives⁶

$$G(z) = \frac{b_1z^2 + b_2z + b_3}{z^3 + a_1z^2 + a_2z + a_3} = \frac{Y(z)}{U(z)}. \quad (5.6)$$

We break up the transfer function into two parts:

$$G(z) = G_z(z)G_p(z),$$

where $G_z(z)$ contains the “zeros” of the system and $G_p(z)$ contains the “poles.” That is

$$\begin{aligned} G_z(z) &= b_1z^2 + b_2z + b_3 \\ G_p(z) &= \frac{1}{z^3 + a_1z^2 + a_2z + a_3}. \end{aligned}$$

Let $V(z) = G_p(z)U(z)$. Then

$$v[k+3] + a_1v[k+2] + a_2v[k+1] + a_3v[k] = u[k].$$

For this example, we will choose the present and two advanced versions of $v[k]$ to be the model’s state vector.⁷

⁶ This is called a *rational-polynomial* form transfer function (in z), because it comprises a quotient of two polynomials (in the variable z).

$$x[k] = \begin{bmatrix} v[k+2] & v[k+1] & v[k] \end{bmatrix}^T.$$

Then

$$\underbrace{\begin{bmatrix} v[k+3] \\ v[k+2] \\ v[k+1] \end{bmatrix}}_{x[k+1]} = \underbrace{\begin{bmatrix} -a_1 & -a_2 & -a_3 \\ 1 & 0 & 0 \\ 0 & 1 & 0 \end{bmatrix}}_A \underbrace{\begin{bmatrix} v[k+2] \\ v[k+1] \\ v[k] \end{bmatrix}}_{x[k]} + \underbrace{\begin{bmatrix} 1 \\ 0 \\ 0 \end{bmatrix}}_B u[k].$$

⁷ This is a choice. There are other equally valid choices, as we will see.

This is the state equation for this system for this choice of state.

We now add a description of the system’s zeros:

$$\begin{aligned} Y(z) &= G_z(z)V(z) \\ &= [b_1z^2 + b_2z + b_3] V(z), \end{aligned}$$

or

$$\begin{aligned} y[k] &= b_1v[k+2] + b_2v[k+1] + b_3v[k] \\ &= \underbrace{\begin{bmatrix} b_1 & b_2 & b_3 \end{bmatrix}}_C x[k]. \end{aligned}$$

In summary, we have the state-space model:

$$\begin{aligned} \mathbf{x}[k+1] &= \begin{bmatrix} -a_1 & -a_2 & -a_3 \\ 1 & 0 & 0 \\ 0 & 1 & 0 \end{bmatrix} \mathbf{x}[k] + \begin{bmatrix} 1 \\ 0 \\ 0 \end{bmatrix} u[k] \\ y[k] &= \begin{bmatrix} b_1 & b_2 & b_3 \end{bmatrix} \mathbf{x}[k] + \begin{bmatrix} 0 \end{bmatrix} u[k]. \end{aligned}$$

Note that there are many other equally valid state-space models of this particular transfer function. We will soon see how they are related.

Also, this particular example was for a transfer function that had fewer zeros than poles. If the transfer function had an equal number of zeros and poles, we would have started the example by performing polynomial long division. For example, consider

$$G(z) = \frac{dz^3 + (da_1 + b_1)z^2 + (da_2 + b_2)z + (da_3 + b_3)}{z^3 + a_1z^2 + a_2z + a_3}.$$

We first perform polynomial long division and find

$$G(z) = d + \frac{b_1z^2 + b_2z + b_3}{z^3 + a_1z^2 + a_2z + a_3} = \frac{Y(z)}{U(z)}.$$

Following essentially the same steps as before,

$$\begin{aligned} \mathbf{x}[k+1] &= \begin{bmatrix} -a_1 & -a_2 & -a_3 \\ 1 & 0 & 0 \\ 0 & 1 & 0 \end{bmatrix} \mathbf{x}[k] + \begin{bmatrix} 1 \\ 0 \\ 0 \end{bmatrix} u[k] \\ y[k] &= \begin{bmatrix} b_1 & b_2 & b_3 \end{bmatrix} \mathbf{x}[k] + \begin{bmatrix} d \end{bmatrix} u[k]. \end{aligned}$$

We see that systems having an equal number of poles and zeros have a nonzero state-space D matrix. In our battery models, this direct-feedthrough term represents an equivalent-series-resistance term, as the output has a component that is instantaneously related to the input.

While it can be instructive to work through an example like this by hand, it is cumbersome to do so routinely. The MathWorks' Control System Toolbox for MATLAB provides the command `[A, B, C, D] = tf2ss (num, den, Ts)` to convert a rational-polynomial transfer function form to a state-space form.

5.1.4 Converting state space to transfer function

In the prior example, we saw that it is possible to convert from a difference equation (or transfer function) to a state-space form quite easily. Now, we'll see that translating in the reverse direction is also straightforward.

We start with the state-space equations

$$\begin{aligned}\mathbf{x}[k+1] &= \mathbf{Ax}[k] + \mathbf{Bu}[k] \\ \mathbf{y}[k] &= \mathbf{Cx}[k] + \mathbf{Du}[k].\end{aligned}$$

Next, take the z -transform of both sides of both equations

$$\begin{aligned}z\mathbf{X}(z) - z\mathbf{x}[0] &= \mathbf{AX}(z) + \mathbf{BU}(z) \\ \mathbf{Y}(z) &= \mathbf{CX}(z) + \mathbf{DU}(z).\end{aligned}$$

Rearranging the state equation to solve for $\mathbf{X}(z)$ gives⁸

$$\begin{aligned}(z\mathbf{I} - \mathbf{A})\mathbf{X}(z) &= \mathbf{BU}(z) + z\mathbf{x}[0] \\ \mathbf{X}(z) &= (z\mathbf{I} - \mathbf{A})^{-1}\mathbf{BU}(z) + (z\mathbf{I} - \mathbf{A})^{-1}z\mathbf{x}[0].\end{aligned}$$

Substituting $\mathbf{X}(z)$ into the output equation gives⁹

$$\mathbf{Y}(z) = \underbrace{[\mathbf{C}(z\mathbf{I} - \mathbf{A})^{-1}\mathbf{B} + \mathbf{D}]}_{\text{transfer function of system}} \mathbf{U}(z) + \underbrace{\mathbf{C}(z\mathbf{I} - \mathbf{A})^{-1}z\mathbf{x}[0]}_{\text{response to initial conditions}}.$$

By definition, the transfer function of a system assumes that the initial conditions are zero. For this assumption,

$$G(z) = \frac{\mathbf{Y}(z)}{\mathbf{U}(z)} = \mathbf{C}(z\mathbf{I} - \mathbf{A})^{-1}\mathbf{B} + \mathbf{D}.$$

Note that $(z\mathbf{I} - \mathbf{A})^{-1} = \frac{\text{adj}(z\mathbf{I} - \mathbf{A})}{\det(z\mathbf{I} - \mathbf{A})}$, so we can write a system's transfer function as

$$G(z) = \frac{\mathbf{C} \text{adj}(z\mathbf{I} - \mathbf{A})\mathbf{B} + \mathbf{D} \det(z\mathbf{I} - \mathbf{A})}{\det(z\mathbf{I} - \mathbf{A})}.$$

From this, we make an extremely important observation: the poles of the system are where $\det(z\mathbf{I} - \mathbf{A}) = 0$, which (by definition) are the eigenvalues of \mathbf{A} . Since the poles determine stability, character of response, and speed of response, we can learn a lot about system behavior from only the \mathbf{A} matrix.

5.1.5 Transformation of state-space models

As alluded to earlier, state-space representations of a particular system's dynamics are not unique. The selection of the state vector $\mathbf{x}[k]$ is somewhat arbitrary. To see this, let's analyze a transformation of Eqs. (5.4) and (5.5), where we let $\mathbf{x}[k] = \mathbf{T}\mathbf{w}[k]$, and where \mathbf{T} is a constant square invertible (similarity) transformation matrix. Then,

$$\begin{aligned}(\mathbf{T}\mathbf{w}[k+1]) &= \mathbf{A}(\mathbf{T}\mathbf{w}[k]) + \mathbf{B}\mathbf{u}[k] \\ \mathbf{y}[k] &= \mathbf{C}(\mathbf{T}\mathbf{w}[k]) + \mathbf{D}\mathbf{u}[k].\end{aligned}$$

⁸We have to be careful when factoring $\mathbf{X}(z)$ from the two terms in which it appears since z is a scalar and \mathbf{A} is a matrix. We must write $z\mathbf{I} - \mathbf{A}$ instead of $z - \mathbf{A}$ to have compatible dimensions for the subtraction.

⁹The entire first term (including $\mathbf{U}(z)$) is sometimes called the zero-state solution, and the second term is sometimes called the zero-input solution.

Multiplying the first equation by T^{-1} gives

$$\begin{aligned} \mathbf{w}[k+1] &= \underbrace{\mathbf{T}^{-1} \mathbf{A} \mathbf{T}}_{\bar{\mathbf{A}}} \mathbf{w}[k] + \underbrace{\mathbf{T}^{-1} \mathbf{B}}_{\bar{\mathbf{B}}} \mathbf{u}[k] \\ \mathbf{y}[k] &= \underbrace{\mathbf{C} \mathbf{T}}_{\bar{\mathbf{C}}} \mathbf{w}[k] + \underbrace{\mathbf{D}}_{\bar{\mathbf{D}}} \mathbf{u}[k]. \end{aligned}$$

So, we have a revised discrete-time state-space form with the state $\mathbf{w}[k]$ and matrices $\bar{\mathbf{A}}$, $\bar{\mathbf{B}}$, $\bar{\mathbf{C}}$, and $\bar{\mathbf{D}}$.

$$\mathbf{w}[k+1] = \bar{\mathbf{A}} \mathbf{w}[k] + \bar{\mathbf{B}} \mathbf{u}[k] \quad (5.7)$$

$$\mathbf{y}[k] = \bar{\mathbf{C}} \mathbf{w}[k] + \bar{\mathbf{D}} \mathbf{u}[k]. \quad (5.8)$$

The input-to-state behavior of Eq. (5.7) is different from Eq. (5.4), but the overall coupled input-to-output behavior of Eqs. (5.7) and (5.8) is the same as that of Eqs. (5.4) and (5.5). We can see this by computing the transfer functions of the two representations, where we use $H_1(z)$ to denote the transfer function of the \mathbf{x} -state system and $H_2(z)$ to denote the transfer function of the \mathbf{w} -state system

$$\begin{aligned} H_1(z) &= \mathbf{C}(z\mathbf{I} - \mathbf{A})^{-1} \mathbf{B} + \mathbf{D} \\ &= \mathbf{C} \mathbf{T} \mathbf{T}^{-1}(z\mathbf{I} - \mathbf{A})^{-1} \mathbf{T} \mathbf{T}^{-1} \mathbf{B} + \mathbf{D} \\ &= (\mathbf{C} \mathbf{T})[\mathbf{T}^{-1}(z\mathbf{I} - \mathbf{A})\mathbf{T}]^{-1}(\mathbf{T}^{-1} \mathbf{B}) + \mathbf{D} \\ &= \bar{\mathbf{C}}(z\mathbf{I} - \bar{\mathbf{A}})^{-1} \bar{\mathbf{B}} + \bar{\mathbf{D}} = H_2(z). \end{aligned}$$

So, the transfer function has not been changed by the similarity transform.

From this exercise, we conclude that it is possible to arrive at multiple state-space representations having identical input-output relationships but different $(\mathbf{A}, \mathbf{B}, \mathbf{C}, \mathbf{D})$ matrices. As an example, consider the transformation of

$$\begin{aligned} \mathbf{A} &= \begin{bmatrix} -a_1 & -a_2 & -a_3 \\ 1 & 0 & 0 \\ 0 & 1 & 0 \end{bmatrix}, & \mathbf{B} &= \begin{bmatrix} 1 \\ 0 \\ 0 \end{bmatrix}, \\ \mathbf{C} &= \begin{bmatrix} b_1 & b_2 & b_3 \end{bmatrix}, & \mathbf{D} &= \begin{bmatrix} 0 \end{bmatrix} \end{aligned}$$

with

$$\mathbf{T} = \mathbf{T}^{-1} = \begin{bmatrix} 0 & 0 & 1 \\ 0 & 1 & 0 \\ 1 & 0 & 0 \end{bmatrix}.$$

Note that multiplying on the right by \mathbf{T} flips the original entries left to right; multiplying on the left flips the original entries top to bottom.

For this transformation matrix, we first compute the transformed state-transition matrix

$$\begin{aligned}\bar{A} &= T^{-1}AT = \begin{bmatrix} 0 & 0 & 1 \\ 0 & 1 & 0 \\ 1 & 0 & 0 \end{bmatrix} \begin{bmatrix} -a_1 & -a_2 & -a_3 \\ 1 & 0 & 0 \\ 0 & 1 & 0 \end{bmatrix} \begin{bmatrix} 0 & 0 & 1 \\ 0 & 1 & 0 \\ 1 & 0 & 0 \end{bmatrix} \\ &= \begin{bmatrix} 0 & 1 & 0 \\ 0 & 0 & 1 \\ -a_3 & -a_2 & -a_1 \end{bmatrix}.\end{aligned}$$

Next, consider the transformed input matrix

$$\bar{B} = T^{-1}B = \begin{bmatrix} 0 & 0 & 1 \\ 0 & 1 & 0 \\ 1 & 0 & 0 \end{bmatrix} \begin{bmatrix} 1 \\ 0 \\ 0 \end{bmatrix} = \begin{bmatrix} 0 \\ 0 \\ 1 \end{bmatrix},$$

output matrix

$$\bar{C} = CT = \begin{bmatrix} b_1 & b_2 & b_3 \end{bmatrix} \begin{bmatrix} 0 & 0 & 1 \\ 0 & 1 & 0 \\ 1 & 0 & 0 \end{bmatrix} = \begin{bmatrix} b_3 & b_2 & b_1 \end{bmatrix},$$

and direct feedthrough term $\bar{D} = D = 0$.

To verify that we arrive at the same transfer function, we evaluate

$$\begin{aligned}G(z) &= \bar{C}(zI - \bar{A})^{-1}\bar{B} + \bar{D} \\ &= \begin{bmatrix} b_3 & b_2 & b_1 \end{bmatrix} \left(\begin{bmatrix} z & 0 & 0 \\ 0 & z & 0 \\ 0 & 0 & z \end{bmatrix} - \begin{bmatrix} 0 & 1 & 0 \\ 0 & 0 & 1 \\ -a_3 & -a_2 & -a_1 \end{bmatrix} \right)^{-1} \begin{bmatrix} 0 \\ 0 \\ 1 \end{bmatrix} \\ &= \begin{bmatrix} b_3 & b_2 & b_1 \end{bmatrix} \left(\begin{bmatrix} z & -1 & 0 \\ 0 & z & -1 \\ a_3 & a_2 & z + a_1 \end{bmatrix} \right)^{-1} \begin{bmatrix} 0 \\ 0 \\ 1 \end{bmatrix} \\ &= \frac{\begin{bmatrix} b_3 & b_2 & b_1 \end{bmatrix} \begin{bmatrix} z^2 + a_1z + a_2 & a_1 + z & 1 \\ -a_3 & z^2 + a_1z & z \\ -a_3z & -a_2z - a_3 & z^2 \end{bmatrix} \begin{bmatrix} 0 \\ 0 \\ 1 \end{bmatrix}}{z^3 + a_1z^2 + a_2z + a_3} \\ &= \frac{\begin{bmatrix} b_3 & b_2 & b_1 \end{bmatrix} \begin{bmatrix} 1 \\ z \\ z^2 \end{bmatrix}}{z^3 + a_1z^2 + a_2z + a_3} = \frac{b_1z^2 + b_2z + b_3}{z^3 + a_1z^2 + a_2z + a_3},\end{aligned}$$

which is the same transfer function as in Eq. (5.6), which is what we started with before the transformations.

5.1.6 Discrete-time Markov parameters

It turns out that the discrete unit-pulse response of a state-space system has a special form that will be important to us later. For example,

let's look at the unit-pulse response of a single-input state-space system.¹⁰ The unit-pulse input is defined as

$$u[k] = \begin{cases} 1, & k = 0; \\ 0, & k \neq 0. \end{cases}$$

The system response to the unit-pulse input can be found by evaluating the state and output equations recursively

$$\begin{aligned} y[0] &= Cx[0] + Du[0] = D, & x[1] &= Ax[0] + Bu[0] = B \\ y[1] &= Cx[1] + Du[1] = CB, & x[2] &= Ax[1] + Bu[1] = AB \\ y[2] &= Cx[2] + Du[2] = CAB, & x[3] &= Ax[2] + Bu[2] = A^2B \\ &\vdots & & \\ y[k] &= CA^{k-1}B, & k \geq 1. & \end{aligned}$$

These pulse-response values, $\{D, CB, CAB, CA^2B, CA^3B, \dots\}$ are called the *Markov parameters* of the system. They turn out to be of critical importance to realizing our transfer functions, as we will see.

Specifically, we define the Markov parameters to be:

$$g_k = \begin{cases} D, & k = 0; \\ CA^{k-1}B, & k > 0. \end{cases}$$

To be clear:

- For single-input single-output (SISO) systems, the Markov parameters are scalars.
- For a single-input multioutput (SIMO) system, the Markov parameters are (column) vectors.
 - The i th entry (row) of each Markov parameter is computed as the unit-pulse response from the input to the i th output.
 - Equivalently, the entire vector Markov parameter is the unit-pulse response from the input to the vector output.
- For multi-input single-output (MISO) systems, the above results can be generalized, and the Markov parameters are row vectors.
 - The j th entry (column) of each Markov parameter is computed via the unit-pulse response from the j th input to the output.
- For multi-input multioutput (MIMO) systems, the Markov parameters are matrices.
 - The (i,j) th entries yield the the unit-pulse response from the j th input to the i th output.
 - Equivalently, the j th column of each Markov parameter is a vector (as in the SIMO case), which is computed as the unit-pulse response from the j th input to the vector output.

¹⁰Note that, by definition, $x[0] = 0$ when finding a unit-pulse response.

As an example, consider finding the discrete unit-pulse response for a state-space system defined by

$$A = \begin{bmatrix} 0.5 & 0 \\ 0 & 1 \end{bmatrix}, \quad B = \begin{bmatrix} 1 \\ 0 \end{bmatrix}, \quad C = \begin{bmatrix} 1 & -1 \end{bmatrix}, \quad D = 0.$$

The Markov parameters are given by

$$\begin{aligned} g_k &= \{D, CB, CAB, CA^2B, CA^3B, \dots\} \\ &= \{0, 1, 0.5, 0.25, \dots\}. \end{aligned}$$

This is illustrated in Fig. 5.2, where MATLAB's `impulse` command (from the Control System Toolbox) is used to confirm this result:

```
A = [0.5 0; 0 1]; B = [1; 0]; C = [1 -1]; D = 0;
sys = ss(A,B,C,D,-1); % "-1" = discrete-time model with unknown T
[y,k] = impulse(sys,0:15);
stem(k,y,'filled');
```

5.2 Equations describing the solid dynamics

We have now quickly previewed state-space models, with the claim that there will be a method to represent our battery models in that particular form. We continue by beginning to investigate that claim, with the first step being to create transfer-function models for the variables of interest. In this chapter, we look at representing c_s as a transfer function; in the next chapter we look at the remainder of the model equations.

Note that in Chap. 3, we used symbols *without* an over-line to indicate point-wise values for variables of interest (i.e., c_s , c_e , ϕ_s , ϕ_e , and j). Then, in Chap. 4 we used symbols *with* an over-line to indicate volume-average versions of these point-wise variables (i.e., \bar{c}_e , $\bar{\phi}_s$, $\bar{\phi}_e$, and \bar{j}). We now drop the over-line notation, because otherwise the equations get so highly decorated that they are impossible to parse. We are still talking about the volume-average quantities of Chap. 4.

5.2.1 Finding the transfer function $\tilde{C}_{s,e}(s)/J(s)$

To find the transfer function for c_s , we follow the approach by Jacobsen and West.¹¹ We start with the underlying partial-differential equation

$$\frac{\partial c_s(r, t)}{\partial t} = \frac{1}{r^2} \frac{\partial}{\partial r} \left(D_s r^2 \frac{\partial c_s(r, t)}{\partial r} \right),$$

with standard boundary conditions

$$D_s \frac{\partial c_s(0, t)}{\partial r} = 0, \quad \text{and} \quad D_s \frac{\partial c_s(R_s, t)}{\partial r} = -j(t), \quad t \geq 0,$$

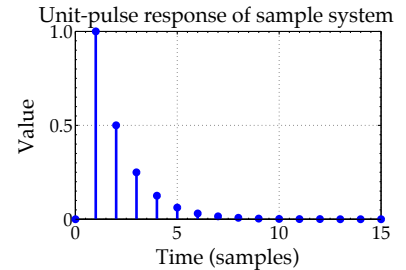


Figure 5.2: Discrete unit-pulse response.

¹¹ Jacobsen, T., and West, K., "Diffusion Impedance in Planar, Cylindrical and Spherical Symmetry," *Electrochimica Acta*, 40(2), 1995, pp. 255–62.

and with initial equilibrium concentration,

$$c_s(r, 0) = c_{s,0}, \quad 0 \leq r \leq R_s.$$

Note that we run into problems solving this PDE directly if $c_{s,0} \neq 0$. To enforce a homogeneous PDE in later steps, we define $\tilde{c}_s(r, t) = c_s(r, t) - c_{s,0}$. The “tilde” notation denotes the difference between an absolute quantity and its equilibrium set-point, resulting in a *debiased* variable.

We also assume that D_s is constant, and so the differential equations for \tilde{c}_s become

$$\frac{\partial \tilde{c}_s(r, t)}{\partial t} = \frac{D_s}{r^2} \frac{\partial}{\partial r} \left(r^2 \frac{\partial \tilde{c}_s(r, t)}{\partial r} \right),$$

with boundary conditions,

$$D_s \frac{\partial \tilde{c}_s(0, t)}{\partial r} = 0, \quad \text{and} \quad D_s \frac{\partial \tilde{c}_s(R_s, t)}{\partial r} = -j(t), \quad t \geq 0,$$

and with initial equilibrium concentration,

$$\tilde{c}_s(r, 0) = 0, \quad 0 \leq r \leq R_s.$$

We proceed by taking the Laplace transform of the underlying equation

$$\begin{aligned} s \tilde{C}_s(r, s) - \tilde{c}_s(r, 0) &= \frac{D_s}{r^2} \frac{\partial}{\partial r} \left(r^2 \frac{\partial \tilde{C}_s(r, s)}{\partial r} \right) \\ s \tilde{C}_s(r, s) &= \frac{D_s}{r^2} \left(2r \frac{\partial \tilde{C}_s(r, s)}{\partial r} + r^2 \frac{\partial^2 \tilde{C}_s(r, s)}{\partial r^2} \right). \end{aligned}$$

This is a second-order differential equation in r , which may be written as

$$\frac{\partial^2 \tilde{C}_s(r, s)}{\partial r^2} + \frac{2}{r} \frac{\partial \tilde{C}_s(r, s)}{\partial r} - \frac{s}{D_s} \tilde{C}_s(r, s) = 0.$$

The solution to this homogeneous differential equation has the form

$$\begin{aligned} \tilde{C}_s(r, s) &= \frac{A}{r} \exp \left(r \sqrt{\frac{s}{D_s}} \right) + \frac{B}{r} \exp \left(-r \sqrt{\frac{s}{D_s}} \right) \\ &= \frac{A}{r} \exp(\beta(r)) + \frac{B}{r} \exp(-\beta(r)), \end{aligned}$$

where we define $\beta(r) = r \sqrt{s/D_s}$. We note that $\beta(r)$ is also a function of s , but we omit this dependence in the notation for compactness.

The constants A and B are chosen to satisfy the boundary conditions of the problem. Consider first the outer boundary condition at $r = R_s$, which is

$$D_s \frac{\partial \tilde{c}_s(r, t)}{\partial r} \Big|_{r=R_s} = -j(t).$$

The equivalent Laplace-domain boundary condition is

$$D_s \frac{\partial \tilde{C}_s(r, s)}{\partial r} \bigg|_{r=R_s} = -J(s).$$

To substitute this into our result, we will need to compute $\partial \tilde{C}_s(r, s)/\partial r$, which is

$$\begin{aligned} \frac{\partial \tilde{C}_s(r, s)}{\partial r} &= \frac{A \sqrt{\frac{s}{D_s}} r \exp(\beta(r)) - B \exp(-\beta(r))}{r^2} \\ &\quad - \frac{A \exp(\beta(r)) + B \sqrt{\frac{s}{D_s}} r \exp(-\beta(r))}{r^2} \\ &= \frac{A(\beta(r) - 1) \exp(\beta(r)) - B(1 + \beta(r)) \exp(-\beta(r))}{r^2}. \end{aligned}$$

We substitute $r = R_s$ and the boundary condition

$$\begin{aligned} \frac{\partial \tilde{C}_s(r, s)}{\partial r} \bigg|_{r=R_s} &= \frac{A(\beta(R_s) - 1) \exp(\beta(R_s)) - B(1 + \beta(R_s)) \exp(-\beta(R_s))}{R_s^2} \\ \frac{J(s)}{D_s} &= \frac{A(\beta(R_s) - 1) \exp(\beta(R_s)) - B(1 + \beta(R_s)) \exp(-\beta(R_s))}{R_s^2}. \end{aligned}$$

This gives us an expression for $J(s)$,

$$J(s) = -\frac{D_s}{R_s^2} (A(\beta(R_s) - 1) \exp(\beta(R_s)) - B(1 + \beta(R_s)) \exp(-\beta(R_s))).$$

If we immediately substitute the second boundary condition at $r = 0$, we run into some divide-by-zero issues. So, instead, we substitute $r = r_\delta$, which we think of as a very small value. We will then later take the limit as $r_\delta \rightarrow 0$.

$$0 = \frac{A(\beta(r_\delta) - 1) \exp(\beta(r_\delta)) - B(1 + \beta(r_\delta)) \exp(-\beta(r_\delta))}{r_\delta^2}.$$

This allows us to write

$$\begin{aligned} \frac{A(\beta(r_\delta) - 1) \exp(\beta(r_\delta))}{r_\delta^2} &= \frac{B(1 + \beta(r_\delta)) \exp(-\beta(r_\delta))}{r_\delta^2} \\ A &= B \frac{(1 + \beta(r_\delta)) \exp(-\beta(r_\delta))}{(\beta(r_\delta) - 1) \exp(\beta(r_\delta))}. \end{aligned}$$

We take the limit as $r_\delta \rightarrow 0$, and find that $A = -B$.

We are now ready to construct the transfer function $\tilde{C}_s(s, r)/J(s)$

$$\begin{aligned} \frac{\tilde{C}_s(r, s)}{J(s)} &= \frac{-R_s^2}{D_s r} \left[\frac{A \exp(\beta(r)) + B \exp(-\beta(r))}{A(\beta(R_s) - 1) \exp(\beta(R_s)) - B(1 + \beta(R_s)) \exp(-\beta(R_s))} \right] \\ &= \frac{-R_s^2}{D_s r} \left[\frac{A}{-A} \right] \left[\frac{\exp(\beta(r)) - \exp(-\beta(r))}{(1 - \beta(R_s)) \exp(\beta(R_s)) - (1 + \beta(R_s)) \exp(-\beta(R_s))} \right] \\ &= \frac{R_s^2}{D_s r} \left[\frac{\exp(\beta(r)) - \exp(-\beta(r))}{(1 - \beta(R_s)) \exp(\beta(R_s)) - (1 + \beta(R_s)) \exp(-\beta(R_s))} \right]. \end{aligned}$$

This expression can be used to determine the lithium concentration anywhere within the particle. However, we are most interested in determining the concentration at the *surface* of the particle, where $r = R_s$. So we substitute $r = R_s$ and denote $\tilde{C}_{s,e}(s) = \tilde{C}_s(R_s, s)$

$$\frac{\tilde{C}_{s,e}(s)}{J(s)} = \frac{R_s}{D_s} \left[\frac{\exp(\beta(R_s)) - \exp(-\beta(R_s))}{(1 - \beta(R_s)) \exp(\beta(R_s)) - (1 + \beta(R_s)) \exp(-\beta(R_s))} \right].$$

To compact the notation yet again, write $\beta(R_s)$ as simply β ,

$$\begin{aligned} \frac{\tilde{C}_{s,e}(s)}{J(s)} &= \frac{R_s}{D_s} \left[\frac{\exp(\beta) - \exp(-\beta)}{(1 - \beta) \exp(\beta) - (1 + \beta) \exp(-\beta)} \right] \\ &= \frac{R_s}{D_s} \left[\frac{\frac{\exp(\beta) - \exp(-\beta)}{\exp(\beta) - \exp(-\beta)}}{\frac{\exp(\beta) - \exp(-\beta)}{\exp(\beta) - \exp(-\beta)} - \beta \frac{\exp(\beta) + \exp(-\beta)}{\exp(\beta) - \exp(-\beta)}} \right] \\ &= \frac{R_s}{D_s} \left[\frac{1}{1 - \beta \coth(\beta)} \right]. \end{aligned}$$

To recap to this point, re-expanding notation,¹²

$$\tilde{C}_{s,e}(s) = \frac{R_s}{D_s} \left[\frac{1}{1 - R_s \sqrt{s/D_s} \coth(R_s \sqrt{s/D_s})} \right] J(s). \quad (5.9)$$

5.2.2 Removing the integrator pole

While not immediately obvious by looking at the transfer function, it turns out that $\tilde{C}_{s,e}(s)/J(s)$ is unstable: it has a pole at $s = 0$, which corresponds to integration dynamics. This is intuitively clear, however, because we know that a constant influx of lithium to a particle will result in an ever-increasing concentration of lithium within that particle.

This will be important when we look at how to convert the transfer function to a state-space model. To make a stable transfer function, define $\Delta\tilde{C}_{s,e}(s) = \tilde{C}_{s,e}(s) - \tilde{C}_{s,\text{avg}}(s)$, where $\tilde{C}_{s,\text{avg}}(s)$ is the bulk (average) concentration in the solid, less $c_{s,0}$.

Note that we can write $\tilde{c}_{s,\text{avg}}(t_1)$ for arbitrary time t_1 as

$$\tilde{c}_{s,\text{avg}}(t_1) = \int_0^{t_1} \frac{\text{Influx of Li, [mol s}^{-1}\text{]}}{\text{Volume of particle [m}^3\text{]}} dt.$$

The volume of a sphere of radius R_s is $\frac{4}{3}\pi R_s^3$ [m³] and the influx of lithium is $-j(t)$ [mol m⁻² s⁻¹], occurring over the surface area of $4\pi R_s^2$ [m²]. This gives¹³

$$\begin{aligned} \tilde{c}_{s,\text{avg}}(t_1) &= \int_0^{t_1} \frac{-j(t) \cdot 4\pi R_s^2}{\frac{4}{3}\pi R_s^3} dt = -\frac{3}{R_s} \int_0^{t_1} j(t) dt \\ \frac{d}{dt} \tilde{c}_{s,\text{avg}}(t) &= -\frac{3}{R_s} j(t). \end{aligned}$$

¹² We call $\tilde{C}_{s,e}(s)/J(s)$ a *transcendental* form transfer function (in s), since it is not represented by a quotient of two polynomials (in the variable s). That is, it is not a *rational-polynomial* transfer function.

¹³ This result is perfectly general. We made no assumptions on how the lithium concentration is distributed inside the particle.

Taking Laplace transforms, we find:

$$\frac{\tilde{C}_{s,\text{avg}}(s)}{J(s)} = -\frac{3}{R_s} \frac{1}{s}.$$

Therefore,

$$\begin{aligned} \frac{\Delta \tilde{C}_{s,e}(s)}{J(s)} &= \frac{\tilde{C}_{s,e}(s)}{J(s)} - \frac{\tilde{C}_{s,\text{avg}}(s)}{J(s)} \\ &= \frac{R_s}{D_s} \left[\frac{1}{1 - \beta \coth(\beta)} \right] + \frac{3}{R_s s} \\ &= \frac{R_s}{D_s} \left[\frac{1 + \frac{3D_s}{sR_s^2} (1 - \beta \coth(\beta))}{1 - \beta \coth(\beta)} \right] \\ &= \frac{R_s}{D_s} \left[\frac{1 + \frac{3}{\beta^2} (1 - \beta \coth(\beta))}{1 - \beta \coth(\beta)} \right] \\ &= \frac{R_s}{D_s} \left[\frac{\beta^2 + 3 (1 - \beta \coth(\beta))}{\beta^2 (1 - \beta \coth(\beta))} \right] \\ &= \frac{R_s}{D_s} \left[\frac{(\beta^2 + 3) - 3\beta \coth(\beta)}{\beta^2 (1 - \beta \coth(\beta))} \right]. \end{aligned}$$

Finally, expanding notation, we have

$$\frac{\Delta \tilde{C}_{s,e}(s)}{J(s)} = \frac{\frac{sR_s^2}{D_s} + 3 - 3R_s \sqrt{\frac{s}{D_s}} \coth \left(R_s \sqrt{\frac{s}{D_s}} \right)}{sR_s \left(1 - R_s \sqrt{\frac{s}{D_s}} \coth \left(R_s \sqrt{\frac{s}{D_s}} \right) \right)}. \quad (5.10)$$

5.3 State-space realization

At this point, we have found a transfer-function model that relates input flux to transient variations in the surface concentration of lithium around some average value. For this specific case, it turns out to be possible to find all the poles and zeros of the transfer function using a simple numeric method, and to use that information to make a discrete-time state-space model.¹⁴ However, for the transfer functions we develop in Chap. 6, this cannot be done. So, we must turn to alternative implementation approaches.

One method is to use nonlinear optimization to select poles and zeros of a rational-polynomial transfer function to attempt to match its frequency response to that of the transcendental transfer function. Then, standard methods for converting rational-polynomial transfer functions to state-space models can be used. Unfortunately, however, this approach is fraught with problems. In particular, nonlinear optimization is very sensitive to the initial model guess, is unbounded in time and computation, and is not guaranteed to converge to a global optimum.

¹⁴ Smith, K., *Electrochemical Modeling, Estimation and Control of Lithium Ion Batteries*, Ph.D. dissertation, The Pennsylvania State University, 2006.

We introduce another approach, which gives us a discrete-time state-space approximate model directly from our transfer functions. This system-identification problem for state-space systems is sometimes called the “realization problem.” That is, we wish to find a realization (a set of A , B , C , and D matrices) that describes a system’s dynamics. For now, we assume that we are able to find the Markov parameters of our transfer functions.

The problem is then: given a system’s Markov parameters, find the system dimension n and (A, B, C, D) , up to a similarity transform.

5.3.1 The Ho–Kalman state-space realization method

An early (maybe the *first*) state-space realization method was introduced by Ho and Kalman.¹⁵ It is key to the discrete-time realization algorithm we will develop. To derive the Ho–Kalman method, notice that something curious happens when we multiply the following matrices together

$$\underbrace{\begin{bmatrix} C \\ CA \\ CA^2 \\ \vdots \\ CA^{n-1} \end{bmatrix}}_{\mathcal{O}} \underbrace{\begin{bmatrix} B & AB & A^2B & \cdots & A^{n-1}B \end{bmatrix}}_C = \begin{bmatrix} CB & CAB & CA^2B & \cdots & CA^{n-1}B \\ CAB & CA^2B & CA^3B & & \\ CA^2B & CA^3B & CA^4B & & \\ \vdots & & \ddots & & \vdots \\ CA^{n-1}B & & \cdots & & CA^{2n-2}B \end{bmatrix}.$$

For reasons beyond the scope of our discussion here, \mathcal{O} is called the *observability matrix* and C is called the *controllability matrix* of our state-space system.¹⁶

Notice that the product of \mathcal{O} and C is a block Hankel matrix—a matrix having constant skew diagonals (i.e., it is an upside-down block Toeplitz matrix). Note also that the values on the skew diagonals are the Markov parameters of the system (excluding g_0 and g_k for $k > 2n - 1$). That is,

$$\mathcal{H} = \mathcal{O}C = \begin{bmatrix} g_1 & g_2 & \cdots & g_n \\ g_2 & g_3 & & \\ \vdots & & \ddots & \vdots \\ g_n & & \cdots & g_{2n-1} \end{bmatrix}.$$

¹⁵ Ho, B.L., and Kalman, R.E., “Effective Construction of Linear State Variable Models from Input/Output Functions,” *Regelungstechnik*, 14(12), 1966, pp. 545–8.

¹⁶ It should be evident from the equation, but we point out for clarity, that the controllability matrix C and the output matrix C are different quantities, even though the notation looks quite similar.

The Ho–Kalman method assumes that we know the Markov parameters. Knowledge of g_0 gives us D directly. Knowledge of the rest of the Markov parameters will ultimately result in A , B , and C .

To use Ho–Kalman, we must first form the Hankel matrix \mathcal{H} . The next step is to factor $\mathcal{H} = \mathcal{O}\mathcal{C}$ into its \mathcal{O} and \mathcal{C} components. The third step is to use \mathcal{O} and \mathcal{C} to find A , B , and C .

ISSUE I: We don't know n . So, how do we form \mathcal{H} in the first place?

That is, when do we stop adding pulse-response values to \mathcal{H} ?

PRELIMINARY ANSWER: The rank of \mathcal{H} is equal to the system order n . Keep adding data until the rank doesn't increase.

ISSUE II: How do we compute A , B , and C from \mathcal{O} and \mathcal{C} ?

ANSWER: Our estimate $\hat{\mathcal{C}}$ of C is extracted as the first block row of \mathcal{O} ; our estimate $\hat{\mathcal{B}}$ of B is extracted as the first block column of \mathcal{C} . We'll see how to get our estimate $\hat{\mathcal{A}}$ of A shortly.

ISSUE III: How do we factor \mathcal{H} into \mathcal{O} and \mathcal{C} ?

ANSWER: It doesn't matter, at least in principle. Any matrices \mathcal{O} and \mathcal{C} such that $\mathcal{O}\mathcal{C} = \mathcal{H}$ are okay.

To see this latter point, consider what happens to \mathcal{O} and \mathcal{C} when the state-space model undergoes a similarity transformation. Recall that $\bar{A} = T^{-1}AT$, $\bar{B} = T^{-1}B$, and $\bar{C} = CT$. The observability and controllability matrices of the new representation are

$$\begin{aligned}\bar{\mathcal{O}} &= \begin{bmatrix} \bar{C} \\ \bar{C}\bar{A} \\ \vdots \\ \bar{C}\bar{A}^{n-1} \end{bmatrix} = \begin{bmatrix} CT \\ CTT^{-1}AT \\ \vdots \\ CT(T^{-1}AT)^{n-1} \end{bmatrix} = \mathcal{O}T \\ \bar{\mathcal{C}} &= \begin{bmatrix} \bar{B} & \bar{A}\bar{B} & \cdots & \bar{A}^{n-1}\bar{B} \end{bmatrix} \\ &= \begin{bmatrix} T^{-1}B & T^{-1}ATT^{-1}B & \cdots & (T^{-1}AT)^{n-1}T^{-1}B \end{bmatrix} = T^{-1}\mathcal{C}.\end{aligned}$$

Therefore, $\bar{\mathcal{O}}\bar{\mathcal{C}} = (\mathcal{O}T)(T^{-1}\mathcal{C}) = \mathcal{O}\mathcal{C}$. If we factor \mathcal{H} one way, we end up with a representation that has one set of \mathcal{O} and \mathcal{C} . If we factor \mathcal{H} any other way, we end up with a representation that has an alternate set of $\bar{\mathcal{O}}$ and $\bar{\mathcal{C}}$. But, these representations are related via a similarity transformation T .

That is, no matter how we factor \mathcal{H} , we end up with different A , B , and C matrices, but the same input–output relationship (same transfer function, same unit-pulse response, but different state descriptions). For example, we could choose to let $\mathcal{O} = I$, and then $\mathcal{C} = \mathcal{H}$. This will result in an A , B , and C that are in *observability canonical form*. Or, we could choose to let $\mathcal{C} = I$, and then $\mathcal{O} = \mathcal{H}$.

This will result in an A , B , and C that are in *controllability canonical form*.

ISSUE IV: Is there a “best” way to factor \mathcal{H} ?

ANSWER: Yes, using the singular value decomposition (SVD). We now review this critical tool.

5.3.2 Singular value decomposition (SVD)

An important result from linear algebra is that any rectangular matrix $A \in \mathbb{R}^{m \times n}$, where $\text{rank}(A) = r$, can be factored into the form

$$A = U\Sigma V^T, \quad (5.11)$$

where

- $U = [u_1, \dots, u_m] \in \mathbb{R}^{m \times m}$, and $U^T U = I$, and u_i are the *left or output singular vectors* of A .
- $V = [v_1, \dots, v_n] \in \mathbb{R}^{n \times n}$, and $V^T V = I$, and v_i are the *right or input singular vectors* of A .
- The matrix $\Sigma \in \mathbb{R}^{m \times n}$ is a (zero-padded) diagonal matrix containing the *singular values* σ_i of the matrix A . That is,

$$\Sigma = \begin{bmatrix} \sigma_1 & & 0 & 0 \\ & \ddots & & 0 \\ 0 & & \sigma_m & 0 \end{bmatrix}, \quad \text{or} \quad \Sigma = \begin{bmatrix} \sigma_1 & & 0 \\ & \ddots & \\ 0 & & \sigma_n \end{bmatrix}, \quad \text{or}$$

$$\Sigma = \begin{bmatrix} \sigma_1 & & 0 \\ & \ddots & \\ 0 & & \sigma_n \\ 0 & 0 & 0 \end{bmatrix},$$

when $m < n$, $m = n$, and $m > n$, respectively, where $\sigma_1 \geq \dots \geq \sigma_r > 0$, and $\sigma_i = 0$ for $i > r$.

The factored form of Eq. (5.11) is called the (full) *singular value decomposition* of the matrix A . In MATLAB, the singular value decomposition is computed via `svd` or `svds`.

We often write the full SVD in partitioned form, with matrix partitions based on the rank r of A :

$$A = \left[\begin{array}{c|c} U_1 & U_2 \end{array} \right] \left[\begin{array}{c|c} \Sigma_1 & \mathbf{0}_{r \times (n-r)} \\ \hline \mathbf{0}_{(m-r) \times r} & \mathbf{0}_{(m-r) \times (n-r)} \end{array} \right] \left[\begin{array}{c} V_1^T \\ V_2^T \end{array} \right],$$

where $A = U_1 \Sigma_1 V_1^T$ is known as the *compact SVD*.

We can view the operation $y = Ax$ as $y = (U\Sigma V^T)x$ by decomposing the operation into (1) computing coefficients of x along the input directions v_1, \dots, v_r (rotating by V^T); (2) scaling the coefficients by σ_i

(dilation); and (3) reconstituting the output along output directions $\mathbf{u}_1, \dots, \mathbf{u}_r$. This is illustrated in Fig. 5.3. Note that \mathbf{v}_1 is the most sensitive (highest gain) input direction and \mathbf{u}_1 is the highest gain output direction. We have $A\mathbf{v}_1 = \sigma_1 \mathbf{u}_1$.

An important result is that the singular values themselves are related to the matrix norm. In particular, the two-norm of a matrix is equal to the maximum singular value of the matrix: $\|A\|_2 = \sigma_1$. Thus, overall, the SVD gives a picture of gain as a function of input/output directions.

As an example, consider $A \in \mathbb{R}^{4 \times 4}$ with $\Sigma = \text{diag}(10, 7, 0.1, 0.05)$. Then, input components along directions \mathbf{v}_1 and \mathbf{v}_2 are amplified (by a factor of about 10) and come out mostly along the plane spanned by \mathbf{u}_1 and \mathbf{u}_2 . Input components along directions \mathbf{v}_3 and \mathbf{v}_4 are attenuated (by a factor of about 10). The gain $\|Ax\|_2 / \|\mathbf{x}\|_2$ can range between 10 and 0.05. Because the gain is always greater than zero, we can also conclude that A is nonsingular. For some applications you might say that A is *effectively* rank 2 (this will be important for us later).

5.3.3 Low-rank approximations via the SVD

Suppose that $A \in \mathbb{R}^{m \times n}$ has $\text{rank}(A) = r$, with SVD $A = U\Sigma V^T = \sum_{i=1}^r \sigma_i \mathbf{u}_i \mathbf{v}_i^T$. We want to approximate A by \hat{A} , where $\text{rank}(\hat{A}) \leq p < r$ such that $\hat{A} \approx A$ in the sense that $\|A - \hat{A}\|_2$ is minimized. Then, the optimal rank p approximant to A is $\hat{A} = \sum_{i=1}^p \sigma_i \mathbf{u}_i \mathbf{v}_i^T$ and hence

$$\|A - \hat{A}\|_2 = \left\| \sum_{i=p+1}^r \sigma_i \mathbf{u}_i \mathbf{v}_i^T \right\|_2 = \sigma_{p+1}$$

because σ_{p+1} is the maximum remaining singular value.

INTERPRETATION: SVD dyads $\mathbf{u}_i \mathbf{v}_i^T$ are ranked in order of “importance”; we take p of them to get a rank p approximant.

APPLICATION: We can use this idea to simplify models.

This latter point is very useful. For example, suppose that $\mathbf{y} = A\mathbf{x} + \mathbf{w}$ where $A \in \mathbb{R}^{100 \times 30}$ has singular values 10, 7, 2, 0.5, 0.01, ..., 0.0001. If $\|\mathbf{x}\|_2$ is on the order of 1, and the unknown error or noise \mathbf{w} has norm on the order of 0.1, then the terms $\sigma_i \mathbf{u}_i \mathbf{v}_i^T \mathbf{x}$ for $i = 5, \dots, 30$ are substantially smaller than the noise term \mathbf{w} . So, we can approximate $\mathbf{y} = A\mathbf{x} + \mathbf{w}$ by the much simplified model $\mathbf{y} = \sum_{i=1}^4 \sigma_i \mathbf{u}_i \mathbf{v}_i^T \mathbf{x} + \mathbf{w}$.

5.3.4 Implementing the Ho–Kalman method

Recall state-space realization “ISSUE 1,” how do we form the Hankel matrix \mathcal{H} if we don’t know the dimension of the system state n ? To

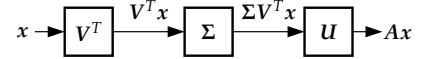


Figure 5.3: Visualizing a matrix multiplication via the SVD of the matrix.

address this issue, consider the infinite, skew-diagonal matrix \mathcal{H}_∞ where

$$\mathcal{H}_\infty = \begin{bmatrix} g_1 & g_2 & g_3 & g_4 & \cdots \\ g_2 & g_3 & g_4 & g_5 & \cdots \\ g_3 & g_4 & g_5 & g_6 & \cdots \\ g_4 & g_5 & g_6 & g_7 & \cdots \\ \vdots & \vdots & \vdots & \vdots & \ddots \end{bmatrix},$$

where the entries g_k correspond to the Markov parameters for the given system. This form is called an *infinite Hankel matrix*, or the *Hankel operator*.

We can also define a finite Hankel matrix, formed by the first k block rows and l block columns of \mathcal{H}

$$\mathcal{H}_{k,l} = \begin{bmatrix} g_1 & g_2 & g_3 & \cdots & g_l \\ g_2 & g_3 & g_4 & \cdots & g_{l+1} \\ g_3 & g_4 & g_5 & \cdots & g_{l+2} \\ \vdots & \vdots & \vdots & & \vdots \\ g_k & g_{k+1} & g_{k+2} & \cdots & g_{k+l-1} \end{bmatrix}.$$

This finite Hankel matrix can be factored into $\mathcal{H}_{k,l} = \mathcal{O}_k \mathcal{C}_l$ where

$$\mathcal{O}_k = \begin{bmatrix} \mathcal{C} \\ \mathcal{C}A \\ \vdots \\ \mathcal{C}A^{k-1} \end{bmatrix}, \quad \mathcal{C}_l = \begin{bmatrix} B & AB & A^2B & \cdots & A^{l-1}B \end{bmatrix}.$$

The approach we will take is to make a $\mathcal{H}_{k,l}$ of larger size than we expect to need for a hypothesized value of n . That is, $k > n$ and $l > n$. Therefore $\mathcal{O}_k \neq \mathcal{O}$ and $\mathcal{C}_l \neq \mathcal{C}$ even though the matrices have the same general form. We call \mathcal{O}_k the *extended observability matrix* and \mathcal{C}_l the *extended controllability matrix*.

We then apply the SVD to $\mathcal{H}_{k,l}$

$$\begin{aligned} \mathcal{H}_{k,l} &= \mathcal{U}\Sigma\mathcal{V}^T = \mathcal{U}\Sigma^{1/2}\Sigma^{1/2}\mathcal{V}^T \\ &= \mathcal{U}\Sigma^{1/2}\mathcal{T}\mathcal{T}^{-1}\Sigma^{1/2}\mathcal{V}^T \\ &= \underbrace{(\mathcal{U}\Sigma^{1/2}\mathcal{T})}_{\mathcal{O}_k} \underbrace{(\mathcal{T}^{-1}\Sigma^{1/2}\mathcal{V}^T)}_{\mathcal{C}_l}. \end{aligned}$$

The factoring of $\mathcal{H}_{k,l}$ into \mathcal{O}_k and \mathcal{C}_l depends on the choice of transformation matrix \mathcal{T} , but the input-output behavior of the resulting model does not depend on \mathcal{T} . The only restriction is that \mathcal{T} must be invertible; we generally choose \mathcal{T} to be the identity matrix, $\mathcal{T} = \mathcal{I}$, for simplicity. This solves “ISSUE III” and “ISSUE IV.”

The system order n can be determined by the number of nonzero singular values. However, “noise” on the unit-pulse response values

that make up $\mathcal{H}_{k,l}$ (even numeric roundoff noise) cause the SVD to have more than n nonzero singular values. So, in practice, we look at the first several singular values and make a judgment where there is a significant drop-off in the magnitude of the singular values, choosing to retain a model having a number of states equal to the number of significant singular values.

We are left with the final question: How to decompose further into (A, B, C) to solve “issue II”?

Note the shift property of a Hankel matrix. If we shift \mathcal{H} up by one block row, we get $\mathcal{H}_{k+1,l}^\uparrow = \mathcal{O}_k A \mathcal{C}_l$.

$$\begin{aligned}\mathcal{H}_{k+1,l}^\uparrow &= \begin{bmatrix} g_2 & g_3 & g_4 & \cdots & g_{l+1} \\ g_3 & g_4 & g_5 & \cdots & g_{l+2} \\ \vdots & \vdots & \vdots & & \vdots \\ g_k & g_{k+1} & g_{k+2} & \cdots & g_{k+l-1} \\ g_{k+1} & g_{k+2} & g_{k+3} & \cdots & g_{k+l} \end{bmatrix} \\ &= \begin{bmatrix} CAB & CA^2B & CA^3B & \cdots & CA^lB \\ CA^2B & CA^3B & CA^4B & & CA^{l+1}B \\ \vdots & \vdots & \vdots & \ddots & \vdots \\ CA^{k-1}B & CA^kB & CA^{k+1}B & \cdots & CA^{k+l-2}B \\ CA^kB & CA^{k+1}B & CA^{k+2}B & \cdots & CA^{k+l-1}B \end{bmatrix} \\ &= \mathcal{O}_{k+1}^\uparrow \mathcal{C}_l = \mathcal{O}_k \mathcal{C}_{l+1}^\leftarrow = \mathcal{O}_k A \mathcal{C}_l.\end{aligned}$$

There are a variety of ways that we can use these relationships to solve for our estimate \hat{A} of A . One of these uses the matrix pseudo-inverse operation, giving $\hat{A} = \mathcal{O}_k^\dagger \mathcal{H}_{k+1,l}^\uparrow \mathcal{C}_l^\dagger$.

In MATLAB, if $0k$ is the extended observability matrix, Cl is the extended controllability matrix, and HankelUp is the shifted Hankel matrix $\mathcal{H}_{k+1,l}^\uparrow$, we can compute either

```
Ahat = pinv(0k)*HankelUp*pinv(Cl);
```

or

```
Ahat = (0k\HankelUp)/Cl;
```

As before, we extract our estimate \hat{B} of B from the first block column of the extended controllability matrix \mathcal{C}_l , we extract our estimate \hat{C} of C from the first block row of the extended observability matrix \mathcal{O}_k , and we set our estimate \hat{D} of D to $\hat{D} = g_0$.

5.3.5 Summary: Algorithm steps for the Ho–Kalman method

The following steps comprise the Ho–Kalman method for converting a discrete unit-pulse response to a state-space representation.

STEP I: Collect the discrete unit-pulse response values into two Hankel matrices: (1) an original finite Hankel matrix $\mathcal{H}_{k,l}$, and (2) a shifted version $\mathcal{H}_{k+1,l}^\uparrow$ of the original Hankel matrix.

STEP II: Compute the SVD of the (unshifted) Hankel matrix $\mathcal{H}_{k,l}$, and identify the system order n as the number of “large” singular values.

STEP III: Compute the extended observability and controllability matrices, using appropriately dimensioned SVD components. (We typically use $T = I$.)

STEP IV: Identify estimates $(\hat{A}, \hat{B}, \hat{C})$ of the system matrices (A, B, C) . Set estimate \hat{D} of D to $\hat{D} = g_0$.

As an example, suppose that a unit-pulse input to some single-input single-output system yields the following response:

$$y = (0, 1, 1, 2, 3, 5, 8, 13, 21, 34, 55, 89, \dots).$$

We recognize this output as the Fibonacci sequence generated by

$g_k = g_{k-1} + g_{k-2}$ with initial conditions $g_0 = 0$ and $g_1 = 1$.

A typical realization for this sequence is given by the state-space system

$$A = \begin{bmatrix} 0 & 1 \\ 1 & 1 \end{bmatrix}, \quad B = \begin{bmatrix} 1 \\ 1 \end{bmatrix}, \quad C = \begin{bmatrix} 1 & 0 \end{bmatrix}, \quad D = 0. \quad (5.12)$$

We'll try to come up with an equivalent realization based on only the unit-pulse response. In MATLAB, we can define this state-space system and find the unit-pulse response as

```
% Define true system, compute the Markov parameters as "y"
A = [0 1; 1 1]; B = [1; 1]; C = [1 0]; D = 0; dt = 1;
sysTrue = ss(A,B,C,D,dt);      % "typical" Fibonacci ss model
y = dt*impulse(sysTrue);       % scale by dt to get unit-pulse response
```

Next, we form the required Hankel matrices, which turn out to be

$$\mathcal{H}_{4,4} = \begin{bmatrix} 1 & 1 & 2 & 3 \\ 1 & 2 & 3 & 5 \\ 2 & 3 & 5 & 8 \\ 3 & 5 & 8 & 13 \end{bmatrix}, \quad \mathcal{H}_{5,4}^\uparrow = \begin{bmatrix} 1 & 2 & 3 & 5 \\ 2 & 3 & 5 & 8 \\ 3 & 5 & 8 & 13 \\ 5 & 8 & 13 & 21 \end{bmatrix}.$$

This was accomplished using the MATLAB code

```
% Form H{4,4} and shifted H{5,4}. Note: Do not include "zero-th"
% parameter (first element of y), which corresponds to the matrix D.
bigHankel = hankel(y(2:end)); % don't forget to omit h(0) term = y(1)
H = bigHankel(1:4,1:4);      % for this example, keep only 4x4 portion
Hup = bigHankel(2:5,1:4);    % shifted H{5,4}
```

The SVD of $\mathcal{H}_{4,4}$ yields

$$\sigma_1 = 54.56, \quad \sigma_2 = 0.43988, \quad \sigma_i = 0, \quad i \geq 3$$

which indicates that $n = 2$. In MATLAB,

```
% Compute singular values of Hankel matrix
[U,S,V] = svd(H);

% Identify system order off-line as n = 2 based on values of S
n = 2;
```

We now extract the two left columns of U and V

$$U = V = \begin{bmatrix} -0.1876 & 0.7947 \\ -0.3035 & -0.4911 \\ -0.4911 & 0.3035 \\ -0.7947 & -0.1876 \end{bmatrix}.$$

We compute the extended controllability and observability matrices

$$\mathcal{C}_l = \Sigma^{1/2} V^T = \begin{bmatrix} -0.8507 & -1.3764 & -2.2270 & -3.6034 \\ 0.5257 & -0.3249 & 0.2008 & -0.1241 \end{bmatrix}$$

$$\mathcal{O}_k = U \Sigma^{1/2} = \mathcal{C}_l^T.$$

In MATLAB,

```
% Compute extended observability and controllability matrices, sized to
% the order for the system inferred by the singular values.
Us = U(:,1:n); Ss = S(1:n,1:n); Vs = V(:,1:n);
Ok = Us*sqrtm(Ss); Cl = sqrtm(Ss)*Vs';
```

Finally, we identify the system matrices $(\hat{A}, \hat{B}, \hat{C})$ up to similarity transform, and \hat{D} from g_0

$$\hat{A} = \mathcal{O}_k^\dagger \mathcal{H}_{k+1,l}^\dagger \mathcal{C}_l^\dagger = \begin{bmatrix} 1.6180 & 0 \\ 0 & -0.6180 \end{bmatrix}$$

$$\hat{B} = \mathcal{C}_l(1:n, 1:m) = \mathcal{C}_l(1:2, 1) = \begin{bmatrix} -0.8057 \\ 0.5257 \end{bmatrix}$$

$$\hat{C} = \mathcal{O}_k(1:p, 1:n) = \mathcal{O}_k(1, 1:2) = \begin{bmatrix} -0.8057 & 0.5257 \end{bmatrix}$$

$$\hat{D} = g_0 = 0.$$

The numeric results above were found using the following MATLAB code:

```
% Identify system assuming p = m = 1 (SISO), using shifted Hankel matrix
Ahat = (Ok\Hup)/Cl; Bhat = Cl(:,1); Chat = Ok(:,1,:); Dhat = y(1);
sysEst = ss(Ahat, Bhat, Chat, Dhat, dt);
```

Now, let's compare the true system of Eq. (5.12) and the identified ("estimated") system. Fig. 5.4 shows the poles and zeros of the true and estimated systems. Both systems have two poles and one zero, and the locations of the estimated system's dynamics are indistinguishable from those of the true system. In Fig. 5.5, we see the unit-pulse responses of the true and estimated system. Again, the two responses cannot be told apart.

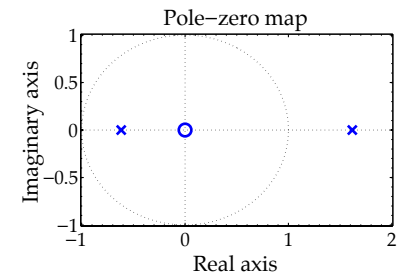


Figure 5.4: Pole-zero map of true and estimated systems for Fibonacci example.

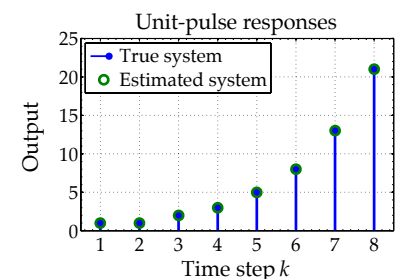


Figure 5.5: Fibonacci sequence example using the Ho-Kalman method.

COMMENTS: Selecting an appropriate amount of output data to store may require iteration (“how big an \mathcal{H} do I need?”). Generally, we would add data until $\text{rank}(\mathcal{H}_{k,l}) = \text{rank}(\mathcal{H}_{k-1,l-1})$, or until the next singular value is “insignificant.”

REMAINING QUESTION: If we start with a generic continuous-time transfer function, from whence come the g_k ? The answer to this question turns out to be the key to applying the Ho–Kalman method to finding a state-space realization for our battery transfer functions. We explore it next.

5.4 Discrete-time realization algorithm (DRA)

Given a (possibly multi-input multioutput) continuous-time transfer function $H(s)$ in the Laplace domain such that $Y(s) = H(s)U(s)$, and a sampling period, T_s , we want to derive a reduced-order discrete-time state-space realization of the form

$$\begin{aligned}\mathbf{x}[k+1] &= \mathbf{A}\mathbf{x}[k] + \mathbf{B}\mathbf{u}[k] \\ \mathbf{y}[k] &= \mathbf{C}\mathbf{x}[k] + \mathbf{D}\mathbf{u}[k].\end{aligned}$$

The method that we develop is called the *discrete-time realization algorithm*, or DRA.¹⁷

A *sufficient* condition for the DRA to operate is that $H(s)$ be an element of the Hardy space \mathcal{H}_∞ , which implies that it is a strictly stable and proper system. This is not a *necessary* condition to be able to find a state-space realization, however, as we will later generalize the method to work with systems having an isolated pole at the origin of the s -plane (i.e., an integrator).

Note that we do not restrict $H(s)$ to be formulated as a quotient of polynomials in the Laplace variable “ s ” (for which well-known methods exist to find the discrete-time system). This is important for us to be able to find realizations for transcendental transfer functions like those in Eqs. (5.9) and (5.10).

For simplicity, we describe the DRA for single-input single-output $H(s)$, but the result may be generalized to multi-input and/or multioutput $H(s)$, as will be needed in the next chapter. We will describe the additional considerations for multi-input multioutput systems in the examples presented then.

The overall DRA process, starting with the continuous-time transfer function $H(s)$ is:

STEP 1: Sample the continuous-time transfer function $H(s)$ in the frequency domain at a high rate, and take the inverse discrete Fourier transform (IDFT) of the samples to get an approximation to the continuous-time impulse response $h(t)$.

¹⁷ This method was first published in Lee, J.L., Chemistruck, A., and Plett, G.L., “Discrete-Time Realization of Transcendental Impedance Functions, with Application to Modeling Spherical Solid Diffusion,” *Journal of Power Sources*, 206, 2012, pp. 367–377. The method developed in this book is identical in all major respects, but varies slightly in some of the details with the aim of improving clarity.

STEP 2: Use $h(t)$ to approximate the continuous-time step response $h_{\text{step}}(t)$, also sampled at the high rate.

STEP 3: Compute the discrete-time unit-pulse response values g_k with inter-sample period T_s from the continuous-time step response $h_{\text{step}}(t)$, assuming a sample and hold circuit connected to the system input.

STEP 4: Generate a discrete-time state-space realization using the deterministic Ho–Kalman algorithm. This algorithm returns the reduced order \hat{A} , \hat{B} , and \hat{C} matrices from the discrete-time unit-pulse response sequence in Step 3. The order of the system is determined from the ordered singular values of the Hankel matrix computed as part of the algorithm. The \hat{D} matrix is found by the initial value theorem.

We note that a transfer function having a pole at the origin does not meet the strictly stable requirement. However, we will also show that this pole can be accounted for automatically.

We now proceed to discuss the sample-and-hold framework, the Ho–Kalman method, and accounting for a possible pole at $s = 0$ in more detail.

5.4.1 Building the DRA from the end to the beginning

STEP 4: We now build the discrete-time realization algorithm in backward order. We start by recognizing that if we know a system’s unit-pulse response, we can use the Ho–Kalman algorithm to find its state-space representation. Therefore, we focus on finding the unit-pulse response.

STEP 3: How do we find the unit-pulse response? Let’s assume that we know the system’s continuous-time step response $h_{\text{step}}(t)$. Then, we can find the unit-pulse response as illustrated in Fig. 5.6. Notice that if a unit-step input results in a unit-step response, then (because of time invariance) a time-shifted unit-step input will result in a time-shifted unit-step response. Here, we consider a time shift equal to T_s , the desired sampling period of the final discrete-time state-space system.

Then, if we use an input equal to the difference between the unit-step function and the time-shifted unit-step function, the output will be the difference between the unit-step response and the time-shifted unit-step response (because of linearity). This modified input is the unit-pulse function of duration T_s , so the modified output must be the unit-pulse response. We sample this continuous-time unit-pulse response every T_s seconds to find the discrete-time unit-pulse response.

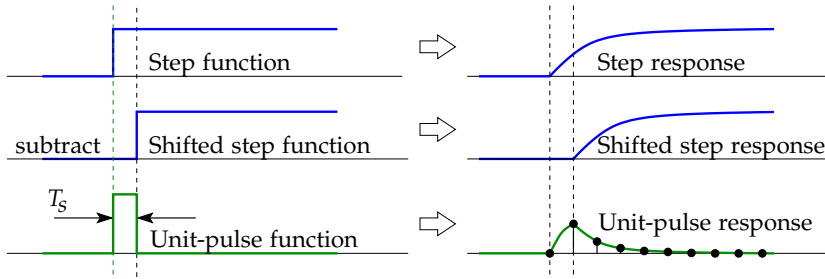


Figure 5.6: Converting a continuous-time step response to a discrete-time unit-pulse response.

That is, the continuous-time response to a unit pulse of length T_s seconds is

$$h_{\text{pulse}}(t) = h_{\text{step}}(t) - h_{\text{step}}(t - T_s),$$

and the discrete-time unit-pulse response is then $g_k = h_{\text{pulse}}(kT_s)$.

STEP 2: So, if we can find the system's continuous-time step response, we can find a discrete-time state-space realization. But, how do we find the continuous-time step response? Let's assume that we know the continuous-time impulse response $h(t)$. Then,

$$h_{\text{step}}(t) = \int_0^t h(\tau) d\tau.$$

In fact, since the DRA is a numeric algorithm, we can't deal with continuous time directly. Instead, we select a fast sample frequency F_1 such that $T_1 = \frac{1}{F_1} \ll T_s$. Then, the finely sampled continuous-time step response is

$$h_{\text{step}}(kT_1) = T_1 \sum_{i=0}^{k-1} h(iT_1).$$

STEP 1: So, if we can find the system's finely sampled continuous-time impulse response, we can find a state-space representation. But, how do we find the finely sampled continuous-time impulse response?

One approach is to approximate the continuous-time impulse response via a "discrete equivalent" method.¹⁸ We use the bilinear transform to write a high-sample-rate discrete-time approximation to the original continuous-time transfer function

$$H(z) \approx H(s)|_{s=\frac{2}{T_1} \frac{z-1}{z+1}},$$

where T_1 is the same emulation sampling period as before.¹⁹

We now recognize that the discrete Fourier transform (DFT) of a sequence is related to its z -transform via the relationship

$$H[f] = H(z) \Big|_{z=\exp(j2\pi f/N)} = H(s) \Big|_{s=\frac{2}{T_1} \left[\frac{e^{j2\pi f/N} - 1}{e^{j2\pi f/N} + 1} \right]}$$

¹⁸ Franklin, G.F., Powell, J.D., and Workman, M., *Digital Control of Dynamic Systems*, 3rd ed., Addison-Wesley, 1998, pp. 187–210.

¹⁹ To arrive at an accurate estimation of the continuous-time transfer function, the sampling frequency $F_1 = 1/T_1$ must be high enough to capture the system dynamics. As a rule of thumb, the sampling frequency must be at least 20 times as great as the bandwidth of the system to get a rough approximation in the frequency domain. A higher emulation sampling frequency gives more accurate results.

$$= H(s)|_{s=\frac{2j}{T_1} \tan(\pi f/N)}, \quad 0 \leq f < N,$$

where N is the number of points chosen for the underlying sequence and is usually chosen to be a power of 2 for efficient computations.

The inverse DFT of $H[f]$ gives $h(nT_1)$, which is the approximation of the continuous-time impulse response at the emulation sampling period, T_1

$$h(nT_1) = \frac{1}{N} \sum_{f=0}^{N-1} H[f] e^{j2\pi f n/N},$$

which is indexed from $n = 0$ to $n = N - 1$.

We can now do the complete conversion from $H(s)$ to a state-space model. We note, though, that while the final discrete-time state-space D matrix is the first Markov parameter, it can often be better found numerically by using the initial value theorem,

$$D = g_0 = h[0] = \lim_{s \rightarrow \infty} H(s).$$

5.5 Step-by-step examples of the DRA

In this section, we look at three examples to illustrate the operation of the DRA. The first two are rational-polynomial transfer functions, which we use because we can calculate the exact solution using other methods. We can then compare the exact solutions to the approximate solutions obtained by the DRA. The third does not have a closed-form solution, but we can use a 1D parabolic-elliptic partial-differential-equation solver to find an accurate near-exact solution against which to compare the DRA solution. We find excellent agreement between the exact solutions and DRA solutions in all cases.

5.5.1 Example 1: Rational-polynomial transfer function

We first apply the DRA method to a simple second-order system:

$$H_1(s) = \frac{s^2 + 20s + 80}{s^2 + 2s + 8}.$$

We require a discrete-time realization with a sampling period of $T_s = 0.1$ seconds.

To begin, we compute the Bode plot for $H_1(s)$ to estimate the system bandwidth, to select an appropriate fast sampling rate T_1 . In MATLAB, we use the following code:

```
omega = linspace(-1,3,100); % create freq. axis in rad/sec
s = 1j*omega; % create s = j*omega
H = (s.^2+20*s+80)./(s.^2+2*s+8); % compute cplx. freq. response
semilogx(omega,20*log10(abs(H))); % display the magnitude response
```

The magnitude response of $H_1(s)$ is shown in Fig. 5.7. We note that the bandwidth is on the order of 3 rad s^{-1} , or about 0.5 Hz.

STEP 1: We select the high-rate sampling frequency $F_1 = 256 \text{ Hz}$, which is (much) greater than 20 times the system bandwidth. The following code samples the transfer function at discrete frequencies, and the inverse DFT yields an approximate continuous-time impulse response.

```

F1 = 256; T1 = 1/F1;                                % Interp. freq. of 256 Hz
minTlen = 6.5;                                     % min. h(t) length in sec.
N = 2^(ceil(log2(minTlen*F1)));                   % # of samples at rate F1
f = 0:N-1;                                         % normalized freq. vector
s = (2j/T1)*tan(pi*f/N);                          % substitution to get Hd[f]
Hd = (s.^2+20*s+80)./(s.^2+2*s+8);               % Hd[f]
hd = real(ifft(Hd)) * F1;                          % approximation to h(t)
td = T1*(0:N-1);                                   % time vector for h(t)
plot(td,hd,'bx','markersize',8); hold on % plot h(t)

H1 = tf([1 20 80],[1 2 8]);                      % true transfer function
[himpTrue,timpTrue] = impulse(H1,5);               % true impulse response
plot(timpTrue,himpTrue,'r'); axis([0 5 -8 23]); % plot on top

```

Fig. 5.8 compares the approximate continuous-time impulse response computed via the inverse DFT to the exact continuous-time impulse response of $H_1(s)$. The two solutions are coincident, showing that the DFT method gives a good approximation to the impulse response.

STEP 2: The approximation to the continuous-time step response is found by doing a cumulative summation of the impulse response. This is accomplished via the MATLAB code:

```

hstep = T1*cumsum(hd);                            % h_s(t)
plot(td,hstep,'bx','markersize',8); hold on       % plot h_s(t)

[hstepTrue,tstepTrue] = step(H1,5);               % true step resp.
plot(tstepTrue,hstepTrue,'r'); axis([0 5 0 15]); % plot on top

```

Fig. 5.9 shows a comparison between the DRA-approximated step response and the true step response of the system. Again, we see excellent agreement between the two signals.

STEP 3: We now resample the continuous-time approximate step response at the final sample rate T_s and compute the discrete-time pulse response as $h_{\text{step}}[k] - h_{\text{step}}[k - 1]$. The MATLAB code to accomplish this is:

```

Ts = 0.1; tdisc = 0:Ts:6.5;                      % final time vector
hdisc = [0 diff(interp1(td,hstep,tdisc))];        % h[k]
stem(tdisc,hdisc,'filled'); hold on

```

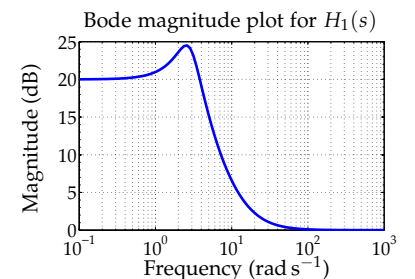


Figure 5.7: Bode magnitude plot for $H_1(s)$.

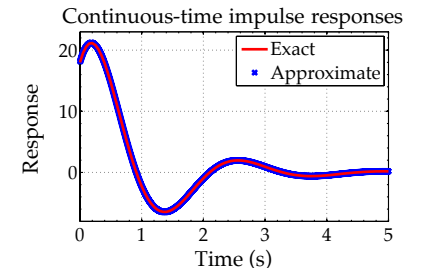


Figure 5.8: Exact and approximate (via DRA Step 1) continuous-time impulse responses for $H_1(s)$.

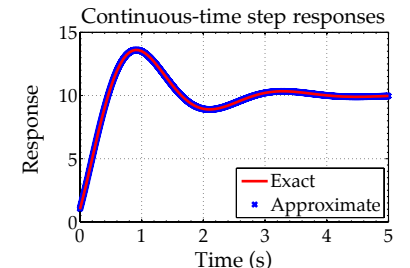


Figure 5.9: Exact and approximate (via DRA Step 2) continuous-time step responses for $H_1(s)$.

```
[himpDiscTrue,timpDiscTrue] = impulse(c2d(H1,Ts),5);
% next line scales IMPULSE in new MATLAB to give unit-pulse resp.
himpDiscTrue = Ts*himpDiscTrue;
plot(timpDiscTrue,himpDiscTrue,'r.','markersize',8);
axis([-0.01 5 -0.8 2.3]);
```

Note that in older versions of MATLAB the `impulse` command computes unit-pulse responses for discrete-time systems; for newer versions of MATLAB, it attempts to approximate a continuous-time impulse response in discrete time, and its output must be scaled by the sampling period T_s to achieve the true unit-pulse response.

Fig. 5.10 shows the comparison between the unit-pulse responses produced by the DRA approximate method and MATLAB's exact method. Again, there is excellent agreement, except at the single point $t = 0$. This is often the case because of some properties of the inverse DFT, but it causes no problems since the unit-pulse response value at $t = 0$ is not used by the Ho–Kalman algorithm in Step 3, and the D matrix (which is equal to the unit-pulse response value at $t = 0$) is computed analytically from $H_1(s)$ as

$$D = g_0 = \lim_{s \rightarrow \infty} H_1(s) = 1.$$

STEP 4: The deterministic Ho–Kalman algorithm is used to find a state-space realization from the approximate discrete-time unit-pulse response from Step 2. Sixty-five points from the discrete-time unit-pulse response are used, which allows a maximum Hankel matrix of 32×32 (allowing for the need to shift one Hankel matrix up by one row). That is, we form $\mathcal{H}_{32,32}$ and $\mathcal{H}_{33,32}^\uparrow$, and then compute and plot the singular values of the Hankel matrix $\mathcal{H}_{32,32}$. Fig. 5.11 shows the singular values on a logarithmic scale, and the following MATLAB code does the computation.

```
bigHankel = hankel(hdisc(2:66)); % don't forget to omit h(0) term!
% for this example, keep only 32x32 portion
Hankel = bigHankel(1:32,1:32);
HankelUp = bigHankel(2:33,1:32); % shifted Hankel matrix
[U, S, V] = svd(Hankel); % compute singular values
plot(log10(diag(S)), 'bx', 'markersize', 8); axis([0 33 -20 5]);
```

The SVD of the Hankel matrix gives insight into the order of the system. We see from the figure that the first two singular values are more than three orders of magnitude greater than the third singular value, so we select a reduced-order model dimension $n = 2$.²⁰

```
n = 2; % select via singular values
Us = U(:,1:n); % Compute extended observability, controllability
Ss = S(1:n,1:n); % matrices, sized to the order for the system
```

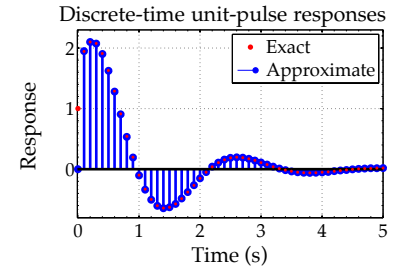


Figure 5.10: Exact and approximate (via DRA Step 3) discrete-time unit-pulse responses for $H_1(s)$.

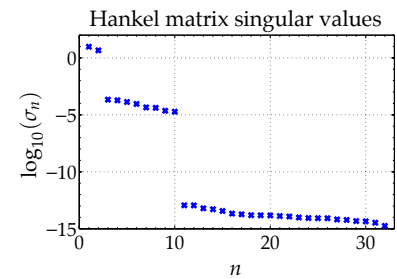


Figure 5.11: The 32 singular values of $\mathcal{H}_{32,32}$ for $H_1(s)$.

²⁰ For this example, we know that the system order is two, so why are the singular values for $n > 2$ not equal to zero as they were for the Fibonacci example? There are two reasons: (1) we are approximating the discrete-time unit-pulse response using the DFT method, and some noise is introduced in this approximation, and (2) numeric precision is not exact, so we would expect some “noise floor” in the computed singular values simply due to roundoff error in floating-point mathematics. Here, reason 1 is most likely the dominant effect, but reason 2 can become more significant when the size of the Hankel matrix is large.

```

Vs = V(:,1:n); % inferred by the singular values.
Ok = Us*sqrtm(Ss); Cl = sqrtm(Ss)*Vs';

Ahat = (Ok\HankelUp)/Cl; % calculate A from Ok and Cl
Bhat = Cl(1:n,1); Chat = Ok(1,1:n); % calculate B and C
Dhat = 1; % calculated manually
sysDRA = ss(Ahat,Bhat,Chat,Dhat,Ts); % final DRA state-space sys.

```

Truncating to the first two states only, the Ho-Kalman algorithm gives a state-space realization with the following estimated \hat{A} , \hat{B} , and \hat{C} matrices

$$\hat{A} = \begin{bmatrix} 0.8529 & -0.2375 \\ 0.2375 & 0.8938 \end{bmatrix}, \quad \hat{B} = \begin{bmatrix} -1.53 \\ 0.6254 \end{bmatrix},$$

$$\hat{C} = \begin{bmatrix} -1.53 & -0.6254 \end{bmatrix}.$$

An estimate of the D matrix is found from the initial value theorem and, for this example, $\hat{D} = \lim_{s \rightarrow \infty} H_1(s) = [1]$. We verify this by examining the high-frequency magnitude response of $H_1(s)$ in Fig. 5.7, which is 0 dB, or 1 in linear units.

We validate the DRA-produced model by looking at the true discrete-time unit-pulse response and the final DRA-model unit-pulse response, as plotted in Fig. 5.12 using the following code:

```

% next line scales IMPULSE in new MATLAB to give unit-pulse resp.
[himpDRA,tempDRA] = impulse(sysDRA,5); himpDRA = Ts*himpDRA;
stem(tempDRA,himpDRA,'filled'); hold on
plot(tempDiscTrue,himpDiscTrue,'r.', 'markersize',8);
axis([-0.01 5 -0.8 2.3]);

```

The figure shows that the final DRA model unit-pulse response agrees very well with the exact unit-pulse response (note that $h[0]$ has been corrected by the explicit calculation of the \hat{D} matrix in Step 4). Because the unit-pulse responses agree very well, the response of the reduced-order model to any input signal $u[k]$ will also agree well with the exact response.

5.5.2 Dealing with one or more poles in $H(s)$ at the origin

The DRA does not work, without modification, for unstable systems. The problem is in Step 1: the continuous-time impulse response must decay to (very close to) zero in the period NT_1 , or else the inverse DFT will seriously alias its approximation to the impulse response. So, an unstable system must be stabilized by removal of the unstable dynamics prior to Step 1; these unstable dynamics can be added back into the final model.

Here, we consider a common case where $H(s)$ has a pole at $s = 0$. This corresponds to integration dynamics, which appear in a number

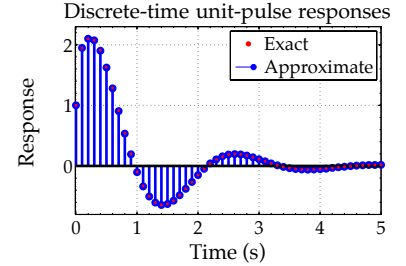


Figure 5.12: Exact and final-model approximate (via DRA Step 4) discrete-time unit-pulse responses for $H_1(s)$.

of our battery transfer functions. We can separate the stable part of $H(s)$ from the integration dynamics by writing

$$H(s) = H^*(s) + \frac{\text{res}_0}{s}.$$

We can find res_0 as $\text{res}_0 = \lim_{s \rightarrow 0} sH(s)$. This limit can often be found analytically (we can do so for all our transfer functions, as we have closed-form representations of them) or numerically by substituting a very small value of s in $sH(s)$.

Then, $H^*(s)$ no longer has the pole at the origin, and we can execute the DRA using it as the starting transfer function. Afterward, we take the state-space system defined by \hat{A} , \hat{B} , \hat{C} , and \hat{D} from the DRA and augment it with dynamics that describe the integration pole that was previously removed.

The discrete-time equivalent to an integrator can be implemented as

$$x_i[k+1] = x_i[k] + T_s u[k].$$

We combine this with the DRA-produced state-space form

$$\begin{aligned} \underbrace{\begin{bmatrix} x[k+1] \\ x_i[k+1] \end{bmatrix}}_{x_{\text{aug}}[k+1]} &= \underbrace{\begin{bmatrix} \hat{A} & \mathbf{0} \\ \mathbf{0} & 1 \end{bmatrix}}_{\hat{A}_{\text{aug}}} \underbrace{\begin{bmatrix} x[k] \\ x_i[k] \end{bmatrix}}_{x_{\text{aug}}[k]} + \underbrace{\begin{bmatrix} \hat{B} \\ T_s \end{bmatrix}}_{\hat{B}_{\text{aug}}} u[k] \\ y[k] &= \underbrace{\begin{bmatrix} \hat{C} & \text{res}_0 \end{bmatrix}}_{\hat{C}_{\text{aug}}} \underbrace{\begin{bmatrix} x[k] \\ x_i[k] \end{bmatrix}}_{x_{\text{aug}}[k]} + D u[k] \end{aligned}$$

where the dotted lines delineate boundaries between block sub-matrices of the overall augmented state-space matrices \hat{A}_{aug} , \hat{B}_{aug} , and \hat{C}_{aug} .

5.5.3 Example 2: Rational-polynomial transfer function with pole at origin

We illustrate this process with a second example. Here, we consider the continuous-time transfer function

$$H_2(s) = \frac{1}{s} \left(\frac{1}{s^2 + 6s + 2} \right).$$

This example is very similar to the first one—so we include MATLAB code only for the steps that are significantly different—but is dissimilar in the sense that it has an unstable integrator pole at $s = 0$. Fig. 5.13 shows the Bode magnitude plot for $H_2(s)$, where the integration dynamics can be observed in that the low-frequency response not converge to a constant value.

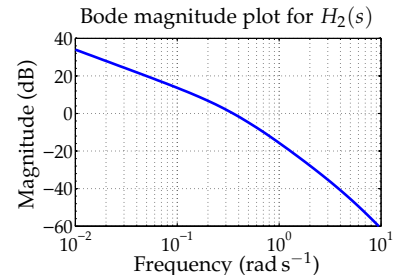


Figure 5.13: Bode magnitude plot for $H_2(s)$.

We desire to create a discrete-time state-space model with a final sampling period of $T_s = 0.5$ s. However, prior to DRA Step 1, we must remove the pole at the origin. This is accomplished by first calculating the residue for this pole. In this example, the residue can be computed analytically as

$$\text{res}_0 = \lim_{s \rightarrow 0} sH(s) = 0.5.$$

The reduced transfer function $H_2^*(s)$ with the pole at the origin removed is

$$H_2^*(s) = \frac{1}{s} \left(\frac{1}{s^2 + 6s + 2} \right) - \frac{0.5}{s}. \quad (5.13)$$

Fig. 5.14 shows the Bode magnitude response of $H_2^*(s)$, where the low-frequency response shows that the integrator has been successfully removed.

STEP 1: $H_2^*(s)$ is sampled at 256 Hz, which is (much) more than 50 times greater than the system bandwidth. When performing this sampling, we have a choice. We could implement it as Eq. (5.13) or via analytically reducing it as

$$\begin{aligned} H_2^*(s) &= \frac{1}{s} \left(\frac{1}{s^2 + 6s + 2} \right) - \frac{0.5}{s} \left(\frac{s^2 + 6s + 2}{s^2 + 6s + 2} \right) \\ &= \frac{-0.5}{s} \left(\frac{s^2 + 6s}{s^2 + 6s + 2} \right) \\ &= -0.5 \left(\frac{s + 6}{s^2 + 6s + 2} \right), \end{aligned} \quad (5.14)$$

and then implementing Eq. (5.14). That is, in DRA Step 1, we could implement either²¹

```
Hd = 1./(s.^3+6*s.^2+2*s) - 0.5./s; % Hd[f]
Hd(1) = -6/4; % analytic solution
```

where $\lim_{s \rightarrow 0} H_2^*(s) = -6/64$, or

```
Hd = -0.5*(s+6)./(s.^2+6*s+2); % Hd[f]
```

Fig. 5.15 compares the approximate continuous-time impulse response computed via the inverse DFT to the exact continuous-time impulse response of $H_2^*(s)$. The two solutions are coincident, except at time $t = 0$, showing that the DFT method gives a good approximation to the impulse response. The spurious single point (which is a property of the DFT when there is a discontinuity in a response) is not of great concern, since the integration in Step 2 eliminates this deviation.

STEP 2: The approximation to the continuous-time step response of $H_2^*(s)$ is calculated as in the first example and plotted in Fig. 5.16.

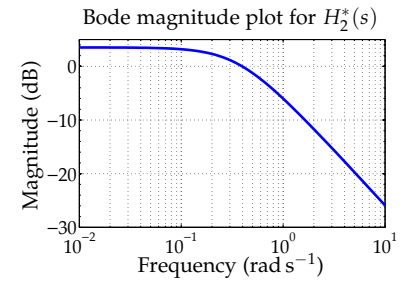


Figure 5.14: Bode magnitude plot for $H_2^*(s)$.

²¹ If we use the first method, we will find that the first element in the vector Hd will be NaN (not-a-number) due to the division by zero when $s = 0$. This has to be specifically corrected by the statement Hd(1) = -6/64.

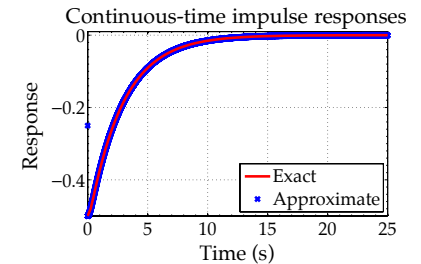


Figure 5.15: Exact and approximate (via DRA Step 1) continuous-time impulse responses for $H_2^*(s)$.

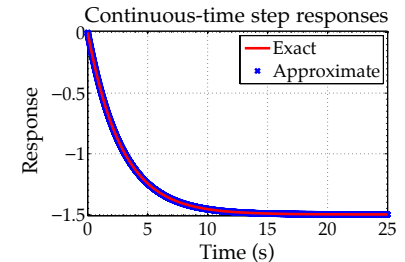


Figure 5.16: Exact and approximate (via DRA Step 2) continuous-time impulse responses for $H_2^*(s)$.

STEP 3: This step response is sampled at $T_s = 0.1$ seconds and differenced to yield the discrete-time unit-pulse response, plotted in Fig. 5.17.

STEP 4: The system Hankel matrix is generated from the discrete-time unit-pulse response found in Step 3. Sixty-four discrete time points are used, resulting in a 32×32 Hankel matrix.

Fig. 5.18 depicts the 32 singular values of the system Hankel matrix. The first two singular values are two orders of magnitude greater than the third, indicating that $H_2^*(s)$ is a second-order system.

The Ho–Kalman algorithm generates the \hat{A} , \hat{B} , and \hat{C} matrices after truncating all but the first two states. We find that

$$\begin{aligned}\hat{A} &= \begin{bmatrix} 0.8394 & 0.03663 \\ -0.03663 & 0.05771 \end{bmatrix}, & \hat{B} &= \begin{bmatrix} 0.4913 \\ -0.05112 \end{bmatrix}, \\ \hat{C} &= \begin{bmatrix} -0.4913 & 0.05112 \end{bmatrix}.\end{aligned}$$

In this example, we also compute $\hat{D} = \lim_{s \rightarrow \infty} H_2^*(s) = 0$, which can also be quite easily seen in the high-frequency response of Fig. 5.14.

This state-space representation for $H_2^*(s)$ is augmented to include the pole at the origin. This is accomplished using the MATLAB code

```
Aaug = [Ahat zeros(n,1); 1 zeros(1,n)];
Baug = [Bhat; Ts];
Caug = [Chat, res0];
sysDRA = ss(Aaug,Baug,Caug,Dhat,Ts) % final DRA state-space sys.
```

The resulting discrete-time realization of $H_2(s)$ is

$$\begin{aligned}\hat{A}_{\text{aug}} &= \begin{bmatrix} 0.8394 & 0.03663 & 0 \\ -0.03663 & 0.05771 & 0 \\ 0 & 0 & 1 \end{bmatrix}, & \hat{B}_{\text{aug}} &= \begin{bmatrix} 0.4913 \\ 0.05112 \\ 0.5 \end{bmatrix}, \\ \hat{C}_{\text{aug}} &= \begin{bmatrix} -0.4913 & 0.05112 & 0.5 \end{bmatrix}, & \hat{D} &= [0].\end{aligned}$$

Fig. 5.19 shows a close comparison of the unit-pulse response found from the DRA-produced model and the exact solution.

5.5.4 Example 3: Transcendental transfer function

In the first two examples, we approximated rational-polynomial transfer functions using the DRA method to illustrate its behavior. For those examples, the order of the system was known *a priori*, and the exact answer could be calculated analytically. We will now demonstrate the DRA with an infinite-order distributed-parameter system, for which the exact answer cannot be calculated analytically, but for which the DRA works just as well.

Specifically we model the Jacobsen–West transfer function of lithium diffusion in a single particle, Eq. (5.9). This transfer function

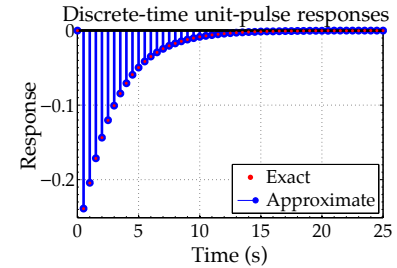


Figure 5.17: Exact and approximate (via DRA Step 3) discrete-time unit-pulse responses for $H_2^*(s)$.

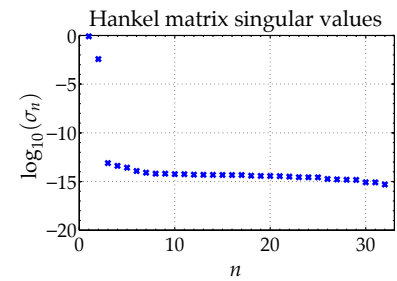


Figure 5.18: The 32 singular values of $\mathcal{H}_{32,32}$ for $H_2^*(s)$.

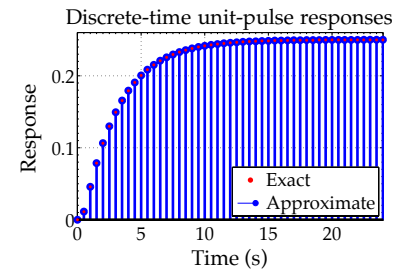


Figure 5.19: Exact and final-model approximate (via DRA Step 4) discrete-time unit-pulse responses for $H_2(s)$.

has a pole at the origin, which can be removed analytically, as given by Eq. (5.10). We repeat these equations here: the Jacobsen–West transfer function is

$$H_3(s) = \frac{\tilde{C}_{s,e}(s)}{J(s)} = \frac{R_s}{D_s} \left[\frac{1}{1 - R_s \sqrt{s/D_s} \coth(R_s \sqrt{s/D_s})} \right],$$

and the integrator-removed transfer function is

$$\begin{aligned} H_3^*(s) &= \frac{\Delta \tilde{C}_{s,e}(s)}{J(s)} = \frac{\tilde{C}_{s,e}(s)}{J(s)} - \frac{\tilde{C}_{s,\text{avg}}(s)}{J(s)} \\ &= \frac{\frac{sR_s^2}{D_s} + 3 - 3R_s \sqrt{\frac{s}{D_s}} \coth\left(R_s \sqrt{\frac{s}{D_s}}\right)}{sR_s \left(1 - R_s \sqrt{\frac{s}{D_s}} \coth\left(R_s \sqrt{\frac{s}{D_s}}\right)\right)}, \end{aligned}$$

where

$$\frac{\tilde{C}_{s,\text{avg}}(s)}{J(s)} = \frac{-\text{res}_0}{s} = \frac{-3/R_s}{s}.$$

Parameter values for the transfer functions used in this example are listed in Table 5.1, from which we can compute that $\text{res}_0 = 3 \times 10^5$.

Parameter name	Interpretation	Value
T_s	Sampling period	1 s
R_s	Particle radius	8×10^{-6} m
D_s	Diffusivity	10^{-12} m ² s ⁻¹
$c_{s,e}(0)$	Initial lithium concentration	10,000 mol m ⁻³

The Bode magnitude plot of $H_3(s)$ is shown in Fig. 5.20. We see that this transfer function has an integrator (pole at $s = 0$) by the low-frequency behavior that does not converge to a flat line, but rather to a slope of -20 dB per decade. We also see curious high-frequency behavior, where the slope is -10 dB per decade. This slope cannot be implemented by a finite number of poles (whose slopes would all be -20 dB per decade) or zeros (whose slopes would all be $+20$ dB per decade), but instead by some combination of poles and zeros that add together in a stair-step method to approximate the slope of -10 dB per decade.

This slope of -10 dB per decade is characteristic of distributed-parameter systems such as diffusion equations. We will see a number of other examples of this in the next chapter, when we develop transfer-function models of lithium-ion battery cells.

The Bode magnitude plot of $H_3^*(s)$ is shown in Fig. 5.21. We see that the integrator has been successfully removed (but that the high-frequency behavior is still characterized by a slope of -10 dB per decade).

Table 5.1: Parameter values used in example 3.

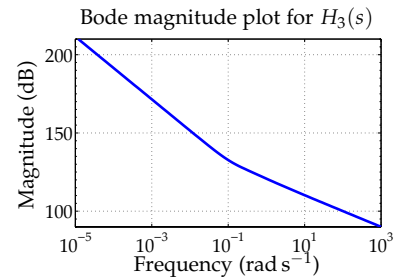


Figure 5.20: Bode magnitude plot for $H_3(s)$.

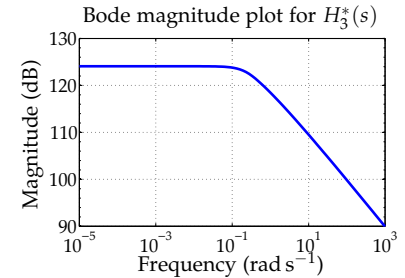


Figure 5.21: Bode magnitude plot for $H_3^*(s)$.

STEP 1: In the first DRA step, we choose the fast sample rate to be 256 Hz, and we sample $H_3^*(s)$ to give an approximate continuous-time impulse response of length 256 s. The frequency vector for $H_3^*(s)$ can be calculated using Eq. (5.9) as

```
beta = Rs*sqrt(s/Ds);
Hd = (Rs/Ds)*(1./(1-beta.*coth(beta))) + (3/Rs)./s;
Hd(1) = -Rs/(5*Ds); % analytic solution
```

where MATLAB numerically removes the integrator pole, or using Eq. (5.10)

```
beta = Rs*sqrt(s/Ds);
Hd = (beta.^2+3-3*beta.*coth(beta))./(s.*Rs.*(1-beta.*coth(beta)));
Hd(1) = -Rs/(5*Ds); % analytic solution
```

Note that both computations of Hd initially produce NaN for $s = 0$ due to numeric attempts to evaluate zero divided by zero. This entry must be manually replaced by a value computed analytically

$$\lim_{s \rightarrow 0} H_3^*(s) = \lim_{s \rightarrow 0} \frac{\frac{sR_s^2}{D_s} + 3 - 3R_s \sqrt{\frac{s}{D_s}} \coth\left(R_s \sqrt{\frac{s}{D_s}}\right)}{sR_s \left(1 - R_s \sqrt{\frac{s}{D_s}} \coth\left(R_s \sqrt{\frac{s}{D_s}}\right)\right)} = -\frac{R_s}{5D_s}.$$

This limit is quite difficult to find by hand, as a direct computation returns 0/0. We must use l'Hôpital's rule repeatedly (in this case, five times) until an answer is reached. When using transcendental transfer functions, we recommend computer tools such as Mathematica for symbolic manipulation.

This approximate continuous-time impulse response is shown in Fig. 5.22. Note that since there is no way to solve for this impulse response exactly, we can show only the DRA-approximated response.

STEP 2: The approximate continuous-time step response is calculated by performing a cumulative sum of the impulse response of Step 1. Fig. 5.23 shows the approximation of the continuous-time step response. Again, there is no known exact solution to the continuous-time step response for this system against which to compare this result.

STEP 3: The approximate continuous-time step response is sampled at $T_s = 1$ second and differenced to produce the discrete-time unit-pulse response, shown in Fig. 5.24.

STEP 4: The Hankel matrix is formed, and its singular values are plotted in Fig. 5.25. $H_3^*(s)$ represents a distributed-parameter system that actually has an infinite number of poles. However, we see from this plot that only a few of these poles are significant to the solution. In particular, we choose to use a reduced-order model dimension

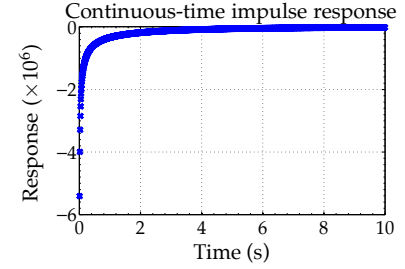


Figure 5.22: DRA-approximated impulse response for $H_3^*(s)$.

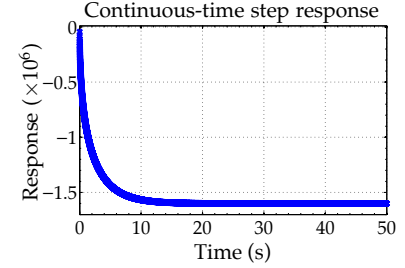


Figure 5.23: DRA-approximated step response for $H_3^*(s)$.

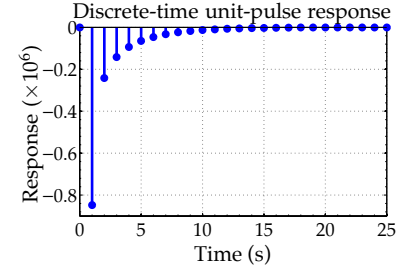


Figure 5.24: DRA-approximated unit-pulse response for $H_3^*(s)$.

$p = 2$ in the results we present here. This demonstrates a tradeoff between the complexity and accuracy of the solution.

The Ho–Kalman algorithm generates the \hat{A} , \hat{B} , and \hat{C} matrices to approximate $H_3^*(s)$ after truncating all but the first two states. We find that

$$\begin{aligned}\hat{A} &= \begin{bmatrix} 0.3808 & 0.3073 \\ 0.3073 & 0.4091 \end{bmatrix}, & \hat{B} &= \begin{bmatrix} 909.4 \\ -145.3 \end{bmatrix}, \\ \hat{C} &= \begin{bmatrix} -909.4 & 145.3 \end{bmatrix}.\end{aligned}$$

In this example, we also compute $\hat{D} = \lim_{s \rightarrow \infty} H_3^*(s) = 0$, which can also be quite easily seen in the high-frequency response of Fig. 5.21.

This state-space realization is augmented with the integrator state to give the final third-order state-space model of the diffusion equation $H_3(s)$. The final realization is given by

$$\begin{aligned}\hat{A}_{\text{aug}} &= \begin{bmatrix} 0.3808 & 0.3073 & 0 \\ 0.3073 & 0.4091 & 0 \\ 0 & 0 & 1 \end{bmatrix}, & \hat{B}_{\text{aug}} &= \begin{bmatrix} 909.4 \\ -145.3 \\ 1 \end{bmatrix}, \\ \hat{C}_{\text{aug}} &= \begin{bmatrix} -909.4 & 145.3 & -3.75 \times 10^5 \end{bmatrix}, & \hat{D} &= [0].\end{aligned}$$

We demonstrate the accuracy of the DRA-produced model by simulating a 10-second discharge pulse where the surface lithium flux (leaving the particle) was $j = 1 \times 10^{-5} \text{ mol m}^{-2} \text{ s}^{-1}$, followed by a 10-second rest. The augmented state-space model was simulated with this input to produce $\tilde{c}_{s,e}[k]$, and $c_{s,e}[k]$ was computed as $c_{s,e}[k] = \tilde{c}_{s,e}[k] + c_{s,0}$. The following MATLAB code was used:

```
cs0 = 10000;
uk = 1e-5*[ones(1,10),zeros(1,10)];
[cseTilde,tk] = lsim(sysDRA,uk);
cse = cseTilde + cs0;
```

We compare this approximate result against a “true” result produced by simulating the differential equation using MATLAB’s 1D parabolic-elliptic partial differential equation solver. The following code was used:

```
function [cse,t] = simCsePDE
dr = 0.1e-6; % Radial resolution = 0.1 micro-meter
dt = 0.001; % Time step in simulation, s
Tfinal = 20; % Length of simulation, s
Rp = 8e-6; % Radius of particle = 10 micro-meters
Ds = 1e-12; % Solid diffusivity, m^2/s
j = 1e-5; % mol/m^2/s

x = 0:dr:Rp; % locations for solution
t = 0:dt:Tfinal; % time steps for solution

options = odeset('RelTol',1e-8,'AbsTol',1e-10);
sol = pdepe(2,@csefun,@cseic,@csebc,x,t,options);
```

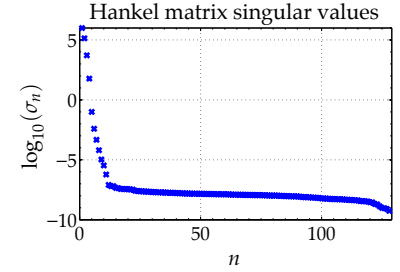


Figure 5.25: The 128 singular values of $\mathcal{H}_{128,128}$ for $H_3^*(s)$.

```

cse = sol(:,end,1);

function[c,f,s] = csefun(~,~,~,DuDx)
  c = 1/Ds; f = DuDx; s = 0;
end

function u0 = cseic(~,~)
  c0 = 10000; u0 = c0;
end

function[pl,ql,pr,qr] = csebc(~,~,~,~,~,t)
  pl = 0; ql = 1; qr = Ds; pr = 0;
  if t<Tfinal/2, pr=j; end
end

end

```

The code comprises nested functions, where the main function initializes variables and calls MATLAB's solver with pointers (function handles) to nested helper functions: `csefun` implements the parameter values of the PDE; `cseic` implements the initial conditions; and `csebc` implements the boundary conditions. Note that we achieve good results with the PDE solver only if a fine time step is used: here, we have used a 1 ms step size, which makes the PDE solver execute much more slowly than the DRA-produced model.

Fig. 5.26 compares the exact PDE solution with the DRA-model solution. We see that the third-order DRA model results agree very closely with the PDE solution at the sampling points. Somewhat greater accuracy could be obtained from the DRA model by retaining more singular values from the Hankel matrix, but at the cost of higher computational complexity of the final model.

5.6 Eigensystem realization algorithm (ERA)

We have seen that the DRA is a very effective way to convert a continuous-time transfer function into an approximate reduced-order discrete-time state-space model. With some practice in selecting T_1 , N , T_s , and the number of singular values retained by the Ho–Kalman method, the discrete-time model can produce results indistinguishable from the original continuous-time counterpart.

In some situations, however, we find that the required final sample period T_s is quite small relative to the duration of the impulse response of the system being modeled. This requires that T_1 be similarly small for the interpolation in Step 3 to be accurate, and it requires N to be large to capture the duration of the impulse response. The effect of these is that the Hankel matrices produced in Step 4 can be *very* large, and the process of finding the singular values of the unshifted Hankel matrix can become intractable.

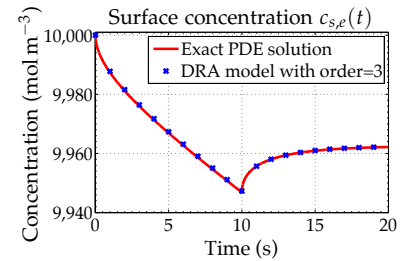


Figure 5.26: Comparing reduced-order DRA final model to exact PDE simulation.

This problem can be alleviated, in part, by using the `svds` command in MATLAB instead of the `svd` command to find the singular values of the Hankel matrix. While `svd` finds all of the singular values of the matrix (most of which we end up discarding), `svds` finds only the n most significant singular values, where n is a parameter specified by the user. This speeds up the operation greatly when an idea of the maximum model size that might be of interest is known a priori.

This modification may still not be enough; that is, MATLAB may run out of memory when computing the singular values, or the computation may take too long to be tractable.

The solution to this problem can be found in an extension to the Ho–Kalman method, first applied to the identification of the dynamics of flexible structures by Juang and Pappa.²² In their application, they wished to identify a realization (\hat{A} , \hat{B} , \hat{C} , and \hat{D}) and then to determine a continuous-time model of the modes (eigenvalues of the continuous-time \hat{A} matrix) from that. They called their algorithm the *Eigensystem Realization Algorithm* (ERA) because it results in an eigensystem (i.e., a modal description of the system). Here, we are interested in only the first part of the algorithm, the realization part, but we still refer to only the first part as the ERA.

The major feature of the ERA that is of interest to us is that it is able to deal with faulty sensors or incomplete unit-pulse-response data. In the original application, the authors were concerned with cases where the measured unit-pulse response was corrupted by saturation of the sensors, data dropout from a communications link, an intermittent bit failure, or an external noise source that temporarily affected the data measured by the system. Their ERA still uses a Hankel-matrix approach that bears a great deal of similarity to Ho–Kalman, but it allows removing rows and columns from the Hankel matrix that correspond to “bad” data. In our application, we don’t need to remove corrupted unit-pulse-response data; however, the ERA allows us to remove from the Hankel matrices long segments of the unit-pulse response that don’t contain much information, thus greatly reducing the size of the matrices and making the computations possible.

To define the ERA, we begin by forming an $r \times s$ generalized Hankel matrix

$$\mathcal{H}_{r,s}[k-1] = \begin{bmatrix} \mathbf{g}_k & \mathbf{g}_{k+t_1} & \cdots & \mathbf{g}_{k+t_{s-1}} \\ \mathbf{g}_{j_1+k} & \mathbf{g}_{j_1+k+t_1} & \cdots & \mathbf{g}_{j_1+k+t_{s-1}} \\ \vdots & \vdots & & \vdots \\ \mathbf{g}_{j_{r-1}+k} & \mathbf{g}_{j_{r-1}+k+t_1} & \cdots & \mathbf{g}_{j_{r-1}+k+t_{s-1}} \end{bmatrix}_{rp \times ms}$$

where j_k ($k = 1, \dots, r-1$) and t_k ($k = 1, \dots, s-1$) are arbitrary

²²Juang, J.N., and Pappa, R.S., “Eigen-system Realization Algorithm for Modal Parameter Identification and Model Reduction,” *Journal of Guidance, Control, and Dynamics*, 8(5), 1985, pp. 620–27.

integers. Note that this is the same as the Hankel matrix used by the Ho–Kalman method, except that we have deleted all *block* rows and all *block* columns that have “bad” data in them. We will assume that $\mathcal{H}_{r,s}[0]$ (which starts with g_1) and $\mathcal{H}_{r,s}[1]$ (which starts with g_2) are available.

We now define *generalized controllability* and *observability matrices*

$$\mathcal{C}_s = \begin{bmatrix} \mathbf{B}, & \mathbf{A}^{t_1} \mathbf{B}, & \dots, & \mathbf{A}^{t_{s-1}} \mathbf{B} \end{bmatrix}_{n \times ms}, \quad \mathcal{O}_r = \begin{bmatrix} \mathbf{C} \\ \mathbf{C} \mathbf{A}^{j_1} \\ \vdots \\ \mathbf{C} \mathbf{A}^{j_r-1} \end{bmatrix}_{rp \times n}.$$

With these definitions, we note that $\mathcal{H}_{r,s}[k] = \mathcal{O}_r \mathbf{A}^k \mathcal{C}_s$. In particular, $\mathcal{H}_{r,s}[0] = \mathcal{O}_r \mathcal{C}_s$ and $\mathcal{H}_{r,s}[1] = \mathcal{O}_r \mathbf{A} \mathcal{C}_s$.

The method for finding a realization is similar to Ho–Kalman. We first take the compact SVD of $\mathcal{H}_{r,s}[0]$:

$$\mathcal{H}_{r,s}[0] = \mathbf{U} \Sigma \mathbf{V}^T,$$

where $\mathbf{U} \in \mathbb{R}^{rp \times n}$, $\mathbf{V} \in \mathbb{R}^{ms \times n}$, and $\Sigma = \text{diag}(\sigma_1, \dots, \sigma_n)$. As with Ho–Kalman, we set $\mathcal{O}_r = \mathbf{U} \Sigma^{1/2}$ and $\mathcal{C}_s = \Sigma^{1/2} \mathbf{V}^T$.

We then set $\widehat{\mathbf{B}}$ to be the left block column of \mathcal{C}_s , $\widehat{\mathbf{C}}$ to be the top block row of \mathcal{O}_r , and $\widehat{\mathbf{D}} = g_0$. Finally, we set $\widehat{\mathbf{A}} = \mathcal{O}_r^\dagger \mathcal{H}_{r,s}[1] \mathcal{C}_s^\dagger$.

As an example consider again the Fibonacci sequence from page 193. This time, the pulse-response experiment yields the following outputs

$$y = (0, 1, 1, 2, 32.12, 724.1, 87.4, 13, 21, 34, 55, 89, 144, 233, 377, 610 \dots)$$

The float-valued quantities in entries y_4, y_5, y_6 are suspicious (all others are integers) and thus will be discarded (label them *).

$$y = (0, 1, 1, 2, *, *, 13, 21, 34, 55, 89, 144, 233, 377, 610 \dots)$$

We can immediately set $\widehat{\mathbf{D}} = g_0 = 0$. We can then form a 7×9 Hankel matrix from g_k , $k > 0$:

$$\mathcal{H}_{7,9} = \begin{bmatrix} 1 & 1 & 2 & * & * & * & 13 & 21 & 34 \\ 1 & 2 & * & * & * & 13 & 21 & 34 & 55 \\ 2 & * & * & * & 13 & 21 & 34 & 55 & 89 \\ * & * & * & 13 & 21 & 34 & 55 & 89 & 144 \\ * & * & 13 & 21 & 34 & 55 & 89 & 144 & 233 \\ * & 13 & 21 & 34 & 55 & 89 & 144 & 233 & 377 \\ 13 & 21 & 34 & 55 & 89 & 144 & 233 & 377 & 610 \end{bmatrix}.$$

To remove the suspect data, we could delete rows 2 through 6 and columns 3 through 6. This corresponds to index sets: $j_k = \{6, 7, 8\}$ and $t_k = \{1, 6, 7\}$.

This deletion leaves us with 4×4 Hankel matrices²³

$$\mathcal{H}_{r,s}[0] = \begin{bmatrix} g_1 & g_2 & g_7 & g_8 \\ g_7 & g_8 & g_{13} & g_{14} \\ g_8 & g_9 & g_{14} & g_{15} \\ g_9 & g_{10} & g_{15} & g_{16} \end{bmatrix} = \begin{bmatrix} 1 & 1 & 13 & 21 \\ 13 & 21 & 233 & 377 \\ 21 & 34 & 377 & 610 \\ 34 & 55 & 610 & 987 \end{bmatrix}$$

$$\mathcal{H}_{r,s}[1] = \begin{bmatrix} g_2 & g_3 & g_8 & g_9 \\ g_8 & g_9 & g_{14} & g_{15} \\ g_9 & g_{10} & g_{15} & g_{16} \\ g_{10} & g_{11} & g_{16} & g_{17} \end{bmatrix} = \begin{bmatrix} 1 & 2 & 21 & 34 \\ 21 & 34 & 377 & 610 \\ 34 & 55 & 610 & 987 \\ 55 & 89 & 987 & 1,597 \end{bmatrix}.$$

²³ Note that $\mathcal{H}_{r+1,s}^\uparrow[0] \neq \mathcal{H}_{r,s}[1]$, which is why we needed to change how we denote of the Hankel matrix from that used when describing the Ho–Kalman method.

The following MATLAB code also produces these matrices

```
% Store the Markov parameters
y = [0,1,1,2,32.12,724.1,87.4,13,21,34,55,89,144,233,377,610,987,1597];

% Form modified Hankel matrices.
% Note: Do not include "zero-th" parameter (first element of y).
% Corresponds to the matrix D.
j = [0 6 7 8]; % Pad "j" and "t" with "0" at front to make loop
t = [0 1 6 7]; % that makes Hankel matrices easier to code
H0 = zeros(length(j),length(t)); H1 = H0;
for ind1 = 1:length(t)
    for ind2 = 1:length(j)
        H0(ind2,ind1) = y(t(ind1)+j(ind2)+2);
        H1(ind2,ind1) = y(t(ind1)+j(ind2)+3);
    end
end
```

Once the modified Hankel matrices are formed, they are processed as follows:

```
% Step 1: Compute singular values of Hankel matrix
[U,S,V] = svd(H0);

% [Identify system order off-line as n = 2 based on values of S]
n = 2;

% Step 2: Compute extended observability and controllability matrices,
% sized to the order for the system inferred by the singular values.
Us = U(:,1:n); Ss = S(1:n,1:n); Vs = V(:,1:n);
Or = Us*sqrtm(Ss); Cs = sqrtm(Ss)*Vs';

% Step 3: Identify the system assuming p = m = 1 (SISO), using the
% shifted Hankel matrix
Ahat = (Or\H1)/Cs; Bhat = Cs(:,1); Chat = Or(1,:); Dhat = y(1);
```

When this code is executed, the SVD of $\mathcal{H}_{r,s}[0]$ yields

$$\sigma_1 = 1,436.6 \quad \sigma_2 = 0.326 \quad \sigma_i = 0, \quad i \geq 3,$$

which indicates that $n = 2$. Note that the split of SVD magnitude has dramatically changed.

We now extract the two left columns of U and V

$$U = \begin{bmatrix} -0.0172 & 0.9976 \\ -0.3090 & 0.0450 \\ -0.4999 & -0.0516 \\ -0.8089 & -0.0066 \end{bmatrix}, \quad V = \begin{bmatrix} -0.0293 & 0.8493 \\ -0.0473 & -0.5249 \\ -0.5249 & 0.0473 \\ -0.8493 & -0.0293 \end{bmatrix}.$$

Again, note that U no longer equals V .

The generalized observability and controllability matrices are

$$\mathcal{O}_r = U \Sigma^{1/2} = \begin{bmatrix} -0.6526 & 0.5696 \\ -11.7109 & 0.0257 \\ -18.9487 & -0.0294 \\ -30.6596 & -0.0037 \end{bmatrix}$$

$$\mathcal{C}_s = \Sigma^{1/2} V^T = \begin{bmatrix} -1.1090 & -1.7939 & -19.8959 & -32.1922 \\ 0.4849 & -0.2997 & 0.0270 & -0.0167 \end{bmatrix}.$$

Using this result, we identify the system matrices \hat{A} , \hat{B} , and \hat{C}

$$\hat{A} = \mathcal{O}_r^\dagger \mathcal{H}_{r,s}[1] \mathcal{C}_s^\dagger = \begin{bmatrix} 1.6180 & 0.0012 \\ 2.6275 \times 10^{-7} & -0.6180 \end{bmatrix}$$

$$\hat{B} = \mathcal{C}_s(1 : n, 1 : m) = \mathcal{C}_s(1 : 2, 1) = \begin{bmatrix} -1.1090 \\ 0.4849 \end{bmatrix}$$

$$\hat{C} = \mathcal{O}_r(1 : p, 1 : n) = \mathcal{O}_r(1, 1 : 2) = \begin{bmatrix} -0.6526 & 0.5696 \end{bmatrix}.$$

These system matrices are quite different from those computed in the Ho–Kalman example, but give identical transfer function, unit-pulse response, and pole-zero mapping. This is illustrated in Fig. 5.27, where the unit-pulse responses of the true and estimated (using the ERA) system are drawn. Note that this figure is indistinguishable from Fig. 5.5, which was created using the Ho–Kalman algorithm instead.

When using the ERA as part of the DRA, the only change is to replace the Ho–Kalman code in Step 4 with code to implement the ERA instead. The index vectors j_k and t_k must be chosen to capture the essence of the unit-pulse response without requiring all samples. In our experience that means keeping all the first samples until the response decays to a nearly exponential shape, and then short segments of the response until it becomes vanishingly small.

5.7 Where to from here?

We have now introduced the discrete-time state-space form, which is the form that our final model of a battery cell will take. We have also seen our first example of a battery-related transcendental transfer

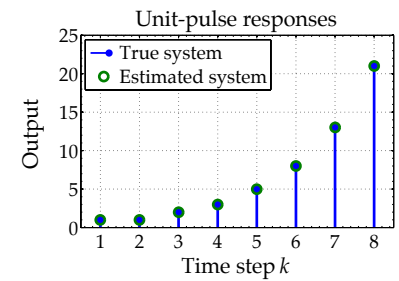


Figure 5.27: Fibonacci sequence example using ERA algorithm.

function, and have developed the discrete-time realization algorithm as a method for converting from a continuous-time transcendental transfer function into a discrete-time state-space form. An example of a diffusion equation, which will also be important in the next chapter, shows that the DRA-produced final model very accurately approximates the PDE solution, but at a much lower computational complexity.

The next step is to develop transfer function models for all cell variables of interest. We will then use the DRA to convert these into a lithium-ion cell model that can predict cell voltage as well as cell internal variables. We will then show, via simulation, that the DRA-produced final reduced-order model of a lithium-ion cell agrees very closely with the full-order model simulated in COMSOL.

5.8 Partial glossary

This section gives a glossary of the most important variables defined in this chapter.

- $\mathbf{0}_{k \times l}$ is a matrix comprising k rows and l columns, where every matrix entry is zero.
- \mathbf{A} is the *state transition matrix* of a discrete-time state-space model form (cf. p. 175).
- $\hat{\mathbf{A}}$ is an estimate of \mathbf{A} .
- \mathbf{A}_c is the *state transition matrix* of a continuous-time state-space model form (cf. p. 174).
- \mathbf{B} is the *input matrix* of a discrete-time state-space model form (cf. p. 175).
- $\hat{\mathbf{B}}$ is an estimate of \mathbf{B} .
- \mathbf{B}_c is the *input matrix* of a continuous-time state-space model form (cf. p. 174).
- \mathbf{C} is the *output matrix* of a discrete-time state-space model form (cf. p. 175).
- \mathbf{C} is the *controllability matrix* of a state-space model form. It has 1 block row and n block columns, where n is the dimension of the state vector \mathbf{x} (cf. p. 187).
- $\hat{\mathbf{C}}$ is an estimate of \mathbf{C} .
- \mathbf{C}_c is the *output matrix* of a continuous-time state-space model form (cf. p. 174).
- \mathbf{C}_l is the *extended controllability matrix* of a state-space model form. It has 1 block row and l block columns, where l is generally greater than the dimension of the state vector \mathbf{x} (cf. p. 191).

- $c_{s,0}$ is the initial equilibrium set-point value for lithium concentration in a solid particle (cf. p. 183).
- $\tilde{c}_s(r, t)$ is the debiased lithium concentration: $\tilde{c}_s(r, t) = c_s(r, t) - c_{s,0}$ (cf. p. 183).
- D is the *feedthrough matrix* of a discrete-time state-space model form (cf. p. 175).
- \hat{D} is an estimate of D .
- D_c is the *feedthrough matrix* of a continuous-time state-space model form (cf. p. 174).
- g_k are the *Markov parameters* of a discrete-time state-space model form. For single-input single-output systems, they comprise the set of discrete-time pulse-response values. For multi-input and/or multioutput systems, they are generalized versions of pulse-response values (cf. p. 181).
- $H(s)$ is the Laplace-domain *transfer function* of a continuous-time linear time-invariant system.
- $H(z)$ is the *z-domain transfer function* of a discrete-time linear time-invariant system.
- \mathcal{H} is the *Hankel matrix* of a state-space model form. It has n block rows and n block columns (cf. p. 187).
- $\mathcal{H}_{k,l}$ is an *extended Hankel matrix* of a state-space model form. It has k block rows and l block columns (cf. p. 191).
- \mathcal{H}_∞ is the *infinite Hankel matrix* or *Hankel operator* of a state-space model form. It has an infinite number of block rows and block columns (cf. p. 191).
- $h(t)$ is the *impulse response* of a continuous-time system (cf. p. 174).
- $h_{\text{pulse}}(t)$ is the *unit-pulse response* of a continuous-time system for a pulse duration of T_s (cf. p. 197).
- $h_{\text{step}}(t)$ is the *step response* of a continuous-time system (cf. p. 197).
- I is the *identity matrix*. It is always square.
- \mathcal{O} is the *observability matrix* of a state-space model form. It has n block rows and 1 block column, where n is the dimension of the state vector x (cf. p. 187).
- \mathcal{O}_k is the *extended observability matrix* of a state-space model form. It has k block rows and 1 block column, where k is generally greater than the dimension of the state vector x (cf. p. 191).
- Σ is a matrix containing the *singular values* of a singular-value decomposition of a matrix (cf. p. 189).
- σ_i is the i th singular value of a matrix (cf. p. 189).

- U is a matrix containing the *left* or *output singular vectors* of a singular-value decomposition of a matrix (cf. p. 189).
- u is the *input signal* to a state-space model form (cf. p. 175).
- V is a matrix containing the *right* or *input singular vectors* of a singular-value decomposition of a matrix (cf. p. 189).
- x is the *state vector* of a state-space model form (cf. p. 175).
- y is the *output signal* from a state-space model form (cf. p. 175).

6

Reduced-Order Models

To see the progress we've made, we encourage you to look back to Fig. 3.1. We've studied equivalent-circuit-based empirical models, which had the advantage of simplicity, but had the disadvantage of not being able to produce predictions of internal cell behaviors. Turning to physics-based modeling approaches, we've developed microscale homogeneous-material models, and we've used volume-averaging techniques to convert them to continuum-scale coupled PDE models.

These models are still too complex to use in an embedded-system type of application. They must be simplified. But, now we know an approach to doing so: we've seen how to convert a continuous-time and space PDE to a discrete-time ODE via finding transfer functions and using the discrete-time realization algorithm. We will now extend this method to make a simple coupled ODE model of all the internal cell behaviors that we might care to monitor.

The focus of this chapter, then, is to develop transfer functions for all internal cell variables of interest, run the DRA on these transfer functions, and verify the results.

6.1 A one-dimensional model of $j^{neg}(z, t)$

In Chap. 5, we derived a transfer function, $\tilde{C}_{s,e}(s)/J(s)$, that allows us to compute the lithium surface concentration $c_{s,e}(t)$ for a single particle if we know the local value of lithium flux at that point, $j(t)$. By implementing this transfer function in a reduced-order model created by the DRA, we have transformed the infinite-order radial pseudo dimension into a small finite-order ODE. However, we still need an infinite set of these ODEs if we are to solve for lithium surface concentration at every x coordinate in the cell!

In this chapter, we look at ways to make a one-dimensional reduced-order cell model. The outcome of this process will be a small finite-order ODE that is able to compute all cell variables of interest at

6.1	1D model of $j^{neg}(z, t)$	217
6.2	1D model of $\tilde{c}_{s,e}^{neg}(z, t)$	225
6.3	1D model of $\tilde{\phi}_s^{neg}(z, t)$	226
6.4	j^{pos} , $\tilde{c}_{s,e}^{pos}$, and $\tilde{\phi}_s^{pos}$	227
6.5	1D model of $c_e(x, t)$	229
6.6	1D model of $\tilde{\phi}_e(x, t)$	241
6.7	T.F. summary	244
6.8	Computing cell voltage	246
6.9	Frequency response	248
6.10	Multioutput DRA	249
6.11	Full cell model	252
6.12	Simulation example	253
6.13	Model blending	256
6.14	Where to from here?	266
6.15	Modal-solution code	266
6.16	Partial glossary	269

any desired set of x locations in the cell. To do so, we will first find transfer functions for each variable since, once we have the transfer functions, we already know how to convert them to a discrete-time reduced-order state-space system using the DRA.

We follow the approach first proposed by Lee et al.¹ with some minor modifications to the nomenclature to clarify presentation. Lee's work, in turn, was inspired by the pioneering work of Smith et al., who derived transfer functions for the first several variables of interest.² Lee et al. developed additional transfer functions for the variables that were not considered by Smith, and showed how all transfer functions could be implemented via the DRA.

Because we are now considering a model for the entire cell rather than a single electrode or point in an electrode, we must be very careful to specify the cell region for which a particular result applies and the cell region from which a particular parameter value is taken. When appropriate in the equations we develop, we will use superscript "neg" to denote a negative-electrode quantity; "sep" to denote a separator quantity; and "pos" to denote a positive-electrode quantity.

We will initially focus on modeling the cell's internal variables for the negative electrode. We will omit the superscript "neg" until the final result is obtained so that the presentation is not overly cluttered. However, the reader should understand that all variables and constants in the next sections refer to negative-electrode quantities. We will later see that it is quite simple to generalize results to the positive electrode.

We make two fundamental assumptions when creating the reduced-order models:

1. We assume locally linear behavior. Since the actual equations are nonlinear, we linearize the nonlinear equations using Taylor series;
2. We assume that electrolyte potential $\phi_e(x, t)$ is predominantly a function of the reaction flux density $j(x, t)$ and, consequently, that the effect of electrolyte concentration $c_e(x, t)$ on $\phi_e(x, t)$ is minimal.

We begin by linearizing the Butler–Volmer kinetic relationship. Recall Eq. (4.19):

$$j = k_0 c_e^{1-\alpha} (c_{s,\max} - c_{s,e})^{1-\alpha} c_{s,e}^\alpha \left\{ \exp\left(\frac{(1-\alpha)F}{RT}\eta\right) - \exp\left(-\frac{\alpha F}{RT}\eta\right) \right\},$$

where $\eta = \phi_s - \phi_e - U_{\text{ocp}}(c_{s,e}) - FR_{\text{film}}j$. Note the new term in the overpotential calculation, $FR_{\text{film}}j$, which models the voltage drop due to lithium flux through the ionic resistance of the electrode's surface film.

¹ Lee, J.L., Chemistruck, A., and Plett, G.L., "One-Dimensional Physics-Based Reduced-Order Model of Lithium-Ion Dynamics," *Journal of Power Sources*, 220, 2012, pp. 430–448.

² Smith, K., Rahn, C.D., and Wang, C-Y, "Control Oriented 1D Electrochemical Model of Lithium Ion Battery," *Energy Conversion and Management*, 48, 2007, pp. 2,565–78.

We rearrange the Butler–Volmer equation, expanding the overpotential term and defining $\phi_{s-e} = \phi_s - \phi_e$,

$$\begin{aligned} & \frac{j}{k_0 (c_e)^{1-\alpha} (c_{s,\max} - c_{s,e})^{1-\alpha} (c_{s,e})^\alpha} \\ &= \exp\left(\frac{(1-\alpha)F}{RT} (\phi_{s-e} - U_{\text{ocp}}(c_{s,e}) - FR_{\text{film}}j)\right) \\ &\quad - \exp\left(-\frac{\alpha F}{RT} (\phi_{s-e} - U_{\text{ocp}}(c_{s,e}) - FR_{\text{film}}j)\right). \end{aligned} \quad (6.1)$$

We see that j appears on both sides of this expression, and because of the nonlinear nature of the right-hand side, we cannot solve for j in closed form, in general.

Our approach is to find separate Taylor-series expansions of both sides of Eq. (6.1), then equate them to make an overall linear approximation to it. The linearization setpoint p^* is defined as: $p^* = \{c_{s,e} = c_{s,0}, c_e = c_{e,0}, \phi_{s-e} = U_{\text{ocp}}(c_{s,0}), j = 0\}$, where $c_{s,0}$ is the initial equilibrium bulk-average concentration of lithium in the solid, $c_{e,0}$ is the electrolyte average concentration of lithium, and U_{ocp} is the open-circuit-potential relationship of the electrode material at the given concentration.

Linearizing the left-hand side (LHS) of Eq. (6.1), we get:

$$\begin{aligned} \text{LHS} &\approx \underbrace{\text{LHS}(p^*)}_{0} + \underbrace{\frac{\partial \text{LHS}}{\partial c_{s,e}} \Big|_{p^*}}_0 (c_{s,e} - c_{s,0}) + \underbrace{\frac{\partial \text{LHS}}{\partial c_e} \Big|_{p^*}}_0 (c_e - c_{e,0}) + \underbrace{\frac{\partial \text{LHS}}{\partial j} \Big|_{p^*}}_j j \\ &= \frac{1}{k_0 (c_{e,0})^{1-\alpha} (c_{s,\max} - c_{s,0})^{1-\alpha} (c_{s,0})^\alpha} j \\ &= j/j_0, \end{aligned}$$

where we have defined the constant

$$j_0 = k_0 (c_{e,0})^{1-\alpha} (c_{s,\max} - c_{s,0})^{1-\alpha} (c_{s,0})^\alpha.$$

Linearizing the right-hand side (RHS) of Eq. (6.1), we get:

$$\begin{aligned} \text{RHS} &\approx \underbrace{\text{RHS}(p^*)}_{0} + \underbrace{\frac{\partial \text{RHS}}{\partial \phi_{s-e}} \Big|_{p^*}}_0 (\phi_{s-e} - U_{\text{ocp}}(c_{s,0})) \\ &\quad + \underbrace{\frac{\partial \text{RHS}}{\partial c_{s,e}} \Big|_{p^*}}_0 (c_{s,e} - c_{s,0}) + \underbrace{\frac{\partial \text{RHS}}{\partial j} \Big|_{p^*}}_j j \\ &= \frac{F}{RT} (\phi_{s-e} - U_{\text{ocp}}(c_{s,0})) - \frac{F}{RT} \left[\frac{\partial U_{\text{ocp}}}{\partial c_{s,e}} \Big|_{c_{s,0}} \right] (c_{s,e} - c_{s,0}) \\ &\quad - \frac{F^2 R_{\text{film}}}{RT} j. \end{aligned}$$

Equating the linearized LHS = RHS and defining debiased variables $\tilde{c}_{s,e} = c_{s,e} - c_{s,0}$ and $\tilde{\phi}_{s-e} = \phi_{s-e} - U_{\text{ocp}}(c_{s,0})$, we get

$$\frac{j}{j_0} = \frac{F}{RT} \tilde{\phi}_{s-e} - \frac{F}{RT} \left[\frac{\partial U_{\text{ocp}}}{\partial c_{s,e}} \Big|_{c_{s,0}} \right] \tilde{c}_{s,e} - \frac{F^2 R_{\text{film}}}{RT} j.$$

Rearranging allows us to solve for $\tilde{\phi}_{s-e}$

$$\begin{aligned} \tilde{\phi}_{s-e} &= \left(\frac{RT}{j_0 F} + F R_{\text{film}} \right) j + \left[\frac{\partial U_{\text{ocp}}}{\partial c_{s,e}} \Big|_{c_{s,0}} \right] \tilde{c}_{s,e} \\ &= F(R_{\text{ct}} + R_{\text{film}}) j + \left[\frac{\partial U_{\text{ocp}}}{\partial c_{s,e}} \Big|_{c_{s,0}} \right] \tilde{c}_{s,e}, \end{aligned} \quad (6.2)$$

if we define the *charge-transfer resistance*

$$R_{\text{ct}} = \frac{RT}{j_0 F^2}. \quad (6.3)$$

Before proceeding, we take a brief diversion that will give us some insight into the function of R_{ct} . Rearranging the prior result gives

$$F(R_{\text{ct}} + R_{\text{film}})j = \phi_s - \phi_e - U_{\text{ocp}}(c_{s,0}) - \left[\frac{\partial U_{\text{ocp}}}{\partial c_{s,e}} \Big|_{c_{s,0}} \right] \tilde{c}_{s,e}.$$

Notice that the last two terms are a Taylor-series linearization of $U_{\text{ocp}}(c_{s,e})$, so we rewrite as

$$\begin{aligned} F(R_{\text{ct}} + R_{\text{film}})j &= \phi_s - \phi_e - U_{\text{ocp}}(c_{s,e}) \\ F R_{\text{ct}} j &= \phi_s - \phi_e - U_{\text{ocp}}(c_{s,e}) - F R_{\text{film}} j \\ &= \eta. \end{aligned}$$

So, the linearized model has

$$\eta = F R_{\text{ct}} j. \quad (6.4)$$

This helps explain the *charge-transfer resistance* terminology. Since η is a voltage and Fj is current density in A m^{-2} , R_{ct} in Ωm^2 is the linearized resistance of the activation polarization of the Butler–Volmer equation that models the voltage drop beyond open-circuit-potential over the interface between solid and electrolyte. Note that this resistance is a function of state of charge since j_0 is a function of $c_{s,0}$.

Based on this understanding, we can also define a total *solid-electrolyte interfacial resistance*

$$R_{s,e} = R_{\text{ct}} + R_{\text{film}},$$

so Eq. (6.2) becomes

$$\tilde{\phi}_{s-e} = F R_{s,e} j + \left[\frac{\partial U_{\text{ocp}}}{\partial c_{s,e}} \Big|_{c_{s,0}} \right] \tilde{c}_{s,e}, \quad (6.5)$$

We'll lay these results aside for now, and proceed to examine the cell potentials ϕ_s and ϕ_e . Our first step is to define a dimensionless spatial variable $z = x/L$, where L is the electrode thickness.

- The location $z = 0$ represents the current-collector interface;
- The location $z = 1$ represents the separator interface.

This dimensionless variable makes the equations somewhat more compact than if we were to proceed using x , makes it easier to interpret the equations since the length scale is normalized between zero and one (i.e., we don't need to remember L), and will ultimately make the equations for the positive electrode very similar to the equations for the negative electrode.

Recall the solid-phase charge conservation equation from Eq. (4.4), specialized to one spatial dimension and transformed to normalized variable z ,³

$$\frac{\sigma_{\text{eff}}}{L^2} \frac{\partial^2}{\partial z^2} \phi_s = a_s F j, \quad (6.6)$$

with boundary conditions from Sect. 4.11.1

$$\left. \frac{\sigma_{\text{eff}}}{L} \frac{\partial \phi_s}{\partial z} \right|_{z=0} = \frac{-i_{\text{app}}}{A} \quad \text{and} \quad \left. \frac{\partial \phi_s}{\partial z} \right|_{z=1} = 0,$$

where i_{app} is the cell applied current in amperes. Also recall the electrolyte-phase charge conservation equation from Eq. (4.6), also specialized to one spatial dimension and normalized

$$\frac{\kappa_{\text{eff}}}{L^2} \frac{\partial^2}{\partial z^2} \phi_e + \frac{\kappa_{D,\text{eff}}}{L^2} \frac{\partial^2}{\partial z^2} \ln c_e = -a_s F j,$$

with boundary conditions from Sect. 4.11.2

$$\begin{aligned} \left. \kappa_{\text{eff}} \frac{\partial \phi_e}{\partial z} + \kappa_{D,\text{eff}} \frac{\partial \ln c_e}{\partial z} \right|_{z=0} &= 0 \\ \left. \frac{\kappa_{\text{eff}}}{L} \frac{\partial \phi_e}{\partial z} + \frac{\kappa_{D,\text{eff}}}{L} \frac{\partial \ln c_e}{\partial z} \right|_{z=1} &= \frac{i_{\text{app}}}{A}. \end{aligned}$$

By assumption 2, we ignore the electrolyte concentration in these last equations, giving

$$\frac{\kappa_{\text{eff}}}{L^2} \frac{\partial^2}{\partial z^2} \phi_e = -a_s F j, \quad (6.7)$$

with boundary conditions

$$\left. \frac{\partial \phi_e}{\partial z} \right|_{z=0} = 0 \quad \text{and} \quad \left. \frac{\kappa_{\text{eff}}}{L} \frac{\partial \phi_e}{\partial z} \right|_{z=1} = \frac{i_{\text{app}}}{A}.$$

We subtract Eq. (6.7) from Eq. (6.6) to arrive at a single static PDE for phase potential difference $\phi_{s-e} = \phi_s - \phi_e$,

$$\frac{\partial^2}{\partial z^2} \phi_{s-e} = a_s F L^2 \left(\frac{1}{\sigma_{\text{eff}}} + \frac{1}{\kappa_{\text{eff}}} \right) j \quad (6.8)$$

³ In the transformation, we have replaced $\partial(\cdot)/\partial x$ with $(1/L)\partial(\cdot)/\partial z$, via change of variables. We have also assumed that σ_{eff} is uniform throughout the electrode.

with boundary conditions

$$\frac{\sigma_{\text{eff}}}{L} \frac{\partial \phi_{s-e}}{\partial z} \Big|_{z=0} = \frac{-\kappa_{\text{eff}}}{L} \frac{\partial \phi_{s-e}}{\partial z} \Big|_{z=1} = \frac{-i_{\text{app}}}{A}.$$

This PDE expresses ϕ_{s-e} in terms of j . If we were able to eliminate j from the equation, we would have a homogeneous PDE for ϕ_{s-e} , which we could then solve. This, in turn, would allow us to solve for the other variables using the equations in which it appears.

In an effort to eliminate j , we take the Laplace transform of Eq. (6.5), noticing that all signals are functions of both time and space, to get

$$\tilde{\Phi}_{s-e}(z, s) = FR_{s,e}J(z, s) + \left[\frac{\partial U_{\text{ocp}}}{\partial c_{s,e}} \Big|_{c_{s,0}} \right] \tilde{C}_{s,e}(z, s).$$

To treat the rightmost term, write

$$\tilde{C}_{s,e}(z, s) = \frac{\tilde{C}_{s,e}(z, s)}{J(z, s)} J(z, s).$$

In Chap. 5, we determined the transfer function $\tilde{C}_{s,e}(s) / J(s)$ for a single spatial location using the PDEs developed from the Jacobsen–West paper (cf. Eq. (5.9)). But, in the solid, we are assuming that diffusion happens along only the r dimension (not the z dimension), so transfer functions at any location $z = z_1$ have the same form as any other location $z = z_2$, and so we can write $\tilde{C}_{s,e}(z, s) / J(z, s) = \tilde{C}_{s,e}(s) / J(s)$. This gives (remembering that $\beta = R_s \sqrt{s/D_s}$)

$$\begin{aligned} \tilde{\Phi}_{s-e}(z, s) &= \left(FR_{s,e} + \left[\frac{\partial U_{\text{ocp}}}{\partial c_{s,e}} \Big|_{c_{s,0}} \right] \frac{\tilde{C}_{s,e}(s)}{J(s)} \right) J(z, s) \\ &= F \left(R_{s,e} + \left[\frac{\partial U_{\text{ocp}}}{\partial c_{s,e}} \Big|_{c_{s,0}} \right] \frac{R_s}{FD_s} \left[\frac{1}{1 - \beta \coth(\beta)} \right] \right) J(z, s). \end{aligned}$$

Note that since $\tilde{\phi}_{s-e} = \phi_{s-e} - U_{\text{ocp}}(c_{s,0})$, we also have $\frac{\partial^2 \tilde{\phi}_{s-e}}{\partial z^2} = \frac{\partial^2 \phi_{s-e}}{\partial z^2}$, so we can write Eq. (6.8) as

$$\begin{aligned} \frac{\partial^2 \tilde{\phi}_{s-e}(z, t)}{\partial z^2} &= a_s F L^2 \left(\frac{1}{\sigma_{\text{eff}}} + \frac{1}{\kappa_{\text{eff}}} \right) j(z, t) \\ \frac{\partial^2 \tilde{\Phi}_{s-e}(z, s)}{\partial z^2} &= a_s F L^2 \left(\frac{1}{\sigma_{\text{eff}}} + \frac{1}{\kappa_{\text{eff}}} \right) J(z, s) \\ &= \frac{a_s L^2 \left(\frac{1}{\sigma_{\text{eff}}} + \frac{1}{\kappa_{\text{eff}}} \right)}{R_{s,e} + \frac{R_s}{FD_s} \left[\frac{\partial U_{\text{ocp}}}{\partial c_{s,e}} \Big|_{c_{s,0}} \right] \left[\frac{1}{1 - \beta \coth(\beta)} \right]} \tilde{\Phi}_{s-e}(z, s) \end{aligned}$$

with boundary conditions

$$\frac{\sigma_{\text{eff}}}{L} \frac{\partial \tilde{\Phi}_{s-e}(z, s)}{\partial z} \Big|_{z=0} = \frac{-\kappa_{\text{eff}}}{L} \frac{\partial \tilde{\Phi}_{s-e}(z, s)}{\partial z} \Big|_{z=1} = \frac{-I_{\text{app}}(s)}{A}.$$

For convenience of notation, we define dimensionless variable $\nu^{\text{neg}}(s)$ (to which we will refer simply as $\nu(s)$ in the remainder of the sections describing transfer functions in the negative electrode) as⁴

$$\nu^{\text{neg}}(s) = \frac{L^{\text{neg}} \sqrt{\frac{a_s^{\text{neg}}}{\sigma_{\text{eff}}^{\text{neg}}} + \frac{a_s^{\text{neg}}}{\kappa_{\text{eff}}^{\text{neg}}}}}{\sqrt{R_{s,e}^{\text{neg}} + \frac{R_s^{\text{neg}}}{FD_s^{\text{neg}}} \left[\frac{\partial U_{\text{ocp}}^{\text{neg}}}{\partial c_{s,e}^{\text{neg}}} \Big|_{c_{s,0}^{\text{neg}}} \right] \left[\frac{1}{1 - R_s^{\text{neg}} \sqrt{s/D_s^{\text{neg}}} \coth(R_s^{\text{neg}} \sqrt{s/D_s^{\text{neg}}})} \right]}}, \quad (6.9)$$

which gives us the homogeneous PDE

$$\frac{\partial^2 \tilde{\Phi}_{s-e}(z,s)}{\partial z^2} - \nu^2(s) \tilde{\Phi}_{s-e}(z,s) = 0.$$

The generic solution to this PDE is

$$\tilde{\Phi}_{s-e}(z,s) = k_1 \cosh(\nu(s)z) + k_2 \sinh(\nu(s)z),$$

where k_1 and k_2 are chosen to satisfy the boundary conditions. Since our boundary conditions are expressed as gradients, we compute

$$\frac{\partial \tilde{\Phi}_{s-e}(z,s)}{\partial z} = k_1 \nu(s) \sinh(\nu(s)z) + k_2 \nu(s) \cosh(\nu(s)z).$$

From the boundary condition at $z = 0$, we have

$$\begin{aligned} \frac{\sigma_{\text{eff}}}{L} \frac{\partial \tilde{\Phi}_{s-e}(z,s)}{\partial z} \Big|_{z=0} &= \frac{\sigma_{\text{eff}}}{L} k_2 \nu(s) = \frac{-I_{\text{app}}(s)}{A} \\ k_2 &= \frac{-I_{\text{app}}(s)L}{A \sigma_{\text{eff}} \nu(s)}. \end{aligned} \quad (6.10)$$

From the boundary condition at $z = 1$, we have

$$\begin{aligned} \frac{-\kappa_{\text{eff}}}{L} \frac{\partial \tilde{\Phi}_{s-e}(z,s)}{\partial z} \Big|_{z=1} &= \frac{-\kappa_{\text{eff}}}{L} \left[k_1 \nu(s) \sinh(\nu(s)) - \frac{I_{\text{app}}(s)L}{A \sigma_{\text{eff}}} \cosh(\nu(s)) \right] \\ \frac{-I_{\text{app}}(s)}{A} &= \frac{-\kappa_{\text{eff}}}{L} \left[k_1 \nu(s) \sinh(\nu(s)) - \frac{I_{\text{app}}(s)L}{A \sigma_{\text{eff}}} \cosh(\nu(s)) \right] \\ k_1 \nu(s) \sinh(\nu(s)) &= \frac{I_{\text{app}}(s)L}{A \kappa_{\text{eff}}} \left[1 + \frac{\kappa_{\text{eff}}}{\sigma_{\text{eff}}} \cosh(\nu(s)) \right] \\ k_1 &= \frac{I_{\text{app}}(s)L}{A \nu(s) \sinh(\nu(s))} \left[\frac{1}{\kappa_{\text{eff}}} + \frac{1}{\sigma_{\text{eff}}} \cosh(\nu(s)) \right]. \end{aligned} \quad (6.11)$$

Substituting these values of k_1 and k_2 into $\tilde{\Phi}_{s-e}(z,s)$ gives

$$\begin{aligned} \tilde{\Phi}_{s-e}(z,s) &= \frac{I_{\text{app}}(s)L}{A \nu(s) \sinh(\nu(s))} \left[\frac{1}{\kappa_{\text{eff}}} + \frac{1}{\sigma_{\text{eff}}} \cosh(\nu(s)) \right] \cosh(\nu(s)z) \\ &+ \frac{-I_{\text{app}}(s)L}{A \sigma_{\text{eff}} \nu(s)} \sinh(\nu(s)z) \end{aligned}$$

⁴This is the Greek letter “nu” and not the English letter “v”. We use this notation to be consistent with Smith et al. (cf. reference in footnote 2). We can interpret $\nu^2(s)$ as a ratio of frequency-dependent and SOC-dependent impedances, where the numerator represents the impedance in the x dimension across the electrode, and the denominator represents the impedance in the r dimension across the solid–electrolyte interface and via diffusion into the particle.

$$\begin{aligned}\frac{\tilde{\Phi}_{s-e}(z, s)}{I_{app}(s)} &= \frac{L}{A\nu(s) \sinh(\nu(s))} \left[\frac{1}{\kappa_{\text{eff}}} \cosh(\nu(s)z) \right. \\ &\quad \left. + \frac{1}{\sigma_{\text{eff}}} (\cosh(\nu(s)) \cosh(\nu(s)z) - \sinh(\nu(s)) \sinh(\nu(s)z)) \right].\end{aligned}$$

Some trigonometric manipulations give us the following final form

$$\frac{\tilde{\Phi}_{s-e}^{\text{neg}}(z, s)}{I_{app}(s)} = \frac{L^{\text{neg}} \left[\sigma_{\text{eff}}^{\text{neg}} \cosh(\nu^{\text{neg}}(s)z) + \kappa_{\text{eff}}^{\text{neg}} \cosh(\nu^{\text{neg}}(s)(z-1)) \right]}{A\sigma_{\text{eff}}^{\text{neg}} \kappa_{\text{eff}}^{\text{neg}} \nu^{\text{neg}}(s) \sinh(\nu^{\text{neg}}(s))}, \quad (6.12)$$

where the superscript “neg” for $\tilde{\Phi}_{s-e}$ reminds us that this transfer function applies to the negative-electrode region only.⁵

We can now write

$$\frac{J(z, s)}{I_{app}(s)} = \frac{J(z, s)}{\tilde{\Phi}_{s-e}(z, s)} \frac{\tilde{\Phi}_{s-e}(z, s)}{I_{app}(s)} = \frac{\nu^2(s)}{a_s F L^2 \left(\frac{1}{\kappa_{\text{eff}}} + \frac{1}{\sigma_{\text{eff}}} \right)} \frac{\tilde{\Phi}_{s-e}(z, s)}{I_{app}(s)}.$$

Expanding gives

$$\frac{J^{\text{neg}}(z, s)}{I_{app}(s)} = \nu^{\text{neg}}(s) \frac{\sigma_{\text{eff}}^{\text{neg}} \cosh(\nu^{\text{neg}}(s)z) + \kappa_{\text{eff}}^{\text{neg}} \cosh(\nu^{\text{neg}}(s)(z-1))}{a_s^{\text{neg}} F L^{\text{neg}} A (\kappa_{\text{eff}}^{\text{neg}} + \sigma_{\text{eff}}^{\text{neg}}) \sinh(\nu^{\text{neg}}(s))}. \quad (6.13)$$

Summarizing to this point, we have now developed a transfer-function that relates the applied cell current $i_{\text{app}}(t)$ to the reaction flux $j(z, t)$ at any z location in the negative electrode. Much like the Jacobsen–West transfer function from the previous chapter, this result also involves transcendental functions of s . However, we have seen that the DRA is able to make high-fidelity low-order discrete-time ODE approximate versions of transcendental transfer functions: the same will be true here as well.

Later in the chapter we’ll see examples that illustrate that a low-order DRA model based on this transfer function $J(z, s) / I_{app}(s)$ can accurately predict reaction flux at any location in the electrode. To see why this is possible, Fig. 6.1 plots the magnitude responses of $J(z, s) / I_{app}(s)$ for several normalized z locations in the negative electrode. Parameter values used by the transfer functions in these plots are the same as those used in the full-cell example later in this chapter. Note that while the transfer functions *appear* very complicated mathematically, the magnitude responses are actually quite simple in nature. So, it turns out to be possible to approximate their behavior closely with a low-order state-space model.

The transfer function for $\tilde{\Phi}_{s-e}^{\text{neg}}(z, s)$ in Eq. (6.12) turns out to have integrator dynamics (a pole at $s = 0$). Referring back to Eq. (6.2), we see why this is the case: $\tilde{\phi}_{s-e}(z, t)$ has a component based on $\tilde{c}_{s,e}(z, t)$, which we have already seen has an integrator (in Example 3 in Chap. 5). When running the DRA with Eq. (6.12), we must

⁵ All of the tricky trigonometric manipulations and integrals involving hyperbolic functions in this chapter were performed with the aid of Mathematica.

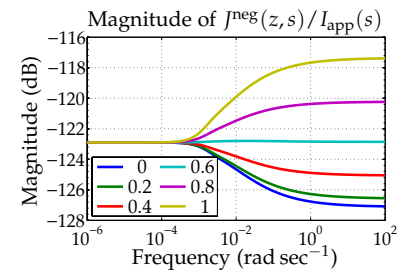


Figure 6.1: Example magnitude responses of $J^{\text{neg}}(z, s) / I_{\text{app}}(s)$ at six different z locations across the negative electrode.

(Adapted from Fig. 3 in Lee, J.L., Chemistruck, A., and Plett, G.L., “One-Dimensional Physics-Based Reduced-Order Model of Lithium-Ion Dynamics,” *Journal of Power Sources*, 220, 2012, pp. 430–448.)

first subtract the integrator dynamics

$$\begin{aligned} \frac{[\tilde{\Phi}_{s,e}^{\text{neg}}(z,s)]^*}{I_{\text{app}}(s)} &= \frac{\tilde{\Phi}_{s,e}^{\text{neg}}(z,s)}{I_{\text{app}}(s)} - \frac{\text{res}_0}{s} \\ &= \frac{\tilde{\Phi}_{s,e}^{\text{neg}}(z,s)}{I_{\text{app}}(s)} + \frac{1}{\varepsilon_s^{\text{neg}} AFL^{\text{neg}}_s} \left[\frac{\partial U_{\text{ocp}}}{\partial c_{s,e}} \Big|_{c_{s,0}} \right]. \end{aligned} \quad (6.14)$$

The resulting magnitude response is plotted in Fig. 6.2. As with Fig. 6.1, the plot shows the simplicity of the transfer function despite the apparent complexity of Eq. (6.12).

6.2 A one-dimensional model of $\tilde{c}_{s,e}^{\text{neg}}(z,t)$

Using the transfer function for $J(z,s)/I_{\text{app}}(s)$, it is straightforward to develop a transfer function relating $i_{\text{app}}(t)$ to $\tilde{c}_{s,e}(z,t)$. We start by writing

$$\begin{aligned} \frac{\tilde{C}_{s,e}(z,s)}{I_{\text{app}}(s)} &= \frac{\tilde{C}_{s,e}(z,s)}{J(z,s)} \frac{J(z,s)}{I_{\text{app}}(s)} \\ &= \frac{R_s}{D_s} \left[\frac{1}{1 - R_s \sqrt{s/D_s} \coth(R_s \sqrt{s/D_s})} \right] \frac{J(z,s)}{I_{\text{app}}(s)}. \end{aligned}$$

Substituting Eq. (6.13), we get our final form:

$$\begin{aligned} \frac{\tilde{C}_{s,e}^{\text{neg}}(z,s)}{I_{\text{app}}(s)} &= \left[\frac{\sigma_{\text{eff}}^{\text{neg}} \cosh(\nu^{\text{neg}}(s)z) + \kappa_{\text{eff}}^{\text{neg}} \cosh(\nu^{\text{neg}}(s)(z-1))}{a_s^{\text{neg}} FL^{\text{neg}} AD_s^{\text{neg}} (\kappa_{\text{eff}}^{\text{neg}} + \sigma_{\text{eff}}^{\text{neg}}) \sinh(\nu^{\text{neg}}(s))} \right] \times \\ &\quad \left[\frac{R_s^{\text{neg}} \nu^{\text{neg}}(s)}{1 - R_s^{\text{neg}} \sqrt{s/D_s^{\text{neg}}} \coth(R_s^{\text{neg}} \sqrt{s/D_s^{\text{neg}}})} \right]. \end{aligned} \quad (6.15)$$

As before, this is a transcendental transfer function, which has an infinite number of poles and zeros. However, also as before, we'll be able to use this transfer function via the DRA to make excellent low-order models of $\tilde{c}_{s,e}(z,t)$. Fig. 6.3 plots the magnitude responses of $\tilde{C}_{s,e}(z,s)/I_{\text{app}}(s)$ for several normalized z locations in the negative electrode. We see again that while the transfer functions *appear* very complicated, the magnitude responses are actually quite simple.

We also recognize from the magnitude response that there is an integrator pole at $s = 0$ in this transfer function. Fig. 6.4 shows the magnitude response with this pole removed via

$$\begin{aligned} \frac{[\tilde{C}_{s,e}^{\text{neg}}(z,s)]^*}{I_{\text{app}}(s)} &= \frac{\tilde{C}_{s,e}^{\text{neg}}(z,s)}{I_{\text{app}}(s)} - \frac{\text{res}_0}{s} \\ &= \frac{\tilde{C}_{s,e}^{\text{neg}}(z,s)}{I_{\text{app}}(s)} + \frac{1}{\varepsilon_s^{\text{neg}} AFL^{\text{neg}}_s}. \end{aligned} \quad (6.16)$$

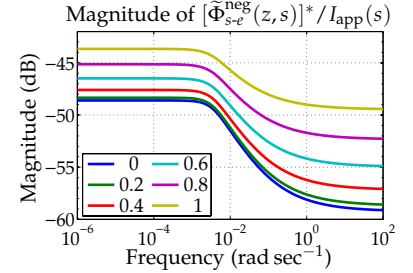


Figure 6.2: Example magnitude responses of $[\tilde{\Phi}_{s,e}^{\text{neg}}(z,s)]^*/I_{\text{app}}(s)$ at six different z locations across the negative electrode.

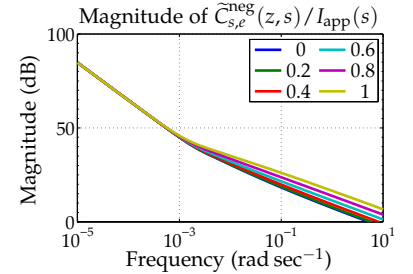


Figure 6.3: Example magnitude responses of $\tilde{C}_{s,e}^{\text{neg}}(z,s)/I_{\text{app}}(s)$ at six different z locations across the negative electrode.

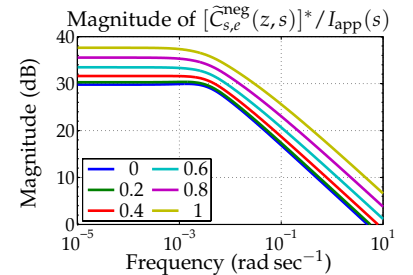


Figure 6.4: Example magnitude responses of $[\tilde{C}_{s,e}^{\text{neg}}(z,s)]^*/I_{\text{app}}(s)$ at six different z locations across the negative electrode.

(Adapted from Fig. 1 in Lee, J.L., Chemistruck, A., and Plett, G.L., "One-Dimensional Physics-Based Reduced-Order Model of Lithium-Ion Dynamics," *Journal of Power Sources*, 220, 2012, pp. 430–448.)

6.3 A one-dimensional model of $\tilde{\phi}_s^{neg}(z, t)$

We now wish to develop an independent transfer function for $\phi_s(z, t)$.

We begin by recalling Eq. (6.6):

$$\frac{\sigma_{\text{eff}}}{L^2} \frac{\partial^2}{\partial z^2} \phi_s(z, t) = a_s F j(z, t). \quad (6.17)$$

We will arrive at a transfer function for $\phi_s(z, t)$ by integrating this expression twice.

First, recall from Eq. (4.14) that we have a definition for the electronic current i_s flowing through the solid: $\varepsilon_s \mathbf{i}_s = -\sigma_{\text{eff}} \nabla \phi_s$. Specializing to the one-dimensional case, we have

$$\varepsilon_s i_s(x, t) = -\sigma_{\text{eff}} \frac{\partial \phi_s(x, t)}{\partial x}. \quad (6.18)$$

Then, changing variables from absolute position x to relative position $z = x/L$ gives

$$\varepsilon_s i_s(z, t) = -\frac{\sigma_{\text{eff}}}{L} \frac{\partial \phi_s(z, t)}{\partial z}.$$

This allows us to rewrite Eq. (6.17) as

$$-\frac{\varepsilon_s}{L} \frac{\partial i_s(z, t)}{\partial z} = a_s F j(z, t),$$

with limiting cases $i_s(0, t) = i_{\text{app}}(t) / (\varepsilon_s A)$ and $i_s(1, t) = 0$. Taking Laplace transforms gives

$$-\frac{\varepsilon_s}{L} \frac{\partial I_s(z, s)}{\partial z} = a_s F J(z, s).$$

We then integrate from zero to z to get an expression for $I_s(z, s)$

$$\begin{aligned} -\frac{\varepsilon_s}{L} \int_0^z \frac{\partial I_s(\zeta, s)}{\partial \zeta} d\zeta &= a_s F \int_0^z J(\zeta, s) d\zeta \\ -\frac{\varepsilon_s}{L} (I_s(z, s) - I_s(0, s)) &= a_s F \int_0^z J(\zeta, s) d\zeta \\ I_s(z, s) &= I_s(0, s) - \frac{a_s F L}{\varepsilon_s} \int_0^z J(\zeta, s) d\zeta \\ \frac{I_s(z, s)}{I_{\text{app}}(s)} &= \frac{1}{\varepsilon_s A} - \frac{a_s F L}{\varepsilon_s} \int_0^z \frac{J(\zeta, s)}{I_{\text{app}}(s)} d\zeta. \end{aligned}$$

Substituting $J(z, s) / I_{\text{app}}(s)$ from Eq. (6.13) and integrating gives

$$\frac{I_s(z, s)}{I_{\text{app}}(s)} = \frac{\sigma_{\text{eff}} (\sinh(\nu(s)) - \sinh(z\nu(s))) - \kappa_{\text{eff}} \sinh((z-1)\nu(s))}{\varepsilon_s A (\kappa_{\text{eff}} + \sigma_{\text{eff}}) \sinh(\nu(s))}.$$

We now wish to find $\phi_s(z, t)$ from $i_s(z, t)$. We start with the Laplace transform of Eq. (6.18)

$$\frac{\partial \Phi_s(z, s)}{\partial z} = -\frac{\varepsilon_s L}{\sigma_{\text{eff}}} I_s(z, s).$$

We then integrate from zero to z to get an expression for $\Phi_s(z, s)$

$$\begin{aligned}\frac{\partial \Phi_s(z, s)}{\partial z} &= -\frac{\varepsilon_s L}{\sigma_{\text{eff}}} I_s(z, s) \\ \int_0^z \frac{\partial \Phi(\zeta, s)}{\partial \zeta} d\zeta &= -\frac{\varepsilon_s L}{\sigma_{\text{eff}}} \int_0^z I_s(\zeta, s) d\zeta \\ \Phi(z, s) - \Phi(0, s) &= -\frac{\varepsilon_s L}{\sigma_{\text{eff}}} \int_0^z I_s(\zeta, s) d\zeta.\end{aligned}$$

We define $\tilde{\phi}_s(z, t) = \phi_s(z, t) - \phi_s(0, t)$, which then gives, in the negative electrode

$$\begin{aligned}\frac{\tilde{\Phi}_s^{\text{neg}}(z, s)}{I_{\text{app}}(s)} &= -L^{\text{neg}} \left[\frac{\kappa_{\text{eff}}^{\text{neg}} (\cosh(\nu^{\text{neg}}(s)) - \cosh((z-1)\nu^{\text{neg}}(s)))}{A\sigma_{\text{eff}}^{\text{neg}}(\kappa_{\text{eff}}^{\text{neg}} + \sigma_{\text{eff}}^{\text{neg}})\nu^{\text{neg}}(s) \sinh(\nu^{\text{neg}}(s))} \right. \\ &\quad \left. + \frac{\sigma_{\text{eff}}^{\text{neg}} (1 - \cosh(z\nu^{\text{neg}}(s)) + z\nu^{\text{neg}}(s) \sinh(\nu^{\text{neg}}(s)))}{A\sigma_{\text{eff}}^{\text{neg}}(\kappa_{\text{eff}}^{\text{neg}} + \sigma_{\text{eff}}^{\text{neg}})\nu^{\text{neg}}(s) \sinh(\nu^{\text{neg}}(s))} \right].\end{aligned}\quad (6.19)$$

In the negative electrode, we define $\phi_s(0, t) = 0$, so we have $\tilde{\phi}_s(z, t) = \phi_s(z, t)$. (In the positive electrode, it is somewhat more complicated, as we will see in Sect. 6.4.) Fig. 6.5 shows the magnitude response of Eq. (6.19) at several z locations. As we've seen before, even though the transfer function is quite complicated, the magnitude response is quite simple, which leads to a relatively simple reduced-order model.

6.4 Positive-electrode variables $j^{\text{pos}}(z, t)$, $\tilde{c}_{s,e}^{\text{pos}}(z, t)$, and $\tilde{\phi}_s^{\text{pos}}(z, t)$

We have so far focused on deriving transfer functions of variables of interest for the negative electrode: j , $c_{s,e}$, and ϕ_s . Now, we look at deriving the same transfer functions for the positive electrode.

Starting with $\tilde{\Phi}_{s,e}(z, s)$, the derivation for the positive electrode remains unchanged up until the point where we find that

$$\frac{\partial^2 \tilde{\Phi}_{s,e}(z, s)}{\partial z^2} - \nu^2(s) \tilde{\Phi}_{s,e}(z, s) = 0,$$

where we now think of $\nu(s)$ as describing the positive-electrode variables. That is, $\nu(s) = \nu^{\text{pos}}(s)$ where

$$\nu^{\text{pos}}(s) = \frac{L^{\text{pos}} \sqrt{\frac{a_s^{\text{pos}}}{\sigma_{\text{eff}}^{\text{pos}}} + \frac{a_s^{\text{pos}}}{\kappa_{\text{eff}}^{\text{pos}}}}}{\sqrt{R_{s,e}^{\text{pos}} + \frac{R_s^{\text{pos}}}{FD_s^{\text{pos}}} \left[\frac{\partial U_{\text{ocp}}^{\text{pos}}}{\partial c_{s,e}^{\text{pos}}} \Big|_{c_{s,0}^{\text{pos}}} \right] \left[\frac{1}{1 - R_s^{\text{pos}} \sqrt{s/D_s^{\text{pos}}} \coth(R_s^{\text{pos}} \sqrt{s/D_s^{\text{pos}}})} \right]}}. \quad (6.20)$$

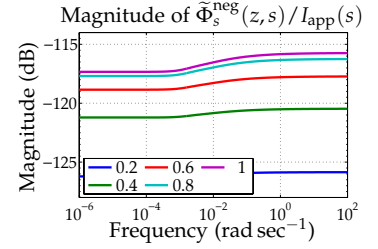


Figure 6.5: Example magnitude responses of $\tilde{\Phi}_s^{\text{neg}}(z, s) / I_{\text{app}}(s)$ for five different z locations across the negative electrode.

However, the boundary conditions are different. To be careful, we write them in terms of x rather than z :

$$\sigma_{\text{eff}} \frac{\partial \tilde{\Phi}_{s-e}(x, s)}{\partial x} \Big|_{x=L^{\text{tot}}} = -\kappa_{\text{eff}} \frac{\partial \tilde{\Phi}_{s-e}(x, s)}{\partial x} \Big|_{x=L^{\text{tot}}-L^{\text{pos}}} = \frac{-I_{\text{app}}(s)}{A}.$$

As for the negative electrode, we define $z = 0$ to be the location of the current collector, and $z = 1$ to be at the separator boundary. That gives the relationship

$$x = L^{\text{tot}} - zL^{\text{pos}}.$$

To rewrite these boundary conditions in terms of z , note that

$$\frac{\partial \tilde{\Phi}_{s-e}}{\partial z} = \frac{\partial \tilde{\Phi}_{s-e}}{\partial x} \frac{\partial x}{\partial z} = -L^{\text{pos}} \frac{\partial \tilde{\Phi}_{s-e}}{\partial x}.$$

This allows us to write

$$\frac{\sigma_{\text{eff}}}{L^{\text{pos}}} \frac{\partial \tilde{\Phi}_{s-e}(z, s)}{\partial z} \Big|_{z=0} = \frac{-\kappa_{\text{eff}}}{L^{\text{pos}}} \frac{\partial \tilde{\Phi}_{s-e}(z, s)}{\partial z} \Big|_{z=1} = \frac{+I_{\text{app}}(s)}{A}.$$

Note the sign changes from before, which cause us to solve the PDE with k_1 and k_2 constants having equal magnitude to those found before, but opposite sign. This has the net effect that all positive-electrode transfer functions are of the same form as their negative-electrode counterparts except:

1. We use $\nu^{\text{pos}}(s)$ instead of $\nu^{\text{neg}}(s)$.
2. We use L^{pos} , a_s^{pos} , $\kappa_{\text{eff}}^{\text{pos}}$, $\sigma_{\text{eff}}^{\text{pos}}$ instead of L^{neg} , a_s^{neg} , $\kappa_{\text{eff}}^{\text{neg}}$, and $\sigma_{\text{eff}}^{\text{eng}}$, respectively.
3. We multiply the transfer function by -1 .

Therefore, for the positive electrode,

$$\frac{\tilde{\Phi}_{s-e}^{\text{pos}}(z, s)}{I_{\text{app}}(s)} = \frac{-L^{\text{pos}} \left[\sigma_{\text{eff}}^{\text{pos}} \cosh(\nu^{\text{pos}}(s)z) + \kappa_{\text{eff}}^{\text{pos}} \cosh(\nu^{\text{pos}}(s)(z-1)) \right]}{A \sigma_{\text{eff}}^{\text{pos}} \kappa_{\text{eff}}^{\text{pos}} \nu^{\text{pos}}(s) \sinh(\nu^{\text{pos}}(s))}. \quad (6.21)$$

We can compute $\Phi_{s-e}^{\text{pos}}(z, s) = \tilde{\Phi}_{s-e}^{\text{pos}}(z, s) + U_{\text{ocp}}^{\text{pos}}(c_{s,0}^{\text{pos}})$, where we are now considering the OCP function for the positive-electrode material, not the negative-electrode material, and $c_{s,0}$ as the linearization setpoint concentration for the positive electrode.

Likewise, since all the transfer functions we have studied so far depend on $\tilde{\Phi}_{s-e}(z, s)$,

$$\frac{J^{\text{pos}}(z, s)}{I_{\text{app}}(s)} = -\nu^{\text{pos}}(s) \frac{\sigma_{\text{eff}}^{\text{pos}} \cosh(\nu^{\text{pos}}(s)z) + \kappa_{\text{eff}}^{\text{pos}} \cosh(\nu^{\text{pos}}(s)(z-1))}{a_s^{\text{pos}} F L^{\text{pos}} A (\kappa_{\text{eff}}^{\text{pos}} + \sigma_{\text{eff}}^{\text{pos}}) \sinh(\nu^{\text{pos}}(s))}, \quad (6.22)$$

and

$$\frac{\tilde{C}_{s,e}^{\text{pos}}(z,s)}{I_{\text{app}}(s)} = - \left[\frac{\sigma_{\text{eff}}^{\text{pos}} \cosh(\nu^{\text{pos}}(s)z) + \kappa_{\text{eff}}^{\text{pos}} \cosh(\nu^{\text{pos}}(s)(z-1))}{a_s^{\text{pos}} F L^{\text{pos}} A D_s^{\text{pos}} (\kappa_{\text{eff}}^{\text{pos}} + \sigma_{\text{eff}}^{\text{pos}}) \sinh(\nu^{\text{pos}}(s))} \right] \times \left[\frac{R_s^{\text{pos}} \nu^{\text{pos}}(s)}{1 - R_s^{\text{pos}} \sqrt{s/D_s^{\text{pos}}} \coth(R_s^{\text{pos}} \sqrt{s/D_s^{\text{pos}}})} \right]. \quad (6.23)$$

We can compute $C_{s,e}^{\text{pos}}(z,s) = \tilde{C}_{s,e}^{\text{pos}}(z,s) + c_{s,0}^{\text{pos}}$, where $c_{s,0}^{\text{pos}}$ is the linearization setpoint value for the positive electrode.

Finally,

$$\frac{\tilde{\Phi}_s^{\text{pos}}(z,s)}{I_{\text{app}}(s)} = L^{\text{pos}} \left[\frac{\kappa_{\text{eff}}^{\text{pos}} (\cosh(\nu^{\text{pos}}(s)) - \cosh((z-1)\nu^{\text{pos}}(s)))}{A \sigma_{\text{eff}}^{\text{pos}} (\kappa_{\text{eff}}^{\text{pos}} + \sigma_{\text{eff}}^{\text{pos}}) \nu^{\text{pos}}(s) \sinh(\nu^{\text{pos}}(s))} \right. \\ \left. + \frac{\sigma_{\text{eff}}^{\text{pos}} (1 - \cosh(z\nu^{\text{pos}}(s)) + z\nu^{\text{pos}}(s) \sinh(\nu^{\text{pos}}(s)))}{A \sigma_{\text{eff}}^{\text{pos}} (\kappa_{\text{eff}}^{\text{pos}} + \sigma_{\text{eff}}^{\text{pos}}) \nu^{\text{pos}}(s) \sinh(\nu^{\text{pos}}(s))} \right]. \quad (6.24)$$

We could compute $\phi_s^{\text{pos}}(z,t) = \tilde{\phi}_s^{\text{pos}}(z,t) + \phi_s^{\text{pos}}(0,t)$ if we knew how to compute $\phi_s^{\text{pos}}(0,t)$. However, $\phi_s^{\text{pos}}(0,t) = v(t)$, the overall cell voltage, which we do not yet know how to compute. We will see how to do so in Sect. 6.8. Then, we compute $\phi_s(z,t) = \tilde{\phi}_s(z,t) + v(t)$ in the positive electrode.

6.5 A one-dimensional model of $c_e(x,t)$

6.5.1 An outline of the approach

The next variable that we tackle is $c_e(x,t)$ over the entire cell width. We will begin by deriving an ordinary-differential equation solution to the PDE equation of lithium concentration in the electrolyte:

$$\frac{\partial \varepsilon_e(x) c_e(x,t)}{\partial t} = \nabla \cdot (D_{e,\text{eff}}(x) \nabla c_e(x,t)) + a_s(x) (1 - t_+^0) j \quad (6.25)$$

where the boundary conditions are

$$\frac{\partial c_e(0,t)}{\partial x} = 0 \quad \text{and} \quad \frac{\partial c_e(L^{\text{tot}},t)}{\partial x} = 0,$$

and the initial distribution is $c_e(x,0) = c_{e,0}$.

ASSUME: We assume that $D_{e,\text{eff}}$ and ε_e are uniform (constant) over each region of the cell, but may have different values in the negative electrode, separator, and positive electrode, respectively.

We also define $\tilde{c}_e(x,t) = c_e(x,t) - c_{e,0}$. This converts Eq. (6.25) into the following form, which is solvable via transfer functions:

$$\frac{\partial \varepsilon_e(x) \tilde{c}_e(x,t)}{\partial t} = \nabla \cdot (D_{e,\text{eff}}(x) \nabla \tilde{c}_e(x,t)) + a_s(x) (1 - t_+^0) j \quad (6.26)$$

where the boundary conditions are

$$\frac{\partial \tilde{c}_e(0, t)}{\partial x} = 0 \quad \text{and} \quad \frac{\partial \tilde{c}_e(L^{\text{tot}}, t)}{\partial x} = 0,$$

and the initial distribution is $\tilde{c}_e(x, 0) = 0$.

We desire to show the following intermediate result: the reduced-order solution involves first-order ordinary-differential equation "modes," each having the form:

$$\frac{d}{dt} \tilde{c}_{e,n}(t) = -\lambda_n \tilde{c}_{e,n}(t) + j_n(t),$$

where the electrolyte concentration is the weighted summation of the solution to each of these differential equations:

$$\tilde{c}_e(x, t) = \sum_{n=0}^{\infty} \tilde{c}_{e,n}(t) \Psi(x; \lambda_n).$$

We then derive a transfer-function solution $\tilde{C}_e(x, s) / I_{\text{app}}(s)$ based on $\tilde{c}_e(x, t)$.

6.5.2 Sturm–Liouville problem and Green's identity

In the course of finding a representation for $\tilde{c}_e(x, t)$ that can be converted into a transfer function, we will find that we can write Eq. (6.25) in terms of a *Sturm–Liouville problem*, which is an ordinary differential equation having the generic form

$$\frac{d}{dx} \left[p(x) \frac{d\Psi(x)}{dx} \right] + q(x) \Psi(x) + \lambda w(x) \Psi(x) = 0 \quad (6.27)$$

over a finite closed interval $[a, b]$. We don't prove it here, but it is important to note that

1. There are an infinite number of solutions to the Sturm–Liouville problem, each of which is indexed by a distinct real eigenvalue λ . The set of solutions can be ordered such that

$$\lambda_0 < \lambda_1 < \lambda_2 < \dots < \lambda_n < \dots \rightarrow \infty.$$

2. Corresponding to each eigenvalue λ_n is a unique (up to a normalization constant) eigenfunction $\Psi(x; \lambda_n)$ that has exactly n zero crossings in (a, b) .
3. The normalized eigenfunctions form a basis that is orthonormal with respect to the weighting function $w(x)$ such that

$$\int_a^b \Psi(x; \lambda_n) \Psi(x; \lambda_m) w(x) dx = \delta_{mn}, \quad (6.28)$$

where $\delta_{mn} = 0$ if $m \neq n$ and $\delta_{mn} = 1$ if $m = n$.

We will also need *Green's identity*, which we can quickly derive. Define a linear operator, L ,

$$L \equiv \frac{d}{dx} \left[p(x) \frac{d}{dx} \right] + q(x).$$

Then, the Sturm–Liouville problem can be rewritten as

$$L(\Psi(x)) + \lambda w(x) \Psi(x) = 0.$$

For *any* two functions, v and u , we can write

$$\begin{aligned} L(v) &= \frac{d}{dx} \left[p(x) \frac{dv}{dx} \right] + q(x)v \\ L(u) &= \frac{d}{dx} \left[p(x) \frac{du}{dx} \right] + q(x)u. \end{aligned}$$

Multiplying the first equation by u , the second equation by v , and subtracting gives

$$\begin{aligned} uL(v) - vL(u) &= u \frac{d}{dx} \left(p \frac{dv}{dx} \right) + uqv - v \frac{d}{dx} \left(p \frac{du}{dx} \right) - vqu \\ &= u \frac{d}{dx} \left(p \frac{dv}{dx} \right) - v \frac{d}{dx} \left(p \frac{du}{dx} \right). \end{aligned}$$

We integrate by parts to get

$$\begin{aligned} \int_a^b \left[u \frac{d}{dx} \left(p \frac{dv}{dx} \right) - v \frac{d}{dx} \left(p \frac{du}{dx} \right) \right] dx \\ &= \int_a^b u \frac{d}{dx} \left(p \frac{dv}{dx} \right) dx - \int_a^b v \frac{d}{dx} \left(p \frac{du}{dx} \right) dx \\ &= \left[p \frac{dv}{dx} u \Big|_a^b - \int_a^b p \left(\frac{du}{dx} \right) \left(\frac{dv}{dx} \right) dx \right] \\ &\quad - \left[p \frac{du}{dx} v \Big|_a^b - \int_a^b p \left(\frac{du}{dx} \right) \left(\frac{dv}{dx} \right) dx \right]. \end{aligned}$$

The integrals in the right-hand side cancel, yielding Green's identity

$$\int_a^b [uL(v) - vL(u)] dx = p \left(u \frac{dv}{dx} - v \frac{du}{dx} \right) \Big|_a^b. \quad (6.29)$$

6.5.3 Solution to the homogeneous PDE

Having reviewed these fundamental mathematical results, we now use the *separation of variables* approach to solve the electrolyte-concentration PDE. To do so, we first find the solution in terms of an infinite series of eigenfunctions, and then truncate the solution to use only the first few terms of the expansion.

We begin by solving the homogeneous PDE (that is, with $j = 0$). Solving the homogeneous boundary value problem gives the eigenvalues λ_n and the eigenfunctions $\Psi(x; \lambda_n)$ that will be used for both the homogeneous and inhomogeneous solutions. We then generalize this solution to find the forced PDE solution.

The homogeneous problem is given by

$$\frac{\partial \tilde{c}_e(x, t)}{\partial t} = \frac{1}{\varepsilon_e(x)} \frac{\partial}{\partial x} D_{e,\text{eff}}(x) \frac{\partial \tilde{c}_e(x, t)}{\partial x}, \quad (6.30)$$

with boundary conditions

$$\frac{\partial \tilde{c}_e(0, t)}{\partial x} = 0 \quad \text{and} \quad \frac{\partial \tilde{c}_e(L^{\text{tot}}, t)}{\partial x} = 0,$$

and the initial condition, $\tilde{c}_e(x, 0) = 0$.

There are also internal boundary conditions where the three regions of the cell join. First, we assume continuity:

$$\begin{aligned} \tilde{c}_e((L^{\text{neg}})^-, t) &= \tilde{c}_e((L^{\text{neg}})^+, t) \\ \tilde{c}_e((L^{\text{neg}} + L^{\text{sep}})^-, t) &= \tilde{c}_e((L^{\text{neg}} + L^{\text{sep}})^+, t), \end{aligned}$$

where the superscripts “ $-$ ” and “ $+$ ” indicate that the function is evaluated slightly to the left or right of the boundary, respectively.

We also need to say something about the slope of the concentration function on either side of an internal boundary. Notice what happens when we use the product rule on the right-hand side of the PDE:

$$\frac{\partial}{\partial x} D_{e,\text{eff}}(x) \frac{\partial \tilde{c}_e(x, t)}{\partial x} = D_{e,\text{eff}}(x) \frac{\partial^2 \tilde{c}_e(x, t)}{\partial x^2} + \left(\frac{\partial \tilde{c}_e(x, t)}{\partial x} \right) \left(\frac{\partial D_{e,\text{eff}}(x)}{\partial x} \right).$$

There is no physical problem with the first term in this expression, but the second term evaluates to scaled Dirac delta functions at region boundaries in general because of the discontinuity in $D_{e,\text{eff}}(x)$.

This doesn't make physical sense, so we constrain the solution to eliminate these delta functions by effectively multiplying them by zero

$$\begin{aligned} \frac{\partial}{\partial x} D_{e,\text{eff}}(x) \frac{\partial \tilde{c}_e(x, t)}{\partial x} &= \lim_{x^+ - x^- \rightarrow 0} \frac{1}{x^+ - x^-} \left[D_{e,\text{eff}}(x^+) \left[\frac{\partial \tilde{c}_e(x, t)}{\partial x} \Big|_{x=x^+} \right] \right. \\ &\quad \left. - D_{e,\text{eff}}(x^-) \left[\frac{\partial \tilde{c}_e(x, t)}{\partial x} \Big|_{x=x^-} \right] \right] = 0 \end{aligned}$$

at the boundaries where $x = L^{\text{neg}}$ or $x = L^{\text{neg}} + L^{\text{sep}}$. This gives:

$$\begin{aligned} D_{e,\text{eff}}^{\text{neg}} \frac{\partial \tilde{c}_e(x, t)}{\partial x} \Big|_{x=(L^{\text{neg}})^-} &= D_{e,\text{eff}}^{\text{sep}} \frac{\partial \tilde{c}_e(x, t)}{\partial x} \Big|_{x=(L^{\text{neg}})^+} \\ D_{e,\text{eff}}^{\text{sep}} \frac{\partial \tilde{c}_e(x, t)}{\partial x} \Big|_{x=(L^{\text{neg}} + L^{\text{sep}})^-} &= D_{e,\text{eff}}^{\text{pos}} \frac{\partial \tilde{c}_e(x, t)}{\partial x} \Big|_{x=(L^{\text{neg}} + L^{\text{sep}})^+}. \end{aligned}$$

The separation-of-variables method assumes that the solution can be broken up into the product of a function of time only, $h(t)$, and a function of position only, $\Psi(x)$; that is,

$$\tilde{c}_e(x, t) = h(t)\Psi(x).$$

It remains to find $h(t)$ and $\Psi(x)$. Substituting the assumed form into the original PDE gives

$$\frac{dh(t)}{dt}\Psi(x) = \frac{1}{\varepsilon_e(x)} \frac{\partial}{\partial x} D_{e,\text{eff}}(x) h(t) \frac{\partial \Psi(x)}{\partial x}.$$

We separate time-dependent variables on one side, and position dependent variables on the other as

$$\frac{1}{h(t)} \frac{dh(t)}{dt} = \frac{1}{\varepsilon_e(x)\Psi(x)} \frac{\partial}{\partial x} D_{e,\text{eff}}(x) \frac{\partial \Psi(x)}{\partial x}.$$

Since the left-hand side is a function of time only, and the right-hand side is a function of position only, and they are equal for all time and all position, they must both be equal to a constant, which we will label as $-\lambda$.⁶

$$\begin{aligned} \frac{dh(t)}{dt} &= -\lambda h(t) \\ \frac{\partial}{\partial x} D_{e,\text{eff}} \frac{\partial \Psi(x)}{\partial x} &= -\lambda \varepsilon_e(x) \Psi(x). \end{aligned}$$

Note that there are an infinite number of λ that solve these equations, and each distinct value of λ yields different $h(t)$ and $\Psi(x)$. So, we rethink the notation and change $h(t) \mapsto h(t; \lambda)$ and change $\Psi(t) \mapsto \Psi(t; \lambda)$, which means that both h and Ψ are *parameterized* by a particular value of λ . Rewriting gives

$$\frac{dh(t; \lambda)}{dt} = -\lambda h(t; \lambda) \quad (6.31)$$

$$\frac{\partial}{\partial x} D_{e,\text{eff}}(x) \frac{\partial \Psi(x; \lambda)}{\partial x} = -\lambda \varepsilon_e(x) \Psi(x; \lambda). \quad (6.32)$$

The solution to Eq. (6.31) has the form

$$h(t; \lambda) = h(0; \lambda) e^{-\lambda t}.$$

The solution to Eq. (6.32) determines the eigenfunctions $\Psi(x; \lambda)$, each of which is divided into three parts: one each for the negative-electrode, separator, and positive-electrode regions. For the negative electrode region, we have (where k_1 and k_2 are (possibly) functions of λ , but this dependence has been omitted for brevity)

$$\Psi^{\text{neg}}(x; \lambda) = k_1 \cos(\sqrt{\lambda \varepsilon_e^{\text{neg}} / D_{e,\text{eff}}^{\text{neg}}} x) + k_2 \sin(\sqrt{\lambda \varepsilon_e^{\text{neg}} / D_{e,\text{eff}}^{\text{neg}}} x).$$

⁶ λ has units s^{-1} and so is a kind of frequency. $\lambda = 0$ corresponds to dc; small λ correspond to low frequencies; large λ correspond to high frequencies.

The boundary condition at $x = 0$ eliminates the $\sin(\cdot)$ term, leaving us with

$$\Psi^{\text{neg}}(x; \lambda) = k_1 \cos \left(\sqrt{\lambda \varepsilon_e^{\text{neg}} / D_{e,\text{eff}}^{\text{neg}}} x \right).$$

For the separator region, we have

$$\Psi^{\text{sep}}(x; \lambda) = k_3 \cos \left(\sqrt{\lambda \varepsilon_e^{\text{sep}} / D_{e,\text{eff}}^{\text{sep}}} x \right) + k_4 \sin \left(\sqrt{\lambda \varepsilon_e^{\text{sep}} / D_{e,\text{eff}}^{\text{sep}}} x \right).$$

For this region, the $\sin(\cdot)$ term is not automatically eliminated, and the two functions must be scaled so that the interior boundary conditions are met automatically. To compact notation, we define

$$\omega_1 = L^{\text{neg}} \sqrt{\frac{\lambda \varepsilon_e^{\text{neg}}}{D_{e,\text{eff}}^{\text{neg}}}} \quad \text{and} \quad \omega_2 = L^{\text{neg}} \sqrt{\frac{\lambda \varepsilon_e^{\text{sep}}}{D_{e,\text{eff}}^{\text{sep}}}}.$$

Then, for continuity,

$$k_1 \cos(\omega_1) = k_3 \cos(\omega_2) + k_4 \sin(\omega_2).$$

For the first derivative criterion:

$$\begin{aligned} D_{e,\text{eff}}^{\text{neg}} \left[-k_1 \frac{\omega_1}{L^{\text{neg}}} \sin(\omega_1) \right] \\ = D_{e,\text{eff}}^{\text{sep}} \left[-k_3 \frac{\omega_2}{L^{\text{neg}}} \sin(\omega_2) + k_4 \frac{\omega_2}{L^{\text{neg}}} \cos(\omega_2) \right]. \end{aligned}$$

We now have two equations and two unknowns (k_3 and k_4), which can be solved in terms of the unknown k_1 , which we will determine later

$$\begin{bmatrix} \cos(\omega_2) & \sin(\omega_2) \\ -D_{e,\text{eff}}^{\text{sep}} \omega_2 \sin(\omega_2) & D_{e,\text{eff}}^{\text{sep}} \omega_2 \cos(\omega_2) \end{bmatrix} \begin{bmatrix} k_3 \\ k_4 \end{bmatrix} \\ = k_1 \begin{bmatrix} \cos(\omega_1) \\ -D_{e,\text{eff}}^{\text{neg}} \omega_1 \sin(\omega_1) \end{bmatrix}.$$

Finally, for the positive-electrode region, we have

$$\Psi^{\text{pos}}(x; \lambda) = k_5 \cos \left(\sqrt{\lambda \varepsilon_e^{\text{pos}} / D_{e,\text{eff}}^{\text{pos}}} x \right) + k_6 \sin \left(\sqrt{\lambda \varepsilon_e^{\text{pos}} / D_{e,\text{eff}}^{\text{pos}}} x \right).$$

We define

$$\omega_3 = (L^{\text{neg}} + L^{\text{sep}}) \sqrt{\frac{\lambda \varepsilon_e^{\text{sep}}}{D_{e,\text{eff}}^{\text{sep}}}} \quad \text{and} \quad \omega_4 = (L^{\text{neg}} + L^{\text{sep}}) \sqrt{\frac{\lambda \varepsilon_e^{\text{pos}}}{D_{e,\text{eff}}^{\text{pos}}}}.$$

Then, for continuity,

$$k_3 \cos(\omega_3) + k_4 \sin(\omega_3) = k_5 \cos(\omega_4) + k_6 \sin(\omega_4).$$

For the first derivative criterion,

$$\begin{aligned} D_{e,\text{eff}}^{\text{sep}} & \left[-k_3 \frac{\omega_3}{L^{\text{neg}} + L^{\text{sep}}} \sin(\omega_3) + k_4 \frac{\omega_3}{L^{\text{neg}} + L^{\text{sep}}} \cos(\omega_3) \right] \\ & = D_{e,\text{eff}}^{\text{pos}} \left[-k_5 \frac{\omega_4}{L^{\text{neg}} + L^{\text{sep}}} \sin(\omega_4) + k_6 \frac{\omega_4}{L^{\text{neg}} + L^{\text{sep}}} \cos(\omega_4) \right]. \end{aligned}$$

We again have two equations and two unknowns (now in k_5 and k_6), which can be solved in terms of k_3 and k_4

$$\begin{aligned} & \begin{bmatrix} \cos(\omega_4) & \sin(\omega_4) \\ -D_{e,\text{eff}}^{\text{pos}} \omega_4 \sin(\omega_4) & D_{e,\text{eff}}^{\text{pos}} \omega_4 \cos(\omega_4) \end{bmatrix} \begin{bmatrix} k_5 \\ k_6 \end{bmatrix} \\ & = \begin{bmatrix} \cos(\omega_3) & \sin(\omega_3) \\ -D_{e,\text{eff}}^{\text{sep}} \omega_3 \sin(\omega_3) & D_{e,\text{eff}}^{\text{sep}} \omega_3 \cos(\omega_3) \end{bmatrix} \begin{bmatrix} k_3 \\ k_4 \end{bmatrix}. \end{aligned}$$

So, assuming that we can find k_1 , we now have

$$\Psi(x; \lambda) = \begin{cases} \Psi^{\text{neg}}(x; \lambda), & 0 \leq x < L^{\text{neg}}; \\ \Psi^{\text{sep}}(x; \lambda), & L^{\text{neg}} \leq x < L^{\text{neg}} + L^{\text{sep}}; \\ \Psi^{\text{pos}}(x; \lambda), & L^{\text{neg}} + L^{\text{sep}} \leq x \leq L^{\text{tot}}. \end{cases} \quad (6.33)$$

We find k_1 via the third property of Sturm–Liouville theory in Sect. 6.5.2.

We choose its value to force the eigenfunctions to be orthonormal

with respect to the weighting function $\varepsilon_e(x)$. That is, we select k_1 such that

$$\int_0^{L^{\text{tot}}} \Psi^2(x; \lambda) \varepsilon_e(x) dx = 1.$$

The final boundary condition $\partial\Psi(L^{\text{tot}}; \lambda)/\partial x = 0$ imposes the condition that allows us to solve for λ_n . Generally, this cannot be done in closed form. So, we use numeric methods to search an interval for zero crossings of $d\Psi(L^{\text{tot}}; \lambda)/dx$ as a function of λ . An example is shown in Fig. 6.6. In this example, the first 10 roots are located at

$$\{\lambda_n\} = \{0, 0.0039, 0.0106, 0.0298, 0.0538, 0.0782, 0.1151, 0.1620, 0.1936, 0.2676\},$$

where we denote the ordered set of eigenvalues as $\{\lambda_n\}$. Then, the solution to the homogeneous problem is the superposition

$$\tilde{c}_e(x, t) = \sum_{n=0}^{\infty} h(0; \lambda) \Psi(x; \lambda_n) e^{-\lambda_n t}.$$

6.5.4 Solution to the forced PDE

We now generalize the solution from the homogeneous case to the inhomogeneous case to solve

$$\frac{\partial \tilde{c}_e(x, t)}{\partial t} = \frac{1}{\varepsilon_e(x)} \frac{\partial}{\partial x} D_{e,\text{eff}}(x) \frac{\partial \tilde{c}_e(x, t)}{\partial x} + \frac{a_s(x)(1 - t_+^0)}{\varepsilon_e(x)} j(x, t). \quad (6.34)$$

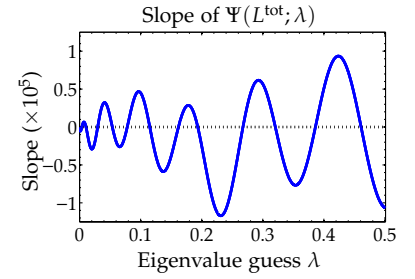


Figure 6.6: Finding eigenvalues by locating zero crossings.

Our approach is to transform $\tilde{c}_e(x, t)$ into a series expansion using the eigenfunctions of the homogeneous solution $\Psi(x; \lambda_n)$ as a basis set.

We rely on the fact that any piecewise smooth function can be expanded in terms of the eigenfunctions.

$$\tilde{c}_e(x, t) = \sum_{n=0}^{\infty} \tilde{c}_{e,n}(t) \Psi(x; \lambda_n), \quad (6.35)$$

where $\tilde{c}_{e,n}(t)$ are the generalized Fourier coefficients of $\tilde{c}_e(x, t)$.

Taking the partial derivative of Eq. (6.35) with respect to time gives

$$\frac{\partial \tilde{c}_e(x, t)}{\partial t} = \sum_{n=0}^{\infty} \frac{d\tilde{c}_{e,n}(t)}{dt} \Psi(x; \lambda_n). \quad (6.36)$$

Then, substituting into the original PDE gives

$$\sum_{n=0}^{\infty} \frac{d\tilde{c}_{e,n}(t)}{dt} \Psi(x; \lambda_n) = \frac{1}{\varepsilon_e(x)} \frac{\partial}{\partial x} D_{e,\text{eff}}(x) \frac{\partial \tilde{c}_e(x, t)}{\partial x} + \frac{a_s(x)(1 - t_+^0)}{\varepsilon_e(x)} j(x, t). \quad (6.37)$$

To reduce the left-hand side of Eq. (6.37), we multiply both sides by $\Psi(x; \lambda_m) \varepsilon_e(x)$ and integrate from 0 to L^{tot} .

$$\begin{aligned} & \int_0^{L^{\text{tot}}} \sum_{n=0}^{\infty} \frac{d\tilde{c}_{e,n}(t)}{dt} \Psi(x; \lambda_n) \Psi(x; \lambda_m) \varepsilon_e(x) dx \\ &= \int_0^{L^{\text{tot}}} \Psi(x; \lambda_m) \frac{\partial}{\partial x} D_{e,\text{eff}}(x) \frac{\partial \tilde{c}_e(x, t)}{\partial x} dx \\ &+ \int_0^{L^{\text{tot}}} a_s(x)(1 - t_+^0) j(x, t) \Psi(x; \lambda_m) dx. \end{aligned}$$

Because $\int_0^{L^{\text{tot}}} \Psi(x; \lambda_n) \Psi(x; \lambda_m) \varepsilon_e(x) dx = \delta_{mn}$, the integral on the left is nonzero only when $m = n$. Therefore,

$$\begin{aligned} \frac{d\tilde{c}_{e,n}(t)}{dt} &= \int_0^{L^{\text{tot}}} \Psi(x; \lambda_n) \frac{\partial}{\partial x} D_{e,\text{eff}}(x) \frac{\partial \tilde{c}_e(x, t)}{\partial x} dx \\ &+ \int_0^{L^{\text{tot}}} a_s(x)(1 - t_+^0) j(x, t) \Psi(x; \lambda_n) dx. \end{aligned} \quad (6.38)$$

We want to simplify the first term on the right-hand side, and we do this by using Green's identity. Note that $\Psi(x; \lambda)$ are the solutions to a Sturm–Liouville problem with $p(x) = 1$, $q(x) = 0$, and $w(x) = \varepsilon_e(x)$.

We focus again on the first term:

$$\int_0^{L^{\text{tot}}} \Psi(x; \lambda_n) \frac{\partial}{\partial x} D_{e,\text{eff}}(x) \frac{\partial \tilde{c}_e(x, t)}{\partial x} dx.$$

We use Green's identity with $v = \Psi(x)$, $u = \tilde{c}_e(x, t)$, and $p = D_{e,\text{eff}}(x)$

$$\int_0^{L^{\text{tot}}} \left[\tilde{c}_e(x, t) \frac{\partial}{\partial x} D_{e,\text{eff}}(x) \frac{\partial \Psi(x)}{\partial x} - \Psi(x; \lambda_n) \frac{\partial}{\partial x} D_{e,\text{eff}}(x) \frac{\partial \tilde{c}_e(x, t)}{\partial x} \right] dx$$

$$= D_{e,\text{eff}}(x) \left(\tilde{c}_e(x, t) \frac{\partial \Psi(x; \lambda_n)}{\partial x} - \Psi(x; \lambda_n) \frac{\partial \tilde{c}_e(x, t)}{\partial x} \right) \Big|_0^{L^{\text{tot}}}. \quad (6.39)$$

In our problem, the right-hand side goes to zero because of boundary conditions

$$\frac{\partial \Psi(x; \lambda_n)}{\partial x} \Big|_{x \in \{0, L^{\text{tot}}\}} = \frac{\partial \tilde{c}_e(x, t)}{\partial x} \Big|_{x \in \{0, L^{\text{tot}}\}} = 0.$$

Therefore,

$$\int_0^{L^{\text{tot}}} \tilde{c}_e(x, t) \frac{\partial}{\partial x} D_{e,\text{eff}}(x) \frac{\partial \Psi(x)}{\partial x} dx = \int_0^{L^{\text{tot}}} \Psi(x; \lambda_n) \frac{\partial}{\partial x} D_{e,\text{eff}}(x) \frac{\partial \tilde{c}_e(x, t)}{\partial x} dx.$$

The left-hand side can be written as

$$\int_0^{L^{\text{tot}}} \tilde{c}_e(x, t) \frac{\partial}{\partial x} D_{e,\text{eff}}(x) \frac{\partial \Psi(x)}{\partial x} dx = -\lambda_n \int_0^{L^{\text{tot}}} \tilde{c}_e(x, t) \Psi(x; \lambda_n) \varepsilon_e(x) dx, \quad (6.40)$$

via Eq. (6.32).

Substituting, we get

$$\int_0^{L^{\text{tot}}} \Psi(x) \frac{\partial}{\partial x} D_{e,\text{eff}}(x) \frac{\partial \tilde{c}_e(x, t)}{\partial x} dx = -\lambda_n \int_0^{L^{\text{tot}}} \tilde{c}_e(x, t) \Psi(x; \lambda_n) \varepsilon_e(x) dx.$$

Using this in Eq. (6.38),

$$\begin{aligned} \frac{d\tilde{c}_{e,n}(t)}{dt} &= -\lambda_n \int_0^{L^{\text{tot}}} \tilde{c}_e(x, t) \Psi(x; \lambda_n) \varepsilon_e(x) dx \\ &\quad + \int_0^{L^{\text{tot}}} a_s(x) (1 - t_+^0) j(x, t) \Psi_n(x) dx \\ &= -\lambda_n \tilde{c}_{e,n}(t) + \underbrace{\int_0^{L^{\text{tot}}} a_s(x) (1 - t_+^0) j(x, t) \Psi_n(x) dx}_{j_n(t)}, \end{aligned} \quad (6.41)$$

where $j_n(t)$ is the modal input to $\tilde{c}_{e,n}(t)$.

6.5.5 Example of $\tilde{c}_e(x, t)$ using eigenfunction method

To illustrate the results to date, consider a cell with the following properties.

$$\begin{array}{lll} L^{\text{neg}} = 128 \mu\text{m} & \varepsilon_e^{\text{neg}} = 0.357 & D_{e,\text{eff}}^{\text{neg}} = 1.60 \times 10^{-11} \text{ m}^2/\text{s} \\ L^{\text{sep}} = 76 \mu\text{m} & \varepsilon_e^{\text{sep}} = 0.724 & D_{e,\text{eff}}^{\text{sep}} = 4.62 \times 10^{-11} \text{ m}^2/\text{s} \\ L^{\text{pos}} = 190 \mu\text{m} & \varepsilon_e^{\text{pos}} = 0.444 & D_{e,\text{eff}}^{\text{pos}} = 2.22 \times 10^{-11} \text{ m}^2/\text{s} \end{array}$$

We look for a solution to the electrolyte concentration as a function of position when the concentration is initially uniform at $1,000 \text{ mol m}^{-3}$, and a 10-A step of current has been applied to the cell for 3 s, where

j is assumed to be uniform in each electrode region and zero in the separator.

First, we find the eigenfunctions. The first six, $\Psi(x; \lambda_0)$ through $\Psi(x; \lambda_5)$, are shown in Fig. 6.7. We can quickly double-check to see if we have found the right ones (since the numeric search to find λ_n might miss some if the search parameters are not initialized with good initial guesses) by counting the number of zero crossings of each eigenfunction. Per property 2 of the Sturm–Liouville theory in Sect. 6.5.2, we know that $\Psi(x; \lambda_0)$ should have no zero crossings, $\Psi(x; \lambda_1)$ should have one zero crossing, and so forth. Also, the slope of every eigenfunction should be zero at both cell boundaries. The figure shows that this is indeed the case.

Next, having identified the eigenfunctions, we use them with Eq. (6.41) to solve for the generalized Fourier coefficients $\tilde{c}_{e,n}(t)$ for $0 \leq n \leq 10$. Finally, we compute $\tilde{c}_e(x, t)$ using Eq. (6.35).

Results are shown in Fig. 6.8. The red line shows the exact PDE solution, and the blue line shows the approximate solution using eigenfunctions zero through 10. It is possible to improve the solution by using additional eigenfunctions but there is a point of diminishing returns. (MATLAB code for this example is listed in Sect. 6.15.)

6.5.6 A transfer-function model for $\tilde{c}_{e,n}(x, t)$

To compute $\tilde{c}_e(x, t)$ via transfer-function methods, we note that $\tilde{c}_e(x, t)$ is formed from a summation of $\tilde{c}_{e,n}(t)$ terms. So, we can compute $\tilde{c}_e(x, t)$ if we know $\tilde{c}_{e,n}(t)$; therefore, we proceed by finding a transfer function for $\tilde{c}_{e,n}(t)$.

We begin by taking Laplace transforms of Eq. (6.41), rewritten here

$$\begin{aligned} \frac{d}{dt} \tilde{c}_{e,n}(t) &= -\lambda_n \tilde{c}_{e,n}(t) + j_n(t) \\ s \tilde{C}_{e,n}(s) - \tilde{c}_{e,n}(0) &= -\lambda_n \tilde{C}_{e,n}(s) + J_n(s). \end{aligned}$$

Because debiased variable $\tilde{c}_e(x, t)$ has zero initial value, so too does $\tilde{c}_{e,n}(t)$ and

$$\begin{aligned} s \tilde{C}_{e,n}(s) &= -\lambda_n \tilde{C}_{e,n}(s) + J_n(s) \\ \frac{\tilde{C}_{e,n}(s)}{I_{app}(s)} &= \frac{1}{s + \lambda_n} \frac{J_n(s)}{I_{app}(s)}. \end{aligned}$$

To solve this, we need to find a transfer function for $j_n(t)$ first.

We begin by writing,

$$\begin{aligned} j_n(t) &= \int_0^{L^{\text{tot}}} a_s(x) (1 - t_+^0) j(x, t) \Psi(x; \lambda_n) dx \\ &= \int_0^{L^{\text{neg}}} a_s^{\text{neg}} (1 - t_+^0) j^{\text{neg}}(x, t) \Psi(x; \lambda_n) dx \end{aligned}$$

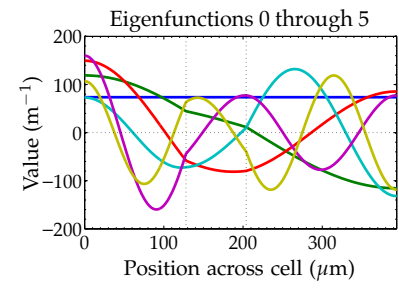


Figure 6.7: Eigenfunctions for the example.

(Adapted from Fig. 4 in Lee, J.L., Chemistruck, A., and Plett, G.L., “One-Dimensional Physics-Based Reduced-Order Model of Lithium-Ion Dynamics,” *Journal of Power Sources*, 220, 2012, pp. 430–448.)

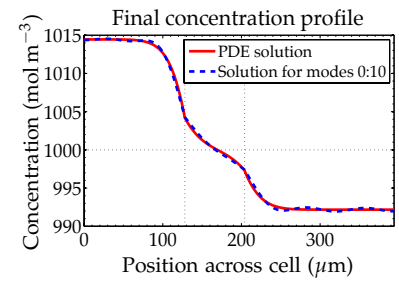


Figure 6.8: Solution for electrolyte concentration.

$$\begin{aligned}
& + \int_{L^{\text{neg}}+L^{\text{sep}}}^{L^{\text{tot}}} a_s^{\text{pos}} (1-t_+^0) j^{\text{pos}}(x, t) \Psi(x; \lambda_n) dx \\
& = j_n^{\text{neg}}(t) + j_n^{\text{pos}}(t).
\end{aligned}$$

Looking at the negative-electrode term first:

$$\begin{aligned}
j_n^{\text{neg}}(t) & = a_s^{\text{neg}} (1-t_+^0) \int_0^{L^{\text{neg}}} j^{\text{neg}}(x, t) \Psi(x; \lambda_n) dx \\
\frac{j_n^{\text{neg}}(s)}{I_{\text{app}}(s)} & = a_s^{\text{neg}} (1-t_+^0) \int_0^{L^{\text{neg}}} \frac{J^{\text{neg}}(x/L^{\text{neg}}, s)}{I_{\text{app}}(s)} \Psi(x; \lambda_n) dx,
\end{aligned}$$

where the integrand evaluates $J^{\text{neg}}(z, s) / I_{\text{app}}(s)$ from Eq. (6.13) at $z = x/L^{\text{neg}}$.

The transfer function is (computed in Mathematica)

$$\begin{aligned}
\frac{J_n^{\text{neg}}(s)}{I_{\text{app}}(s)} & = \frac{k_1 (1-t_+^0) \omega_n^{\text{neg}} \sin(\omega_n^{\text{neg}}) \left(\kappa_{\text{eff}}^{\text{neg}} + \sigma_{\text{eff}}^{\text{neg}} \cosh(\nu^{\text{neg}}(s)) \right) \nu^{\text{neg}}(s)}{AF(\kappa_{\text{eff}}^{\text{neg}} + \sigma_{\text{eff}}^{\text{neg}}) \left((\omega_n^{\text{neg}})^2 + (\nu^{\text{neg}}(s))^2 \right) \sinh(\nu^{\text{neg}}(s))} \\
& + \frac{k_1 (1-t_+^0) \left(\kappa_{\text{eff}}^{\text{neg}} + \sigma_{\text{eff}}^{\text{neg}} \cos(\omega_n^{\text{neg}}) \right) (\nu^{\text{neg}}(s))^2}{AF(\kappa_{\text{eff}}^{\text{neg}} + \sigma_{\text{eff}}^{\text{neg}}) \left((\omega_n^{\text{neg}})^2 + (\nu^{\text{neg}}(s))^2 \right)}, \quad (6.42)
\end{aligned}$$

where $\omega_n^{\text{neg}} = L^{\text{neg}} \sqrt{\lambda_n \epsilon_e^{\text{neg}} / D_{e,\text{eff}}^{\text{neg}}}$.

Looking at the positive electrode now,

$$\begin{aligned}
j_n^{\text{pos}}(t) & = a_s^{\text{pos}} (1-t_+^0) \int_{L^{\text{tot}}-L^{\text{pos}}}^{L^{\text{tot}}} j^{\text{pos}}(x, t) \Psi(x; \lambda_n) dx \\
\frac{J_n^{\text{pos}}(s)}{I_{\text{app}}(s)} & = a_s^{\text{pos}} (1-t_+^0) \int_{L^{\text{tot}}-L^{\text{pos}}}^{L^{\text{tot}}} \frac{J^{\text{pos}}((L^{\text{tot}}-x)/L^{\text{pos}}, s)}{I_{\text{app}}(s)} \Psi(x; \lambda_n) dx,
\end{aligned}$$

where the integrand evaluates $J^{\text{pos}}(z, s) / I_{\text{app}}(s)$ from Eq. (6.22) at $z = (L^{\text{tot}}-x)/L^{\text{pos}}$.

The transfer function is (computed in Mathematica)

$$\begin{aligned}
\frac{J_n^{\text{pos}}(s)}{I_{\text{app}}(s)} & = \frac{k_5 (1-t_+^0) \omega_n^{\text{pos}} \sin(\omega_n^{\text{sep}}) \left(\kappa_{\text{eff}}^{\text{pos}} + \sigma_{\text{eff}}^{\text{pos}} \cosh(\nu^{\text{pos}}(s)) \right) \nu^{\text{pos}}(s)}{AF(\kappa_{\text{eff}}^{\text{pos}} + \sigma_{\text{eff}}^{\text{pos}}) \left((\omega_n^{\text{pos}})^2 + (\nu^{\text{pos}}(s))^2 \right) \sinh(\nu^{\text{pos}}(s))} \\
& - \frac{k_5 (1-t_+^0) \omega_n^{\text{pos}} \sin(\omega_n^{\text{tot}}) \left(\sigma_{\text{eff}}^{\text{pos}} + \kappa_{\text{eff}}^{\text{pos}} \cosh(\nu^{\text{pos}}(s)) \right) \nu^{\text{pos}}(s)}{AF(\kappa_{\text{eff}}^{\text{pos}} + \sigma_{\text{eff}}^{\text{pos}}) \left((\omega_n^{\text{pos}})^2 + (\nu^{\text{pos}}(s))^2 \right) \sinh(\nu^{\text{pos}}(s))} \\
& - \frac{k_5 (1-t_+^0) \left(\sigma_{\text{eff}}^{\text{pos}} \cos(\omega_n^{\text{sep}}) + \kappa_{\text{eff}}^{\text{pos}} \cos(\omega_n^{\text{tot}}) \right) (\nu^{\text{pos}}(s))^2}{AF(\kappa_{\text{eff}}^{\text{pos}} + \sigma_{\text{eff}}^{\text{pos}}) \left((\omega_n^{\text{pos}})^2 + (\nu^{\text{pos}}(s))^2 \right)} \\
& + \frac{k_6 (1-t_+^0) \omega_n^{\text{pos}} \cos(\omega_n^{\text{tot}}) \left(\sigma_{\text{eff}}^{\text{pos}} + \kappa_{\text{eff}}^{\text{pos}} \cosh(\nu^{\text{pos}}(s)) \right) \nu^{\text{pos}}(s)}{AF(\kappa_{\text{eff}}^{\text{pos}} + \sigma_{\text{eff}}^{\text{pos}}) \left((\omega_n^{\text{pos}})^2 + (\nu^{\text{pos}}(s))^2 \right) \sinh(\nu^{\text{pos}}(s))}
\end{aligned}$$

$$\begin{aligned}
& - \frac{k_6(1-t_+^0)\omega_n^{\text{pos}} \cos(\omega_n^{\text{sep}}) \left(\kappa_{\text{eff}}^{\text{pos}} + \sigma_{\text{eff}}^{\text{pos}} \cosh(\nu^{\text{pos}}(s)) \right) \nu^{\text{pos}}(s)}{AF(\kappa_{\text{eff}}^{\text{pos}} + \sigma_{\text{eff}}^{\text{pos}}) \left((\omega_n^{\text{pos}})^2 + (\nu^{\text{pos}}(s))^2 \right) \sinh(\nu^{\text{pos}}(s))} \\
& - \frac{k_6(1-t_+^0) \left(\sigma_{\text{eff}}^{\text{pos}} \sin(\omega_n^{\text{sep}}) + \kappa_{\text{eff}}^{\text{pos}} \sin(\omega_n^{\text{tot}}) \right) (\nu^{\text{pos}}(s))^2}{AF(\kappa_{\text{eff}}^{\text{pos}} + \sigma_{\text{eff}}^{\text{pos}}) \left((\omega_n^{\text{pos}})^2 + (\nu^{\text{pos}}(s))^2 \right)}, \tag{6.43}
\end{aligned}$$

where $\omega_n^{\text{pos}} = L^{\text{pos}} \sqrt{\varepsilon_e^{\text{pos}} \lambda_n / D_{e,\text{eff}}^{\text{pos}}}$, $\omega_n^{\text{tot}} = L^{\text{tot}} \sqrt{\varepsilon_e^{\text{pos}} \lambda_n / D_{e,\text{eff}}^{\text{pos}}}$, and $\omega_n^{\text{sep}} = \omega_n^{\text{tot}} - \omega_n^{\text{pos}}$.

Overall, we have

$$\frac{\tilde{C}_{e,n}(s)}{I_{\text{app}}(s)} = \frac{1}{s + \lambda_n} \left[\frac{J_n^{\text{neg}}(s)}{I_{\text{app}}(s)} + \frac{J_n^{\text{pos}}(s)}{I_{\text{app}}(s)} \right]. \tag{6.44}$$

Yes, this is a mess. The good news is that we'll develop tools that deal with the mess quite nicely.

6.5.7 A transfer function model for $\tilde{c}_e(x, t)$

Our final step is to take the results developed so far in this section and turn them into a transfer function for $\tilde{c}_e(x, t)$. Recall that

$$\tilde{c}_e(x, t) = \sum_{n=0}^{\infty} \tilde{c}_{e,n}(t) \Psi(x; \lambda_n).$$

The first mode in this solution, $n = 0$, is the dc term and is zero because $\tilde{c}_{e,0} = 0$. We further truncate the summation to M terms for a computable approximate result

$$\tilde{c}_e(x, t) \approx \sum_{n=1}^M \tilde{c}_{e,n}(t) \Psi(x; \lambda_n).$$

Then, we can arrive at a transfer function for any desired x location of the cell as

$$\frac{\tilde{C}_e(x, s)}{I_{\text{app}}(s)} = \sum_{n=1}^M \frac{\tilde{C}_{e,n}(s)}{I_{\text{app}}(s)} \Psi(x; \lambda_n), \tag{6.45}$$

where $\tilde{C}_{e,n}(s) / I_{\text{app}}(s)$ is defined in Eq. (6.44). The value for M is chosen as a tradeoff between computation and accuracy. Note, however, that the summation is performed only when computing $\tilde{C}_e(x, s) / I_{\text{app}}(s)$ as part of the DRA process. It is not performed during the implementation of the final ODE. Therefore, M can be chosen to be quite large without incurring substantial delay in executing the DRA algorithm; it can be chosen to be any value at all without incurring any real-time processing delay in the final ODE.

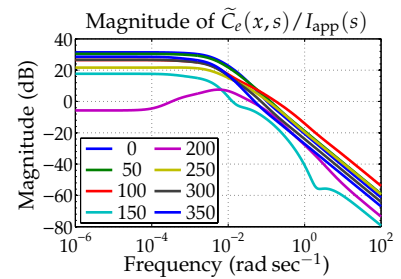


Figure 6.9: Example magnitude plots for $\tilde{C}_e(x, s) / I_{\text{app}}(s)$ at eight different x locations (in μm) across the cell.

Fig. 6.9 shows an example magnitude-response plot for the transfer function $\tilde{C}_e(x, s)/I_{\text{app}}(s)$. Once again we note the simplicity of the function despite the mathematical complexity involved in its derivation.

6.6 A one-dimensional model of $\tilde{\phi}_e(x, t)$

We now wish to develop an independent transfer function for $\phi_e(x, t)$. We begin by recalling the differential equation, Eq. (4.6), that governs ϕ_e , which in one dimension is

$$\kappa_{\text{eff}} \frac{\partial^2}{\partial x^2} \phi_e(x, t) + \kappa_{D,\text{eff}} \frac{\partial^2}{\partial x^2} \ln \tilde{c}_e(x, t) = -a_s F j(x, t). \quad (6.46)$$

We will arrive at a transfer function for $\phi_e(x, t)$ by integrating this expression twice.

First, recall from Eq. (4.18) that we have a definition for the ionic current \mathbf{i}_e flowing through the electrolyte: $\varepsilon_e \mathbf{i}_e = -\kappa_{\text{eff}} \nabla \phi_e - \kappa_{D,\text{eff}} \nabla \ln c_e$. Again, specializing to one dimension, we have

$$\varepsilon_e i_e(x, t) = -\kappa_{\text{eff}} \frac{\partial}{\partial x} \phi_e(x, t) - \kappa_{D,\text{eff}} \frac{\partial}{\partial x} \ln c_e(x, t). \quad (6.47)$$

This allows us to rewrite Eq. (6.46) as

$$\varepsilon_e \frac{\partial}{\partial x} i_e(x, t) = a_s F j(x, t).$$

Integrating from zero to x and noting that $i_e(0, t) = 0$ gives

$$i_e(x, t) = \begin{cases} \int_0^x \frac{a_s^{\text{neg}} F}{\varepsilon_e^{\text{neg}}} j^{\text{neg}}(\xi, t) d\xi, & 0 \leq x \leq L^{\text{neg}}; \\ \frac{i_{\text{app}}(t)}{\varepsilon_e^{\text{sep}} A}, & L^{\text{neg}} \leq x \leq L^{\text{neg}} + L^{\text{sep}}; \\ \frac{i_{\text{app}}(t)}{\varepsilon_e^{\text{pos}} A} + \int_{L^{\text{neg}} + L^{\text{sep}}}^x \frac{a_s^{\text{pos}} F}{\varepsilon_e^{\text{pos}}} j^{\text{pos}}(\xi, t) d\xi, & L^{\text{neg}} + L^{\text{sep}} \leq x \leq L^{\text{tot}}. \end{cases}$$

A transfer function for $i_e(x, t)$ in the negative electrode is

$$\begin{aligned} \frac{i_e(x, s)}{I_{\text{app}}(s)} &= \frac{a_s^{\text{neg}} F}{\varepsilon_e^{\text{neg}}} \int_0^x \frac{j^{\text{neg}}(\xi/L^{\text{neg}}, s)}{I_{\text{app}}(s)} d\xi, \\ &= \frac{\kappa_{\text{eff}}^{\text{neg}} \left(\sinh(\nu^{\text{neg}}(s)) - \sinh \left(\frac{(L^{\text{neg}} - x)\nu^{\text{neg}}(s)}{L^{\text{neg}}} \right) \right)}{\varepsilon_e^{\text{neg}} A (\kappa_{\text{eff}}^{\text{neg}} + \sigma_{\text{eff}}^{\text{neg}}) \sinh(\nu^{\text{neg}}(s))} \\ &\quad + \frac{\sigma_{\text{eff}}^{\text{neg}} \sinh \left(\frac{x\nu^{\text{neg}}(s)}{L^{\text{neg}}} \right)}{\varepsilon_e^{\text{neg}} A (\kappa_{\text{eff}}^{\text{neg}} + \sigma_{\text{eff}}^{\text{neg}}) \sinh(\nu^{\text{neg}}(s))}. \end{aligned}$$

A transfer function for $i_e(x, t)$ in the separator is

$$\frac{i_e(x, s)}{I_{\text{app}}(s)} = \frac{1}{\varepsilon_e^{\text{sep}} A}.$$

A transfer function for $i_e(x, t)$ in the positive electrode is

$$\begin{aligned} \frac{I_e(x, s)}{I_{app}(s)} &= \frac{1}{\varepsilon_e^{\text{pos}} A} + \frac{a_s^{\text{pos}} F}{\varepsilon_e^{\text{pos}}} \int_{L^{\text{neg}} + L^{\text{sep}}}^x \frac{J^{\text{pos}}((L^{\text{tot}} - \xi)/L^{\text{pos}}, s)}{I_{app}(s)} d\xi \\ &= \frac{\kappa_{\text{eff}}^{\text{pos}} \left(\sinh(\nu^{\text{pos}}(s)) - \sinh \left(\frac{(x - L^{\text{neg}} - L^{\text{sep}})}{L^{\text{pos}}} \nu^{\text{pos}}(s) \right) \right)}{\varepsilon_e^{\text{pos}} A (\kappa_{\text{eff}}^{\text{pos}} + \sigma_{\text{eff}}^{\text{pos}}) \sinh(\nu^{\text{pos}}(s))} \\ &\quad + \frac{\sigma_{\text{eff}}^{\text{pos}} \sinh \left(\frac{(L^{\text{tot}} - x)}{L^{\text{pos}}} \nu^{\text{pos}}(s) \right)}{\varepsilon_e^{\text{pos}} A (\kappa_{\text{eff}}^{\text{pos}} + \sigma_{\text{eff}}^{\text{pos}}) \sinh(\nu^{\text{pos}}(s))}. \end{aligned}$$

We now integrate Eq. (6.47) from zero to x to obtain ϕ_e :

$$\phi_e(x, t) - \phi_e(0, t) = \int_0^x \frac{-\varepsilon_e i_e(\xi, t)}{\kappa_{\text{eff}}} + \frac{2RT}{F} (1 - t_+^0) \frac{\partial \ln c_e(\xi, t)}{\partial \xi} d\xi.$$

Define $\tilde{\phi}_e(x, t) = \phi_e(x, t) - \phi_e(0, t)$. Then, $\tilde{\phi}_e(x, t)$ comprises two parts:

$$\begin{aligned} [\tilde{\phi}_e(x, t)]_1 &= \int_0^x \frac{-\varepsilon_e i_e(\xi, t)}{\kappa_{\text{eff}}} d\xi, \\ [\tilde{\phi}_e(x, t)]_2 &= \int_0^x \frac{2RT}{F} (1 - t_+^0) \frac{\partial \ln c_e(\xi, t)}{\partial \xi} d\xi. \end{aligned}$$

The first part, $[\tilde{\phi}_e(x, t)]_1$, can be determined via transfer functions; the second part, $[\tilde{\phi}_e(x, t)]_2$, can be determined via known $c_e(x, t)$.

Let's continue to look at the first part. In the negative electrode,

$$\begin{aligned} \frac{[\tilde{\Phi}_e(x, s)]_1}{I_{app}(s)} &= \int_0^x \frac{-\varepsilon_e^{\text{neg}} I_e(\xi, s)}{\kappa_{\text{eff}}^{\text{neg}} I_{app}(s)} d\xi \\ &= -\frac{L^{\text{neg}} \sigma_{\text{eff}}^{\text{neg}} (\cosh(\frac{x}{L^{\text{neg}}} \nu^{\text{neg}}(s)) - 1)}{A \kappa_{\text{eff}}^{\text{neg}} (\kappa_{\text{eff}}^{\text{neg}} + \sigma_{\text{eff}}^{\text{neg}}) \nu^{\text{neg}}(s) \sinh(\nu^{\text{neg}}(s))} - \frac{x}{A (\kappa_{\text{eff}}^{\text{neg}} + \sigma_{\text{eff}}^{\text{neg}})} \\ &\quad - \frac{L^{\text{neg}} \kappa_{\text{eff}}^{\text{neg}} (\cosh(\frac{(L^{\text{neg}} - x)}{L^{\text{neg}}} \nu^{\text{neg}}(s)) - \cosh(\nu^{\text{neg}}(s)))}{A \kappa_{\text{eff}}^{\text{neg}} (\kappa_{\text{eff}}^{\text{neg}} + \sigma_{\text{eff}}^{\text{neg}}) \nu^{\text{neg}}(s) \sinh(\nu^{\text{neg}}(s))}. \end{aligned} \quad (6.48)$$

At the negative-electrode/separator boundary, we have

$$\frac{[\tilde{\Phi}_e(L^{\text{neg}}, s)]_1}{I_{app}(s)} = -\frac{L^{\text{neg}} ((\sigma_{\text{eff}}^{\text{neg}} - \kappa_{\text{eff}}^{\text{neg}}) \tanh(\frac{\nu^{\text{neg}}(s)}{2}))}{A \kappa_{\text{eff}}^{\text{neg}} (\kappa_{\text{eff}}^{\text{neg}} + \sigma_{\text{eff}}^{\text{neg}}) \nu^{\text{neg}}(s)} - \frac{L^{\text{neg}}}{A (\kappa_{\text{eff}}^{\text{neg}} + \sigma_{\text{eff}}^{\text{neg}})}.$$

In the separator, we then have

$$\begin{aligned} \frac{[\tilde{\Phi}_e(x, s)]_1}{I_{app}(s)} &= -\frac{L^{\text{neg}} ((\sigma_{\text{eff}}^{\text{neg}} - \kappa_{\text{eff}}^{\text{neg}}) \tanh(\frac{\nu^{\text{neg}}(s)}{2}))}{A \kappa_{\text{eff}}^{\text{neg}} (\kappa_{\text{eff}}^{\text{neg}} + \sigma_{\text{eff}}^{\text{neg}}) \nu^{\text{neg}}(s)} \\ &\quad - \frac{L^{\text{neg}}}{A (\kappa_{\text{eff}}^{\text{neg}} + \sigma_{\text{eff}}^{\text{neg}})} - \frac{x - L^{\text{neg}}}{A \kappa_{\text{eff}}^{\text{sep}}}. \end{aligned} \quad (6.49)$$

At the separator/positive-electrode boundary, we have

$$\begin{aligned} \frac{[\tilde{\Phi}_e(L^{\text{neg}} + L^{\text{sep}}, s)]_1}{I_{\text{app}}(s)} &= -\frac{L^{\text{neg}} \left((\sigma_{\text{eff}}^{\text{neg}} - \kappa_{\text{eff}}^{\text{neg}}) \tanh \left(\frac{\nu^{\text{neg}}(s)}{2} \right) \right)}{A \kappa_{\text{eff}}^{\text{neg}} (\kappa_{\text{eff}}^{\text{neg}} + \sigma_{\text{eff}}^{\text{neg}}) \nu^{\text{neg}}(s)} \\ &\quad - \frac{L_{\text{neg}}}{A(\kappa_{\text{eff}}^{\text{neg}} + \sigma_{\text{eff}}^{\text{neg}})} - \frac{L^{\text{sep}}}{A \kappa_{\text{eff}}^{\text{sep}}}. \end{aligned}$$

In the positive electrode, we have

$$\begin{aligned} \frac{[\tilde{\Phi}_e(x, s)]_1}{I_{\text{app}}(s)} &= -\frac{L^{\text{neg}} \left((\sigma_{\text{eff}}^{\text{neg}} - \kappa_{\text{eff}}^{\text{neg}}) \tanh \left(\frac{\nu^{\text{neg}}(s)}{2} \right) \right)}{A \kappa_{\text{eff}}^{\text{neg}} (\kappa_{\text{eff}}^{\text{neg}} + \sigma_{\text{eff}}^{\text{neg}}) \nu^{\text{neg}}(s)} - \frac{L_{\text{neg}}}{A(\kappa_{\text{eff}}^{\text{neg}} + \sigma_{\text{eff}}^{\text{neg}})} \\ &\quad - \frac{L^{\text{sep}}}{A \kappa_{\text{eff}}^{\text{sep}}} - \frac{L^{\text{pos}} \left(1 - \cosh \left(\frac{(L^{\text{neg}} + L^{\text{sep}} - x)}{L^{\text{pos}}} \nu^{\text{pos}}(s) \right) \right)}{A(\kappa_{\text{eff}}^{\text{pos}} + \sigma_{\text{eff}}^{\text{pos}}) \sinh(\nu^{\text{pos}}(s)) \nu^{\text{pos}}(s)} \\ &\quad - \frac{L^{\text{pos}} \sigma_{\text{eff}}^{\text{pos}} \left(\cosh(\nu^{\text{pos}}(s)) - \cosh \left(\frac{(L^{\text{tot}} - x)}{L^{\text{pos}}} \nu^{\text{pos}}(s) \right) \right)}{A \kappa_{\text{eff}}^{\text{pos}} (\kappa_{\text{eff}}^{\text{pos}} + \sigma_{\text{eff}}^{\text{pos}}) \sinh(\nu^{\text{pos}}(s)) \nu^{\text{pos}}(s)} \\ &\quad - \frac{(x - L^{\text{neg}} - L^{\text{sep}})}{A(\kappa_{\text{eff}}^{\text{pos}} + \sigma_{\text{eff}}^{\text{pos}})}. \end{aligned} \quad (6.50)$$

Finally, at the cell boundary, we have

$$\begin{aligned} \frac{[\tilde{\Phi}_e(L^{\text{tot}}, s)]_1}{I_{\text{app}}(s)} &= -\frac{L^{\text{neg}} \left((\sigma_{\text{eff}}^{\text{neg}} - \kappa_{\text{eff}}^{\text{neg}}) \tanh \left(\frac{\nu^{\text{neg}}(s)}{2} \right) \right)}{A \kappa_{\text{eff}}^{\text{neg}} (\kappa_{\text{eff}}^{\text{neg}} + \sigma_{\text{eff}}^{\text{neg}}) \nu^{\text{neg}}(s)} - \frac{L_{\text{neg}}}{A(\kappa_{\text{eff}}^{\text{neg}} + \sigma_{\text{eff}}^{\text{neg}})} \\ &\quad - \frac{L^{\text{sep}}}{A \kappa_{\text{eff}}^{\text{sep}}} - \frac{L^{\text{pos}} \left((\sigma_{\text{eff}}^{\text{pos}} - \kappa_{\text{eff}}^{\text{pos}}) \tanh \left(\frac{\nu^{\text{pos}}(s)}{2} \right) \right)}{A \kappa_{\text{eff}}^{\text{pos}} (\kappa_{\text{eff}}^{\text{pos}} + \sigma_{\text{eff}}^{\text{pos}}) \nu^{\text{pos}}(s)} \\ &\quad - \frac{L_{\text{pos}}}{A(\kappa_{\text{eff}}^{\text{pos}} + \sigma_{\text{eff}}^{\text{pos}})}. \end{aligned}$$

An example magnitude response, at different x locations spanning the cell, is shown in Fig. 6.10.

Now, we focus on the second term of $\tilde{\phi}_e(x, t)$.

$$\begin{aligned} [\tilde{\phi}_e(x, t)]_2 &= \frac{2RT(1 - t_+^0)}{F} \int_0^x \frac{\partial \ln c_e(\xi, t)}{\partial \xi} d\xi \\ &= \frac{2RT(1 - t_+^0)}{F} [\ln c_e(x, t) - \ln c_e(0, t)]. \end{aligned}$$

To compute $\tilde{\phi}_e(x, t)$, we must compute its two parts and add them. Then, to recover $\phi_e(x, t)$ from $\tilde{\phi}_e(x, t)$, we must compute $\phi_e(0, t)$:

$$\begin{aligned} \phi_e(0, t) &= \phi_s^{\text{neg}}(0, t) - \phi_{s-e}^{\text{neg}}(0, t) \\ &= 0 - (\tilde{\phi}_{s-e}^{\text{neg}}(0, t) + U_{\text{ocp}}^{\text{neg}}(c_{s,0})) \\ \phi_e(x, t) &= \tilde{\phi}_e(x, t) - \tilde{\phi}_{s-e}^{\text{neg}}(0, t) - U_{\text{ocp}}^{\text{neg}}(c_{s,0}). \end{aligned}$$

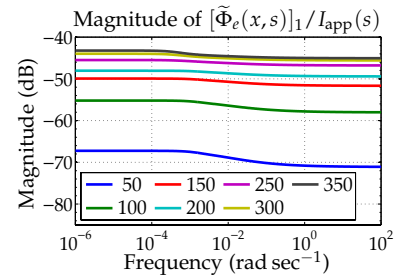


Figure 6.10: Example magnitude responses of $[\tilde{\Phi}_e(x, s)]_1 / I_{\text{app}}(s)$ at seven different x locations (in μm) across the cell.

6.7 Summary of transfer functions

We have now defined all the transfer functions of a linearized pseudo-2D porous-electrode model. This has been an intense process, with mathematically complex results. Before proceeding, we take a brief step back to summarize the transfer functions of the model. Recall that z is a normalized unitless spatial variable in the electrodes that takes on value zero at the current collectors and one at the electrode/separator interface, and that x is the spatial variable across the cell and takes on value zero at the negative-electrode current collector and L^{tot} at the positive-electrode current collector. The electrode-domain transfer functions are written in terms of z and the cell-wide transfer functions are written in terms of x . This is illustrated in Fig. 6.11.

Negative electrode		Separator		Positive electrode	
$\phi_s^{\text{neg}}(z, t)$	$\phi_e(x, t)$	$\phi_e(x, t)$	$\phi_e(x, t)$	$\phi_s^{\text{pos}}(z, t)$	
$c_{s,e}^{\text{neg}}(z, t)$	$c_e(x, t)$	$c_e(x, t)$	$c_e(x, t)$	$c_{s,e}^{\text{pos}}(z, t)$	
$j^{\text{neg}}(z, t)$				$j^{\text{pos}}(z, t)$	
$\phi_{s-e}^{\text{neg}}(z, t)$				$\phi_{s-e}^{\text{pos}}(z, t)$	
$z = 0$	$z = 1$			$z = 1$	$z = 0$
$x = 0$	$x = L^{\text{neg}}$	$x = L^{\text{neg}} + L^{\text{sep}}$		$x = L^{\text{tot}}$	

Figure 6.11: Summary of notation describing cell variables in reduced-order model.
(Adapted from Fig. 4 in Lee, J.L., Chemistruck, A., and Plett, G.L., "One-Dimensional Physics-Based Reduced-Order Model of Lithium-Ion Dynamics," *Journal of Power Sources*, 220, 2012, pp. 430–448.)

Common to all of the transfer functions is the dimensionless function $\nu(s)$, which is given in Eq. (6.9) for the negative electrode and in Eq. (6.20) for the positive electrode. In the following, we assume that the discrete-time realization algorithm from Chap. 5 will be used to convert the transcendental transfer functions into a discrete-time multioutput state-space model that can then compute the corresponding time-domain quantities in real time. Since the majority of these transfer functions have been linearized and debiased (by removing a constant offset) in their development, the following discussion also shows how to add the correct bias back into the computed signals.

Reaction flux: The local reaction-flux transfer function $J(z, s) / I_{\text{app}}(s)$ is given by Eq. (6.13) for the negative electrode and Eq. (6.22) for the positive electrode.

Solid surface concentration: Lithium concentration in the solid is denoted as $c_s(r, z, t)$. Here, we are concerned only with the concentration of lithium at the surface of the particles, as that is what determines reaction rate and cell voltage. The surface concentration is denoted as $c_{s,e}(z, t)$. Furthermore, we define a debiased surface concentration that subtracts out the equilibrium concentration:

$\tilde{c}_{s,e}(z, t) = c_{s,e}(z, t) - c_{s,0}$. The transfer function of the debiased surface concentration $\tilde{C}_{s,e}(z, s) / I_{app}(s)$ is given by Eq. (6.15) in the negative electrode and by Eq. (6.23) in the positive electrode. Once the debiased surface concentration is computed, the true surface concentration can be found as $c_{s,e}(z, t) = \tilde{c}_{s,e}(z, t) + c_{s,0}$.

Potential in solid: Solid potential in an electrode is denoted as $\phi_s(z, t)$.

We define a debiased solid potential that subtracts out the potential at the electrode's current collector where $z = 0$: $\tilde{\phi}_s(z, t) = \phi_s(z, t) - \phi_s(0, t)$. The transfer function $\tilde{\Phi}_s(z, s) / I_{app}(s)$ of the debiased solid potential is given by Eq. (6.19) for the negative electrode and by Eq. (6.24) for the positive electrode. And, since we define the potential of the negative-electrode current collector to be zero, we have $\phi_s(z, t) = \tilde{\phi}_s(z, t)$ in the negative electrode. In the positive electrode, we have that $\phi_s(z, t) = \tilde{\phi}_s(z, t) + v(t)$, where $v(t)$ is the cell voltage and can be found as described in Sect. 6.8.

Potential in electrolyte: Electrolyte potential is denoted as $\phi_e(x, t)$.

We define a debiased electrolyte potential that subtracts out the potential at the negative current collector where $x = 0$: $\tilde{\phi}_e(x, t) = \phi_e(x, t) - \phi_e(0, t)$. Furthermore, we break up $\tilde{\phi}_e(x, t)$ into two parts: $\tilde{\phi}_e(x, t) = [\tilde{\phi}_e(x, t)]_1 + [\tilde{\phi}_e(x, t)]_2$. The transfer function $[\tilde{\Phi}_e(x, s)]_1 / I_{app}(s)$ for x locations in the negative electrode is given by Eq. (6.48). For x locations in the separator, this transfer function is given by Eq. (6.49), and for x locations in the positive electrode, this transfer function is given by Eq. (6.50).

Once the appropriate $[\tilde{\phi}_e(x, t)]_1$ is computed, we further calculate

$$\tilde{\phi}_e(x, t) = [\tilde{\phi}_e(x, t)]_1 + \frac{2RT(1 - t_+^0)}{F} \ln \left(\frac{c_e(x, t)}{c_e(0, t)} \right),$$

where $c_e(x, t)$ is computed as described in the "concentration in electrolyte" summary item. Finally:

$$\begin{aligned} \phi_e(x, t) &= \tilde{\phi}_e(x, t) + \phi_e(0, t) \\ &= \tilde{\phi}_e(x, t) - \phi_{s-e}^{\text{neg}}(0, t), \end{aligned}$$

where (debiased) $\tilde{\phi}_{s-e}(0, t)$ at $x = 0$ is found via the transfer function in Eq. (6.12). Note that the transfer function $\tilde{\Phi}_{s-e}^{\text{neg}}(z, s) / I_{app}(s)$ has a pole at the origin, which is removed prior to using the DRA to give the $[\tilde{\Phi}_{s-e}^{\text{neg}}(z, s)]^* / I_{app}(s)$ transfer function in Eq. (6.14).

The integrator response could be added back manually, as in $\tilde{\phi}_{s-e}(t) = \tilde{\phi}_{s-e}^*(t) + (\tilde{\phi}_{s-e}^{\text{res}0}) x_i(t)$, where $x_i(t)$ is the integrator state of the DRA model, but better performance is obtained by looking deeper at what is actually happening.

Recall that

$$c_{s,\text{avg}}(t) = \left(\tilde{c}_{s,e}^{\text{res}0} \right) x_i(t) + c_{s,0},$$

and note that

$$\tilde{\phi}_{s-e}^{\text{res0}} = \frac{\partial U_{\text{ocp}}}{\partial c_{s,e}} \Big|_{c_{s,0}} \times \tilde{c}_{s,e}^{\text{res0}}.$$

Therefore, we can write

$$\phi_{s-e}^{\text{neg}} = [\tilde{\phi}_{s-e}^{\text{neg}}]^* + \left(U_{\text{ocp}}^{\text{neg}}(c_{s,0}^{\text{neg}}) + \left[\frac{\partial U_{\text{ocp}}^{\text{neg}}}{\partial c_{s,e}^{\text{neg}}} \right]_{c_{s,0}^{\text{neg}}} \left(\tilde{c}_{s,\text{avg}}^{\text{neg}} - c_{s,0}^{\text{neg}} \right) \right),$$

where the second term on the right-hand side is equal to the first two terms of the Taylor-series expansion of $U_{\text{ocp}}^{\text{neg}}(c_{s,\text{avg}}^{\text{neg}})$ around the starting average concentration $c_{s,0}^{\text{neg}}$. Therefore, we find that we achieve more accurate results if we implement $[\tilde{\Phi}_{s-e}^{\text{neg}}(z, s)]^* / I_{\text{app}}(s)$ and then compute

$$\phi_{s-e}^{\text{neg}}(0, t) = [\tilde{\phi}_{s-e}^{\text{neg}}(0, t)]^* + U_{\text{ocp}}^{\text{neg}}(c_{s,\text{avg}}^{\text{neg}}(t)).$$

Finally:

$$\phi_e(x, t) = \tilde{\phi}_e(x, t) - [\tilde{\phi}_{s-e}^{\text{neg}}(0, t)]^* - U_{\text{ocp}}^{\text{neg}}(c_{s,\text{avg}}^{\text{neg}}(t)).$$

Concentration in electrolyte: Lithium concentration in the electrolyte is denoted $c_e(x, t)$. We define a debiased electrolyte concentration that subtracts out the average concentration: $\tilde{c}_e(x, t) = c_e(x, t) - c_{e,0}$. We use an eigenfunction expansion to express the transfer function of $\tilde{c}_e(x, t)$ in terms of M weighted partial transfer functions, per Eq. (6.45), where M is at least as large as the anticipated reduced-order-model system order. Details of finding the eigenfunctions $\Psi(x; \lambda_k)$ are given in Sect. 6.5.3. The individual partial transfer functions are expressed in Eq. (6.44). The two parts of this transfer function are found in Eqs. (6.42) and (6.43).

6.8 Computing cell voltage

One of the more important applications of a cell model is to be able to predict cell voltage response to variations in input current.

Cell terminal voltage can be written (in z coordinates) as $v(t) = \phi_s^{\text{pos}}(0, t) - \phi_s^{\text{neg}}(0, t)$. To implement this equation, however, we run into a problem: to compute $\phi_s^{\text{pos}}(0, t)$, we must already know $v(t)$ to debias $\tilde{\phi}_s^{\text{pos}}(0, t)$!

The solution to this dilemma is to write the local overpotential as $\eta = \phi_s - \phi_e - U_{\text{ocp}} - FR_{\text{film}}j$. Thus, we can write (mixing x coordinates and z coordinates as appropriate, and treating η as a z -coordinate variable):

$$v(t) = \eta^{\text{pos}}(0, t) + \phi_e^{\text{pos}}(L^{\text{tot}}, t) + U_{\text{ocp}}^{\text{pos}}(c_{s,e}^{\text{pos}}(0, t)) + FR_{\text{film}}^{\text{pos}}j^{\text{pos}}(0, t) \\ - \eta^{\text{neg}}(0, t) - \phi_e^{\text{neg}}(0, t) - U_{\text{ocp}}^{\text{neg}}(c_{s,e}^{\text{neg}}(0, t)) - FR_{\text{film}}^{\text{neg}}j^{\text{neg}}(0, t).$$

This is an improvement, because we already know how to compute most of these terms. One that we have not discussed, however, is $\eta(z, t)$. One possible method to compute its value is

$$\begin{aligned}\eta^{\text{pos}}(z, t) &= FR_{\text{ct}}^{\text{pos}} j^{\text{pos}}(z, t) \\ \eta^{\text{neg}}(z, t) &= FR_{\text{ct}}^{\text{neg}} j^{\text{neg}}(z, t),\end{aligned}$$

using Eq. (6.4). This can be an adequate small-signal approximation, but, the true nonlinear nature of the overpotential can most easily be seen via the Butler–Volmer equation. Recall that

$$\begin{aligned}j &= k_0 c_e^{1-\alpha} (c_{s,\text{max}} - c_{s,e})^{1-\alpha} c_{s,e}^\alpha \\ &\times \left(\exp\left(\frac{(1-\alpha)F}{RT}\eta\right) - \exp\left(-\frac{\alpha F}{RT}\eta\right) \right).\end{aligned}$$

If we assume that the charge-transfer coefficient $\alpha = 0.5$, as is often the case, we can then write

$$j = 2k_0 \sqrt{c_e(c_{s,\text{max}} - c_{s,e})c_{s,e}} \sinh\left(\frac{F}{2RT}\eta\right).$$

This can be inverted to solve for the overpotential

$$\eta = \frac{2RT}{F} \operatorname{asinh}\left(\frac{j}{2k_0 \sqrt{c_e(c_{s,\text{max}} - c_{s,e})c_{s,e}}}\right). \quad (6.51)$$

A linearization of Eq. (6.51) gives Eq. (6.4). However, computing the overpotential directly using the nonlinear relationship in Eq. (6.51) results in better voltage predictions. Specifically,

$$\begin{aligned}\eta^{\text{pos}}(z, t) &= \frac{2RT}{F} \operatorname{asinh}\left(\frac{j^{\text{pos}}(z, t)}{2k_0^{\text{pos}} \sqrt{c_e(z, t)(c_{s,\text{max}}^{\text{pos}} - c_{s,e}^{\text{pos}}(z, t))c_{s,e}^{\text{pos}}(z, t)}}\right) \\ \eta^{\text{neg}}(z, t) &= \frac{2RT}{F} \operatorname{asinh}\left(\frac{j^{\text{neg}}(z, t)}{2k_0^{\text{neg}} \sqrt{c_e(z, t)(c_{s,\text{max}}^{\text{neg}} - c_{s,e}^{\text{neg}}(z, t))c_{s,e}^{\text{neg}}(z, t)}}\right).\end{aligned}$$

With either of these definitions, then, we can write cell voltage as

$$\begin{aligned}v(t) &= F[R_{\text{film}}^{\text{pos}} j^{\text{pos}}(0, t) - R_{\text{film}}^{\text{neg}} j^{\text{neg}}(0, t)] + [\tilde{\phi}_e(L^{\text{tot}}, t)]_1 \\ &\quad + [\eta^{\text{pos}}(0, t) - \eta^{\text{neg}}(0, t)] + [\tilde{\phi}_e(L^{\text{tot}}, t)]_2 \\ &\quad + [U_{\text{ocp}}^{\text{pos}}(c_{s,e}^{\text{pos}}(0, t)) - U_{\text{ocp}}^{\text{neg}}(c_{s,e}^{\text{neg}}(0, t))],\end{aligned} \quad (6.52)$$

where the first line of the equation comprises the linear portion of the voltage equation, and the following two lines comprise the terms computed as nonlinear functions of linear model outputs.

6.9 Frequency response and cell impedance

The voltage equation can also be manipulated to form the linearized small-signal frequency response of the cell, which is the negative of the impedance spectrum. We start with Eq. (6.52), using an already linearized overpotential, and note that the remaining nonlinear terms are

$$[\tilde{\phi}_e(L^{\text{tot}}, t)]_2 \quad \text{and} \quad \left[U_{\text{ocp}}^{\text{pos}}(c_{s,e}^{\text{pos}}(0, t)) - U_{\text{ocp}}^{\text{neg}}(c_{s,e}^{\text{neg}}(0, t)) \right].$$

Writing out the first term, we have

$$[\tilde{\phi}_e(L^{\text{tot}}, t)]_2 = \frac{2RT(1 - t_+^0)}{F} [\ln(c_e(L^{\text{tot}}, t) - \ln(c_e(0, t))].$$

Linearizing the logarithm via Taylor-series expansion gives

$$\begin{aligned} \ln(c_e) &\approx \ln(c_{e,0}) + \left[\frac{\partial \ln c_e}{\partial c_e} \right]_{c_{e,0}} (c_e - c_{e,0}) \\ &= \ln(c_{e,0}) + \left(\frac{c_e - c_{e,0}}{c_{e,0}} \right) = \ln(c_{e,0}) + \frac{\tilde{c}_e}{c_{e,0}}. \end{aligned}$$

So

$$[\tilde{\phi}_e(L^{\text{tot}}, t)]_2 \approx \frac{2RT(1 - t_+^0)}{F} \left[\frac{\tilde{c}_e(L^{\text{tot}}, t) - \tilde{c}_e(0, t)}{c_{e,0}} \right].$$

Using a similar means, the open-circuit-potential relationships can be linearized

$$\begin{aligned} U_{\text{ocp}}(c_{s,e}) &\approx U_{\text{ocp}}(c_{s,0}) + \left[\frac{\partial U_{\text{ocp}}(c_{s,e})}{\partial c_{s,e}} \right]_{c_{s,0}} (c_{s,e} - c_{s,0}) \\ &= U_{\text{ocp}}(c_{s,0}) + \left[\frac{\partial U_{\text{ocp}}(c_{s,e})}{\partial c_{s,e}} \right]_{c_{s,0}} \tilde{c}_{s,e}. \end{aligned}$$

So a linearized model of cell voltage is then

$$\begin{aligned} v(t) &\approx FR_{s,e}^{\text{pos}} j^{\text{pos}}(0, t) - FR_{s,e}^{\text{neg}} j^{\text{neg}}(0, t) + [\tilde{\phi}_e(L^{\text{tot}}, t)]_1 \\ &\quad + \frac{2RT(1 - t_+^0)}{F} \left[\frac{\tilde{c}_e(L^{\text{tot}}, t) - \tilde{c}_e(0, t)}{c_{e,0}} \right] \\ &\quad + \left[U_{\text{ocp}}^{\text{pos}}(c_{s,0}^{\text{pos}}) - U_{\text{ocp}}^{\text{neg}}(c_{s,0}^{\text{neg}}) \right] \\ &\quad + \left[\frac{\partial U_{\text{ocp}}^{\text{pos}}(c_{s,e}^{\text{pos}})}{\partial c_{s,e}^{\text{pos}}} \right]_{c_{s,0}^{\text{pos}}} \tilde{c}_{s,e}^{\text{pos}}(0, t) - \left[\frac{\partial U_{\text{ocp}}^{\text{neg}}(c_{s,e}^{\text{neg}})}{\partial c_{s,e}^{\text{neg}}} \right]_{c_{s,0}^{\text{neg}}} \tilde{c}_{s,e}^{\text{neg}}(0, t). \end{aligned}$$

We define a debiased voltage

$$\tilde{v}(t) = v(t) - \left[U_{\text{ocp}}^{\text{pos}}(c_{s,0}^{\text{pos}}) - U_{\text{ocp}}^{\text{neg}}(c_{s,0}^{\text{neg}}) \right].$$

Then the transfer function from applied current to variations in cell voltage around its equilibrium setpoint (with the open-circuit voltage offset removed) is

$$\begin{aligned} \frac{\tilde{V}(s)}{I_{\text{app}}(s)} = & FR_{s,e}^{\text{pos}} \frac{J^{\text{pos}}(0,s)}{I_{\text{app}}(s)} - FR_{s,e}^{\text{neg}} \frac{J^{\text{neg}}(0,s)}{I_{\text{app}}(s)} + \frac{[\tilde{\Phi}_e(L^{\text{tot}}, s)]_1}{I_{\text{app}}(s)} \\ & + \frac{2RT(1-t_+^0)}{Fc_{e,0}} \left[\frac{\tilde{C}_e(L^{\text{tot}}, s)}{I_{\text{app}}(s)} - \frac{\tilde{C}_e(0,s)}{I_{\text{app}}(s)} \right] \\ & + \left[\frac{\partial U_{\text{ocp}}^{\text{pos}}(c_{s,e}^{\text{pos}})}{\partial c_{s,e}^{\text{pos}}} \right]_{c_{s,0}^{\text{pos}}} \frac{\tilde{C}_{s,e}^{\text{pos}}(0,s)}{I_{\text{app}}(s)} - \left[\frac{\partial U_{\text{ocp}}^{\text{neg}}(c_{s,e}^{\text{neg}})}{\partial c_{s,e}^{\text{neg}}} \right]_{c_{s,0}^{\text{neg}}} \frac{\tilde{C}_{s,e}^{\text{neg}}(0,s)}{I_{\text{app}}(s)}, \end{aligned} \quad (6.53)$$

where the individual transfer functions are as defined earlier in this chapter.

Note that since cell voltage is equal to open-circuit voltage minus current times generalized impedance,

$$v(t) = \text{OCV}(z(t)) - Zi_{\text{app}}(t),$$

we have $\tilde{v}(t) = -Zi_{\text{app}}(t)$, and

$$Z(s) = -\frac{\tilde{V}(s)}{I_{\text{app}}(s)}.$$

This relationship produces the impedance spectrum, which can be compared with results from laboratory electrochemical impedance spectroscopy (EIS) tests.

6.10 Multioutput DRA

We have now derived all of the necessary continuous-time transfer functions required to model the internal dynamics of a lithium-ion cell. Proceeding, our goal is to approximate these transfer functions with a reduced-order discrete-time state-space model of the form⁷

$$\begin{aligned} \mathbf{x}[k+1] &= \hat{\mathbf{A}}\mathbf{x}[k] + \hat{\mathbf{B}}i_{\text{app}}[k] \\ \mathbf{y}[k] &= \hat{\mathbf{C}}\mathbf{x}[k] + \hat{\mathbf{D}}i_{\text{app}}[k]. \end{aligned}$$

We will use the DRA from Chap. 5 to find the state-space matrices from the transfer functions derived in this chapter.

So far, the only examples of using the DRA that we have seen have been for single-input single-output systems. However, the DRA can also work with multi-input single-output, single-input multioutput, or multi-input multioutput transfer functions. Here, we are considering the case of a single input $i_{\text{app}}(t)$ and multiple outputs, where the outputs comprise the set of transfer functions that the user would

⁷ The “hat” symbol on the state matrices reminds us that the DRA produces a reduced-order *approximate* system description to an infinite-order ideal description.

like to implement. The overall multioutput transfer function being implemented by the DRA is then the vertical concatenation of all single-output subtransfer functions. For example, if the user would like to determine $j^{\text{neg}}(0, t)$ and $c_{s,e}^{\text{pos}}(1, t)$, the overall transfer function would be

$$H(s) = \begin{bmatrix} \frac{j^{\text{neg}}(0,s)}{I_{\text{app}}(s)} \\ \frac{\tilde{C}_{s,e}^{\text{pos}}(1,s)}{I_{\text{app}}(s)} \end{bmatrix}.$$

Before implementing DRA Step 1, $H(s)$ must be strictly stable (e.g., it may not contain a pole at $s = 0$, which corresponds to integration dynamics). If $H(s)$ has a pole at $s = 0$, this pole must first be removed, resulting in $H^*(s)$.⁸ In the final state-space representation, we augment the realization with an integrator state to account for removal of the pole in the DRA. The reduced-order approximation to the original system via the augmented discrete-time state-space model is:

$$\underbrace{\begin{bmatrix} x[k+1] \\ x_i[k+1] \end{bmatrix}}_{x_{\text{aug}}[k+1]} = \underbrace{\begin{bmatrix} \hat{A} & \mathbf{0} \\ \mathbf{0} & 1 \end{bmatrix}}_{\hat{A}_{\text{aug}}} \underbrace{\begin{bmatrix} x[k] \\ x_i[k] \end{bmatrix}}_{x_{\text{aug}}[k]} + \underbrace{\begin{bmatrix} \hat{B} \\ T_s \end{bmatrix}}_{\hat{B}_{\text{aug}}} i_{\text{app}}[k]$$

$$y[k] = \underbrace{\begin{bmatrix} \hat{C} & \mathbf{res}_0 \end{bmatrix}}_{\hat{C}_{\text{aug}}} \underbrace{\begin{bmatrix} x[k] \\ x_i[k] \end{bmatrix}}_{x_{\text{aug}}[k]} + D i_{\text{app}}[k]$$

where \mathbf{res}_0 is a column vector containing the residues of the transfer functions with a pole at the origin.

The length of the output vector depends on the number of z locations (for the electrode-domain properties) and x locations (for the cell-scale properties) chosen by the user for evaluation. For example, solving for the six variables $[\tilde{\phi}_{s-e}]^*$, j , $\tilde{c}_{s,e}$, $\tilde{\phi}_s$, $[\tilde{\phi}_e]_1$, and \tilde{c}_e at four spatial locations each (e.g., both current collectors and both electrode-separator interfaces) produces a total of 24 outputs. The output $y(t)$ then has the following structure:

$$y(t) = \begin{bmatrix} [\tilde{\phi}_{s-e}(z, t)]^* \\ j(z, t) \\ \tilde{c}_{s,e}(z, t) \\ \tilde{\phi}_s(z, t) \\ [\tilde{\phi}_e(x, t)]_1 \\ \tilde{c}_e(x, t) \end{bmatrix}, \quad (6.54)$$

where each variable is a four-vector corresponding to the four spatial locations evaluated.⁹

DRA Step 1 requires we select a high-rate sampling frequency F_1 to approximate the impulse response of the continuous-time system.

⁸ The only two transfer functions derived in this chapter that have a pole at $s = 0$ are for $c_{s,e}$ and ϕ_{s-e} . The “starred” integrator-removed versions of these transfer functions are given in the sections where they are derived.

⁹ The attentive reader will have observed that we don't need to compute all of these: $\tilde{\phi}_s(0, t) = 0$ (at both current collectors) and we also find that $[\tilde{\phi}_e(0, t)]_1$ is zero as well. We can reduce $y(t)$ to a 21-vector and will still be able to compute the same quantities.

We find that the results are not very sensitive to F_1 , but that it is important that the duration of the truncated impulse response is long enough to capture the slow time constants in the model.

While the elements of the output vector $y(t)$ of the DRA have physical meaning, the only state variable within the state vector $x(t)$ that has independent physical interpretation is the integrator state. If this state is $x_i(t)$, then we have that the average concentration of lithium in the solid is equal to

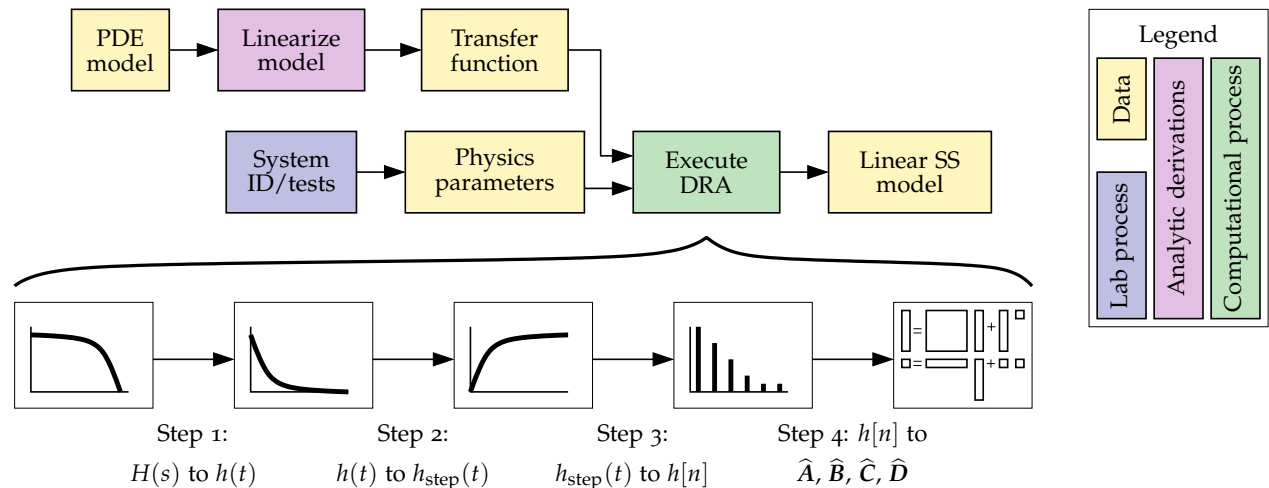
$$c_{s,\text{avg}}(t) = c_{s,0} + \left(\tilde{c}_{s,e}^{\text{res0}} \right) x_i(t).$$

In the two electrodes, via Eq. (6.16), this becomes

$$\begin{aligned} c_{s,\text{avg}}^{\text{neg}}(t) &= c_{s,0}^{\text{neg}} - \left(\frac{1}{\varepsilon_s^{\text{neg}} AFL^{\text{neg}}} \right) x_i(t) \\ c_{s,\text{avg}}^{\text{pos}}(t) &= c_{s,0}^{\text{pos}} + \left(\frac{1}{\varepsilon_s^{\text{pos}} AFL^{\text{pos}}} \right) x_i(t). \end{aligned}$$

As the average concentration of lithium in an electrode is related to the state of charge of the electrode via an affine transformation, the value of the integrator state is key to being able to estimate cell SOC.

Fig. 6.12 illustrates the process to generate a linearized state-space model of cell dynamics. The PDE models were derived in Chap. 3 and 4. This chapter described how to linearize the model to create transfer functions. The DRA from Chap. 5 uses these transfer functions to produce the state-space model.



Comparing this figure to the corresponding diagram for creating an equivalent-circuit model (Fig. 2.27), we see significant differences. The equivalent-circuit model was created via nonlinear optimization and current–voltage cell-test data; the physics-based reduced-order

Figure 6.12: Depiction of procedural steps used to compute linear state-space model of linearized debiased variables. (Adapted from Fig. 1 in Lee, J.L., Aldrich, L., Stetzel, K., and Plett, G.L., "Extended Operating Range for Reduced-Order Model of Lithium-Ion Cells," *Journal of Power Sources*, 255, 2014, pp. 85–100.)

model is created via considerable (one-time) mathematical work to obtain transfer-function derivations, but then by a linear-algebra optimal order-reduction methodology.

6.11 Full cell model

The state-space model produced by the DRA can undergo some mathematical transformations to put in a standard form. Sect. 6.13.2 describes how to do so, within a context we will soon encounter where it is a requirement to do so. For now, we simply assume that it is possible to convert the DRA output to a state-space system having a diagonal \hat{A} matrix and a \hat{B} matrix comprising only units values. We furthermore sort the diagonal of the \hat{A} matrix so that the integrator state is the bottom entry of the $x_{\text{aug}}[x]$ vector. With these transformations, the model state equation can be visualized as drawn in Fig. 6.13, which shows a model having four states plus an integrator state. With this configuration, which we find works quite well in practice, a state update is performed with four multiplications (we don't need to multiply by one for the integrator state) and five additions, which is computationally very fast.

Four general-purpose states modeling all nonintegral internal cell dynamics

Integrator state

New states

$$\begin{array}{c} \text{New states} \\ \hline \end{array} = \begin{array}{c} \text{Prior states} \\ \hline \end{array} + \begin{array}{c} \text{Input matrix} \\ \hline \end{array}$$

Model input = current

0 0 0 0
0 0 0 0
0 0 0 0
0 0 0 0
0 0 0 1

Figure 6.13: Visualizing the state equation.

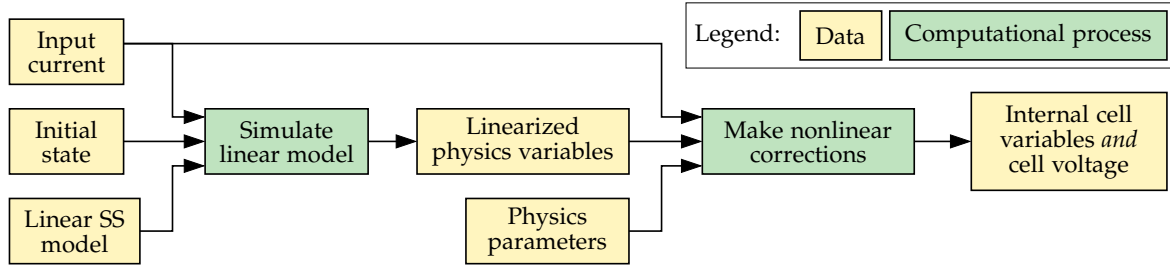
The linear output equation can be visualized as drawn in Fig. 6.14. The number of rows in $y[k]$ depends on the number of transfer functions the user has requested that the DRA produce. The example represented in Eq. (6.54) had 24 outputs, so the \hat{C} matrix would be 24×5 in size. The \hat{C} matrix is generally full, without structure, except that we know that the column associated with the integrator state is zero except for outputs that have an integration component. These multiply-by-zeros could be skipped in an implementation. Also, the \hat{D} matrix is generally full; however, we know that rows corresponding to outputs computing either $\tilde{c}_{s,e}$ or \tilde{c}_e have zero entries, so these multiplications could be skipped.

Linear outputs

$$\begin{array}{c} \text{Linear outputs} \\ \vdots \\ \hline \end{array} = \begin{array}{c} \text{Model input = current} \\ \vdots \\ \hline \end{array} + \begin{array}{c} \text{Input matrix} \\ \vdots \\ \hline \end{array}$$

Figure 6.14: Visualizing the output equation.

Overall, the process for simulating a reduced-order model is visualized in Fig. 6.15. It is somewhat more complicated than the equivalent-circuit-model counterpart in Fig. 2.28 but has the great advantage of being able to compute all internal cell variables in addition to the cell voltage, whereas the equivalent-circuit model can compute the cell voltage only.



6.12 Simulation example

In this section, we use simulation to demonstrate the performance of the reduced-order model as compared to the full-order PDEs describing the porous-electrode model. The parameters of the cell being simulated are those published by Doyle et al.¹⁰ and are listed in Table 6.1. The cell input current for the simulation is based on the Environmental Protection Agency's (EPA) Urban Dynamometer Driving Schedule (UDDS), which was developed to represent city driving conditions for light-duty vehicles. Fig. 6.16 shows the UDDS profile of current versus time, scaled to achieve a maximum absolute rate of 2C, which for this cell corresponds to 41 A.

We compare the ROM results to full-order model (FOM) simulations of the pseudo-2D porous-electrode model, which we implemented in COMSOL Multiphysics. In all cases, the simulation is initialized with a cell SOC of 60 %. We compute DRA outputs and PDE outputs for the five main cell variables (j , $c_{s,e}$, c_e , ϕ_s , and ϕ_e) at four different spatial locations across the cell (at both current collectors and at both electrode/separator interfaces). The reduced-order state-space model therefore has one input (cell current) and 18 linear outputs (one for $[\tilde{\phi}_{s-e}(0,t)]$, two for the nonzero $\tilde{\phi}_s(1,t)$ transfer functions, three for the nonzero $[\tilde{\phi}_e(x,t)]_1$ transfer functions, and four for each of the others).

When approximating the electrolyte concentration, we use eigenvalue/eigenfunction pairs λ_k and $\Psi(x; \lambda_k)$ for $k = 1, \dots, 10$. For

Figure 6.15: Depiction of procedural steps used to simulate physics-based reduced-order model.

(Adapted from Fig. 2 in Lee, J.L., Aldrich, L., Stetzel, K., and Plett, G.L., "Extended Operating Range for Reduced-Order Model of Lithium-Ion Cells," *Journal of Power Sources*, 255, 2014, pp. 85–100.)

¹⁰ Doyle, M., Newman, J., Gozdz, A.S., Schmutz, C.N., and Tarascon, J.-M., "Comparison of Modeling Predictions with Experimental Data from Plastic Lithium Ion Cells," *Journal of the Electrochemical Society*, 143, 1996, pp. 1890–1903.

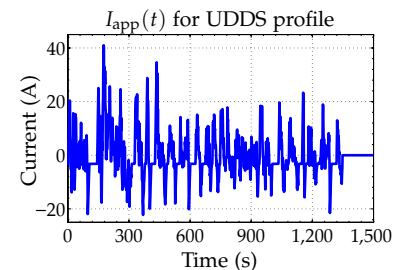


Figure 6.16: Profile of cell current versus time for the UDDS cycle.

Symbol	Units	Negative electrode	Separator	Positive electrode
L	μm	128	76	190
R_s	μm	12.5	—	8.5
A	m^2	1	1	1
σ	S m^{-1}	100	—	3.8
ε_s	$\text{m}^3 \text{m}^{-3}$	0.471	—	0.297
ε_e	$\text{m}^3 \text{m}^{-3}$	0.357	0.724	0.444
brug	—	1.5	—	1.5
$c_{s,\text{max}}$	mol m^{-3}	26,390	—	22,860
$c_{e,0}$	mol m^{-3}	2,000	2,000	2,000
θ_{min}	—	0.05	—	0.78
θ_{max}	—	0.53	—	0.17
D_s	$\text{m}^2 \text{s}^{-1}$	3.9×10^{-14}	—	1.0×10^{-13}
D_e	$\text{m}^2 \text{s}^{-1}$	7.5×10^{-11}	7.5×10^{-11}	7.5×10^{-11}
t_+^0	—	0.363	0.363	0.363
k	$\text{mol}^{-1/2} \text{m}^{5/2} \text{s}^{-1}$	1.94×10^{-11}	—	2.16×10^{-11}
α	—	0.5	—	0.5
R_{film}	Ωm^2	0.0	—	—

We compute $\sigma_{\text{eff}} = \sigma \varepsilon_s^{\text{brug}}$, $\kappa_{\text{eff}} = \kappa \varepsilon_e^{\text{brug}}$, $D_{e,\text{eff}} = D_e \varepsilon_e^{\text{brug}}$.

In the electrolyte, conductivity is a function of concentration:

$$\begin{aligned} \kappa(c_e) = & 4.1253 \times 10^{-2} + 5.007 \times 10^{-4} c_e - 4.7212 \times 10^{-7} c_e^2 \\ & + 1.5094 \times 10^{-10} c_e^3 - 1.6018 \times 10^{-14} c_e^4. \end{aligned}$$

For the negative electrode, the open-circuit potential function is:

$$U_{\text{ocp}}^{\text{neg}}(\theta) = -0.16 + 1.32 \exp(-3.0\theta) + 10.0 \exp(-2,000.0\theta).$$

For the positive electrode, the open-circuit potential function is:

$$\begin{aligned} U_{\text{ocp}}^{\text{pos}}(\theta) = & 4.19829 + 0.0565661 \tanh(-14.5546\theta + 8.60942) \\ & - 0.0275479 \left[\frac{1}{(0.998432 - \theta)^{0.4924656}} - 1.90111 \right] \\ & - 0.157123 \exp(-0.04738\theta^6) + 0.810239 \exp[-40(\theta - 0.133875)]. \end{aligned}$$

Table 6.1: Cell parameters for simulation.

(From: Doyle, M., Newman, J., Gozdz, A.S., Schmutz, C.N., and Tarascon, J-M, "Comparison of Modeling Predictions with Experimental Data from Plastic Lithium Ion Cells," *Journal of the Electrochemical Society*, 143, 1996, pp. 1890-1903.)

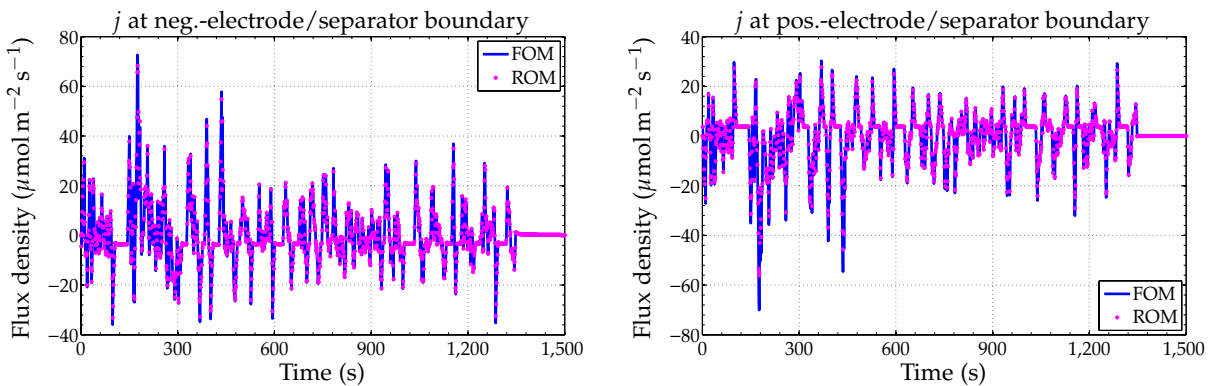
the simulation runs presented here, the DRA high-rate sampling frequency was chosen as $F_1 = 2$ Hz and the sampling period of the computed discrete-time reduced-order model was chosen as $T_s = 1$ s. The computational complexity required to run the DRA and the accuracy of the resulting reduced-order model predictions are not sensitive to either of these parameters. We use a ROM having exactly five state variables in its state vector $x_{\text{aug}}(t)$.

The ERA was used in Step 4 of the DRA (replacing the Ho–Kalman algorithm), with the j_k index set comprising

$$j_k = \{ 0 \dots 4,000, 5,000 \dots 5,100, 6,000 \dots 6,050, 7,000 \dots 7,050, \\ 8,000 \dots 8,050, 10,000 \dots 10,050, 12,000 \dots 12,050, \\ 14,000 \dots 14,050, 16,000 \dots 16,050, 18,000 \dots 18,050, \\ 19,000 \dots 19,050, 20,000 \dots 20,050 \},$$

and $t_k = j_k$. This index set was not optimized, but chosen to place a good deal of emphasis on early time samples in the unit-pulse responses, but to also include some time samples at significant time delays to capture some of the slower time constants. With such a large index set, the DRA requires significant memory resources (to compute the SVD) and takes considerable time. A shorter index set could be used to reduce memory and time requirements, with some loss in accuracy.

Results of comparing flux-density predictions of this ROM to those of the FOM at the electrode/separator interfaces are presented in Fig. 6.17. The electrochemical reactions at the electrode/separator interface are more dynamic than at the current collectors and are therefore more difficult for the ROM to match. Even so, the ROM and FOM results match very well.



Likewise, ROM versus FOM comparisons for the internal cell potentials are presented in Fig. 6.18. They also match well.

Figure 6.17: Butler–Volmer flux at electrode/separator boundaries. (Adapted from Fig. 8 in Lee et al., *Journal of Power Sources*, 220, 2012, pp. 430–448.)

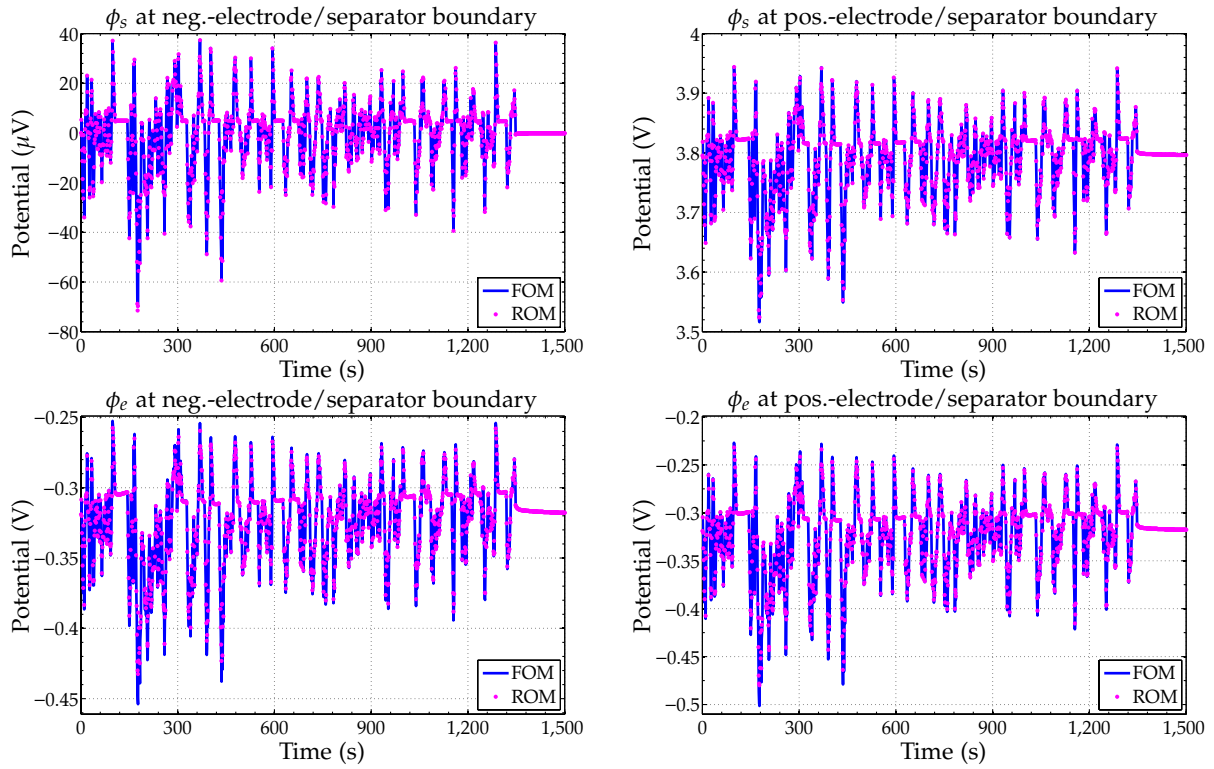


Figure 6.18: Solid- and electrolyte-phase potentials.

(Adapted from Fig. 8 in Lee et al., *Journal of Power Sources*, 220, 2012, pp. 430–448.)

Finally, ROM versus FOM comparisons for internal concentrations are presented in Fig. 6.19. These do not match quite as well as the other variables, but they match well enough to be useful.

The output cell voltage for the ROM is calculated from the electrochemical variables using Eq. (6.52). The results of the fifth-order ROM and the rigorous PDE model are shown in Fig. 6.20. The cell voltage RMS error between the FOM and the ROM is about 1 mV. The right frame shows a detailed view of the simulation during the period of the greatest mismatch.

6.13 Model blending

The ROM we've developed to this point was derived by linearizing the pseudo-2D porous-electrode PDE model around a specific operational setpoint. However, as model dynamics can vary with temperature and SOC, we find that a single model is often not sufficient. To model the cell over a wide range of both temperature and SOC, we use a model-blending approach.¹¹ The basic idea is to precompute ROMs at multiple state-of-charge and temperature setpoints and then—during operation—use these to generate a best “average” ROM specialized for the present instantaneous SOC and temperature.

¹¹ This section is based on Lee, J.L., Aldrich, L., Stetzel, K., and Plett, G.L., “Extended Operating Range for Reduced-Order Model of Lithium-Ion Cells,” *Journal of Power Sources*, 255, 2014, pp. 85–100.

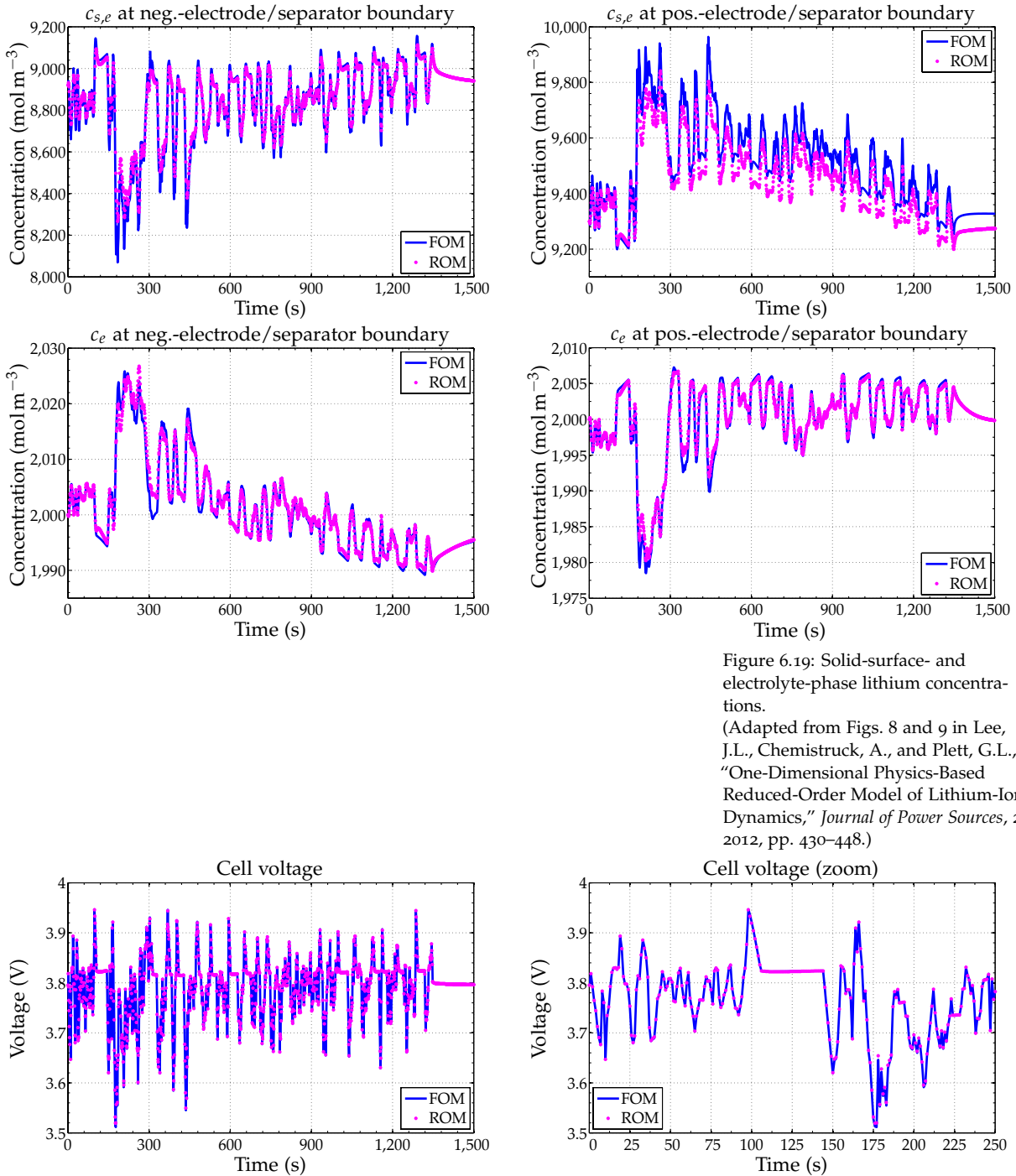


Figure 6.19: Solid-surface- and electrolyte-phase lithium concentrations.

(Adapted from Figs. 8 and 9 in Lee, J.L., Chemistruck, A., and Plett, G.L., "One-Dimensional Physics-Based Reduced-Order Model of Lithium-Ion Dynamics," *Journal of Power Sources*, **220**, 2012, pp. 430–448.)

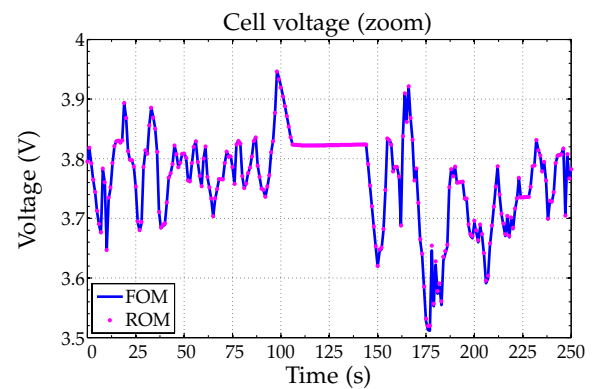


Figure 6.20: Cell voltage for UDDS test. (Left frame adapted from Fig. 10 in Lee, J.L., Chemistruck, A., and Plett, G.L., "One-Dimensional Physics-Based Reduced-Order Model of Lithium-Ion Dynamics," *Journal of Power Sources*, **220**, 2012, pp. 430–448.)

Note that the computational requirements of creating a ROM from a specific SOC and temperature setpoint is high; the computation requirement of averaging precomputed ROMs is low—this approach avoids executing the DRA to generate a ROM in real time during operation. In this chapter we desire to use model blending to extend the ROM’s useful SOC operating range. In Chap. 7, we will investigate how models change as functions of temperature: for now, we assume that it is possible to produce ROMs indicative of operation in the neighborhood of a particular SOC and temperature linearization setpoint.

Although it is considered an ad hoc method, model blending is one of the most popular approaches to modeling nonlinear systems. This method typically works well when the scheduling variables change slowly during operation, as is the case with cell SOC and temperature and when the variation in model parameter values is smooth with respect to a change in the scheduling variables.

6.13.1 Blending the models

Individual reduced-order models are generated *a priori* using the DRA over the expected operating range of temperatures and states of charge. For simplicity, we assume that the setpoints are generated as the Cartesian product of a temperature vector and an SOC vector, so that they fall on a rectangular grid.

These precomputed models are blended in real time using bilinear interpolation to generate a time-varying state-space model, as illustrated in Fig. 6.21. We define SOC_0 to be the nearest SOC setpoint value among the precomputed models that is less than or equal to the cell’s present operating SOC value, and SOC_1 to be the nearest SOC setpoint that exceeds the cell’s present operating SOC value. Similarly, we define T_0 to be the nearest temperature setpoint value among the precomputed models that is less than or equal to the cell’s present operating temperature, and T_1 to be the nearest temperature setpoint value that exceeds the cell’s present operating temperature. We then define blending factors θ_z and θ_T as

$$\theta_z = \frac{SOC - SOC_0}{SOC_1 - SOC_0} \quad \text{and} \quad \theta_T = \frac{T - T_0}{T_1 - T_0}.$$

The value of the time-varying blended \hat{A}_k matrix is found from¹²

$$\hat{A}_k = (1 - \theta_T) \left((1 - \theta_z) \hat{A}_{0,0} + \theta_z \hat{A}_{1,0} \right) + \theta_T \left((1 - \theta_z) \hat{A}_{0,1} + \theta_z \hat{A}_{1,1} \right),$$

where $\hat{A}_{0,0}$ is the \hat{A} matrix of the precomputed model at SOC_0 and T_0 , $\hat{A}_{0,1}$ at SOC_0 and T_1 , $\hat{A}_{1,0}$ at SOC_1 and T_0 , and $\hat{A}_{1,1}$ at SOC_1 and T_1 . The time-varying blended \hat{B}_k , \hat{C}_k , and \hat{D}_k matrices can be found

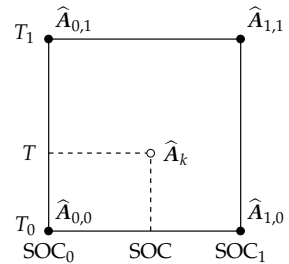


Figure 6.21: Bilinear interpolation of the \hat{A} matrix.

(Adapted from Fig. 3 in Lee, J.L., Aldrich, L., Stetzel, K., and Plett, G.L., “Extended Operating Range for Reduced-Order Model of Lithium-Ion Cells,” *Journal of Power Sources*, 255, 2014, pp. 85–100.)

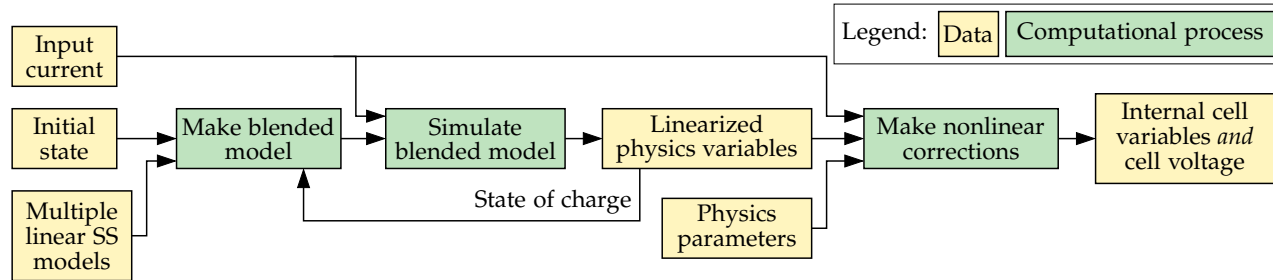
¹² We drop the “aug” subscript in the following, assuming that all matrices and vectors correspond to an augmented system when an integrator state is needed.

in the same manner (although we see some simplifications in the next section, which make it unnecessary to blend $\widehat{\mathbf{B}}_k$). The state-space equations are then modified with these time-varying blended matrices to become

$$\mathbf{x}[k+1] = \widehat{\mathbf{A}}_k \mathbf{x}[k] + \widehat{\mathbf{B}}_k i_{\text{app}}[k] \quad (6.55)$$

$$\mathbf{y}[k] = \widehat{\mathbf{C}}_k \mathbf{x}[k] + \widehat{\mathbf{D}}_k i_{\text{app}}[k]. \quad (6.56)$$

Fig. 6.22 illustrates the real-time aspect of the overall model-blending approach. During operation, the present cell SOC and temperature are used to generate blended state-space matrices. The model state vector $\mathbf{x}[k]$ is updated using these time-varying matrices, and the linearized outputs $\mathbf{y}[k]$ are computed from the updated state vector. The SOC calculated at each time step from the internal states is fed back into the linear model as an input to this blending process.



6.13.2 Sorting the model

One complication when implementing the model-blending scheme arises from the fact that state-space models are not unique. An infinite number of different state descriptions with corresponding $\{\widehat{\mathbf{A}}, \widehat{\mathbf{B}}, \widehat{\mathbf{C}}, \widehat{\mathbf{D}}\}$ represent the same input-output relationship. This fact poses a potential problem when model blending because for the method to work all elements of the matrix $\widehat{\mathbf{A}}_{0,0}$ must be consistent in meaning with the corresponding elements of the matrices $\widehat{\mathbf{A}}_{1,0}$, $\widehat{\mathbf{A}}_{0,1}$, and $\widehat{\mathbf{A}}_{1,1}$. If not, unrelated elements will be averaged together, producing a meaningless result. The DRA itself does not guarantee that models generated at different temperature and SOC setpoints will exhibit a consistent state-space description.

There is a simple remedy, however, which is to transform all pre-computed models into a common framework. We do so as follows. We begin by supposing that a linear discrete-time state-space model produced by the DRA is of the form

$$\mathbf{x}^{(0)}[k+1] = \widehat{\mathbf{A}}^{(0)} \mathbf{x}^{(0)}[k] + \widehat{\mathbf{B}}^{(0)} i_{\text{app}}[k]$$

Figure 6.22: Simulating a cell using model-blending approach.
(Adapted from Fig. 4 in Lee, J.L., Aldrich, L., Stetzel, K., and Plett, G.L., "Extended Operating Range for Reduced-Order Model of Lithium-Ion Cells," *Journal of Power Sources*, 255, 2014, pp. 85–100.)

$$\mathbf{y}[k] = \widehat{\mathbf{C}}^{(0)} \mathbf{x}^{(0)}[k] + \widehat{\mathbf{D}} i_{\text{app}}[k].$$

The superscript “(0)” on several of the model terms indicates that these matrices and signals arise from the untransformed model produced directly from the DRA. We will use superscripts “(1),” “(2),” and “(3)” in the following to indicate different stages of model transformation.

For the first transformation, we define a new state vector $\mathbf{x}^{(1)}[k]$, such that $\mathbf{x}^{(0)}[k] = \mathbf{T}^{(1)} \mathbf{x}^{(1)}[k]$, where $\mathbf{T}^{(1)}$ is some square invertible matrix. We have an equivalent input–output relationship between $i_{\text{app}}[k]$ and $\mathbf{y}[k]$ if we write

$$\begin{aligned} \mathbf{x}^{(1)}[k+1] &= \underbrace{(\mathbf{T}^{(1)})^{-1} \widehat{\mathbf{A}}^{(0)} \mathbf{T}^{(1)}}_{\widehat{\mathbf{A}}^{(1)}} \mathbf{x}^{(1)}[k] + \underbrace{(\mathbf{T}^{(1)})^{-1} \widehat{\mathbf{B}}^{(0)}}_{\widehat{\mathbf{B}}^{(1)}} i_{\text{app}}[k] \\ \mathbf{y}[k] &= \underbrace{\widehat{\mathbf{C}}^{(0)} \mathbf{T}^{(1)}}_{\widehat{\mathbf{C}}^{(1)}} \mathbf{x}^{(1)}[k] + \widehat{\mathbf{D}} i_{\text{app}}[k]. \end{aligned}$$

We have great freedom in choosing the transformation matrix $\mathbf{T}^{(1)}$, so long as it is invertible.

Consider first choosing $\mathbf{T}^{(1)} = \mathbf{V}$, where \mathbf{V} is a matrix whose columns are the eigenvectors of $\widehat{\mathbf{A}}^{(0)}$. The resulting $\widehat{\mathbf{A}}^{(1)}$ matrix will be diagonal.¹³ The diagonal elements of $\widehat{\mathbf{A}}^{(1)}$ are called the *poles* of the system and represent the dynamic time constants. Already, this first transformation has uncovered some physical meaning in the model. Also, the storage requirements of the transformed model are reduced, as the $n \times n$ dimension $\widehat{\mathbf{A}}^{(1)}$ matrix will contain only n nonzero values (on its diagonal), and computation requirements will be reduced, since only the diagonal elements of the $\widehat{\mathbf{A}}$ matrices need to be blended and fewer multiplies are needed to implement $\widehat{\mathbf{A}}^{(1)} \mathbf{x}^{(1)}[k]$ than to implement $\widehat{\mathbf{A}}^{(0)} \mathbf{x}^{(0)}[k]$.

Since eigenvectors are unique only up to a scaling factor, we can use this remaining degree of freedom to simplify our matrices further. Here, we elect to normalize the $\widehat{\mathbf{B}}$ matrix to have units value elements. This, of course, presupposes that there are no zero elements in $\widehat{\mathbf{B}}$, which is guaranteed if the system is completely controllable. The Ho–Kalman algorithm used in the DRA always produces a minimal state-space description, so we have this guarantee.

Thus, we then apply a second transformation, choosing $\mathbf{T}^{(2)} = \text{diag}(\widehat{\mathbf{B}}^{(1)})$. In the resulting transformed model, $\widehat{\mathbf{B}}^{(2)}$ contains only ones, and $\widehat{\mathbf{A}}^{(2)}$ will be unchanged from $\widehat{\mathbf{A}}^{(1)}$. This transformation has resulted in $\widehat{\mathbf{B}}^{(2)}$ and $\widehat{\mathbf{C}}^{(2)}$ matrices that are all scaled in a consistent way. It also reduces storage requirements, as $\widehat{\mathbf{B}}^{(2)}$ is known to always contain only ones, which do not need to be stored. Computation has

¹³ For this to be possible, the $\widehat{\mathbf{A}}^{(0)}$ matrix must be diagonalizable, requiring that the eigenvectors in \mathbf{V} be linearly independent. In our experience, the output of the DRA has always resulted in a diagonalizable $\widehat{\mathbf{A}}^{(0)}$ matrix; however, we know of no guarantee of this. In cases where the eigenvectors are linearly dependent, it is always possible to choose a transformation to put the $\widehat{\mathbf{A}}^{(1)}$ matrix into a Jordan form, which is what should be done instead.

also been reduced, as the $\widehat{\mathbf{B}}$ matrices do not need to be blended (they are all the same) and because the multiplication $\widehat{\mathbf{B}}_k i_{\text{app}}[k]$ is simply a repetition of the elements of $i_{\text{app}}[k]$, without multiplication.

Finally, we choose a third transformation matrix $\mathbf{T}^{(3)}$ to permute the elements of $\widehat{\mathbf{A}}^{(2)}$ such that $\widehat{\mathbf{A}}^{(3)}$ remains diagonal, but its elements appear in order of ascending magnitude. The $\widehat{\mathbf{B}}^{(3)}$ matrix remains all ones. For any particular temperature and SOC setpoint, we define the final scaled and sorted precomputed model as having $\widehat{\mathbf{A}} = \widehat{\mathbf{A}}^{(3)}$, $\widehat{\mathbf{B}} = \widehat{\mathbf{B}}^{(3)} = \mathbf{1}_{n \times 1}$, and $\widehat{\mathbf{C}} = \widehat{\mathbf{C}}^{(3)}$. The model $\widehat{\mathbf{D}}$ matrix is unchanged from the one produced by the DRA.

6.13.3 Stability of the blended model

Another concern to address is whether the model-blending method guarantees a stable time-varying model. It is intuitively appealing that linear time-varying combinations of stable time-invariant systems should be stable, but this is not always the case, depending on how the systems are connected.

With the method we propose, the model blending will always result in a stable system. To see this, consider the following. The blended model is computed using a weighted sum of the four nearest DRA matrices using bilinear interpolation. The state-space model can be written

$$\begin{aligned}\mathbf{x}[k+1] &= \widehat{\mathbf{A}}_k \mathbf{x}[k] + \widehat{\mathbf{B}}_k i_{\text{app}}[k] \\ \mathbf{y}[k] &= \widehat{\mathbf{C}}_k \mathbf{x}[k] + \widehat{\mathbf{D}}_k i_{\text{app}}[k]\end{aligned}$$

where $\widehat{\mathbf{A}}_k$ is diagonal with diagonal entries $0 \leq a_{ii} < 1$ except for the integrator pole where $a_{ii} = 1$. The $\widehat{\mathbf{B}}_k$ matrix of each ROM is $\begin{bmatrix} 1 & 1 & \dots & 1 \end{bmatrix}^T$. The state vector, $\mathbf{x}[k]$, can be found as

$$\mathbf{x}[k] = \left(\prod_{j=0}^{k-1} \widehat{\mathbf{A}}_{k-1-j} \right) \mathbf{x}[0] + \sum_{i=0}^{k-1} \left(\prod_{j=0}^{k-i-2} \widehat{\mathbf{A}}_{k-1-j} \right) \widehat{\mathbf{B}}_i i_{\text{app}}[i]$$

where $\widehat{\mathbf{A}}_k \equiv \mathbf{I}$ for $k < 0$. Using the triangle inequality, the infinity norm of the state vector is

$$\|\mathbf{x}[k]\|_\infty \leq \left\| \left(\prod_{j=0}^{k-1} \widehat{\mathbf{A}}_{k-1-j} \right) \mathbf{x}[0] \right\|_\infty + \left\| \sum_{i=0}^{k-1} \left(\prod_{j=0}^{k-i-2} \widehat{\mathbf{A}}_{k-1-j} \right) \widehat{\mathbf{B}}_i i_{\text{app}}[i] \right\|_\infty. \quad (6.57)$$

To demonstrate bounded-input bounded-output (BIBO) stability, we require that the input be bounded: $\|i_{\text{app}}[k]\|_\infty < \gamma < \infty$, where γ is some arbitrary finite bounding value.

Note that by the operations performed in Sect. 6.13.2, the diagonalization of the \hat{A}_k matrix has caused the individual states to become decoupled. In particular, every model will have the exact same integrator pole value where $a_{ii} = 1$, which does not then require blending between models. To ensure that the time-varying model is stable, we need look only at the nonintegrator dynamics, where $0 \leq a_{ii} < 1$.

To show that a bounded input always results in a bounded output, we look at the terms on the right-hand side of Eq. (6.57). Taking advantage of the fact that we have diagonalized all \hat{A}_k matrices, the first term is bounded by

$$\left\| \left(\prod_{j=0}^{k-1} \hat{A}_{k-1-j} \right) \mathbf{x}[0] \right\|_{\infty} \leq (\max_a)^k \|\mathbf{x}[0]\|_{\infty},$$

where $\max_a = \max_{i,k} (a_{k,ii}) < 1$. Thus, this term is always finite if $\|\mathbf{x}_0\|_{\infty} < \infty$. Turning to the second term on the right-hand side of Eq. (6.57) we have

$$\left\| \sum_{i=0}^{k-1} \left(\prod_{j=0}^{k-i-2} \hat{A}_{k-1-j} \right) \hat{B}_i i_{\text{app}}[i] \right\|_{\infty} \leq \sum_{i=0}^{k-1} \left\| \left(\prod_{j=0}^{k-i-2} \hat{A}_{k-1-j} \right) \right\|_{\infty} \left\| \hat{B}_i i_{\text{app}}[i] \right\|_{\infty}. \quad (6.58)$$

Because all of the values in the \hat{A} matrix are less than 1, we can write

$$\left\| \left(\prod_{j=0}^{k-i-2} \hat{A}_{k-1-j} \right) \right\|_{\infty} \leq (\max_a)^{k-i-1}.$$

Eq. (6.58) is simplified to

$$\left\| \sum_{i=0}^{k-1} \left(\prod_{j=0}^{k-i-2} \hat{A}_{k-1-j} \right) \hat{B}_i i_{\text{app}}[i] \right\|_{\infty} \leq \gamma (\max_a)^{k-1} \sum_{i=0}^{k-1} \left(\frac{1}{\max_a} \right)^i.$$

The formula for the geometric series is used to give

$$\begin{aligned} \left\| \sum_{i=0}^{k-1} \left(\prod_{j=0}^{k-i-2} \hat{A}_{k-1-j} \right) \hat{B}_i i_{\text{app}}[i] \right\|_{\infty} &\leq \gamma (\max_a)^{k-1} \left[\frac{1 - \left(\frac{1}{\max_a} \right)^k}{1 - \left(\frac{1}{\max_a} \right)} \right] \\ &\leq \gamma \left[\frac{(\max_a)^{k-1} - \left(\frac{1}{\max_a} \right)}{1 - \frac{1}{\max_a}} \right] < \infty. \end{aligned}$$

Both terms on the right-hand side of Eq. (6.57) are finite. Therefore, $\|\mathbf{x}[k]\|_{\infty} < \infty$.

The infinity norm of the output equation is defined as

$$\|\mathbf{y}[k]\|_{\infty} = \left\| \hat{C}_k \mathbf{x}[k] + \hat{D}_k i_{\text{app}}[k] \right\|_{\infty}.$$

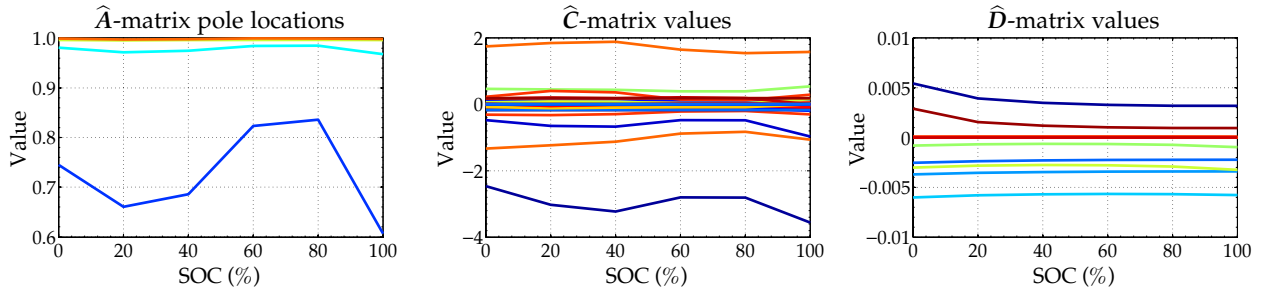


Figure 6.23: SOC-dependent model values.

To show BIBO stability, this norm must be finite. Using the triangle inequality gives

$$\begin{aligned}\|\mathbf{y}[k]\|_{\infty} &\leq \|\hat{\mathbf{C}}_k \mathbf{x}[k]\|_{\infty} + \|\hat{\mathbf{D}}_k i_{\text{app}}[k]\|_{\infty} \\ &\leq \|\hat{\mathbf{C}}_k\|_{\infty} \|\mathbf{x}[k]\|_{\infty} + \|\hat{\mathbf{D}}_k\|_{\infty} \|i_{\text{app}}[k]\|_{\infty}.\end{aligned}$$

Since $\|\mathbf{x}[k]\|_{\infty} < \infty$ and the $\hat{\mathbf{C}}_k$ and $\hat{\mathbf{D}}_k$ matrices are finite, we have that $\|\mathbf{y}[k]\|_{\infty} < \infty$, which shows BIBO stability.

6.13.4 Smoothness of the model matrices versus SOC

For the model-blending approach to work, the reduced-order state-space model matrices must have smoothly changing parameters over the expected SOC range. Then, blending model values via interpolation between setpoints for any specific operational SOC will compute a numeric result that is close to what would have been computed if a dedicated ROM had been precomputed at that SOC via the DRA. In effect, the smoothness (or lack thereof) of the model parameters dictates the number of precomputed setpoint ROMs needed to be able to capture the changing dynamics of the system accurately with a blended model.

The setpoint model matrices do vary in a sufficiently smooth manner. This is shown in Fig. 6.23 for the cell described by Table 6.1. For each setpoint ROM, the diagonal $\hat{\mathbf{A}}$ matrix has one integrator term (with “pole” equal to 1.0 in every case); the value of the remaining four “poles” are plotted in the first frame as a functions of SOC. We see that all demonstrate smooth variation, such that we would expect model blending to yield good intermediate models in-between stored precomputed models. Similar results are shown in the figure for the model $\hat{\mathbf{C}}$ - and $\hat{\mathbf{D}}$ -matrix values.¹⁴

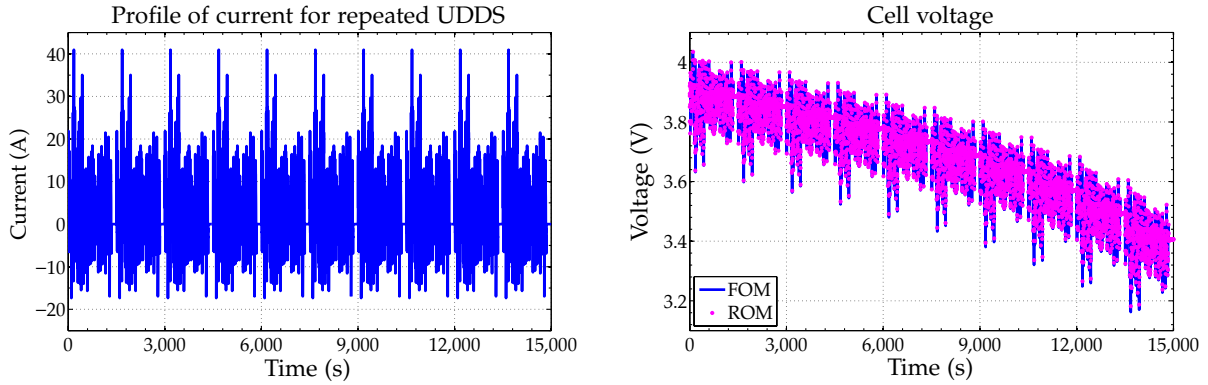
6.13.5 Results from the blended model

This section presents simulation results to provide insight into the impact of changing SOC.¹⁵ For this scenario, we use a charge-depleting

¹⁴ Note that two $\hat{\mathbf{D}}$ -matrix values have noticeably larger value at low SOC. The blended model is capturing the SOC dependence of the equivalent series resistance term.

¹⁵ To reproduce these results, see <http://mocha-java.uccs.edu/BMS1/CH06/ROM.zip>.

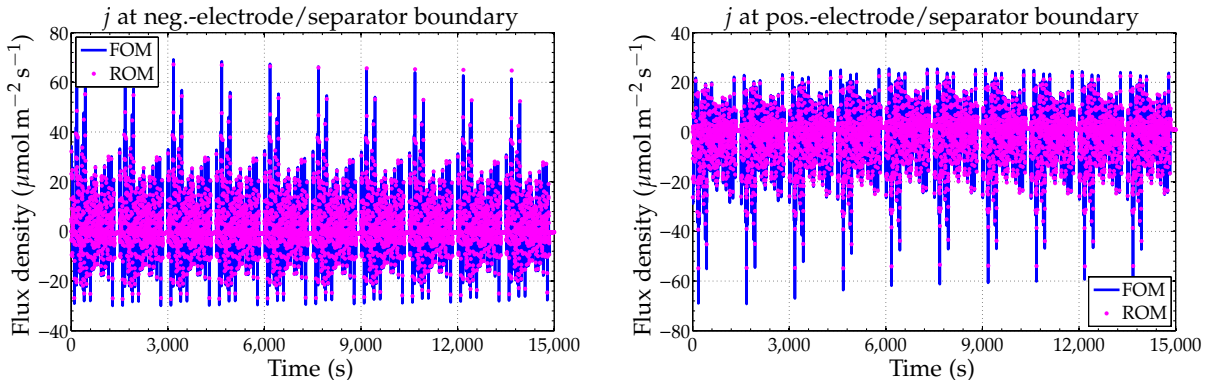
UDDS cycle, which reduces cell SOC by about 5.5 %. The cell is run through 10 consecutive repetitions of this charge-depleting UDDS cycle. This input is shown in the left frame of Fig. 6.24.



During the simulation, the cell discharges from 80 % to about 25 % SOC. The right frame of Fig. 6.24 depicts the ROM and FOM predictions of cell voltage. Root-mean-squared error was 2.47 mV.

We also show cell internal variables for this simulation. Reaction flux density at the electrode/separator interfaces are presented in Fig. 6.25. The electrochemical reactions at the electrode/separator interface are more dynamic than at the current collectors and are therefore more difficult for the ROM to match. Even so, the ROM and FOM results match very well.

Figure 6.24: Cell voltage for UDDS test. (Right frame adapted from Fig. 10 in Lee, J.L., Aldrich, L., Stetzel, K., and Plett, G.L., "Extended Operating Range for Reduced-Order Model of Lithium-Ion Cells," *Journal of Power Sources*, 255, 2014, pp. 85–100.)



Likewise, ROM versus FOM comparisons for the internal cell potentials are presented in Fig. 6.26. They also match well.

Finally, ROM versus FOM comparisons for internal concentrations are presented in Fig. 6.27. These do not match quite as well as the other variables, but they match well enough to be useful.

Adding more states to the reduced-order model (increasing from five states to 10 states) does not have a significant impact on any of

Figure 6.25: Butler–Volmer flux density at electrode/separator boundaries.

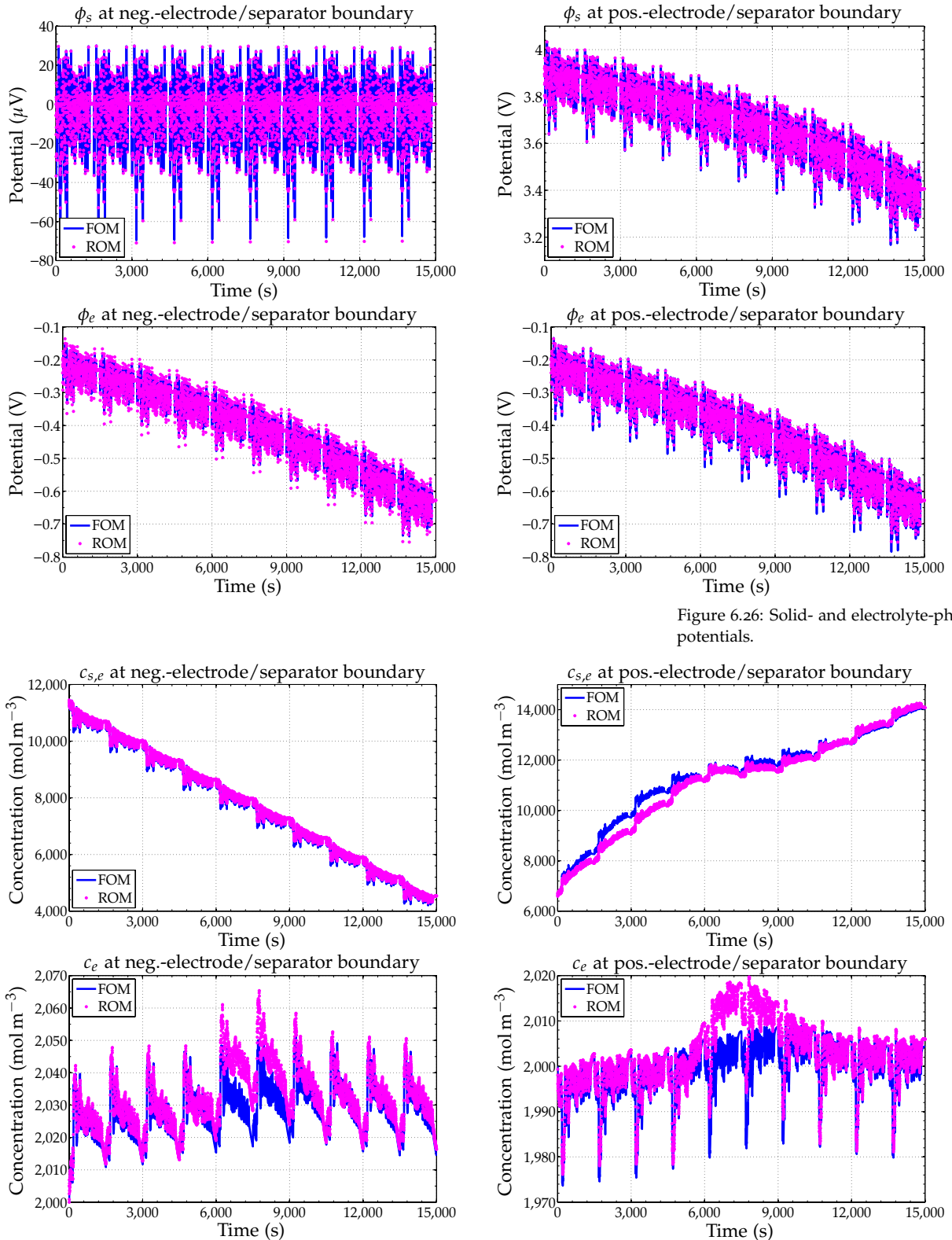


Figure 6.26: Solid- and electrolyte-phase potentials.

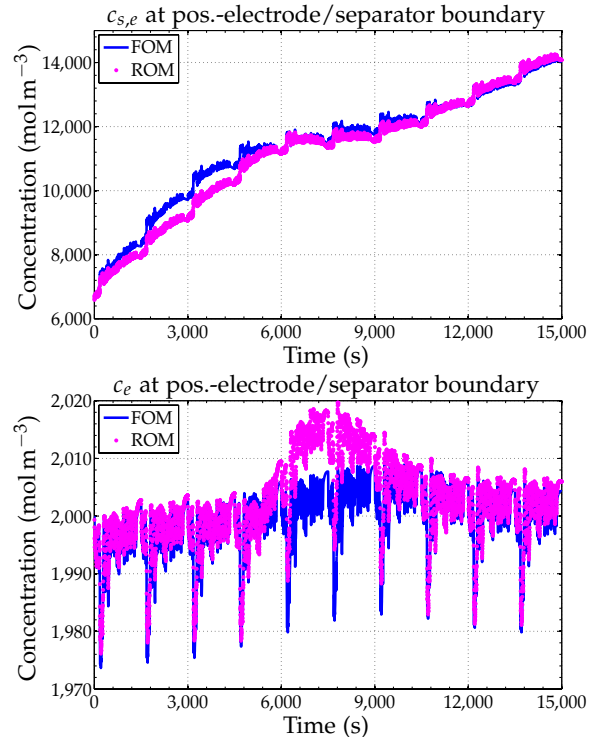


Figure 6.27: Solid-surface- and electrolyte-phase lithium concentrations.

the results except for the electrolyte concentration. Fig. 6.28 shows simulations of these variables, which have improved greatly over the center part of the simulation. However, despite this improvement, the cell voltage prediction (and error) stays very nearly the same, as it is not very sensitive to electrolyte concentration.

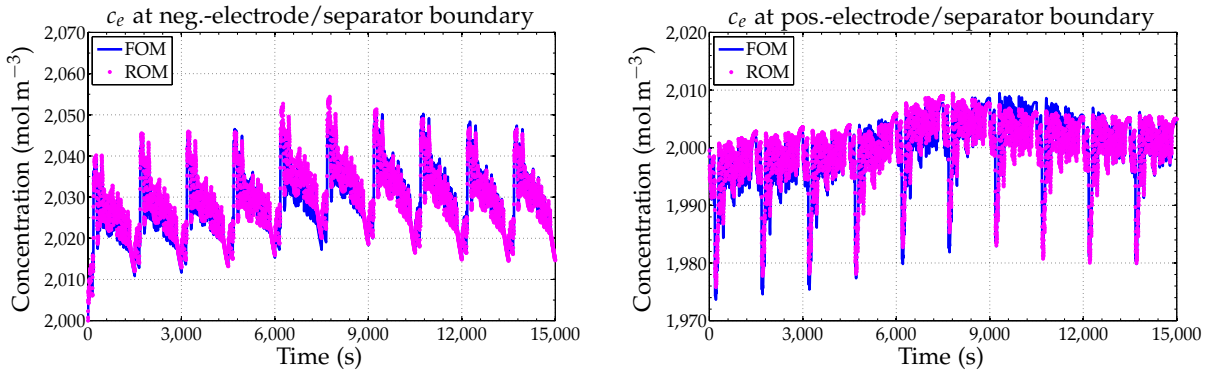


Figure 6.28: Electrolyte-phase lithium concentrations for a 10-state ROM.

6.14 Where to from here?

We now have a reduced-order physics-based model of cell dynamics that agrees very closely with the continuum-scale predictions. This model executes in very reasonable time, having only five states.

However, this model operates only around a single temperature setpoint: we require a thermal model for lithium-ion cells. This is what we look at next.

6.15 Modal-solution code

Perhaps the most challenging of the transfer functions to develop and understand is the one for concentration of lithium in the electrolyte. This section contains MATLAB code to find eigenvalues (it produces Fig. 6.6), eigenfunctions (it produces Fig. 6.7), and a solution assuming simplified uniform reaction flux density (it produces Fig. 6.8). While we do not devote space to explaining the code, the hope is that it can be illustrative by comparing to the equations in this chapter.

```
function eigenFunctions
%
% Simulate electrolyte concentration equation:
%
% Declare simulation parameters
Tfinal = 10; % total length of current pulse [s]
dt = 0.001; % time step for PDE solution [s]
i_app = 10; % cell applied current [A]
modes = 10; % number of eigenvalue terms in modal solution
```

```

% Declare cell parameters (Doyle cell)
La = 128; Ls = 76; Lc = 190; L = La+Ls+Lc; % widths, in micro-meters
dx = 1e-6; % 1 micro-meter
La_abs = La*dx; Lc_abs = Lc*dx; Ls_abs = Ls*dx; L_abs = L*dx;
L1 = La_abs; L2 = La_abs+Ls_abs;
A = 1; % cell area of 1 m^2
eps1 = 0.357; eps2 = 0.724; eps3 = 0.444; % vol frac, D per region
D = 7.5e-11; D1 = D*eps1^1.5; D2 = D*eps2^1.5; D3=D*eps3^1.5;
tplus = 0.363; % transference number [u/l]
c0 = 1000; % initial electrolyte concentration [mol/m3]
Far = 96485; % Faraday's constant

% -----
% First, simulate PDE solution using built-in MATLAB solver
x = 0:dx:L_abs; t = 0:dt:Tfinal;
ce = pdepe(0,@pdepde,@pdeic,@pdebc,x,t);

% -----
% Now, find eigenfns: Compute y3prime(lambda) at x=L to find lambda
lambda = 0:1e-4:0.5;
y3prime = lambdaFn(lambda); % get derivative of y3prime at x=L

% Search for the roots of y3prime == 0: Initialize 'theRoots' to known
% eigenvalue of zero, search for eigenvalues k=2 and following
theRoots = 0; k = 2; dL=0.0001;
while 1,
    if lambdaFn((k-1)*dL)*lambdaFn(k*dL)<0, % sign change!
        theRoots = [theRoots,fzero(@lambdaFn,[(k-1)*dL k*dL])]; %#ok<AGROW>
        if length(theRoots)>modes, break; end
    end
    k = k+1;
end

% compute the eigenfunctions for these eigenvalues, then normalize
Psi = eigenFunction(theRoots(1:modes+1)');
epsX = zeros(1,L+1); epsX((0:La)+1) = eps1;
epsX((La:La+Ls)+1) = eps2; epsX((La+Ls:L)+1) = eps3;
for k = 1:modes+1, % normalize
    Psi(k,:) = Psi(k,:)/sqrt(trapz((0:L)*dx,Psi(k,:).^2.*epsX));
end

% -----
% Next, find the modal solution
c_en = zeros([modes+1 Tfinal/dt+1]);
Afact = theRoots(1:modes+1)'; Bfact = 0*Afact;
for k = 1:length(Afact),
    v1 = zeros(size(epsX));
    v1((0:La)+1) = (1-tplus)/(Far*A*La_abs);
    v1((La+Ls:L)+1) = -(1-tplus)/(Far*A*Lc_abs);
    Bfact(k) = trapz((0:L)*dx,Psi(k,:).*v1);
end
c_en(1,1) = c0*trapz((0:L)*dx,Psi(1,:).*epsX);

% Simulate the c_{e,n} ODEs using Euler's forward method
for t = 2:size(c_en,2),
    c_en(:,t) = c_en(:,t-1) + dt*(-Afact.*c_en(:,t-1)) + dt*i_app*Bfact;
end

tstep = size(c_en,2); % time step at which to examine solution
modeApprox = c0 + c_en(2:end,tstep)'*Psi(2:modes+1,:);

```

```

% -----
% Plot results
figure(1); clf; plot(lambda,y3prime/1e5,'-',[0 0.5],[0 0],'k:');
title('Slope of PSI(Ltot,L)');
xlabel('Eigenvalue guess L'); ylabel('Slope (x1e5)');

figure(2); clf; plot(0:L,c0+ce(tstep,:),'r',0:L,modeApprox,'b-');
yl = ylim; xlim([0 L]); hold on;
title('Final concentration profile');
xlabel('Position across cell (um)'); ylabel('Conc. (mol/m3)');
legend('PDE solution',sprintf('Solution for modes 0:%d',modes));
plot([0 L],[1000 1000],'k',[La La],yl,'k',[La+Ls La+Ls],yl,'k');
plot([0 L],[1000 1000],'k',[La La],yl,'k',[La+Ls La+Ls],yl,'k');

if modes > 5,
figure(3); clf; plot(0:L,Psi(1:6,:)); yl = ylim; xlim([0 L]);
title('Eigenfunctions 0 through 5'); hold on;
xlabel('Position across cell (um)'); ylabel('Value (m^{-1})');
plot([La La],yl,'k',[La+Ls La+Ls],yl,'k',[0 L],[0 0],'k');
end

% -----
% Eigenfunction solver helper functions
function y3prime = lambdaFn(lambda)
% "k" values solved symbolically based on normalizing constant k1
k1 = 1; sle1 = sqrt(lambda*eps1/D1);
sle2 = sqrt(lambda*eps2/D2); sle3 = sqrt(lambda*eps3/D3);
k3 = k1.*cos(sle1*L1).*cos(sle2*L1) + ...
    D1*sle1.*sin(sle1*L1).*sin(sle2*L1)/(D2*sle2));
k4 = k1.*cos(sle1*L1).*sin(sle2*L1) - ...
    D1*sle1.*cos(sle1*L1).*sin(sle2*L1)/(D2*sle2));

k5 = k3.*cos(sle2*L2).*cos(sle3*L2) + ...
    D2*sle2.*sin(sle2*L2).*sin(sle3*L2)/(D3*sle3)) + ...
    k4.*sin(sle2*L2).*cos(sle3*L2) - ...
    D2*sle2.*cos(sle2*L2).*sin(sle3*L2)/(D3*sle3));
k6 = k3.*cos(sle2*L2).*sin(sle3*L2) - ...
    D2*sle2.*sin(sle2*L2).*cos(sle3*L2)/(D3*sle3)) + ...
    k4.*sin(sle2*L2).*sin(sle3*L2) + ...
    D2*sle2.*cos(sle2*L2).*cos(sle3*L2)/(D3*sle3));
y3prime = -k5.*sle3.*sin(sle3*L_abs) + k6.*sle3.*cos(sle3*L_abs);
y3prime(lambda == 0) = 0;
end

function Psi = eigenFunction(lambda)
% "k" values solved symbolically based on normalizing constant k1
k1 = 1; sle1 = sqrt(lambda*eps1/D1);
sle2 = sqrt(lambda*eps2/D2); sle3 = sqrt(lambda*eps3/D3);
k3 = k1.*cos(sle1*L1).*cos(sle2*L1) + ...
    D1*sle1.*sin(sle1*L1).*sin(sle2*L1)/(D2*sle2));
k4 = k1.*cos(sle1*L1).*sin(sle2*L1) - ...
    D1*sle1.*cos(sle1*L1).*sin(sle2*L1)/(D2*sle2));

k5 = k3.*cos(sle2*L2).*cos(sle3*L2) + ...
    D2*sle2.*sin(sle2*L2).*sin(sle3*L2)/(D3*sle3)) + ...
    k4.*sin(sle2*L2).*cos(sle3*L2) - ...
    D2*sle2.*cos(sle2*L2).*sin(sle3*L2)/(D3*sle3));
k6 = k3.*cos(sle2*L2).*sin(sle3*L2) - ...
    D2*sle2.*sin(sle2*L2).*cos(sle3*L2)/(D3*sle3)) + ...
    k4.*sin(sle2*L2).*sin(sle3*L2) + ...
    D2*sle2.*cos(sle2*L2).*cos(sle3*L2)/(D3*sle3));
Psi = zeros(length(lambda),L+1);

```

```

x = 0:La;
Psi(:,x+1) = k1.*cos(sle1*x*dx);
x = La:La+Ls;
Psi(:,x+1) = k3(:,ones(size(x))).*cos(sle2*x*dx) + ...
k4(:,ones(size(x))).*sin(sle2*x*dx);
x = La+Ls:L;
Psi(:,x+1) = k5(:,ones(size(x))).*cos(sle3*x*dx) + ...
k6(:,ones(size(x))).*sin(sle3*x*dx);
Psi(lambda == 0,:) = k1;
end

% -----
% PDE solver helper functions
function [c,f,s] = pdepde(x,~,~,DuDx)
if x <= La_abs,
    c = eps1; f = D1*DuDx; s = (1-tplus)*i_app/(Far*A*La_abs);
elseif x <= La_abs+Ls_abs,
    c = eps2; f = D2*DuDx; s = 0;
else
    c = eps3; f = D3*DuDx; s = -(1-tplus)*i_app/(Far*A*Lc_abs);
end
end

function u0 = pdeic(~) % initial conditions
u0 = 0; % initialize to 0, and add in c0 later for better numerics
end

function [pl,ql,pr,qr] = pdebc(~,~,~,~,~) % boundary conditions
pl = 0; ql = 1; pr = 0; qr = 1;
end
end

```

6.16 Partial glossary

This section provides a glossary of the most important variables defined in this chapter.

- $c_{e,0}$ [mol m³] is the steady-state concentration of lithium in the electrolyte when the cell is at rest (cf. p. 219).
- $\tilde{c}_e(x, t)$ [mol m³] is the debiased concentration of lithium in the electrolyte: $\tilde{c}_e = c_e - c_{e,0}$ (cf. p. 229).
- $c_{s,\text{avg}}(t)$ [mol m³] is the average concentration of lithium in an electrode (cf. p. 245).
- $c_{s,0}$ [mol m³] is the steady-state concentration of lithium in the electrode solid particles at a particular setpoint cell state-of-charge (cf. p. 219).
- $\tilde{c}_{s,e}(x, t)$ [mol m³] is the debiased solid-surface concentration of an electrode particle: $\tilde{c}_{s,e} = c_{s,e} - c_{s,0}$ (cf. p. 220).
- $[\tilde{c}_{s,e}(x, t)]^*$ [mol m³] is the debiased solid-surface concentration of an electrode particle, with its integrator term removed (cf. p. 225).
- $h(t; \lambda)$ [mol m⁻²] is the time-varying part of a separation-of-variables PDE solution (cf. p. 233).

- $i_{\text{app}}(t)$ [A] is the cell applied current (cf. p. 221).
- j_0 [mol m² s⁻¹] is the steady-state exchange flux density of lithium between solid and electrolyte when the cell is at rest (cf. p. 219).
- $j_n(t)$ [mol m⁻³ s⁻¹] is the modal input to $\tilde{c}_{e,n}(t)$ (cf. p. 237).
- λ [s⁻¹] is an eigenvalue relating to one solution of a Sturm–Liouville problem, used in a separation-of-variables PDE solution (cf. p. 233).
- $\nu(s)$ [u/l] is a square-root impedance ratio that is common to all the electrochemical-variable transfer functions (cf. p. 223).
- $\tilde{\phi}_e(x, t)$ [V] is the debiased electrolyte potential: $\tilde{\phi}_e(x, t) = \phi_e(x, t) - \phi_e(0, t)$ (cf. p. 242).
- $[\tilde{\phi}_e(x, t)]_1$ [V] is the linear portion of $\tilde{\phi}_e(x, t)$ (cf. p. 242).
- $[\tilde{\phi}_e(x, t)]_2$ [V] is the nonlinear portion of $\tilde{\phi}_e(x, t)$ (cf. p. 242).
- $\tilde{\phi}_s(x, t)$ [V] is the debiased solid potential: $\tilde{\phi}_s = \phi_s - \phi_s(0)$ where $\phi_s(0)$ is the potential of the solid at the current-collector interface: $\phi_s^{\text{neg}}(0) = 0$ and $\phi_s^{\text{pos}}(0) = v(t)$ (cf. p. 227).
- $\phi_{s-e}(x, t)$ [V] is the solid–electrolyte potential difference (cf. p. 219).
- $\tilde{\phi}_{s-e}(x, t)$ [V] is the debiased solid–electrolyte potential difference: $\tilde{\phi}_{s-e} = \phi_{s-e} - U_{\text{ocp}}(c_{s,0})$ (cf. p. 220).
- $[\tilde{\phi}_{s-e}(x, t)]^*$ [V] is the debiased solid–electrolyte potential difference, with its integrator term removed (cf. p. 225).
- $\Psi(x; \lambda)$ [m⁻¹] is the spatially varying part of a separation-of-variables PDE solution (cf. p. 233).
- R_{ct} [Ωm²] is the charge-transfer resistance of an electrode particle (cf. p. 220).
- R_{film} [Ωm²] is the resistance of a surface film on an electrode particle (cf. p. 218).
- $R_{s,e}$ [Ωm²] is the total solid–electrolyte interfacial resistance of an electrode particle (cf. p. 220).
- z [u/l] is a dimensionless value between 0 and 1 indicating a spatial location in an electrode. $z = 0$ at the current collector and $z = 1$ at the electrode/separator interface (cf. p. 221).

7

Thermal Modeling

Up until now we have assumed that the cell we are modeling is at a constant temperature, which is rarely the case in reality. When considering thermal aspects of real cells, we must account for how usage of the cell generates (or sinks) heat, how local temperature changes due to heat generation or consumption, flow of heat within the cell and to/from the environment at cell boundaries, and how cell operational parameters change as a function of cell temperature.

In this chapter, we consider thermal aspects of battery-cell performance, resulting in a reduced-order coupled electrochemical–thermal model. We start by defining some important fundamental terms and then develop a microscale thermal model. We will not go back to first principles quite the same way we did in Chap. 3, as that would require far more development than we’re willing to discuss in this book. However, we will point the reader to references that can help with the underlying thermal physics.

In particular, we first derive an equation that describes thermal activity in a single phase k at the microscale

$$\rho_k c_{P,k} \frac{\partial T_k}{\partial t} = \nabla \cdot (\lambda_k \nabla T_k) - \mathbf{i}_k \cdot \nabla \phi_k. \quad (7.1)$$

We then use volume-averaging techniques to describe thermal activity at the continuum scale, which is modeled as

$$\frac{\partial(\rho c_P T)}{\partial t} = \nabla \cdot (\lambda \nabla T) + q. \quad (7.2)$$

The heat-generation terms are also discussed in some detail.

After these PDE models are derived, we show how to make reduced-order models of the heat-generation terms by leveraging some of the same techniques already seen in Chaps. 5–6 and how to make a reduced-order model of Eq. (7.2) with q as its input. Last, we look at how to make a dynamic cell model that operates over a wide temperature range.

7.1	Preliminary definitions	272
7.2	Microscale model	273
7.3	Continuum model	277
7.4	Parameter variation	280
7.5	Reduced-order model	281
7.6	New transfer functions	281
7.7	Heat-generation terms	285
7.8	Heat-flux terms	292
7.9	Uncoupled model results	296
7.10	Coupled model results	297
7.11	Where to from here?	298
7.12	Partial glossary	300

7.1 Preliminary definitions

According to thermodynamic theory, *temperature* is a measure of the tendency of an object to give up energy to its surroundings spontaneously. When two objects are in thermal contact, the one that tends to lose energy spontaneously is at the higher temperature.¹ If we are precise, we can write

$$\frac{1}{T} = \left(\frac{dS}{dU} \right)_{n,V},$$

relating temperature T to entropy S and internal energy U when the number of particles and volume are held constant.

A simpler (but less precise) definition of temperature relates it to the translational kinetic energy associated with the disordered microscopic translational motion of atoms or molecules in a system. (It does not consider the potential energy of the system.) According to this definition of *kinetic temperature*,

$$\left[\frac{1}{2}mv^2 \right]_{\text{average}} = \frac{3}{2}kT,$$

where k is the Boltzmann constant. While this conceptual definition of temperature has some problems, it will be sufficient to understand this chapter.

HEAT can be defined as “thermal energy in transit.”² We talk about *heat flux* and mean that thermal energy is moving from one place to another, tending to change the temperatures of the source and destination. We talk about *heat generation* and mean that thermal energy is being added to a system, tending to increase its temperature. We talk about a *heat sink* and mean that thermal energy is being removed from a system, tending to decrease its temperature.

There are various mechanisms by which thermal energy can travel: conduction, convection, and radiation. *Conduction* is the transfer of thermal energy within a system, molecule by molecule, as one molecule imparts energy to its neighbor. If you hold a metal cooking pot over a fire, it will absorb the energy from the flame (via radiation energy transfer). The molecules absorbing the energy will begin to vibrate more quickly, bumping into the molecules next to them, increasing their energy, and so forth. As this process continues, the heat is transferred from the part directly over the fire to the extremities of the pot.

The ability of a material to conduct heat depends on its macroscopic and microscopic structure. Styrofoam cups and double-paned windows are good thermal insulators because air pockets captured by the styrofoam beads and gas pockets between window panes do not

¹ Schroeder, D., *An Introduction to Thermal Physics*, Addison Wesley, Chap. 1, 2000.

² Blundell, S.J., and Blundell, K.M., *Concepts in Thermal Physics*, Oxford University Press, 2d, Chap. 2, 2010.

conduct heat very well. On the other hand, metals are good thermal conductors due to the tight internal bonding of their atoms. This is why a metal plate seems cold when you touch it—it conducts body heat away from your hand quickly.

Convection is the transfer of thermal energy due to the mass movement of a fluid (liquid or gas) arising from a pressure gradient. *Natural convection* is a function of density: warm fluids are less dense than cold fluids, so warm fluids tend to rise while cold fluids fall. *Forced convection* relies on a fan or pump to augment the natural pressure gradient to speed fluid movement. To extend the prior example, water in the metal cooking pot that is being held over a fire will begin to move via convection, transferring heat.

An object is cooled via convection when a thin layer of fluid in contact with it is first heated via conduction. Conduction alone does not account for the cooling, however, as fluids are generally poor conductors of thermal energy. Instead, the thin layer of fluid heated by conduction carries the heat away from the system by convection; this cycle repeats when a new cooler layer of fluid takes its place. Different fluids have different abilities to remove heat, with liquids generally having a greater capacity than gases.

Radiation is the transfer of thermal energy via electromagnetic waves.³ Radiation does not rely upon any contact between the heat source and the heated object as is the case with both conduction and convection. No mass is exchanged and no medium is required in the process of radiation: heat can be transmitted through empty space. This energy is absorbed when these waves encounter an object. For example, energy traveling from the sun to your skin: you can feel your skin getting warmer as energy is absorbed.

³ For ordinary temperatures—less than “red hot”—the radiation is in the infrared region of the electromagnetic spectrum.

7.2 Microscale thermal model

7.2.1 Enthalpy

Before deriving the microscale thermal model, a concept that needs further development is that of *enthalpy*. This was introduced in Chap. 3 as one of the four quantities known as the *thermodynamic potentials* of a system. Enthalpy is particularly useful here as it can be thought of as the total amount of energy stored by the system that could be released as heat.

For example, if enthalpy H increases, then $\Delta H > 0$, and the system has received energy that could be released as heat. If enthalpy decreases, $\Delta H < 0$, and the system has released energy in the form of heat. So, ΔH must be proportional to a change in internal energy due to heat, Δq .

Enthalpy is related to internal energy but is not equal to internal energy because the first law of thermodynamics states

$$\Delta U = \Delta q + \Delta w \neq \Delta q.$$

To remove the Δw term, enthalpy is defined as $H \equiv U + pV$ and is most useful for constant-pressure calculations. This is not a major constraint as many chemical reactions may be considered to occur under (constant) atmospheric pressure, so we may regard them as constant pressure processes.

The change in enthalpy due to a chemical reaction is then the heat released by the reaction, as we show in the following sketch:

$$\begin{aligned} dH &= dU + d(pV) = dU + p dV + V dp = dU + p dV \\ &= dq + dw + p dV = dq - p dV + p dV = dq. \end{aligned}$$

7.2.2 General thermal energy equation

With this introduction, we are ready to proceed to the rest of the derivation, based on a paper by Gu and Wang.⁴ We begin with a general differential equation result for thermal energy balance that considers multiple species in multiple phases (such as in a battery cell with solid and electrolyte phases, and having electronic and ionic species), based on first principles:⁵

$$\rho_k c_{P,k} \left(\frac{\partial T_k}{\partial t} + \mathbf{v}_k \cdot \nabla T_k \right) = \nabla \cdot (\lambda_k \nabla T_k) - \sum_{\text{species } i} \mathbf{j}_{k,i} \cdot \nabla H_{k,i}. \quad (7.3)$$

Heat generation is apparently absent from this PDE because it is a phenomena that occurs at the boundary between phases due to chemical reactions occurring there. We will introduce its impact when we consider boundary conditions in the continuum-scale model.

The first term on the left-hand side of Eq. (7.3) models energy storage in phase k as an increase in temperature, where ρ_k is the density of phase k , $c_{P,k}$ is the specific heat of phase k , and T_k is the temperature of phase k .

The second term on the left-hand side of Eq. (7.3) is a convection term—local energy changes because warmer or colder materials flow into the region of interest. In this term, \mathbf{v}_k is the average velocity of the mixture.

The first term on the right-hand side models heat flux due to thermal diffusion, where λ_k is the thermal conductivity of phase k . Conductivities of some materials are illustrated in Fig. 7.1. Battery materials have typical thermal conductivities around $5 \text{ W m}^{-1} \text{ K}^{-1}$.

The second term on the right-hand side models heat flux due to material flux, where $\mathbf{j}_{k,i}$ is the molar flux density due to diffusion and

⁴ Gu, W.B., and Wang, C.Y., "Thermal-Electrochemical Modeling of Battery Systems," *Journal of the Electrochemical Society*, 147(8), 2000, pp. 2910–2922.

⁵ Bird, R.B., Stewart, W.E., and Lightfoot, E.N., *Transport Phenomena*, 2d, John Wiley and Sons, 2002. This result is from Table 19.2-4, entry (F) in Bird's book, combined with Bird 19.3-6, as derived in Gu and Wang.

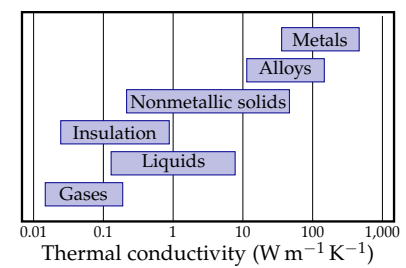


Figure 7.1: Range of thermal conductivities for different kinds of materials.

migration of species i in phase k , relative to the mixture's average velocity \mathbf{v}_k , and H_k is the partial molar enthalpy of species i in phase k , where $H_k = U_k + pV_k$.

We assume that convection within a phase is negligible and drop it from the equation, giving⁶

$$\rho_k c_{P,k} \frac{\partial T_k}{\partial t} = \nabla \cdot (\lambda_k \nabla T_k) - \sum_{\text{species } i} \mathbf{j}_{k,i} \cdot \nabla H_{k,i}.$$

7.2.3 Evaluating the partial molar enthalpy term

To proceed, we need to be able to work with the H_k term. Starting with the definition of partial molar enthalpy, we write (cf. Table 3.1)

$$\begin{aligned} H_{k,i} &= \left(\frac{dH}{dn_{k,i}} \right)_{T,p,n_j \neq k,i} \\ &= \left(\frac{d(G + TS)}{dn_{k,i}} \right)_{T,p,n_j \neq k,i} \\ &= \left(\frac{dG}{dn_{k,i}} \right)_{T,p,n_j \neq k,i} + T \left(\frac{dS}{dn_{k,i}} \right)_{T,p,n_j \neq k,i}. \end{aligned}$$

Recall that the first term is equal to the electrochemical potential $\bar{\mu}_i$. To evaluate the second term, we need the Gibbs–Duhem relationship via Eq. (3.15):

$$\begin{aligned} SdT - Vdp &= - \sum_{i=1}^r n_i d\bar{\mu}_i \\ S &= V \frac{dp}{dT} - \sum_{i=1}^r n_i \frac{d\bar{\mu}_i}{dT} \\ \left(\frac{dS}{dn_{k,i}} \right)_{T,p,n_j \neq k,i} &= - \frac{d\bar{\mu}_{k,i}}{dT}. \end{aligned}$$

Combining, we have

$$H_{k,i} = \bar{\mu}_{k,i} - T \left(\frac{d\bar{\mu}_{k,i}}{dT} \right)_{p,n_j}.$$

Now, recall one definition of the electrochemical potential, via Eqs. (3.13) and (3.17):

$$\begin{aligned} \bar{\mu}_k &= RT \ln(\lambda_k) + z_k F \phi_k \\ H_{k,i} &= RT \ln(\lambda_{k,i}) + z_{k,i} F \phi_{k,i} - T \frac{d(RT \ln(\lambda_{k,i}) + z_{k,i} F \phi_{k,i})}{dT} \\ &= RT \ln(\lambda_{k,i}) + z_{k,i} F \phi_{k,i} - T \frac{dRT \ln(\lambda_{k,i})}{dT} - z_{k,i} FT \frac{d\phi_{k,i}}{dT} \\ &= RT \ln(\lambda_{k,i}) - T \left(R \ln(\lambda_{k,i}) + RT \frac{d \ln(\lambda_{k,i})}{dT} \right) + z_{k,i} F \left(\phi_{k,i} - T \frac{d\phi_{k,i}}{dT} \right) \end{aligned}$$

⁶ The type of convection being considered here is movement of a species within a particular phase internal to the battery cell due to a pressure gradient. This is different from convective heat transfer, which occurs at the boundary of the cell (and will be considered later).

$$= -RT^2 \frac{d \ln(\lambda_{k,i})}{dT} + z_{k,i}F \left(\phi_{k,i} - T \frac{d\phi_{k,i}}{dT} \right).$$

Continuing with the gradient term that we need,

$$\nabla H_{k,i} = -R\nabla \left(T^2 \frac{d \ln(\lambda_{k,i})}{dT} \right) + z_{k,i}F\nabla \left(\phi_{k,i} - T \frac{d\phi_{k,i}}{dT} \right).$$

The first term is closely related to the enthalpy of mixing and is generally ignored in practice. We also ignore the temperature dependence of phase potential. So, we approximate

$$\nabla H_{k,i} = z_{k,i}F\nabla\phi_k.$$

Substituting this into the prior relationship,

$$\rho_k c_{P,k} \frac{\partial T_k}{\partial t} = \nabla \cdot (\lambda_k \nabla T_k) - \sum_{\text{species } i} z_{k,i}F \mathbf{j}_{k,i} \cdot \nabla\phi_k.$$

Noting that the current through phase k results from diffusion and migration of ionic species in the phase under the assumption of electroneutrality where

$$\mathbf{i}_k = \sum_{\text{species } i} z_{k,i}F \mathbf{j}_{k,i},$$

we can rewrite the relationship as

$$\rho_k c_{P,k} \frac{\partial T_k}{\partial t} = \nabla \cdot (\lambda_k \nabla T_k) - \mathbf{i}_k \cdot \nabla\phi_k.$$

We have now derived Eq. (7.1).

7.2.4 Boundary conditions

As we have seen before, any PDE must be accompanied by suitable boundary conditions in order to simulate its dynamics. Here, we are concerned about the boundary between the electrolyte and solid phases.

In a nontrivial derivation, it can be shown that:⁷

$$\lambda_e \nabla T_e \cdot \hat{\mathbf{n}}_e + \lambda_s \nabla T_s \cdot \hat{\mathbf{n}}_s = Fj\eta + Fj\Pi, \quad (7.4)$$

where $\hat{\mathbf{n}}_e$ is a unit normal vector pointing from the electrolyte into the solid at the boundary, and $\hat{\mathbf{n}}_s$ is a unit normal vector pointing from the solid into the electrolyte at the boundary. Subscript “ e ” refers to electrolyte and subscript “ s ” refers to solid. The terms j and η are the Butler–Volmer flux density and Butler–Volmer overpotential, as we have seen previously, and Π is the *Peltier coefficient*, which is equal to

$$\Pi_j = T \frac{\partial U_{\text{ocp},j}}{\partial T}.$$

⁷ Newman, J., “Thermoelectric Effects in Electrochemical Systems,” *Industrial & Engineering Chemical Research*, 24, 1995, pp. 3208–3216.

The *partial molar entropy* term $\partial U_{\text{ocp},j}/\partial T$ has to do with change in open-circuit potential as temperature varies. At different stages of lithiation, more or less order is produced by lithiation, so heat is either generated or sunk. Some representative curves for different materials are shown in Fig. 7.2.

The left-hand side of Eq. (7.4) is the sum of the heat flux into the solid and into the electrolyte. This heat must be generated at the solid–electrolyte interface. The $j\eta$ term models irreversible heat generation due to chemical reactions at the interface and is always positive. The $j\Pi$ term models reversible heat generation and can either be positive or negative. We will see how to evaluate these terms in the next section.

7.3 Continuum thermal model

Now that the microscale thermal model has been developed, our next goal is to use volume averaging over the phases to arrive at a continuum-scale model. Starting with Eq. (7.1), we use volume-averaging theorem 3 on the left-hand side of the equation. We assume that the solid–electrolyte phase boundary is not moving, and get

$$\rho_k c_{P,k} \overline{\left[\frac{\partial T_k}{\partial t} \right]} = \frac{1}{\varepsilon_k} \rho_k c_{P,k} \frac{\partial(\varepsilon_k \bar{T}_k)}{\partial t}.$$

We then use volume-averaging theorem 2 on the first term of the right-hand side of the equation:

$$\overline{\nabla \cdot (\lambda_k \nabla T_k)} = \frac{1}{\varepsilon_k} \left[\nabla \cdot (\varepsilon_k \overline{\lambda_k \nabla T_k}) + \frac{1}{V} \int_{A_{se}} (\lambda_k \nabla T_k) \cdot \hat{\mathbf{n}}_k \, dA \right].$$

We will model $\varepsilon_k \overline{\lambda_k \nabla T_k} \approx \lambda_{\text{eff},k} \nabla \bar{T}_k$, where $\lambda_{\text{eff},k} = \lambda_k \varepsilon_k^{\text{brug}}$, and will assume that the integrand is constant within the small volume V , giving

$$\begin{aligned} \overline{\nabla \cdot (\lambda_k \nabla T_k)} &\approx \frac{1}{\varepsilon_k} \left[\nabla \cdot (\lambda_{\text{eff},k} \nabla \bar{T}_k) + \frac{A_{se} (\lambda_k \nabla T_k) \cdot \hat{\mathbf{n}}_k}{V} \right] \\ &= \frac{1}{\varepsilon_k} [\nabla \cdot (\lambda_{\text{eff},k} \nabla \bar{T}_k) + a_s (\lambda_k \nabla T_k) \cdot \hat{\mathbf{n}}_k]. \end{aligned}$$

The second term on the right-hand side of Eq. (7.1) is more tricky, because we don't have a volume-averaging theorem to help with it. Gu and Wang handle it by "completing the square." Consider:

$$(\mathbf{i}_k - \bar{\mathbf{i}}_k) \cdot (\nabla(\phi_k - \bar{\phi}_k)) = [\mathbf{i}_k \cdot \nabla \phi_k] - [\mathbf{i}_k \cdot \nabla \bar{\phi}_k] - [\bar{\mathbf{i}}_k \cdot \nabla \phi_k] + [\bar{\mathbf{i}}_k \cdot \nabla \bar{\phi}_k].$$

This allows us to write the term of interest as

$$[\mathbf{i}_k \cdot \nabla \phi_k] = [\mathbf{i}_k \cdot \nabla \bar{\phi}_k] + [\bar{\mathbf{i}}_k \cdot \nabla(\phi_k - \bar{\phi}_k)] + (\mathbf{i}_k - \bar{\mathbf{i}}_k) \cdot (\nabla(\phi_k - \bar{\phi}_k)).$$

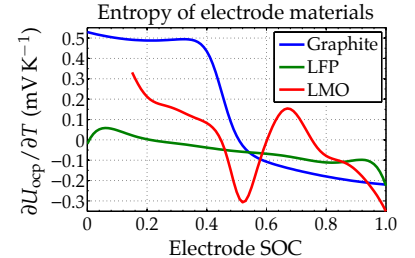


Figure 7.2: Partial molar entropy of some common electrode materials.

We take volume averages of this equation term by term. Because $\nabla\bar{\phi}_k$ is a constant, the volume average of the first term is

$$\begin{aligned}\overline{[\mathbf{i}_k \cdot \nabla \bar{\phi}_k]} &= \frac{1}{V_k} \int_{V_k} [\mathbf{i}_k \cdot \nabla \bar{\phi}_k] dV \\ &= \left(\frac{1}{V_k} \int_{V_k} \mathbf{i}_k dV \right) \cdot \nabla \bar{\phi}_k \\ &= \bar{\mathbf{i}}_k \cdot \nabla \bar{\phi}_k.\end{aligned}$$

For the second term, we use volume-averaging theorem 1:

$$\overline{[\bar{\mathbf{i}}_k \cdot \nabla (\phi_k - \bar{\phi}_k)]} = \underbrace{\bar{\mathbf{i}}_k \cdot \nabla (\bar{\phi}_k - \bar{\phi}_k)}_0 + \bar{\mathbf{i}}_k \cdot \frac{1}{V} \int_{A_{se}} (\phi_k - \bar{\phi}_k) \hat{\mathbf{n}}_k dA,$$

where Gu and Wang show that the integral term is small compared to the other terms, and so this entire expression is dropped.

For the third term, we use the definition of volume averaging:

$$\overline{(\mathbf{i}_k - \bar{\mathbf{i}}_k) \cdot (\nabla (\phi_k - \bar{\phi}_k))} = \frac{1}{V_k} \int_{V_k} (\mathbf{i}_k - \bar{\mathbf{i}}_k) \cdot (\nabla (\phi_k - \bar{\phi}_k)) dV.$$

Gu and Wang did not give any advice for how to evaluate this term but omitted it from their final result, assuming it was negligible.

Combining all results to date:

$$\frac{1}{\varepsilon_k} \rho_k c_{pk} \frac{\partial(\varepsilon_k \bar{T}_k)}{\partial t} = \frac{1}{\varepsilon_k} [\nabla \cdot (\lambda_{\text{eff},k} \nabla \bar{T}_k) + a_s (\lambda_k \nabla T_k) \cdot \hat{\mathbf{n}}_k] - \bar{\mathbf{i}}_k \cdot \nabla \bar{\phi}_k.$$

We now assume that local thermal equilibrium exists in the system, meaning that

$$\bar{T}_s = \bar{T}_e = T,$$

and sum the above equation over the solid and electrolyte phases, giving Eq. (7.2):

$$\frac{\partial(\rho c_P T)}{\partial t} = \nabla \cdot (\lambda \nabla T) + q$$

where

$$\begin{aligned}\rho c_P &= \sum_{k \in \{s,e\}} \varepsilon_k \rho_k c_{P,k} \\ \lambda &= \sum_{k \in \{s,e\}} \lambda_{\text{eff},k},\end{aligned}$$

and the *heat-generation* term q is given by

$$q = \sum_{\text{reaction } j} a_s F \bar{j} (\bar{\eta}_j + \bar{\Pi}_j) - \sum_{\text{species } k} \varepsilon_k \bar{\mathbf{i}}_k \cdot \nabla \bar{\phi}_k.$$

Recall from Eq. (4.18) that the volume-averaged current density through the electrolyte phase is

$$\varepsilon_e \bar{\mathbf{i}}_e = -\kappa_{\text{eff}} \nabla \bar{\phi}_e - \kappa_{D,\text{eff}} \nabla \ln \bar{c}_e.$$

Similarly, recall from Eq. (4.14) that the volume-averaged current density through the solid phase is

$$\varepsilon_s \bar{\mathbf{i}}_s = -\sigma_{\text{eff}} \nabla \bar{\phi}_s.$$

Summarizing (and removing overlines from volume-averaged quantities to clean up notation), heat-generation terms that can be considered in a model (with units W m^{-3}) include:

- Irreversible heat generation due to chemical reactions: $q_i = a_s F j_j \eta_j$ for each chemical reaction j that takes place at the interface,
- Reversible heat generation due to change in entropy: $q_r = a_s F j_j T \frac{\partial U_{\text{ocp},j}}{\partial T}$ for each chemical reaction j that takes place at the interface,
- Joule heating due to electrical potential gradient in the solid: $q_s = \sigma_{\text{eff}} (\nabla \phi_s \cdot \nabla \phi_s)$, and
- Joule heating due to electrochemical potential gradient in electrolyte: $q_e = \kappa_{\text{eff}} (\nabla \phi_e \cdot \nabla \phi_e) + \kappa_{D,\text{eff}} (\nabla \ln c_e \cdot \nabla \phi_e)$.

Sometimes, we also include heat generation due to contact resistance, $q_c = i_{\text{app}}^2 R_{\text{contact}}$.⁸ Heat generation within the current collectors themselves due to electrical resistance of the aluminum or copper sheets is small but can be included by simply lumping it in with the contact resistance.

⁸ Note the different units: q_c had units W m^{-2} . This heat-generation term applies only to current-collector to electrode contact region, and is specified per unit area rather than per unit volume.

7.3.1 Transfer of heat at boundaries

At the cell boundaries, there are three methods we consider by which heat can be conducted into or out of the cell: convection, conduction, and radiation. Conduction can be modeled as a fixed temperature specified at surface. In one dimension, we can write

$$T(x, t)|_{x=0} = T_0, \quad \text{and} \quad T(x, t)|_{x=L} = T_L.$$

It can also be modeled as a fixed heat flux at the surface:

$$-\lambda \frac{\partial T(x, t)}{\partial x} \Big|_{x=0} = \mathbf{q}_0, \quad \text{and} \quad \lambda \frac{\partial T(x, t)}{\partial x} \Big|_{x=L} = \mathbf{q}_L,$$

where the sign of the derivatives flip at $x = L$ to reflect the convention of heat flux into the surface as positive. A special case is the adiabatic (or insulated) surface for which

$$\frac{\partial T(x, t)}{\partial x} \Big|_{x=0} = 0 \quad \text{and/or} \quad \frac{\partial T(x, t)}{\partial x} \Big|_{x=L} = 0.$$

The second type of boundary condition is convection, in which the heat flux to/from the surface is proportional to the difference

between the surface temperature and an ambient fluid temperature, which we denote as T_∞

$$\begin{aligned}-\lambda \frac{\partial T(x, t)}{\partial x} \Big|_{x=0} &= h \left(T_\infty - T(0, t) \right) \\ \lambda \frac{\partial T(x, t)}{\partial x} \Big|_{x=L} &= h \left(T_\infty - T(L, t) \right),\end{aligned}$$

where h is the *heat-transfer* (or convection) *coefficient*. The value of h is a property of the flow conditions of the fluid in contact with the surface and not a property of the surface itself.

A third type of boundary condition is radiation, which can become significant when the surface temperatures are relatively high. Heat transfer to the surface via radiation can be expressed as

$$\begin{aligned}-\lambda^{\text{eff}} \frac{\partial T(x, t)}{\partial x} \Big|_{x=0} &= \epsilon \sigma \left(T_\infty^4 - T^4(0, t) \right) \\ \lambda^{\text{eff}} \frac{\partial T(x, t)}{\partial x} \Big|_{x=L} &= \epsilon \sigma \left(T_\infty^4 - T^4(L, t) \right),\end{aligned}$$

where ϵ [unitless] is the surface emissivity, and $\sigma = 5.670373 \times 10^{-8} \text{ W m}^{-2} \text{ K}^{-4}$ is the Stefan–Boltzmann constant.

The challenge created by this boundary condition is that temperature appears in the fourth power, which makes the problem nonlinear in T and eliminates most hopes of finding an analytical solution. One way to deal with this is to linearize the radiation rate law via a first-order Taylor-series expansion, giving

$$T_\infty^4 - T_s^4 \approx 4T_\infty^3(T_\infty - T_s),$$

where T_s represents the temperature of either surface. The quantity $4\epsilon\sigma T_\infty^3$ can now be viewed as a linearized radiation heat transfer coefficient, denoted h_{rad} .

7.4 Parameter temperature variation

Many parameters in the cell model we have developed so far have values that are temperature dependent. This is usually modeled by the (empirical) Arrhenius relationship, which relates some property of the cell at present temperature T , $\Phi(T)$, to that property at a *reference temperature* T_{ref} , Φ_{ref} via an exponential function with *activation energy* E_0 :

$$\Phi(T) = \Phi_{\text{ref}} \exp \left[\frac{E_0}{R} \left(\frac{1}{T_{\text{ref}}} - \frac{1}{T} \right) \right]. \quad (7.5)$$

7.5 Reduced-order model

To create a reduced-order thermal model, we must be able to do three things:⁹

1. Accurately approximate the four heat-generation terms listed at the end of Sect. 7.3, resulting in a total heat-generation term q .
2. Use the predicted value of q in an approximation to Eq. (7.2) to model change in cell average temperature.
3. Blend models created at different temperature setpoints to approximate the true model having parameters determined by Eq. (7.5).

These are described in the following sections.

7.6 Gradient transfer functions

Our first approach to finding a reduced-order model of the heat-generation terms might be to attempt to find transfer functions between the applied current and the desired quantities, so that the DRA could be used to generate a state-space model. However, there is a fundamental problem with this approach: all four heat-generation terms are nonlinear, so transfer functions don't exist. Further, they are products of terms which themselves are functions of $i_{\text{app}}(t)$, and so are essentially functions of $i_{\text{app}}^2(t)$, and truncating a Taylor-series expansion will not give linearized models that are very helpful.

An approach that we find does work well is to individually compute the quantities that are ultimately multiplied together to predict heat generation. We already know how to compute reduced-order estimates of $j(z, t)$ and $\eta(z, t)$. We further need to be able to compute $\nabla \phi_s(z, t)$, $\nabla \ln c_e(x, t)$, and $\nabla \phi_e(x, t)$. We can find these terms via a transfer-function approach, as we will show in the next subsections.

7.6.1 Gradient of $\phi_s(z, t)$

Recall from Chap. 6 that we defined $\tilde{\phi}_s(z, t) = \phi_s(z, t) - \phi_s(0, t)$. Then the gradient with respect to the spatial coordinate z can be written as

$$\begin{aligned}\nabla_z \tilde{\phi}_s(z, t) &= \nabla_z \phi_s(z, t) - \nabla_z \phi_s(0, t) \\ \nabla_z \phi_s(z, t) &= \nabla_z \tilde{\phi}_s(z, t),\end{aligned}$$

since $\phi_s(0, t)$ is not a function of a spatial dimension. Therefore, if we can find a transfer function for $\nabla_z \tilde{\phi}_s(z, t)$, we can compute the gradient we need for computing Joule heat generation in the solid.

⁹Special thanks to Matt Aldrich for helping to develop and verify the reduced-order model equations and for providing data for the examples.

Recall also from Chap. 6 the transfer function we developed for $\tilde{\Phi}_s(z, s)$ in the negative electrode:

$$\frac{\tilde{\Phi}_s^{\text{neg}}(z, s)}{I_{\text{app}}(s)} = -\frac{L^{\text{neg}} \kappa_{\text{eff}}^{\text{neg}} (\cosh(v^{\text{neg}}(s)) - \cosh((z-1)v^{\text{neg}}(s)))}{A \sigma_{\text{eff}}^{\text{neg}} (\kappa_{\text{eff}}^{\text{neg}} + \sigma_{\text{eff}}^{\text{neg}}) v^{\text{neg}}(s) \sinh(v^{\text{neg}}(s))} - \frac{L^{\text{neg}} \sigma_{\text{eff}}^{\text{neg}} (1 - \cosh(zv^{\text{neg}}(s)) + zv^{\text{neg}}(s) \sinh(v^{\text{neg}}(s)))}{A \sigma_{\text{eff}}^{\text{neg}} (\kappa_{\text{eff}}^{\text{neg}} + \sigma_{\text{eff}}^{\text{neg}}) v^{\text{neg}}(s) \sinh(v^{\text{neg}}(s))}.$$

Taking the derivative of this function with respect to z gives

$$\frac{\nabla_z \tilde{\Phi}_s^{\text{neg}}(z, s)}{I_{\text{app}}(s)} = \frac{L^{\text{neg}} \sigma_{\text{eff}}^{\text{neg}} (\sinh(zv^{\text{neg}}(s)) - \sinh(v^{\text{neg}}(s)))}{A \sigma_{\text{eff}}^{\text{neg}} (\kappa_{\text{eff}}^{\text{neg}} + \sigma_{\text{eff}}^{\text{neg}}) \sinh(v^{\text{neg}}(s))} + \frac{L^{\text{neg}} \kappa_{\text{eff}}^{\text{neg}} \sinh((z-1)v^{\text{neg}}(s))}{A \sigma_{\text{eff}}^{\text{neg}} (\kappa_{\text{eff}}^{\text{neg}} + \sigma_{\text{eff}}^{\text{neg}}) \sinh(v^{\text{neg}}(s))}.$$

The gradient with respect to x can be found as

$$\begin{aligned} \frac{\nabla_x \tilde{\Phi}_s^{\text{neg}}(z, s)}{I_{\text{app}}(s)} \Big|_{\frac{x}{L^{\text{neg}}}} &= \left(\frac{\partial z}{\partial x} \right) \left(\frac{\nabla_z \tilde{\Phi}_s^{\text{neg}}(x/L^{\text{neg}}, s)}{I_{\text{app}}(s)} \right) \\ &= \frac{1}{L^{\text{neg}}} \left(\frac{\nabla_z \tilde{\Phi}_s^{\text{neg}}(x/L^{\text{neg}}, s)}{I_{\text{app}}(s)} \right) \\ &= \left[\frac{\sigma_{\text{eff}}^{\text{neg}} (\sinh(zv^{\text{neg}}(s)) - \sinh(v^{\text{neg}}(s)))}{A \sigma_{\text{eff}}^{\text{neg}} (\kappa_{\text{eff}}^{\text{neg}} + \sigma_{\text{eff}}^{\text{neg}}) \sinh(v^{\text{neg}}(s))} \right. \\ &\quad \left. + \frac{\kappa_{\text{eff}}^{\text{neg}} \sinh((z-1)v^{\text{neg}}(s))}{A \sigma_{\text{eff}}^{\text{neg}} (\kappa_{\text{eff}}^{\text{neg}} + \sigma_{\text{eff}}^{\text{neg}}) \sinh(v^{\text{neg}}(s))} \right] \Big|_{\frac{x}{L^{\text{neg}}}}. \end{aligned}$$

In the positive electrode, the transfer function for $\tilde{\Phi}_s(z, s)$ must be multiplied by -1 , and the gradient with respect to x must also be multiplied by -1 , so the net effect is nil. The same basic transfer function is used for both electrodes, with the substitution of constants appropriate for each electrode, and with $z = (L^{\text{tot}} - x)/L^{\text{pos}}$ substituted in the positive electrode.

7.6.2 Gradient of $\ln c_e(x, t)$

We need to be able to compute $\nabla \ln c_e(x, t)$ to find q_e . Note that

$$\nabla \ln c_e(x, t) = \frac{\nabla c_e(x, t)}{c_e(x, t)},$$

and as we already compute $c_e(x, t)$ as an output of the ROM, we need only to learn how to compute $\nabla c_e(x, t)$.

Recall that $c_e(x, t) = \tilde{c}_e(x, t) + c_{e,0}$, so $\nabla c_e(x, t) = \nabla \tilde{c}_e(x, t)$. We have already derived a transfer function for $\tilde{c}_e(x, t)$, which we wrote as

$$\frac{\tilde{C}_e(x, s)}{I_{\text{app}}(s)} = \sum_{n=1}^M \frac{\tilde{C}_{e,n}(s)}{I_{\text{app}}(s)} \Psi(x; \lambda_n).$$

As only the eigenfunctions in this summation are a function of x , the gradient can be found as

$$\frac{\nabla \tilde{C}_e(x, s)}{I_{\text{app}}(s)} = \sum_{n=1}^M \frac{\tilde{C}_{e,n}(s)}{I_{\text{app}}(s)} (\nabla \Psi(x; \lambda_n)).$$

All of the hard work computing $\tilde{C}_{e,n}(s)$ is reused; the only change is that we must multiply these terms by the gradients of the original eigenfunctions inside the summation, not by the eigenfunctions themselves.

Recall that the eigenfunctions were defined by Eq. (6.33):

$$\Psi(x; \lambda) = \begin{cases} \Psi^{\text{neg}}(x; \lambda), & 0 \leq x < L^{\text{neg}}; \\ \Psi^{\text{sep}}(x; \lambda), & L^{\text{neg}} \leq x < L^{\text{neg}} + L^{\text{sep}}; \\ \Psi^{\text{pos}}(x; \lambda), & L^{\text{neg}} + L^{\text{sep}} \leq x \leq L^{\text{tot}}; \end{cases}$$

where

$$\begin{aligned} \Psi^{\text{neg}}(x; \lambda) &= k_1 \cos \left(\sqrt{\lambda \varepsilon_e^{\text{neg}} / D_{e,\text{eff}}^{\text{neg}}} x \right) \\ \Psi^{\text{sep}}(x; \lambda) &= k_3 \cos \left(\sqrt{\lambda \varepsilon_e^{\text{sep}} / D_{e,\text{eff}}^{\text{sep}}} x \right) + k_4 \sin \left(\sqrt{\lambda \varepsilon_e^{\text{sep}} / D_{e,\text{eff}}^{\text{sep}}} x \right) \\ \Psi^{\text{pos}}(x; \lambda) &= k_5 \cos \left(\sqrt{\lambda \varepsilon_e^{\text{pos}} / D_{e,\text{eff}}^{\text{pos}}} x \right) + k_6 \sin \left(\sqrt{\lambda \varepsilon_e^{\text{pos}} / D_{e,\text{eff}}^{\text{pos}}} x \right). \end{aligned}$$

Then,

$$\begin{aligned} \nabla \Psi^{\text{neg}}(x; \lambda) &= -k_1 \sqrt{\frac{\lambda \varepsilon_e^{\text{neg}}}{D_{e,\text{eff}}^{\text{neg}}}} \sin \left(\sqrt{\frac{\lambda \varepsilon_e^{\text{neg}}}{D_{e,\text{eff}}^{\text{neg}}}} x \right) \\ \nabla \Psi^{\text{sep}}(x; \lambda) &= k_4 \sqrt{\frac{\lambda \varepsilon_e^{\text{sep}}}{D_{e,\text{eff}}^{\text{sep}}}} \cos \left(\sqrt{\frac{\lambda \varepsilon_e^{\text{sep}}}{D_{e,\text{eff}}^{\text{sep}}}} x \right) - k_3 \sqrt{\frac{\lambda \varepsilon_e^{\text{sep}}}{D_{e,\text{eff}}^{\text{sep}}}} \sin \left(\sqrt{\frac{\lambda \varepsilon_e^{\text{sep}}}{D_{e,\text{eff}}^{\text{sep}}}} x \right) \\ \nabla \Psi^{\text{pos}}(x; \lambda) &= k_6 \sqrt{\frac{\lambda \varepsilon_e^{\text{pos}}}{D_{e,\text{eff}}^{\text{pos}}}} \cos \left(\sqrt{\frac{\lambda \varepsilon_e^{\text{pos}}}{D_{e,\text{eff}}^{\text{pos}}}} x \right) - k_5 \sqrt{\frac{\lambda \varepsilon_e^{\text{pos}}}{D_{e,\text{eff}}^{\text{pos}}}} \sin \left(\sqrt{\frac{\lambda \varepsilon_e^{\text{pos}}}{D_{e,\text{eff}}^{\text{pos}}}} x \right). \end{aligned}$$

7.6.3 Gradient of $\phi_e(x, t)$

To compute the gradient of $\phi_e(x, t)$, recall that we have previously defined $\tilde{\phi}_e(x, t) = \phi_e(x, t) - \phi_e(0, t)$. Therefore, $\nabla \tilde{\phi}_e(x, t) = \nabla \phi_e(x, t) - \nabla \phi_e(0, t)$, or

$$\nabla \phi_e(x, t) = \nabla \tilde{\phi}_e(x, t).$$

Recall also that we wrote $\tilde{\phi}_e(x, t)$ as having two parts:

$$\tilde{\phi}_e(x, t) = [\tilde{\phi}_e(x, t)]_1 + [\tilde{\phi}_e(x, t)]_2.$$

The first part, $[\tilde{\phi}_e(x, t)]_1$, can be determined via transfer functions; the second part, $[\tilde{\phi}_e(x, t)]_2$, can be determined via known $c_e(x, t)$.

Similarly, the gradient of the first part can also be found via transfer functions, and the gradient of the second part will furthermore require $c_e(x, t)$.

Let's continue to look at the first part. In the negative electrode, we had Eq. (6.48), which was

$$\begin{aligned} \frac{[\tilde{\Phi}_e(x, s)]_1}{I_{app}(s)} = & -\frac{L^{\text{neg}} \sigma_{\text{eff}}^{\text{neg}} (\cosh(\frac{x}{L^{\text{neg}}} \nu^{\text{neg}}(s)) - 1)}{A \kappa_{\text{eff}}^{\text{neg}} (\kappa_{\text{eff}}^{\text{neg}} + \sigma_{\text{eff}}^{\text{neg}}) \nu^{\text{neg}}(s) \sinh(\nu^{\text{neg}}(s))} - \frac{x}{A (\kappa_{\text{eff}}^{\text{neg}} + \sigma_{\text{eff}}^{\text{neg}})} \\ & - \frac{L^{\text{neg}} \kappa_{\text{eff}}^{\text{neg}} (\cosh(\frac{(L^{\text{neg}} - x)}{L^{\text{neg}}} \nu^{\text{neg}}(s)) - \cosh(\nu^{\text{neg}}(s)))}{A \kappa_{\text{eff}}^{\text{neg}} (\kappa_{\text{eff}}^{\text{neg}} + \sigma_{\text{eff}}^{\text{neg}}) \nu^{\text{neg}}(s) \sinh(\nu^{\text{neg}}(s))}. \end{aligned}$$

The corresponding gradient, computed with the aid of Mathematica, is

$$\begin{aligned} \frac{\nabla [\tilde{\Phi}_e(x, s)]_1}{I_{app}(s)} = & \frac{\kappa_{\text{eff}}^{\text{neg}} \left(\sinh\left(\frac{(L^{\text{neg}} - x) \nu^{\text{neg}}(s)}{L^{\text{neg}}}\right) - \sinh(\nu^{\text{neg}}(s)) \right)}{A \kappa_{\text{eff}}^{\text{neg}} (\kappa_{\text{eff}}^{\text{neg}} + \sigma_{\text{eff}}^{\text{neg}}) \sinh(\nu^{\text{neg}}(s))} \\ & - \frac{\sigma_{\text{eff}}^{\text{neg}} \sinh\left(\frac{x \nu^{\text{neg}}(s)}{L^{\text{neg}}}\right)}{A \kappa_{\text{eff}}^{\text{neg}} (\kappa_{\text{eff}}^{\text{neg}} + \sigma_{\text{eff}}^{\text{neg}}) \sinh(\nu^{\text{neg}}(s))}. \end{aligned}$$

In the separator, we had Eq. (6.49), which was

$$\begin{aligned} \frac{[\tilde{\Phi}_e(x, s)]_1}{I_{app}(s)} = & -\frac{L^{\text{neg}} \left((\sigma_{\text{eff}}^{\text{neg}} - \kappa_{\text{eff}}^{\text{neg}}) \tanh\left(\frac{\nu^{\text{neg}}(s)}{2}\right) \right)}{A \kappa_{\text{eff}}^{\text{neg}} (\kappa_{\text{eff}}^{\text{neg}} + \sigma_{\text{eff}}^{\text{neg}}) \nu^{\text{neg}}(s)} \\ & - \frac{L_{\text{neg}}}{A (\kappa_{\text{eff}}^{\text{neg}} + \sigma_{\text{eff}}^{\text{neg}})} - \frac{x - L^{\text{neg}}}{A \kappa_{\text{eff}}^{\text{sep}}}. \end{aligned}$$

The corresponding gradient is

$$\frac{\nabla [\tilde{\Phi}_e(x, s)]_1}{I_{app}(s)} = -\frac{1}{A \kappa_{\text{eff}}^{\text{sep}}}.$$

In the positive electrode, we had Eq. (6.50), which was

$$\begin{aligned} \frac{[\tilde{\Phi}_e(x, s)]_1}{I_{app}(s)} = & -\frac{L^{\text{neg}} \left((\sigma_{\text{eff}}^{\text{neg}} - \kappa_{\text{eff}}^{\text{neg}}) \tanh\left(\frac{\nu^{\text{neg}}(s)}{2}\right) \right)}{A \kappa_{\text{eff}}^{\text{neg}} (\kappa_{\text{eff}}^{\text{neg}} + \sigma_{\text{eff}}^{\text{neg}}) \nu^{\text{neg}}(s)} - \frac{L_{\text{neg}}}{A (\kappa_{\text{eff}}^{\text{neg}} + \sigma_{\text{eff}}^{\text{neg}})} \\ & - \frac{L_{\text{sep}}}{A \kappa_{\text{eff}}^{\text{sep}}} - \frac{L^{\text{pos}} \left(1 - \cosh\left(\frac{(L^{\text{neg}} + L^{\text{sep}} - x)}{L^{\text{pos}}} \nu^{\text{pos}}(s)\right) \right)}{A (\kappa_{\text{eff}}^{\text{pos}} + \sigma_{\text{eff}}^{\text{pos}}) \sinh(\nu^{\text{pos}}(s)) \nu^{\text{pos}}(s)} \\ & - \frac{L^{\text{pos}} \sigma_{\text{eff}}^{\text{pos}} \left(\cosh(\nu^{\text{pos}}(s)) - \cosh\left(\frac{(L^{\text{tot}} - x)}{L^{\text{pos}}} \nu^{\text{pos}}(s)\right) \right)}{A \kappa_{\text{eff}}^{\text{pos}} (\kappa_{\text{eff}}^{\text{pos}} + \sigma_{\text{eff}}^{\text{pos}}) \sinh(\nu^{\text{pos}}(s)) \nu^{\text{pos}}(s)} \\ & - \frac{(x - L^{\text{neg}} - L_{\text{sep}})}{A (\kappa_{\text{eff}}^{\text{pos}} + \sigma_{\text{eff}}^{\text{pos}})}. \end{aligned}$$

The corresponding gradient is

$$\frac{\nabla [\tilde{\Phi}_e(x, s)]_1}{I_{app}(s)} = \frac{\kappa_{\text{eff}}^{\text{pos}} \left(\sinh\left(\frac{\nu^{\text{pos}}(s) (L^{\text{pos}} - L^{\text{tot}} + x)}{L^{\text{pos}}}\right) - \sinh(\nu^{\text{pos}}(s)) \right)}{A \kappa_{\text{eff}}^{\text{pos}} (\kappa_{\text{eff}}^{\text{pos}} + \sigma_{\text{eff}}^{\text{pos}}) \sinh(\nu^{\text{pos}}(s))}$$

$$-\frac{\sigma_{\text{eff}}^{\text{pos}} \sinh\left(\frac{(L^{\text{tot}}-x)\nu^{\text{pos}}(s)}{L^{\text{pos}}}\right)}{Ak_{\text{eff}}^{\text{pos}}(\kappa_{\text{eff}}^{\text{pos}} + \sigma_{\text{eff}}^{\text{pos}}) \sinh(\nu^{\text{pos}}(s))}.$$

Now we focus on the second term of $\tilde{\phi}_e(x, t)$:

$$\begin{aligned} [\tilde{\phi}_e(x, t)]_2 &= \frac{2RT(1-t_+^0)}{F} [\ln c_e(x, t) - \ln c_e(0, t)] \\ \nabla [\tilde{\phi}_e(x, t)]_2 &= \frac{2RT(1-t_+^0)}{F} \left[\frac{\nabla c_e(x, t)}{c_e(x, t)} - \frac{\nabla c_e(0, t)}{c_e(0, t)} \right] \\ &= \frac{2RT(1-t_+^0)}{F} \frac{\nabla c_e(x, t)}{c_e(x, t)}. \end{aligned}$$

As we already compute $c_e(x, t)$ as an output of the ROM and have seen how to compute $\nabla c_e(x, t)$, we have all the terms necessary to compute $\nabla[\tilde{\phi}_e(x, t)]_2$, and therefore we can compute $\nabla\phi_e(x, t)$.

7.7 Heat-generation terms

We are now ready to investigate different reduced-order approximations to the heat-generation terms of Sect. 7.3. Depending on the accuracy requirements of an application, we can take different approaches, with different computational demands. So, to illustrate the tradeoffs, we will use several examples throughout this section to compare the results predicted by the different approaches. The different reduced-order models are labeled ROM1 through ROM4, and the equations used as their basis are listed in Table 7.1 for reference.

Heat-gen. term:	\bar{q}_r	\bar{q}_i	\bar{q}_s	\bar{q}_e
ROM1	Eq. (7.6)	Eq. (7.8)	Eq. (7.11)	Eq. (7.13)
ROM2	Eq. (7.6)	Eq. (7.9)	Eq. (7.11)	Eq. (7.14)
ROM3	Eq. (7.6)	Eq. (7.10)	Eq. (7.12)	Eq. (7.15)
ROM4	Eq. (7.7)	Eq. (7.10)	Eq. (7.12)	Eq. (7.15)

We use the same basic cell as was used in the examples in Chap. 6, where the cell parameters are listed in Table 6.1. To compute the heat-generation terms, we must also know the partial molar entropy relationships. For the negative electrode, we use the graphite curve in Fig. 7.2, and for the positive electrode, we use the LMO curve. These relationships are¹⁰

$$\begin{aligned} \frac{\partial U_{\text{ocp}}^{\text{neg}}(\theta)}{\partial \theta} &= \frac{344.1347148 \exp(-32.9633287\theta + 8.316711484)}{1 + 749.0756003 \exp(-34.79099646\theta + 8.887143624)} \\ &\quad - 0.8520278805\theta + 0.36229929\theta^2 + 0.2698001697. \end{aligned}$$

Table 7.1: Equations defining the different heat-generation reduced-order models.

¹⁰ From: Srinivasan, V., and Wang, C.Y., "Analysis of Electrochemical and Thermal Behavior of Li-Ion Cells," *Journal of The Electrochemical Society*, 150(1), 2003, pp. A98–A106.

$$\begin{aligned}
\frac{\partial U_{\text{ocp}}^{\text{pos}}(\theta)}{\partial \theta} = & 4.31274309 \exp(0.571536523\theta) - 4.14532933 \\
& + 1.281681122 \sin(-4.9916739\theta) \\
& - 0.090453431 \sin(-20.9669665\theta + 12.5788250) \\
& - 0.0313472974 \sin(31.7663338\theta - 22.4295664) \\
& + 8.147113434\theta - 26.064581\theta^2 + 12.7660158\theta^3 \\
& - 0.184274863 \exp\left(-\left(\frac{\theta - 0.5169435168}{0.04628266783}\right)^2\right).
\end{aligned}$$

The three examples that we consider are (1) a simple discharge pulse followed by a charge pulse, around 50 % state of charge; (2) a full 1C discharge starting at 100 %; and (3) a charge-neutral UDDS profile, around 60 % (the same profile used in Chap. 6). These profiles are drawn in Fig. 7.3.

7.7.1 Reversible heat-generation term $q_r[z, k]$

We first consider the reversible heat-generation term, specialized to a single chemical reaction occurring at the solid–electrolyte boundary:

$$q_r[z, k] = a_s F T j[z, k] \frac{\partial U_{\text{ocp}}(c_{s,e}[z, k])}{\partial T},$$

assuming that temperature is relatively constant across an electrode. From Chap. 6, we have already found transfer functions for $j[z, k]$ and $c_{s,e}[z, k]$. We can approximate the average reversible heat generation across the electrode as

$$\begin{aligned}
\bar{q}_r[k] &= \int_0^1 a_s F T j[z, k] \frac{\partial U_{\text{ocp}}(c_{s,e}[z, k])}{\partial T} dz \\
&\approx a_s F T \sum_i j[z_i, k] \frac{\partial U_{\text{ocp}}(c_{s,e}[z_i, k])}{\partial T} \Delta z_i.
\end{aligned} \tag{7.6}$$

That is, $j[z, k]$ and $c_{s,e}[z, k]$ are evaluated at a number of z locations across the electrode, the entropy function is evaluated at each $c_{s,e}$ point, and an approximation is made to the integral to compute the average heat generation using a rectangular integration summation. For an even better approximation, a trapezoidal integration can be performed, which amounts to using different weighting constants for every z_i point. In the simulations that follow, we will use the set of $z_i \in \{0, 0.25, 0.5, 0.75, 1\}$ with trapezoidal integration in the results labeled ROM1 through ROM3.

Computing $j[z, k]$ and $c_{s,e}[z, k]$ at multiple z locations incurs a fair amount of real-time computation in the $Cx_k + Di_{\text{app}}$ step. It is possible to make a cruder approximation to \bar{q}_r and reduce the amount of computation required. That is, if we assume $c_{s,e} \approx c_{\text{avg}}$

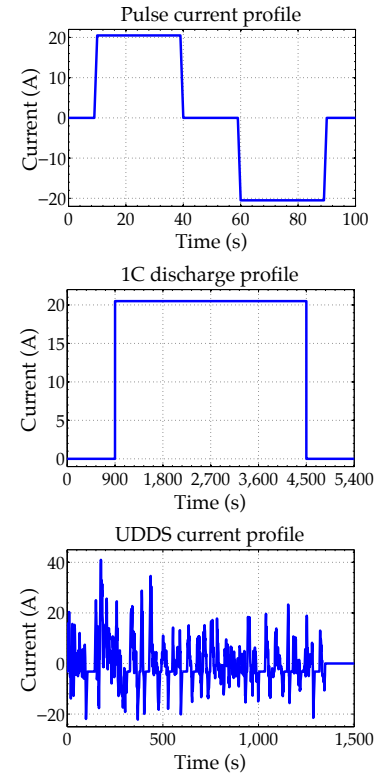


Figure 7.3: Cell input current profiles used to illustrate thermal model results.

across the electrode, then we have

$$\begin{aligned}\bar{q}_r &= \int_0^1 a_s F T j[z, k] \frac{\partial U_{\text{ocp}}(c_{\text{avg}}[k])}{\partial T} dz \\ &= a_s F T \frac{\partial U_{\text{ocp}}(c_{\text{avg}}[k])}{\partial T} \int_0^1 j[z, k] dz \\ &= \frac{i_{\text{app}}[k] T}{A} \frac{\partial U_{\text{ocp}}(c_{\text{avg}}[k])}{\partial T}.\end{aligned}\quad (7.7)$$

In the simulations that follow, we will use this method in results labeled ROM4.

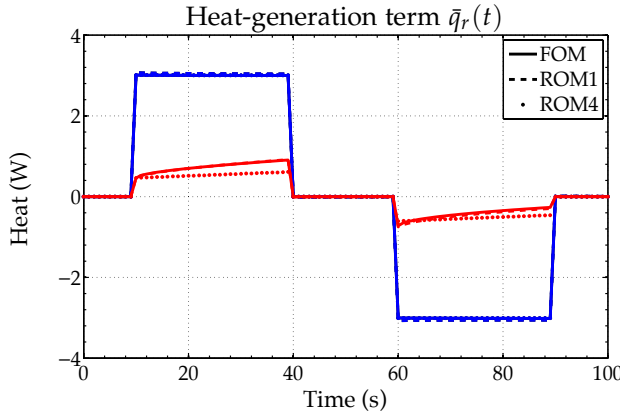


Figure 7.4: Reversible heat generated via pulses: blue lines are for negative electrode; red lines are for positive electrode.

Fig. 7.4 shows sample results when the cell input current is the sequence of discharge and charge pulses. The solid line shows the full-order model result, and the decorated lines show different reduced-order model results. In this case, both ROM1 and ROM4 gave similar predictions that were quite close to the truth, primarily because the simulation was not long enough for significant gradients in the solid surface concentration to arise. Had they done so (as we shall see later), we would find ROM1 to be noticeably better than ROM4. The choice of which ROM to use depends on the application.

7.7.2 Irreversible heat-generation term $q_i[z, k]$

We next consider the irreversible heat-generation term, specialized to a single chemical reaction occurring at the solid–electrolyte boundary,

$$q_i[z, k] = a_s F j[z, k] \eta[z, k].$$

From Chap. 6, we have already found a transfer function for $j[z, k]$ and have seen how to compute $\eta[z, k]$ from a nonlinear relationship. We can approximate the average irreversible heat generation across the electrode as

$$\bar{q}_i[k] = \int_0^1 a_s F T j[z, k] \eta[z, k] dz$$

$$\approx a_s F T \sum_i j[z_i, k] \eta[z_i, k] \Delta z_i. \quad (7.8)$$

As before, we can also use a trapezoidal integration approximation. In the simulations that follow, we will use the set of $z_i \in \{0, 0.25, 0.5, 0.75, 1\}$ with trapezoidal integration in the results labeled ROM1.

For a reduction in computational complexity that incurs only a modest loss of accuracy, we can linearize the $\eta(z, t)$ term and recall $\eta[z, k] \approx R_{ct} j[z, k]$. This allows us to write

$$\bar{q}_i[k] \approx a_s F T R_{ct} \sum_i j^2[z_i, k] \Delta z_i.$$

The advantage of this form is that it is the product of two terms found via fully linear transfer functions. We will see this form in the other heat-generation terms as well, so we take some time to examine it in general.

Consider a generic heat-generation term, in discrete time

$$q[z, k] = y_1[z, k] y_2[z, k]$$

where $y_1[z, k]$ and $y_2[z, k]$ are both purely linear terms computed as output from the state-space reduced-order model (that is, there are no nonlinear corrections applied to the terms). Then,

$$\begin{aligned} \bar{q}[k] &= \int_0^1 y_1[z, k] y_2[z, k] dz \\ &= \int_0^1 [\mathbf{C}_1 \mathbf{x}[k] + \mathbf{D}_1 u[k]] [\mathbf{C}_2 \mathbf{x}[k] + \mathbf{D}_2 u[k]] dz. \end{aligned}$$

The terms written inside square brackets are scalars and so are equal to their own transpose. This allows us to write

$$\begin{aligned} \bar{q}[k] &= \int_0^1 \left[\mathbf{x}^T[k] \mathbf{C}_1^T + u^T[k] \mathbf{D}_1^T \right] [\mathbf{C}_2 \mathbf{x}[k] + \mathbf{D}_2 u[k]] dz \\ &= \mathbf{x}^T[k] \underbrace{\left\{ \int_0^1 \mathbf{C}_1^T \mathbf{C}_2 dz \right\}}_{\{\mathbf{CC}\}} \mathbf{x}[k] + u^T[k] \underbrace{\left\{ \int_0^1 \mathbf{D}_1^T \mathbf{D}_2 dz \right\}}_{\{\mathbf{DD}\}} u[k] \\ &\quad + \mathbf{x}^T[k] \underbrace{\left\{ \int_0^1 \mathbf{C}_1^T \mathbf{D}_2 + \mathbf{C}_2^T \mathbf{D}_1 dz \right\}}_{\{\mathbf{CD}\}} u[k] \\ &= \mathbf{x}^T[k] \{\mathbf{CC}\} \mathbf{x}[k] + \mathbf{x}^T[k] \{\mathbf{CD}\} u[k] + u^T[k] \{\mathbf{DD}\} u[k] \end{aligned}$$

The \mathbf{C} and \mathbf{D} matrices are produced by the DRA from the appropriate transfer functions, and the integrals are approximated from these matrices using a one-time computation, resulting in constant precomputed $\{\mathbf{CC}\}$, $\{\mathbf{CD}\}$, and $\{\mathbf{DD}\}$ matrices.

Expressing the heat generation in this form allows us to consider a number of different approximations to the original result, at different levels of complexity. The integral involving $C_1^T C_2$ requires the most computations, resulting in an $n \times n$ output at every z value. The integral involving $C_i^T D_j$ has fewer computations, resulting in an $n \times 1$ vector for every z value. The integral involving $D_1^T D_2$ has the fewest computations, resulting in a 1×1 scalar at every z value. If we are able to drop terms from the approximation without losing too much fidelity, we can reduce the real-time computation load of estimating a heat-generation term.

In the following simulations, results labeled ROM2 use the full expression

$$\bar{q}_i[k] = \mathbf{x}^T[k] \{CC\} \mathbf{x}[k] + \mathbf{x}^T[k] \{CD\} i_{\text{app}}[k] + \{DD\} i_{\text{app}}^2[k]. \quad (7.9)$$

Results labeled ROM3 and ROM4 use a simpler computation

$$\bar{q}_i[k] = \{DD\} i_{\text{app}}^2[k]. \quad (7.10)$$

Note that this corresponds to an “ $i^2 \times R$ ” type of heat generation we would expect from a lumped resistance. The other scenarios give better approximations to the heat generation within an electrode, which is a distributed system.

In the ROM2 through ROM4 results that follow for the irreversible heat-generation term, we selected $y_1[z, k] = y_2[z, k] = j[z, k]$ and computed

$$\bar{q}_i[k] \approx a_s FTR_{\text{ct}} \int_0^1 y_1[z, k] y_2[z, k] \, dz$$

using the three different approaches above.

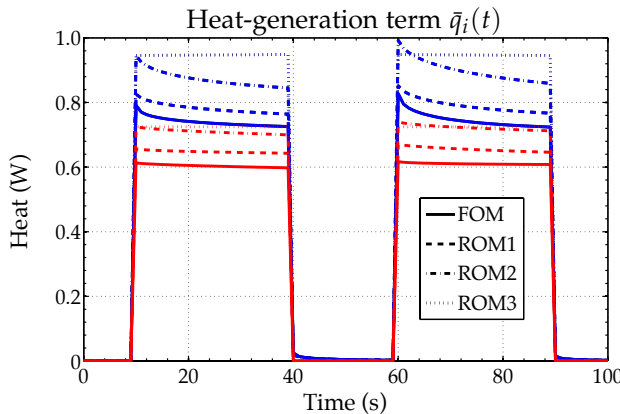


Figure 7.5: Irreversible heat generated via pulses: blue lines are for negative electrode; red lines are for positive electrode.

Fig. 7.5 shows sample results when the cell input current is the sequence of discharge and charge pulses. As before, the solid line

shows the full-order model result, and the decorated lines show different reduced-order model results. In this case, ROM1 is significantly better than ROM2, which itself is significantly better than ROM3. The fidelity of predictions required by the application will dictate which ROM to use.

7.7.3 Joule heating in solid term $q_s[z, k]$

We now consider the heat-generation term corresponding to Joule heating in the solid, expressed as $q_s = \sigma_{\text{eff}}(\nabla\phi_s \cdot \nabla\phi_s)$. We have already seen that we can express $\nabla\phi_s$ as a purely linear transfer function, so we can use the same approaches as we did with irreversible heat generation.

In the simulations that follow, we select $y_1[z, k] = y_2[z, k] = \sqrt{\sigma_{\text{eff}}}\nabla\phi_s[z, k]$ and compute

$$\bar{q}_s[k] = \int_0^1 y_1[z, k] y_2[z, k] \, dz$$

where results labeled ROM1 or ROM2 use the full expression

$$\bar{q}_s[k] = \mathbf{x}^T[k] \{CC\} \mathbf{x}[k] + \mathbf{x}^T[k] \{CD\} i_{\text{app}}[k] + \{DD\} i_{\text{app}}^2[k]. \quad (7.11)$$

Results labeled ROM3 and ROM4 use a simpler computation:

$$\bar{q}_s[k] = \{DD\} i_{\text{app}}^2[k]. \quad (7.12)$$

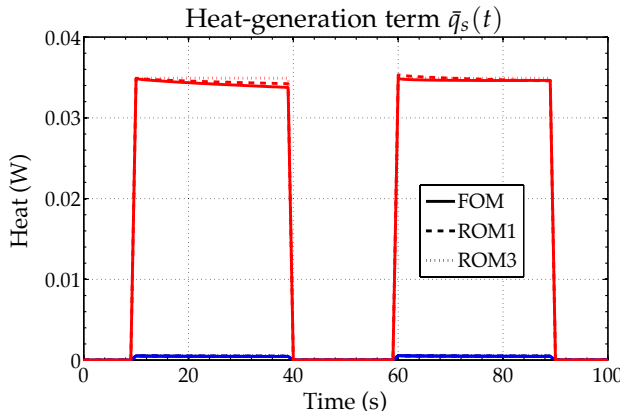


Figure 7.6: Heat generated via Joule heating in solid from pulses: blue lines are for negative electrode; red lines are for positive electrode.

Fig. 7.6 shows sample results when the cell input current is the sequence of discharge and charge pulses. The solid line shows the full-order model result, and the decorated lines show different reduced-order model results. In this case, all reduced-order models produce nearly indistinguishable results. Further, a close examination of the vertical scale shows that the $\bar{q}_s[k]$ term is by far the smallest heat-generation term, so even large relative errors are not significant when

total heat generation is computed. Therefore, ROM3 is probably sufficient for most applications.

7.7.4 Joule heating in electrolyte term $q_e[x, k]$

Finally, we consider the heat-generation term corresponding to Joule heating in the electrolyte. We take a few steps to convert it into a combination of signals at our disposal:

$$\begin{aligned}
q_e &= \kappa_{\text{eff}}(\nabla\phi_e \cdot \nabla\phi_e) + \kappa_{D,\text{eff}}(\nabla \ln c_e \cdot \nabla\phi_e) \\
&= \kappa_{\text{eff}} \left((\nabla[\tilde{\phi}_e]_1)^2 + 2(\nabla[\tilde{\phi}_e]_1 \nabla[\tilde{\phi}_e]_2) + (\nabla[\tilde{\phi}_e]_2)^2 \right) \\
&\quad + \kappa_{D,\text{eff}} \left(\frac{\nabla\tilde{c}_e}{c_e} (\nabla[\tilde{\phi}_e]_1 + \nabla[\tilde{\phi}_e]_2) \right) \\
&= \kappa_{\text{eff}} \left((\nabla[\tilde{\phi}_e]_1)^2 + \frac{4RT(1-t_+^0)}{Fc_e} (\nabla[\tilde{\phi}_e]_1 \nabla\tilde{c}_e) + \left(\frac{2RT(1-t_+^0)\nabla\tilde{c}_e}{Fc_e} \right)^2 \right) \\
&\quad + \kappa_{\text{eff}} \left(\frac{2RT(t_+^0-1)}{F} \frac{\nabla\tilde{c}_e}{c_e} \left(\nabla[\tilde{\phi}_e]_1 + \frac{2RT(1-t_+^0)\nabla\tilde{c}_e}{Fc_e} \right) \right) \\
&= \kappa_{\text{eff}} (\nabla[\tilde{\phi}_e]_1)^2 - \frac{\kappa_{D,\text{eff}}}{c_e} \nabla[\tilde{\phi}_e]_1 \nabla\tilde{c}_e.
\end{aligned}$$

To compute this result, we will need to have the DRA produce a ROM that can generate $\nabla[\tilde{\phi}_e]_1$, \tilde{c}_e , and $\nabla\tilde{c}_e$ at different locations across the cell to create proper averages. For best results, we use $\kappa_{\text{eff}}(c_e(x, t))$ instead of the $\kappa_{\text{eff}}(c_{e,0})$ that we usually use. Further, we recognize that the denominator of the transfer function for $\nabla[\tilde{\phi}_e]_1$ in all regions of the cell includes a κ_{eff} term. The DRA-produced ROM uses $\kappa_{\text{eff}}(c_{e,0})$ when making the linearized transfer function. However for best results, the output of the ROM should be multiplied by $\kappa_{\text{eff}}(c_{e,0})/\kappa_{\text{eff}}(c_e(x, t))$ since κ_{eff} is a strong function of c_e and $\nabla[\tilde{\phi}_e]_1$ is a strong function of κ_{eff} . Writing this out more explicitly, the heat-generation terms used for ROM1 results presented below use

$$q_e[x, k] = \kappa_{\text{eff}}(c_e[x, k]) \left(\frac{\kappa_{\text{eff}}(c_{e,0})}{\kappa_{\text{eff}}(c_e[x, k])} \nabla[\tilde{\phi}_e]_1 \right)^2 - \frac{\kappa_{D,\text{eff}}}{c_e[x, k]} \nabla[\tilde{\phi}_e]_1 \nabla\tilde{c}_e. \quad (7.13)$$

A simpler version assumes that $c_e[x, k] \approx c_{e,0}$. Results for ROM2 through ROM4 assume linearized results:

$$q_e[x, k] = \kappa_{\text{eff}} (\nabla[\tilde{\phi}_e]_1)^2 - \frac{\kappa_{D,\text{eff}}}{c_{e,0}} \nabla[\tilde{\phi}_e]_1 \nabla\tilde{c}_e.$$

Then, the method from Sect. 7.7.2 can be used on both parts of this expression. Results for ROM2 use the full linearized expression; results for ROM3 and ROM4 retain only the $\{\mathbf{DD}\}$ terms.

That is, for the first term we select $y_1[x, k] = y_2[x, k] = \sqrt{\kappa_{\text{eff}}/L^{\text{tot}}} \nabla[\tilde{\phi}_e[x, k]]_1$ and for the second term we select $y_3[x, k] = \sqrt{\kappa_{D,\text{eff}}/(c_{e,0}L^{\text{tot}})} \nabla[\tilde{\phi}_e[x, k]]_1$

and $y_4[x, k] = \nabla \tilde{c}_e[x, k]$ and compute

$$\bar{q}_e[k] = \frac{\kappa_{\text{eff}}}{L^{\text{tot}}} \int_0^{L^{\text{tot}}} y_1[x, k] y_2[x, k] \, dx - \frac{\kappa_{D, \text{eff}}}{c_{e,0} L^{\text{tot}}} \int_0^{L^{\text{tot}}} y_3[x, k] y_4[x, k] \, dx$$

where results labeled ROM1 or ROM2 use the full expression

$$\begin{aligned} \bar{q}_e[k] = & x^T[k] \{CC_1 - CC_2\} x[k] + x^T[k] \{CD_1 - CD_2\} i_{\text{app}}[k] \\ & + \{DD_1 - DD_2\} i_{\text{app}}^2[k], \end{aligned} \quad (7.14)$$

where the matrix subscripts indicate the integral from which they were computed. Results labeled ROM3 and ROM4 use a simpler computation:

$$\bar{q}_e[k] = \{DD_1 - DD_2\} i_{\text{app}}^2[k]. \quad (7.15)$$

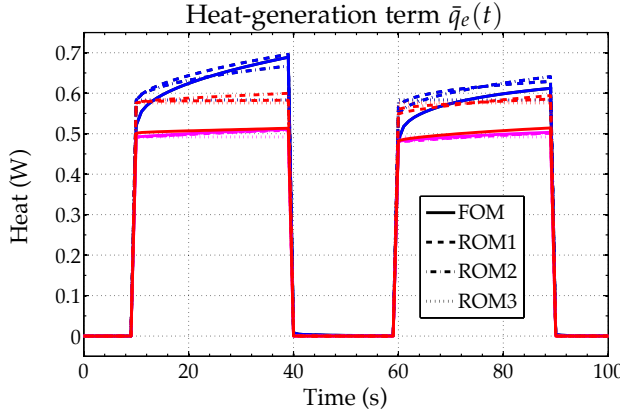


Figure 7.7: Heat generated via Joule heating in electrolyte from pulses: blue lines are for negative electrode; magenta lines are for separator; red lines are for positive electrode.

Fig. 7.7 shows sample results when the cell input current is the sequence of discharge and charge pulses. The solid line shows the full-order model result, and the decorated lines show different reduced-order model results. In this case, all ROMs gave fairly similar predictions to one another, although ROM1 appears to be more robust over a variety of simulation scenarios.

As a point of comparison, the total heat generated is modeled and displayed in Fig. 7.8 for the pulses and 1C discharge scenarios.¹¹ We see that the predictions of the ROMs are quite similar. The only large discrepancy is with ROM4 for the 1C discharge case, and this error is due to the crude model of $\bar{q}_r(t)$.

¹¹ The 1C discharge simulations use model blending, as discussed briefly in Sect. 7.10. Results for UDDS simulations are not shown as the plots are too “busy”; however, all ROMs match the FOM quite well.

7.8 Heat-flux terms

Now that we have seen how to approximate the heat-generation terms of the thermal model, we turn our attention to modeling heat

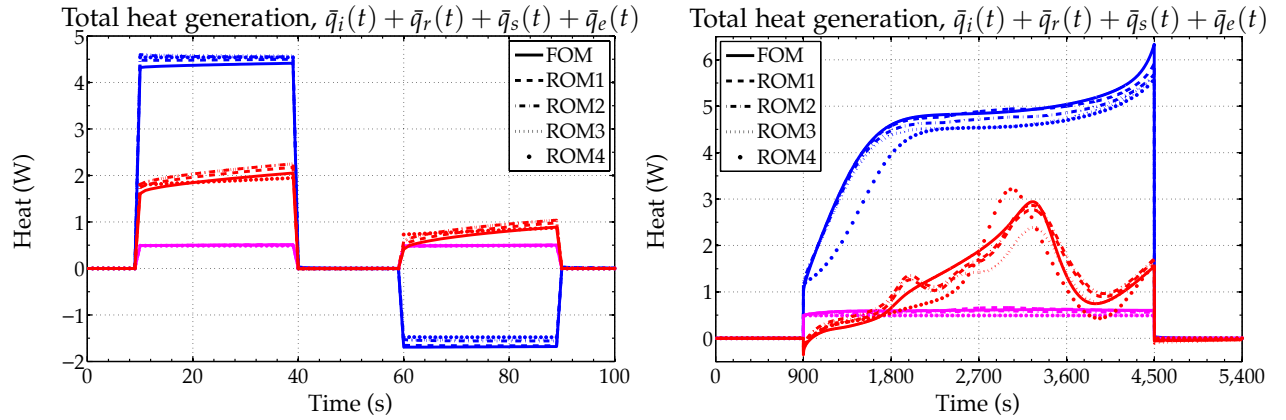


Figure 7.8: Total heat generated from 1C pulses (left) and a full 1C discharge (right): blue lines are for negative electrode; magenta are for separator; red lines are for positive electrode.

flux, leading to an expression for average cell temperature. We start with the underlying PDE

$$\rho c_P \frac{\partial T(x, t)}{\partial t} = \nabla \cdot (\lambda \nabla T(x, t)) + q(x, t) \quad (7.16)$$

having convective boundary conditions

$$-\lambda \frac{\partial T(x, t)}{\partial x} \Big|_{x=0} = h(T_\infty - T(0, t)) \quad (7.17)$$

$$\lambda \frac{\partial T(x, t)}{\partial x} \Big|_{x=L} = h \left(T_\infty - T(L, t) \right). \quad (7.18)$$

The constants ρ , c_P , and λ may be different in the three regions of the cell, but are assumed to be homogeneous within each region. Also, a radiative boundary condition may be approximated using

$$T_\infty^4 - T_s^4 \approx 4T_\infty^3(T_\infty - T_s)$$

as discussed earlier.

To solve this PDE, we might consider using separation of variables, as we did when exploring the PDE governing the concentration of lithium in the electrolyte, $c_e(x, t)$ in Chap. 6. However, since temperature tends to be fairly uniform across the x dimension of the cell, we use a simpler approach here, which is sufficient if all we want is average temperature of the cell and not an accurate model of the entire profile of $T(x, t)$.

Assume that we can closely approximate $T(x, t)$ as

$$T(x, t) \approx T_\infty + a(t) + b(t) \sin \left(\frac{\pi x}{L_{\text{tot}}} \right).$$

This allows for a fairly flat temperature profile over the cell cross section—which we observe in full-order-model simulations—but retains some curvature, as needed to satisfy the boundary conditions

in Eqs. (7.17) and (7.18). The $a(t)$ term primarily models the overall temperature bias versus the ambient temperature T_∞ , and $b(t)$ the nonuniformity of temperature versus cross-sectional position x .

For this assumed model, the derivatives that we need to solve the PDE can be written as

$$\begin{aligned}\frac{\partial T(x, t)}{\partial t} &= \frac{da(t)}{dt} + \frac{db(t)}{dt} \sin\left(\frac{\pi x}{L^{\text{tot}}}\right) \\ \frac{\partial T(x, t)}{\partial x} &= \frac{\pi}{L^{\text{tot}}} b(t) \cos\left(\frac{\pi x}{L^{\text{tot}}}\right) \\ \frac{\partial^2 T(x, t)}{\partial x^2} &= -\left(\frac{\pi}{L^{\text{tot}}}\right)^2 b(t) \sin\left(\frac{\pi x}{L^{\text{tot}}}\right).\end{aligned}$$

Inserting the assumed form of solution into the boundary condition of Eq. (7.17) at $x = 0$ gives

$$\begin{aligned}-\lambda \frac{\pi}{L^{\text{tot}}} b(t) \cos\left(\frac{\pi x}{L^{\text{tot}}}\right) \Big|_{x=0} &= h(T_\infty - (T_\infty + a(t))) \\ -\lambda \frac{\pi}{L^{\text{tot}}} b(t) &= -h a(t) \\ b(t) &= \frac{h L^{\text{tot}}}{\lambda \pi} a(t).\end{aligned}$$

Evaluating the PDE of Eq. (7.16) with the assumed form of solution gives

$$\begin{aligned}\rho c_P \left[\frac{da(t)}{dt} + \frac{h L^{\text{tot}}}{\lambda \pi} \frac{da(t)}{dt} \sin\left(\frac{\pi x}{L^{\text{tot}}}\right) \right] &= -\lambda \left(\frac{\pi}{L^{\text{tot}}}\right)^2 \left(\frac{h L^{\text{tot}}}{\lambda \pi}\right) a(t) \sin\left(\frac{\pi x}{L^{\text{tot}}}\right) \\ &\quad + q(x, t) \\ \rho c_P \left[1 + \frac{h L^{\text{tot}}}{\lambda \pi} \sin\left(\frac{\pi x}{L^{\text{tot}}}\right) \right] \frac{da(t)}{dt} &= -\left(\frac{\pi h}{L^{\text{tot}}}\right) a(t) \sin\left(\frac{\pi x}{L^{\text{tot}}}\right) + q(x, t).\end{aligned}\tag{7.19}$$

We will use this functional form as a basis for finding average cell temperature. To do so, we average both sides of the equation

$$\frac{1}{L^{\text{tot}}} \int_0^{L^{\text{tot}}} \rho c_P \left[1 + \frac{h L^{\text{tot}}}{\lambda \pi} \sin\left(\frac{\pi x}{L^{\text{tot}}}\right) \right] dx \frac{da(t)}{dt} = -\left(\frac{\pi h}{L^{\text{tot}}} \frac{2}{\pi}\right) a(t) + \bar{q}(t),$$

where

$$\bar{q}(t) = \frac{1}{L^{\text{tot}}} \int_0^{L^{\text{tot}}} q(x, t) dx,$$

and we have used

$$\frac{1}{L^{\text{tot}}} \int_0^{L^{\text{tot}}} \sin\left(\frac{\pi x}{L^{\text{tot}}}\right) dx = \frac{2}{\pi}.$$

We rewrite this as

$$\frac{da(t)}{dt} = -\left(\frac{2h}{k_q L^{\text{tot}}}\right) a(t) + \frac{1}{k_q} \bar{q}(t),$$

where the constant

$$\begin{aligned}
k_q &= \frac{1}{L^{\text{tot}}} \int_0^{L^{\text{tot}}} \rho c_P \left[1 + \frac{hL^{\text{tot}}}{\lambda\pi} \sin\left(\frac{\pi x}{L^{\text{tot}}}\right) \right] dx \\
&= \frac{1}{L^{\text{tot}}} \left[\rho^{\text{neg}} c_P^{\text{neg}} \left(\frac{h(L^{\text{tot}})^2}{\lambda^{\text{neg}}\pi^2} \left(1 - \cos\left(\frac{\pi L^{\text{neg}}}{L^{\text{tot}}}\right) \right) \right) \right. \\
&\quad + \rho^{\text{sep}} c_P^{\text{sep}} \left(\frac{h(L^{\text{tot}})^2}{\lambda^{\text{sep}}\pi^2} \left(\cos\left(\frac{\pi L^{\text{neg}}}{L^{\text{tot}}}\right) - \cos\left(\frac{\pi(L^{\text{neg}} + L^{\text{sep}})}{L^{\text{tot}}}\right) \right) \right) \\
&\quad + \rho^{\text{pos}} c_P^{\text{pos}} \left(\frac{h(L^{\text{tot}})^2}{\lambda^{\text{pos}}\pi^2} \left(1 + \cos\left(\frac{\pi(L^{\text{neg}} + L^{\text{sep}})}{L^{\text{tot}}}\right) \right) \right) \\
&\quad \left. + \rho^{\text{neg}} c_P^{\text{neg}} L^{\text{neg}} + \rho^{\text{sep}} c_P^{\text{sep}} L^{\text{sep}} + \rho^{\text{pos}} c_P^{\text{pos}} L^{\text{pos}} \right].
\end{aligned}$$

Recalling that

$$\begin{aligned}
T(x, t) &\approx T_{\infty} + a(t) + b(t) \sin\left(\frac{\pi x}{L^{\text{tot}}}\right) \\
&= T_{\infty} + a(t) \left[1 + \frac{hL^{\text{tot}}}{\lambda\pi} \sin\left(\frac{\pi x}{L^{\text{tot}}}\right) \right],
\end{aligned}$$

we can compute an average temperature

$$\begin{aligned}
T_{\text{avg}}(t) &= T_{\infty} + \frac{a(t)}{L^{\text{tot}}} \int_0^{L^{\text{tot}}} 1 + \frac{hL^{\text{tot}}}{\lambda\pi} \sin\left(\frac{\pi x}{L^{\text{tot}}}\right) dx \\
&= T_{\infty} + C_q a(t)
\end{aligned}$$

where the constant

$$\begin{aligned}
C_q &= \frac{1}{L^{\text{tot}}} \int_0^{L^{\text{tot}}} 1 + \frac{hL^{\text{tot}}}{\lambda\pi} \sin\left(\frac{\pi x}{L^{\text{tot}}}\right) dx \\
&= \frac{1}{L^{\text{tot}}} \left[\left(L^{\text{neg}} + \frac{h(L^{\text{tot}})^2}{\lambda^{\text{neg}}\pi^2} \left(1 - \cos\left(\frac{\pi L^{\text{neg}}}{L^{\text{tot}}}\right) \right) \right) \right. \\
&\quad + \left(L^{\text{sep}} + \frac{h(L^{\text{tot}})^2}{\lambda^{\text{sep}}\pi^2} \left(\cos\left(\frac{\pi L^{\text{neg}}}{L^{\text{tot}}}\right) - \cos\left(\frac{\pi(L^{\text{neg}} + L^{\text{sep}})}{L^{\text{tot}}}\right) \right) \right) \\
&\quad \left. + \left(L^{\text{pos}} + \frac{h(L^{\text{tot}})^2}{\lambda^{\text{pos}}\pi^2} \left(1 + \cos\left(\frac{\pi(L^{\text{neg}} + L^{\text{sep}})}{L^{\text{tot}}}\right) \right) \right) \right] \\
&= 1 + \frac{hL^{\text{tot}}}{\pi^2} \left[\frac{1}{\lambda^{\text{neg}}} \left(1 - \cos\left(\frac{\pi L^{\text{neg}}}{L^{\text{tot}}}\right) \right) \right. \\
&\quad + \frac{1}{\lambda^{\text{sep}}} \left(\cos\left(\frac{\pi L^{\text{neg}}}{L^{\text{tot}}}\right) - \cos\left(\frac{\pi(L^{\text{neg}} + L^{\text{sep}})}{L^{\text{tot}}}\right) \right) \\
&\quad \left. + \frac{1}{\lambda^{\text{pos}}} \left(1 + \cos\left(\frac{\pi(L^{\text{neg}} + L^{\text{sep}})}{L^{\text{tot}}}\right) \right) \right].
\end{aligned}$$

Converting to discrete time using the result from Sect. 2.4, we have the one-state ODE model for cell average temperature

$$a[k+1] = A_q a[k] + B_q \bar{q}[k]$$

$$T_{\text{avg}}[k] = C_q a[k] + T_{\infty},$$

where

$$A_q = \exp\left(-\frac{2h}{k_q L^{\text{tot}}} \Delta t\right)$$

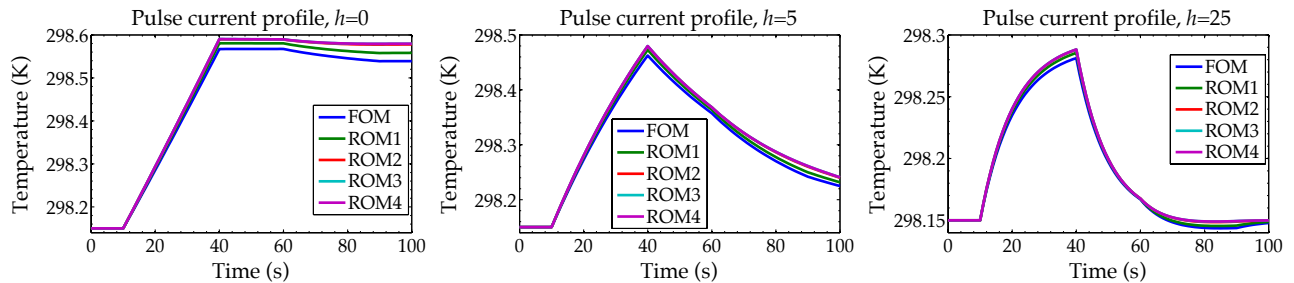
$$B_q = \begin{cases} -\frac{L^{\text{tot}}}{2h} (A_q - 1), & h \neq 0 \\ \frac{\Delta t}{k_q}, & h = 0. \end{cases}$$

7.9 Uncoupled model results

We demonstrate the heat-flux model first using an uncoupled electrochemical-thermal model. In this scenario, the electrochemical model (artificially) operates at a constant temperature of 298.15 K (*i.e.*, 25 °C), independent of the thermal model. The thermal model computes heat-generation terms and predicts temperature change, but the temperature change is not an input to the electrochemical simulation. In Sect. 7.10 we will show results for a coupled electrochemical-thermal model instead.

Results of these simulations to test the heat-flux ROM are shown in Figs. 7.9 through 7.11. In each figure, three different simulation scenarios are shown: one for convection coefficient $h = 0$ (modeling the perfectly insulated or adiabatic case, with no heat transfer to or from the environment), one with $h = 5$ (modeling natural convection), and one with $h = 25$ (modeling forced-air convection).

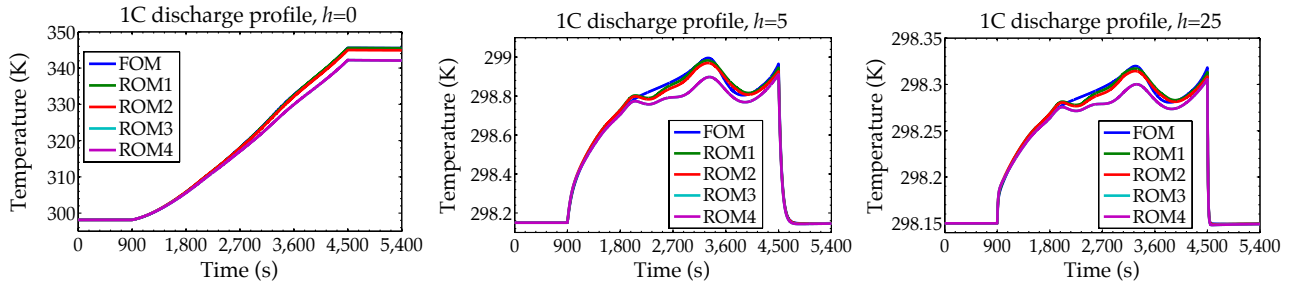
In Fig. 7.9, we see the results for the pulse test. All ROMs agree with the FOM results to within less than one degree over the entire simulation. ROM1 is somewhat better than the others, but they are all similar.



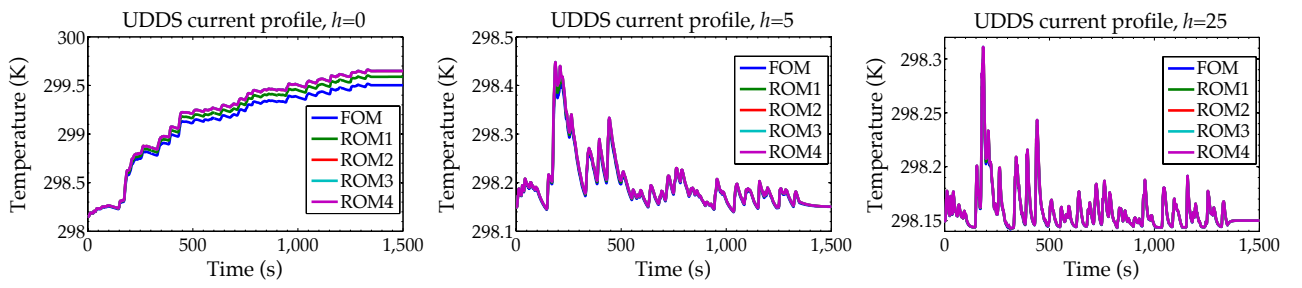
In Fig. 7.10, we see the results for the 1C discharge test. Here, all ROMs do quite well again, although ROM4 is noticeably worse than the others. This is due to the crude approximation of $\bar{q}_r(t)$.

Finally, Fig. 7.11 shows results for the charge-balanced UDDS test. Again, all ROMs do quite well. ROM1 slightly outperforms the

Figure 7.9: Cell average temperature as predicted by the uncoupled FOM and ROMs for the pulse profile and several convection coefficients h .



others, but perhaps not enough to justify the additional complexity.



7.10 Coupled model results

For our next results, we consider a coupled electrochemical–thermal model, where temperature from the thermal model is fed back into the electrochemical model on a sample-by-sample basis. In the electrochemical model, parameter values change according to an Arrhenius relationship via Eq. (7.5). The reference temperature for all parameter values was taken to be 25 °C, the reference values for temperature-varying quantities were the standard values from Table 6.1, and the activation energies for those parameters were those listed in Table 7.2.

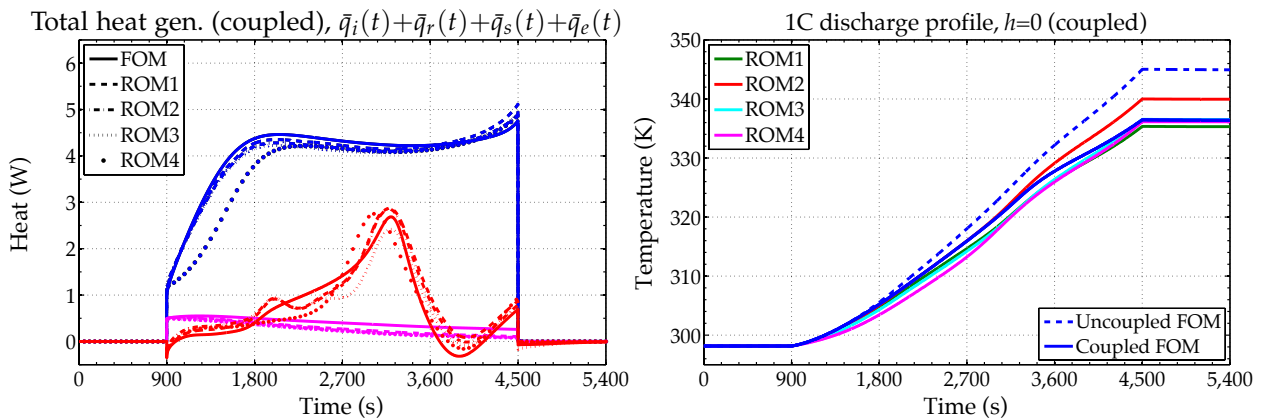
	k^{neg}	k^{pos}	D_s^{neg}	D_s^{pos}	D_e	κ
Activation energy [kJ mol ⁻¹]	30	30	4	20	10	20

Table 7.2: Activation energies for Arrhenius relationship for coupled electrochemical–thermal model simulation.

Full-order model results were from a coupled electrochemical–thermal model implemented in COMSOL. Reduced-order model results were created via blending ROMs created at multiple temperature–SOC setpoints. That is, first, the Arrhenius equation (Eq. (7.5)) was used to find parameter values at different temperature setpoints, and

the DRA was executed off-line to produce reduced-order models at different state-of-charge and temperature setpoints. Then, while the cell model is operating, the electrochemical model updates state of charge, and the thermal model updates temperature. Model blending continuously updates the A , B , C , and D matrices that are used in real time.

For the parameters and profiles used in these simulations there is very little difference between most uncoupled and coupled results. The biggest difference is seen in the adiabatic ($h = 0$) case for the full 1C discharge profile. This is shown in Fig. 7.12.



The left frame shows a comparison between heat-generation predictions by the FOM and the ROMs. (The comparable uncoupled result is in the right frame of Fig. 7.8.) Again, all ROMs except ROM4 predict heat generation in the negative electrode well; all ROMs predict heat generation in the separator nearly equally well; and ROM 1 and ROM 2 do the best at predicting heat generation in the positive electrode.

The right frame shows temperature change versus time. (The comparable uncoupled result is in the left frame of Fig. 7.10.) First, notice the significant difference between the uncoupled and coupled “truth” results predicted by the two different FOMs. Next, we see that ROMs 1 and 2 predict temperature change nearly equally well; ROMs 3 and 4 are not quite as good but may be adequate for many applications.

7.11 Where to from here?

We have now reached the end of this volume on battery modeling. We've come a long way in our understanding!

- We have explored empirical equivalent-circuit type models. These

Figure 7.12: Cell average temperature as predicted by the coupled FOM and ROMs for the 1C discharge profile and $h = 0$.

are both conceptually and computationally simple and can predict cell input–output behaviors well. They provide robust simulations for cell voltage for scenarios similar to those that generated the data that were used to train the models. System identification of model parameters is straightforward using voltage–current input–output data gathered using standard battery-laboratory equipment.

- We have derived microscale physics-based models that describe the internal dynamics of lithium-ion cells at very small length scales. These models apply directly to simulating mass and charge conservation in homogeneous solid active materials and in homogeneous electrolyte, separately. Parameters for these models (e.g., conductivities, diffusivities) are found by electrochemical laboratory tests on the raw materials that make up the cell. Simulations of cells using microscale models are intractable due to the vast amount of computation required.
- We have seen how to create volume-averaged continuum-scale models from the microscale models. These consider the average behavior of lithium concentration and potential in the solid and electrolyte over small neighborhoods and are simplified enough to be suitable for simulating full cells on a desktop computer. However, simulations are still too computationally complex to be considered on an embedded-systems battery-management system.
- We have also seen how to convert the continuum-scale models into linearized transfer functions, from which the discrete-time realization algorithm can compute physics-based reduced-order models. These models incorporate all the best features of the empirical and physics-based approaches: they are computationally simple, fast, and robust; further, they use physics to be able to predict cell behaviors outside of typical operating regimes; and they can furthermore compute cell electrochemical internal variables. The last is very useful to be able to predict (and control) aging.
- Finally, we have studied thermal effects at the microscale, continuum-scale, and reduced-order cell scale levels. The physics-based reduced-order models can compute all the terms needed to evaluate heat generation and temperature change in a cell. This can either improve the fidelity of an open-loop simulation or be used in a battery-management system to assist with thermal management and control.

These models are now ready to be used. In the second volume of this series, we discuss practical applications of battery models to the problems of proper battery management and control, focusing on

methods that use equivalent-circuit type models. The general outline of the book is

- An introduction to battery-management systems and the hardware and software requirements. There is some discussion of the kinds of electronics needed, but the focus of the book is on software methods, or *algorithms*.
- Generalizing from the battery-cell models seen in this volume to discover how to simulate battery packs of interconnected cells. It also considers simulating the load to which the battery pack is connected.
- The largest single section of the book explores how to estimate the internal state of all cells in a battery pack using only a cell model and voltage–current–temperature measured data. The particular focus is on state-of-charge estimation using some simple methods, as well as some methods based on nonlinear Kalman filtering. It also addresses practical robustness concerns and computational-complexity issues.
- An additional substantial section of the book considers state-of-health estimation for all cells in the battery pack. We show why estimating resistance is “easy” and why estimating total capacity is “hard.” Some simple methods for estimating health are considered, and then an optimal method for total-capacity estimation.
- We consider cell balancing: why is it needed, how can it be done, and what balancing speed is necessary.
- Finally, we examine power-limits estimation. We first consider power limits based on maintaining all cells within some prescribed voltage operating window, and then explain how power limits based on cell electrochemistry can improve on these greatly.

7.12 Partial glossary

This section gives a glossary of the most important variables defined in this chapter.

- c_P [$\text{J kg}^{-1} \text{K}^{-1}$] is the *specific heat* of a material (cf. p. 274).
- h [$\text{W m}^{-2} \text{K}^{-1}$] is a *heat-transfer coefficient* describing heat transfer at a boundary (cf. p. 280).
- H_k [J mol^{-1}] is the *partial molar enthalpy* of a material (cf. p. 275).
- λ [W K^{-1}] is the *thermal conductivity* of a material (cf. p. 274).
- Π [V K^{-1}] is the *Peltier coefficient* of a material (cf. p. 276).
- q [W m^{-3}] is a *heat-generation term* (cf. p. 278).

- ρ [kg m^{-3}] is the *density* of a material (cf. p. 274).
- T_∞ [K] is the *ambient temperature* (cf. p. 280).

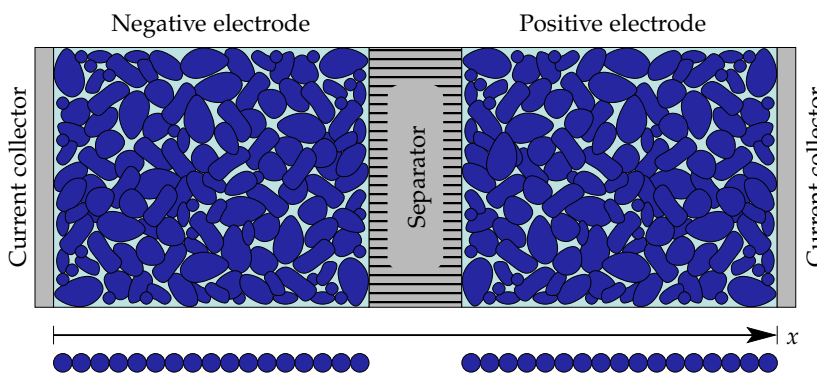
A

Supercapacitors

A.1 The same but different

Supercapacitors, sometimes known as *ultracapacitors* or electrochemical double-layer capacitors (EDLC), are electrochemical energy storage devices that share some similarities to the lithium-ion cells we have studied in this book. They have energy density about one tenth that of lithium-ion cells but power density of 10 or more times that of lithium-ion. In addition, they will tolerate many more charge and discharge cycles than most batteries. They are especially well suited for applications requiring long life and high power but low energy.

The structure of a supercapacitor is essentially the same as that of a lithium-ion battery cell and is depicted in Fig. A.1. There are negative and positive electrodes, current collectors, and a separator. The electrodes are composed of small particles, with the voids filled by an electrolyte solution.



Because of these similarities, we can leverage the math required to develop PDE full-order models and discrete-time reduced-order models of lithium-ion cells and apply it to understanding supercapacitors as well. So, enjoy this bonus appendix chapter!

A.1	The same but different	303
A.2	Charge storage	304
A.3	Continuum model	305
A.4	1D model of $\tilde{\phi}_{s-e}^{neg}(z, t)$	307
A.5	1D model of $\tilde{\phi}_s^{neg}(z, t)$	310
A.6	1D model of $\tilde{\phi}_e^{neg}(z, t)$	311
A.7	$\tilde{\phi}_{s-e}^{pos}$, $\tilde{\phi}_s^{pos}$ and $\tilde{\phi}_e^{pos}$	312
A.8	Supercapacitor voltage	313
A.9	Implement FOM	314
A.10	Implement ROM	315
A.11	Simulation results	316
A.12	Identifying parameters	317
A.13	Partial glossary	322

Figure A.1: Schematic of a supercapacitor, from a continuum-model perspective.

A.2 Charge storage

Charge can be stored in a supercapacitor via two mechanisms:

- With the so-called *nonfaradaic* mechanism, charge is stored electrostatically across the solid–electrolyte boundary. The solid particles develop a positive or negative charge, and the ions in the electrolyte immediately adjacent to the particles develop an opposite charge. No chemical reaction occurs at the particle surface.

The region in the electrolyte adjacent to the particle develops two layers of ordered charges, hence this region is called the “double layer.” The separation of charge is generally less than 1 nm, which is much smaller than in a conventional capacitor. This, combined with the enormous surface area of the particles in a porous electrode, leads to a very high capacitance value.

Fig. A.2 shows a particle and surrounding electrolyte in discharged and charged configurations. When discharged, positive and negative charges are disordered, with no net charge storage. When charged, positive (or negative) charges build up on the surface of the solid, and negative (or positive) charges build up in the electrolyte immediately adjacent to the particle.

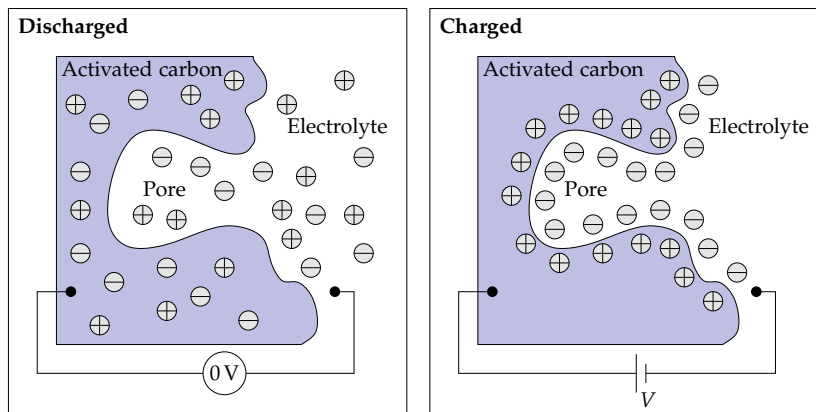


Figure A.2: Electrostatic charge storage in an electric double layer via a nonfaradaic mechanism.

- With the *faradaic* mechanism, charge is stored electrochemically with electron charge transfer, which can occur because of a redox reaction (as with a traditional electrochemical battery cell) or via intercalation (as with a lithium-ion battery cell). This is not truly a capacitor (since charge is not stored electrostatically), so this mechanism is sometimes termed *pseudocapacitance*. Faradaic-mechanism supercapacitors can store much more charge than nonfaradaic-mechanism supercapacitors, but with reduced life expectancy and reduced power capabilities.

At present, most supercapacitors available for sale are nonfaradaic, relying on a double-layer mechanism for charge storage. Some are

pseudocapacitors, and some are hybrids having one nonfaradaic electrode and one faradaic electrode. Generally, positive and negative electrodes can be of different geometry and composition, but most often they are identical to each other. The most commonly used material for the solid particles in a double-layer capacitor is activated carbon; pseudocapacitors are often made with at least one electrode comprising a metal oxide or a conducting polymer.

A.3 Continuum model

Our goal is to develop equations describing the internal and external behaviors of a supercapacitor, much as we have already done for a lithium-ion battery cell. We omit the microscale derivations and jump directly to the continuum-scale model by employing analogies to our experience with lithium-ion battery cells. From the continuum model, we will develop transfer functions to describe the supercapacitor internal variables. Then, the DRA will be used to build discrete-time state-space approximate models.

As with the lithium-ion cell model, the supercapacitor model has equations describing potential in its solid particles and potential in its electrolyte. Unlike a lithium-ion battery cell, the supercapacitor models assume constant concentration of charge carriers in the electrolyte, so electrolyte concentration variation $c_e(x, t)$ does not need to be modeled. Also, we do not consider intercalation, so solid concentration $c_{s,e}(x, t)$ does not need to be modeled.¹

The derivation of the supercapacitor continuum-scale model in this appendix merges elements of the nonfaradaic approach of Srinivasan and Weidner and the faradaic approach of Lin et al., although a slightly different path is taken, and notation is modified to be compatible with what we've used throughout this book.² We begin with derivations for the negative-electrode quantities and later generalize to the positive-electrode quantities as well. We start by assuming the continuum-scale models of electronic current through the solid and ionic current through the electrolyte:

$$\varepsilon_s^{\text{neg}} \mathbf{i}_s^{\text{neg}}(x, y, z, t) = -\sigma_{\text{eff}}^{\text{neg}} \nabla \phi_s^{\text{neg}}(x, y, z, t) \quad (\text{A.1})$$

$$\varepsilon_e^{\text{neg}} \mathbf{i}_e^{\text{neg}}(x, y, z, t) = -\kappa_{\text{eff}}^{\text{neg}} \nabla \phi_e^{\text{neg}}(x, y, z, t). \quad (\text{A.2})$$

Note the similarities to Eqs. (4.14) and (4.18). However, because of the assumption of uniform electrolyte concentration, we omit the term from Eq. (4.18) that is dependent on the concentration gradient.

We specialize to a one-dimensional model, so we can write

$$\varepsilon_s^{\text{neg}, \text{neg}} \mathbf{i}_s^{\text{neg}}(x, t) = -\sigma_{\text{eff}}^{\text{neg}} \frac{\partial \phi_s^{\text{neg}}(x, t)}{\partial x} \quad (\text{A.3})$$

¹ To consider pseudocapacitors having an intercalation faradaic mechanism, the techniques from Chap. 6 can be employed directly to make a model.

² Nonfaradaic from: Srinivasan, V., and Weidner, J.W., "Mathematical Modeling of Electrochemical Capacitors," *Journal of the Electrochemical Society*, 146(5), 1999, pp. 1,650–1,658. Faradaic from: Lin, C., Ritter, J.A., Popov, B.N., and White, R.E., "A Mathematical Model of an Electrochemical Capacitor with Double-Layer and Faradaic Processes," *Journal of the Electrochemical Society*, 146(9), 1999, pp. 3,168–3,175.

$$\varepsilon_e^{\text{neg}} i_e^{\text{neg}}(x, t) = -\kappa_{\text{eff}}^{\text{neg}} \frac{\partial \phi_e^{\text{neg}}(x, t)}{\partial x}. \quad (\text{A.4})$$

We next define a normalized spatial dimension $z = x/L^{\text{neg}}$ in the negative electrode. Then, by change of variables,

$$\varepsilon_s^{\text{neg}} i_s^{\text{neg}}(z, t) = -\frac{\sigma_{\text{eff}}^{\text{neg}}}{L^{\text{neg}}} \frac{\partial \phi_s^{\text{neg}}(z, t)}{\partial z} \quad (\text{A.5})$$

$$\varepsilon_e^{\text{neg}} i_e^{\text{neg}}(z, t) = -\frac{\kappa_{\text{eff}}^{\text{neg}}}{L^{\text{neg}}} \frac{\partial \phi_e^{\text{neg}}(z, t)}{\partial z}, \quad (\text{A.6})$$

where the total current at any z location is the sum

$$\frac{i_{\text{app}}(t)}{A} = \varepsilon_s i_s(z, t) + \varepsilon_e i_e(z, t). \quad (\text{A.7})$$

The solid-current equation has boundary conditions

$$\left. \frac{\sigma_{\text{eff}}^{\text{neg}}}{L^{\text{neg}}} \frac{\partial \phi_s^{\text{neg}}(z, t)}{\partial z} \right|_{z=0} = \frac{-i_{\text{app}}(t)}{A} \quad \text{and} \quad \left. \frac{\partial \phi_s^{\text{neg}}(z, t)}{\partial z} \right|_{z=1} = 0.$$

Likewise, the electrolyte-current equation has boundary conditions

$$\left. \frac{\partial \phi_e^{\text{neg}}(z, t)}{\partial z} \right|_{z=0} = 0 \quad \text{and} \quad \left. \frac{\kappa_{\text{eff}}^{\text{neg}}}{L^{\text{neg}}} \frac{\partial \phi_e(z, t)}{\partial z} \right|_{z=1} = \frac{i_{\text{app}}(t)}{A}.$$

We define the solid-electrolyte potential difference as

$$\phi_{s-e}(z, t) = \phi_s(z, t) - \phi_e(z, t),$$

and find that its boundary conditions are

$$\left. \frac{\sigma_{\text{eff}}^{\text{neg}}}{L^{\text{neg}}} \frac{\partial \phi_{s-e}(z, t)}{\partial z} \right|_{z=0} = \left. \frac{-\kappa_{\text{eff}}^{\text{neg}}}{L^{\text{neg}}} \frac{\partial \phi_{s-e}(z, t)}{\partial z} \right|_{z=1} = \frac{-i_{\text{app}}(t)}{A}.$$

Charge flux out of the electrolyte and into the surface layer is denoted as i_n , such that

$$\nabla \cdot (\varepsilon_s i_s) = -a_s i_n \quad \text{or} \quad \varepsilon_s \frac{\partial i_s}{\partial x} = -a_s i_n \quad (\text{A.8})$$

$$\nabla \cdot (\varepsilon_e i_e) = a_s i_n \quad \text{or} \quad \varepsilon_e \frac{\partial i_e}{\partial x} = a_s i_n \quad (\text{A.9})$$

for uniform ε_s and ε_e , and where i_n is the sum of the nonfaradaic current density flowing into the double layer plus the faradaic current density flowing into the surface-layer chemical reaction.

The double layer is modeled using a standard capacitor equation as an analogy:

$$i_{\text{dl}} = C \frac{\partial \phi_{s-e}}{\partial t}, \quad (\text{A.10})$$

where i_{dl} is the *double-layer current density*, and C is the specific capacitance of the active materials.

To model the faradaic process, we begin by defining faradaic current density i_f flowing into the surface layer and *faradaic charge* Q_f stored by the surface layer such that electrode *faradaic state of charge* θ_f can be written as

$$\theta_f = \frac{Q_f - Q_{f,0\%}}{Q_{f,100\%} - Q_{f,0\%}},$$

where $Q_{f,0\%}$ is the faradaic charge of a fully discharged (fully reduced) electrode, and $Q_{f,100\%}$ is the faradaic charge of a fully charged (fully oxidized) electrode. The charge varies according to

$$\frac{\partial Q_f}{\partial t} = a_s i_f,$$

where i_f is the *faradaic current density*. Then, we model the kinetics of i_f using a Butler–Volmer equation.

$$i_f = i_0 \left[\exp \left(\frac{(1-\alpha)F}{RT} (\phi_{s-e} - U_f(Q_f)) \right) - \exp \left(-\frac{\alpha F}{RT} (\phi_{s-e} - U_f(Q_f)) \right) \right], \quad (\text{A.11})$$

where $U_f(Q_f)$ models the state-of-charge dependent rest voltage of the faradaic process.

In the model, if there is no nonfaradaic process one simply sets $C = 0$ so that $i_{\text{dl}} = 0$ in Eq. (A.10). Similarly, if there is no nonfaradaic process, one sets $i_0 = 0$ so that $i_f = 0$ in Eq. (A.11).

A.4 A one-dimensional model of $\tilde{\phi}_{s-e}^{\text{neg}}(z, t)$

We desire to make a reduced-order discrete-time approximation to this continuum PDE model of a supercapacitor. We will use a very similar approach to the one taken in Chap. 6 to make a ROM of a lithium-ion cell. In particular, we will start by linearizing the PDEs and making transfer functions.

Beginning with Eq. (A.11), we define a linearization setpoint $p^* = \{Q_f = Q_0, \phi_{s-e} = \phi_{s-e,0}\}$ and write

$$\begin{aligned} i_f &\approx \underbrace{i_f(p^*)}_{0} + \frac{\partial i_f}{\partial \phi_{s-e}} \bigg|_{p^*} (\phi_{s-e} - \phi_{s-e,0}) + \frac{\partial i_f}{\partial Q_f} \bigg|_{p^*} (Q_f - Q_0) \\ i_f &\approx \frac{i_0 F}{RT} \tilde{\phi}_{s-e} - \frac{i_0 F}{RT} \left[\frac{\partial U_f}{\partial Q_f} \bigg|_{Q_0} \right] \tilde{Q}_f \end{aligned}$$

where we have defined $\tilde{\phi}_{s-e} = \phi_{s-e} - \phi_{s-e,0}$ and $\tilde{Q}_f = Q_f - Q_0$. Note that the initial solid–electrolyte potential difference is the sum of the

potential across the double layer plus the potential caused by the faradaic storage. Therefore, we can write $\phi_{s-e,0} = U_{dl,0} + U_f(Q_0)$, and $\tilde{\phi}_{s-e} = \phi_{s-e} - U_{dl,0} - U_f(Q_0)$.

We rearrange to solve for $\tilde{\phi}_{s-e}$ in time and Laplace domains

$$\begin{aligned}\tilde{\phi}_{s-e}(z, t) &= \frac{RT}{i_0 F} i_f(z, t) + \left[\frac{\partial U_f}{\partial Q_f} \Big|_{Q_0} \right] \tilde{Q}_f(z, t) \\ \tilde{\Phi}_{s-e}(z, s) &= \frac{RT}{i_0 F} I_f(z, s) + \left[\frac{\partial U_f}{\partial Q_f} \Big|_{Q_0} \right] \tilde{Q}_f(z, s).\end{aligned}$$

Note also that in the time and Laplace domains we have

$$\begin{aligned}\frac{\partial \tilde{Q}_f(z, t)}{\partial t} &= a_s i_f(z, t) \\ s \tilde{Q}_f(z, s) &= a_s I_f(z, s).\end{aligned}$$

Combining these results, we can write

$$\tilde{\Phi}_{s-e}(z, s) = \left[\frac{RT}{i_0 F} + \frac{a_s}{s} \left[\frac{\partial U_f}{\partial Q_f} \Big|_{Q_0} \right] \right] I_f(z, s). \quad (\text{A.12})$$

In this equation, we observe a charge-transfer resistance

$$R_{ct} = \frac{RT}{i_0 F},$$

which is equivalent to what we saw in Eq. (6.3) for a lithium-ion battery, and an overall faradaic impedance³

$$Z_f = \left[\frac{RT}{i_0 F} + \frac{a_s}{s} \left[\frac{\partial U_f}{\partial Q_f} \Big|_{Q_0} \right] \right].$$

The total current density entering the surface layer is $i_n(z, t) = i_{dl}(z, t) + i_f(z, t)$. Using Eqs. (A.10) and (A.11), we have

$$I_n(z, s) = sC \tilde{\Phi}_{s-e}(z, s) + \frac{1}{\left[\frac{RT}{i_0 F} + \frac{a_s}{s} \left[\frac{\partial U_f}{\partial Q_f} \Big|_{Q_0} \right] \right]} \tilde{\Phi}_{s-e}(z, s). \quad (\text{A.13})$$

Note that this is a current-divider equation. The impedance of the double-layer process is $Z_{dl} = 1/sC$ and the impedance of the faradaic process is Z_f . The total current density entering the surface layer is split between current densities entering due to the two different mechanisms.

We set this result aside for now and refer back to Eqs. (A.8) and (A.9). Subtracting κ_{eff} times Eq. (A.8) from σ_{eff} times (A.9) gives

$$a_s (\kappa_{\text{eff}} + \sigma_{\text{eff}}) i_n = -\kappa_{\text{eff}} \epsilon_s \frac{\partial i_s}{\partial x} + \sigma_{\text{eff}} \epsilon_e \frac{\partial i_e}{\partial x}.$$

³ If there is no faradaic process, Z_f is infinite. In the equations that follow, this is accomplished by setting $i_0 = 0$ and $\partial U_f / \partial Q_f = \infty$ in the limit.

Then, by Eqs. (A.3) and (A.4),

$$\begin{aligned} a_s(\kappa_{\text{eff}} + \sigma_{\text{eff}})i_n &= \kappa_{\text{eff}}\sigma_{\text{eff}} \frac{\partial^2 \phi_s}{\partial x^2} - \kappa_{\text{eff}}\sigma_{\text{eff}} \frac{\partial^2 \phi_e}{\partial x^2} \\ &= \kappa_{\text{eff}}\sigma_{\text{eff}} \frac{\partial^2 \tilde{\phi}_{s-e}}{\partial x^2}. \end{aligned}$$

Changing from the x coordinate system to the z coordinate system, we get

$$a_s(\kappa_{\text{eff}} + \sigma_{\text{eff}})i_n = \frac{\kappa_{\text{eff}}\sigma_{\text{eff}}}{L^2} \frac{\partial^2 \tilde{\phi}_{s-e}}{\partial z^2},$$

and taking the Laplace transform, we find

$$a_s(\kappa_{\text{eff}} + \sigma_{\text{eff}})I_n(z, s) = \frac{\kappa_{\text{eff}}\sigma_{\text{eff}}}{L^2} \frac{\partial^2 \tilde{\Phi}_{s-e}(z, s)}{\partial z^2}. \quad (\text{A.14})$$

Combining Eqs. (A.13) and (A.14), we arrive at

$$\frac{a_s L^2 (\kappa_{\text{eff}} + \sigma_{\text{eff}})}{\kappa_{\text{eff}}\sigma_{\text{eff}}} \left(sC + \left[\frac{RT}{i_0 F} + \frac{a_s}{s} \left[\frac{\partial U_f}{\partial Q_f} \Big|_{Q_0} \right] \right]^{-1} \right) \tilde{\Phi}_{s-e}(z, s) = \frac{\partial^2 \tilde{\Phi}_{s-e}(z, s)}{\partial z^2}.$$

Define, for the negative electrode,⁴

$$\begin{aligned} \nu^{\text{neg}}(s) &= L^{\text{neg}} \sqrt{\frac{a_s^{\text{neg}}}{\kappa_{\text{eff}}^{\text{neg}}} + \frac{a_s^{\text{neg}}}{\sigma_{\text{eff}}^{\text{neg}}}} \\ &\times \sqrt{sC^{\text{neg}} + \left[\frac{RT}{i_0^{\text{neg}} F} + \frac{a_s^{\text{neg}}}{s} \left[\frac{\partial U_f^{\text{neg}}}{\partial Q_f^{\text{neg}}} \Big|_{Q_0^{\text{neg}}} \right] \right]^{-1}}. \end{aligned}$$

Then,

$$\frac{\partial^2 \tilde{\Phi}_{s-e}(z, s)}{\partial z^2} - \nu^2(s) \tilde{\Phi}_{s-e}(z, s) = 0. \quad (\text{A.15})$$

The generic solution to this PDE is

$$\tilde{\Phi}_{s-e}(z, s) = k_1 \cosh(\nu(s)z) + k_2 \sinh(\nu(s)z),$$

where k_1 and k_2 are chosen to satisfy the boundary conditions. Since our boundary conditions are expressed as gradients, we differentiate

$$\frac{\partial \tilde{\Phi}_{s-e}(z, s)}{\partial z} = k_1 \nu(s) \sinh(\nu(s)z) + k_2 \nu(s) \cosh(\nu(s)z).$$

From our boundary condition at $z = 0$, we have

$$\begin{aligned} \frac{\sigma_{\text{eff}}}{L} \frac{\partial \tilde{\Phi}_{s-e}(z, s)}{\partial z} \Big|_{z=0} &= \frac{\sigma_{\text{eff}}}{L} k_2 \nu(s) = \frac{-I_{\text{app}}(s)}{A} \\ k_2 &= \frac{-I_{\text{app}}(s)L}{A\sigma_{\text{eff}}\nu(s)}. \end{aligned}$$

⁴ Note, we can rearrange this as

$$\nu^2(s) = \frac{L^2 \left(\frac{a_s}{\kappa_{\text{eff}}} + \frac{a_s}{\sigma_{\text{eff}}} \right)}{\left(\frac{1}{Z_{\text{dl}}^{-1} + Z_f^{-1}} \right)}.$$

We recognize the numerator to be in the same form as for $\nu^2(s)$ for a battery cell. The denominator is the generalized impedance of a capacitor in parallel with the impedance of the faradaic process. Thus, $\nu^2(s)$ has the same basic interpretation as for a battery: it is the ratio of the impedance of the electrode in the x dimension to the impedance of the electrode in the r dimension (the impedance of charging the double-layer/faradaic process in this case).

From our boundary condition at $z = 1$, we have

$$\begin{aligned} \frac{-\kappa_{\text{eff}}}{L} \frac{\partial \tilde{\Phi}_{s-e}(z, s)}{\partial z} \bigg|_{z=1} &= \frac{-\kappa_{\text{eff}}}{L} \left[k_1 \nu(s) \sinh(\nu(s)) - \frac{I_{\text{app}}(s)L}{A\sigma_{\text{eff}}} \cosh(\nu(s)) \right] \\ \frac{-I_{\text{app}}(s)}{A} &= \frac{-\kappa_{\text{eff}}}{L} \left[k_1 \nu(s) \sinh(\nu(s)) - \frac{I_{\text{app}}(s)L}{A\sigma_{\text{eff}}} \cosh(\nu(s)) \right] \\ k_1 \nu(s) \sinh(\nu(s)) &= \frac{I_{\text{app}}(s)L}{A\kappa_{\text{eff}}} \left[1 + \frac{\kappa_{\text{eff}}}{\sigma_{\text{eff}}} \cosh(\nu(s)) \right] \\ k_1 &= \frac{I_{\text{app}}(s)L}{A\nu(s) \sinh(\nu(s))} \left[\frac{1}{\kappa_{\text{eff}}} + \frac{1}{\sigma_{\text{eff}}} \cosh(\nu(s)) \right]. \end{aligned}$$

Note that these are exactly the same as Eqs. (6.10) and (6.11) for the corresponding development for batteries.

Substituting these values of k_1 and k_2 into $\tilde{\Phi}_{s-e}(z, s)$ gives

$$\begin{aligned} \tilde{\Phi}_{s-e}(z, s) &= \frac{I_{\text{app}}(s)L}{A\nu(s) \sinh(\nu(s))} \left[\frac{1}{\kappa_{\text{eff}}} + \frac{1}{\sigma_{\text{eff}}} \cosh(\nu(s)) \right] \cosh(\nu(s)z) \\ &\quad + \frac{-I_{\text{app}}(s)L}{A\sigma_{\text{eff}}\nu(s)} \sinh(\nu(s)z) \\ \frac{\tilde{\Phi}_{s-e}(z, s)}{I_{\text{app}}(s)} &= \frac{L}{A\nu(s) \sinh(\nu(s))} \left[\frac{1}{\kappa_{\text{eff}}} \cosh(\nu(s)z) \right. \\ &\quad \left. + \frac{1}{\sigma_{\text{eff}}} (\cosh(\nu(s)) \cosh(\nu(s)z) - \sinh(\nu(s)) \sinh(\nu(s)z)) \right]. \end{aligned}$$

Some trigonometric manipulations give us the following final form

$$\frac{\tilde{\Phi}_{s-e}^{\text{neg}}(z, s)}{I_{\text{app}}(s)} = L^{\text{neg}} \frac{\sigma_{\text{eff}}^{\text{neg}} \cosh(\nu^{\text{neg}}(s)z) + \kappa_{\text{eff}}^{\text{neg}} \cosh(\nu^{\text{neg}}(s)(z-1))}{A\sigma_{\text{eff}}^{\text{neg}} \kappa_{\text{eff}}^{\text{neg}} \nu^{\text{neg}}(s) \sinh(\nu^{\text{neg}}(s))}. \quad (\text{A.16})$$

This has exactly the same form as for a lithium-ion cell, as we saw in Eq. (6.12), but with a different definition of $\nu(s)$.

A.5 A one-dimensional model of $\tilde{\phi}_s^{\text{neg}}(z, t)$

To find a transfer function for $\phi_s^{\text{neg}}(z, t)$, we first find a transfer function for $i_s^{\text{neg}}(z, t)$. We begin by multiplying Eq. (A.5) by κ_{eff} :

$$\varepsilon_s \kappa_{\text{eff}} i_s(z, t) = -\frac{\kappa_{\text{eff}} \sigma_{\text{eff}}}{L} \frac{\partial \phi_s(z, t)}{\partial z}.$$

Now, we multiply Eq. (A.7) by σ_{eff} , after substituting Eq. (A.6), to get

$$\sigma_{\text{eff}} \frac{i_{\text{app}}(t)}{A} = \varepsilon_s \sigma_{\text{eff}} i_s(z, t) - \frac{\kappa_{\text{eff}} \sigma_{\text{eff}}}{L} \frac{\partial \phi_e(z, t)}{\partial z}.$$

Adding these two equations gives

$$\varepsilon_s (\kappa_{\text{eff}} + \sigma_{\text{eff}}) i_s(z, t) = \sigma_{\text{eff}} \frac{i_{\text{app}}(t)}{A} + \frac{\kappa_{\text{eff}} \sigma_{\text{eff}}}{L} \frac{\partial \phi_{s-e}(z, t)}{\partial z}.$$

We take Laplace transforms:

$$\varepsilon_s I_s(z, s) = \frac{\sigma_{\text{eff}}}{\kappa_{\text{eff}} + \sigma_{\text{eff}}} \frac{I_{\text{app}}(s)}{A} + \frac{1}{L} \left(\frac{\kappa_{\text{eff}} \sigma_{\text{eff}}}{\kappa_{\text{eff}} + \sigma_{\text{eff}}} \right) \frac{\partial \tilde{\Phi}_{s-e}(z, s)}{\partial z}.$$

After substituting Eq. (A.16) and performing symbolic manipulations (using Mathematica), we arrive at the following transfer function:

$$\begin{aligned} \varepsilon_s \frac{I_s^{\text{neg}}(z, s)}{I_{\text{app}}(s)} &= \frac{\kappa_{\text{eff}}^{\text{neg}} \sinh(\nu^{\text{neg}}(s)(1-z)) - \sigma_{\text{eff}}^{\text{neg}} \sinh(\nu^{\text{neg}}(s)z)}{A(\kappa_{\text{eff}}^{\text{neg}} + \sigma_{\text{eff}}^{\text{neg}}) \sinh(\nu^{\text{neg}}(s))} \\ &+ \frac{\sigma_{\text{eff}}^{\text{neg}}}{A(\kappa_{\text{eff}}^{\text{neg}} + \sigma_{\text{eff}}^{\text{neg}})}. \end{aligned} \quad (\text{A.17})$$

Now, starting with Eq. (A.5), we can write

$$\begin{aligned} \frac{\partial \phi_s(z, t)}{\partial z} &= -\frac{L \varepsilon_s}{\sigma_{\text{eff}}} i_s(z, t) \\ \phi_s(z, t) - \phi_s(0, t) &= -\frac{L \varepsilon_s}{\sigma_{\text{eff}}} \int_0^z i_s(\zeta, t) d\zeta. \end{aligned}$$

Define $\tilde{\phi}_s(z, t) = \phi_s(z, t) - \phi_s(0, t)$. In the negative electrode, $\phi_s(z, t) = \tilde{\phi}_s(z, t)$; in the positive electrode, $\phi_s(z, t) = \tilde{\phi}_s(z, t) + v(t)$.

$$\begin{aligned} \tilde{\phi}_s(z, t) &= -\frac{L \varepsilon_s}{\sigma_{\text{eff}}} \int_0^z i_s(\zeta, t) d\zeta \\ \tilde{\Phi}_s(z, s) &= -\frac{L \varepsilon_s}{\sigma_{\text{eff}}} \int_0^z I_s(\zeta, s) d\zeta. \end{aligned}$$

Substituting Eq. (A.17) and simplifying gives

$$\begin{aligned} \frac{\tilde{\Phi}_s^{\text{neg}}(z, s)}{I_{\text{app}}(s)} &= -L^{\text{neg}} \frac{\sigma_{\text{eff}}^{\text{neg}} + \kappa_{\text{eff}}^{\text{neg}} \cosh(\nu^{\text{neg}}(s)) + z \nu^{\text{neg}}(s) \sigma_{\text{eff}}^{\text{neg}} \sinh(\nu^{\text{neg}}(s))}{A \sigma_{\text{eff}}^{\text{neg}} (\kappa_{\text{eff}}^{\text{neg}} + \sigma_{\text{eff}}^{\text{neg}}) \nu^{\text{neg}}(s) \sinh(\nu^{\text{neg}}(s))} \\ &+ L^{\text{neg}} \frac{\sigma_{\text{eff}}^{\text{neg}} \cosh(\nu^{\text{neg}}(s)z) + \kappa_{\text{eff}}^{\text{neg}} \cosh(\nu^{\text{neg}}(s)(1-z))}{A \sigma_{\text{eff}}^{\text{neg}} (\kappa_{\text{eff}}^{\text{neg}} + \sigma_{\text{eff}}^{\text{neg}}) \nu^{\text{neg}}(s) \sinh(\nu^{\text{neg}}(s))}. \end{aligned} \quad (\text{A.18})$$

This has exactly the same form as for a lithium-ion cell, as we saw in Eq. (6.19) but with a different definition of $\nu(s)$.

A.6 A one-dimensional model of $\tilde{\phi}_e^{\text{neg}}(z, t)$

To find a transfer function for $\phi_e^{\text{neg}}(z, t)$, we begin by finding a transfer function for $i_e^{\text{neg}}(z, t)$. Rearrange Eq. (A.7) to get

$$\varepsilon_e i_e(z, t) = \frac{i_{\text{app}}(t)}{A} - \varepsilon_s i_s(z, t).$$

Therefore,

$$\varepsilon_e \frac{i_e^{\text{neg}}(z, s)}{I_{\text{app}}(s)} = \frac{1}{A} - \varepsilon_s \frac{I_s^{\text{neg}}(z, s)}{I_{\text{app}}(s)}.$$

Substituting Eq. (A.17) and simplifying gives

$$\varepsilon_e \frac{I_e^{\text{neg}}(z, s)}{I_{\text{app}}(s)} = \frac{\sigma_{\text{eff}}^{\text{neg}} \sinh(\nu^{\text{neg}}(s)z) - \kappa_{\text{eff}}^{\text{neg}} \sinh(\nu^{\text{neg}}(s)(1-z))}{A(\kappa_{\text{eff}}^{\text{neg}} + \sigma_{\text{eff}}^{\text{neg}}) \sinh(\nu^{\text{neg}}(s))} + \frac{\kappa_{\text{eff}}^{\text{neg}}}{A(\kappa_{\text{eff}}^{\text{neg}} + \sigma_{\text{eff}}^{\text{neg}})}. \quad (\text{A.19})$$

To find $\phi_e(z, t)$ in an electrode, write

$$\begin{aligned} \phi_e(z, t) &= \phi_s(z, t) - \phi_{s-e}(z, t) \\ &= \tilde{\phi}_s(z, t) + \phi_s(0, t) - \tilde{\phi}_{s-e}(z, t) - U_{\text{dl},0} - U_f(Q_0). \end{aligned}$$

Define

$$\tilde{\phi}_e(z, t) = \phi_e(z, t) - \phi_s(0, t) + U_{\text{dl},0} + U_f(Q_0). \quad (\text{A.20})$$

Then,

$$\frac{\tilde{\Phi}_e(z, s)}{I_{\text{app}}(s)} = \frac{\tilde{\Phi}_s(z, s)}{I_{\text{app}}(s)} - \frac{\tilde{\Phi}_{s-e}(z, s)}{I_{\text{app}}(s)}.$$

After substitution and simplification, this yields

$$\begin{aligned} \frac{\tilde{\Phi}_e^{\text{neg}}(z, s)}{I_{\text{app}}(s)} &= -L^{\text{neg}} \frac{(\kappa_{\text{eff}}^{\text{neg}})^2 \cosh(\nu^{\text{neg}}(s)) + (\sigma_{\text{eff}}^{\text{neg}})^2 \cosh(\nu^{\text{neg}}(s)z)}{A\sigma_{\text{eff}}^{\text{neg}}\kappa_{\text{eff}}^{\text{neg}}(\kappa_{\text{eff}}^{\text{neg}} + \sigma_{\text{eff}}^{\text{neg}})\nu^{\text{neg}}(s) \sinh(\nu^{\text{neg}}(s))} \\ &\quad - L^{\text{neg}} \frac{1 + \cosh(\nu^{\text{neg}}(s)(1-z)) + z\nu^{\text{neg}}(s) \sinh(\nu^{\text{neg}}(s))}{A(\kappa_{\text{eff}}^{\text{neg}} + \sigma_{\text{eff}}^{\text{neg}})\nu^{\text{neg}}(s) \sinh(\nu^{\text{neg}}(s))}. \end{aligned} \quad (\text{A.21})$$

A.7 Positive-electrode variables $\tilde{\phi}_{s-e}^{\text{pos}}$, $\tilde{\phi}_s^{\text{pos}}$ and $\tilde{\phi}_e^{\text{pos}}$

Following the same approach as we used for the model of the lithium-ion cell, we find that all positive-electrode transfer functions are of the same form as their negative-electrode counterparts except:

1. We use $\nu^{\text{pos}}(s)$ instead of $\nu^{\text{neg}}(s)$.
2. We use L^{pos} , a_s^{pos} , $\kappa_{\text{eff}}^{\text{pos}}$, $\sigma_{\text{eff}}^{\text{pos}}$ (etc.) instead of L^{neg} , a_s^{neg} , $\kappa_{\text{eff}}^{\text{neg}}$, and $\sigma_{\text{eff}}^{\text{neg}}$ (etc.), respectively.
3. We multiply the transfer function by -1 .

Therefore, for the positive electrode, we have impedance ratio

$$\begin{aligned} \nu^{\text{pos}}(s) &= L^{\text{pos}} \sqrt{\frac{a_s^{\text{pos}}}{\kappa_{\text{eff}}^{\text{pos}}} + \frac{a_s^{\text{pos}}}{\sigma_{\text{eff}}^{\text{pos}}}} \\ &\times \sqrt{sC^{\text{pos}} + \left[\frac{RT}{i_0^{\text{pos}}F} + \frac{a_s^{\text{pos}}}{s} \left[\frac{\partial U_f^{\text{pos}}}{\partial Q_f^{\text{pos}}} \right]_{Q_0^{\text{pos}}} \right]^{-1}} \end{aligned}$$

and

$$\frac{\tilde{\Phi}_{s-e}^{\text{pos}}(z, s)}{I_{\text{app}}(s)} = -L^{\text{pos}} \frac{\sigma_{\text{eff}}^{\text{pos}} \cosh(\nu^{\text{pos}}(s)z) + \kappa_{\text{eff}}^{\text{pos}} \cosh(\nu^{\text{pos}}(s)(z-1))}{A \sigma_{\text{eff}}^{\text{pos}} \kappa_{\text{eff}}^{\text{pos}} \nu^{\text{pos}}(s) \sinh(\nu^{\text{pos}}(s))} \quad (\text{A.22})$$

$$\begin{aligned} \frac{\tilde{\Phi}_s^{\text{pos}}(z, s)}{I_{\text{app}}(s)} &= L^{\text{pos}} \frac{\sigma_{\text{eff}}^{\text{pos}} + \kappa_{\text{eff}}^{\text{pos}} \cosh(\nu^{\text{pos}}(s)) + z \nu^{\text{pos}}(s) \sigma_{\text{eff}}^{\text{pos}} \sinh(\nu^{\text{pos}}(s))}{A \sigma_{\text{eff}}^{\text{pos}} (\kappa_{\text{eff}}^{\text{pos}} + \sigma_{\text{eff}}^{\text{pos}}) \nu^{\text{pos}}(s) \sinh(\nu^{\text{pos}}(s))} \\ &\quad - L^{\text{pos}} \frac{\sigma_{\text{eff}}^{\text{pos}} \cosh(\nu^{\text{pos}}(s)z) + \kappa_{\text{eff}}^{\text{pos}} \cosh(\nu^{\text{pos}}(s)(1-z))}{A \sigma_{\text{eff}}^{\text{pos}} (\kappa_{\text{eff}}^{\text{pos}} + \sigma_{\text{eff}}^{\text{pos}}) \nu^{\text{pos}}(s) \sinh(\nu^{\text{pos}}(s))} \end{aligned} \quad (\text{A.23})$$

$$\begin{aligned} \frac{\tilde{\Phi}_e^{\text{pos}}(z, s)}{I_{\text{app}}(s)} &= L^{\text{pos}} \frac{(\kappa_{\text{eff}}^{\text{pos}})^2 \cosh(\nu^{\text{pos}}(s)) + (\sigma_{\text{eff}}^{\text{pos}})^2 \cosh(\nu^{\text{pos}}(s)z)}{A \sigma_{\text{eff}}^{\text{pos}} \kappa_{\text{eff}}^{\text{pos}} (\kappa_{\text{eff}}^{\text{pos}} + \sigma_{\text{eff}}^{\text{pos}}) \nu^{\text{pos}}(s) \sinh(\nu^{\text{pos}}(s))} \\ &\quad + L^{\text{pos}} \frac{1 + \cosh(\nu^{\text{pos}}(s)(1-z)) + z \nu^{\text{pos}}(s) \sinh(\nu^{\text{pos}}(s))}{A (\kappa_{\text{eff}}^{\text{pos}} + \sigma_{\text{eff}}^{\text{pos}}) \nu^{\text{pos}}(s) \sinh(\nu^{\text{pos}}(s))}. \end{aligned} \quad (\text{A.24})$$

A.8 Supercapacitor voltage

Fig. A.3 illustrates the supercapacitor internal potentials while the device is experiencing a constant-current charge profile. This figure gives insight into how we can use the expressions we have developed already to compute a supercapacitor voltage signal.

Notice that the overall supercapacitor voltage can be written as the sum of the voltages over every region of the device. That is,

$$v(t) = v^{\text{neg}}(t) + v^{\text{sep}}(t) + v^{\text{pos}}(t).$$

We can write

$$\begin{aligned} v^{\text{neg}}(t) &= \phi_e^{\text{neg}}(1, t) - \underbrace{\phi_s^{\text{neg}}(0, t)}_0 \\ &= \tilde{\phi}_e^{\text{neg}}(1, t) + \underbrace{\phi_s^{\text{neg}}(0, t)}_0 - U_{\text{dl},0}^{\text{neg}} - U_f^{\text{neg}}(Q_0^{\text{neg}}), \end{aligned}$$

where we have substituted Eq. (A.20). Similarly,

$$v^{\text{pos}}(t) = \phi_s^{\text{pos}}(0, t) - \phi_e^{\text{pos}}(1, t) = -\tilde{\phi}_e^{\text{pos}}(1, t) + U_{\text{dl},0}^{\text{pos}} + U_f^{\text{pos}}(Q_0^{\text{pos}}),$$

where we have again substituted Eq. (A.20). Finally,

$$v^{\text{sep}}(t) = -i_{\text{app}}(t) \frac{L^{\text{sep}}}{A \kappa_{\text{eff}}^{\text{sep}}}.$$

Overall, then, we have

$$\begin{aligned} v(t) &= \tilde{\phi}_e^{\text{neg}}(1, t) - \tilde{\phi}_e^{\text{pos}}(1, t) - i_{\text{app}}(t) \frac{L^{\text{sep}}}{A \kappa_{\text{eff}}^{\text{sep}}} \\ &\quad - U_f^{\text{neg}}(Q_0^{\text{neg}}) + U_f^{\text{pos}}(Q_0^{\text{pos}}) - U_{\text{dl},0}^{\text{neg}} + U_{\text{dl},0}^{\text{pos}}. \end{aligned}$$

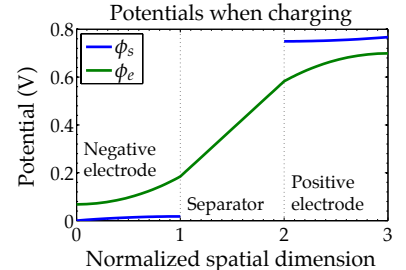


Figure A.3: Illustration of potentials inside supercapacitor while charging.

If we define a debiased voltage

$$\tilde{v}(t) = \tilde{\phi}_e^{\text{neg}}(1, t) - \tilde{\phi}_e^{\text{pos}}(1, t) - i_{\text{app}}(t) \frac{L^{\text{sep}}}{A\kappa_{\text{eff}}^{\text{sep}}},$$

then we can make a transfer function for the supercapacitor voltage

as

$$\frac{\tilde{V}(s)}{I_{\text{app}}(s)} = \frac{\tilde{\Phi}_e^{\text{neg}}(1, s)}{I_{\text{app}}(s)} - \frac{\tilde{\Phi}_e^{\text{pos}}(1, s)}{I_{\text{app}}(s)} - \frac{L^{\text{sep}}}{A\kappa_{\text{eff}}^{\text{sep}}},$$

where we reuse transfer functions from Eqs. (A.21) and (A.24), evaluated at $z = 1$, to compute the electrolyte potentials.

A.9 Implementing the full-order model

Recalling Eqs. (A.1) through (A.11), we can construct PDEs suitable for implementation in COMSOL or a similar PDE solver. Starting with Eqs. (A.8) and (A.1),

$$\begin{aligned} \nabla \cdot (\varepsilon_s i_s) &= -a_s i_n \\ \nabla \cdot (\sigma_{\text{eff}} \nabla \phi_s) &= a_s i_n, \end{aligned}$$

we substitute $i_n = i_{\text{dl}} + i_f$ via Eqs. (A.10) and (A.11), which give

$$\begin{aligned} i_n &= C \left[\frac{\partial \phi_s}{\partial t} - \frac{\partial \phi_e}{\partial t} \right] + i_0 \left[\exp \left(\frac{(1-\alpha)F}{RT} (\phi_{s-e} - U_f(Q_f)) \right) \right. \\ &\quad \left. - \exp \left(-\frac{\alpha F}{RT} (\phi_{s-e} - U_f(Q_f)) \right) \right], \end{aligned}$$

to yield the overall relationship

$$\begin{aligned} \frac{\partial \phi_s}{\partial t} &= \frac{\nabla \cdot (\sigma_{\text{eff}} \nabla \phi_s)}{a_s C L^2} + \frac{\partial \phi_e}{\partial t} - \frac{i_0}{C} \left[\exp \left(\frac{(1-\alpha)F}{RT} (\phi_{s-e} - U_f(Q_f)) \right) \right. \\ &\quad \left. - \exp \left(-\frac{\alpha F}{RT} (\phi_{s-e} - U_f(Q_f)) \right) \right], \end{aligned}$$

where the divergence and gradient operators are with respect to normalized length z .

We follow similar steps to find a PDE for ϕ_e . Starting with Eqs. (A.9) and (A.2),

$$\begin{aligned} \nabla \cdot (\varepsilon_s i_e) &= a_s i_n \\ \nabla \cdot (\kappa_{\text{eff}} \nabla \phi_e) &= -a_s i_n, \end{aligned}$$

we substitute $i_n = i_{\text{dl}} + i_f$, to yield the overall relationship:

$$\frac{\partial \phi_e}{\partial t} = \frac{\nabla \cdot (\kappa_{\text{eff}} \nabla \phi_e)}{a_s C L^2} + \frac{\partial \phi_s}{\partial t} + \frac{i_0}{C} \left[\exp \left(\frac{(1-\alpha)F}{RT} (\phi_{s-e} - U_f(Q_f)) \right) \right]$$

$$- \exp \left(-\frac{\alpha F}{RT} \left(\phi_{s-e} - U_f(Q_f) \right) \right) \Bigg],$$

where the divergence and gradient operators are again with respect to normalized length z .

For boundary conditions in the negative electrode, we know that at the current collector

$$\frac{i_{\text{app}}(t)}{A} = \varepsilon_s^{\text{neg}} i_s^{\text{neg}}(0, t) = -\sigma_{\text{eff}}^{\text{neg}} \nabla \phi_s^{\text{neg}}(0, t).$$

So,

$$\frac{\partial \phi_s^{\text{neg}}(x, t)}{\partial x} \Big|_{x=0} = -\frac{i_{\text{app}}(t)}{\sigma_{\text{eff}}^{\text{neg}} A} \quad \text{or} \quad \frac{\partial \phi_s^{\text{neg}}(z, t)}{\partial z} \Big|_{z=0} = -\frac{i_{\text{app}}(t) L^{\text{neg}}}{\sigma_{\text{eff}}^{\text{neg}} A}.$$

We also know

$$\varepsilon_e^{\text{neg}} i_e^{\text{neg}}(0, t) = 0 = -\kappa_{\text{eff}}^{\text{neg}} \nabla \phi_e^{\text{neg}}(0, t)$$

so

$$\frac{\partial \phi_e^{\text{neg}}(x, t)}{\partial x} \Big|_{x=0} = \frac{\partial \phi_e^{\text{neg}}(z, t)}{\partial z} \Big|_{z=0} = 0.$$

At the separator boundary,

$$\frac{i_{\text{app}}(t)}{A} = \varepsilon_e^{\text{neg}} i_e^{\text{neg}}(L^{\text{neg}}, t) = -\kappa_{\text{eff}}^{\text{neg}} \nabla \phi_e^{\text{neg}}(L^{\text{neg}}, t).$$

So

$$\frac{\partial \phi_e^{\text{neg}}(x, t)}{\partial x} \Big|_{x=L^{\text{neg}}} = -\frac{i_{\text{app}}(t)}{\kappa_{\text{eff}}^{\text{neg}} A} \quad \text{or} \quad \frac{\partial \phi_e^{\text{neg}}(z, t)}{\partial z} \Big|_{z=1} = -\frac{i_{\text{app}}(t) L^{\text{neg}}}{\kappa_{\text{eff}}^{\text{neg}} A}.$$

We also know

$$\varepsilon_s^{\text{neg}} i_s^{\text{neg}}(L^{\text{neg}}, t) = 0 = -\sigma_{\text{eff}}^{\text{neg}} \nabla \phi_s^{\text{neg}}(L^{\text{neg}}, t)$$

so

$$\frac{\partial \phi_s^{\text{neg}}(x, t)}{\partial x} \Big|_{x=L^{\text{neg}}} = \frac{\partial \phi_s^{\text{neg}}(z, t)}{\partial z} \Big|_{z=1} = 0.$$

In the positive electrode, we must multiply the boundary conditions by -1 and replace the “neg” parameters and variables with “pos” equivalents.

Finally, we set $\phi_s^{\text{neg}}(0, t) = 0$ and $\phi_s^{\text{pos}}(z = 0, t) = v(t)$.

A.10 Implementing the reduced-order model

A reduced-order model can be created using the DRA to implement any set of transfer functions at any set of locations in the supercapacitor. There are no special considerations needed for supercapacitors versus lithium-ion battery cells.

A.11 Simulation results

To demonstrate the effectiveness of the reduced-order supercapacitor models, this section presents results for both a nonfaradaic example and a faradaic example. The parameters for the nonfaradaic example are listed in Table A.1 and are taken from Srinivasan and Weidner. The parameters for the faradaic example are listed in Table A.2 and are taken from Lin et al. The reduced-order models had four dynamic states plus one integrator state.

Parameter	Units	Electrode	Separator
a_s	$\text{m}^2 \text{m}^{-3}$	3×10^8	—
C	F m^{-2}	0.3	—
L	μm	150	100
ϵ_e	—	0.25	0.7
ϵ_s	—	0.75	—
κ_{eff}	S m^{-1}	8.4	39.2
σ_{eff}	S m^{-1}	10^7	—

Table A.1: Parameters for nonfaradaic simulation ($A = 1 \text{ m}^2$).

(From: Srinivasan, V., and Weidner, J.W., "Mathematical Modeling of Electrochemical Capacitors," *Journal of the Electrochemical Society*, 146(5), 1999, pp. 1,650–1,658.)

Parameter	Units	Electrode	Separator
a_s	$\text{m}^2 \text{m}^{-3}$	4.5×10^8	—
C	F m^{-2}	0.2	—
L	μm	50	25
ϵ_e	—	0.25	0.25
ϵ_s	—	0.7	—
κ_{eff}	S m^{-1}	10	47
σ_{eff}	S m^{-1}	10^7	—
i_0	A m^{-2}	0.1	—
$Q_{f,0\%}$	C m^{-3}	0	—
$Q_{f,100\%}$	C m^{-3}	4.51×10^6	—
α	—	0.5	—
$U_f^{\text{neg}}(\theta_f)$	V	$0.5\theta_f$	—
$U_f^{\text{pos}}(\theta_f)$	V	$0.5(1 + \theta_f)$	—

Table A.2: Parameters for faradaic simulation ($A = 1 \text{ m}^2$).

(From: Lin, C., Ritter, J.A., Popov, B.N., and White, R.E., "A Mathematical Model of an Electrochemical Capacitor with Double-Layer and Faradaic Processes," *Journal of the Electrochemical Society*, 146(9), 1999, pp. 3,168–3,175.)

In both cases, the initial supercapacitor voltage was set to 0.5 V. In the nonfaradaic case, this was accomplished by setting $U_{\text{dl}}^{\text{neg}} = -0.25 \text{ V}$ and $U_{\text{dl}}^{\text{pos}} = 0.25 \text{ V}$. In the faradaic case, this was accomplished by setting $U_{\text{dl}}^{\text{neg}} = U_{\text{dl}}^{\text{pos}} = 0 \text{ V}$, $\theta_{f,0}^{\text{neg}} = 0.5$, and $\theta_{f,0}^{\text{pos}} = 0.5$. The supercapacitor was initially at rest. It was then exercised with a 1,000-A charge pulse, followed by a brief rest to allow voltage relaxation, followed by a 1,000-A discharge pulse.

Results for the nonfaradaic case are shown in Fig. A.4, and results for the faradaic case are shown in Fig. A.5. In both cases, the ROM and FOM results are nearly indistinguishable. Zooming in on the fine details shows that there is some imprecision at the discontinuities in current, as the ROM has a finite number of time constants versus the infinite number of time constants for the FOM. Adding states to the ROM would improve this, but there is a point of diminishing return.

A.12 Identifying parameters

Before concluding this appendix, we would like to be able to identify all the parameters of a supercapacitor simply from current–voltage input–output data. For example, we would like to determine the parameters listed in Table A.1 for a nonfaradaic supercapacitor and the parameters listed in Table A.2 for a faradaic supercapacitor. Here, we describe an approach to doing so, which does not provide the full list of parameters, but which does provide all parameters needed to evaluate any of the transfer functions considered in this appendix.

For brevity, we consider only the commonly encountered non-faradaic case where negative and positive electrodes are identical. Then, cell voltage can be written as

$$\frac{\tilde{V}(s)}{I_{\text{app}}(s)} = 2 \frac{\tilde{\Phi}_e^{\text{neg}}(1, s)}{I_{\text{app}}(s)} - \frac{L^{\text{sep}}}{A\kappa_{\text{eff}}^{\text{sep}}}.$$

We define the following constants:

$$\begin{aligned} R^{\text{sep}} &= \frac{L^{\text{sep}}}{A\kappa_{\text{eff}}^{\text{sep}}} \\ R_0 &= \frac{2L^{\text{neg}}}{A(\kappa_{\text{eff}}^{\text{neg}} + \sigma_{\text{eff}}^{\text{neg}})} + R^{\text{sep}} \\ R_{ss} &= \frac{2L^{\text{neg}}(\kappa_{\text{eff}}^{\text{neg}} + \sigma_{\text{eff}}^{\text{neg}})}{3A(\kappa_{\text{eff}}^{\text{neg}}\sigma_{\text{eff}}^{\text{neg}})} + R^{\text{sep}} \\ C_{\text{tot}} &= a_s^{\text{neg}} A C^{\text{neg}} L^{\text{neg}}. \end{aligned}$$

These values correspond to the separator ohmic resistance and to terms that can be measured from a step-response test, such as depicted in Fig. A.6. We see that R_0 is the resistance describing the instantaneous change in voltage due to the step input, R_{ss} is the resistance describing the steady-state difference in voltage between an ideal capacitor response to a step input (drawn as a dashed green line) and the actual response, and C_{tot} is the total capacitance of one electrode in the supercapacitor. We find that we can then write

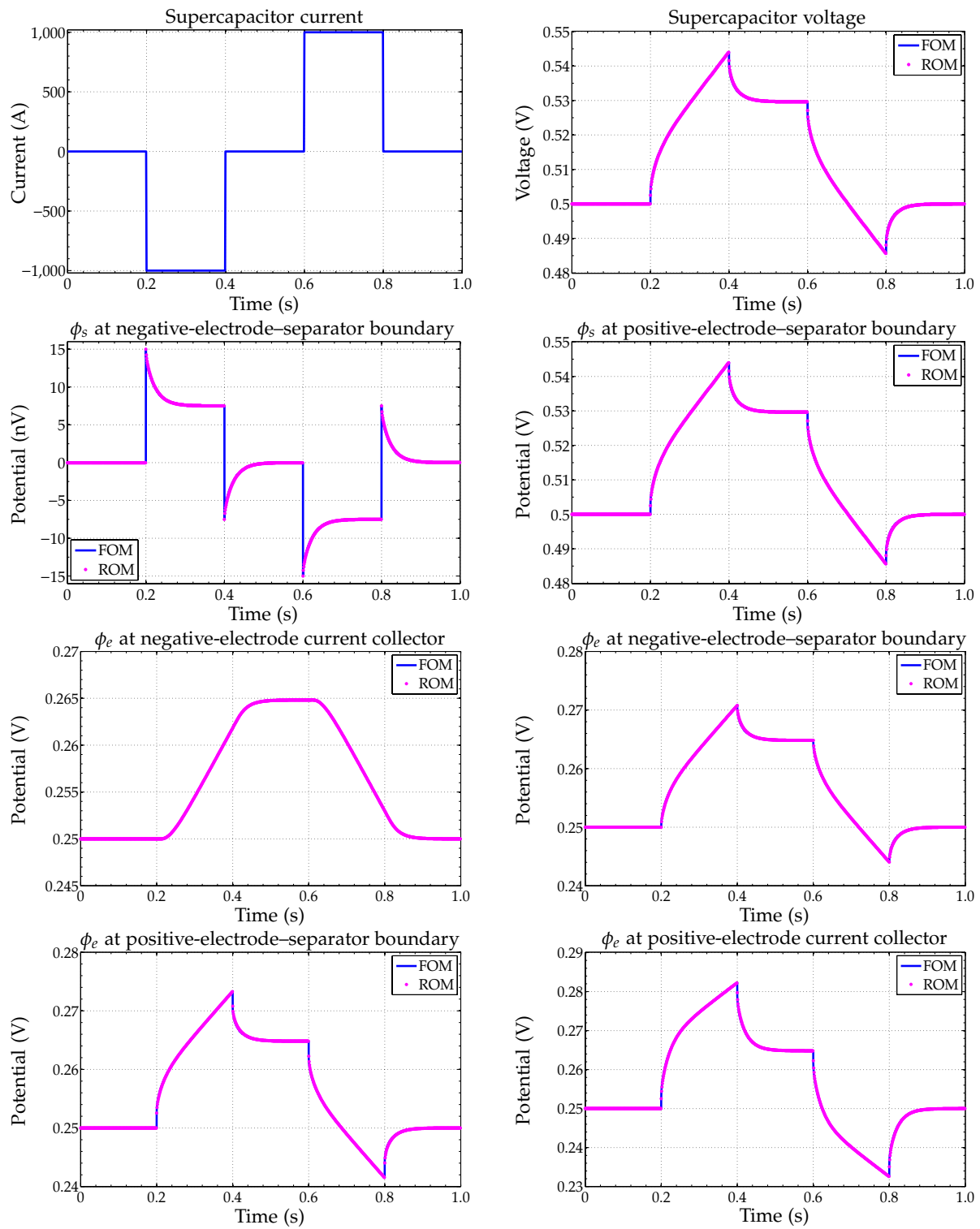


Figure A.4: Nonfaradaic results.

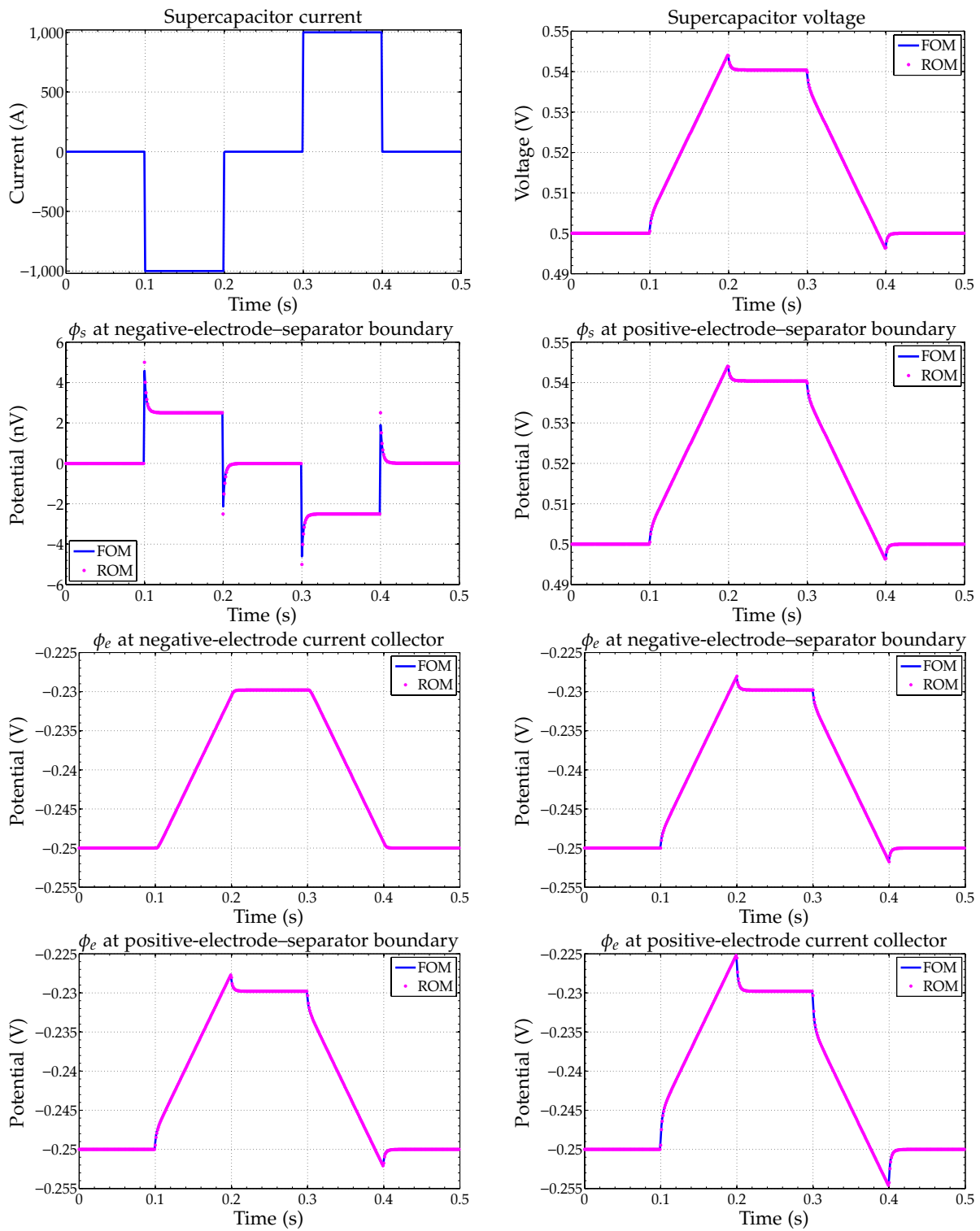


Figure A.5: Faradaic results.

$v^{\text{neg}}(s)$ in terms of these quantities:

$$\begin{aligned} v^{\text{neg}}(s) &= L^{\text{neg}} \sqrt{s C^{\text{neg}} \left(\frac{a_s^{\text{neg}}}{\kappa_{\text{eff}}^{\text{neg}}} + \frac{a_s^{\text{neg}}}{\sigma_{\text{eff}}^{\text{neg}}} \right)} \\ &= \sqrt{\frac{3s}{2} C_{\text{tot}} (R_{ss} - R^{\text{sep}})}. \end{aligned}$$

After some further manipulation, we find that we can write

$$\begin{aligned} \frac{\tilde{\Phi}_e^{\text{neg}}(1, s)}{I_{\text{app}}(s)} &= \left(R_0 - \frac{3}{2} R_{ss} + \frac{1}{2} R^{\text{sep}} \right) \frac{\coth(v^{\text{neg}}(s))}{v^{\text{neg}}(s)} \\ &\quad - \frac{1}{2} (R_0 - R^{\text{sep}}) \left(1 + \frac{2}{v^{\text{neg}}(s) \sinh(v^{\text{neg}})} \right). \end{aligned}$$

That is, the cell voltage can be written uniquely in terms of the four quantities R^{sep} , R_0 , R_{ss} , and C_{tot}

$$\begin{aligned} \frac{\tilde{V}(s)}{I_{\text{app}}(s)} &= (2R_0 - 3R_{ss} + R^{\text{sep}}) \frac{\coth(v^{\text{neg}}(s))}{v^{\text{neg}}(s)} \\ &\quad - (R_0 - R^{\text{sep}}) \left(1 + \frac{2}{v^{\text{neg}}(s) \sinh(v^{\text{neg}})} \right) - \frac{L^{\text{sep}}}{A \kappa_{\text{eff}}^{\text{sep}}}. \quad (\text{A.25}) \end{aligned}$$

This poses a problem. Table A.1 lists 11 independent parameters (including A) that determine a supercapacitor's dynamics. However, we can determine at most four from current–voltage measurements. The step-response test itself can supply only three of these values— R_{ss} can be determined via fitting a measured frequency response to Eq. (A.25).

There is a solution, however. If we are willing to consider groups of parameters, we can rewrite all the transfer functions of this appendix in terms of the four identifiable quantities. First, we further define

$$\kappa_{\text{tot}}^{\text{neg}} = \frac{A}{L^{\text{neg}}} \kappa_{\text{eff}}^{\text{neg}}, \quad \kappa_{\text{tot}}^{\text{sep}} = \frac{A}{L^{\text{sep}}} \kappa_{\text{eff}}^{\text{sep}}, \quad \text{and} \quad \sigma_{\text{tot}}^{\text{neg}} = \frac{A}{L^{\text{neg}}} \sigma_{\text{eff}}^{\text{neg}}.$$

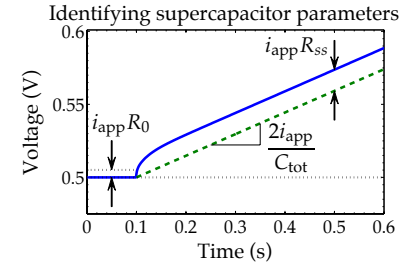
Then, we rewrite

$$R_0 = \frac{2}{\kappa_{\text{tot}}^{\text{neg}} + \sigma_{\text{tot}}^{\text{neg}}} + R^{\text{sep}} \quad (\text{A.26})$$

$$R_{ss} = \frac{2(\kappa_{\text{tot}}^{\text{neg}} + \sigma_{\text{tot}}^{\text{neg}})}{3(\kappa_{\text{tot}}^{\text{neg}} \sigma_{\text{tot}}^{\text{neg}})} + R^{\text{sep}}. \quad (\text{A.27})$$

The transfer functions in this appendix can be written in terms of these new variables. Consider, for example, the negative electrode

$$\frac{\tilde{\Phi}_{s-e}^{\text{neg}}(z, s)}{I_{\text{app}}(s)} = \frac{\sigma_{\text{tot}}^{\text{neg}} \cosh(v^{\text{neg}}(s)z) + \kappa_{\text{tot}}^{\text{neg}} \cosh(v^{\text{neg}}(s)(z-1))}{\sigma_{\text{tot}}^{\text{neg}} \kappa_{\text{tot}}^{\text{neg}} v^{\text{neg}}(s) \sinh(v^{\text{neg}}(s))} \quad (\text{A.28})$$



Identifying supercapacitor parameters
Figure A.6: Measurements made from step response.

$$\begin{aligned} \frac{\tilde{\Phi}_s^{\text{neg}}(z, s)}{I_{\text{app}}(s)} &= -\frac{\sigma_{\text{tot}}^{\text{neg}} + \kappa_{\text{tot}}^{\text{neg}} \cosh(\nu^{\text{neg}}(s)) + z\nu^{\text{neg}}(s)\sigma_{\text{tot}}^{\text{neg}} \sinh(\nu^{\text{neg}}(s))}{\sigma_{\text{tot}}^{\text{neg}}(\kappa_{\text{tot}}^{\text{neg}} + \sigma_{\text{tot}}^{\text{neg}})\nu^{\text{neg}}(s) \sinh(\nu^{\text{neg}}(s))} \\ &\quad + \frac{\sigma_{\text{tot}}^{\text{neg}} \cosh(\nu^{\text{neg}}(s)z) + \kappa_{\text{tot}}^{\text{neg}} \cosh(\nu^{\text{neg}}(s)(1-z))}{\sigma_{\text{tot}}^{\text{neg}}(\kappa_{\text{tot}}^{\text{neg}} + \sigma_{\text{tot}}^{\text{neg}})\nu^{\text{neg}}(s) \sinh(\nu^{\text{neg}}(s))} \end{aligned} \quad (\text{A.29})$$

$$\begin{aligned} \frac{\tilde{\Phi}_e^{\text{neg}}(z, s)}{I_{\text{app}}(s)} &= \frac{-(\kappa_{\text{tot}}^{\text{neg}})^2 \cosh(\nu^{\text{neg}}(s)) + (\sigma_{\text{tot}}^{\text{neg}})^2 \cosh(\nu^{\text{neg}}(s)z)}{\sigma_{\text{tot}}^{\text{neg}}\kappa_{\text{tot}}^{\text{neg}}(\kappa_{\text{tot}}^{\text{neg}} + \sigma_{\text{tot}}^{\text{neg}})\nu^{\text{neg}}(s) \sinh(\nu^{\text{neg}}(s))} \\ &\quad - \frac{1 + \cosh(\nu^{\text{neg}}(s)(1-z)) + z\nu^{\text{neg}}(s) \sinh(\nu^{\text{neg}}(s))}{(\kappa_{\text{tot}}^{\text{neg}} + \sigma_{\text{tot}}^{\text{neg}})\nu^{\text{neg}}(s) \sinh(\nu^{\text{neg}}(s))}. \end{aligned} \quad (\text{A.30})$$

So, if we are able to derive $\kappa_{\text{tot}}^{\text{neg}}$ and $\sigma_{\text{tot}}^{\text{neg}}$ from the four known quantities, we can compute all the transfer functions. Rearranging Eqs. (A.26) and (A.27), we have

$$\begin{aligned} \frac{1}{\kappa_{\text{tot}}^{\text{neg}}} + \frac{1}{\sigma_{\text{tot}}^{\text{neg}}} &= \frac{3}{2}(R_{ss} - R^{\text{sep}}) \\ \frac{1}{\kappa_{\text{tot}}^{\text{neg}} + \sigma_{\text{tot}}^{\text{neg}}} &= \frac{1}{2}(R_0 - R^{\text{sep}}). \end{aligned}$$

Combining these equations, we have that

$$\begin{aligned} (\kappa_{\text{tot}}^{\text{neg}})^2 - c_1\kappa_{\text{tot}}^{\text{neg}} + c_2 &= 0 \\ (\sigma_{\text{tot}}^{\text{neg}})^2 - c_1\sigma_{\text{tot}}^{\text{neg}} + c_2 &= 0, \end{aligned}$$

where

$$c_1 = \frac{2}{R_0 - R^{\text{sep}}} \quad \text{and} \quad c_2 = \frac{2c_1}{3(R_{ss} - R^{\text{sep}})}.$$

Since the equations describing $\kappa_{\text{tot}}^{\text{neg}}$ and $\sigma_{\text{tot}}^{\text{neg}}$ are identical, we must assign the two solutions of the quadratic equation to the two variables using side information. For any realistic supercapacitor, the electronic conductivity will be much higher than the ionic conductivity, which makes this choice for us.

So while we have not been able to identify all parameters in Table A.1 from cell-test data, we have identified a sufficient subset of quantities to be able to compute any signal of interest. Table A.3 lists the true and estimated parameter values using only data from the step response to initialize estimates and data from the noise-free frequency response to refine the estimates. The estimated parameter values match the true parameter values to many significant digits. If any specific nonlumped parameter value from the table is needed, the supercapacitor will have to be opened, and independent electrochemical laboratory measurements taken on the internals to determine the missing information.

Before concluding, we make one final comment based on observing Eq. (A.26). In practice, $\sigma_{\text{tot}}^{\text{neg}}$ tends to be a very large value such

Parameter	True value	Estimated value
C_{tot}	1.350000×10^4	1.350000×10^4
R_{sep}	2.548462×10^{-6}	2.548462×10^{-6}
R_{ss}	1.448877×10^{-5}	1.448877×10^{-5}
$R_0 - R_{\text{sep}}$	2.999997×10^{-11}	2.999992×10^{-11}
$\kappa_{\text{sep}}^{\text{tot}}$	3.923936×10^5	3.923936×10^5
$\kappa_{\text{neg}}^{\text{tot}}$	5.583333×10^4	5.583333×10^4
$\sigma_{\text{neg}}^{\text{tot}}$	6.666667×10^{10}	6.666679×10^{10}

Table A.3: Results of parameter estimation.

that $R_0 \approx R^{\text{sep}}$ to many significant decimal places. The frequency-response data collected to disambiguate these two quantities will need to be very accurate.

A.13 Partial glossary

This section gives a glossary of the most important variables defined in this appendix, which builds on the definitions given in earlier chapters. Units are also given—the notation [u/l] is specified for a unitless quantity. Note that all variables are at least potentially functions of space and time.

- C [F m^{-2}] is the *double-layer specific capacitance* (cf. p. 307).
- C_{tot} [F] is an electrode's *total capacitance* (cf. p. 317).
- i_{dl} [A m^{-2}] is the *double-layer current density* (cf. p. 307).
- i_f [A m^{-2}] is the *faradaic current density* (cf. p. 307).
- Q_f [C m^{-3}] is the *faradaic charge density* (cf. p. 307).
- R_0 [Ω] is the *series resistance* of the capacitor (cf. p. 317).
- R_{sep} [Ω] is the *separator resistance* (cf. p. 317).
- R_{ss} [Ω] is the *steady-state resistance* of the capacitor to a steplike input (cf. p. 317).
- θ_f [u/l] is the faradaic state-of-charge of an electrode. For a symmetric cell, $\theta_f^{\text{neg}} = 1 - \theta_f^{\text{pos}}$ (cf. p. 307).

About the Author

GREGORY L. PLETT is a professor of electrical and computer engineering at the University of Colorado Colorado Springs (UCCS). His research since 2001 has been focused on applications of control-systems theory to the management and control of high-capacity battery systems such as found in hybrid and electric vehicles. Current investigations include physics-based reduced-order modeling of ideal lithium-ion dynamics, system identification of physics-based model parameters using only current–voltage input–output data, physics-based reduced-order modeling of degradation mechanisms in electrochemical cells, estimation of cell internal state and degradation state, state-of-charge, state-of-health and state-of-life estimation, power and energy prediction to extend life, and battery pack fast charging. Research is both theoretical and empirical: the UCCS High-Capacity Battery Research and Test Laboratory houses equipment to test cells, modules, and battery packs and is home to custom battery-management system and hardware battery-pack simulator projects, which together enable cutting-edge research in advanced but practical algorithm prototyping. He offers courses in control systems and in battery modeling and management to support this research. Dr. Plett holds a bachelor of engineering in computer systems engineering degree from Carleton University (Ontario, Canada) and master of science and Ph.D. degrees in electrical engineering from Stanford University (Stanford, California). He is a senior member of the Institute of Electrical and Electronic Engineers and life member of the Electrochemical Society.

Index

- $\langle \cdot \rangle$ notation, 142
- $\overline{\cdot}$ notation, 143
- (\cdot) notation, 32
- $[\cdot]$ notation, 32
- Activated complex, 112
- Activation energy, 111, 280
- Activity, 90
 - Absolute (via molality), 91
 - Absolute (via molarity), 90
 - Mean molal coefficient, 104
 - Mean molar coefficient, 110
- Anion, 6
- Anode, *see* Negative electrode
- Arrhenius relationship, 111, 280
- Atomic number, 10
- Atomic weight, 10
- Avagadro's number N_A , 68
- Battery, 2
- Bruggeman's exponent, 154
- C-rate, 3
- Capacity
 - Charge, 52
 - Discharge, 31, 52
 - Energy, 3
 - Nominal, 3
 - Total, 31, 52, 124, 163
- Cathode, *see* Positive electrode
- Cation, 6
- Cell, 2
 - Cylindrical, 20
 - Pouch, 20
 - Primary, 2, 8
 - Prismatic, 20
 - Rechargeable, *see* Cell, secondary
 - Secondary, 2, 8
- Charge number, 92
- Charge-transfer coefficient α , 114
- Charge-transfer resistance, 220
- Chemical potential, 88
- Concentrated solution theory, 81
- Conduction, 272
- Conductivity, 71, 109
 - Effective, 154, 160
- Constrictivity, 154
- Controllability matrix, 187
 - Extended, 191
 - Generalized, 210
- Convection, 95, 273
 - Forced, 273
 - Natural, 273
- Corrosion, 25
- Coulombic efficiency, 31, 48
- Current collector, 7
- Density, 274
- Depth of discharge, 32
- Diffusion, 95
- Diffusivity, 76
 - Effective, 158
 - Maxwell–Stefan, 98
- Dirac delta function $\delta(\mathbf{x}, t)$, 138
 - Integrating, 140
 - Sifting property, 138
- Dither, 52
- Divergence ($\nabla \cdot$), 73
- Electrochemical double-layer capacitor, *see* Supercapacitor
- Electrochemical potential, 88
- Electrochemical series, 8
- Electrolyte, 6, 19
 - Binary, 91
 - Salt, 19
- Electrolyte concentration c_e
 - Continuum scale, 137
- Microscale, 67
- Reduced-order model (debiased), 240
- Reduced-order model modal term, 240
- Electrolyte current density i_e
 - Continuum scale, 160
 - Microscale, 110
 - Reduced-order model, 241
- Electrolyte potential ϕ_e
 - Continuum scale, 137
 - Microscale, 68
 - Reduced-order model (debiased), 242
- Electromotive force, *see* Voltage, cell
- Energy, 3
- Energy density, 4
- Energy efficiency, 31
- Enthalpy, 81, 273
 - Partial molar, 275
- Entropy, 84
 - Partial molar, 277
- Environment, 81
- Equivalent circuit model, *see* Model, equivalent circuit
- Equivalent series resistance, 33, 177
- Exact differential, 83
- Exchange current density i_0 , 116
- Extensive variable, 86
- Faradaic capacitance, 304
- Faraday's constant F , 69
- Film resistance, 218
- Finite difference method, 78, 164
- Finite element method, 165
- Finite volume method, 127, 164
- Flux density, 69, 76
- Formation, 23
- Frequency response, 174, 248

- Gibbs free energy, 81, 85
 Gibbs–Duhem equation, 89
 Gradient, 142, 144
 Gradient (∇), 71
 Green's identity, 231
- Heat, 272
 Flux, 272
 Generation, 272
 Sink, 272
 Heat generation, 278
 Contact resistance, 279
 Irreversible, 279
 Joule heating, 279
 Reversible, 279
 Heat-transfer coefficient, 280
 Helmholtz free energy, 81
 Hysteresis, 41, 51
- $\hat{\mathbf{i}}$ unit vector, 71
 Impedance
 Reduced-order model, 249
 Impedance ratio $\nu^2(s)$
 Lithium-ion cell, 223
 Supercapacitor, 309
 Impulse response, 174
 Indicator function $\gamma_a(\mathbf{x}, t)$, 138
 Gradient, 140
 Inexact differential, 83
 Insertion electrode, 11, 13
 Intensive variable, 86
 Intercalation, 13, 16
 Internal energy, 81
 Intrinsic phase average, 143
- $\hat{\mathbf{j}}$ unit vector, 71
 Jacobsen–West transfer function
 $\tilde{C}_{s,e}(s)/J(s)$, 185
- $\hat{\mathbf{k}}$ unit vector, 71
 Kinetics, 81, 111
- Liebnitz' rule, 75
 Lithium flux density j
 Continuum scale, 137
 Microscale, 68
 Reduced-order model, 224, 228
- Markov parameter, 181
 Maxwell–Stefan theory, 95
 Migration, 95
- Model
 Cell scale, 67
 Continuum scale, 66, 135
 Empirical, *see* Model, equivalent circuit
 Enhanced self-correcting, 44
 Equivalent circuit, 29, 65
 Microscale, 66
 Molecular scale, 66
 Physics-based, 65
 Pseudo-two-dimensional, 152
 Single particle, 127
 State space, 174
 Molality, 87
 Molarity, 87
 Mole, 68
 Mole fraction, 97
- Negative electrode, 5, 16
 Graphite, 16, 51, 123
 Lithium titanate oxide, 16, 123
 Silicon, 16
 Nonfaradaic capacitance, 304
- Observability matrix, 187
 Extended, 191
 Generalized, 210
 Ohm's law, 71
 Open-circuit potential, 118, 122
 Open-circuit voltage, *see* Voltage, open circuit
 Output equation, 174
 Overpotential η , 115, 118, 220
 Oxidant, 112
 Oxidation reaction, 5
- Peltier coefficient, 276
 Periodic table, 10
 Phase, 136
 Phase average, 142
 Phase transition, 14
 Polarization, 34
 Positive electrode, 6, 17
 Lithium cobalt oxide, 17, 51, 123
 Lithium iron phosphate, 18, 51, 123
 Lithium manganese oxide, 17, 51, 123
 Lithium nickel cobalt aluminum oxide, 17, 124
 Lithium nickel manganese cobalt oxide, 17, 51, 124
- Power, 3
 Pseudocapacitance, *see* Faradaic capacitance
- Radiation, 273
 Randles circuit, 40
 Reaction rate constant k_0 , 117
 Normalized k_0^{norm} , 118
 Redox reaction, 5
 Reductant, 112
 Reduction reaction, 5
 Reversible process, 84
 Room temperature, 32
- Separator, 7, 19
 Singular value decomposition, 189
 Solid concentration c_s
 Continuum scale, 137
 Microscale, 67
 Solid current density i_s
 Continuum scale, 155
 Microscale, 75
 Reduced-order model, 226
 Solid electrolyte interphase, 24, 25, 123
 Solid potential ϕ_s
 Continuum scale, 137
 Microscale, 67
 Reduced-order model (debiased), 227, 229
 Solid surface concentration $c_{s,e}$
 Reduced-order model (debiased), 225, 229
 Reduced-order model (debiased, integrator-removed), 225
 Solid–electrolyte interfacial resistance, 220
 Solute, 6
 Solvent, 6, 19
 Specific energy, 4
 Specific heat, 274
 State (of model), 174
 State equation, 174
 State function, 83
 State of charge, 30, 126, 164
 Stoichiometric coefficient, 92
 Sturm–Liouville problem, 230
 Supercapacitor, 303
 System, 81
 System identification, 54, 66
 Subspace, 56

- Temperature, 272
Kinetic, 272
Reference, 280
Thermodynamic potential, 81, 273
Thermodynamics, 81
First law, 83
Second law, 84
Tortuosity, 154
Total concentration, 97
Transfer function, 174, 178
- Rational polynomial, 176, 185
Transcendental, 185
Transference number, 102
Ultracapacitor, *see* Supercapacitor
Vector field, 69
Voltage
Cell, 7
Diffusion, 34
- Nominal, 2
Open circuit, 30, 45, 122
Reduced-order model, 247
Volume fraction, 143
Volume-averaging
Theorem 1, 136
Theorem 2, 136
Theorem 3, 136
Warburg impedance, 40

Recent Artech House Titles in Power Engineering

Dr. Jianhui Wang, Series Editor

The Advanced Smart Grid: Edge Power Driving Sustainability, Second Edition, Andres Carvallo and John Cooper

Battery Management Systems, Volume I: Battery Modeling, Gregory L. Plett

Battery Management Systems for Large Lithium Ion Battery Packs, Davide Andrea

Battery Power Management for Portable Devices, Yevgen Barsukov and Jinrong Qian

Design and Analysis of Large Lithium-Ion Battery Systems, Shriram Santhanagopalan, Kandler Smith, Jeremy Neubauer, Gi-Heon Kim, Matthew Keyser, and Ahmad Pesaran

Designing Control Loops for Linear and Switching Power Supplies: A Tutorial Guide, Christophe Basso

Electric Systems Operations: Evolving to the Modern Grid, Mani Vadari

Energy Harvesting for Autonomous Systems, Stephen Beeby and Neil White

GIS for Enhanced Electric Utility Performance, Bill Meehan

Introduction to Power Electronics, Paul H. Chappell

Power Line Communications in Practice, Xavier Carcelle

Power System State Estimation, Mukhtar Ahmad

A Systems Approach to Lithium-Ion Battery Management, Phil Weicker

Signal Processing for RF Circuit Impairment Mitigation in Wireless Communications, Huang, Zhu, Leung

Synergies for Sustainable Energy, Elvin Yüzügüllü

For further information on these and other Artech House titles, including previously considered out-of-print books now available through our In-Print-Forever® (IPF®) program, contact:

Artech House
685 Canton Street
Norwood, MA 02062
Phone: 781-769-9750
Fax: 781-769-6334
e-mail: artech@artechhouse.com

Artech House
16 Sussex Street
London SW1V 4RW UK
Phone: +44 (0)20 7596-8750
Fax: +44 (0)20 7630-0166
e-mail: artech-uk@artechhouse.com

Find us on the World Wide Web at: www.artechhouse.com

